








EX LIBRIS  
UNIVERSITATIS  
ALBERTENSIS

---

The Bruce Peel  
Special Collections  
Library





Digitized by the Internet Archive  
in 2025 with funding from  
University of Alberta Library

<https://archive.org/details/0162011368220>











**University of Alberta**

**Library Release Form**

**Name of Author:** **Matthias Grobe**

**Title of Thesis:** **Origin and Formation of Dolostone in the Devonian  
Brilon Reef Complex, Northeastern Rhenish  
Schiefergebirge, Germany.**

**Degree:** **Doctor of Philosophy**

**Year this Degree Granted:** **1999**

Permission is hereby granted to the University of Alberta Library to reproduce single copies of this thesis and to lend or sell such copies for private, scholarly or scientific research purposes only.

The author reserves all other publication and other rights in association with the copyright in the thesis, and except as hereinbefore provided, neither the thesis nor any substantial portion thereof may be printed or otherwise reproduced in any material form whatever without the author's prior written permission.







**University of Alberta**

**Origin and Formation of Dolostone in the Devonian Brilon Reef Complex,  
Northeastern Rhenish Schiefergebirge, Germany.**

by

**Matthias Grobe**



A thesis submitted to the Faculty of Graduate Studies and Research in partial fulfillment  
of the requirements for the degree of Doctor of Philosophy.

Department of Earth and Atmospheric Sciences

Edmonton, Alberta  
Fall 1999





**University of Alberta**

**Faculty of Graduate Studies and Research**

The undersigned certify that they have read, and recommend to the Faculty of Graduate Studies and Research for acceptance, a thesis entitled “**Origin and Formation of Dolostone in the Devonian Brilon Reef Complex, Northeastern Rhenish Schiefergebirge, Germany**” by **Matthias Grobe**, in partial fulfillment of the requirements for the degree of **Doctor of Philosophy**.





## ABSTRACT

The Middle to Upper Devonian Brilon Reef Complex in the Northeastern Rhenish Schiefergebirge hosts several dolostone intervals of variable thickness that show striking petrographic similarities with pervasively dolomitized hydrocarbon reservoir rocks and host rocks of MVT-deposits in Western Canada. Although not of economic significance, the Brilon Reef Complex serves as a case study to enhance the understanding of the origin and formation of dolostone.

The Middle and Upper Devonian carbonates of the so-called “Massenkalk”, which make up the bulk of the complex, can be mapped as facies types characteristic of fore-reef, reef-core, and back-reef (lagoonal) depositional environments. The stratigraphic correlation of drill cores is complicated by (1) the scarcity of index fossils; (2) lateral changes in lithofacies; (3) displacements, fracturing, and brecciation due to Variscan (thrust) and post-Variscan (normal) faults; and (4) the effects of other post-sedimentary processes (e.g., karst).

The dolostone intervals consist of grey matrix dolomite (dolomite Type 1) and two types of coarse crystalline milky-white dolomite (occurring as a recrystallization product of grey matrix dolomite and as saddle dolomite cement) followed by sulfide minerals and late calcite cements. The distribution of dolostone and associated sulfide mineralization appears to be largely controlled by post-Variscan fracturing in the vicinity of deep-reaching, NNW-SSE trending faults. Carbonate facies types as well as pre-Variscan diagenesis and textures related to the Variscan deformation do not appear to have any significant influence on the distribution of dolostone in the Brilon Reef Complex.

Based on petrographic, geochemical, and microthermometric data, dolomitization, limestone recrystallization, dolomite recrystallization, dolomite cementation, sulfide mineralization, calcitization, and calcite cementation in the Brilon Reef Complex are the result of at least four episodic pulses of highly saline, hydrothermal fluids (salinity between 16 and 26 equiv. wt.% NaCl,  $T_h = 70$  to  $120^\circ\text{C}$ ) during a distinct phase of regional uplift and wrench tectonics in the Late Cretaceous/Early Tertiary. Seismic pumping and hydrothermal convection along the NNW-SSE trending faults may have been the driving mechanism for





the episodic ascent and circulation of the dolomitizing and ore-forming fluids.

Present-day saline groundwaters in the adjacent Münsterland Cretaceous Basin are saline to highly saline (TDS up to 250000 mg/l), ascend on NNW-SSE trending faults, and have the same range of Sr isotope compositions as the investigated carbonates from the Brilon Reef Complex. However, the hydrochemical and isotope data show that parts of the regional aquifer in this basin and the underlying Paleozoic strata have been flushed by sub-recent meteoric water. Thus, these waters do not bear a direct genetic relationship with the fault-controlled hydrothermal mineralization in the Brilon Reef Complex, and, consequently, the possibility that formation fluids from the MCB were driven into the Brilon Reef Complex to generate dolomites, sulfides, and calcites in the fracture systems remains elusive.

The comparison of the results of this study with one local example from the Northern Rhenish Schiefergebirge and with the regional example of pervasive dolomitization in the Western Canada Sedimentary Basin emphasizes the point that occurrences of ancient dolostone have to be interpreted within their local and regional geologic and paleohydrogeologic context.





## ACKNOWLEDGEMENTS

This thesis was financially supported by funds from a Natural Science and Engineering Research Council (NSERC) operating grant to Hans G. Machel (University of Alberta), supplemented by research grants from the Geological Society of America (GSA) and the American Association of Petroleum Geologists (AAPG) Grants-in-Aid Program to the author. Furthermore, the author gratefully acknowledges scholarships from the German Academic Exchange Service (DAAD) and the University of Alberta (Ph.D. recruitment scholarship, G.L. Cumming scholarship). Financial assistance to enable the author to present parts of this thesis at conferences was kindly provided by the University of Alberta, the International Association of Sedimentologists (IAS), and the Geological Society of America (GSA).

I would like to thank Hans Machel and Pat Cavell for valuable discussions and editorial work at many stages of the completion of this thesis. I am indebted to Dieter Stoppel (Bundesanstalt für Geowissenschaften und Rohstoffe, Hannover, Germany), Klaus Steuerwald, Heinrich Heuser, and Volker Wrede (all Geologisches Landesamt Nordrhein-Westfalen, Krefeld, Germany) for logistic support and insightful discussions during fieldwork in Germany. Discussions with Harald Huebscher, Mark Hearn, Rob Hardie, Mikel Erkiaga Aguirre, Dinu Pana, Taro Yamashita, Arjun Keswani, Ben Rostron, Carsten Reinhold, Maja Buschkühle, Barbara Sander, Karsten Michael, and Tony Lemay provided many helpful insights and ideas.

A warm thanks to Adele, Anne Louise, Barb, Brent, Christian, Dagmar, Danie, Donna, Horst, Jeanine, Jochen, Karen, Karina, Karsten, Maja, Mark, Mette, Mikel, Niko, Rob, Simon, Sünne, Traute, and Yoav for their friendship and support during the last couple of years. A special thanks goes out to my parents for their moral support and wisdom. A loving thank you to my wife Barbara and my son Jaron for all their love, support and happiness they bring into my life.



# TABLE OF CONTENTS

## CHAPTER 1

### GENERAL INTRODUCTION

1.1 Definitions .....	1
1.2 Rationale .....	1
1.2 Study area .....	5
1.3 Previous work .....	11
1.3.1 Sedimentary history .....	11
1.3.2 Structural history .....	15
1.3.3 Burial and thermal history .....	16
1.3.4 Diagenetic history and occurrences of dolomite .....	19
1.4 Objectives .....	21
1.5 References .....	22

## CHAPTER 2

### CARBONATE FACIES, STRATIGRAPHY, AND POST-VARISCAN DIAGENESIS OF THE DEVONIAN BRILON REEF COMPLEX AND THEIR RELATIONSHIP TO THE DISTRIBUTION OF DOLOSTONE

2.1 Introduction and previous work .....	28
2.2 Objectives .....	31
2.3 Database and Methods .....	32
2.4 Carbonate facies and stratigraphy of the investigated drill cores .....	35
2.4.1 Upper boundary of the “Massenkalk” .....	36
2.4.2 Lower boundary of the “Massenkalk” .....	36
2.4.3 Facies types within the “Massenkalk” .....	37
2.4.4 Facies distribution within the “Massenkalk” .....	45
2.4.4.1 Fore-reef (facies zones If to IVf) .....	45
2.4.4.2 Reef-core (facies zones IV/V and V) .....	48
2.4.4.3 Back-reef (facies zones IVb to Ib) .....	49
2.4.5 Stratigraphic correlation of the investigated drill cores .....	49
2.4.5.1 Biostratigraphy .....	49
2.4.5.2 Lithostratigraphy .....	50
2.4.6 General trends in facies development .....	52
2.5 General diagenetic framework .....	54
2.5.1 Pre-Variscan diagenesis .....	57
2.5.2 Variscan deformation .....	57
2.5.3. Post-Variscan textural and mineralogical changes .....	60





2.5.3.1 Phase 20: fracturing and scalenohedral calcite cement . .	65
2.5.3.2 Phase 21: fracturing, dolomitization (dolomite Type 1), calcite dissolution . . . . .	65
2.5.3.3 Phase 22: fracturing, dolomite recrystallization (dolomite Type 2), dolomite cementation (dolomite Type 3) . . . . .	68
2.5.3.4 Phase 23: base metal sulfides . . . . .	71
2.5.3.5 Phase 24: fracturing, dolomite dissolution, calcitization, calcite cementation . . . . .	74
2.5.3.6 Phase 25: fracturing, several generations of calcite cement . . . . .	74
2.5.3.7 Karst . . . . .	79
2.5.4 Integration into regional paragenetic sequence and timing of dolomitization . . . . .	80
2.6 Distribution of dolostone intervals . . . . .	82
2.6.1 Spatial relationship to sedimentary facies . . . . .	82
2.6.2 Spatial relationship to post-sedimentary textures . . . . .	86
2.7 Association of dolomite types with sulfide mineralization . . . . .	91
2.8 Controls on the distribution of dolostone in the Brilon Reef Complex . . . .	92
2.9 Genetic implications of petrographic observations . . . . .	92
2.10 References . . . . .	94

## CHAPTER 3

### PETROGRAPHIC, GEOCHEMICAL, AND FLUID INCLUSION EVIDENCE FOR FAULT-CONTROLLED HYDROTHERMAL DOLOMITIZATION IN THE BRILON REEF COMPLEX

3.1 Introduction . . . . .	97
3.2 Methods . . . . .	100
3.3 Results and discussion . . . . .	106
3.3.1 Petrographic changes of the limestone host rock adjacent to dolostone intervals . . . . .	106
3.3.2 Stable isotopes . . . . .	111
3.3.2.1 Characterization of pre- and post-Variscan carbonate phases . . . . .	111
3.3.2.2 Stable isotope trends within the dolostone intervals . . .	119
3.3.2.3 Stable isotope trends in the undolomitized limestone host rock . . . . .	121
3.3.3 Trace elements . . . . .	125
3.3.3.1 Pre-Variscan carbonate phases . . . . .	125
3.3.3.2 Post-Variscan carbonate phases . . . . .	125
3.3.4 Strontium isotopes . . . . .	130
3.3.5 Fluid inclusion microthermometry . . . . .	133
3.3.5.1 Dolomite Type 3 (saddle dolomite) . . . . .	133





3.3.4.2 Sphalerite .....	136
3.3.4.3 Clear scalenohedral calcite cement (CSC) .....	136
3.3.6 Post-Variscan fluid flow events in the Brilon Reef Complex ....	137
3.3.6 Timing of fluid flow events, origin of fluids, and hydrologic driving mechanism .....	142
3.4 References .....	147

## CHAPTER 4

### OXYGEN, HYDROGEN, AND STRONTIUM ISOTOPIC COMPOSITIONS OF SALINE GROUNDWATERS IN THE MÜNSTERLAND CRETACEOUS BASIN: CLUES TO THEIR ORIGIN AND EVOLUTION

4.1 Introduction .....	153
4.1.1 Background .....	153
4.1.2 Geographic location and geologic framework .....	160
4.1.3 Hydrogeological framework .....	162
4.1.4 Paleohydrogeologic history .....	165
4.2 Data base and analytical methods .....	170
4.2.1 Hydrochemistry .....	171
4.2.2 Stable isotope analysis .....	171
4.2.3 Strontium isotope analysis .....	171
4.3 Results .....	172
4.3.1 Temperature and pH .....	172
4.3.2 Total dissolved solids (TDS) and specific electrical conductivity	173
4.3.3 Stable isotope composition .....	175
4.3.4 Hydrochemical composition .....	178
4.3.5 Strontium isotope composition .....	184
4.4 Discussion .....	188
4.4.1 Present-day movement of brines .....	188
4.4.2 Origin and evolution of the saline groundwaters .....	188
4.4.2.1 Origin of the water .....	189
4.4.2.2 Dissolution of halite .....	190
4.4.2.3 Sources of Sr .....	192
4.4.2.4 Mixing relations and effects of water-rock interactions	194
4.5 Conclusions .....	196
4.6 References .....	204



## CHAPTER 5

### SYNOPSIS

5.1 Restatement of objectives .....	210
5.2 Integration of results and interpretations .....	210
5.2.1 Carbonate facies distribution and stratigraphy .....	217
5.2.2 Diagenetic and tectonic framework .....	218
5.2.3 Controls on the distribution of dolostone .....	219
5.2.4 Evidence for hydrothermal dolomitization .....	220
5.2.5 Evidence for dolomite recrystallization .....	221
5.2.6 Composition of dolomitizing and mineralizing fluids .....	222
5.2.7 Origin of dolomitizing and mineralizing fluids .....	223
5.2.8 Origin and evolution of saline groundwaters in the Münsterland Cretaceous Basin .....	226
5.3 Comparison with other examples of dolomitization in Devonian carbonates .....	227
5.3.1 Dornap Carbonate Complex, northern Rhenish Schiefergebirge, Germany .....	227
5.3.2 Western Canada Sedimentary Basin .....	229
5.4 Contributions to original knowledge .....	234
5.5 Future work .....	235
5.6 References .....	237





## LIST OF TABLES

### CHAPTER 2

Table 2.1: Core identifications, abbreviations, locations, elevations and total lengths of drill core .....	32
Table 2.2: Integration of the succession of post-Variscan textural and mineralogical changes into regional paragenesis .....	81

### CHAPTER 3

Table 3.1: Succession of post-sedimentary textural and mineralogical changes .....	101
Table 3.2: Petrographic characteristics of post-Variscan dolomite types, sphalerite, and calcite cements .....	103
Table 3.3: List of samples of micritic limestones .....	107
Table 3.4a: Results of stable isotope, trace element, and Sr-isotope analysis of micritic limestone matrix. ....	111
Table 3.4b: Results of stable isotope, trace element, and Sr-isotope analysis of calcite fossils and one radiaxial-fibrous cement .....	112
Table 3.5a: Average crystal sizes from thin sections and results of stable isotope, trace element, and Sr-isotope analysis of dolomite Type 1 .....	113
Table 3.5b: Average crystal sizes from thin sections and results of stable isotope, trace element, and Sr-isotope analysis of dolomite Type 2 .....	114
Table 3.5c: Average crystal sizes from thin sections and results of stable isotope, trace element, and Sr-isotope analysis of dolomite Type 3. ....	114
Table 3.5d: Results of stable isotope, trace element, and Sr-isotope of calcite cements	115
Table 3.6: Results of microprobe analysis of samples of dolomite types 1, 2, 3 .....	126

### CHAPTER 4

Table 4.1: Paleohydrogeologic evolution of the Ruhr District .....	166
Table 4.2: Chemical composition of seawater .....	172
Table 4.3: Molar percentages of major cations and anions, molar ratios of Na and Cl, and ratios of K and Na concentrations. ....	178

### CHAPTER 5

Table 5.1: Characteristics of dolomitizing and mineralizing fluids in the Brilon Reef Complex .....	223
---	-----





## LIST OF FIGURES

### CHAPTER 1

Figure 1.1: Summary of current dolomitization models and predicted dolomite distribution patterns in carbonate buildups .....	3
Figure 1.2: Geographic location of the Devonian Brilon Reef Complex .....	5
Figure 1.3: (a) Paleogeographic map of the Middle Devonian of Central Europe .....	7
(b) Location of the Brilon Reef Complex .....	7
Figure 1.4: Simplified geologic map of the Brilon Reef Complex .....	9
Figure 1.5: Schematic diagram of the stratigraphy of the Brilon area .....	12
Figure 1.6: Post-Variscan erosion of Paleozoic sediments in the northern Rhenish Schiefergebirge .....	17
Figure 1.7: Isoreflectance lines in the Warstein-Brilon area .....	18

### CHAPTER 2

Figure 2.1: Simplified geologic map of the Brilon Reef Complex .....	30
Figure 2.2: Carbonate classification by Dunham .....	33
Figure 2.3: Facies model for Middle to Late Devonian reef carbonates .....	34
Figure 2.4: Schematic representation of the facies distribution along a N-S cross-section at the end of the Frasnian. ....	46
Figure 2.5: Succession of post-sedimentary textural and/or mineralogical changes of the Middle and Upper Devonian "Massenkalk" .....	55
Figure 2.6: Schematic representation of the post-Variscan paragenetic succession ....	61
Figure 2.7 a: Distribution of dolostone in investigated drill cores from the southern margin and central part of the Brilon Reef Complex .....	83
Figure 2.7 b: Distribution of dolostone in investigated drill cores the northeastern part of the Brilon Reef Complex .....	85
Figure 2.8a: Distribution of dolostone intervals in the Devonian Brilon Reef Complex along cross-section B-B' .....	87
Figure 2.8 b: Distribution of dolostone intervals in the Devonian Brilon Reef Complex along cross-section B'-C .....	89
Figure 2.8 c: Distribution of dolostone intervals in the north-eastern part of the Devonian Brilon Reef Complex .....	90

### CHAPTER 3

Figure 3.1: Simplified geologic map of the Brilon Reef Complex .....	98
Figure 3.2: Carbon and oxygen isotope compositions of pre-Variscan and post-Variscan carbonates .....	116
Figure 3.3: Cross plots of average crystal size versus $\delta^{18}\text{O}$ - and $\delta^{13}\text{C}$ -values of dolomite types .....	120
Figure 3.4: Stable isotope compositions of all limestone samples (including calcite fossils) plotted against vertical distance to the nearest dolostone interval ....	121
Figure 3.5: Stable isotope (O and C) trends in limestone host rock adjacent to dolostone intervals in drill core Almerfeld .....	123
Figure 3.6: Trace element (Mn and Fe) concentrations and Fe/Mn-ratios .....	130



Figure 3.7: Ranges in Sr isotope compositions for the investigated carbonate mineral phases from the Brilon Reef Complex .....	131
Figure 3.8: Results of microthermometric analysis of primary, pseudosecondary, and secondary fluid inclusions in dolomite Type 3, sphalerite, and clear scalenohedral calcite. ....	134
Figure 3.9: Fluid flow events and characteristics of fluid types .....	138
Figure 3.10: Temporal coincidence of phases of fault tectonics in the area of the Münsterland Cretaceous Basin, phases of uplift of the Rhenish Massif, and mineralization phases in the eastern Rhenish Schiefergebirge .....	145

## CHAPTER 4

Figure 4.1: Map of the Münsterland Cretaceous Basin .....	155
Figure 4.2: Schematic cross-section A-B .....	157
Figure 4.3: Overview over the geologic history of the Münsterland Cretaceous Basin .....	161
Figure 4.4: Temperature vs depth plot .....	173
Figure 4.5: Depth vs total dissolved solids (TDS) plot .....	174
Figure 4.6: Stable isotope compositions of saline groundwaters of the MCB .....	176
Figure 4.7: Plot of molar concentrations of Na and Cl .....	179
Figure 4.8: Cross plot of $\text{SO}_4$ and Sr concentrations .....	179
Figure 4.9a: Cross plot of Mg and Cl concentrations .....	181
Figure 4.9b: Cross plot of K and Cl concentrations .....	181
Figure 4.10a: Cross plot of Ca and Cl concentrations .....	182
Figure 4.10b: Cross plot of Sr and Cl concentrations .....	182
Figure 4.11a: Cross plot of K and Na concentrations .....	183
Figure 4.11b: Cross plot of K/Na concentration ratios and Cl concentrations .....	183
Figure 4.12: $^{87}\text{Sr}/^{86}\text{Sr}$ ratio versus Cl and versus K concentration. ....	185
Figure 4.13: $^{87}\text{Sr}/^{86}\text{Sr}$ ratio versus Sr concentration and $1/\text{Sr}$ concentration .....	187
Figure 4.14: Schematic N-S cross sections illustrating the paleohydrogeologic history of the Münsterland Cretaceous Basin from the Late Carboniferous to Recent ...	197

## CHAPTER 5

Figure 5.1: Schematic N-S and W-E cross-section through the Brilon Reef Complex in the Frasnian .....	211
Figure 5.2: Schematic N-S and W-E cross-section through the Brilon Reef Complex in the Late Carboniferous .....	211
Figure 5.3: Schematic N-S and E-W cross-section through the Brilon Reef Complex during the Variscan Orogeny .....	213
Figure 5.4: Schematic N-S and E-W cross-section through the Brilon Reef Complex from the Permian to the Early Cretaceous .....	213
Figure 5.5: Schematic N-S and W-E cross-sections through the Brilon Reef Complex during the Late Cretaceous/Early Tertiary .....	215
Figure 5.6: Schematic N-S and W-E cross-sections through the Brilon Reef Complex at present. ....	215





## LIST OF PLATES

### CHAPTER 2

Plate 2.1: Facies types of fore-reef character within the “Massenkalk” . . . . .	39
Plate 2.2: Facies types of reef-core character within the “Massenkalk” . . . . .	41
Plate 2.3: Facies types of back-reef character within the “Massenkalk”. . . . .	43
Plate 2.4: Fabrics indicative of mechanical deformation during the Variscan Orogeny .	58
Plate 2.5: Post-Variscan textural and mineralogical changes . . . . .	66
Plate 2.6: Post-Variscan textural and mineralogical changes . . . . .	69
Plate 2.7: Post-Variscan textural and mineralogical changes . . . . .	72
Plate 2.8: Post-Variscan textural and mineralogical changes. . . . .	75
Plate 2.9: Post-Variscan textural and mineralogical changes . . . . .	77

### CHAPTER 3

Plate 3.1: SEM photographs of 4 samples of micritic limestone matrix . . . . .	109
--	-----



## LIST OF APPENDICES

### APPENDIX 1

Schematic lithologs, gamma-ray curves, carbonate facies and stratigraphy of the investigated drill cores from the Brilon Reef Complex ..... 243

### APPENDIX 2

Table of petrographic characteristics of dolostone intervals ..... 270

### APPENDIX 3

Carbonate sample dissolution procedure for ICP analysis ..... 288

### APPENDIX 4

Results of fluid inclusion microthermometry ..... 291

### APPENDIX 5

Results of field measurements, analyses of chemical and isotopic composition of saline groundwater samples from the Münsterland Cretaceous Basin ..... 295

### APPENDIX 6

List of publications and abstracts ..... 300

### APPENDIX 7

Grobe, M. and Machel, H.G. 1996, Postvariszische Dolomitisierung des devonischen Briloner Riffkomplexes, nordöstliches Rheinisches Schiefergebirge, Deutschland. - Zentralblatt für Geologie und Paläontologie Teil 1, 1995, p. 131-143. .... 301

### APPENDIX 8

Grobe, M. and Machel, H.G., 1997, Petrographische und stabile Isotopendaten ( C und O) für störungskontrollierte hydrothermal Mineralisation im devonischen Briloner Riffkomplex, Deutschland. - Zentralblatt für Geologie und Paläontologie Teil 1, 1996, p. 397-413. .... 314





# CHAPTER 1

## GENERAL INTRODUCTION

### 1.1 Definitions

In this thesis the term “reef” is defined as a marine biogenic wave-resistant structure that is topographically elevated above the seafloor (Fagerstrom 1987). The term “bioherm” refers to a biogenic moundlike, domelike, lenslike, or reeflike mass of carbonate rock enclosed or surrounded by rock of different lithological character, whereas “biostrom” refers to a distinctly bedded and widely extensive or broadly lenticular, blanketlike mass of biogenic carbonate rock (Cumings 1932). Several reefs form reef systems, very large reef systems are called reef provinces (Fagerstrom 1987). A reef complex consists of reef systems and all genetically related sediments (i.e., reef derived detritus as well as sediments that form as a result of the influence of reef growth on the adjacent sedimentary environment).

The term “dolostone” is used in this thesis for the rock composed largely of the mineral dolomite in order to avoid confusion between the rock and the mineral, as suggested by Shrock (1948). The term “pervasive dolostone” is used for regionally extensive units of dolostone (e.g., in the Devonian of western Canada; Machel and Mountjoy 1987; Machel et al. 1994).

### 1.2 Rationale

Middle and Upper Devonian carbonate buildups are common in western Canada, Australia, China, and Central Europe. Whereas in western Canada most Devonian carbonate buildups are extensively dolomitized and play a dominant role as hydrocarbon reservoir rocks and host rocks for base metal sulfide deposits, dolomite is relatively scarce in the Devonian carbonates of Central Europe, Australia, and China (Mountjoy 1994).

The recognition of the economic potential of dolostone has generated a great interest in its formation, which is reflected in a plethora of research publications on this topic (e.g., papers in Pray and Murray 1965; Zenger et al. 1980; Shukla and Baker 1988; Purser et al.



1994, and references cited therein). The search for a unifying model to explain the origin and formation of ancient and recent occurrences of dolomite has led to the proposal and subsequent controversial discussion of a number of different dolomitization models, invoking a variety of fluids, transport processes, and diagenetic settings (for summaries and discussions see Morrow 1982; Land 1986; Machel and Mountjoy 1986; Hardie 1987; Morrow 1998) (Figure 1.1). It has become obvious that dolomite can form under various chemical and physical conditions as long as three basic requirements are satisfied (Morrow 1982): (1) the existence of a sufficient supply of  $\text{Mg}^{2+}$  and  $\text{CO}_3^{2-}$ ; (2) the presence of a long-lasting and efficient delivery mechanism for these ions, which, at the same time is able to remove excess  $\text{Ca}^{2+}$ , and 3) a 'construction site' that is conducive to dolomitization.. Due to the fact that, in the study of ancient systems, the direct determination of these parameters is generally not possible, the distribution, texture, and geochemical composition of an investigated ancient dolostone occurrence commonly are matched with those predicted by perceived or possible models (e.g., Wilson et al. 1990; Amthor et al. 1993; Braithwaite and Rizzi 1997) (Figure 1.1). In many cases the results are ambiguous and usually require the establishment of a case-specific genetic interpretation within the framework of the specific geologic history of the study area.

The Devonian Brilon Reef Complex in the northeastern Rhenish Schiefergebirge, Germany, hosts intervals of dolostone of various thicknesses (decimeters to hundreds of meters) associated with minor base metal sulfide mineralization, that were encountered in drill cores during a drilling program of the "Bundesanstalt für Geowissenschaften und Rohstoffe" (= German Geological Survey) in the late 1970's (Brinckmann 1981). It was selected to serve as a case study to investigate the origin and formation of dolostone for the following reasons.

(1) Intervals of dolostone in drill cores show striking petrographic similarities with occurrences of pervasive dolostone in western Canada, the origin and timing of which are still controversial (Machel and Mountjoy 1987; Qing and Mountjoy 1992, 1994, 1995; Amthor et al. 1993; Nesbitt and Muehlenbachs 1994; Garven and Sverjensky 1994; Mountjoy 1994; Mountjoy and Amthor 1994; Morrow and Aulstead 1995; Shields and Brady 1995; Machel et al. 1996; Morrow 1998; Wendte 1998).







**Figure 1.1:** Summary of current dolomitization models and predicted dolomite distribution patterns (in grey) in carbonate buildups. Models A to D1 are km scale, models D2 and D3 are basin scale. Arrows denote flow directions, dashed lines in C1 and C2 represent isotherms. KV = vertical hydraulic conductivity, KH = horizontal hydraulic conductivity. Models A to D2 modified from Amthor et al. (1993). Hydrologic models D3 and D4 modified after Garven (1995); predicted dolomite pattern D3 after Morrow (1998); predicted dolomite pattern D4 after Braithwaite and Rizzi (1997).




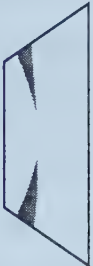
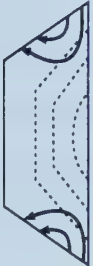





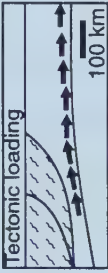

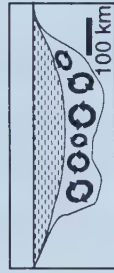
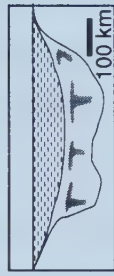


Dolomitization Model	Source of $Mg^{2+}$	Delivery Mechanism	Hydrologic Model	Predicted Dolomite Patterns
A. Reflux Dolomitization	seawater	storm recharge, evaporative pumping density-driven flow		
B. Mixing Zone (Dorag) Dolomitization	seawater	tidal pumping		
C1. Seawater Dolomitization	normal seawater	slope convection ( $K_v > K_h$ )		
C2. Seawater Dolomitization	normal seawater	slope convection ( $K_h > K_v$ )		
D1. Burial Dolomitization (local scale)	basinal shales	compaction-driven flow		
D2. Burial Dolomitization (regional scale)	various subsurface fluids	tectonic expulsion topography-driven flow		
D3. Burial Dolomitization (regional scale)	various subsurface fluids	thermo-density convection		
D4. Burial Dolomitization (local and regional scales)	various subsurface fluids	tectonic reactivation of faults (seismic pumping)		

Figure 1.1

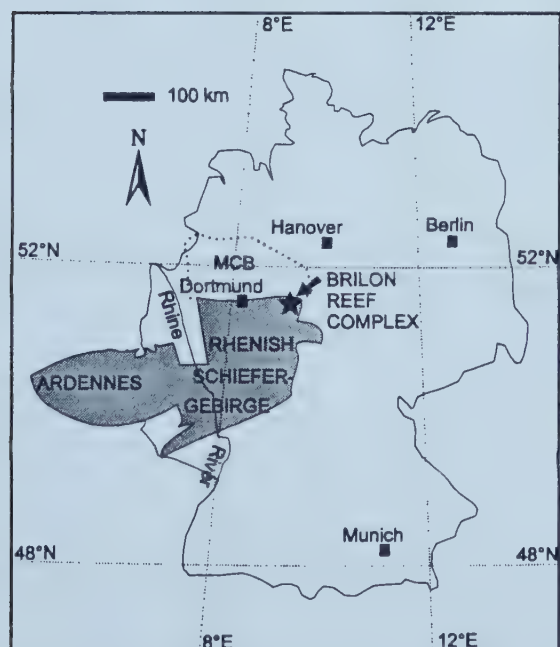


(2) The reef complex has been drilled extensively, providing the opportunity to investigate in detail the spatial relationships between sedimentary facies, tectonic structures, and dolomitization within large parts of the reef complex. Available material includes original core descriptions, geophysical logs, and bulk geochemical analyses, from 35 completely cored wells drilled during a program carried out by the “Bundesanstalt für Geowissenschaften und Rohstoffe” (= German Geological Survey) from 1974 to 1979 (Brinckmann 1981).

(3) No study focusing on the dolomitized intervals had been carried out at the Brilon Reef Complex, although several researchers noted the occurrence of such dolomite and its association with base metal sulfides in the Brilon Reef Complex (Schriel 1954; Machel 1979, 1990a; Brinckmann 1981; Moritz 1983; Schaeffer 1984; Wizisk 1995).

### 1.3 Study area

The Brilon Reef Complex is located in the northeastern Rhenish Schiefergebirge in Germany, approximately 80 km east of the city of Dortmund (Figure 1.2).



**Figure 1.2:** Geographic location of the Devonian Brilon Reef Complex in the northeastern Rhenish Schiefergebirge, Germany. Stippled line depicts the outline of the Münsterland Cretaceous Basin (MCB).

The reef complex is exposed at the surface over an area of approximately 80 km<sup>2</sup> and has been the site of small-scale mining and quarrying activities for Pb-Zn ores and limestone, respectively, over the past millenium (Schriel 1954; Bruns 1996). The Rhenish





Schiefergebirge is the exposed part of the Rhenish Massif that consists of Paleozoic (Ordovician to Carboniferous) sedimentary and volcanic rocks that were deformed in the Variscan Orogeny at the end of the Carboniferous. East of the Rhine River, the tectonically deformed rocks of the Rhenish Massif extend from their outcrops in the Rhenish Schiefergebirge northward into the subsurface below the Mesozoic sedimentary cover of the Münsterland Cretaceous Basin (Figure 1.2). The Brilon Reef Complex represents one of the largest Devonian carbonate buildups in the Rhenish Schiefergebirge. It is part of a NE-SW trending belt of carbonate buildups that formed on the southern shelf margin of the Old Red Continent during the Middle and Late Devonian (Figure 1.3). Predominant reef-building organisms were stromatoporoids occurring in various growth forms as well as tabulate corals (e.g., Witzisk 1995). The reef complex is bordered and intersected by a number of faults (Figure 1.4) that significantly influenced the distribution of sedimentary facies (Bär 1966; Wahba 1978) and particularly the diagenetic/hydrothermal evolution (Schriell 1956; Schaeffer 1984, 1986; Werner 1990).





**Figure 1.3:** (a) Paleogeographic map of the Middle Devonian of Central Europe, modified from Ziegler (1990). (b) Location of the Brilon Reef Complex in the northeastern Rhenish Schiefergebirge on the southern shelf margin of the Old Red Continent; modified from Burchette (1981). (c) Location of Devonian carbonate buildups (black objects) in the northeastern Rhenish Schiefergebirge; modified from Krebs (1974).



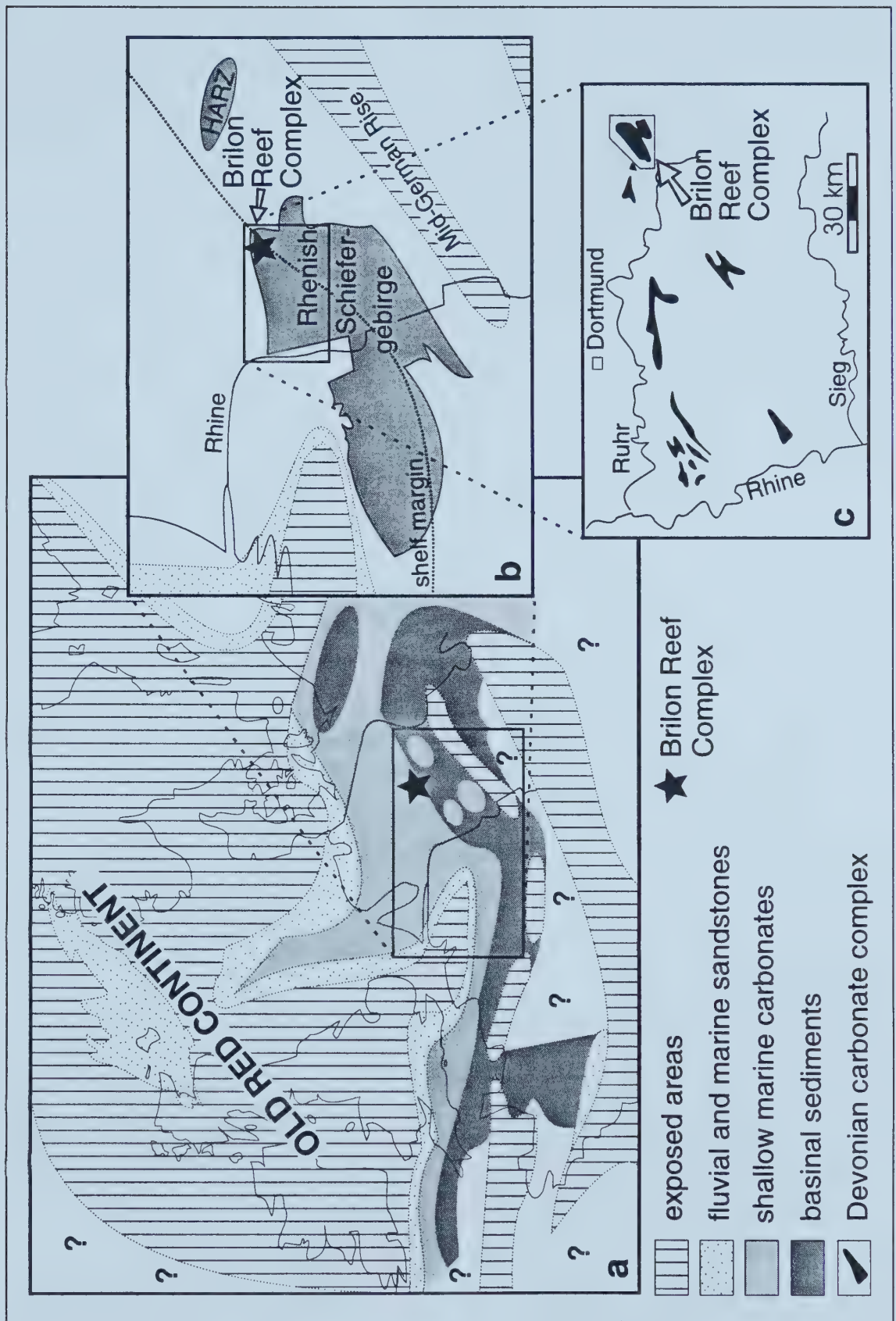


Figure 1.3





**Figure 1.4:** Simplified geologic map of the Brilon Reef Complex with locations of wells; compiled from Wahba (1978), Brinckmann et al. (1981), and Wizisk (1995). Insert map for orientation is the same as Figure 1.3c.

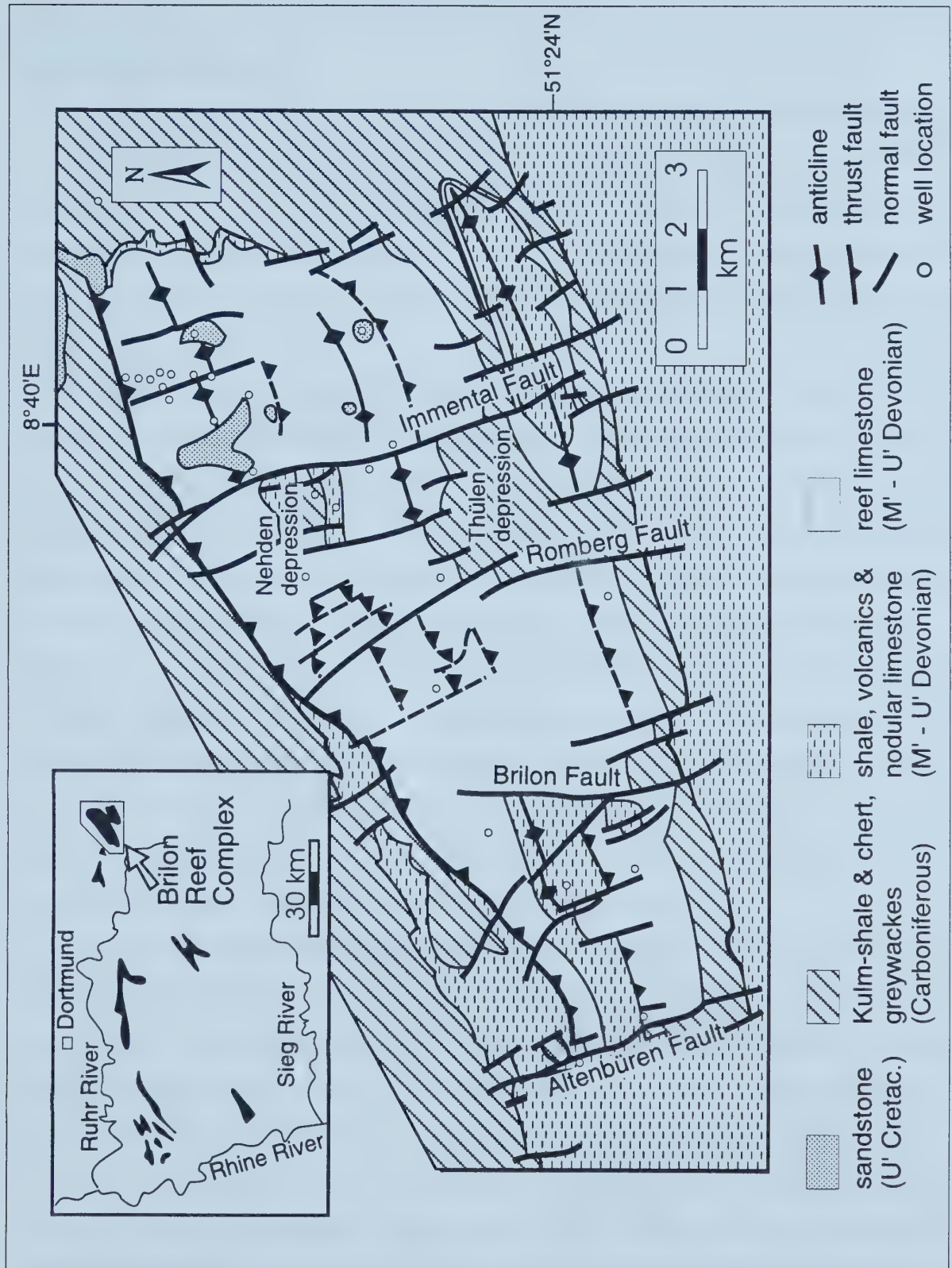


Figure 1.4





## 1.4 Previous work

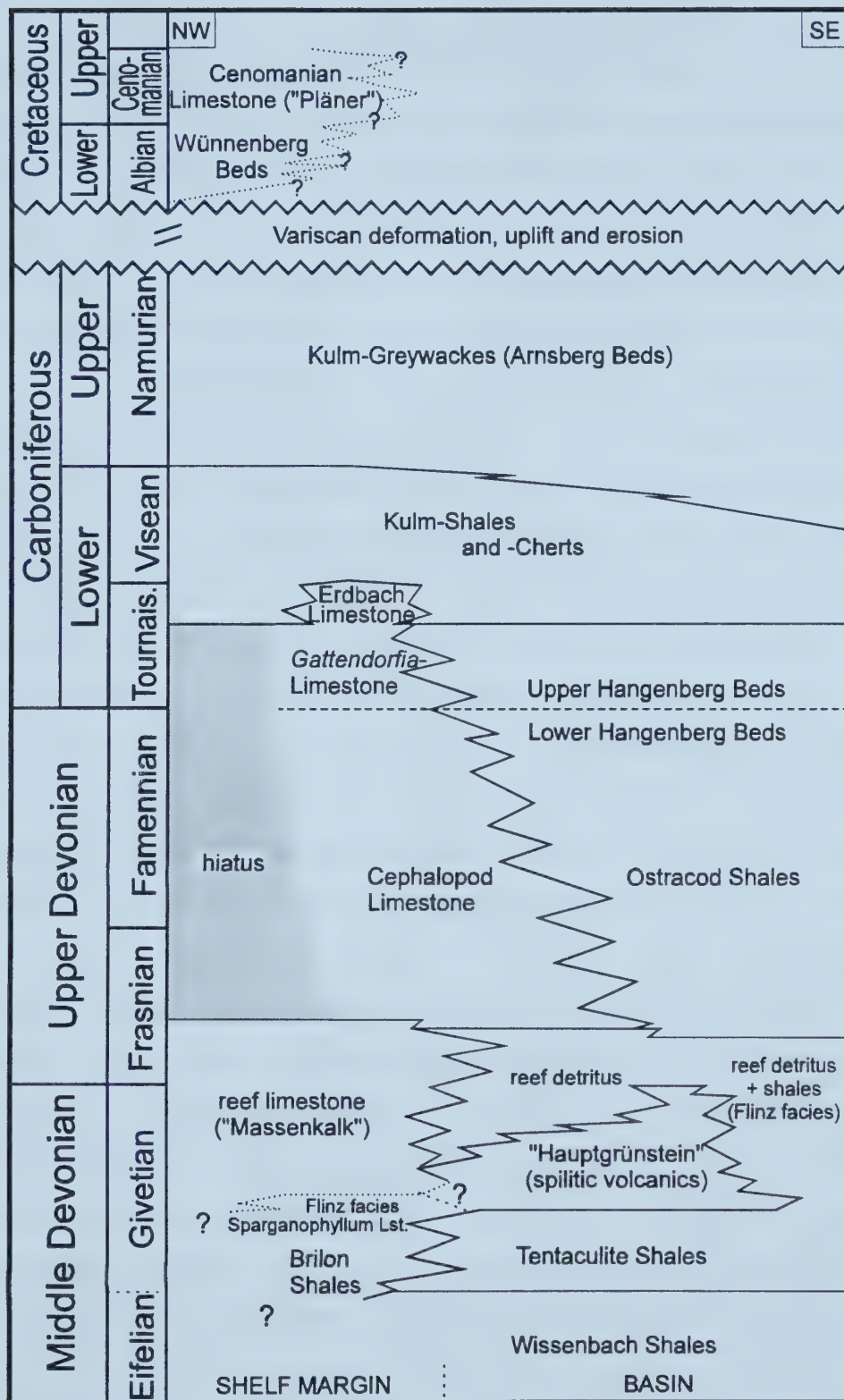
### 1.4.1 Sedimentary history

The general sedimentary history of the Brilon Reef Complex has been well studied (Jux 1960; Bär 1966; Krebs 1968a, 1971a, b, 1974, Wahba 1978; Machel 1979; 1990b; Brinckmann 1981; Moritz 1983; Staedter and Koch 1987; May 1987a, b; Malmshiemer et al. 1990, 1991; Hong 1992; Wizisk 1995). However, many questions remain unanswered, mainly due to the structural complexity and the lack of sufficient biostratigraphic data (Wizisk 1995).

Beginning in the early Middle Devonian (Eifelian), monotonous fossil-poor shales and siltstones (Wissenbach Shales, Tentaculite Shales) were deposited south and southeast of the shelf margin (Paeckelmann 1936) (Figure 1.5), while fossil-rich calcareous shales with intercalated limestone lenses and beds (Brilon Shales) formed on the shelf margin (Müller 1990). The overlying fossil-rich *Sparganophyllum* Limestone has been encountered only in the southwestern part of the Brilon area and probably represents the first stage of biostromal reef growth on the shelf edge (Errenst 1993). The *Sparganophyllum* Limestone is overlain by crinoid-rich calcareous and bituminous shales with intercalated beds of reef-derived detritus (“Flinz facies”) (Müller 1990). The “Flinz facies” is considered to represent the typical sedimentation in off-reef areas in the eastern Rhenish Schiefergebirge, time-equivalent to the Middle and Upper Devonian biostromal and biohermal carbonates, which are collectively called “Massenkalk” (Krebs 1968) (Figure 1.5).

Reef growth in the southern part of the area began in the Upper Givetian, simultaneously with basaltic volcanic activity that led to the formation of spilitic volcanic deposits (altered basalts and volcanic tuffs of the “Hauptgrünstein”) in the nearby basin south of the shelf margin (Sunkel 1990). According to Krebs (1968, 1974), the Middle to Upper Devonian carbonate buildups of the eastern Rhenish Schiefergebirge can be divided into an initial biostromal “bank-type Massenkalk” (“Schwelm facies”) and a subsequent biohermal “reef-type Massenkalk” (“Dorp facies”), which in some places is followed by a “cap-type Massenkalk” (“Iberg facies”). There is still considerable uncertainty regarding of when reef growth began in the northern part of the area (Brinckmann 1981; Wizisk 1995; questionmarks in Figure 1.5).





**Figure 1.5:** Schematic diagram of the stratigraphy of the Brilon area; modified from Malsheimer et al. (1990) and Wizisk (1995).





The results of the federal drilling project (Brinckmann 1981) led to a better understanding of the sedimentary evolution of the Brilon Reef Complex. The occurrence of specimens of the thick-shelled brachiopod *Stringocephalus burtini*, which is stratigraphically restricted to the Givetian, in the “Schwelm facies” and the “Dorp facies”, and the intercalation of both facies, was interpreted to mean that they were deposited contemporaneously and interfingered laterally (Brinckmann 1981). These observations stand in contrast to the original definition by Krebs (1968), because carbonates of the so-called “Schwelm facies” in the Brilon Reef Complex are not necessarily restricted to an initial platform phase, but also occur as lagoonal deposits that formed during the main phase of reef growth (“Dorp facies”). While Krebs (1968, 1971a, b, 1974) had interpreted the Brilon Reef Complex as an atoll, with reef core facies enclosing a central lagoon, Brinckmann (1981) used the new data from the federal drilling project to differentiate between an early phase of reef growth at the northern margin of the complex, beginning in the Middle Devonian (possibly as early as Eifelian), and a later phase of reef growth at the southern margin beginning in the Late Givetian as a result of synsedimentary block-faulting with concomitant tilting of the area. Continued reef growth at the northern and southern margins during the Late Givetian and Frasnian is inferred to have led to the formation of an atoll (Brinckmann 1981). More recent work has shown that the northern part of the reef complex is dominated by a succession of lagoonal sediments, and that most of the reef core facies is concentrated on the southern and southeastern margin of the reef complex (May 1987a, b; Stritzke 1989, 1990; Machel 1990b; Malmshamer 1990, 1991; Wizisk 1995). A reconstruction of the northern margin of the reef complex is complicated by the lack of outcrops and core control except in the northeastern part of the reef complex (Wizisk 1995). The fact that, in the case of the Brilon Reef Complex, the terms “Schwelm facies” and “Dorp facies” have been used ambiguously with regards to stratigraphic age and depositional environment, caused Wizisk (1995) to abandon the terms altogether. Using drill cores and measured sections at the southern margin of the reef complex, Machel (1979, 1990b), Städter and Koch (1987), and Wizisk (1995) recognized the regressive character of the main phase of reef development. During the main phase of reef growth, the rate of carbonate accumulation exceeded the rate of subsidence, resulting in the progradation of shallow water



depositional environments over deeper water depositional environments. Machel (1990b) suggested that the apparent atoll-shape of the Brilon Reef Complex may be the result of differential compaction of sediments on a carbonate platform that had relatively steep slopes but did not possess a ring of reef-core facies.

Whatever the facies relationships in detail, reef growth ceased during the Frasnian, probably caused by an interplay of several factors that had a negative effect on the productivity of the reef organisms, e.g., rising relative sea-level (Bär 1966; Machel 1979, 1990b) and climatic cooling (Malmsheimer et al. 1991). Although it is clear that the basin became deeper, it is not known how much of this development was due to eustatic sea level rise, to tectonic subsidence, or to both. Drowning as a major cause for reef demise is indicated by the fact that the reef is capped by Upper Devonian and Lower Carboniferous condensed pelagic cephalopod limestones that interfinger with red and green shales and siltstones (Ostracod Shales/Lower and Upper Hangenberg Beds) towards the basin (Figure 1.5). Locally, the Lower Carboniferous cephalopod limestone (*Gattendorfia*-Limestone) is overlain by crinoidal limestone (Erdbach Limestone). During the Lower Carboniferous the basin further deepened and shales and cherts of the Kulm facies with intercalated beds of carbonate detritus were deposited. All these sediments occur in deep-reaching (up to about 600 m) subvertical fractures within the reefal carbonates of the Brilon Complex. This observation has been interpreted as an indication for the development of karst during a phase of subaerial exposure in the Lower Carboniferous (Bär 1966, 1968). However, the lack of diagenetic features indicative of subaerial exposure, the fact that pelagic sediments follow on top of the reef, and the similarity of the fracture-filling materials to Upper Devonian/Lower Carboniferous cephalopod limestones and Lower Carboniferous crinoidal limestones ("Erdbach limestone"), respectively, all point to a submarine origin of these fractures (Füchtbauer and Richter 1983; Machel 1990b), i.e., they probably are neptunian dykes. The Kulm-shales and -cherts were followed by Upper Carboniferous flysch-type greywackes (Arnsberg Beds) that indicate the advance of the Variscan deformation front from the south.

Folding and thrusting during the Variscan orogeny near the end of the Carboniferous Period and subsequent uplift led to the erosion of most of the Carboniferous



strata in the area of the Brilon Reef Complex, except for remnants in the deep reaching neptunian dykes and within the Nehden and Thülen depressions where some Carboniferous sediments are preserved (Figures 1.4 and 1.5). Except for a marine ingression at the transition from the Lower to Upper Cretaceous (Albian/Cenomanian), which deposited marginal-marine, glauconitic sandstones and conglomerates (Wünnenberg Beds, Albian) followed by marine limestones and marly limestones (Cenomanian limestone), the Brilon area remained subaerially exposed until today (Brinckmann 1981; Hong 1992). Erosional remnants of these Cretaceous sediments frequently occur in karst cavities and unconformably overly the Middle and Upper Devonian reefal carbonates in the eastern part of the reef complex (Figure 1.4).

#### ***1.4.2 Structural history***

The structural history of the Brilon Reef Complex can be divided into 3 stages: (1) extensional synsedimentary tectonic movements, (2) compressional tectonic deformation during the Variscan orogeny, and (3) extensional tectonic movements during post-Variscan times (Schriel 1954; Bär 1966; Wahba 1978; Brinckmann 1981; Werner 1990). The Variscan tectonism resulted in a north- to northwestward thrusting of the tectonically competent carbonate rocks over the tectonically less competent Upper Devonian and Lower Carboniferous strata (Machel 1990a). In general, the carbonate strata form broad, SW-NE trending folds that are further structured by regional fault systems. One fault system trends SW-NE, parallel to the fold axes and the other one trends NNW-SSE dividing the reef complex into a series of fault blocks (Figure 1.4). The former consists of reverse and thrust faults that formed during the Variscan deformation. The latter consists of subvertical normal faults, some of which (e.g., Altenbüren Fault, Romberg Fault, Immental Fault) are probably of pre-Variscan, synsedimentary origin (Bär 1966; Wahba 1978; Werner 1990). Post-Variscan extensional tectonics caused reactivation of the NNW-SSE trending normal faults. According to Schriel (1954) and Schaeffer (1984, 1986), hydrothermal activity along many of these faults during the Mesozoic and Early Tertiary resulted in base metal sulfide mineralization (pyrite/marcasite, sphalerite, galena), associated with calcite, dolomite, and barite.



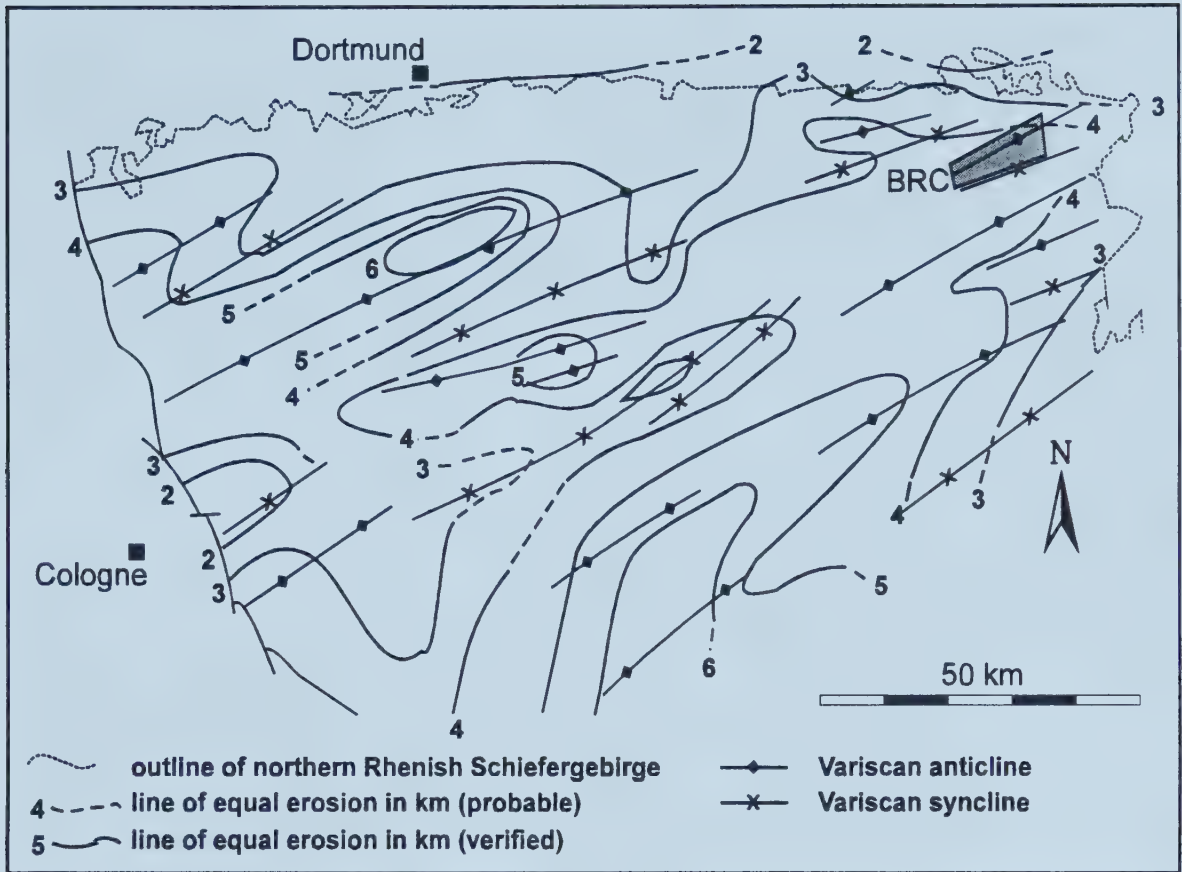


### ***1.4.3 Burial and thermal history***

Due to the structural complexities the burial history of the Brilon Reef Complex is difficult to constrain. Estimates for the maximum burial depth of the northern Rhenish Schiefergebirge vary considerably, ranging from 1000-1500 m (Moritz 1983) to up to 6000 m (Oncken 1982a, b, 1984; Büker et al. 1995). Machel (1990a) estimated a burial depth of “probably more than 2000 m” prior to the Variscan Orogeny, basing this interpretation on field data of the thicknesses of the Upper Devonian to Upper Carboniferous strata in the Brilon area by PaECKELmann (1936) and Clausen and Leuteritz (1979).

Generally, data on the coalification of organic material and on illite crystallinity of Devonian and Lower Carboniferous rocks from the northeastern Rhenish Schiefergebirge indicate a very low-grade metamorphism (Wolf 1972, 1975; Paproth and Wolf 1973; Kalkreuth 1979) with temperatures between 200 and 300°C. The coincidence of tectonic structures (i.e., Variscan synclines and anticlines) and lines of equal coalification in large parts of the northern Rhenish Schiefergebirge indicates that coalification of organic material was largely completed prior to the onset of the Variscan deformation (Wolf 1972; Paproth and Wolf 1973; Teichmüller et al. 1979; Kalkreuth 1979; Oncken 1984). However, a reconstruction of the regional burial history is complicated by the fact that rocks of the same stratigraphic age show significant differences in the degree of coalification. Oncken (1984) attributes this to local differences in pre-Variscan subsidence and paleogeothermal gradients. Paleogeothermal gradients calculated from coalification profiles range between 35 and 70°C/km (Oncken 1984). For a detailed discussion of the calculation of paleogeothermal gradients from coalification profiles, the reader is referred to Oncken (1984). For the Brilon area, Oncken (1984) gives a paleogeothermal gradient of about 60°C/km and estimates that about 4 to 5 km of Carboniferous sediments must have been removed (Figure 1.6).





**Figure 1.6:** Post-Variscan erosion of Paleozoic sediments in the northern Rhenish Schiefergebirge (in km), estimated from coalification gradients (modified from Oncken 1984). In the area of the Brilon Reef Complex (BRC), about 4 to 5 km of Carboniferous sediments have been eroded.

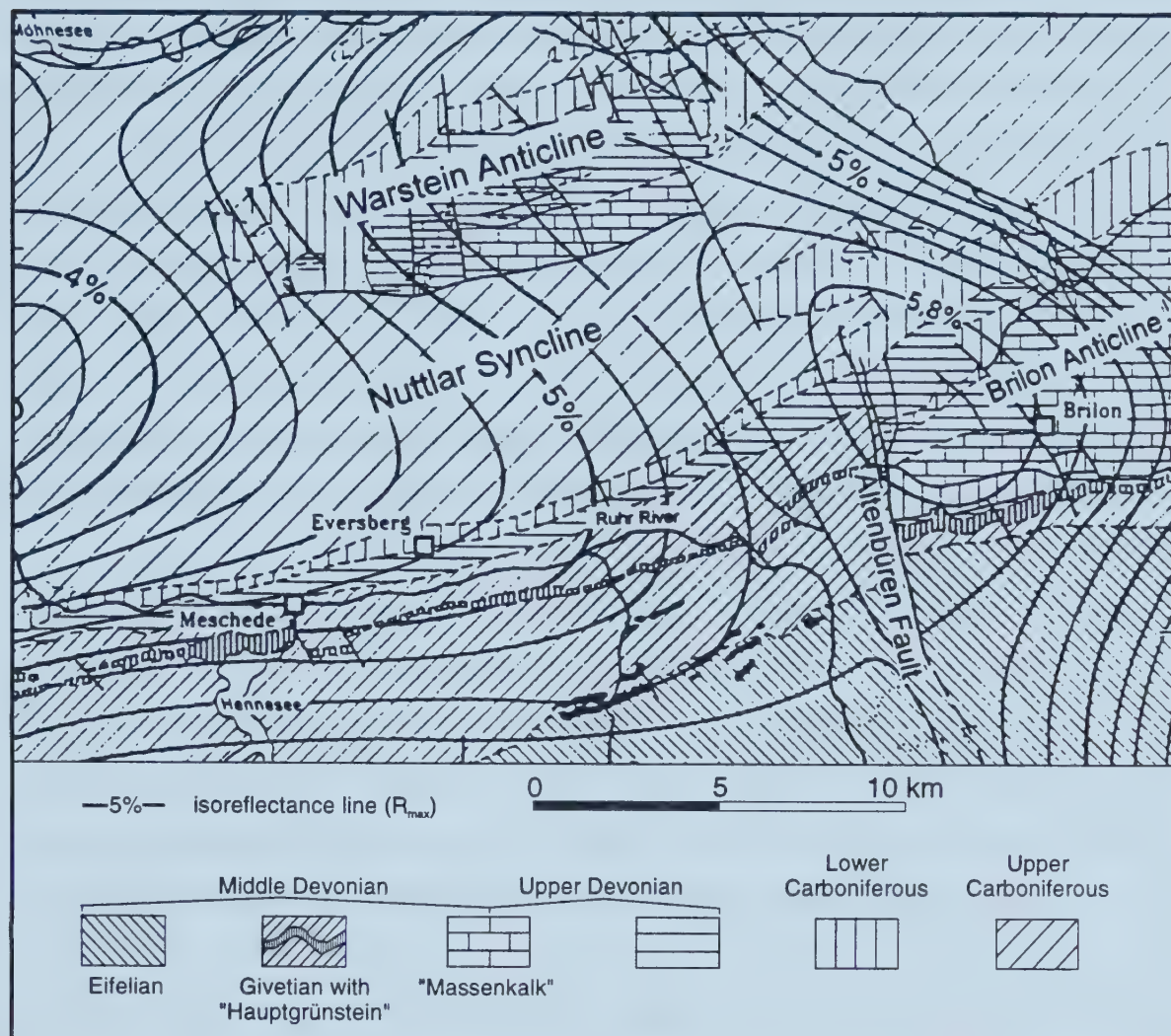
Büker et al. (1995) used vitrinite reflectance data, apatite fission track analysis, and data from Rock-Eval pyrolysis to construct a two-dimensional model of the thermal evolution of Carboniferous and Devonian sedimentary rocks of the eastern Ruhr basin and the northern Rhenish Schiefergebirge about 60 km west of the Brilon area. They concluded, that about 5800 m of Carboniferous sediments must have been eroded in the western part of the northern Rhenish Schiefergebirge.

In the eastern part of the region (i.e., the Warstein-Brilon area; Figure 1.7), a coalification maximum was found, oriented perpendicular to the Variscan structural trend and parallel to the Altenbüren Fault, indicating a syn- or post-kinematic coalification of organic material (Kalkreuth 1979). This anomaly overprints the thermal record of burial at least in the western part of the Brilon Reef Complex and has been interpreted as evidence





for a possible magmatic intrusion below the Warstein-Brilon area (Kalkreuth 1979).



**Figure 1.7:** Isorefectance lines in the Warstein-Brilon area (modified from Kalkreuth 1979).

Moritz (1983) based his estimation of 1000 to 1500 m for the maximum burial depth on the calculation of the formation temperature (74 to 81°C) of a presumably syn-kinematic dolomite phase from the Brilon Reef Complex under the assumption of a paleogeothermal gradient of 30 to 35°C/km. He ignored the regional evidence for a pre-kinematic very low-grade metamorphism and attributed the high coalification of organic matter exclusively to a post-Variscan thermal event, the timing of which he placed into the Jurassic/Cretaceous (Moritz 1983).

The estimate of Oncken (1984) of a maximum burial depth of 4 to 5 km for the area of the Brilon Reef Complex appears to be the most reasonable one because he based





it on the regional evidence that coalification was largely completed before the Variscan deformation, with the exception of certain areas, such as the Warstein-Brilon area, and took local differences in pre-Variscan subsidence and paleogeothermal gradients into account.

Based on geophysical anomalies (gravity and magnetic data) and data on the coalification of organic matter, the presence of a deep-seated granitic pluton of Lower Permian age has been postulated for the Lippstadt area (Hoyer et al. 1974), which is located in the southeastern Münsterland Cretaceous Basin north of the Warstein-Brilon area in the direction of the northern continuation of the Altenbüren Fault. This presumed pluton has been inferred to have caused the formation of occurrences of a first phase of post-Variscan hydrothermal quartz with temperatures of formation of up to 360°C (Koschinski 1979) in the Warstein area (Schaeffer 1984, 1986). According to Schaeffer (1986), further hydrothermal mineralization events in the northeastern Rhenish Schiefergebirge occurred during the Mesozoic and Tertiary as the result of extensional tectonics that enabled hydrothermal mineralizing fluids to ascend episodically along deep-reaching faults. In the southeastern Münsterland Cretaceous Basin, thermal events in the Late Cretaceous and Tertiary are indicated by the occurrence of vein mineralizations and hydrocarbons in the Cretaceous sediments that overly the deformed Paleozoic (Lommerzheim 1991).

#### ***1.4.4 Diagenetic history and occurrences of dolomite***

The pre-Variscan diagenetic history of the Brilon Reef Complex has been the subject of detailed investigations of selected cores by Machel (1979, 1990a) and Moritz (1983). Little detailed work has been done on the post-Variscan alteration, except for the investigation by Moritz (1983) and a regional study of the post-Variscan mineralization that included some samples from the Brilon Reef Complex (Schaeffer 1984, 1986).

Reports of surface exposures of dolomite in the area of the Brilon Reef Complex are rare (Schriel 1954; Steuerwald, personal communication 1997). These dolomite occurrences are mainly restricted to faults and fractures and their immediate vicinity and are mineralized locally with base metal sulfides (Schriel 1954). Dolomite formation prior to the Variscan deformation is restricted to internal sediments (dolomite I and II of Machel 1979, 1990a; dolomite I of Moritz 1983) and stylolites (dolomite III of Machel 1979, 1990a) and



is volumetrically insignificant (Machel 1990a). Machel (1979, 1990a) described intervals of massive dolostone in the lowermost 100 m of the Romberg drill core, consisting of three dolomite types (so-called dolomite IVa, IVb, and V). Based on petrographic data, he interpreted the timing of the first two types as being either syn- or post-Variscan and suggested a hydrothermal origin. He placed the third type in a post-Variscan phase and suggested a possible genetic relationship with the post-Cretaceous land surface, based on a personal communication with Brinckmann (Machel 1979, 1990a). Brinckmann (1981) described mineralized dolomite-breccia zones in several cores in the northeastern part of the reef complex. Fracturing and brecciation seems to have preceded one or several phases of dolomitization, which was followed by dissolution and subsequent base metal sulfide mineralization. Moritz (1983) reported one syn-Variscan dolomite type (his dolomite II, probably equivalent to Machel's dolomite IVa) and two post-Variscan dolomite types (his dolomites III and IV) from the investigation of the cores Brilon 2, Romberg 1, Nehden 3, and Madfeld 1. Dolomite II and III both occur as replacement of limestone and as cavity filling saddle dolomite cement. According to his work, dolomite III forms the major volume of dolomite in the Brilon Reef Complex and seems to be restricted to the margins of the reef complex. Moritz (1983) related this dolomitization event to the late stages of a Jurassic/Cretaceous hydrothermal mineralization event. Dolomite IV occurs exclusively as fracture filling cement (saddle dolomite) with a sharp boundary to the adjacent lime- or dolostone (Moritz 1983). Its formation was attributed to a subsequent hydrothermal mineralization event during the Tertiary (Moritz 1983).

In a regional study of the post-Variscan mineralization in the northeastern Rhenish Schiefergebirge, Schaeffer (1984, 1986) identified two dolomitization events and placed them within a regional paragenetic sequence. He related both generations to hydrothermal mineralization events, one in the Late Cretaceous/Early Tertiary, the other in the Tertiary. His work, however, was mostly based on samples from quarries and mines in the eastern Rhenish Schiefergebirge.

It is important to note that most of the interpretations above are based on observations from a relatively small number of outcrop and drillcore samples from the Brilon Reef Complex. All previous workers agree that dolomitization in the Brilon Reef





Complex did not occur prior to the Variscan deformation. This already excludes those dolomitization models that invoke dolomitization at the sea-floor or during pre-orogenic burial. Interpretations about the number and timing of dolomitization events differ from one author to the other. Little is known about the spatial distribution and extent of dolostone bodies and their association with base metal sulfide mineralization. The lack of sufficient petrographic and geochemical data in previous studies did not allow any confident conclusions about the origin and composition of the dolomitizing and mineralizing fluids.

## **1.5 Objectives**

The major objective of this thesis is to elucidate the spatial distribution, origin and timing of dolomitization and associated base metal mineralization in the Brilon Reef Complex, using petrographic and geochemical methods. In particular, the objectives are

- (1) to determine the primary controls on dolomitization by investigating the relationships between the spatial distribution of dolostone and sedimentary facies, diagenetic phases, and tectonic structures (Chapter 2);
- (2) to study the effects of dolomitization and associated base metal mineralization on the undolomitized limestone hostrock adjacent to the dolostone intervals by identifying petrographic and geochemical trends (Chapter 3);
- (3) to determine the temperatures and compositions of the dolomitizing and mineralizing fluids using microthermometric data from fluid inclusions in suitable diagenetic phases (saddle dolomite, sphalerite, calcite cement) in conjunction with geochemical data (Chapter 3);
- (4) to test one working hypothesis on the origin, timing, and movement of the dolomitizing and mineralizing fluids, using the data from the Brilon Reef Complex, presented in chapters 2 and 3, in conjunction with new hydrochemical data from a regional pilot study on the origin and evolution of saline groundwaters that presently occur in the adjacent Münsterland Cretaceous Basin (Chapters 4).





## 1.6 References

- Amthor, J.E., Mountjoy, E.W., and Machel, H.G., 1993, Subsurface dolomites in the Upper Devonian Leduc Formation buildups, central part of Rimbey-Meadowbrook reef trend, Alberta, Canada. *Bulletin of Canadian Petroleum Geology*, 41, p. 164-185.
- Bär, P., 1966, Stratigraphie, Fazies und Tektonik am Briloner Massenkalksattel (Ostsauerland). Unpublished Dissertation, University of Giessen, 55 p.
- Bär, P., 1968, Die oberdevonische/unterkarbonische Schichtlücke über dem Massenkalk des Briloner und Messinghäuser Sattels (Ostsauerland). *Neues Jahrbuch der Geologie und Paläontologie Abhandlungen*, 131, p. 263-288.
- Braithwaite, C.J.R. and Rizzi, G., 1997, The geometry and petrogenesis of hydrothermal dolomites at Navan, Ireland. *Sedimentology*, 44, p. 421-440.
- Brinckmann, J., 1981, Projekt Rhenohertzynikum, Untersuchung der Metallverteilung in geosynklinalen Sedimenten des Rhenohertzynikums in stratiformen Konzentrationen. Bericht über das Kernbohrprogramm im Briloner Riffkalkkomplex. Unpublished report of the Bundesanstalt für Geowissenschaften und Rohstoffe, 129 p.
- Brinckmann, J., Clausen, C.-D., Müller, H., and Stoppel, D., 1989, Geologische Übersichtskarte der Brilon-Warsteiner Riffkarbonate und ihrer Umrahmung. *Geologisches Jahrbuch*, D95 (1990).
- Bruns, A., 1996, Bergbau um Brilon. In: M. Senger (ed.), *Bergbau im Sauerland*, p. 193-196.
- Büker, C., Littke, R., and Welte, D.H., 1995, 2D-modelling of the thermal evolution of Carboniferous and Devonian sedimentary rocks of the eastern Ruhr basin and northern Rhenish Massif, Germany. *Zeitschrift der deutschen Geologischen Gesellschaft*, 146, p. 321-339.
- Burchette, T. P., 1981, European Devonian reefs: a review of current concepts and models. In: D.F. Toomey (ed.), *European Fossil Reef Models*, Society of Economic Paleontologists and Mineralogists Special Publication, 30, p. 85-142.
- Clausen, C.D. and Leuteritz, K., 1979, Übersicht über die Geologie des Warsteiner Sattels und seiner näheren Umgebung. *Aufschluß*, Sonderband, 29, p. 1-32.
- Cumings, E.R., 1932, Reefs or bioherms? *Geological Society of America Bulletin*, 42, 331-352.
- Errenst, C., 1993, Litho- und biofazielle Untersuchungen im Sparganophyllumkalk der Bohrungen SP6 (Plettenberg) und Brilon II (Brilon) - ein Vergleich. Unpublished Diplom mapping project report, Ruhr-University Bochum, 52 p.
- Fagerstrom, J.A., 1987, *The evolution of reef communities*. 600 p. New York, Wiley-Interscience.



- Füchtbauer, H. and Richter, D. K., 1983, Relations between submarine fissures, internal breccias and mass flows during Triassic and earlier rifting periods. *Geologische Rundschau*, 72, p. 53-66.
- Garven, G., 1995, Continental-scale groundwater flow and geologic processes. In: Wetherill, G.W., Albee, A.L. and Burke, K.C. (eds.), *Annual Review of Earth and Planetary Sciences*, 23, p.89-118.
- Garven, G. and Sverjensky, D.A., 1994, Paleohydrogeology of the Canadian Rockies and origins of brines, Pb-Zn deposits and dolomitization in the Western Canada Sedimentary Basin: Comment and Reply, *Geology*, 22, p. 1149-1151.
- Hong, T., 1992, Mikrofazies, Paläobiologie und Palökologie im nordöstlichen Teil des Briloner Riffkomplexes (Mittel- und Oberdevon) im Ostsauerland, Deutschland. Reihe Geowissenschaften, D82, Rheinisch-Westfälische Technische Hochschule Aachen, 166 p.
- Hoyer, P., Clausen, C.-D., Leuteritz, K., Teichmüller, R., and Thome, K. N., 1974, Ein Inkohlungsprofil zwischen dem Gelsenkirchener Sattel des Ruhrkohlenbeckens und dem Ostsauerländer Hauptsattel des Rheinischen Schiefergebirges. *Fortschritte in der Geologie von Rheinland und Westfalen*, 24, p. 161-172.
- Jux, U., 1960, Die devonischen Riffe im Rheinischen Schiefergebirge. *Neues Jahrbuch der Geologie und Paläontologie, Abhandlungen*, 110, p. 186-258.
- Kalkreuth, W., 1979, Das Inkohlungsbild des Ostsauerländer Hauptsattels im Rhenohertzynikum mit besonderer Berücksichtigung der Trennflächenanalyse. - *Fortschritte der Geologie von Rheinland und Westfalen*, 27, p. 227 - 321.
- Koschinski, G., 1979, Mikrostrukturelle und mikrothermometrische Untersuchungen an Quarzmineralisationen aus dem östlichen Rheinischen Schiefergebirge. Unpublished Ph.D. thesis, University of Göttingen, 146 p.
- Krebs, W., 1968, Reef development on the Devonian of the Eastern Rhenish Slate Mountains, Germany. In: D.H. Oswald (ed.), *International Symposium on the Devonian System*, Calgary, Alberta Society of Petroleum Geologists, 2, p. 295-306.
- Krebs, W., 1971a, Devonian reef limestones in the Eastern Rhenish Schiefergebirge. In: Müller, G. (ed.), *Sedimentology of parts of central Europe*. 8<sup>th</sup>. International Sedimentology Congress, Heidelberg, Guidebook, p. 45-81.
- Krebs, W., 1971b, Die devonischen Riffe in Mitteleuropa. *Mitteilungen der Technischen Universität Carolo-Wilhelminia*, 6(2/3), p. 1-12.
- Krebs, W., 1974, Devonian Carbonate complexes in Central Europe. In: L.F. Laporte (ed.): *Reefs in time and space - selected examples from the recent and the ancient*. Society of Economic Paleontologists and Mineralogists Special Publication 18, p. 155-208.





- Land, L. S., 1985, The Origin of Massive Dolomite. *Journal of Geologic Education*, 33, p. 112-125.
- Machel, H.G., 1979, Fazies und Diagenese der devonischen Riffcarbonate der Bohrung Romberg (Briloner Riff). Unpublished Diplom-thesis, Technical University of Braunschweig, 231 p.
- Machel, H.G., 1990a, Submarine Frühdiagenese, Spaltenbildungen und prätektogenetische Spätdiagenese des Briloner Riffs. *Geologisches Jahrbuch*, D95, p. 85-137.
- Machel, H.G., 1990b, Faziesinterpretation des Briloner Riffs mit Hilfe eines Faziesmodells für devonische Riffkarbonate. *Geologische Jahrbuch*, D95, p. 45-83.
- Machel, H. G. and Mountjoy, E. W., 1986, Chemistry and environments of dolomitization - a reappraisal. *Earth Science Reviews*, 23, p. 175-222.
- Machel, H.G., and Mountjoy, E.W., 1987, General constraints on extensive pervasive dolomitization - and their application to the Devonian carbonates of western Canada. *Bulletin of Canadian Petroleum Geology*, 35, p. 143-158.
- Machel, H.G., Mountjoy, E.W., and Amthor, J.E., 1994, Dolomitisierung von devonischen Riff- und Plattformkarbonaten in West-Kanada. *Zentralblatt für Geologie und Paläontologie*, Teil I, 1993, h.7/8, p. 941-957.
- Machel, H.G. Mountjoy, E.W., and Amthor, J.E., 1996, Mass balance and fluid flow constraints on regional-scale dolomitization, Late Devonian, Western Canada Sedimentary Basin - Discussion. *Bulletin of Canadian Petroleum Geology*, 44, p. 566-571.
- Malsheimer, K.W., Mensink, H., and Stritzke, R., 1990, Beginn der Riffschutt-Produktion un der Knollenkalk-Sedimentation im Südosten des Briloner Riffs / Sauerland. *Geologisches Jahrbuch*, D95, p. 177-182.
- Malsheimer, K.W., Mensink, H., and Stritzke, R., 1991, Gesteinsvielfalt im Riffgebiet um Brilon. *Geologie und Paläontologie von Westfalen*, 18, p. 67-83.
- May, A., 1987a, Fazies und Stratigraphie des devonischen Massenkalkes zwischen Brilon, Wülfe und Alme (MTB Alme 4517, Sauerland). Unpublished Diplom-mapping project and thesis Ruhr-University Bochum, 61 p.
- May, A., 1987b, Der Massenkalk (Devon) nördlich von Brilon (Sauerland). *Geologie und Paläontologie von Westfalen*, 10, p. 51-84.
- Moritz, W., 1983, Fazies und Diagenese des Briloner Karbonatkomplexes anhand einiger ausgewählter Bohrungen. Unpublished Dissertation, Technical University Braunschweig, 162 p.
- Morrow, D. W., 1982, Diagenesis 2. Dolomite - Part 2: Dolomitization models and ancient dolostones. *Geoscience Canada*, 9, p. 95-107.
- Morrow, D.W., 1998, Regional Subsurface Dolomitization: Models and Constraints. *Geoscience Canada*, 25, p. 57-70.





- Morrow, D.W., and Aulstead, K.L., 1995, The Manetoe Dolomite - a Cretaceous-Tertiary or a Paleozoic event? Fluid inclusion and isotopic evidence. *Bulletin of Canadian Petroleum Geology*, 43, p. 67-280.
- Mountjoy, E.W., 1994, Dolomitization and the character of hydrocarbon reservoirs: Devonian of western Canada. In: A. Parker and B. W. Sellwood (eds.), *Quantitative Diagenesis: Recent Developments and Applications to Reservoir Geology*, p. 33-94.
- Mountjoy, E.W., and Amthor, J.E., 1994, Has burial dolomitization come of age? Some answers from the Western Canada Sedimentary Basin. *Special Publications of the International Association of Sedimentologists*, 21, p. 203-229.
- Müller, H., 1990, Zur Altersfrage und Faunenführung der Briloner Schiefer im nordöstlichen Sauerland (Mitteldevon, Rheinisches Schiefergebirge). *Geologisches Jahrbuch*, D95, p. 7-42.
- Nesbitt, B.E. and Muehlenbachs, K., 1994, Paleohydrogeology of the Canadian Rockies and origins of brines, Pb-Zn deposits and dolomitization in the Western Canada Sedimentary Basin. *Geology*, 22, p. 243-246.
- Oncken, O., 1982a, Determinierung und Entwicklung großtektonischer Strukturen im nördlichen Rhenoherynikum (Beispiel Ebbeantiklinorium). PhD thesis, University of Köln, 189 p.
- Oncken, O., 1982b, Zur Rekonstruktion der Geosynklinalgeschichte mit Hilfe von Inkohlungskurven (am Beispiel Ebbeantiklinorium, Rheinisches Schiefergebirge). *Geologische Rundschau*, 71, p. 579-602.
- Oncken, O., 1984, Zusammenhänge der Strukturgenese des Rheinischen Schiefergebirges. *Geologische Rundschau*, 73, p. 619-649.
- Paeckelmann, W., 1936, *Geologische Karte von Preußen 1:25000*, Blatt Adorf, Alme, Brilon und Madfeld mit Erläuterungen.
- Paproth, E. and Wolf, M., 1973, Zur paläogeographischen Deutung der Inkohlung im Devon und Karbon des nördlichen Rheinischen Schiefergebirges. *Neues Jahrbuch der Geologie und Paläontologie, Monatshefte*, 1973, 469-493.
- Pray, L. C. and Murray, R. C. (eds.), 1965, *Dolomitization and Limestone Diagenesis*. - Society of Economic Paleontologists and Mineralogists Special Publication 13, 180 pp.
- Purser, B., Tucker, M., and Zenger, D. (eds.), 1994, *Dolomites - A volume in honour of Dolomieu*. - International Association of Sedimentologists Special Publication 21, 451 p.
- Qing, H., and Mountjoy, E.W., 1994, Formation of coarsely crystalline, hydrothermal dolomite reservoirs in the Presquile Barrier, Western Canada Sedimentary Basin. *American Association of Petroleum Geologists Bulletin*, 78, p. 55-77.



- Qing, H. and Mountjoy, E.W., 1995, Paleohydrogeology of the Canadian Rockies and origins of brines, Pb-Zn deposits and dolomitization in the Western Canada Sedimentary Basin: Comment and Reply. *Geology*, 23, p. 189-190.
- Schriel, W., 1954, Der Briloner Galmei-Distrikt. *Zeitschrift der deutschen geologischen Gesellschaft*, 106, p. 308-349.
- Schaeffer, R., 1984, Die postvariszischen Mineralisationen im nordöstlichen Rheinischen Schiefergebirge. Braunschweiger geologisch-paläontologische Dissertationen, 3, 206 p.
- Schaeffer, R., 1986, Geochemische Charakteristika und Genese der jungmesozoisch-tertiären Vererzung im Sauerland (Rheinisches Schiefergebirge). *Fortschritte der Geologie von Rheinland und Westfalen*, 34, p. 337-381.
- Shields, M.J. and Brady, P.V., 1995, Mass balance and fluid flow constraints on regional-scale dolomitization, Late Devonian, Western Canada Sedimentary Basin. *Bulletin of Canadian Petroleum Geology*, 42, p. 371-392.
- Shukla, V. and Baker, P. A (eds.), 1988, *Sedimentology and Geochemistry of Dolostones*. - Society of Economic Paleontologists and Mineralogists Special Publication 43, 266 pp.
- Staedter, T., and Koch, R., 1987, Mikrofazielle und diagenetische Entwicklung einer devonischen Karbonatabfolge (Givet) am SE-Rand des Briloner Sattels (Rheinisches Schiefergebirge). *Facies*, 17, p. 215-230.
- Sunkel, G., 1990, Devonischer submariner Vulkanismus im Ostsauerland (Rheinisches Schiefergebirge): Vulkanaufbau, Magmenzusammensetzung und Alteration. *Bochumer geologische und geotechnische Arbeiten*, 34, 250 p.
- Teichmüller, M., Teichmüller R., and Weber, K., 1979, Inkohlung und Illitkristallinität. Vergleichende Untersuchungen im Mesozoikum und Paläozoikum von Westfalen. *Fortschritte in der Geologie von Rheinland und Westfalen*, 27, p. 201-276.
- Zenger, D.H., Dunham, J. B., and Ethington, R. L. (eds.), 1980, *Concepts and Models of Dolomitization*. Society of Economic Paleontologists and Mineralogists, 28, 320 pp.
- Wahba, Y., 1978, Die Geologie des Briloner Massenkalksattels im östlichen Sauerland. Unpublished Dissertation University of Clausthal, 203 p.
- Wendte, J., Qing, H.; Dravis, J.J., Moore, S.L.O., Stasiuk, L.D., and Ward, G., 1998, High-temperature saline (thermoflux) dolomitization of Devonian swan Hills platform and bank carbonates, Wild River area, west-central Alberta. *Bulletin of Canadian Petroleum Geology*, 46, p.210-265.
- Werner, W., 1990, Die epigenetische Markasit-Schwerspat-Zinkblende-Vererzung "Altenbüren" (nordöstliches Rheinisches Schiefergebirge). *Geologisches Jahrbuch*, D95, p. 139-176.



- Wilson, E.N., Hardie, L.A., and Phillips, O.M., 1990, Dolomitization front geometry, fluid flow patterns, and the origin of massive dolomite: the Triassic Latemar buildup, northern Italy. *American Journal of Science*, 290, p. 741-796.
- Wizisk, U., 1995, Mikrofazielle Entwicklungsgeschichte des devonischen Briloner Riffkomplexes (Sauerland). Unpublished Dissertation Ruhr-University Bochum, 79 p.
- Wolf, M., 1972, Beziehungen zwischen Inkohlung und Geotektonik im nördlichen Rheinischen Schiefergebirge. *Neues Jahrbuch der Geologie und Paläontologie, Abhandlungen*, 141, p. 222-257.
- Ziegler, P.A., 1990, *Geological Atlas of Western and Central Europe*. 239 p.





## CHAPTER 2

# CARBONATE FACIES, STRATIGRAPHY, AND POST-VARISCAN DIAGENESIS OF THE DEVONIAN BRILON REEF COMPLEX AND THEIR RELATIONSHIP TO THE DISTRIBUTION OF DOLOSTONE

### 2.1 Introduction and previous work

The Devonian Brilon Reef Complex (Figure 2.1) in the northeastern Rhenish Schiefergebirge, Germany, hosts intervals of dolostone associated with minor base metal sulfide mineralization, that were encountered in drill cores during a program of the “Bundesanstalt für Geowissenschaften und Rohstoffe” (= German Geological Survey) in the late 1970's (Brinckmann 1981). Several of these intervals show striking petrographic similarities with occurrences of pervasive dolostone in western Canada, which serve as prolific hydrocarbon reservoir rocks as well as host rocks for Mississippi Valley Type-(MVT) Pb-Zn sulfide mineralization (Mountjoy and Krebs 1983; Mountjoy 1994; Davies 1996).

Earlier studies of selected cores from the drilling program focused mainly on the detailed description of the sedimentary and diagenetic characteristics of the limestones (Machel 1979, 1990a, b; Moritz 1983; Wizisk 1995). They did not investigate the controls on the formation and distribution of dolostone within the Brilon Reef Complex.

The stratigraphic correlation of the drill cores across the reef complex is limited by the structural complexity and the paucity of suitable biostratigraphic markers (such as conodonts) in most of the drill cores (Brinckmann 1981; Moritz 1983; Hong 1992; Wizisk 1995). The stratigraphic and structural framework of the Devonian and Carboniferous rocks in the area of the Brilon Reef Complex is based mainly on outcrop studies (Bär 1966; Wahba 1978). Attempts to extrapolate the stratigraphic data from the surface into the subsurface failed to yield any satisfactory results (Hong 1992) with two conditional exceptions. Firstly, the Givetian brachiopod *Stringocephalus burtini* has been used to constrain the age of some core intervals to the late Middle Devonian (Brinckmann 1981; Wizisk 1995). Secondly, Brinckmann (1981) mentioned that intervals of dark calcareous shale encountered in drill





**Figure 2.1:** Simplified geologic map of the Brilon Reef Complex in the northeastern Rhenish Schiefergebirge (RSG), Germany; compiled from Wahba (1978), Brinkmann et al. (1989), and Wizisk (1995). Names of wells abbreviated, for full names see Table 2.1. Dotted line A-A' indicates location of schematic cross-section in Figure 2.4. Dotted lines B-B' and B'-C indicate locations of schematic cross-sections in Figure 2.8.

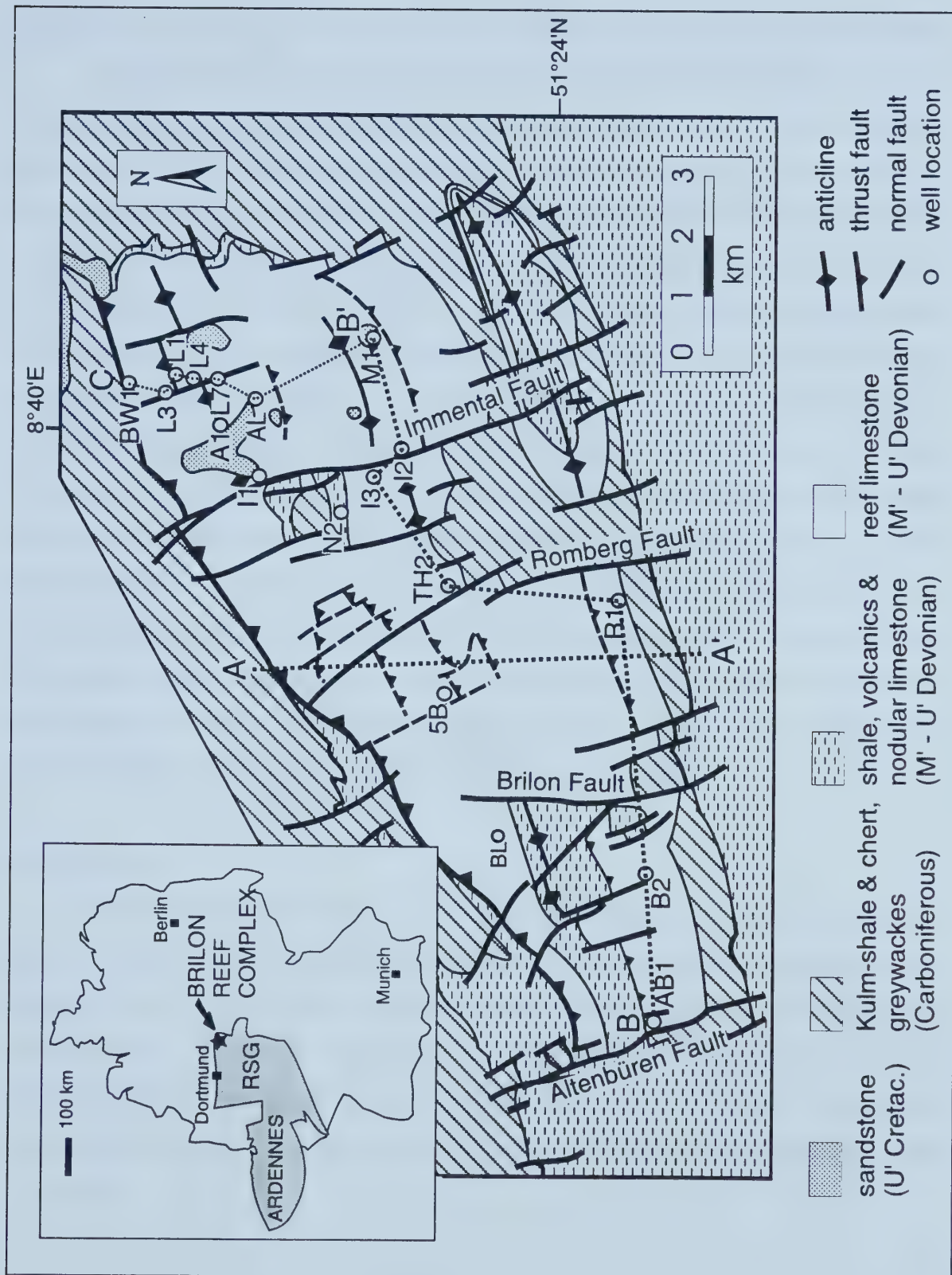


Figure 2.1





cores from the central part of the Brilon Reef Complex may be useful for correlation.

Occurrences of dolomite at the surface are restricted mainly to faults and fractures and their immediate vicinity, and these occurrences are in some cases mineralized with base metal sulfides (Schriel 1954). According to the report by Brinckmann (1981), mineralized dolostone intervals were encountered mainly in the northeastern part of the Brilon Reef Complex. They occur at two depth levels forming “quasi-stratiform” zones (Brinckmann 1981): one at depths between 250 and 430 m below the surface, consisting of mineralized dolomite breccias with varying amounts of sphalerite, galena, and pyrite; the other one at depths below 550 m, consisting of weakly mineralized dolostone mostly devoid of macroscopic mineralization. Brinckmann (1981) estimates that the upper zone has a lateral extent of ca. 1000 m in N-S direction and less than 400 m in E-W direction. The presumed lower zone was penetrated by only two wells that were deep enough to reach it (Loh 1 and Almerfeld). Other occurrences of dolomitized intervals were mentioned in the descriptions of the drill cores that are included in the appendix of Brinckmann’s (1981) report, but were not further expanded upon in the report itself. The report concluded that ore concentrations of the carbonate-hosted base metal sulfide mineralization of the Brilon Reef Complex were too low for mining to be economically viable (Brinckmann 1981).

## **2.2 Objectives**

The objective of this chapter is to investigate the spatial and temporal relationships between the distribution of dolostone and sedimentary facies, diagenetic phases, and tectonic structures in the Brilon Reef Complex, in order to determine the primary controls on dolomitization. The results have important implications for the origin and timing of dolomitization and associated base metal mineralization in the Brilon Reef Complex and provide the framework for the geochemical and microthermometric investigations presented in Chapter 3.



### 2.3 Database and Methods

Of a total of 35 available drill cores from the Brilon Reef Complex, 18 were selected for this study (Figure 2.1, Table 2.1).

core identification	abbreviation	location (UTM coord.)		elevation (m a.S.L.)	total length (m)
		R	H		
Alme 1	A1	34 76 915	57 01 955	390.0	467.0
Almerfeld	AL	34 77 270	57 01 290	418.0	784.4
Altenbüren 1	AB1	34 66 050	56 95 325	485.0	405.0
Auf dem Loh 1	L1	34 77 960	57 02 780	442.3	919.0
Auf dem Loh 3	L3	34 77 890	57 02 950	432.0	485.4
Auf dem Loh 4	L4	34 77 890	57 02 580	447.0	371.4
Auf dem Loh 7	L7	34 77 740	57 02 105	450.0	413.3
Bleiwäsche 1	BW1	34 78 070	57 03 960	375.0	265.2
Blumenstein 1	BL	34 69 600	56 97 934	445.0	746.4
Brilon 2	B2	34 69 055	56 94 570	500.0	615.0
Fünf Brücken	5B	34 71 945	56 98 155	421.0	360.8
Immental 1	I1	34 75 930	57 01 545	435.0	461.2
Immental 2	I2	34 76 395	56 98 890	435.0	513.0
Immental 3	I3	34 76 055	56 99 380	443.0	459.5
Madfeld 1	M1	34 78 610	56 99 460	494.0	452.3
Nehden 2	N2	34 75 510	57 00 003	426.0	639.2
Romberg 1	R1	34 74 050	56 94 965	505.0	765.0
Thülen 2	TH2	34 74 180	56 98 080	415.0	495.0

**Table 2.1:** Core identifications, abbreviations, locations, elevations and total lengths of drill cores from the Brilon Reef Complex; compiled from Brinckmann (1981). For locations, see Figure 2.1.

The primary selection criterion was the presence of dolomitized intervals as reported in the original core descriptions presented in the unpublished report of the drilling program (Brinckmann 1981). During core logging, the Middle and Upper Devonian carbonate rocks (the so-called “Massenkalk” of Krebs 1968) were classified according to the modified carbonate classification by Dunham (1962) (modified by Embry and Klovan 1972, Figure 2.2). The drill cores were investigated at a meter-scale with respect to their gross facies distribution using the carbonate facies model for Middle to Upper Devonian shallow-marine carbonates by Machel and Hunter (1994) (Figure 2.3).



Original components not organically bound during deposition						Original components organically bound during deposition		
of the allochems, less than 10% > 2 mm				of the allochems more than 10% > 2 mm		boundstone		
contains carbonate mud (particles less than 0.03 mm diameter)			mud absent	matrix supported	grain supported	organisms acted as baffles	organisms encrusting and binding	organisms building a rigid framework
mud-supported		grain-supported						
less than 10% grains	more than 10% grains							
mud-stone	wacke-stone	pack-stone	grain stone	float-stone	rud-stone	baffle-stone	bind-stone	frame-stone

**Figure 2.2:** Carbonate classification by Dunham (1962), modified by Embry and Klovan (1972).

The petrographic characteristics and typical fossil content of the carbonate facies types that occur within each facies zone are listed in Figure 2.3. Reasons for choosing the Machel and Hunter (1994) model rather than creating a new classification or using other existing models are:

- (1) it provides a tool for quick and accurate assessment of carbonate facies in core and outcrop using macroscopically identifiable parameters like sorting, rounding, texture, amount of primary micrite, types and amount of primary porosity, fossil assemblage, and typical fossils;
- (2) the model was originally developed on the basis of the Romberg 1 drill core from the Brilon Reef Complex (Machel 1979, 1990a) and is compatible with the results of subsequent studies of the carbonate facies development in the Brilon Reef Complex (Moritz 1983; Hong 1992; Wizisk 1995).

All the drill cores that were selected for this study had already been roughly described in Brinckmann (1981). Detailed descriptions of the carbonate facies types of the Middle and Upper Devonian carbonates of the Brilon Reef Complex can be found in Machel (1979, 1990a), Moritz (1983), May (1987, 1988), Hong (1992), and Wizisk (1995). Striplogs including information on lithology, carbonate facies, and stratigraphy of the investigated drill





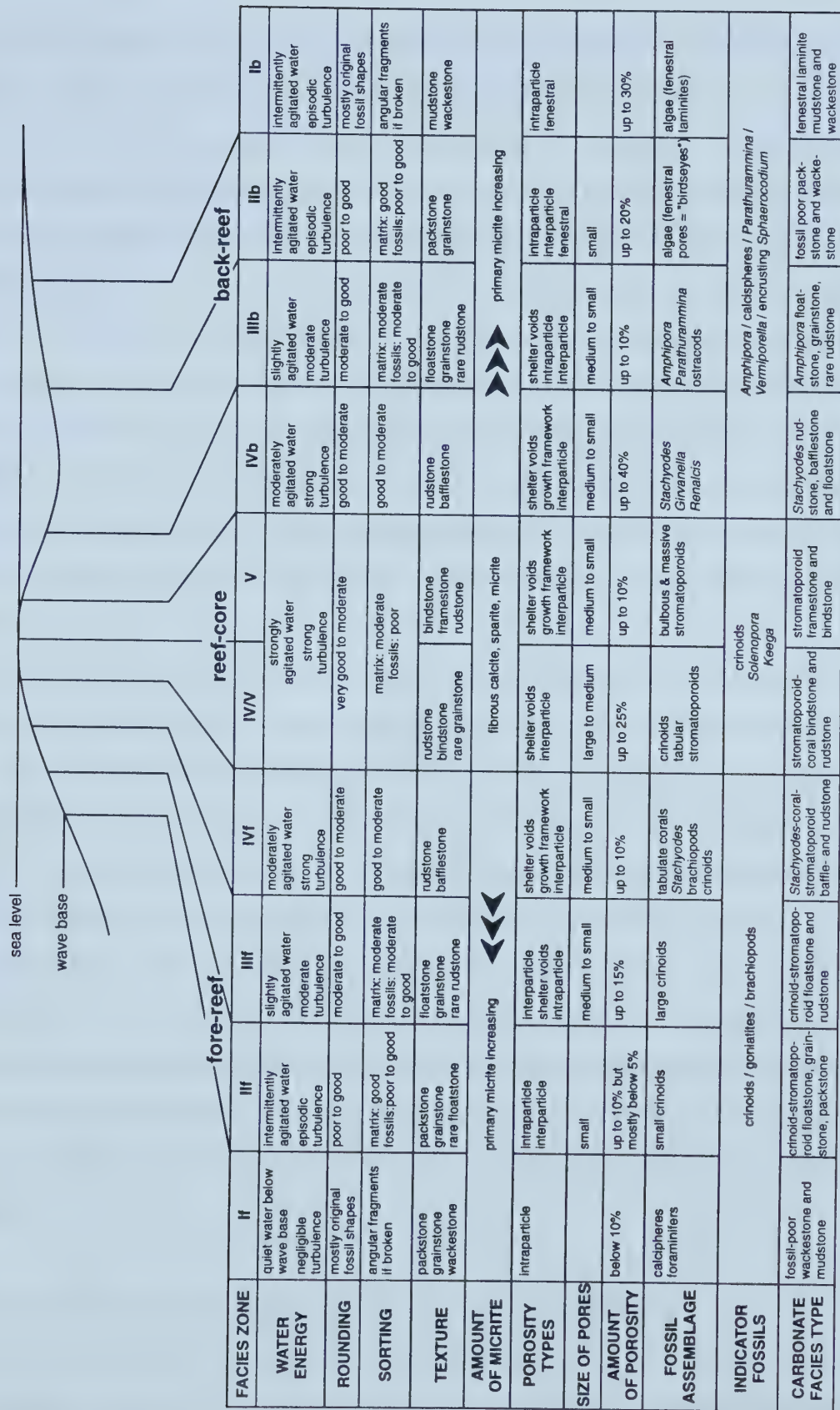


Figure 2.3: Facies model for Middle to Late Devonian reef carbonates, modified from Machel and Hunter (1994).



cores as well as corresponding gamma ray traces (where available) are given in Appendix 1. Stratigraphic ages based on conodont faunas are those reported in Brinckmann (1981) and Machel (1990a). The correlation of the drill cores was attempted using existing biostratigraphic data, the authors observations of the occurrence of macroscopic index fossils (i.e., the Givetian brachiopod *Stringocephalus burtini*), and changes in lithology and facies.

Dolomitized core intervals and the adjacent limestone intervals up to a vertical distance of 30 m from a dolostone/limestone transition were logged in great detail with respect to facies, diagenetic, and structural characteristics to investigate the controls on the distribution of dolomite. A list of the dolomitized intervals and their characteristics is given in Appendix 2. Samples from the dolostone intervals were taken for further petrographic investigations (transmitted light, cathodoluminescence (CL), fluorescence microscopy) to establish a paragenetic sequence and to detect possible relicts of sedimentary and early diagenetic structures.

A total of 163 polished thin sections were produced and stained with Alizarin S and potassium ferricyanide (Dickson 1966) to determine carbonate mineral composition and to estimate the Fe-content of calcites and dolomites. All thin sections were examined by transmitted light microscopy using a Zeiss Jenapol Polarizing Microscope and by CL microscopy using a cold cathode Premier American Technologies ELM-3R Luminoscope. Operating conditions for CL petrography were a beam voltage of 15 to 20 kV and a beam current of 0.5 mA in a 35 to 50 mTorr vacuum under an air atmosphere. Thin sections of dolostones in which the original sedimentary fabric had been obliterated were also examined by UV-microscopy (blue light 450 nm) to identify sedimentary and diagenetic relict fabrics. Dolomite textures were classified according to the classification by Sibley and Gregg (1987). Planar and nonplanar dolomite textures were distinguished based on qualitative inspection in thin section.

## **2.4 Carbonate facies and stratigraphy of the investigated drill cores**

Most of the strata of interest are the so-called “Massenkalk”, which is a series of reefal carbonates of Middle to Upper Devonian age. None of the wells drilled in the area of the Brilon Reef Complex has penetrated both the upper and lower boundary of the





“Massenkalk”. The total thickness of the Middle and Upper Devonian carbonates of the “Massenkalk” has been estimated to be close to 1000 m (Brinckmann 1981).

#### ***2.4.1 Upper boundary of the “Massenkalk”***

Over most of the area of the Brilon Reef Complex, the Middle and Upper Devonian carbonates of the “Massenkalk” lie directly below a thin (about 2 m) cover of soil. In the eastern part of the reef complex erosional remnants of Cretaceous sandstones directly overlie the “Massenkalk” or occur as fillings of karst cavities. In the Madfeld 1 drill core (M1; Figure 2.1), Cretaceous sandstones have been encountered in karst cavities in the uppermost 20 m. In the Nehden 2 drill core (N2; Figure 2.1), Middle Frasnian “Massenkalk” is overlain by Upper Frasnian nodular limestones followed by a succession of Famennian cephalopod-bearing marls and calcareous shales interbedded with dm-thick limestone layers (Brinckmann 1981). All other investigated drill cores start directly within the carbonates of the “Massenkalk”.

#### ***2.4.2 Lower boundary of the “Massenkalk”***

Three of the investigated wells from the southern margin of the Brilon Reef Complex (Altenbüren 1, Brilon 2, Romberg 1) penetrated the lower boundary of the “Massenkalk”. In the Altenbüren 1 drill core, the “Massenkalk” is underlain by 110 m of dark grey calcareous shales interbedded with dark to light grey marls and limestones that are rich in reef-derived fossil detritus (mainly crinoid fragments), followed down-core by 60 m of dark grey bituminous stromatoporoid-coral boundstones with intercalated intervals of dark grey marls, and 200 m of dark grey, fossil-poor calcareous shales and marls. In the deeper parts of the Romberg 1 and Brilon 2 drill cores, intervals of medium grey “Massenkalk” are intercalated with intervals of volcanoclastic tuffs of the Upper Givetian “Hauptgrünstein” intermixed with abundant fossil detritus (stromatoporoids, corals, crinoids). In the Brilon 2 drill core, a 10 m thick interval of dark grey coral-stromatoporoid-crinoid floatstone underlies this unit and is followed down-core by dark grey fossil-poor shales and marls similar to those in the lowermost part of the Altenbüren 1 drill core. The Romberg 1 drill core ends within massive altered basalts of the Upper Givetian “Hauptgrünstein”.





Brinckmann (1981) reported a Middle to Upper Eifelian age for the fossil-poor shales and marls in the deepest part of the Altenbüren 1 drill core and assigned them to the Brilon Shales, together with the petrographically similar unit that was encountered in the lowermost part of the Brilon 2 well. The Brilon Shales were deposited at the shelf edge beyond the shelf and reef facies of the Brilon Reef Complex during the Upper Eifelian and Givetian and represent the transition between the shelf facies and the basin facies (Müller 1990). The units characterized by dark grey fossiliferous stromatoporoid-coral boundstones and coral-stromatoporoid-crinoid floatstones in the Altenbüren 1 and Brilon 2 drill cores, respectively, have been assigned to the Givetian Sparganophyllum limestone (Brinckmann 1981; Errenst 1993), which has been interpreted to represent a first phase of biostromal reef growth on the shelf edge (Krebs 1968; Errenst 1993). The unit between the Sparganophyllum limestone and the “Massenkalk” in the Altenbüren 1 drill core had been interpreted originally as being part of the Brilon Shales by Brinckmann (1981), but its position above the Sparganophyllum limestone and the abundance of reef-derived fossil detritus (mainly crinoid fragments) caused Müller (1990) to re-interpret this unit as “Flinz facies”. The “Flinz facies” represents the typical sedimentation in off-reef areas in the eastern Rhenish Schiefergebirge time-equivalent to the Middle and Upper Devonian biostromal and biohermal carbonates of the “Massenkalk” (Krebs 1968; Müller 1990).

#### ***2.4.3 Facies types within the “Massenkalk”***

The facies model for Middle to Late Devonian shallow marine carbonates by Machel and Hunter (1994) distinguishes between fore-reef, reef-core and back-reef depositional environments (Figure 2.3). It is therefore applicable only to those stages of reef growth when a diversification into distinct facies zones existed. This is generally the case for the diversification and domination stages of reef growth (James 1983), during which the major amount of carbonate sediments accumulates. The preceding pioneer and colonization stages usually do not exhibit a distinct facies zonation, and are volumetrically of minor importance (Machel and Hunter 1994).

All facies types described in Machel and Hunter (1994) were encountered in the carbonates of the “Massenkalk” in the investigated drill cores from the Brilon Reef Complex.



The paleoenvironmental position of a specific core interval was deduced by considering the facies context, i.e., the succession of facies types above and below the interval in question.

Generally, the Middle and Upper Devonian carbonates of the Brilon Reef Complex are dominated by matrix-rich carbonate facies types (e.g., floatstones, packstones, wackestones, mudstones). Grainstones and matrix-poor rudstones rarely occur.

Deposits of the fore-reef are mainly characterized by the occurrence of crinoids with varying proportions of fragments of other reef-derived organisms that decrease in amount and size with increasing distance from the reef core (Figure 2.3). Poorly fossiliferous crinoid wackestones and mudstones with an estimated macrofossil content < 5 % are assigned to facies zone If. Poorly sorted, crinoid-stromatoporoid floatstones, grainstones, and packstones with an estimated macrofossil content between 2 and 30 % are placed in facies zone IIIf (Plate 2.1 a). Crinoid-stromatoporoid floatstones and rudstones with a macrofossil content of 30 to 80 % consisting of reworked thin tabular and small bulbous stromatoporoids in a matrix of crinoid ossicles are characteristic of facies zone IIIIf (Plate 2.1 b). Carbonates of facies zone IVf are *Stachyodes*-coral-stromatoporoid bafflestones and rudstones, which contain > 40 %, poorly sorted, coarse detritus (3 to 20 cm in diameter) in a fine- to medium-grained matrix, consisting mainly of crinoid ossicles (Plate 2.1 c, d).

Deposits of the reef-core are characterized by stromatoporoid-coral rudstones, bindstones and framestones. Carbonates assigned to facies zone IV/V are stromatoporoid-coral bindstones and rudstones with a matrix of generally well sorted crinoid ossicles (plate 2.2 a). Locally, crinoid grainstone layers are present that probably represent channel fills (Plate 2.2 b). Tabular stromatoporoids are common, either in situ (bindstones) or as fragments (rudstones) in a matrix rich in *Stachyodes* and *Thamnopora*. Carbonates of facies zone V are stromatoporoid framestones and bindstones, which are dominated by massive stromatoporoids with diameters of several dm, in some intervals up to 1.5 m, with crinoid detritus (crinoid packstones and rudstones) filling the interstices (Plate 2.2 c, d).







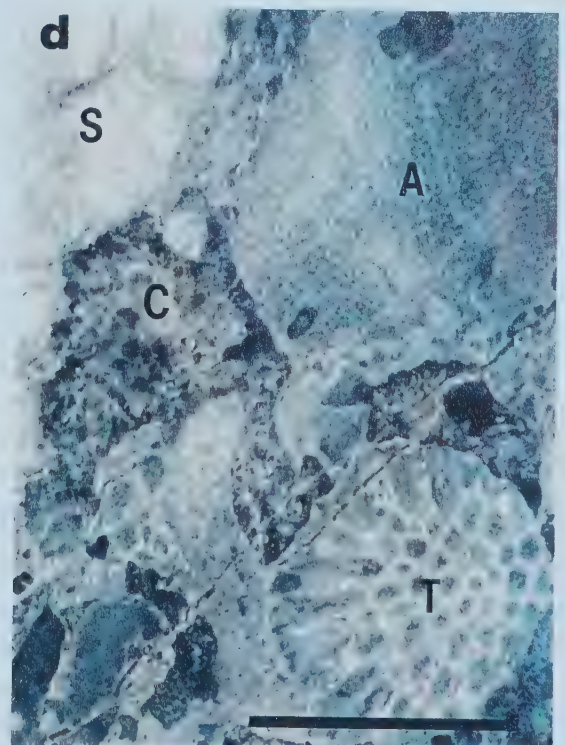
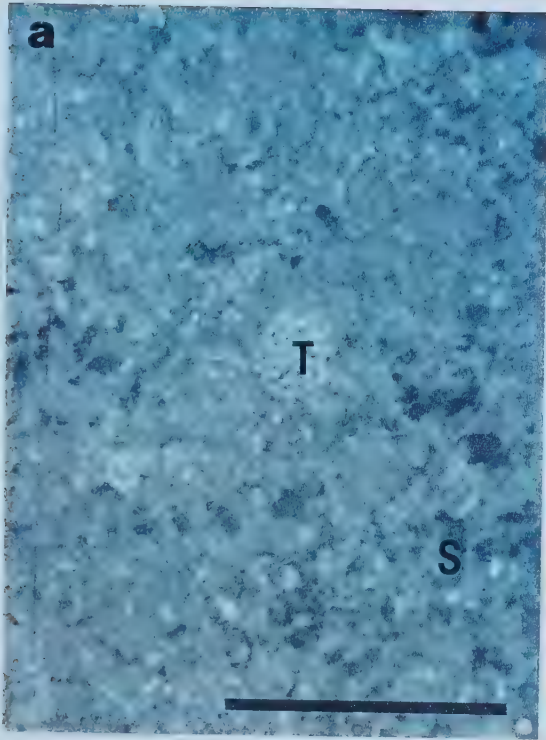
**Plate 2.1:** Facies types of fore-reef character within the “Massenkalk”.

**Plate 2.1a:** Crinoidal packstone with few relics of stromatoporoids (S) and *Thamnopora* (T); facies zone IIIf to If. Romberg 1 (R1) drill core, depth 597.3 m; photo courtesy of H.G. Machel. Scale bar = 1 cm.

**Plate 2.1b:** Crinoid rudstone; facies zone IIIf. Romberg 1 (R1) drill core, depth 406.7 m; photo courtesy of H.G. Machel. Scale bar = 1 cm.

**Plate 2.1c:** Crinoid-stromatoporoid rudstone with large fragment of tabular stromatoporoid (S) in crinoidal floatstone to rudstone matrix; facies zone IVf. Romberg 1 (R1) drill core, depth 696.6 m. Scale bar = 1 cm.

**Plate 2.1d:** Coral-stromatoporoid rudstone with crinoid ossicles (C) in spaces between larger fossil fragments (A = *Alveolites*, S = stromatoporoid, T = *Thamnopora*); facies zone IVf. Romberg 1 (R1) drill core, depth 219.7 m; photo courtesy of H.G. Machel. Scale bar = 1 cm.







**Plate 2.2:** Facies types of reef-core character within the “Massenkalk”.

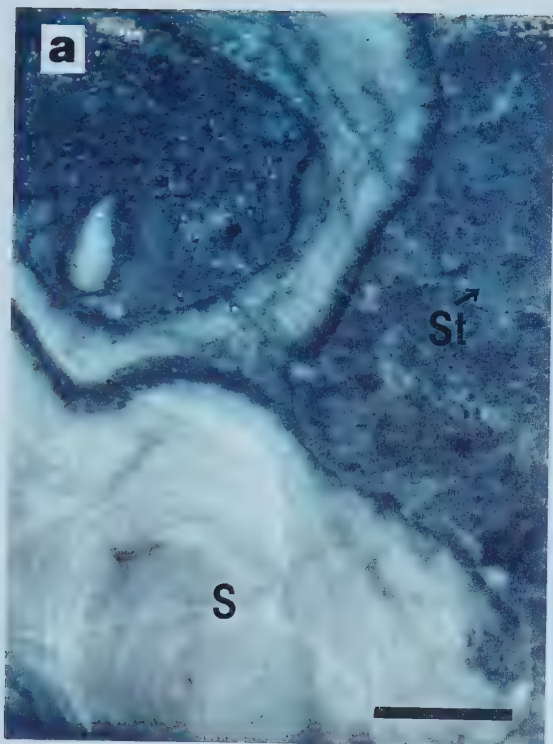
**Plate 2.2a:** Wavy-grown stromatoporoid (S) in stromatoporoid bindstone. Packstone to rudstone matrix consists of crinoid ossicles and fragments of corals and stromatoporoids (e.g., *Stachyodes* = St); facies zone IV/V. Romberg 1 (R1) drill core, depth 129.4 m. Photo courtesy of H.G. Machel. Scale bar = 1 cm.

**Plate 2.2b:** Crinoidal grainstone layer; facies zone IV/V. Bleiwäsche 1 (BW1) drill core, depth 34.6 m. Scale bar = 1 cm.

**Plate 2.2c:** Wavy-grown stromatoporoid with numerous shelter and growth framework pores filled with internal sediment (IS) and several generations of fibrous cements (fc); facies zone V to IV/V. Romberg 1 (R1) drill core, depth 107.2 m. Photo courtesy of H.G. Machel. Scale bar = 1 cm.

**Plate 2.2d:** Massive stromatoporoid (S) framestone with several generations of fibrous calcite cement (fc) in growth framework pores; facies zone V. Bleiwäsche 1 (BW1) drill core, depth 62.2 m. Scale bar = 1 cm.











**Plate 2.3:** Facies types of back-reef character within the “Massenkalk”.

**Plate 2.3a:** Stromatoporoid floatstone to rudstone. Fragments of bulbous stromatoporoids (S), fingerlike and branching stromatoporoids (*Amphipora* and *Stachyodes*), and brachiopod shells (B) in micritic matrix; facies zone IVb/IIIb. Alme 1 (A1) drill core, depth 178.5 m. Scale bar = 1 cm.

**Plate 2.3b:** *Amphipora* floatstone; facies zone IIIb. Auf dem Loh 7 (L7) drill core, depth 404.4 m. Scale bar = 1 cm.

**Plate 2.3c:** Macrofossil-free wackestone with abundant irregularly shaped fenestral pores (arrows) filled with clear calcite; facies zone IIb to Ib. Madfeld 1 (M1) drill core, depth 236.1 m. Scale bar 1 cm.

**Plate 2.3d:** Macrofossil-free mudstone with irregular fenestral laminae (arrows) oriented parallel to bedding and filled with clear calcite; facies zone Ib. Madfeld 1 (M1) drill core, depth 196.1 m. Scale bar = 1 cm.





Deposits of the back-reef environment can be generally identified by the common occurrence of the fingerlike stromatoporoid *Amphipora* and the relative scarcity of crinoids (Machel 1990a; Machel and Hunter 1994). Facies zone IVb is dominated by *Stachyodes* rudstones, bafflestones, and floatstones with fragments of tabular and bulbous stromatoporoids (Plate 2.3 a). *Amphipora* usually occurs scattered throughout the micritic matrix but locally forms also grainstone and rudstone layers (Plate 2.3 b). *Amphipora* floatstones represent the dominant facies type of facies zone IIIb. Bulbous and wavy-laminated stromatoporoid (up to 15 cm in diameter) as well as brachiopods occur in variable proportions. In some places, these organisms appear to be in living position. *Amphipora* rudstone layers and beds dominated by brachiopod shell fragments occur locally. Wackestones and packstones that are almost devoid of macrofossils (except for some fragments of *Amphipora* < 1cm in diameter) and commonly contain irregularly shaped fenestral pores are characteristic of facies zone IIb (Plate 2.3 c). Facies zone Ib is dominated by laminated mudstones to wackestones with abundant fenestral pores that are usually oriented parallel to bedding (Plate 2.3 d).

#### **2.4.4 Facies distribution within the “Massenkalk”**

The facies distribution within the “Massenkalk” for each individual core is given in Appendix 1. The general facies distribution within the Brilon Reef Complex is depicted schematically in Figure 2.4.

##### **2.4.4.1 Fore-reef (facies zones If to IVf)**

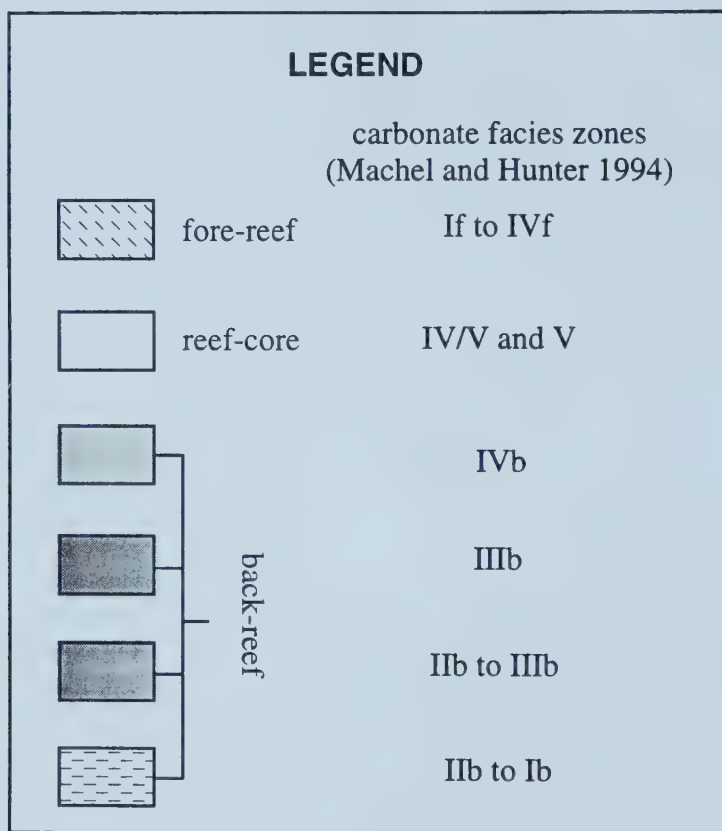
Sedimentary rocks that were deposited in a fore-reef setting occur only in the lower part of the “Massenkalk” in the Brilon 2 and Romberg 1 drill cores at the southern margin of the Brilon Reef Complex (Figure 2.4). In the Brilon 2 drill core, the lower 225 m of the “Massenkalk” are dominated by carbonate breccias in a red calcareous microbreccia matrix with intercalated layers of red, laminated calcareous shale. Breccia components include cm- to dm-sized reef-rock fragments and abundant reef-derived fossil detritus, such as fragments







**Figure 2.4:** Schematic representation of the facies distribution in the Middle and Upper Devonian Brilon Reef Complex along a N-S cross-section (see Figure 2.1) at the end of the Frasnian. The assignment of facies zones follows the facies model for Middle and Late Devonian reef carbonates by Machel and Hunter (1994) (Figure 2.3). For a description of the general stratigraphic succession in the Brilon area, the reader is referred to Chapter 1 (Figure 1.4). See text for further explanation.



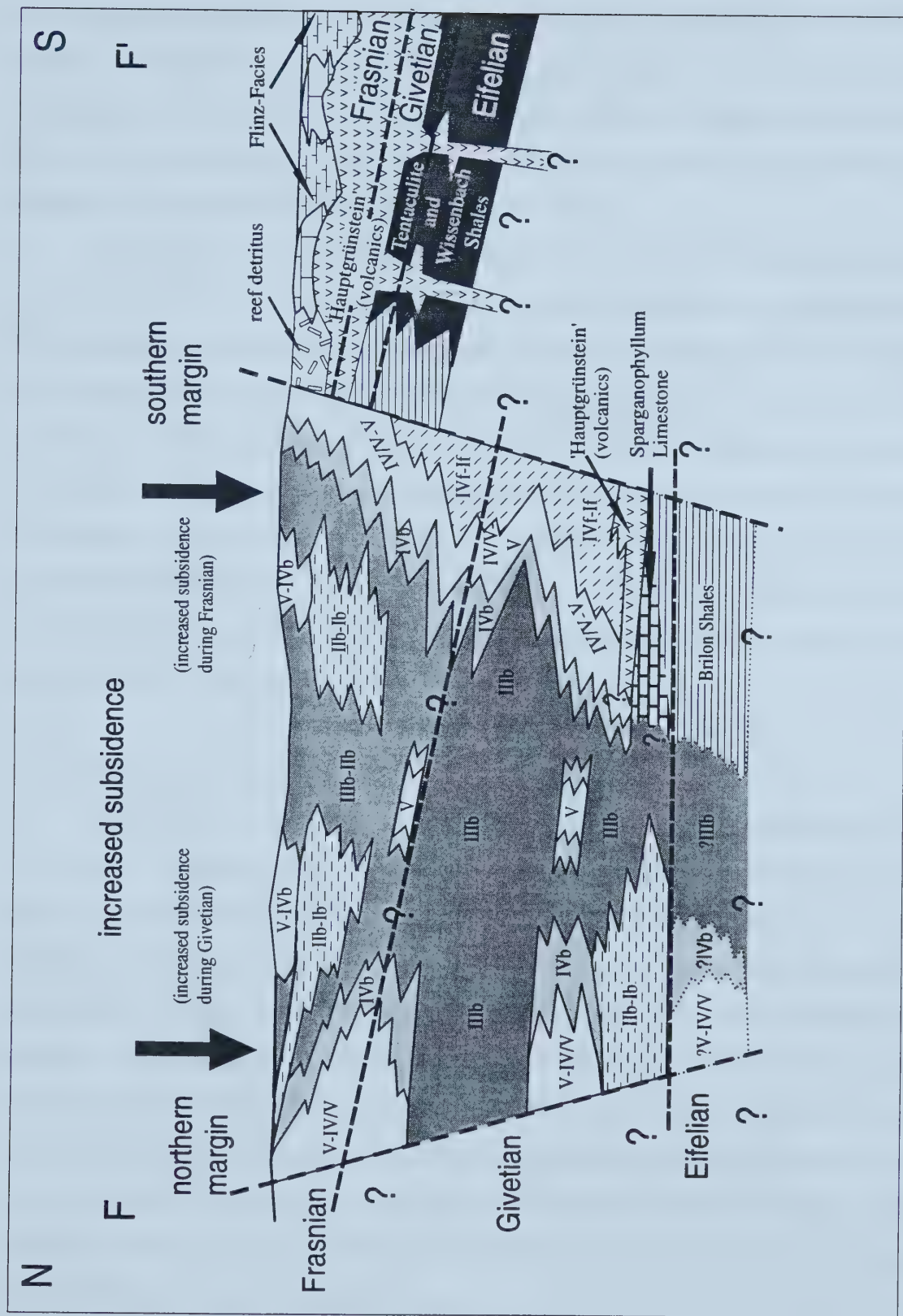


Figure 2.4



of stromatoporoids, tabulate corals, and crinoids. In the microbreccia matrix, fragments of the volcanoclastic material of the “Hauptgrünstein” occur along with mm-sized skeletal detritus (mainly crinoids). Intercalated within these breccias are intervals of crinoid-stromatoporoid floatstones and rudstones (facies zones IIIf and IVf) and stromatoporoid-coral rudstones (facies zones IV/V and V). These carbonate rock types become dominant in the middle part of the drill core (from 303.0 m to 191.8 m).

In the lower part of the Romberg 1 drill core, three breccia intervals similar to those in the Brilon 2 drill core occur between 732.1 m and 633.2 m above the “Hauptgrünstein”. The breccias are interbedded with a succession of crinoid-stromatoporoid-coral floatstones and rudstones (facies zones IIIf and IVf). The recognition of facies types in this interval, however, is difficult because of intense recrystallization and dolomitization. Intervals of facies types of fore-reef character generally occur within the lowermost 500 m of the “Massenkalk” (from 732.1 m to 201.5 m). Generally, intervals that have facies types characteristic of facies zone If and IIIf are relatively rare, whereas facies types that have been assigned to facies zones IIIf and IVf dominate and transitions to facies types indicative of reef-core facies (facies zone IV/V) are common.

#### 2.4.4.2 Reef-core (facies zones IV/V and V)

Three drill cores from the southern margin of the reef complex (Altenbüren 1, Brilon 2, Romberg 1) and one drill core from the northeastern margin (Bleiwäsche 1) contain intervals of reef core facies (facies zones IV/V and V). In the Altenbüren 1 drill core, stromatoporoid framestones and rudstones with *Stachyodes* and *Amphipora* occur in the uppermost 87 m (facies zones V to IVb) overlying *Amphipora* float- and wackestones of the back-reef (facies zone IIIb). In the deeper parts of the Romberg 1 and Brilon 2 drill cores, the alternation between facies types of the fore-reef with those of the reef-core facies is common. At shallower depths, facies types of the reef-core alternate with those of the back-reef facies. In the Bleiwäsche 1 drill core, stromatoporoid framestones and crinoid-stromatoporoid rudstones (facies zones V and IV/V) overly *Amphipora* floatstones and wackestones of the back-reef (facies zones IIIb and IIb).





#### 2.4.4.3 Back-reef (facies zones IVb to Ib)

Facies types that indicate deposition in a back-reef environment predominate in most of the investigated drill cores, except for those which are located on the southern and northeastern margin of the Brilon Reef Complex (see above). Generally, the deeper parts of drill cores from the east-central part of the Brilon Reef Complex are dominated by dark grey, bituminous limestones with variable amounts of biochems floating in a micritic matrix (mostly facies zones IIIb and IVb). Intervals of marly limestones and marls reaching thicknesses between several dm and tens of meters occur locally. In many of these drill cores, light and medium grey limestones are intercalated with dark grey, bituminous limestones. All of these limestones show the same range of textures (mudstones, wackestones, floatstones, rudstones). *Amphipora* floatstones with bulbous and wavy-laminated stromatoporoids, and small tabulate corals represent the most common facies type. Fenestral fabrics, indicative of the peritidal environment of facies zones Ib and IIIb, were observed only in light to medium grey micritic limestones, e.g., in the lower and upper parts of the Loh 1 drill core and in the upper part of the “Massenkalk” in the Madfeld 1 and Romberg 1 drill cores. Intervals of medium and light grey limestones become more abundant and thicker in drill cores located closer to the margins of the reef complex, suggesting lateral transitions between dark grey limestones in the center and medium to light grey limestones at the margins.

#### **2.4.5 Stratigraphic correlation of the investigated drill cores**

##### 2.4.5.1 Biostratigraphy

Biostratigraphic data from the investigated drill cores are rare and insufficient for a confident correlation of the drill cores (Brinckmann 1981). Drill cores from the northern part of the reef complex contain *Stringocephalus burtini* in their deeper sections, indicating a Givetian age for these intervals.

In the lower part of the Blumenstein 1 drill core, which is pervaded by fracture filling breccias, conodont faunas of Late Emsian (at 601 m) and Early to Middle Eifelian age (at 542 m) were found (Brinckmann 1981). Most of the conodont faunas in this part of the core, however, indicate either Frasnian ages or consist of mixtures of elements from Givetian and



Frasnian (locally also Famennian) faunas. A conodont fauna of Late Eifelian/Early Givetian age was reported for a sample from the deepest part of the Loh 1 drill core (at 918 m) (Brinckmann 1981).

The drill cores from the southern margin of the reef complex yielded mostly mixed conodont faunas that were retrieved from Late Devonian and Early Carboniferous fractures (Brinckmann 1981). Conodont faunas of Late Givetian age were reported for samples from the base of the “Massenkalk” above the “Hauptgrünstein” in the Romberg 1 drill core (Machel 1979). All other conodont samples from this core indicate a Middle to Late Devonian age range or represent mixed faunas of Late Devonian to Early Carboniferous age. By projection of the ages of surface samples, Brinckmann (1981) estimated that the position of the Givetian/Frasnian boundary in the Romberg 1 drill core is located probably at a depth of about 450 m. Samples from the Brilon 2 drill core were devoid of conodonts except for two samples from fracture fills at the very top of the drill core (Brinckmann 1981). One sample yielded a conodont fauna of Famennian age, the other one a mixed fauna ranging in age from the Late Eifelian to the Famennian. By analogy with the lower part of the Romberg 1 drill core, the lower part of the Brilon 2 drill core is most likely of Upper Givetian age. Samples of the “Massenkalk” in the Altenbüren 1 drill core contained conodont faunas of Late Givetian age or mixed conodont faunas of Middle and Upper Devonian age (Brinckmann 1981).

In the Nehden 2 drill core, the upper boundary of the “Massenkalk” was dated with conodonts to the Middle Frasnian (Brinckmann 1981). The overlying nodular limestones are of Late Frasnian age and are followed by Famennian cephalopod-bearing marls (Brinckmann 1981).

#### 2.4.5.2 Lithostratigraphy

Brinckmann (1981) used the upper boundary of the dark grey lagoonal limestones as a lithostratigraphic marker in the northeastern part of the reef complex. Furthermore, he suggested that intervals of marly limestones and marls within these dark grey limestones may be useful for correlation of the wells in this area. Although the wells are relatively closely spaced, well correlation is complicated by (1) lateral changes in lithofacies, and (2) faults.



As already pointed out above, the dark grey lagoonal limestones (dominantly facies zones IIIb and IVb) interfinger laterally with medium and light grey lagoonal limestones (dominantly facies zones IIIb to Ib). Likewise, the number and thicknesses of intervals of marly limestones and marls vary from drill core to drill core, which prevents the utilization of these intervals as stratigraphic markers. Synsedimentary fault movements, as suggested by Bär (1966), Wahba (1978), and Werner (1990) for some of the NNW-SSE trending faults (e.g., the Immental, Romberg, Brilon, and Altenbüren Faults) (Figure 2.1), also may have contributed to rapid lateral facies changes. Furthermore, Variscan (thrust) and post-Variscan (normal) faults that can be traced at the surface (Figure 2.1; Wahba 1978; Brinckmann et al. 1989) very likely caused significant displacements, that, however, cannot be quantified without a detailed stratigraphic correlation.

The “Massenkalk” in the Brilon 2 and Romberg 1 drill cores from the southern margin of the reef complex is underlain by and interfingers with volcanoclastics of the “Hauptgrünstein”. There is, however, no clear evidence that the volcanoclastics in both locations were deposited during the same volcanic event, especially when considering that the duration of the volcanic activity in the area lasted from the Late Givetian to the Early Frasnian (Stritzke 1983), and considering the lateral distance of 5 km between the two wells. Outcrop studies have shown that the thickness and lateral extent of the “Hauptgrünstein” vary considerably over short distances, depending on the distance from individual eruption centers (Sunkel 1992). This is confirmed by the observation that no deposits of volcanic origin were encountered in the Altenbüren 1 well, which is located 3 km east of the Brilon 2 well and extends from Upper Givetian “Massenkalk” down to the Eifelian Brilon Shales. Hence, the volcanics cannot be used for stratigraphic correlations either.

Gamma-ray logs were available for most of the investigated wells (see Appendix 1), and were compared to the macroscopic descriptions from core logging. In the investigated drill cores, the excursions of the gamma-ray curve generally coincide with changes in lithology, i.e., shale versus limestone. However, characteristic gamma-ray patterns that are needed for stratigraphic correlation could not be identified at the scale that this study was carried out. This is attributed to the effects of post-sedimentary processes, such as (1) fracturing and subsequent introduction of sediments, which in many places consist of fine-





grained, clay-rich material, into the fractures; (2) tectonic deformation, that resulted in displacements within the sedimentary succession; (3) mineralization, that introduced new mineral material; and (4) karst. In many cases, excursions of the gamma-ray curve coincide with the position of clay-filled fractures and karst cavities, especially in the uppermost 50 to 100 m of most drill cores (see Appendix 1).

#### **2.4.6 General trends in facies development**

The investigation of the carbonate facies and stratigraphy of the drill cores resulted in the recognition of general trends in facies development of the Brilon Reef Complex (Figure 2.4), that mostly confirm the results of previous studies (Brinckmann 1981; Machel 1979, 1990a; Moritz 1983; Hong 1992; Wizisk 1995).

In the northern part, the beginning of carbonate sedimentation cannot be determined because no well penetrated the lower boundary of the “Massenkalk”. At the locations of the Loh 1 and Blumenstein 1 wells, sediments of back-reef character (facies zones IIIb to Ib) were deposited on the shelf as early as the Early Middle Devonian (Eifelian), while in the southern part (Altenbüren 1, Brilon 2), fossil-poor shales and marls of the Brilon shales were deposited at the shelf margin. The Givetian *Sparganophyllum* limestone (Altenbüren 1, Brilon 2) represents a first phase of biostromal reef growth in the southern part of the area (Müller 1990; Errenst 1993) while carbonate accumulation in the northern part continued with deposits of back-reef character. Krebs (1968) interpreted the *Sparganophyllum* limestone as being equivalent to the lowermost part of the “Massenkalk”. This interpretation appears to be correct for the southern part of the area, where the *Sparganophyllum* limestone underlies the “Hauptgrünstein” (Brilon 2) and “Flinz-facies” (Altenbüren 1). In the northern part of the area, however, the sediments time-equivalent to the *Sparganophyllum* limestone probably do not occur at the base but somewhere within the lower part of the “Massenkalk”.

In most of the drill cores from the central and northern part of the reef complex, dark to light grey carbonates of back-reef character predominate. The widespread occurrence of the brachiopod *Stringocephalus burtini* is evidence that most of these carbonates were deposited during the Givetian. After the disappearance of *Stringocephalus burtini*, a shift from subtidal facies zones (IVb and IIIb, predominantly dark grey limestones) to peritidal



facies zones (IIb and Ib, predominantly medium to light grey limestones) occurred. This facies shift has also been determined in drill cores where *Stringocephalus burtini* was not observed (e.g., Madfeld 1, Thülen 2, Immental 2).

Petrographically, the light grey limestones correspond to the “reef-type Massenkalk” or “Dorp facies” of Krebs (1968) and the dark grey bituminous limestones correspond to the “bank-type Massenkalk” or “Schwelm facies” of Krebs (1968). In their original definition, the terms “Schwelm facies” and “Dorp facies” were used in a stratigraphic sense, with the “Schwelm facies” always underlying the “Dorp facies” (Krebs 1968). Within the Brilon Reef Complex, however, this relationship does not completely hold true (see also Brinckmann 1981; Moritz 1983; Hong 1992; Wizisk 1995). For example, the Loh 1 well penetrated light and medium grey lagoonal limestones (dominantly facies zones IIb and Ib) underlying dark grey bituminous limestones (dominantly facies zone IIIb). The petrographic and paleontological characteristics of the dark grey bituminous limestones are generally consistent with their formation on a subtidal carbonate platform or ramp as well as their deposition in a lagoon behind a reef barrier (Hong 1992; Wizisk 1995). Also, the presence of reef core facies at the southern and northeastern margins of the reef complex, the intercalation of dark grey and light to medium grey limestones, and the increasing proportion of medium to light grey limestones from the center toward the margins, support the interpretation that the major portion of the dark grey bituminous limestones formed contemporaneously with the medium to light grey limestones, most likely in a large subtidal lagoon or interior platform behind a platform margin that was, at least on its southern and northeastern side, rimmed by reefs.

Reef growth at the southern margin started in the Late Givetian and ended in the Late Frasnian (Stritzke 1983). At the locations of the Brilon 2 and Romberg 1 wells, a general succession from fore-reef through reef-core to back-reef sedimentation is developed, indicating a progradational character of reef development as described by Machel (1979) and Moritz (1983). The timing of these facies changes in these drill cores is poorly constrained. The transition from the fore-reef dominated older part to the back-reef dominated younger part of the succession in these drill cores, however, may correspond to the facies shift from predominantly subtidal to predominantly peritidal facies zones observed in drill cores from



the central and northern part of the reef complex, and therefore may be useful as a stratigraphic marker for correlation across the reef complex. Unfortunately, the scale at which the drill cores were logged for this study does not provide a high enough resolution to prove this hypothesis.

Drowning as the major cause for the termination of reef growth in the Late Frasnian is indicated by the transition from peri- and subtidal back-reef deposits to open- marine nodular limestones and cephalopod-bearing marls in the Nehden 2 drill core. Similar successions have been described from other wells that penetrated the transition from “Massenkalk” to the overlying Upper Devonian sediments (Brinckmann 1981; Wizisk 1995).

## **2.5 General diagenetic framework**

The post-sedimentary history of the Middle and Upper Devonian carbonates of the Brilon Reef Complex has been recognized to consist of 5 stages (Figure 2.5; Machel 1990b). Stages I to III occurred prior to the Variscan deformation and include synsedimentary early diagenesis (Stage I), diagenesis under a thin sedimentary cover (30 to 150 m) (Stage II), and diagenesis during increasing burial (Stage III). Considering the thickness of the “Massenkalk” of probably close to 1000 m, carbonate sediments were still being deposited at the surface while diagenetic processes of stages I, II, and III were active contemporaneously at different levels in the deeper parts of the sedimentary succession (Machel 1990b). Definite time markers during the pre-Variscan diagenesis are provided by fractures that can be dated by externally derived, younger sediments (Brinckmann 1981; Machel 1990b). Fabrics indicative of mechanical deformation of the Variscan Orogeny (Stage IV) can be used as a time marker to distinguish pre-Variscan from syn- to post-Variscan phases. Textures that cross-cut these fabrics resulted from processes that post-date the Variscan deformation and are grouped in Stage V.







**Figure 2.5:** Succession of post-sedimentary textural and/or mineralogical changes of the Middle and Upper Devonian “Massenkalk” in the Brilon Reef Complex. Data for pre-Variscan diagenesis (phase 1 to 18) are from Machel (1979, 1990b), data for phases 19 to 25 are from this study.

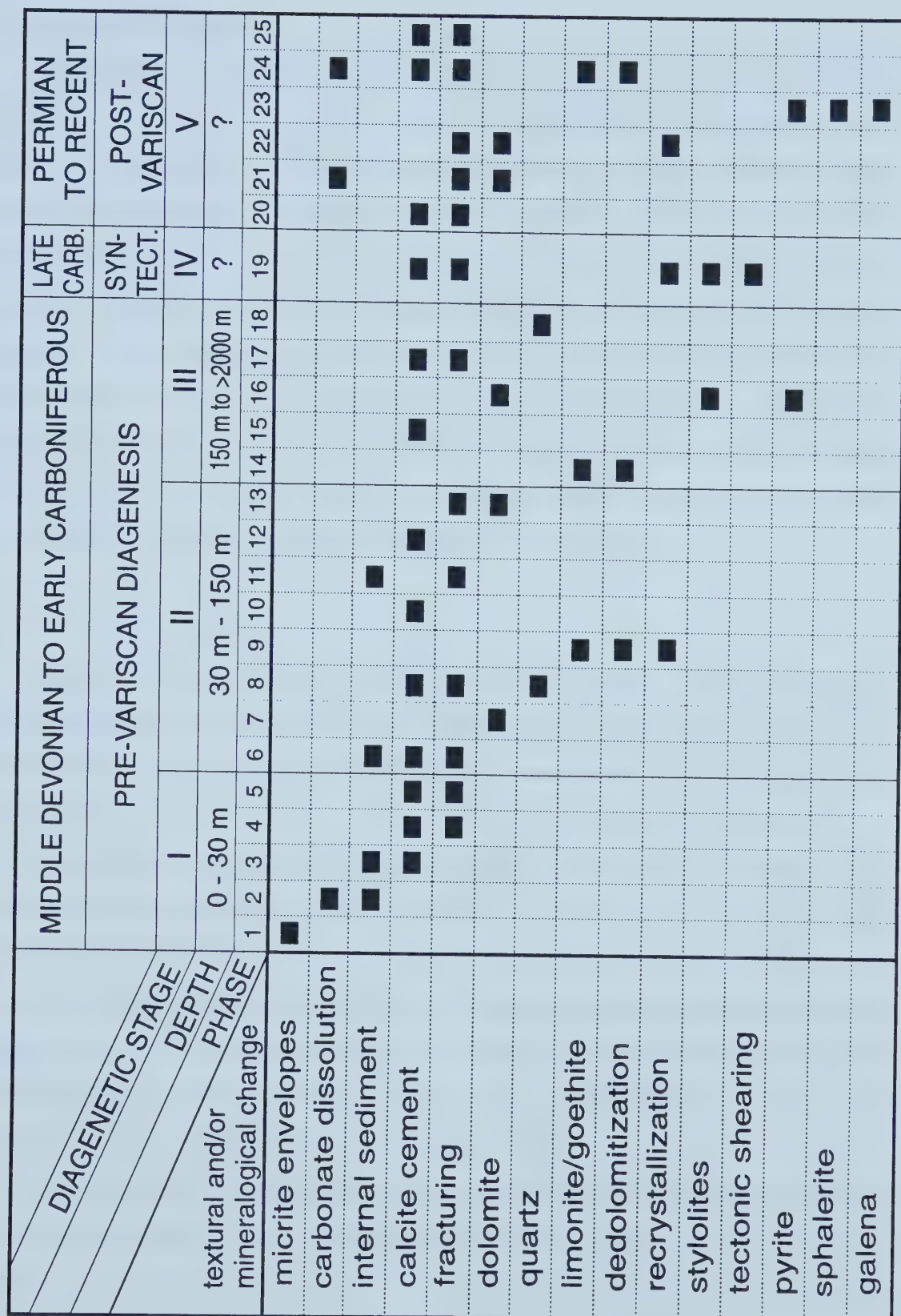


Figure 2.5



### ***2.5.1 Pre-Variscan diagenesis***

The succession of pre-Variscan diagenetic events (stages I to III) in the Brilon Reef Complex has been discussed in detail by Machel (1979, 1990b) and is schematically shown in Figure 2.5. Machel (1979, 1990b) identified 18 distinct pre-Variscan diagenetic phases, including three phases where dolomitization occurred (phases 7, 13, and 16; Figure 2.5). Dolomitization in phases 7 and 13 is associated with fracture-filling sediments of Upper Devonian (Cephalopod limestone) and Lower Carboniferous (Erdbach Limestone) age, respectively. Dolomitization in phase 16 is mainly restricted to stylolites (Machel 1979, 1990b). Small volumes ( $< 1$  vol.-%) of these pre-Variscan dolomites have been identified in all of the investigated drill cores in this study. They usually occur as scattered dolomite rhombs and rarely form larger mosaics. In comparison with dolomites formed during later phases, the pre-Variscan dolomites are volumetrically insignificant.

### ***2.5.2 Variscan deformation***

During the Variscan Orogeny (stage IV, phase 19), a number of fabrics indicative of mechanical deformation developed within the Middle and Upper Devonian “Massenkalk” of the Brilon Reef Complex (Machel 1979, 1990). On a large scale, the “Massenkalk” forms broad SW-NE trending folds which are further structured by thrust faults (Figure 2.1).

Macroscopic fabrics that developed in response to mechanical deformation during the Variscan Orogeny are relatively rare. They include, (1) deformed sutured stylolites (Plate 2.4 a); (2) tectonically oriented and strained fossils (Plate 2.4 b); (3) vertical stylolites (Plate 2.4 c); and shear zones (Plate 2.4 d). Furthermore, Variscan tectonic deformation led to the recrystallization of some of the Devonian carbonates, e.g., the lowermost 200 m of the “Massenkalk” of the Romberg 1 drill core, resulting in the partial obliteration of sedimentary and diagenetic textures (Machel 1979, 1990; Moritz 1983).

Most of the investigated drill cores contain intervals that are intensively fractured and locally brecciated. Fractures and post-sedimentary breccias are generally cemented by coarse-crystalline milky-white calcite, except for syn-sedimentary breccias (e.g., lower part of “Massenkalk” in Brilon 2 drill core), fractures filled with internal sediments, and dolomitized







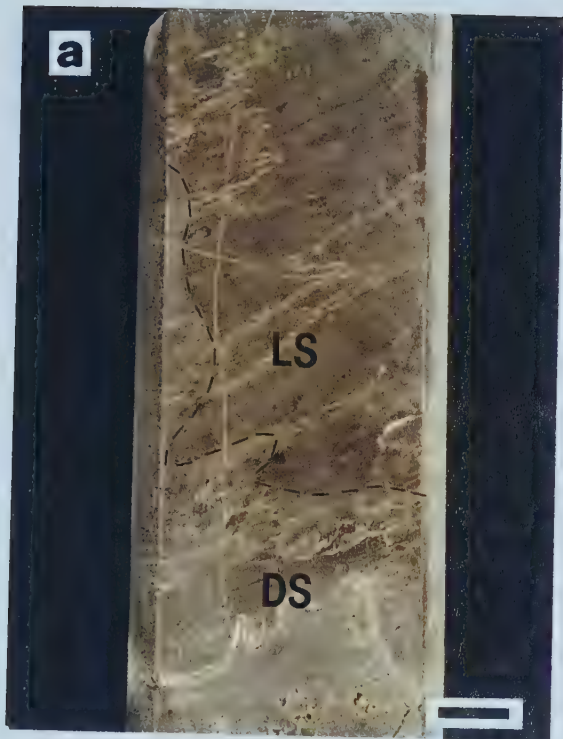
**Plate 2.4:** Fabrics indicative of mechanical deformation during the Variscan Orogeny (phase 19).

**Plate 2.4a:** Deformed sutured stylolites (phase 19) in *Amphipora* wackestone to floatstone (facies zone IIIb) cross-cut by thin subvertical and subhorizontal, undeformed calcite veins (phase 20). In the lower part of the core slab, dolomitization of phase 21 (dolomite Type 1) overprinted deformed stylolites and subvertical calcite vein. Dashed line indicates outline of dolomitization front (LS = limestone, DS = dolostone). Madfeld 1 (M1) drill core, depth 338.5 m. Scale bar = 1 cm.

**Plate 2.4b:** Tectonically oriented and elongated stromatoporoids (probably *Amphipora*) in stromatoporoid floatstone (facies zone IIIb). Almerfeld (AL) drill core, depth 622.0 m. Scale bar = 1 cm.

**Plate 2.4c:** Vertical stylolite (phase 19) with dark residual clay (arrows) in poorly fossiliferous wackestone (facies zone IIb). Auf dem Loh 1 (L1) drill core, depth 674.1 m. Scale bar = 1 cm.

**Plate 2.4d:** Subhorizontal shear zone (phase 19) with white calcite replacing limestone wall rock. Madfeld 1 (M1) drill core, depth 328.1 m. Scale bar 1 cm.







intervals. Milky-white calcite occurs almost throughout most of the paragenetic sequence (Figure 2.5) and cannot be used in isolation to determine the timing of the preceding fracturing or brecciation.

### ***2.5.3. Post-Variscan textural and mineralogical changes***

The post-Variscan history of the Middle and Upper Devonian carbonates of the Brilon Reef Complex is characterized by the reactivation of the NNW-SSE trending normal faults during several tectonic phases in the time period from the Jurassic to the Tertiary (Schaeffer 1986). These faults cross-cut the Variscan folds and thrust faults and presently subdivide the reef complex into a series of fault blocks (Chapter 1; Figure 2.1). Due to the stratigraphic uncertainties, the amounts of throw of these faults are not exactly known. The total vertical throw at the Altenbüren Fault (Figure 2.1) has been estimated to amount to approximately 500 m (Bär 1968; Brinckmann 1981). Schriel (1954) estimated the amount of post-Variscan vertical throw of the Immental Fault to be 100 to 200 m.

Post-Variscan textural and mineralogical changes in the “Massenkalk” of the Brilon Reef Complex were manifold and include repeated fracturing, carbonate cementation, dolomitization, and minor base metal sulfide mineralization (pyrite/marcasite, sphalerite, galena) (Brinckmann 1981; Moritz 1983; Schaeffer 1986; Machel 1990b). In the investigated drill cores, dolomitization crosscuts bedding-planes, pre-Variscan diagenetic textures (such as subhorizontal stylolites), and textures indicative of the Late Carboniferous Variscan deformation (see above; Plate 2.4), and is generally related to fractures. The succession of post-Variscan textural and mineralogical changes that were identified during core logging and subsequent petrographic investigation of samples from the dolomitized intervals is schematically shown in Figure 2.6 and described in detail below.

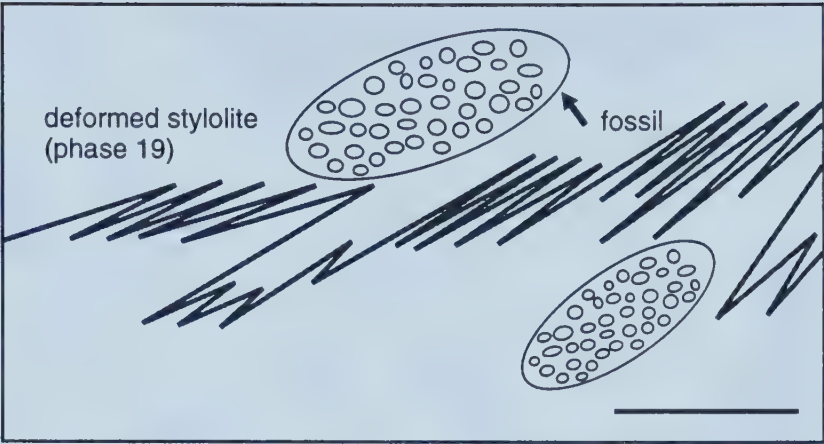






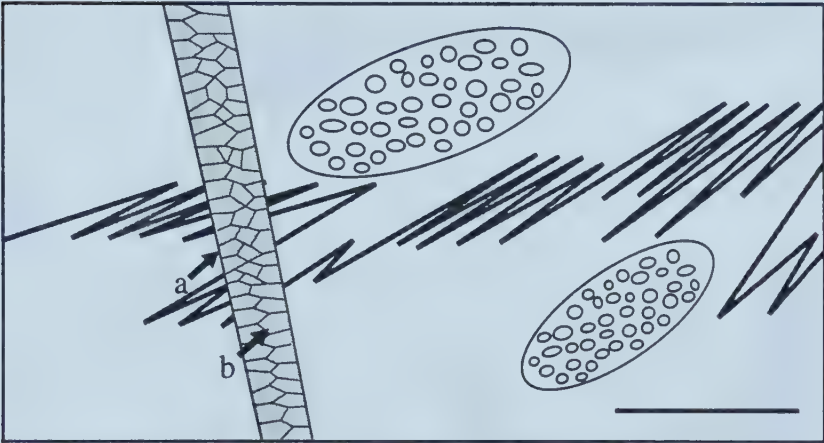
**Figure 2.6 a-g:** Schematic representation of the post-Variscan paragenetic succession in the Brilon Reef Complex based on petrographic observations of samples from dolomitized intervals. Scale bar = 1 cm. See text for further explanation.

**Figure 2.6 a:** Phase 19:  
Precursor limestone  
(*Amphipora* floatstone)  
with stylolite deformed  
during the Variscan de-  
formation.



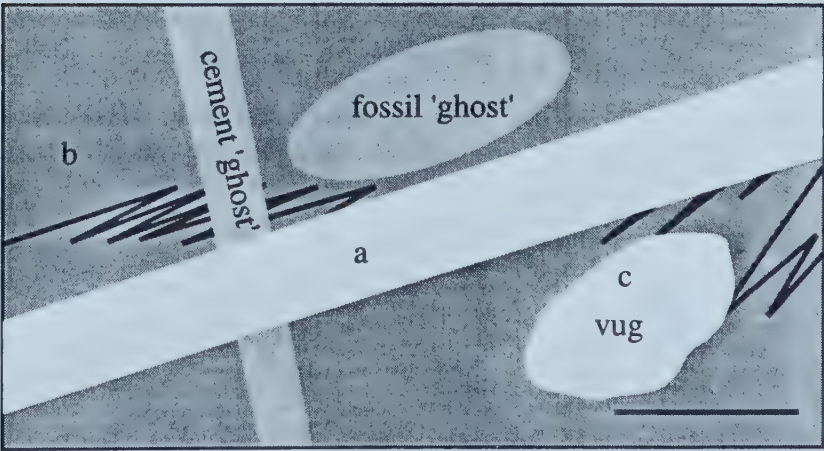
**Figure 2.6 b:** Phase 20:

- (a) fracturing
- (b) scalenohedral calcite



**Figure 2.6 c:** Phase 21:

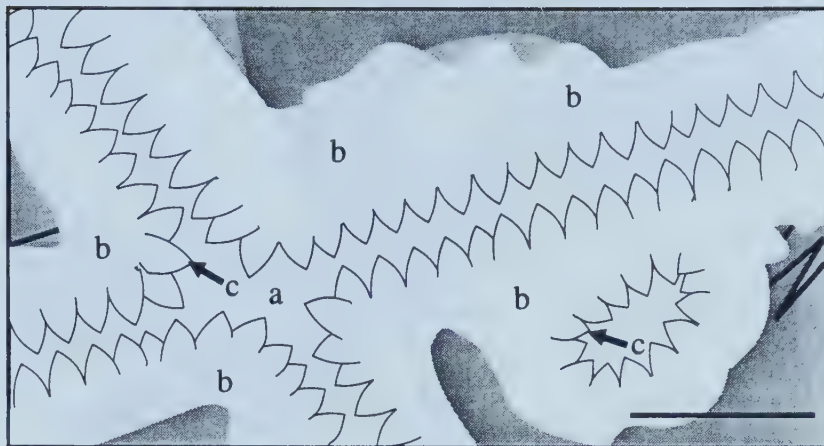
- (a) fracturing
- (b) dolomite Type 1
- (c) calcite dissolution





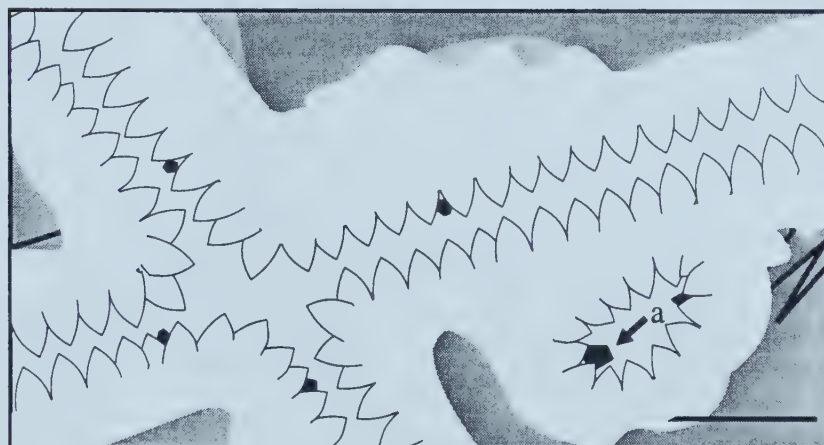
**Figure 2.6 d: Phase 22:**

- (a) fracturing
- (b) dolomite Type 2  
(recrystallization of  
Type 1)
- (c) dolomite Type 3



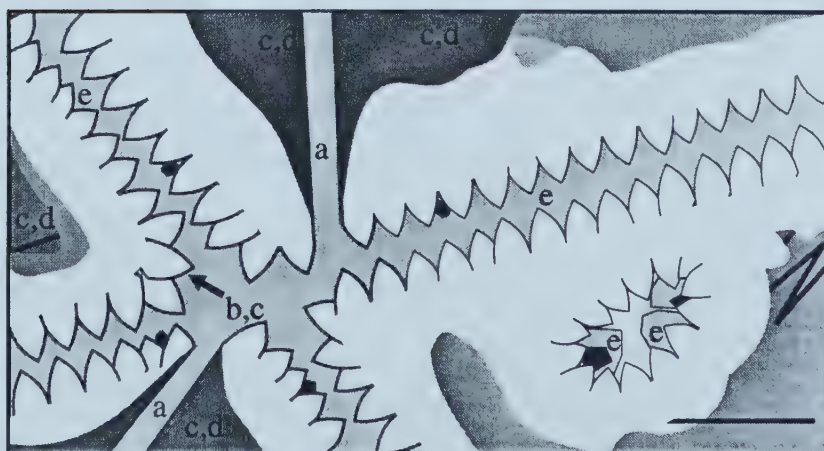
**Figure 2.6 e: Phase 23:**

- (a) base metal sulfides  
(galena, sphalerite,  
pyrite)



**Figure 2.6 f: Phase 24:**

- (a) fracturing
- (b) dolomite dissolution
- (c) limonite/goethite
- (d) calcitization
- (e) calcite cementation

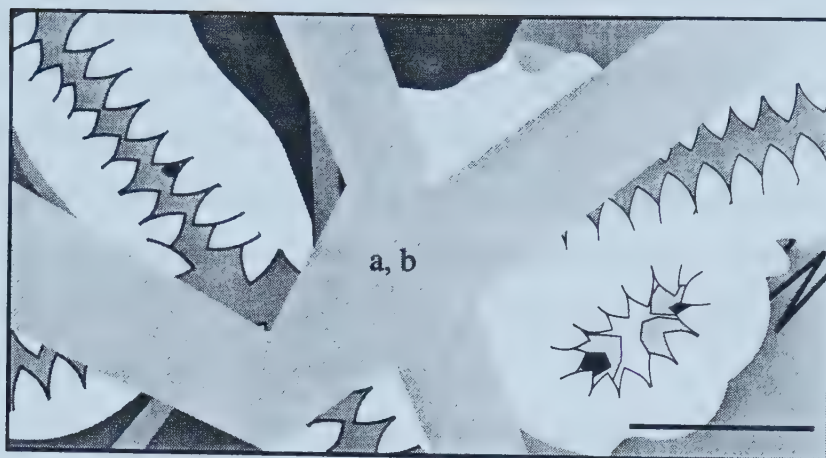






**Figure 2.6 g: Phase 25:**

- (a) fracturing
- (b) calcite cement





#### 2.5.3.1 Phase 20: fracturing and scalenohedral calcite cement

The oldest post-Variscan textural features are calcite-filled fractures (Figure 2.6 b, Plate 2.4 d). In drill core, the fractures seem to be evenly distributed yet randomly oriented and fracture widths range from 0.2 cm to several dm. The fracture-filling calcite cement is milky-white or slightly pink in color. In cases, where crystals grew freely into the fracture space they exhibit a scalenohedral habit. This calcite cement is iron-poor (red color when stained; orange CL) and crystal-sizes range from 100  $\mu\text{m}$  to 2 cm.

This calcite corresponds to the scalenohedral calcite “Wülfrath” of Moritz (1983) and Schaeffer (1984, 1986), that occurs in veins oriented parallel to the NNW-SSE trending post-Variscan normal faults. Its timing is constrained by two lines of evidence: (1) the beginning of intense regional extensional tectonics in the Late Jurassic to Early Cretaceous (Murawski et al. 1983), and (2) the occurrence of Early Cretaceous terrestrial sediments in a karst cavity that cross-cuts a vein of this calcite at the surface (Moritz 1983). Thus, this calcite is most probably Late Jurassic in age.

#### 2.5.3.2 Phase 21: fracturing, dolomitization (dolomite Type 1), calcite dissolution

Although direct evidence is missing, a phase of fracturing probably preceded the formation of dolomite Type 1 (Figure 2.6 c). This claim is supported by the observation that (1) dolostone (phase 21) is confined to the direct vicinity of fractured and brecciated intervals, and that (2) the subsequent, clearly fracture-controlled dolomite types 2 and 3 (phase 22) occur exclusively within the dolostone intervals (see below). This suggests that at least some of the fractures provided pathways for dolomitizing fluids in phase 21 and 22.

Dolomite Type 1 is a fine-crystalline 'grey matrix dolomite' (Plate 2.4 a, Plate 2.5 a, b) with small intercrystal pores, replacing limestone, in some places in a fabric-retentive manner. Generally, its color ranges from dark to light grey, depending on the content of organic matter and clay minerals of the precursor limestone. In those intervals where a hematite-rich red matrix of pre-Variscan breccias was dolomitized (e.g., Brilon 2, Romberg 1, Blumenstein 1), dolomite Type 1 has a red color. It also occurs as replacement of fossil fragments (Plate 2.5 a) and older calcite cements (Figure 2.6 c). In these cases, primary microstructures of the fossil material as well as petrographic characteristics of the calcite







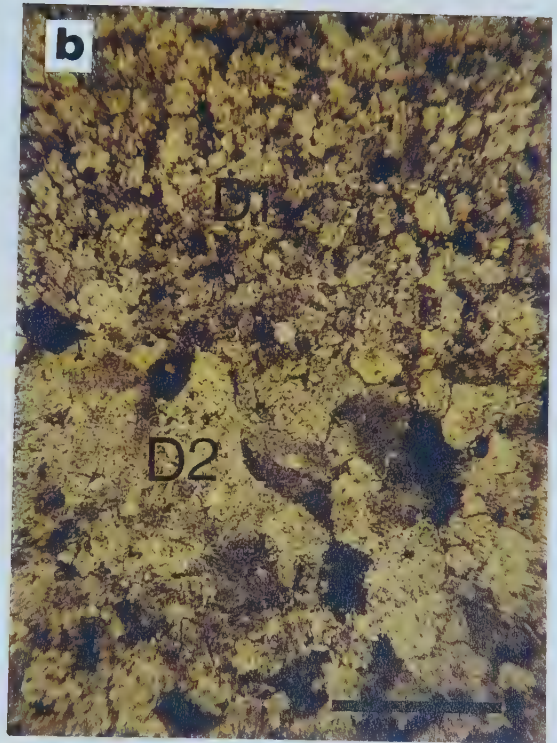
**Plate 2.5:** Post-Variscan textural and mineralogical changes.

**Plate 2.5a:** Core photograph of dolomitized stromatoporoid (?*Amphipora*) floatstone (facies zone IIIb). Dolomite Type 1 (D1) replaced grey matrix and fossils, dolomite Type 2 (D2), originated at subhorizontal fracture at bottom and invaded D1, preferentially where D1 has replaced fossils.

**Plate 2.5b:** Photomicrograph of transition between planar to nonplanar dolomite Type 1 (D1) and nonplanar dolomite Type 2 (D2). Transmitted light; crossed polars. Auf dem Loh 7 (L7), depth 302.5 m. Scale bar = 500  $\mu\text{m}$ .

**Plate 2.5c:** Same as Plate 2.5b, but under CL light. Dolomite Type 1 and Type 2 both show mottled red CL color.

**Plate 2.5d:** Photomicrograph of dolomite Type 2 showing zonation into darker red and lighter red zones under CL light in an area where dolomitized fossil was recrystallized. Auf dem Loh 1 (L1) drill core, depth 576.8 m. Scale bar = 500  $\mu\text{m}$ .





cements that could have been used for their identification have been completely obliterated, resulting in “ghost” structures (Figure 2.6 c). Locally, especially close to the margins of a dolostone interval, fossils are preserved as calcite, but have lost their primary microstructures as a result of recrystallization.

In thin section, dolomite Type 1 appears as planar to nonplanar mosaics of fine- to coarse-crystalline ( $< 50 - 300 \mu\text{m}$ ), sub- to anhedral dolomite crystals (Plate 2.5 b). Cathodoluminescence is mottled red (Plate 2.5 c). Dolomite Type 1 could be identified in almost all of the investigated dolostone intervals.

In some dolostone intervals, a vuggy porosity is developed within dolomite Type 1 (Figure 2.6 c), resulting from the dissolution of calcitic components (probably fossils). The fact that these vugs are restricted to the dolomitized intervals indicates that calcite dissolution took place during and/or after replacement of the limestone by dolomite Type 1.

#### 2.5.3.3 Phase 22: fracturing, dolomite recrystallization (dolomite Type 2), dolomite cementation (dolomite Type 3)

Irregular fractures, ranging in width from several mm to several cm, pervade dolomite Type 1, locally resulting in a breccia-like texture (Plate 2.6 a). At least some of these fractures probably had already formed in phase 21 and provided pathways for dolomitizing fluids that resulted in the formation of dolomite Type 1. Originating from these fractures and from vugs that formed as a result of carbonate dissolution during phase 21, a generally coarse-crystalline ( $< 3 \text{ mm}$ ), milky-white to tan, in some places pinkish, fabric-destructive dolomite (Type 2) occurs as cm- to m-wide halos within dolomitized (Type 1) areas. This suggests that dolomite Type 2 formed via recrystallization of dolomite Type 1.

Dolomite Type 2 appears as nonplanar mosaics of coarse to very coarse-crystalline ( $300 \mu\text{m} - 3 \text{ mm}$ ), sub- to anhedral crystals (Plate 2.5 b). This type is also present where fossils have not been leached but replaced by dolomite Type 1 (Plate 2.5 a). Type 2 usually is almost devoid of visible intercrystal porosity. Some crystals exhibit sweeping extinction in polarized light. The lower crystal size limit of  $300 \mu\text{m}$  seems to correspond with a change in color from grey to milky-white and coincides with the macroscopic boundary between







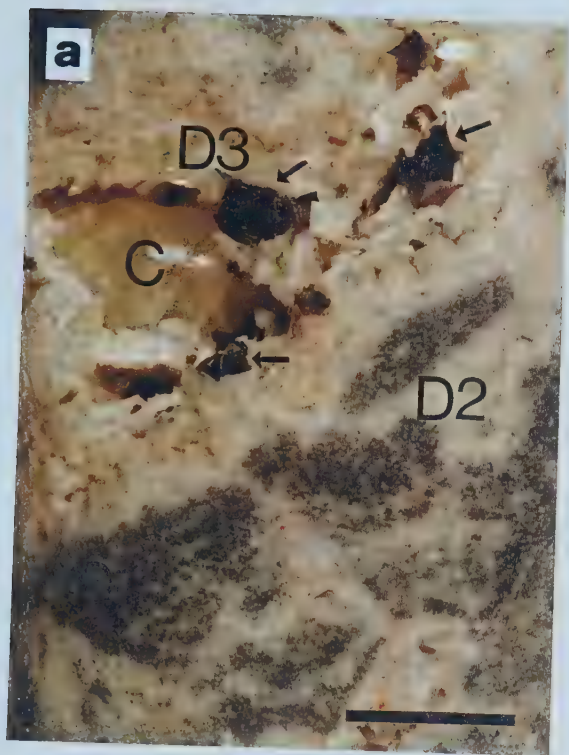
**Plate 2.6:** Post-Variscan textural and mineralogical changes.

**Plate 2.6a:** Core photograph of dolostone, showing relics of dolomite Type 1 (D1; phase 21), strongly invaded by dolomite Type 2 (D2; phase 22), which originates at irregular fractures (phases 21 and 22) and open vugs (phase 21). These fractures and vugs are lined or completely filled by dolomite Type 3 (D3; phase 22), followed by sphalerite (arrows; phase 23) and translucent calcite cement (C; phase 24). Almerfeld (AL) drill core, depth 713.8 m. Scale bar = 1 cm.

**Plate 2.6b:** Photomicrograph depicting dolomite Type 3 (D3; phase 22) with curved crystal faces and sweeping extinction followed by translucent calcite cement (C; phase 24). Transmitted light, crossed polars. Auf dem Loh 7 (L7) drill core, depth 384.6 m. Scale bar = 500  $\mu\text{m}$ .

**Plate 2.6c:** Same as Plate 2.6b, but under CL light. Dolomite Type 3 has mottled red CL-color and exhibits a thin rim with an alternation of red and dull red zones. Subsequent calcite cement has orange CL-color. Rim of dolomite Type 3 is slightly corroded in some places (arrows). Scale bar = 500  $\mu\text{m}$ .

**Plate 2.6d:** Photomicrograph showing CL-zonation of the rim of dolomite Type 3 (arrow). Auf dem Loh 1 (L1) drill core, depth 576.8 m. Scale bar = 500  $\mu\text{m}$ .





Type 1 and 2. Due to the difference in color, boundaries to Type 1 are clearly visible but often appear slightly diffuse. Similar to Type 1, Type 2 generally shows a mottled red CL (Plate 2.5 c). In some samples where dolomitized fossils were recrystallized, it exhibits an alternation of darker and lighter red concentric zones (Plate 2.5 d).

Dolomite Type 3 is commonly present as milky-white to tan dolomite cement that either lines the walls of the fractures and vugs or fills them completely (Plate 2.6 a), thereby partially or completely occluding the pre-existing fracture and vuggy porosity. This dolomite type is characterized by very coarse-crystalline (800  $\mu\text{m}$  - 5 mm), euhedral to subhedral dolomite crystals with curved crystal faces and sweeping extinction (Plate 2.6 b, c). These petrographic characteristics identify Type 3 as saddle dolomite (Radke and Matthis 1980). Transitions to Type 2 are almost impossible to determine with the naked eye due to the similarities in color and crystal size. Type 3 generally has a mottled red CL-color but in some cases exhibits a zonation from a mottled red core to a rim consisting of an alternation of thin zones of darker and lighter red (Plate 2.6 c, d).

#### 2.5.3.4 Phase 23: base metal sulfides

Within many of the dolomitized intervals, precipitation of dolomite Type 3 was followed by minor base metal sulfide precipitation (generally < 1 vol. % over any 1 m-core interval) (Figure 2.6 e). Macroscopically and microscopically, pyrite, sphalerite, and galena are common (Plate 2.6 a, Plate 2.7 a-d). Pyrite occurs in the form of small (< 500  $\mu\text{m}$ ) crystals, with ideal crystal shapes, as well as in the form of irregular masses that can reach dimensions of several mm. Sphalerite is present as translucent, honey-colored, tetrahedral crystals up to 4 mm in diameter (Plate 2.6 a, Plate 2.7 a). Galena crystals usually exhibit a cubic habit and reach sizes of up to 1 cm (Plate 2.7 d). All sulfides overgrow dolomite of Phase 22.

Sphalerite and galena have also been described from Lower Cretaceous sandstones in the eastern part of the Brilon Reef Complex (Figure 2.1) (Schriel 1954; Brinckmann 1981; Schaeffer 1984, 1986), indicating that sulfide mineral formation post-dated the deposition of these sandstones. According to Schaeffer's (1984, 1986) investigation of the post-Variscan paragenetic succession of mineralization in the northeastern Rhenish Schiefergebirge,









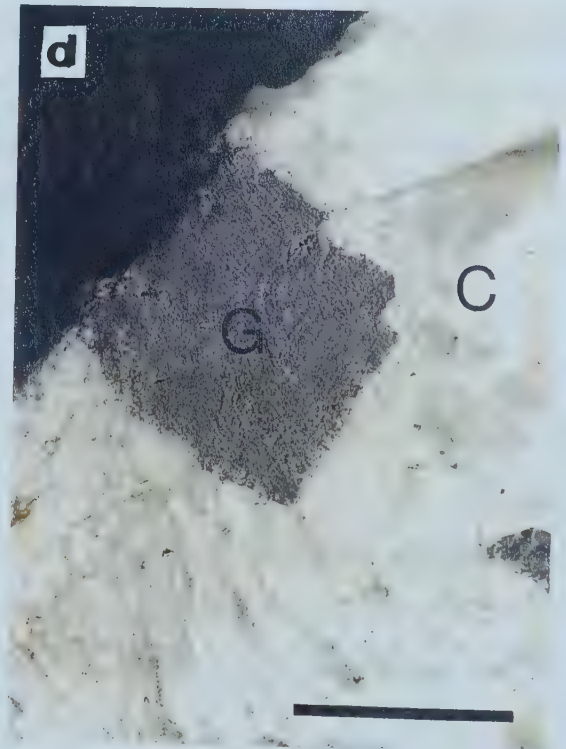
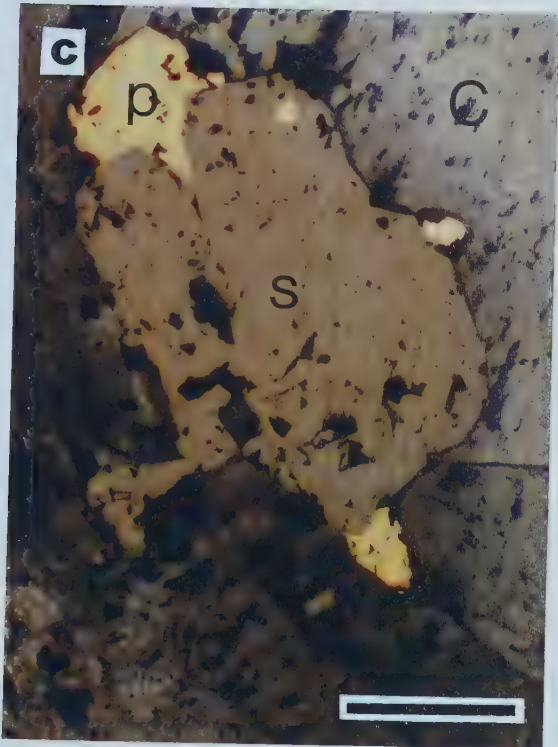
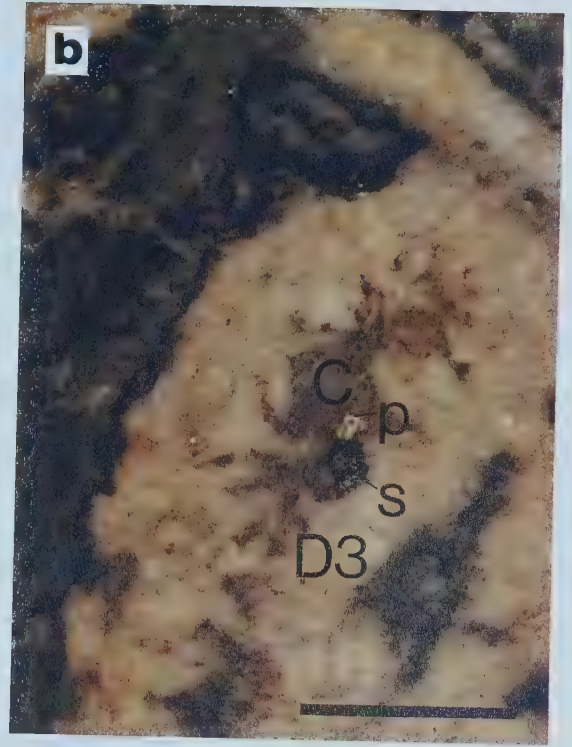
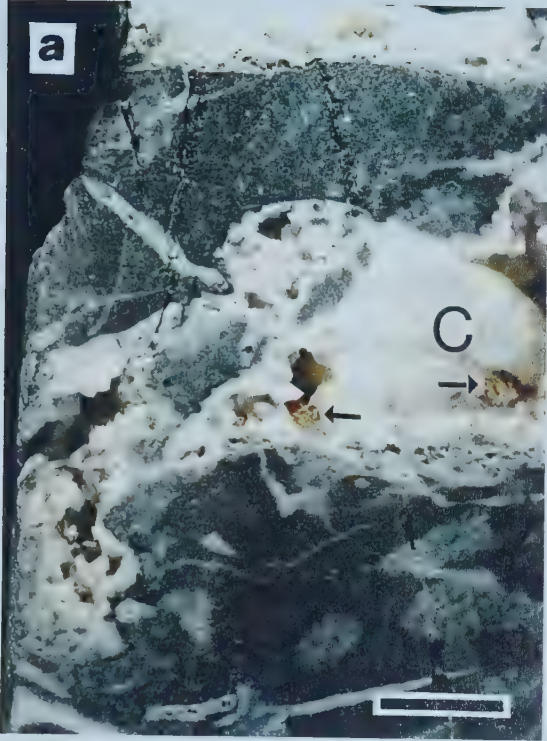
**Plate 2.7:** Post-Variscan textural and mineralogical changes.

**Plate 2.7a:** Core photograph of dolomitized stromatoporoid floatstone with honey-colored sphalerite (arrows; phase 23) following dolomite Type 3 in open vugs. Translucent to white calcite cement (C; phase 24) partially fills remaining vug space. Almerfeld (AL) drill core, depth 726.2 m. Scale bar = 1 cm.

**Plate 2.7b:** Core photograph of dolostone with sphalerite (s) and pyrite (p) (both phase 23), following dolomite Type 3 (D3; phase 22). Translucent calcite (C) fills remaining vug space. Auf dem Loh 1 (L1) drill core, depth 263.4 m. Scale bar = 1 cm.

**Plate 2.7c:** Thin section micrograph of sphalerite (s) and pyrite (p) (both phase 23) following dolomite Type 3 (lower left; phase 22). Remaining void space filled by translucent calcite (C). Reflected light. Almerfeld (AL) drill core, depth 713.8 m. Scale bar = 500  $\mu\text{m}$ .

**Plate 2.7d:** Core photograph of cubic galena crystal (G; phase 23) followed by white to translucent calcite (C; phase 24 or 25). Auf dem Loh 1 (L1), depth 372.5 m. Scale bar = 1 cm.





sphalerite formed during the Early Tertiary (Eocene to Early Miocene).

#### 2.5.3.5 Phase 24: fracturing, dolomite dissolution, calcitization, calcite cementation

Randomly oriented fractures, ranging in width from a few mm to several cm, crosscut most of the dolomitized intervals (Plate 2.8 a; Figure 2.6 f). Originating from these fractures and from remaining pre-existing fracture- and vug-spaces, dolomite dissolution and oxidation of sulfide minerals took place locally, resulting in corrosion features of both dolomite and sulfide minerals and the generation of rusty-brown goethite/limonite rims on corroded crystal surfaces, as well as within corroded crystals (Plate 2.8 b, c, d). Calcitization of all three dolomite types generally occurs within the same areas, suggesting that it simultaneously originated from the same fractures. Generally, dolomite Type 1 appears to have been calcitized most extensively, whereas dolomite Type 2 and 3 are partially preserved in many cases (Plate 2.8 b, d).

Remaining fractures and vugs are partially or completely filled by clear to translucent calcite cement (Plate 2.6 a). In partially filled fractures and vugs this calcite forms scalenohedral crystals up to 1.5 cm in size, that exhibit a two-fold zonation into an iron-poor core (red stain, orange CL) and an iron-rich rim (blue stain, dull-red CL to non-luminescent) in thin section (Plate 2.9 a, b). Under CL-light, the iron-rich rim exhibits a succession of several thin zones, which in some places obliquely cross-cut previous zones (Plate 2.9 b), indicating phases of corrosion followed by phases of calcite precipitation.

#### 2.5.3.6 Phase 25: fracturing, several generations of calcite cement

Post-dating phase 24, further fracturing and calcite cementation took place (Plate 2.9 c, d). The calcite cements are mostly milky-white to clear (in some places slightly pink), and individual crystals range up to several cm in size. Fractures filled with these calcites reach widths of several meters and contain limestone as well as dolostone clasts. Diffuse boundaries between these calcites and all three dolomite types, and the presence of dolomite









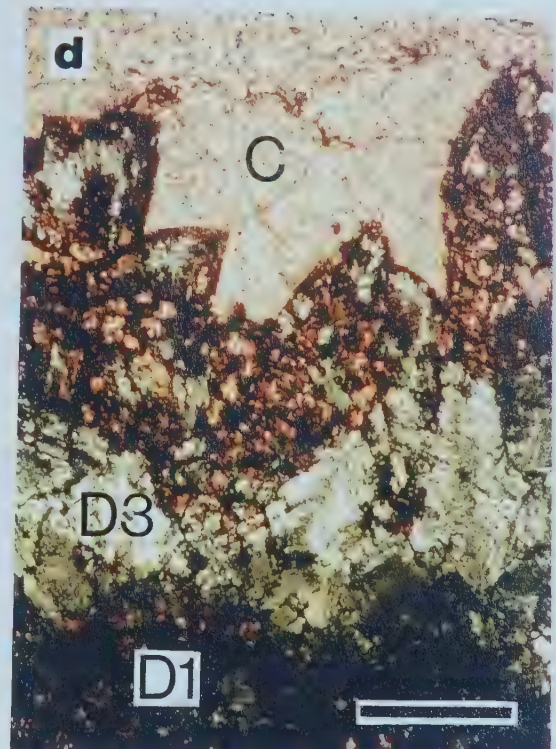
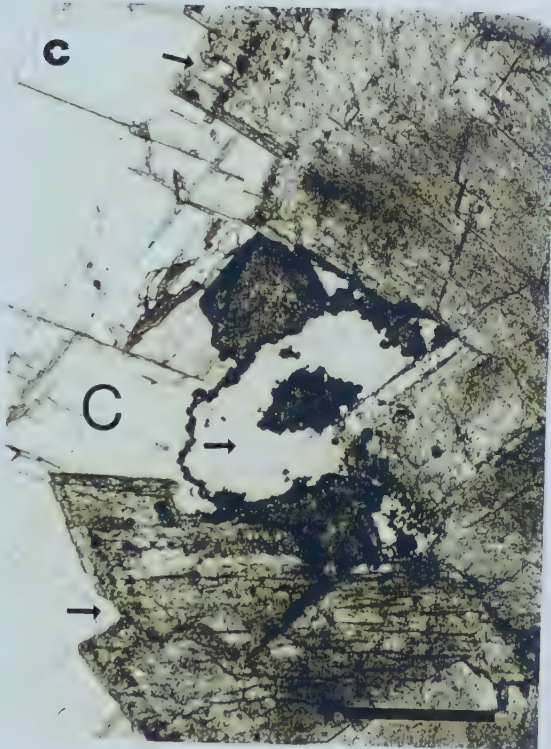
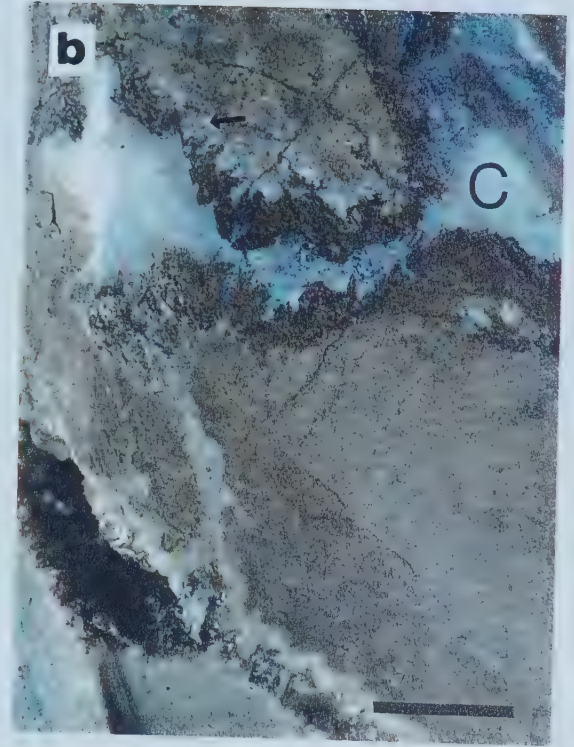
**Plate 2.8:** Post-Variscan textural and mineralogical changes.

**Plate 2.8a:** Photomicrograph of calcite-filled fracture (phase 24) cutting through nonplanar dolomite Type 1 (D1; phase 21). Originating from the fracture, dolomite Type 1 has been partially calcitized (red stain). Stained thin section, transmitted light. Almerfeld (AL) drill core, depth 683.9 m. Scale bar = 500  $\mu\text{m}$ .

**Plate 2.8b:** Core photograph of partially calcitized, vuggy dolostone. Vug-lining dolomite Type 3 (phase 22) in upper part of photograph has been strongly corroded, resulting in the generation of rusty-brown limonite/goethite (phase 24; see also Plate 2.8 d). Vug is filled completely with white to translucent calcite (C; phase 24), that has also calcitized dolomite Type 1 (arrow). Vug-lining dolomite Type 3 in lower part of photograph has only thin rim of brown limonite/goethite, but is otherwise unaffected. Yellow-brown color of calcitized dolomite Type 1 is also due to limonite/goethite (see also Plate 2.8 d). Thülen 2 (TH2) drill core, depth 296.3 m. Scale bar = 1 cm.

**Plate 2.8c:** Photomicrograph of slightly corroded dolomite Type 3 (phase 22) and corroded base metal sulfides (sphalerite/pyrite intergrowth; phase 23) (arrows). Corrosion was contemporaneous with or followed by precipitation of clear calcite cement (C; phase 24). Transmitted light. Almerfeld (AL) drill core, depth 709.5 m. Scale bar = 500  $\mu\text{m}$ .

**Plate 2.8d:** Photomicrograph of stained thin section showing corrosion of dolomite Type 1 (D1; phase 21) and Type 3 (D3; phase 22). Corroded areas are strongly pervaded by calcite (C; phase 24; stained red). Transmitted light. Thülen 2 (TH2) drill core, depth 296.3 m. Scale bar = 500  $\mu\text{m}$ .









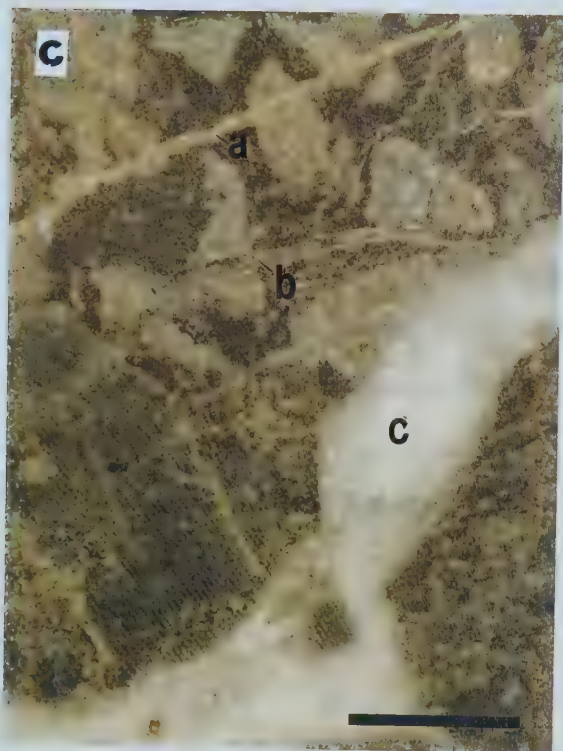
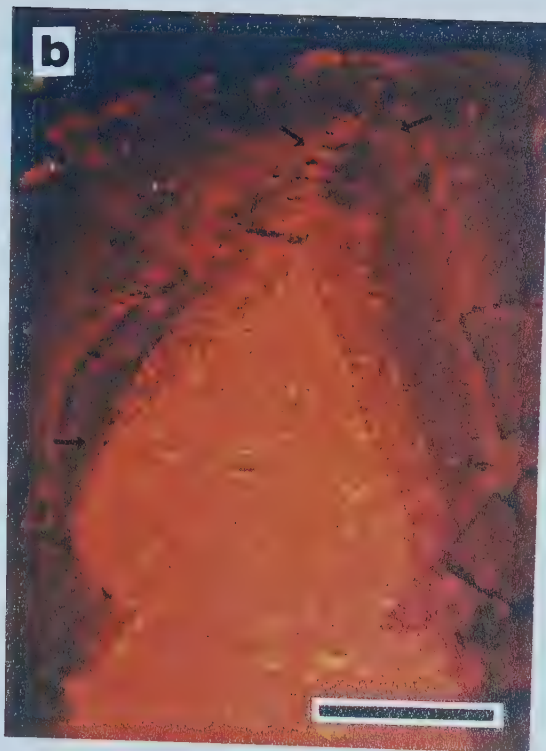
**Plate 2.9:** Post-Variscan textural and mineralogical changes.

**Plate 2.9a:** Photomicrograph of zoned, clear calcite cement (phase 24) showing inclusion-rich zone at the boundary between core and rim. Calcite cement of phase 24 partially or completely fill remaining void space that is lined by dolomite Type 3. Transmitted light. Almerfeld (AL) drill core, depth 726.8 m. Scale bar = 500  $\mu\text{m}$ .

**Plate 2.9b:** Same as in Plate 2.9a, but under CL light. Fe-poor core of the clear calcite cement has orange CL-color, whereas Fe-rich rim exhibits a succession of red and dull-red zones, that cut each other obliquely in some places (arrows), indicating phases of corrosion followed by phases of calcite precipitation. Almerfeld (AL) drill core, depth 726.8 m. Scale bar = 500  $\mu\text{m}$ .

**Plate 2.9c:** Core photograph of dolomitized stromatoporoid floatstone crosscut by fractures of phase 22 (a), 24 (b), and 25 (c). Fracture (a) is filled by dolomite Type 3, fracture (b) by translucent calcite, and fracture (c) by milky-white calcite. Diffuse boundaries between the latter and the dolomitized wall rock (arrows) indicate that calcitization of the wall rock has taken place. Almerfeld (AL) drill core, depth 711.7 m. Scale bar = 1 cm.

**Plate 2.9d:** Core photograph of strongly calcitized dolostone. Yellow-brown color of dolomite types 2 and 3 and rusty-brown rim of calcite-filled vug in upper part of the photograph are due to the generation of limonite/goethite during corrosion of dolomite and sulfide minerals in phase 24. Translucent vug-filling calcite also formed in phase 24, whereas white calcite in the lower left formed in phase 25. Immental 3 (I3) drill core, depth 406.5 m. Scale bar = 1 cm.







inclusions (Plate 2.9 c) indicate that further dolomite replacement by calcite (calcitization) has taken place. Because of its massive volume and relative purity, calcite in fractures of phase 25 has been mined in the Brilon area for several decades, generating prominent trenches that are several meters deep and several tens of meters long in some places.

#### 2.5.3.7 Karst

Karst-textures in the investigated drill cores include solution enlarged cavities as well as cavity- and fracture-filling material (carbonate breccias, brown clay, quartz sandstone). The karst-cavities occur most frequently in the uppermost 100 to 200 m of the drill cores and reach sizes of several meters (Appendix 1). In drill cores from wells that penetrated strongly fractured and brecciated intervals, m-sized cavities filled with brown and grey clays occur even at greater depths (e.g., Alme 1, Almerfeld, Fünf Brücken, Immental 1, Immental 3, Loh 1, Romberg 1). The maximum depths to which karst is developed in the investigated drill cores are 520 m in the Romberg 1 well (Machel 1979) and 660 m in the Loh 1 well.

Except for the marginal-marine quartz sandstone (e.g., uppermost part of Madfeld 1 drill core), which is Lower Cretaceous in age (Brinckmann 1981), and brown clays in the Bleiwäsche 1 drill core containing Middle Jurassic spores (core interval from 213 to 232 m; Stoppel, personal communication, 1995), the ages of the other post-Variscan cavity- and fracture-filling materials found in the investigated drill cores could not be determined. Reports of terrestrial sediments of Triassic, Jurassic and Lower Cretaceous age, as well as fragments of Upper Cretaceous marine limestones from karst cavities within the Middle and Upper Devonian carbonates of the Brilon Reef Complex (e.g., Machel 1979, 1990b) indicate that karst processes were active since the Early Mesozoic and were interrupted only by the Late Cretaceous marine ingression.



#### ***2.5.4 Integration into regional paragenetic sequence and timing of dolomitization***

The succession of post-Variscan textural and mineralogical changes described above, can be integrated into the regional paragenetic sequence for the post-Variscan mineralization in the northeastern Rhenish Schiefergebirge that was established by Schaeffer (1984, 1986) (Table 2.2). He distinguished six phases of post-Variscan mineralization (phases I to VI), each characterized by a specific mineral paragenesis. The paragenetic succession within the core intervals investigated in the present study contains minerals characteristic of Schaeffer's phases II, III, V, and VI. In particular, the scalenohedral calcite (phase 20) corresponds to Schaeffer's calcite II (type "Wülfrath"; phase II). Dolomite types 1, 2, and 3 (phase 21 and 22) correspond to dolomite I (phase III). Schaeffer's dolomite II in phase V, however, which Moritz (1983) had described from the Brilon Reef Complex, could not be identified in any of the investigated drill cores. Galena, sphalerite, and pyrite (phase 23) correspond to galena II, sphalerite I, and pyrite-marcasite II (phase V), respectively. The dissolution of carbonates and oxidation of sulfide minerals with the formation of limonite/goethite and subsequent calcitization and calcite cementation (phase 24) also fall into Schaeffer's phase V, and the zoned scalenohedral crystals of clear calcite (phase 24) correspond to calcite III (type "Freiberg") in Schaeffer's phase V. The fracture-filling calcite cements (phase 25) have not been investigated in detail, but are very likely equivalent to calcite IV (type "Rüdersdorf") of Schaeffer's phase VI.

Following Schaeffer's regional paragenetic sequence (Schaeffer 1984, 1986), the timing of dolomitization (phase 21; dolomite Type 1), dolomite recrystallization (phase 22; dolomite Type 2), and dolomite cementation (phase 22; dolomite Type 3) within the Middle and Upper Devonian carbonates of the Brilon Reef Complex can be constrained to the period from the Late Cretaceous to Early Tertiary (Table 2.2).



SCHAEFFER (1984, 1986)			THIS STUDY	
phase	paragenesis	timing	phase	textural and mineralogical changes
VI	calcite IV (type "Rüdersdorf")	? Pliocene		
	marcasite III			
	barite IV			
V	aragonite I	Tertiary (Oligocene to Early Miocene)		
	fluorite I			
	barite III			
	tetraedrite II			
	calcite III (type "Freiberg")			
	siderite I			
	dolomite II			
	Mn-oxides and hydroxides			
	goethite I			
	pyrite-marcasite II			
	apatite I			
	hematite II			
	chalcopryrite IV			
	sphalerite I			
	galena II			
	chalcedony I			
	quartz III			
IV	barite II galena I	Late Cretaceous to Early Tertiary		
III	hematite I	Late Cretaceous to Early Tertiary		
	chalcopryrite III			
	barite I dolomite I			
II	quartz II	Jurassic to Early Cretaceous		
	chalcopryrite I calcite II (type "Wülfrath")			
I	tetraedrite I chalcopryrite I pyrite-marcasite I calcite I quartz I	Permian (?) to Mesozoic		
			phase 25	calcite cementation fracturing
				calcite cementation calcitization
			phase 24	limonite/goethite dolomite dissolution fracturing
				pyrite
			phase 23	sphalerite galena
			phase 22	dolomite cementation (Type 3) dolomite recrystallization (Type 2) fracturing
			phase 21	calcite dissolution pervasive dolomitization (Type 1) fracturing
			phase 20	scalenohedral calcite fracturing

**Table 2.2:** Integration of the succession of post-Variscan textural and mineralogical changes encountered dolomitized intervals from the Brilon Reef Complex (right) into regional paragenesis of the post-Variscan mineralization in the northeastern Rhenish Schiefergebirge (left) (Schaeffer 1984, 1986).





## 2.6 Distribution of dolostone intervals

Each of the investigated drill cores contains several dolomitized intervals (Figure 2.7 a, b; Appendices 1 and 2), containing and consisting of the three dolomite types described above. Dolostone intervals occur at all depth levels, range in thickness from several dm to tens or even hundreds of meters and constitute between 1 and 83% (M1 and I3), respectively of the total “Massenkalk” section. The lack of a detailed stratigraphic framework (see above) prevents a confident correlation of the dolomitized intervals between wells. Furthermore, the fact that no drill core penetrated the full vertical extent of the Middle and Upper Devonian carbonates of the Brilon Reef Complex implies that each individual drill core represents only part of the carbonate succession. Therefore, the distribution of dolostone intervals within the investigated drill cores is not necessarily representative of their distribution within the whole carbonate body of the Brilon Reef Complex.

### 2.6.1 *Spatial relationship to sedimentary facies*

In many of the intervals the primary sedimentary textures were partially or completely obliterated by recrystallization, dolomitization, carbonate dissolution, and calcitization, so that the carbonate facies type could not be positively identified. Nor did cathodoluminescence and fluorescence microscopy of thin sections from these intervals reveal any conclusive details with respect to their sedimentary facies. In these cases, the sedimentary facies was assumed to be similar to that of the surrounding limestones.

Transitions between dolostones and limestones cross-cut bedding planes and facies boundaries. Intervals of dolostone occur in carbonates of fore-reef, reef-core, and back-reef character (Appendices 1 and 2). Domination of most of the investigated drill cores by float- and wackestones of back-reef character might suggest that these carbonates were preferentially dolomitized. However, the occurrence of dolostone within the relatively few intervals of fore-reef and reef-core character (e.g., Brilon 2, Romberg 1, Bleiwäsche 1) indicates that this is not the case. In the lower part of the Brilon 2 and Romberg 1 drill cores, syn-sedimentary limestone breccias have been dolomitized along with matrix-rich rudstones, floatstones and packstones of fore-reef character. In the Romberg 1 and Bleiwäsche 1 drill cores, dolomitization also affected rudstones of reef-core character.





**Figure 2.7 a:** Distribution of dolostone in investigated drill cores from the southern margin and central part of the Brilon Reef Complex. Numbers below drill core column give the percentage of dolostone section relative to the total "Massenkalk" section, with the exception of drill core AB1, where dolostone occurs within Sparganophyllum limestone. No horizontal scale. For well locations and identifications see Table 2.1. For detailed core logs, see Appendix 1. For list of dolostone intervals, see Appendix 2. See text for further explanation.

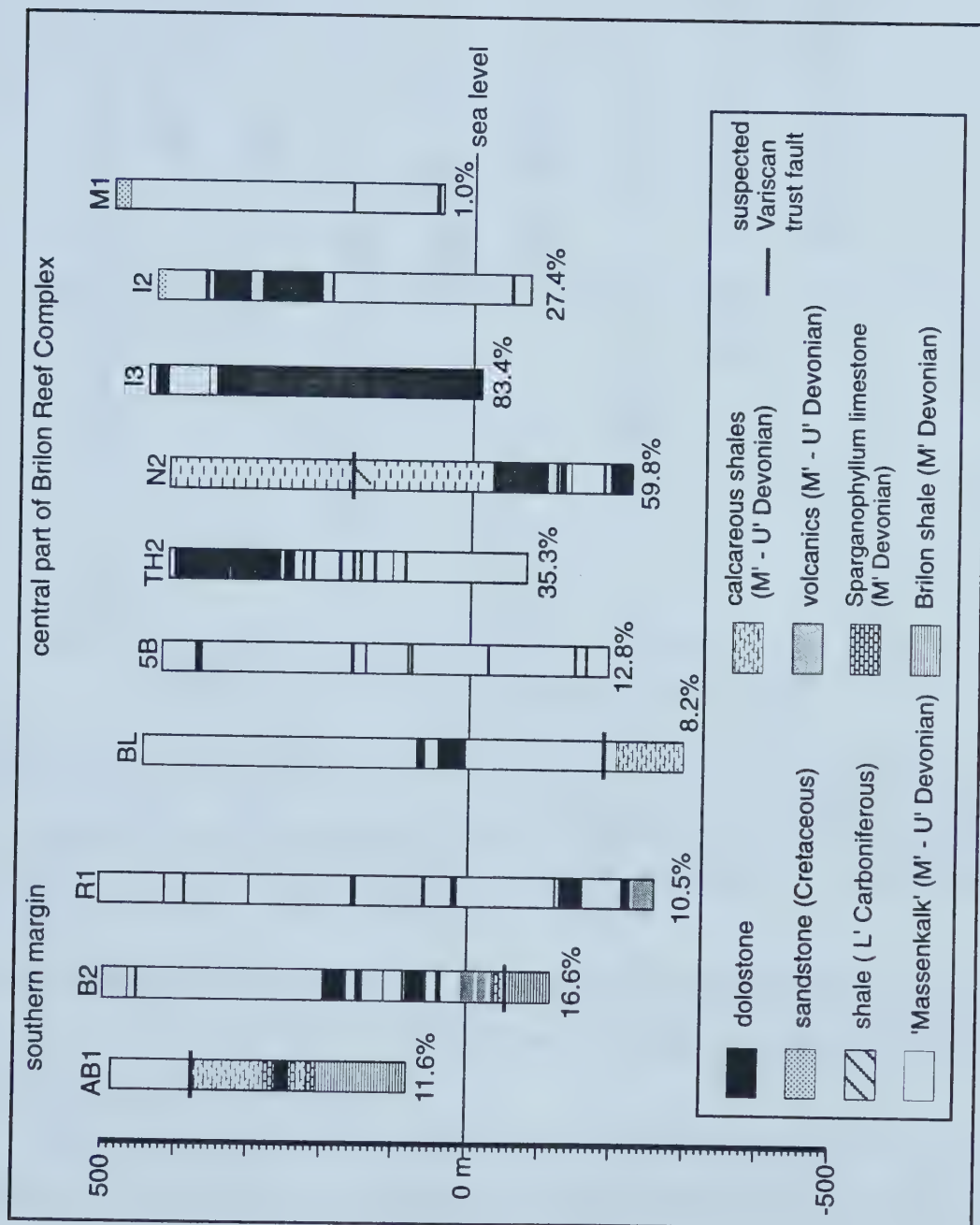
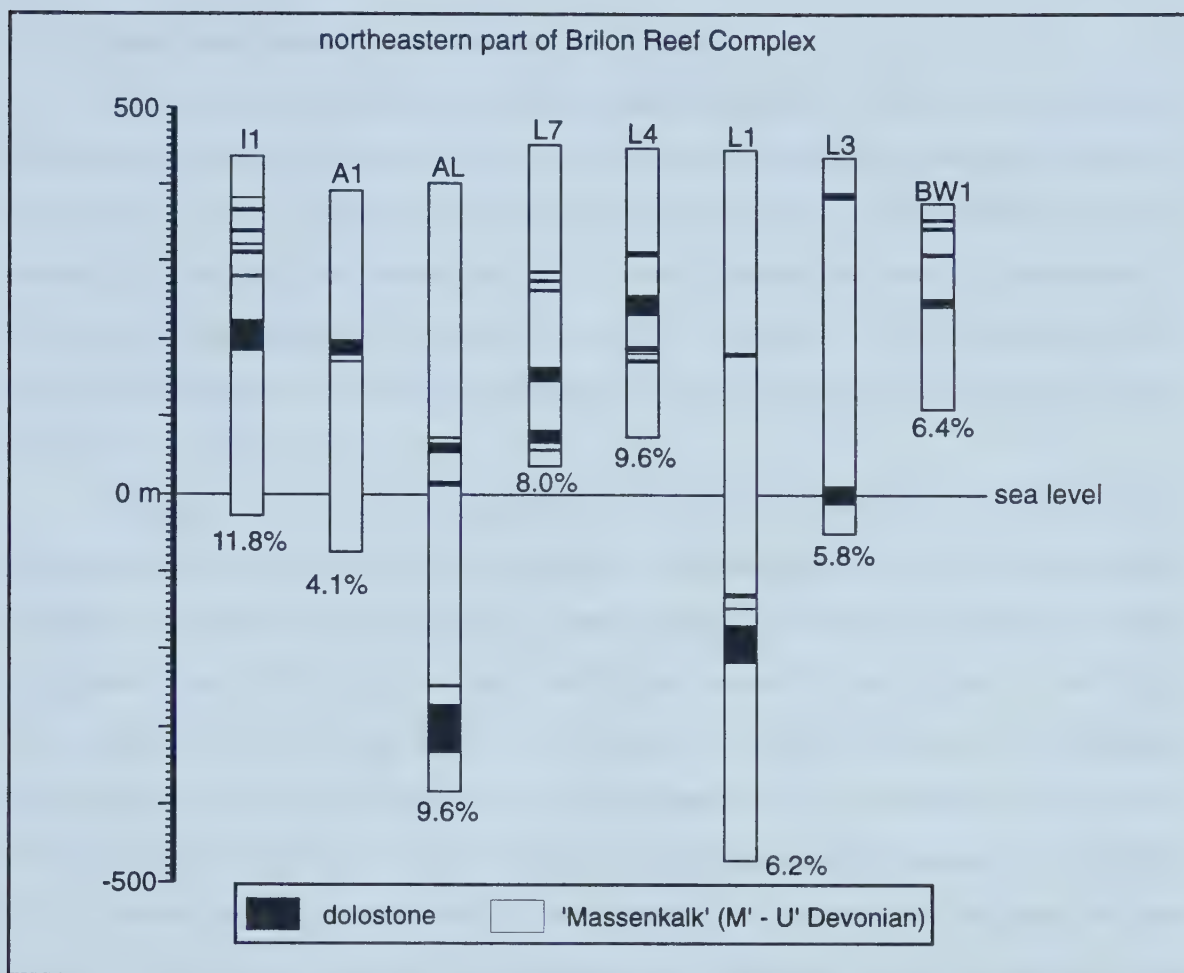


Figure 2.7a







**Figure 2.7 b:** Distribution of dolostone in investigated drill cores the northeastern part of the Brilon Reef Complex. Numbers below drill core columns give the percentage of dolostone section relative to the total “Massenkalk” section. No horizontal scale. For well locations and identifications see Table 2.1. For detailed core logs, see Appendix 1. For list of dolostone intervals, see Appendix 2. See text for further explanation.

In the Altenbüren 1 drill core, parts of the biostromal *Sparganophyllum* limestone, which is under- and overlain by calcareous shales and marls of the Brilon shales and Flinz facies, respectively, have been dolomitized.

The assertion by Brinckmann (1981), that mineralized dolostone intervals in the northeastern part of the Brilon Reef Complex form “quasi-stratiform” zones within the dark-grey bituminous limestones of back-reef character, could not be verified. The number and thicknesses of the dolostone intervals vary considerably from one well to another (Figure 2.7 b) and the stratigraphic uncertainties do not allow a reliable correlation (see above).



### ***2.6.2 Spatial relationship to post-sedimentary textures***

Regardless of the textures of the precursor limestone, most of the investigated dolostone intervals are characterized by the occurrence of post-Variscan fractures (phase 21, phase 22). Generally, drill cores from wells that were drilled close to the NNW-SSE trending normal faults exhibit more numerous post-Variscan fractures and have higher amounts of dolostone (e.g., Immental 1, Immental 2, Immental 3, Thülen 2, Brilon 2) than those from wells drilled at greater distances from these faults (e.g., Madfeld 1, Alme 1, Fünf Brücken) (Figure 2.1, Figure 2.8 a, b, c).

Differences in fracture intensity exist between the upthrown (eastern) and downthrown (western) blocks of the prominent Immental Fault, that cuts through the reef complex from north to south (Figure 2.1). The Immental 2 and Immental 3 wells are located on opposite sides of the fault at a distance of 550 m from each other (Figure 2.1 and Figure 2.8 a), Immental 2 on the upthrown side and Immental 3 on the downthrown side. Compared to the carbonates in the Immental 3 well, the carbonates in the Immental 2 well are less fractured and dolostone intervals are relatively thin. Similarly, the Immental 1 well (Figure 2.8 c) is located on the upthrown side of the Immental Fault and exhibits less post-Variscan fracturing and smaller amounts of dolostone than Immental 3. Furthermore, the upper boundary of the lowermost dolostone interval in the Immental 3 well is located almost at the same depth as the upper boundary of the second (from above) dolostone interval the Immental 2 well. Considering the total vertical throw of at least more than 100 m (Schriel 1954), this indicates, that dolomitization must have occurred after the main vertical displacement at the fault, and serves as further evidence for a fault-controlled origin of the dolostone.

Dolostone in the Altenbüren 1 drill core is restricted to the fractured part of the Sparganophyllum Limestone, which is under- and overlain by relatively compact marls and calcareous shales. Considering the proximity to the Altenbüren Fault, it is somewhat unusual that the fractured and brecciated carbonates of the Massenkalk in the upper part of the Altenbüren 1 drill core were not affected by dolomitization.

Many dolostone intervals experienced repeated fracturing, brecciation, carbonate dissolution, calcitization, and calcite cementation after dolomitization. For example, in large







**Figure 2.8a:** Distribution of dolostone intervals in the Devonian Brilon Reef Complex along cross-section B-B' (see Figure 2.1) showing relationship between amount of dolostone and distance to post-Variscan normal faults. Numbers below drill core column give the percentage of dolostone section relative to the total "Massenkalk" section, with the exception of drill core AB1, where dolostone occurs within Sparganophyllum limestone.

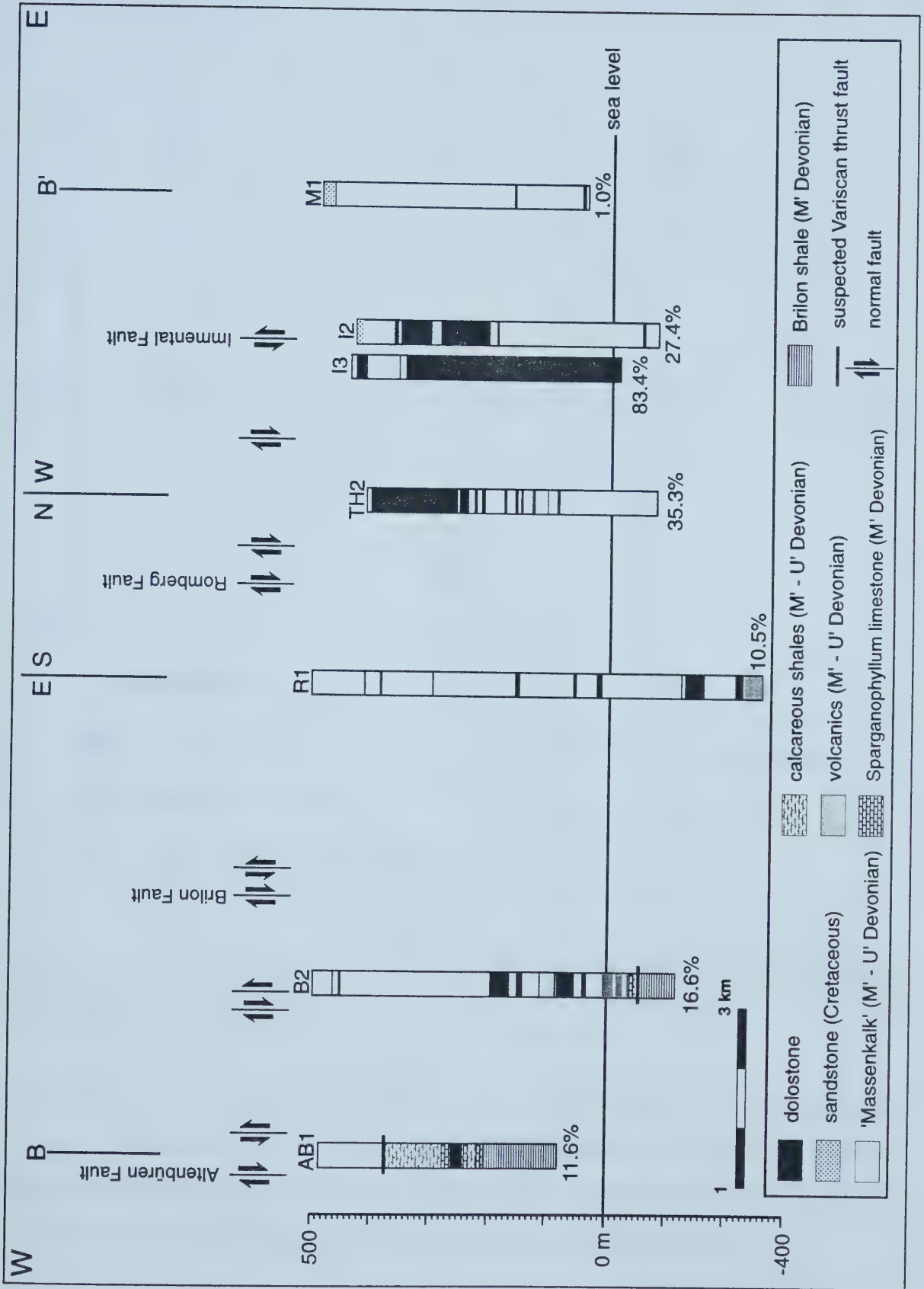
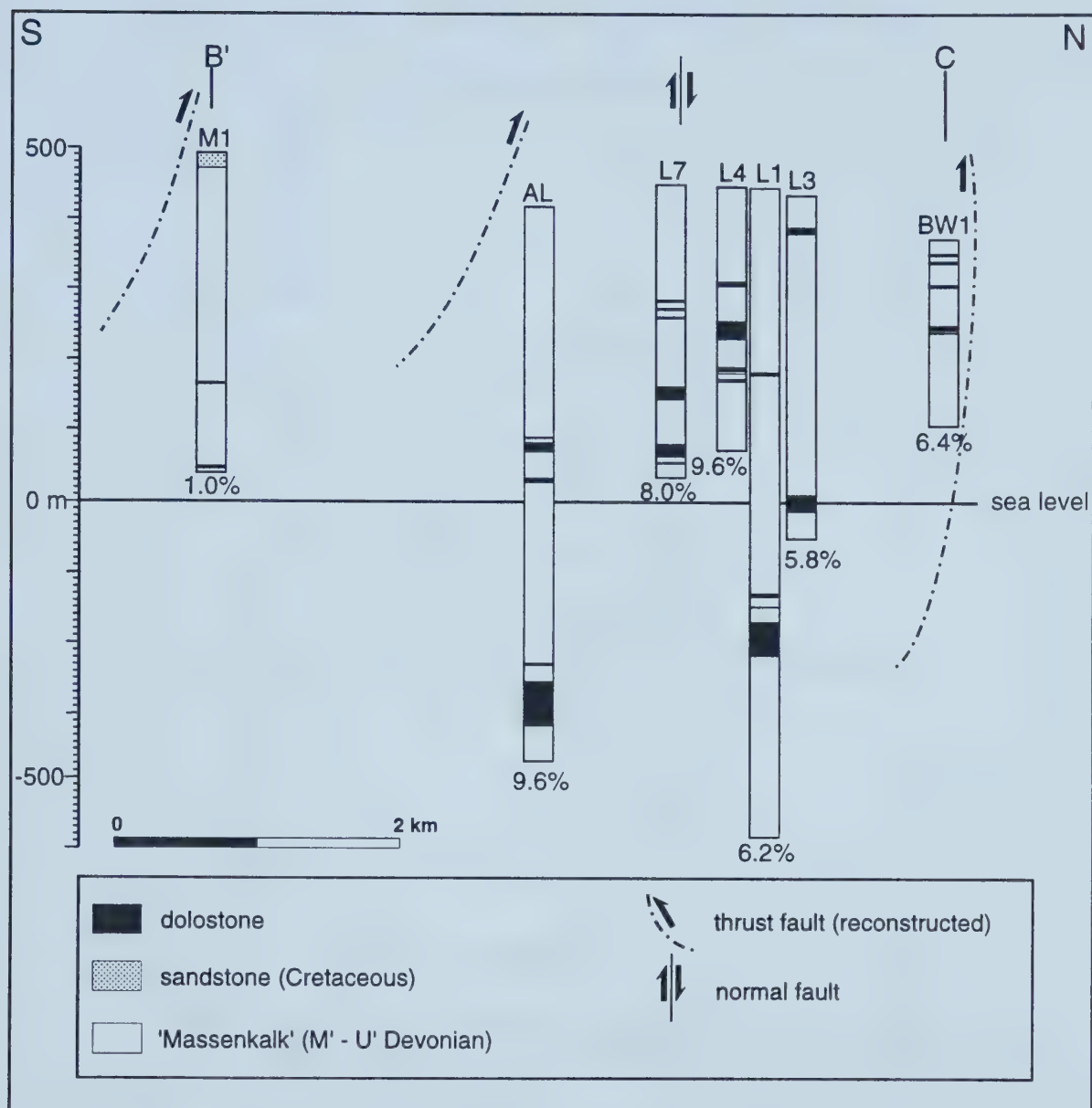


Figure 2.8 a

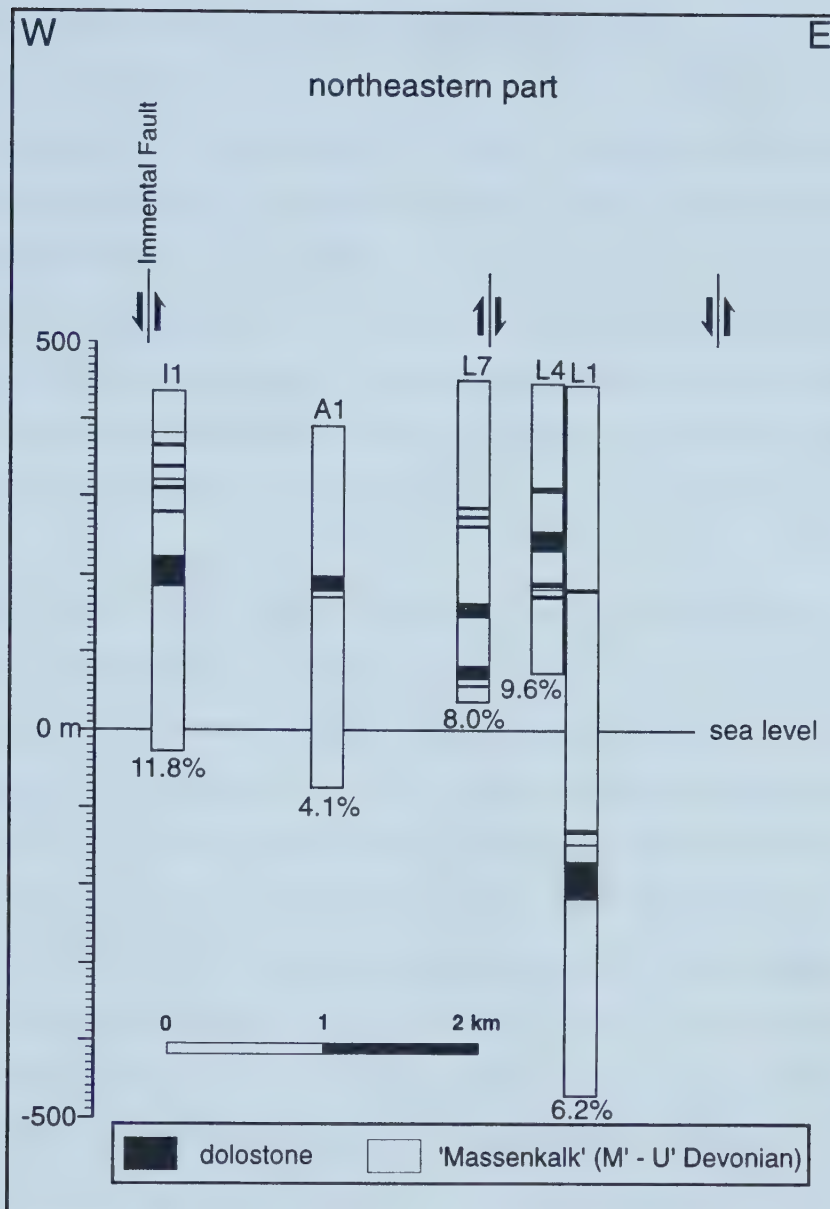




**Figure 2.8 b:** Distribution of dolostone intervals in the Devonian Brilon Reef Complex along cross-section B'-C (see Figure 2.1). Numbers below drill core columns give the percentage of dolostone section relative to the total "Massenkalk" section.

parts of the drill core Immental 3, these processes almost completely obliterated the pre-existing dolomite textures. However, the frequent occurrence of remnants of dolostone within these intervals serve as evidence that the highly fractured and brecciated carbonates had been almost completely dolomitized, except for the uppermost 100 m.





**Figure 2.8 c:** Distribution of dolostone intervals in the north-eastern part of the Devonian Brilon Reef Complex along an E-W trending cross-section from the Immental 1 (I1) to the Loh 1 (L1) well (see Figure 2.1). Numbers below drill core columns give the percentage of dolostone section relative to the total "Massenkalk" section. The number and thicknesses of dolostone intervals are highest close to normal faults (wells I1, L7, and L4) and decrease with increasing distance (wells A1 and L1).





## **2.7 Association of dolomite types with sulfide mineralization**

All three dolomite types occur together in almost all of the investigated dolostone intervals. In particular, dolomite types 2 and 3 have not been found to occur outside of intervals with dolomite Type 1 (or remnants thereof). Type 2 is restricted to the vicinity of fractures and vugs (phases 21, 22), creating cm to m-wide 'halos' within Type 1. Dolomite Type 1 generally predominates in intervals with minor post-Variscan fracturing, whereas Type 2 and 3 commonly predominate in intervals that are strongly fractured. Predominance of Type 2 in intervals characterized by minor fracturing implies that a more intensively fractured zone must be nearby but was not penetrated by the well (e.g., in the drill core Romberg 1).

Base metal sulfide (galena, sphalerite, pyrite) mineralization occurs rather sporadically in the investigated dolostone intervals. Many of the dolostone intervals are practically devoid of macroscopic mineralization. Geochemical data presented in the report by Brinckmann (1981) generally show only slightly elevated Pb and Zn concentrations (below 0.01 wt. %) for bulk analyses over 1 m intervals from most of the investigated dolostone intervals from drill cores (see also Appendix 2). Exceptions are the dolostone intervals in some of the drill cores from the northeastern part of the reef complex (Loh 1, Loh 4, Loh 7) in which concentrations of up to 3.3 wt. % Pb and 1.6 wt. % Zn were measured (Loh 4: interval 260.0 to 261.7 m; Brinckmann 1981). The limestones directly above the dolostone interval within the Sparganophyllum limestone in the Altenbüren 1 drill core, have concentrations of up to 4.5 wt. % Zn and 0.5 wt. % Pb (interval from 213 - 223 m, Brinckmann 1981).

As already stated by Brinckmann (1981), the concentrations of base metals within the dolostone intervals are generally slightly elevated, but too low to be of economic significance. In addition to the minor dolomite-hosted Pb-Zn-sulfide mineralization, Schriel (1954) described several other types of post-Variscan mineralization from outcrops and shallow mines in the Brilon Reef Complex. These include (1) Pb-Zn-Fe-sulfide mineralization on faults and fractures associated with fracture-filling calcite and clays; (2) galena in druses and pods on fractures and voids within fracture-filling calcite and "Massenkalk"; (3) galena associated with barite that replaced Cretaceous sandstone; (4)



galena on calcite filled fractures within (?thrust) fault-breccias at the northeastern margin of the Brilon Reef Complex; (5) galena associated with fracture-filling barite within the “Massenkalk”; (6) Pb-Zn mineralization in karst cavities (sinkholes) associated with clays and calcite cements (Schriel 1954). These types apparently form the major concentrations of base metals in the Brilon Reef Complex that had been mined at the surface in small scale mining operations until the end of the 19<sup>th</sup> century (Schriel 1954; Bruns 1996). Although some of these types had been encountered in several of the drill cores (Brinckmann 1981), their investigation was beyond the scope of this thesis.

## **2.8 Controls on the distribution of dolostone in the Brilon Reef Complex**

The observations presented in the previous sections suggest that, the distribution of dolostone in the Brilon Reef Complex is largely controlled by the amount of post-Variscan fracturing (phases 21 and 22). Carbonate facies type as well as pre-Variscan diagenesis and textures related to the Variscan deformation do not appear to have any significant influence. Rather, the amount of post-Variscan fracturing and the amount of dolostone both generally increase with increasing proximity to the prominent NNW-SSE trending, subvertical normal faults. While it had already been shown that the rare occurrences of dolomite in outcrop were mainly restricted to the direct vicinity of these faults (Schriel 1954), the observations presented here indicate that the faults played an important role for the distribution of dolomite in the subsurface as well. The finding that the major amount of dolostone occurs in the central part of the Brilon Reef Complex close to the Immental Fault contradicts Moritz (1983), who stated that the major amount of dolostone is concentrated at the margins of the Brilon Reef Complex. His misjudgement, however, is mainly due to the fact that his study did not include drill cores from the wells close to the Immental Fault, but rather those from the southern margin and northeastern part of the reef complex.

## **2.9 Genetic implications of petrographic observations**

The spatial distribution of the dolostone intervals, together with the petrographic characteristics of the dolomite types give some clues about their formation. The dolomitizing fluids entered the Brilon Reef Complex via the NNW-SSE trending normal faults and



invaded the limestones along irregular fracture systems that stood in contact with the main faults. The major amount of dolostone formed at the prominent Immental Fault, however, subsequent fracturing, corrosion, and calcitization along this fault resulted in the partial to complete obliteration of dolomite textures.

Nonplanar (or xenotopic) dolomite textures are indicative of dolomite formation at temperatures in excess of 50°C (Gregg and Sibley 1984). The same applies to the presence of saddle dolomite, which characteristically forms in a temperature range between 60 and 150 °C (Radke and Mathis 1980). Of the three types of dolomite found in the investigated dolostone intervals, dolomite Type 1 forms planar (or idiotopic) to nonplanar textures, which makes inferences about the temperature of its formation difficult. Dolomite Type 2 clearly forms nonplanar textures, and Type 3 occurs as saddle dolomite.

The timing of dolomitization has been constrained to the Late Cretaceous to Early Tertiary (see above). During this time, the Devonian carbonates of the Brilon Reef Complex occupied a position close to the surface were overlain only by a thin (probably < 200 m) cover of Cretaceous sediments. Assuming a normal geothermal gradient of 30 °C and a surface temperature of about 20 °C for this time period, temperatures in excess of 50 °C would require a minimum burial depth of at least 1000 m, which appears to be highly unlikely. The evidence for fault- and fracture-control of the dolostone intervals together with the petrographic evidence for formation at elevated temperatures therefore suggest a hydrothermal origin of the post-Variscan dolomite in the Brilon Reef Complex, confirming the suggestions by Machel (1979, 1990b) and Moritz (1983). These findings provide the working hypothesis for the geochemical and microthermometric investigations presented in Chapter 3.





## 2.10 References

- Bär, P., 1966, Stratigraphie, Fazies und Tektonik am Briloner Massenkalksattel (Ostsauerland). Unpublished Dissertation, University of Giessen, 55 p.
- Brinkmann, J., 1981, Projekt Rhenoharzynikum, Untersuchung der Metallverteilung in geosynklinalen Sedimenten des Rhenoharzynikums in stratiformen Konzentrationen. Bericht über das Kernbohrprogramm im Briloner Riffkalk-Komplex. Unpublished report by the Bundesanstalt für Geowissenschaften und Rohstoffe, Hannover, 129 p.
- Brinckmann, J., Clausen, C.-D., Müller, H., and Stoppel, D., 1989, Geologische Übersichtskarte der Brilon-Warsteiner Riffkarbonate und ihrer Umrahmung. Geologisches Jahrbuch, D95 (1990).
- Bruns, A., 1996, Bergbau um Brilon. In: M. Senger (ed.), Bergbau im Sauerland, p. 193-196.
- Davies, G. R., 1996, Hydrothermal dolomite (HTD) reservoir facies: global perspectives on tectonic-structural and temporal linkage between MVT and SEDEX Pb-Zn ore bodies, and subsurface HTD reservoir facies. Canadian Society of Petroleum Geologists Short Course Notes, 167 p.
- Dickson, J. A., 1966, Carbonate identification and genesis as revealed by staining. Journal of Sedimentary Petrology, 36, p. 491-505.
- Dunham, R. J., 1962, Classification of carbonate rocks according to depositional texture. In: Ham, W. E. (Ed.), Classification of Carbonate Rocks, Society of Economic Paleontologists and Mineralogists Special Publication, 14, p. 182-190.
- Errenst, C., 1993, Litho- und biofazielle Untersuchungen im Sparganophyllumkalk der Bohrungen SP6 (Plettenberg) und Brilon II (Brilon) - ein Vergleich. Unpublished Diplom mapping project report, Ruhr-University Bochum, 52 p.
- Embry, A. F. and Klovan, E. J., 1972, Absolute water depth limits of Late Devonian paleoecological zones. Geologische Rundschau, 61, p. 672-686.
- Gregg, J.M. and Sibley, D.F., 1984, Epigenetic dolomitization and the origin of xenotopic dolomite texture. Journal of Sedimentary Petrology, 54, p. 908-931.
- Hong, T., 1992, Mikrofazies, Paläobiologie und Palökologie im nordöstlichen Teil des Briloner Riffkomplexes (Mittel- und Oberdevon) im Ostsauerland, Deutschland. Reihe Geowissenschaften, D82, Rheinisch-Westfälische Technische Hochschule Aachen, 166 p.
- James, N. P., 1983, Reef environment. In: Scholle, P.A., Bebout, D.G., and James, N.P. (eds.), Carbonate Depositional Environments, American Association of Petroleum Geologists Memoir, 33, p. 345-440.
- Krebs, W., 1968, Reef development in the Devonian of the eastern Rhenish Slate Mountains, Germany. International Symposium on the Devonian System, Calgary, 1967, Alberta Society of Petroleum Geologists, 2, p. 295-299.



- Land, L. S., 1985, The Origin of Massive Dolomite. *Journal of Geologic Education*, 33, p. 112-125.
- Machel, H.G., 1979, Fazies und Diagenese der devonischen Riffcarbonate der Bohrung Romberg (Briloner Riff). Unpublished Diplom-thesis, Technische Universität Braunschweig, 231 p.
- Machel, H. G., 1990a, Faziesinterpretation des Briloner Riffs mit Hilfe eines Faziesmodells für devonische Riffkarbonate. *Geologisches Jahrbuch*, Reihe D95, p. 43-83.
- Machel, H. G., 1990b, Submarine Frühdiagenese, Spaltenbildungen und prätektonische Spätdiagenese des Briloner Riffs. *Geologisches Jahrbuch*., Reihe D95, p. 85-137.
- Machel, H. G. and Hunter, I. G., 1994, Facies Models for Middle to Late Devonian Shallow-marine Carbonates, with Comparisons to Modern Reefs: a Guide for Facies Analysis. *Facies*, 30, p. 155-176.
- Machel, H. G. and Mountjoy, E. W., 1986, Chemistry and environments of dolomitization - a reappraisal. *Earth Science Reviews*, 23, p. 175-222.
- May, A., 1987, Der Massenkalk (Devon) nördlich von Brilon (Sauerland). *Geologie und Paläontologie von Westfalen*, 10, p. 51-84.
- May, A., 1988, Fossilführung und Palökologie des lagunären Massenkalkes (Devon) im Sauerland (Rheinisches Schiefergebirge). *Paläontologische Zeitschrift*, 62, p. 175-192.
- Moritz, W., 1983, Fazies und Diagenese des Briloner Karbonatkomplexes anhand einiger ausgewählter Bohrungen. Unpublished Ph.D. thesis, Technische Universität Braunschweig, 180 p.
- Mountjoy, E.W., 1994, Dolomitization and the character of hydrocarbon reservoirs: Devonian of western Canada. In: A. Parker and B. W. Sellwood (eds.), *Quantitative Diagenesis: Recent Developments and Applications to Reservoir Geology*, p. 33-94.
- Müller, H., 1990, Zur Altersfrage und Faunenführung der Briloner Schiefer im nordöstlichen Sauerland (Mitteldevon, Rheinisches Schiefergebirge). *Geologisches Jahrbuch*, Reihe D95, p. 7-42.
- Murawski, H., Albers, H.J., Bender, P., Berners, H.-P., Dürr, St., Huckriede, R., Kauffmann, G., Kowalczyk, G., Meiburg, P., Müller, R., Müller, A., Ritzkowski, S., Schwab, K., Semmel, A., Stapf, K., Walter, R., Winter, K.-P., and Zankl, H., 1983, Regional tectonic setting and geological structure of the Rhenish Massif. In: Fuchs, K., von Gehlen, K., Mälzer, H, Murawski, H., and Semmel, A. (eds.): *Plateau Uplift*, p. 381-403.
- Radke, B.M. and Mathis, R.L., 1980, On the formation and occurrence of saddle dolomite. *Journal of Sedimentary Petrology*, 50, p.1149-1168.



- Schaeffer, R., 1984, Die postvariszischen Mineralisationen im nordöstlichen Rheinischen Schiefergebirge. Braunschweiger geologisch-paläontologische Dissertationen, 3, 206 pp.
- Schaeffer, R., 1986, Geochemische Charakteristika und Genese der jungmesozoisch-tertiären Vererzung im Sauerland (Rheinisches Schiefergebirge). Fortschritte der Geologie von Rheinland und Westfalen, 34, p. 337-381.
- Schriel, W., 1954, Der Briloner Galmei-Distrikt. Zeitschrift der deutschen geologischen Gesellschaft, 106, p. 308-349.
- Sibley, D. F. and Gregg, J. M., 1987, Classification of dolomite rock textures. Journal of Sedimentary Petrology, 57, p. 967-975.
- Stritzke, R., 1983, Die Stratigraphie, Sedimentologie und Paläogeographie der Karbonate im südöstlichen Vorfeld des Briloner Bioherms (Ostsauerland). Dissertation, University of Bochum, 84 pp.
- Sunkel, G., 1990, Devonischer submariner Vulkanismus im Ostsauerland (Rheinisches Schiefergebirge): Vulkanaufbau, Magmenzusammensetzung und Alteration. Bochumer geologische und geotechnische Arbeiten, 34, 250 pp.
- Wahba, Y., 1978, Die Geologie des Briloner Massenkalksattels im östlichen Sauerland. Unpublished Dissertation University of Clausthal, 203 pp.
- Wizisk, U., 1994, Mikrofazielle Entwicklungsgeschichte des devonischen Briloner Riffkomplexes (Sauerland). Unpublished Dissertation, Ruhr-University Bochum, 79 pp.





## CHAPTER 3

# PETROGRAPHIC, GEOCHEMICAL, AND FLUID INCLUSION EVIDENCE FOR FAULT-CONTROLLED HYDROTHERMAL DOLOMITIZATION IN THE BRILON REEF COMPLEX

### 3.1 Introduction

Intervals of dolostone in drill cores from the Devonian Brilon Reef Complex in the northeastern Rhenish Schiefergebirge (Figure 3.1) are characterized by the presence of grey matrix dolomite (dolomite Type 1), coarse crystalline milky-white dolomite occurring as a recrystallization product of grey matrix dolomite (dolomite Type 2), and as saddle dolomite cement (dolomite Type 3), followed by minor amounts of sulfide minerals (sphalerite, pyrite, galena) and late calcite cements. Some of the dolostone intervals show striking petrographic similarities with occurrences of pervasive dolostone in western Canada, which serve as prolific hydrocarbon reservoir rocks as well as host rocks for Mississippi Valley Type- (MVT) Pb-Zn sulfide mineralization (Mountjoy and Krebs 1983; Mountjoy 1994; Davies 1996). Hence, the Brilon Reef Complex may serve as a case study to determine the origin(s) and compositions(s) of dolomitizing and metal-bearing fluids, possible hydrologic drives, and the conditions under which these fluids led to the dolomitization and mineralization of the carbonate host rocks.

The spatial distribution of dolostone intervals and associated minor base metal sulfide mineralization in the Brilon Reef Complex suggests a causal relationship between dolomitization and NNW-SSE-trending, subvertical normal faults (Chapter 2 and Figure 3.1). These faults very likely acted as pathways for the injection of dolomitizing and mineralizing fluids during post-Variscan times. Based on paragenetic constraints, dolomitization and associated base metal sulfide mineralization are thought to have formed during the Late Cretaceous/Early Tertiary (Chapter 2). At this time, the carbonates of the Brilon Reef Complex were overlain only by a thin (probably < 200 m) cover of Upper Cretaceous marginal marine sandstones, marine limestones and marls (Clausen et al. 1982).





**Figure 3.1:** Simplified geologic map of the Brilon Reef Complex in the northeastern Rhenish Schiefergebirge (RSG), Germany; compiled from Wahba (1978), Brinkmann et al. (1989), and Wizisk (1995). Names of wells abbreviated; for full names see Chapter 2, Table 2.1. Stippled line in insert map delineates outline of Münsterland Cretaceous Basin (MCB) north of the Rhenish Schiefergebirge. Numbers in brackets represent the percentage of dolostone of the total “Massenkalk” section penetrated by the drill core. Dolostone contents are highest in the vicinity of NNW-SSE-trending faults in the central part of the Brilon Reef Complex (Immental Fault and Romberg Fault).

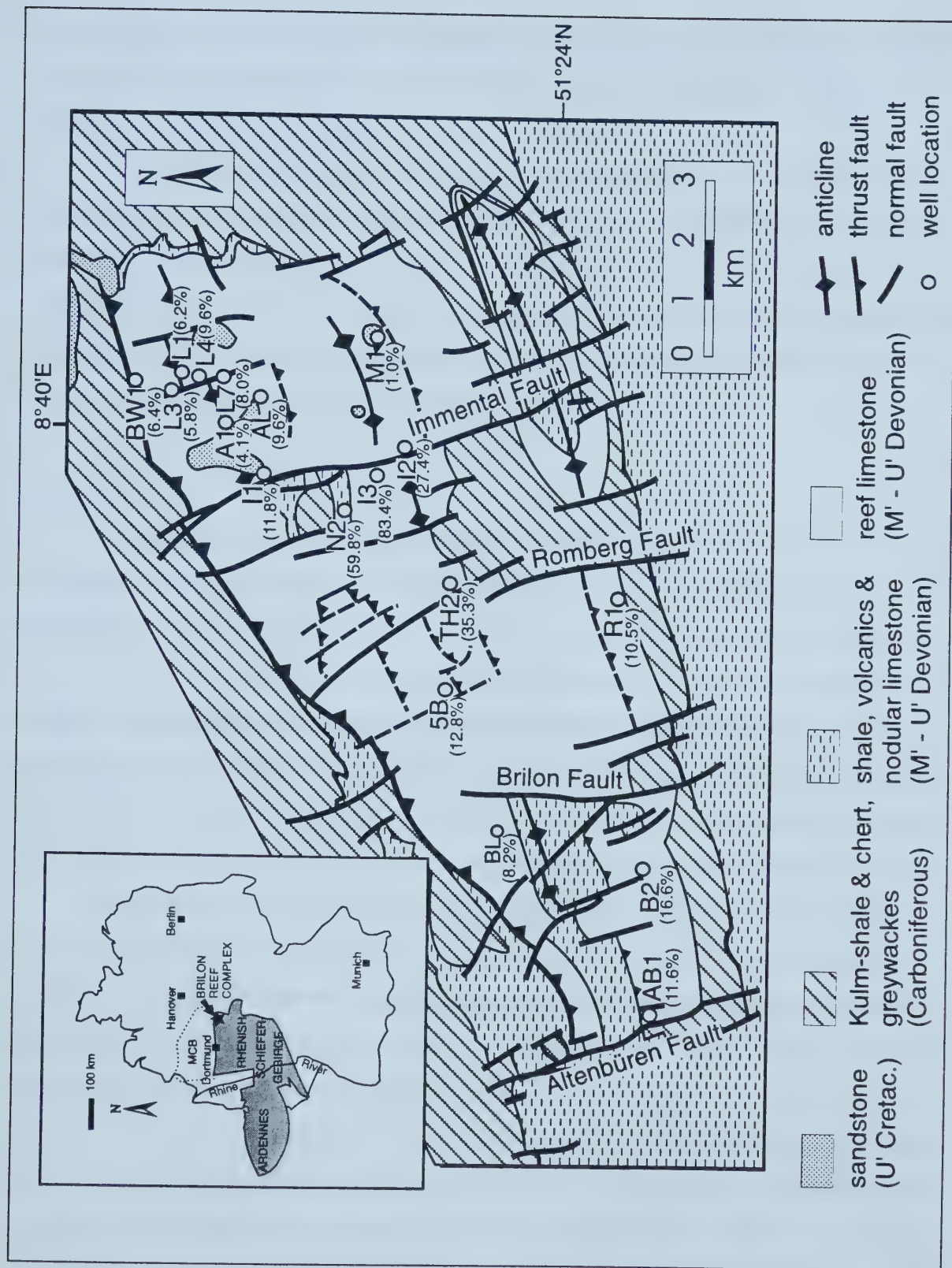


Figure 3.1





Considering the shallow burial depth, nonplanar dolomite textures (dolomite Types 1 and 2) and the presence of saddle dolomite (dolomite Type 3) serve as petrographic evidence for the hydrothermal origin of the dolostone intervals (Chapter 2).

After having established the paragenetic framework for the post-Variscan dolomitization and associated sulfide mineralization in the Brilon Reef Complex based on petrographic observations in Chapter 2, the objectives of Chapter 3 are (1) to furnish further evidence in support of the hypothesis that dolomitization in the Brilon Reef Complex is fault-controlled and hydrothermal in origin and (2) to constrain the composition and timing of the fluids that used these faults as conduits.

### **3.2 Methods**

Limestone samples from selected cores were taken at distances ranging from tens of centimeters to up to 30 m away from the dolostone intervals to investigate the effects of dolomitization on the petrographic features and composition of the undolomitized limestone host rock adjacent to the dolostone intervals. Polished thin sections of these limestone samples were prepared and examined by transmitted and cathodoluminescence microscopy (for equipment specifications and operating conditions, see Chapter 2). Further petrographic investigations were carried out on 16 samples of limestone and dolostone using a Scanning Electron Microscope (JEOL JSM - 6400) at the University of Bilbao, Basque Country.

Based on the results of the petrographic investigations of the dolomitized intervals and their surrounding limestone host rock (Chapter 2), 100 samples were selected for geochemical analysis in order to compare selected pre-Variscan carbonate mineral phases of the limestone host rock (limestone matrix, calcite fossils, one “early” calcite cement) to selected post-Variscan carbonate mineral phases from the dolostone intervals (dolomite Types 1, 2, 3, “late” calcite cements TC and CSC). The “early” calcite cement is a radial-fibrous calcite cement, which formed during phase 4 of the paragenetic succession (Table 3.1; Machel 1979, 1990). Dolomite Type 1 formed during phase 21, dolomite Types 2 and 3 during phase 22, and the post-Variscan calcite cements (TC: vug- and fracture-filling, translucent calcite; CSC: vug- and fracture-lining clear scalenohedral calcite) formed in phase 24 (Table 3.1).





**Table 3.1:** Succession of post-sedimentary textural and mineralogical changes of the Middle and Upper Devonian “Massenkalk” in the Brilon Reef Complex. Data for pre-Variscan diagenesis (phase 1 to 18) are from Machel (1979, 1990), data for phases 19 to 25 are from this study (Chapter 2). Mineral phases selected for geochemical analysis are highlighted in grey and labeled. Paragenetic position of bulk limestone and calcite fossils are not indicated, because they probably represent a continuum from pristine Middle Devonian calcite (e.g., brachiopod shell) to calcite that has been recrystallized during various diagenetic phases.

DIAGENETIC STAGE DEPTH PHASE	MIDDLE DEVONIAN TO EARLY CARBONIFEROUS																		LATE CARB.	PERMIAN TO RECENT					
	PRE-VARISCAN DIAGENESIS																		SYN- TECT.	POST- VARISCAN					
	I 0 - 30 m						II 30 m - 150 m						III 150 m to >2000 m						IV	V					
	1	2	3	4	5	6	7	8	9	10	11	12	13	14	15	16	17	18	19	20	21	22	23	24	25
textural and/or mineralogical change																									
micrite envelopes																									
carbonate dissolution																									
internal sediment																									
calcite cement																									
fracturing																									
dolomite																									
quartz																									
limonite/goethite																									
dedolomitization																									
recrystallization																									
stylolites																									
tectonic shearing																									
pyrite																									
sphalerite																									
galena																									

Table 3.1





Petrographic descriptions of the post-Variscan mineral phases are given in Chapter 2 and are summarized in Table 3.2.

Phase 21	dolomite Type 1	<ul style="list-style-type: none"> <li>- grey matrix dolomite, replacing limestone and fossil fragments;</li> <li>- planar to nonplanar mosaics of fine- to coarse-crystalline (&lt; 50 to 300 <math>\mu\text{m}</math>), sub- to anhedral crystals;</li> <li>- mottled red CL;</li> </ul>
Phase 22	dolomite Type 2	<ul style="list-style-type: none"> <li>- milky-white to tan dolomite, originating at fractures and vugs, creating cm to m-wide halos within dolomite Type 1, suggesting recrystallization;</li> <li>- nonplanar mosaics of coarse- to very coarse-crystalline (300 <math>\mu\text{m}</math> to 3 mm, sub- to anhedral crystals; some crystals with sweeping extinction in polarized light;</li> <li>- mottled red CL;</li> </ul>
	dolomite Type 3	<ul style="list-style-type: none"> <li>- milky-white to tan saddle dolomite cement, partially to completely filling vugs and fractures;</li> <li>- euhedral to subhedral crystals (800 <math>\mu\text{m}</math> to 5 mm) with curved crystal faces and sweeping extinction in polarized light;</li> <li>- mottled red CL, with rims exhibiting alternation of dark and lighter red;</li> </ul>
Phase 23	honey sphalerite	<ul style="list-style-type: none"> <li>- translucent, honey-colored to red, tetrahedral crystals, up to 4 mm in diameter;</li> </ul>
Phase 24	TC	<ul style="list-style-type: none"> <li>- fracture- and vug-filling translucent to clear, poikilotopic calcite cement;</li> <li>- red stain and orange CL, indicating that cement is Fe-poor;</li> </ul>
	CSC	<ul style="list-style-type: none"> <li>- fracture- and vug-lining clear scalenohedral calcite cement with crystals up to 1.5 cm in size;</li> <li>- crystals show zonation into a Fe-poor core (red stain, orange CL) and a Fe-rich rim (blue stain, dull-red CL); rims exhibit succession of several thin zones, which cross-cut previous zones, indicating phases of corrosion followed by phases of calcite precipitation.</li> </ul>

**Table 3.2:** Summary of the petrographic characteristics of post-Variscan dolomite types, sphalerite, and calcite cements in dolostone intervals from the Brilon Reef Complex. For detailed descriptions, see Chapter 2.

Powder samples of carbonate mineral phases ranging in weight from 200 to 350 mg were extracted from thin section offcuts using a low speed dental drill. In the case of a non-luminescent brachiopod shell (*Stringocephalus*), only the inner “secondary” layer was sampled for geochemical analysis, in order to serve as a reference for least-altered Middle Devonian calcite (Diener et al. 1996; Qing et al. 1998). Growth zones of vug-filling scalenohedral calcite cements (CSC) could be sampled separately only in one case. In cases where petrographic observations indicated the possibility of a mixture of calcite and dolomite within a powder sample, its mineralogy was determined by X-ray diffraction. Mixtures of



calcite and dolomite were not further considered.

The average crystal size of dolomite samples was determined by measuring the longest dimension of dolomite crystals encountered at 50 equally spaced points along a linear traverse on a thin section in order to better characterize the three dolomite types and to be able to evaluate variations in their isotopic and chemical compositions (Gregg and Shelton 1990). An attempt was made to carry out these measurements on the area on the thin section that corresponds directly to the area on the thin section offcut, from which powder samples were taken for geochemical analysis.

The carbon and oxygen isotope compositions of 47 calcite and 42 dolomite samples were determined following the standard procedure by McCrea (1950). A 20 to 30 mg aliquot of sample powder was reacted with 100 % phosphoric acid at 25°C for 24 hours (calcite) and one week (dolomite). The resulting CO<sub>2</sub>-gases were analyzed with a Finnigan-MAT 252 mass spectrometer at the University of Alberta. Results were generally reproducible within  $\pm 0.1$  ‰ for  $\delta^{18}\text{O}$  and  $\delta^{13}\text{C}$  and are reported relative to PDB (Pee Dee Belemnite). Values for  $\delta^{18}\text{O}$  of dolomite samples have been corrected for the dolomite - phosphoric acid fractionation by subtracting 0.82 ‰ (Sharma and Clayton 1964).

Powder samples of calcite (39) and dolomite (30) were analyzed for major, minor and trace elements (total of 54 cations analyzed) using a Fisons PQ2 inductively coupled plasma mass spectrometer (ICP-MS) at the Institute for Sedimentary Petroleum Geology in Calgary. Preparation of the sample solutions was carried out using a procedure designed to ensure minimum interference of non-carbonate material utilizing dilute (1.0 N) HCl for dissolution followed by filtering the sample solutions (see Appendix 3). Mg and Ca concentrations were determined using a Dionex 500 liquid chromatograph (ILC) system. Lower detection limits for all elements analyzed by either method are at the ppb level. Of the cations successfully analyzed, only Mg, Ca, Mn, Na, Sr, Pb, and Zn are of direct interest to the objectives of this study. Data for Fe were rejected due to problems with the reliability of the results. The comparison of the element concentrations from each sample with the weight fraction of insoluble residue and with the concentrations of elements characteristic of non-carbonate material (Al, Si, K, Rb) confirms that the contribution by leaching of non-carbonate material can be considered negligible.





Pre-and post-Variscan calcite and dolomite mineral phases in 29 polished thin sections were analyzed on a JEOL JXA-8900R electron microprobe at the University of Alberta in order to check the results from the wet chemical methods and to obtain geochemical information on diagenetic phases that were too small to sample with a dental drill. Operating conditions for the microprobe were 15 kV accelerating voltage, 5 nA beam current at the Faraday cup, 10  $\mu\text{m}$  beam diameter, and peak sample times of 100 seconds (background 50 seconds). Individual spots were analyzed for Mg, Ca, Fe, and Mn. Sr was analyzed in only one sample of a Givetian brachiopod. Detection limits on the electron microprobe are 130 ppm for Mg, 117 ppm for Ca, 130 ppm for Mn, 130 ppm for Fe, and 109 ppm for Sr at a 95 % confidence level for all elements.

For the measurement of the  $^{87}\text{Sr}/^{86}\text{Sr}$  ratios of calcite and dolomite samples, 25 mg aliquots of sample powder were dissolved in 1N HCl. Strontium was extracted from the solutions using standard cation exchange techniques. The Sr isotopic analyses were carried out on a VG 354 thermal ionization mass spectrometer at the University of Alberta. The samples were loaded as a phospho-tantalate gel on a single Re ribbon bead assembly. In-run precision was better than  $4 \times 10^{-5}$  ( $2\sigma$ ). Duplicate analysis of single powder samples were reproducible to within  $1 \times 10^{-4}$  ( $2\sigma$ ). The isotopic ratios of the samples were normalized against the value of the NBS 987 standard (lab long term average: 0.710235).

Fluid inclusion microthermometry was carried out on two-phase (liquid-vapor) fluid inclusions in 2 samples of dolomite Type 3 (phase 22), 1 sphalerite sample (phase 23), and 3 samples of clear euhedral calcite cement (phase 24) to gain information about minimum temperatures of formation ( $T_h$ ), bulk fluid salinities (calculated from the freezing point depression  $T_m\text{-ice}$  expressed as equivalent weight % NaCl), and qualitative information about the cation composition of the inclusion fluids (from eutectic temperature  $T_e$ ) (Appendix 4). The temperature measurements were carried out on a modified Fluid Inc. USGS gas-flow heating-freezing stage with a Doric Trendicator 410A digital thermometric control system attached to a Leitz microscope at the University of Alberta, following standard microthermometry procedures (Roedder 1984; Shepard et al. 1985; Goldstein and Reynolds 1994). Accuracy of microthermometric determinations is within  $\pm 0.2^\circ\text{C}$  for freezing and  $\pm 2.0^\circ\text{C}$  for heating. Fluid inclusions in dolomite Types 1 and 2 are below 2  $\mu\text{m}$





in size and therefore too small to investigate with the equipment used for this study. Inclusions are classified as 1) primary, when a clear relationship to the growth zonation of the respective crystal is evident, 2) pseudosecondary, when a trail of inclusions ends abruptly at a growth zone boundary, and 3) secondary, when a trail of inclusions appears to cut across growth zones of a crystal. No pressure correction was applied, because the post-Variscan mineralization in the Rhenish Schiefergebirge is generally thought to have formed at depths of less than 2 km (Behr et al. 1987).

Correlation coefficients “r” and their significance levels “sig.” were calculated using SPSS 7.0 for Windows.

### **3.3 Results and discussion**

#### ***3.3.1 Petrographic changes of the limestone host rock adjacent to dolostone intervals***

Most of the investigated limestone samples displayed facies variations and various diagenetic and tectonic overprints, which made it impossible to make petrographic comparisons among the samples and to judge if the observed differences were due to the effects of the dolomitization event(s) or not. Of the investigated drill cores, only the Almerfeld drill core (AL) from the eastern part of the Brilon Reef Complex provided samples where petrographic changes could clearly be attributed to the effects of dolomitization (Table 3.3). These samples consist mainly of micritic matrix and have been classified as wacke- and floatstones, according to the carbonate classification by Dunham (1962). All are physically compacted, as indicated by the alignment of clay particles of the more incompetent matrix around fossil components. Crystal sizes within the matrix of all samples are small ( $< 20 \mu\text{m}$ ). Cathodoluminescence microscopy reveals that the calcitic matrix is dominantly non-luminescent to dark red and that there is a trend of increasing dominance of dark red with decreasing distance to the dolostone intervals, and a mottled orange color occurs directly at the contacts between limestone and dolostone (within 0.4 m). The mottled orange color observed in sample AL-654s occurs at a vertical distance of 5.1 m from the closest dolostone interval within the drill core. This mottled-orange luminescence color of calcite also occurs in thin sections of undolomitized remnants of limestone (presumably stromatoporoid fragments) within the dolomitized intervals in the Almerfeld



sample	rock type	vertical distance to dolostone interval	CL-characteristics of micritic limestone matrix
AL-364s	floatstone	20.0 m	non-luminescent to dark red
AL-374s	wackestone	10.0 m	non-luminescent to dark red
AL-381s	floatstone	3.0 m	dark red to non-luminescent
AL-393s	floatstone	3.0 m	non-luminescent to dark red
AL-627.5s	wackestone	20.2 m	non-luminescent to dark red
AL-637.5s	floatstone	10.2 m	non-luminescent to dark red
AL-642.5s	floatstone	5.2 m	non-luminescent to dark red
AL-646.5s	floatstone	1.2 m	dark red to non-luminescent
AL-654s	floatstone	5.1 m	mottled orange
AL-662s	floatstone	10 m	non-luminescent to dark red
AL-669.1s	floatstone	2.9 m	non-luminescent to dark red
AL-671.6	wackestone	0.4 m	dark red to non-luminescent
AL-672.0	wackestone	0.0 m	mottled orange
AL-736s	floatstone	1.9 m	dark red to non-luminescent
AL-742s	floatstone	7.9 m	dark red to non-luminescent
AL-770s	floatstone	18.0 m	non-luminescent to dark red

**Table 3.3:** List of samples of micritic limestones used for petrographic comparison to determine the effects of dolomitization on the petrographic characteristics of the undolomitized limestone host rock in the direct vicinity of dolostone intervals.

drill core as well as in several limestone samples taken close to or directly at limestone-dolostone contacts in other drill cores from the Brilon Reef. The exact distance up to which this texture is developed could not be determined. In the case of the Almerfeld drill core, the change in cathodoluminescence color of the undolomitized limestone matrix appears to extend only from several tens of centimeters (mottled orange CL) to a maximum of several meters distance (dominantly dark red CL) from the limestone-dolostone contact.

A set of four of the above samples (at distances of 10 m, 2.9 m, 0.4 m and 0.0 m from the nearest limestone/dolostone contact) was investigated by scanning electron microscopy (SEM) to identify possible changes in crystal size and habit (Plate 3.1). These investigations



show that with increasing proximity to the dolomitized intervals, the size of calcite crystals that make up the limestone matrix increases from about 2 to about 20  $\mu\text{m}$ , crystal shapes change from subhedral to anhedral, and intercrystalline porosity decreases. The most drastic changes apparently occur within the last 0.4 m, corresponding with the observed changes in cathodoluminescence color.

The changes in CL properties are most likely due to changes in the trace element composition of the investigated samples (Marshall 1988), i.e., the increasing dominance of trace elements that act as CL activators (probably Mn) over those that act as CL quenchers (e.g., Fe) with decreasing distance to the dolostone intervals.





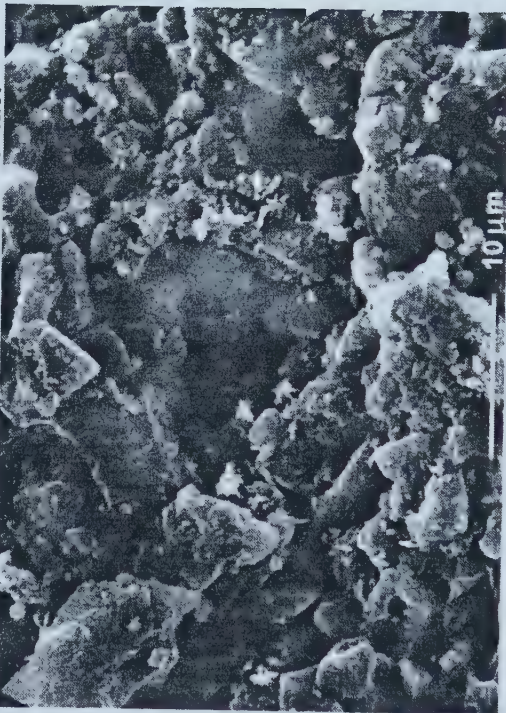


**Plate 3.1:** SEM photographs of 4 samples of micritic limestone matrix taken at 10 m (a) (AL-662.0), 2.9 m (b) (AL-669.1), 0.4 m (c) (AL-671.6), and 0.0 m (d) (AL-672.0) distance from a dolostone interval. Photographs were taken at different magnifications (see scale bars). With decreasing distance to dolostone interval, crystal size increases from 2 to 20  $\mu\text{m}$ , crystal shape changes from euhedral to anhedral, and intercrystalline porosity decreases.

a) 10 m distance from limestone/dolostone contact



c) 0.4 m distance from limestone/dolostone contact



b) 2.9 m distance from limestone/dolostone contact



d) directly at limestone/dolostone contact







### 3.3.2 Stable isotopes

#### 3.3.2.1 Characterization of pre- and post-Variscan carbonate phases

The carbon and oxygen isotope compositions of the following pre- and post-Variscan calcite and dolomite phases were determined: 1. pre-Variscan carbonate mineral phases (Tables 3.4 a and b): micritic limestone (n = 26); calcite fossils (stromatoporoids and tabulate corals, n = 11, non-luminescent brachiopod shell, n = 1); radiaxial-fibrous cement (n = 1); 2. post-Variscan carbonate mineral phases (Tables 3.5 a, b, c, and d): grey matrix dolomite (Type 1; n = 23), milky-white replacement dolomite (Type 2, n = 13); milky-white saddle dolomite cement (Type 3, n = 7); late diagenetic calcite cement (TC, n = 2; CSC, n = 7).

sample	depth m	distance m	$\delta^{13}\text{C}$ ‰ PDB	$\delta^{18}\text{O}$ ‰ PDB	Mn ppm	Sr ppm	Na ppm	Zn ppm	Pb ppm	Sr/Mn	$^{87}\text{Sr}/^{86}\text{Sr}$ $\pm 5 \times 10^{-5}$
AL-364s	364.0	20.0	3.2	-4.0	-	-	-	-	-	-	-
AL-374s	374.0	10.0	2.7	-4.1	98	359	91	12	14	3.66	0.70801
AL-381s	381.0	3.0	3.5	-4.5	254	296	71	22	27	1.17	-
AL-393s	393.0	3.0	3.1	-5.2	110	281	53	14	7	2.56	-
AL-400s	400.0	10.0	4.2	-2.8	60	239	85	7	1	3.96	-
AL-627.5s	627.5	21.1	4.9	-3.2	-	-	-	-	-	-	-
AL-637.5s	637.5	11.1	5.2	-2.9	163	301	51	26	20	1.85	-
AL-648.5	648.5	0.1	1.4	-6.0	-	-	-	-	-	-	-
AL-654s	654.0	3.5	4.4	-4.9	-	-	-	-	-	-	-
AL-669.1s	669.1	2.9	5.0	-4.4	168	312	58	18	9	1.86	0.70816
AL-671.6-8	671.7	0.3	4.0	-5.4	166	318	94	26	2	1.92	0.70825
AL-672.0-2	672.0	0.0	3.0	-7.0	1241	109	92	49	517	0.09	0.70875
AL-736s	736.0	3.5	4.5	-6.1	168	286	83	10	5	1.70	0.70857
AL-742s	742.0	9.5	4.9	-5.9	209	331	62	7	4	1.59	0.70855
AL-770s	770.0	27.5	5.2	-3.7	151	488	106	28	11	3.23	0.70791
L7-163.05	163.1	0.0	1.9	-5.8	549	182	82	41	29	0.33	-
L7-163.9	163.9	0.0	2.2	-9.2	1897	162	345	10	35	0.09	0.70944
L7-190.3	190.3	0.0	2.0	-4.4	-	-	-	-	-	-	-
L7-279s	279.0	10.1	3.2	-3.7	40	197	51	17	4	4.96	0.70806
L7-284s	284.0	5.1	2.1	-5.9	-	-	-	-	-	-	-
L7-288.8s	288.8	0.3	2.5	-5.7	203	220	64	22	9	1.09	-
L7-311.5s	311.5	6.0	2.2	-5.0	135	255	43	17	11	1.89	-
L7-321.5s	321.5	16.0	3.0	-4.8	47	246	59	19	11	5.20	-
L7-363.4s	363.4	4.7	4.0	-3.3	88	374	134	25	37	4.26	-
L7-367.3s	367.3	0.8	4.7	-3.9	-	-	-	-	-	-	-
R1-372.6	372.6	2.6	2.8	-4.4	261	161	117	16	10	0.62	-
average			3.4	-4.9	316	269	92	20	40	2.21	0.70841

**Table 3.4a:** Results of stable isotope, trace element (from ICP-MS), and Sr-isotope analysis of samples of micritic limestone matrix.





sample	depth m	distance m	$\delta^{13}\text{C}$ ‰ PDB	$\delta^{18}\text{O}$ ‰ PDB	Mn ppm	Sr ppm	Na ppm	Zn ppm	Pb ppm	Sr/Mn	$^{87}\text{Sr}/^{86}\text{Sr}$ $\pm 5 \times 10^{-5}$
AL-642.5s	642.5	6.1	5.5	-3.7	147	368	89	8	11	2.50	-
AL-662s	662.0	10.0	4.8	-3.7	50	293	54	8	2	5.80	0.70841
AL-729.6-.8	729.7	0.0	2.5	-9.0	1431	205	84	8	5	0.14	0.70898
B2-435.4	435.4	0.0	-	-	-	-	-	-	-	-	0.70861
L7-188.9	188.9	0.0	2.4	-4.4	648	142	109	13	4	0.22	-
L7-305.5	305.5	0.0	1.6	-8.8	1057	113	67	31	46	0.11	0.70911
*L7-406.0-.1	406.1	10.5	2.5	-4.3	35	702	-	-	-	20.06	0.70789
M-279.7	279.7	>25.0	1.6	-5.1	139	335	89	22	27	2.40	-
R1-17.5	17.5	>25.0	2.9	-4.4	60	177	85	12	3	2.97	0.70824
R1-105.5	105.5	12.2	1.3	-5.2	65	165	72	7	3	2.53	-
R1-325.5	325.5	21.5	3.5	-4.7	124	165	71	7	2	1.33	-
^R1-362.3	362.3	5.4	2.1	-4.0	-	-	-	-	-	-	-
R1-411.2-.4	411.3	22.0	2.7	-5.6	150	183	89	9	3	1.22	0.70837
average			2.8	-5.3	355	259	74	13	11	3.57	0.70852

**Table 3.4b:** Results of stable isotope, trace element (from ICP-MS), and Sr-isotope analysis of samples of calcite fossils and one radiaxial-fibrous cement (indicated by ^). Sample of non-luminescent shell of brachiopod with Mn and Sr concentrations from electron microprobe is indicated by \*.



sample	depth m	average crystal size µm	$\delta^{13}\text{C}$ ‰ PDB	$\delta^{18}\text{O}$ ‰ PDB	Mn ppm	Sr ppm	Na ppm	Zn ppm	Pb ppm	$^{87}\text{Sr}/^{86}\text{Sr}$ $\pm 5 \times 10^{-5}$
AL-648.9	648.9	123	-	-	7017	56	157	35	9	-
AL-681.1.-.2	681.2	51	3.7	-6.9	1377	54	284	45	30	0.70941
AL-699.0	699.0	154	2.9	-8.8	1688	42	346	55	13	-
AL-699.1	699.1	43	3.4	-7.7	1810	38	317	110	7	-
AL-699.5	699.5	134	2.1	-8.8	-	-	-	-	-	-
AL-707.3-.4	707.4	223	2.5	-9.5	-	-	-	-	-	-
AL-709.5-.6	709.6	265	3.3	-10.8	-	-	-	-	-	-
AL-718.6-.8	718.7	121	3.6	-8.4	1265	50	435	54	21	-
AL-720.0-.1	720.1	225	3.7	-10.1	-	-	-	-	-	-
AL-726.2-.3	726.3	175	3.1	-9.4	-	-	-	-	-	-
AL-726.3-.4	726.4	287	3.2	-10.3	-	-	-	-	-	-
AL-726.8	726.8	289	3.0	-11.3	-	-	-	-	-	-
B2-435.4	435.4	96	-	-	-	-	-	-	-	0.70941
B2-441.4	441.4	117	-	-	-	-	-	-	-	0.70893
I1-249.45	249.5	141	-	-	-	-	-	-	-	0.70889
L1-262.4	262.4	138	3.0	-8.2	-	-	-	-	-	-
L1-262.5	262.5	65	3.8	-7.3	4746	44	286	53	398	-
L1-265.9	265.9	165	-	-	3019	40	425	26	50	-
L1-573.9	573.9	172	3.8	-8.8	1930	69	455	70	58	0.70922
L1-576.8	576.8	243	3.5	-9.0	2703	65	419	21	7	-
L1-591.9	591.9	264	3.6	-10.0	1800	52	434	66	30	-
L1-591.9	591.9	-	-	-	1938	57	423	65	34	-
L7-163.05	163.05	54	3.1	-7.6	-	-	-	-	-	-
L7-163.9	163.9	211	2.2	-10.0	-	-	-	-	-	-
L7-166.1	166.1	-	-	-	909	28	295	27	16	-
L7-188.9	188.9	-	-	-	464	44	244	16	5	-
L7-190.3	190.3	-	-	-	386	46	168	14	7	-
L7-292.3	292.3	62	3.6	-7.9	1830	46	331	82	60	0.70944
L7-302.5	302.5	129	3.1	-8.7	1420	40	346	28	199	-
L7-369.1	369.1	109	3.0	-8.5	1053	22	240	38	69	-
L7-384.6	384.6	87	3.0	-8.0	1012	27	266	29	12	-
L7-395.4	395.4	156	3.9	-8.5	941	25	307	26	10	-
average		154	3.2	-8.9	1964	44	325	45	54	0.70922

**Table 3.5a:** Average crystal sizes from thin sections and results of stable isotope, trace element (from ICP-MS), and Sr-isotope analysis of powder samples of dolomite Type 1.



sample	depth m	average crystal size $\mu\text{m}$	$\delta^{13}\text{C}$ ‰ PDB	$\delta^{18}\text{O}$ ‰ PDB	Mn ppm	Sr ppm	Na ppm	Zn ppm	Pb ppm	$^{87}\text{Sr}/^{86}\text{Sr}$ $\pm 5 \times 10^{-5}$
AL-681.1	681.1	382	2.4	-9.2	-	-	-	-	-	0.70873
AL-681.1-.2	681.2	563	3.5	-9.6	-	-	-	-	-	-
AL-681.8-.9	681.9	486	2.1	-9.3	-	-	-	-	-	-
AL-691.5	691.5	387	2.7	-9.1	-	-	-	-	-	-
AL-699.0-.1	699.1	678	1.8	-9.8	2475	27	377	62	12	-
AL-699.5	699.5	476	2.5	-9.4	-	-	-	-	-	-
AL-713.8	713.8	424	3.9	-7.9	6948	69	246	114	5	-
AL-720.0-.1	720.1	743	2.1	-10.8	-	-	-	-	-	-
AL-726.2-.3	726.3	1243	3.0	-10.7	-	-	-	-	-	-
AL-729.6-.8	729.7	1194	-	-	1741	43	405	18	2	-
B2-441.4	441.4	462	-	-	-	-	-	-	-	0.70854
L1-263.4	263.4	543	3.8	-7.6	3057	47	448	17	12	0.70913
L1-573.9	573.9	1254	3.5	-10.2	-	-	-	-	-	-
L7-302.5	302.5	921	2.1	-10.1	1172	29	278	37	35	0.70862
L7-384.6	384.6	767	3.1	-8.4	1225	28	355	33	89	0.70865
average		701	2.8	-9.4	2770	40	351	47	26	0.70873

**Table 3.5b:** Average crystal sizes from thin sections and results of stable isotope, trace element (from ICP-MS), and Sr-isotope analysis of powder samples of dolomite Type 2.

sample	depth m	average crystal size $\mu\text{m}$	$\delta^{13}\text{C}$ ‰ PDB	$\delta^{18}\text{O}$ ‰ PDB	Mn ppm	Sr ppm	Na ppm	Zn ppm	Pb ppm	$^{87}\text{Sr}/^{86}\text{Sr}$ $\pm 5 \times 10^{-5}$
AL-218.6	218.6	1552	-	-	2958	52	372	17	3	-
AL-650.2	650.2	1563	3.5	-8.5	6581	60	417	16	2	-
AL-702.1-.2	702.2	1754	2.4	-10.7	-	-	-	-	-	-
AL-709.5-.6	709.6	2456	3.3	-11.0	-	-	-	-	-	-
AL-718.6-.8	718.7	1567	3.6	-10.4	1769	40	471	19	3	0.70875
AL-726.3-.4	726.4	1987	3.2	-10.3	-	-	-	-	-	-
B2-441.4	441.4	1659	-	-	-	-	-	-	-	0.70855
L7-375.1	375.1	1539	3.7	-8.3	1176	35	336	27	13	-
L7-395.4	395.4	1643	3.8	-8.8	1909	28	282	20	2	-
average		1747	3.4	-9.7	2879	43	376	20	5	0.70865

**Table 3.5c:** Average crystal sizes from thin sections and results of stable isotope, trace element (from ICP-MS), and Sr-isotope analysis of powder samples of dolomite Type 3.





sample	depth m	calcite type	$\delta^{13}\text{C}$ ‰ PDB	$\delta^{18}\text{O}$ ‰ PDB	Mn ppm	Sr ppm	Na ppm	Zn ppm	Pb ppm	$^{87}\text{Sr}/^{86}\text{Sr}$ $\pm 5 \times 10^{-5}$
AL-675.7	675.7	CSC	2.0	-9.1	6784	159	52	26	2	-
AL-709.5-.6	709.6	CSC	2.3	-8.8	-	-	-	-	-	-
AL-713.8	713.8	CSC	-	-	2044	90	80	6	2	0.71210
AL-720.0-.1	720.1	CSC	2.1	-10.7	-	-	-	-	-	-
AL-726.8	726.8	CSC	3.8	-9.2	-	-	-	-	-	0.71233
L7-302.5	302.5	CSC	3.0	-7.6	2299	103	85	9	24	0.71238
L7-375.1	375.1	CSC core	2.8	-7.8	2317	127	116	18	12	0.71058
L7-375.1	375.1	CSC rim	3.2	-7.2	2939	75	123	17	46	0.71371
L7-384.6	384.6	CSC	-	-	2188	98	125	20	14	0.71123
AL-699.0-.1	699.1	TC	-	-	501	19	65	1090	6	-
L1-265.9	265.9	TC	3.1	-6.7	-	-	-	-	-	-
L7-151.5	151.5	TC	2.5	-7.3	834	65	61	4	1	0.71085
T2-256.2	256.2	TC	-	-	489	8	39	444	251	-
		average	2.8	-8.3	2266	83	83	182	40	0.71188

**Table 3.5d:** Results of stable isotope, trace element (from ICP-MS), and Sr-isotope analysis of powder samples of calcite cements CSC and TC of phase 24.

The carbon and oxygen isotope compositions of the analyzed host rock limestones range from +1.4 to +5.5 ‰ PDB and -2.8 to -9.2 ‰ PDB, respectively (Figure 3.2a). Samples of calcite fossils (stromatoporoids and corals) have  $\delta^{13}\text{C}$  values between +1.3 and +3.6 ‰ PDB and  $\delta^{18}\text{O}$  values between -3.6 and -9.0 ‰ PDB. The sample of a non-luminescent shell of a Givetian brachiopod (*Stringocephalus burtini*) has a  $\delta^{13}\text{C}$  value of +2.5 ‰ PDB and a  $\delta^{18}\text{O}$  value of -4.3 ‰ PDB. The single sample of a radiaxial fibrous cement has a  $\delta^{13}\text{C}$  value of +2.1 ‰ PDB and a  $\delta^{18}\text{O}$  value of -4.0 ‰ PDB. The  $\delta^{13}\text{C}$  values of all of the investigated post-Variscan carbonate samples range from +1.8 to +3.9 ‰ PDB, and their  $\delta^{18}\text{O}$  values range from -6.7 to -11.3 ‰ PDB (Type 1: -6.9 to -11.3 ‰ PDB; Types 2 and 3: -7.9 to -11.0 ‰ PDB; late calcite cement: -6.7 to -10.7 ‰ PDB; Figure 3.2b).

A  $\delta^{13}\text{C}$  value of +2 ‰ ( $\pm 1.0$ ) PDB is considered representative of Middle to Upper Devonian seawater (Veizer et al. 1986; Hurley and Lohmann 1989; Lohmann and Walker 1989) (Figure 3.2a). By comparison, the extremely enriched values found in the Brilon limestones are unusual for Devonian carbonates. However, Popp et al. (1986a and b) reported values of up to +4.8 ‰ PDB from Givetian brachiopods, Brand and Morrison (1987) gave values of up to +4.4 ‰ PDB for Devonian brachiopods, and Dunn





**Figure 3.2:** Carbon and oxygen isotope compositions of pre-Variscan (a) and post-Variscan carbonates (b) from the Brilon Reef Complex. Range of  $\delta^{13}\text{C}$  values of Devonian marine calcites from Veizer et. (1986), Hurley and Lohmann (1988), and Lohmann and Walker (1989), range of  $\delta^{18}\text{O}$  values of least altered Devonian calcites from Allan and Wiggins (1993). (c) Summary diagram pointing out the possible processes and changes in conditions that resulted in the shifts of carbon and oxygen isotope compositions of the pre- and post-Variscan carbonates. The  $\delta^{18}\text{O}$  value of  $-6.5\text{‰ PDB}$  defines the boundary between the pre-Variscan ( $\delta^{18}\text{O}$ -value  $> -6.5\text{‰ PDB}$ ) and post-Variscan calcites and dolomites ( $\delta^{18}\text{O}$  value  $< -6.5\text{‰ PDB}$ ). Pre-Variscan calcites with  $\delta^{18}\text{O}$  values lower than  $-6.5\text{‰ PDB}$  have been recrystallized at elevated temperatures and/or under the influence of fluids depleted in  $^{18}\text{O}$  (e.g., meteoric water).

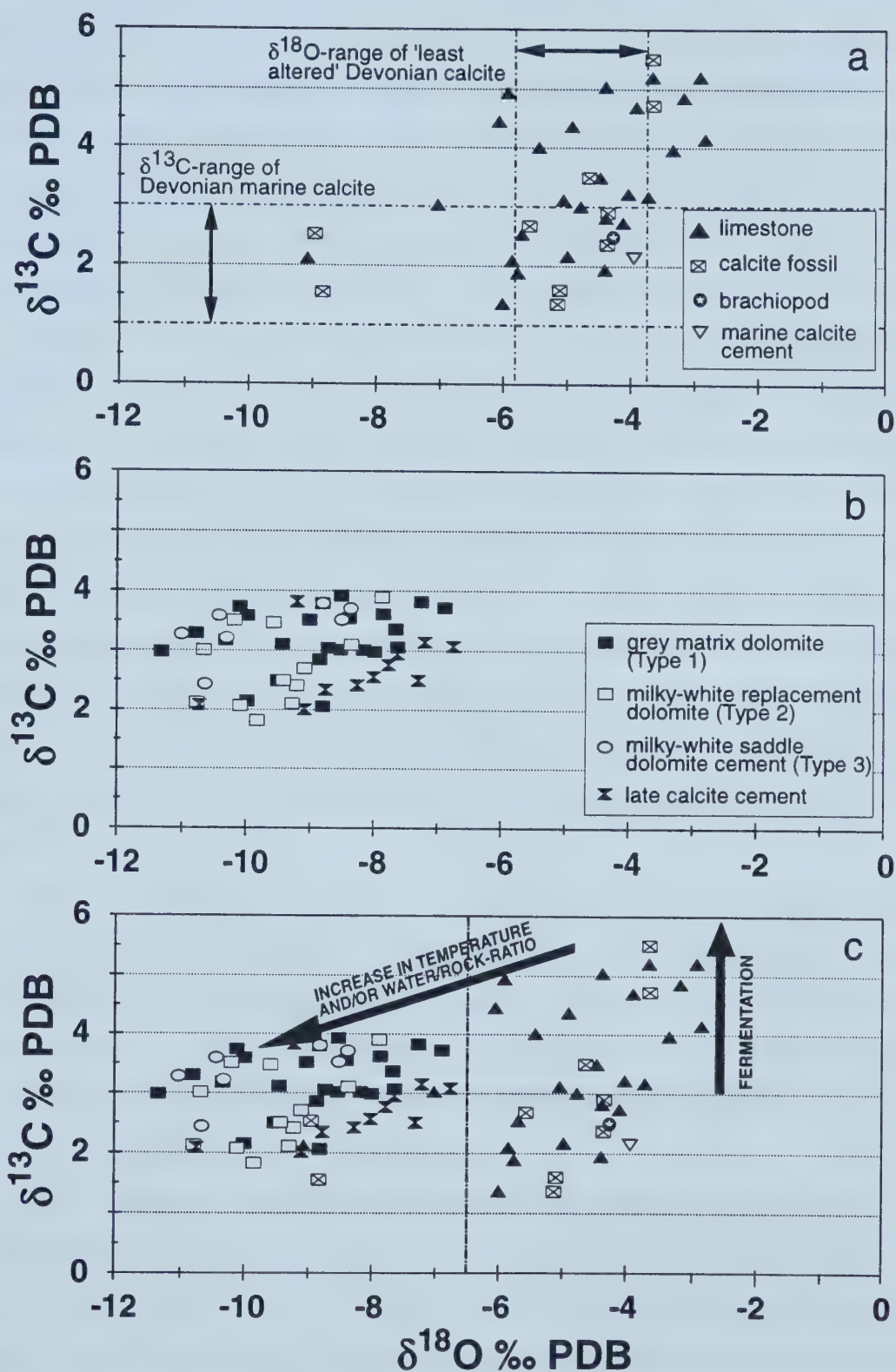


Figure 3.2





(1988) reported values of up to 5.5 ‰ PDB in Frasnian abiotic marine calcite cements. Enrichment of  $^{13}\text{C}$  in carbonates is generally assigned to early-diagenetic fermentation reactions (Hudson 1975; Games and Hayes 1976; Reitsemá 1980; Lohmann et al. 1985) during shallow burial to up to 1000 m (Allan and Wiggins 1993), or to oxidation of organic matter or crude oil to  $\text{CO}_2$  in organic-poor sediments (Deuser 1970). The  $\delta^{13}\text{C}$  values of the post-Variscan carbonate phases (dolomite, calcite) fall within the range of the pre-Variscan carbonate phases, indicating that the carbon is derived mainly from the carbonate host rock.

For a given data set, the heaviest  $\delta^{18}\text{O}$  values are considered to be the best estimate of the primary  $\delta^{18}\text{O}$  value of marine carbonates (O'Neil 1987). On this basis, the primary  $\delta^{18}\text{O}$  value for the Middle and Upper Devonian carbonates of the Brilon Reef Complex is about -2.8 ‰ PDB, which is about 1 ‰ heavier than the upper limit of the range for the 'least altered' Devonian marine calcites reported by Allan and Wiggins (1993) (Figure 3.2a). Most of the pre-Variscan Brilon samples, however, have  $\delta^{18}\text{O}$  values within the range given by Allan and Wiggins (1993). The cause(s) for a possible enrichment of about 1 ‰ in  $\delta^{18}\text{O}$  of the Middle and Upper Devonian marine Brilon carbonates with respect to Allan and Wiggins' (1993) range for the 'least altered' Devonian marine calcites is/are not clear. This difference could be due to local variations in water temperature and/or salinity (e.g., James et al. 1997).

The highly depleted  $\delta^{18}\text{O}$  values of the post-Variscan carbonate phases suggest a possible influence of fluids depleted in  $^{18}\text{O}$  (e.g., meteoric water) and/or formation at elevated temperatures. The relatively large range of  $\delta^{18}\text{O}$  values of the post-Variscan carbonate phases can be attributed to 1) a range of temperatures during precipitation, or during replacement or recrystallization of older carbonate phases; or 2) differences in the water/rock-ratio (Taylor 1979); or 3) a combination of 1) and 2) (Figure 3.2c).

The  $\delta^{18}\text{O}$  value of -6.5 ‰ PDB defines the boundary between the pre-Variscan ( $\delta^{18}\text{O} > -6.5$  ‰ PDB) and post-Variscan calcites and dolomites ( $\delta^{18}\text{O} < -6.5$  ‰ PDB) (Figure 3.2c). Samples with a  $\delta^{18}\text{O}$  value  $< -6.5$  ‰ PDB are recrystallized (limestone matrix, fossil calcites) or formed (dolomite types, late calcite cements) at elevated temperatures and/or under the influence of fluids depleted in  $^{18}\text{O}$ . According to Allan and Wiggins (1993), this value also defines the boundary between early diagenetic dolomite ( $\delta^{18}\text{O} > -6.5$  ‰ PDB) and dolomite that formed at elevated temperatures ( $\delta^{18}\text{O} < -6.5$  ‰ PDB).



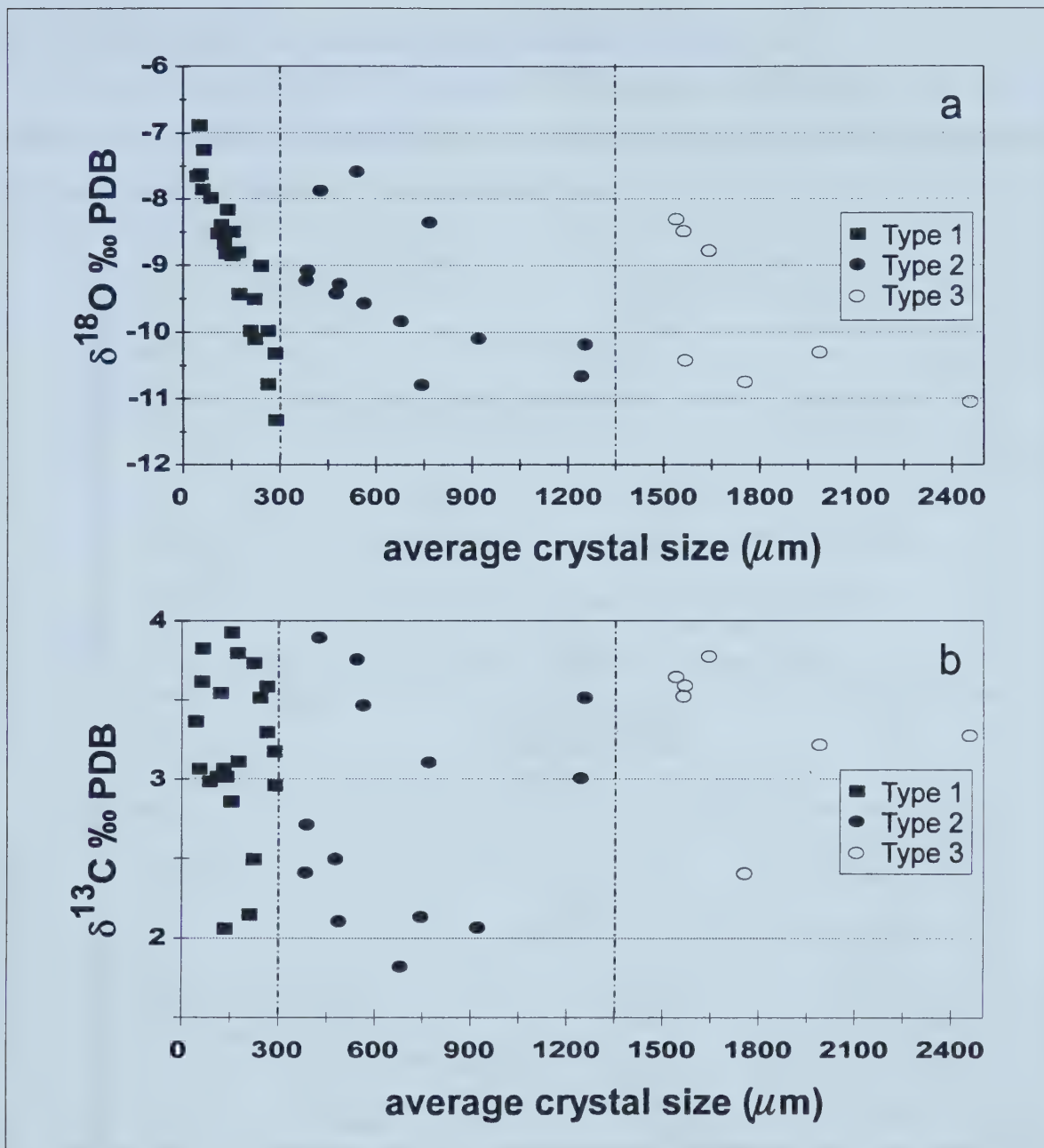
### 3.3.2.2 Stable isotope trends within the dolostone intervals

Where dolomite Type 1 and dolomite Type 2 were analyzed from the same core sample, dolomite Type 2 commonly is more depleted in  $^{18}\text{O}$  (by up to 2.3 ‰) (Tables 3.5a, b, c). Dolomite Type 1 shows a very strong negative correlation  $R = -0.936$ , sig.  $< 0.001$ ,  $N=23$ ) between average crystal size and  $\delta^{18}\text{O}$  value (Figure 3.3a). The values for dolomite Types 2 and 3 are much more scattered and show a weaker negative correlation between average crystal size and  $\delta^{18}\text{O}$  value for the bulk of the sample set (dolomite Type 2:  $r = -0.606$ , sig.  $= 0.028$ ,  $N = 13$ ; dolomite Type 3:  $r = -0.680$ , sig.  $= 0.093$ ,  $N = 7$ ). The petrographic “boundary” between dolomite Type 1 and Type 2 at a crystal size of 300  $\mu\text{m}$  corresponds to a distinct break in  $\delta^{18}\text{O}$  values (Figure 3.3a).

The  $\delta^{13}\text{C}$  value of dolomite Type 2 is either the same ( $\pm 0.1$  ‰) or lower than that of dolomite Type 1 in 7 out of 8 cases where corresponding samples of dolomite Type 1 and 2 were analyzed (Tables 3.5a and b). There is no apparent correlation between average crystal size and  $\delta^{13}\text{C}$  value of the dolomite types (Figure 3.3b).

Together with the petrographic evidence presented in Chapter 2 (i.e., nonplanar texture of dolomite Type 2; dolomite Type 3 as saddle dolomite), the  $\delta^{18}\text{O}$  trends indicate that dolomite Type 2 and 3 both formed at elevated temperatures and possibly from the same fluid. Dolomite Type 2 probably resulted from recrystallization of dolomite Type 1, while dolomite Type 3 (saddle dolomite cement) precipitated as a cement in remaining fractures and vugs. The overlap of the  $\delta^{18}\text{O}$  ranges of dolomite Types 1 and 2 reflects various degrees of recrystallization of dolomite Type 1 to Type 2 (that may or may not be visible petrographically) as a function of temperature and water-rock interaction. Dolomite Type 1 can be fully recrystallized with respect to its  $\delta^{18}\text{O}$  value and still retain its petrographic features that characterize it as grey matrix dolomite (grey color in hand sample, upper crystal size boundary at 300  $\mu\text{m}$ , etc.) (e.g., Machel 1997). On the other hand, dolomite Type 2 may not show complete equilibration of its oxygen isotopes with the fluid that led to its formation (i.e., via recrystallization of dolomite Type 1). A comprehensive discussion of the effects of the factors governing the extent of petrographic changes and isotope equilibration is beyond the scope of this study. These factors include the original crystal size, the amount and distribution of clay and organic material, and the initial  $\delta^{18}\text{O}$  value of the precursor dolomite, as well as the temperature and  $\delta^{18}\text{O}$  value of the dolomitizing (recrystallizing) fluid.





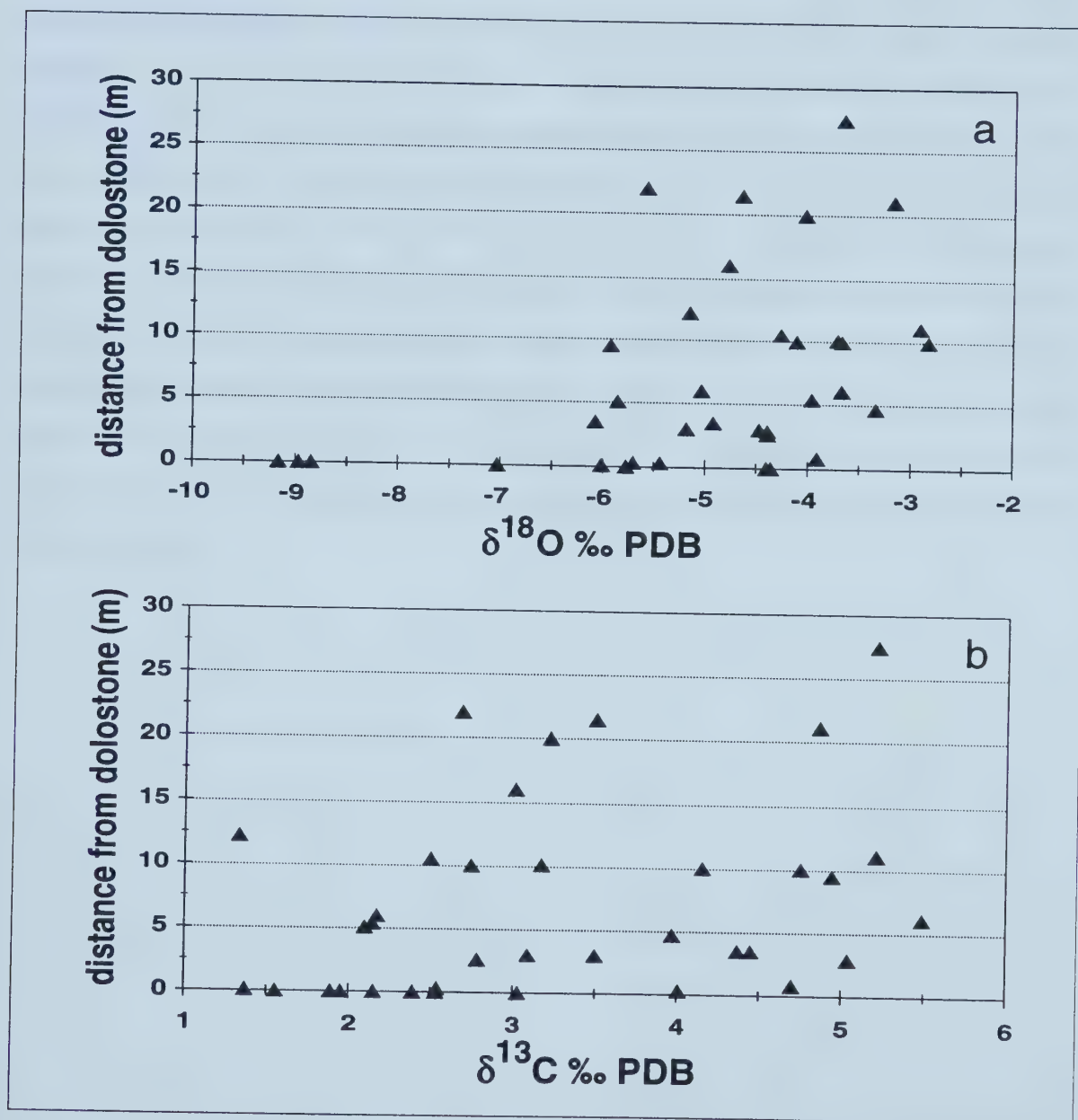
**Figure 3.3:** Cross plots of average crystal size versus  $\delta^{18}\text{O}$ - (a) and  $\delta^{13}\text{C}$ -values (b) of dolomite types from the Brilon Reef Complex. Hatched vertical lines at crystal sizes of 300 and 1350  $\mu\text{m}$  represent petrographic “boundaries” between dolomite Type 1 and Type 2 and dolomite Type 2 and Type 3, respectively. (a) Data for dolomite Type 1 show a very strong negative correlation between average crystal size and  $\delta^{18}\text{O}$  value ( $r=-0.936$ ,  $\text{sig.} < 0.001$ ). Data for dolomite types 2 and 3 display weak negative correlations (Type 2:  $r=-0.606$ ,  $\text{sig.}=0.028$ ; Type 3:  $r=-0.680$ ,  $\text{sig.}=0.093$ ). (b) No correlation between average crystal size and  $\delta^{13}\text{C}$  value is apparent for all three dolomite types (Type 1:  $r= -0.145$ ,  $\text{sig.}=0.510$ ; Type 2:  $r=-0.069$ ,  $\text{sig.}=0.824$ ; Type 3:  $r=0.288$ ,  $\text{sig.}=0.531$ ).





### 3.3.2.3 Stable isotope trends in the undolomitized limestone host rock

Plots of the  $\delta^{18}\text{O}$  and  $\delta^{13}\text{C}$  values of all limestone samples against their vertical distance to the nearest dolostone interval in the drillcores show a large scatter of values over the whole range of distances (Figures 3.4a and 3.4b).



**Figure 3.4:** Stable isotope compositions of all limestone samples (including calcite fossils) plotted against vertical distance to the nearest dolostone interval. Both oxygen (a) and carbon isotopes (b) show a large scatter of values over the whole range of distances. Some samples at the contact to dolostone intervals show very low  $\delta^{18}\text{O}$  values.



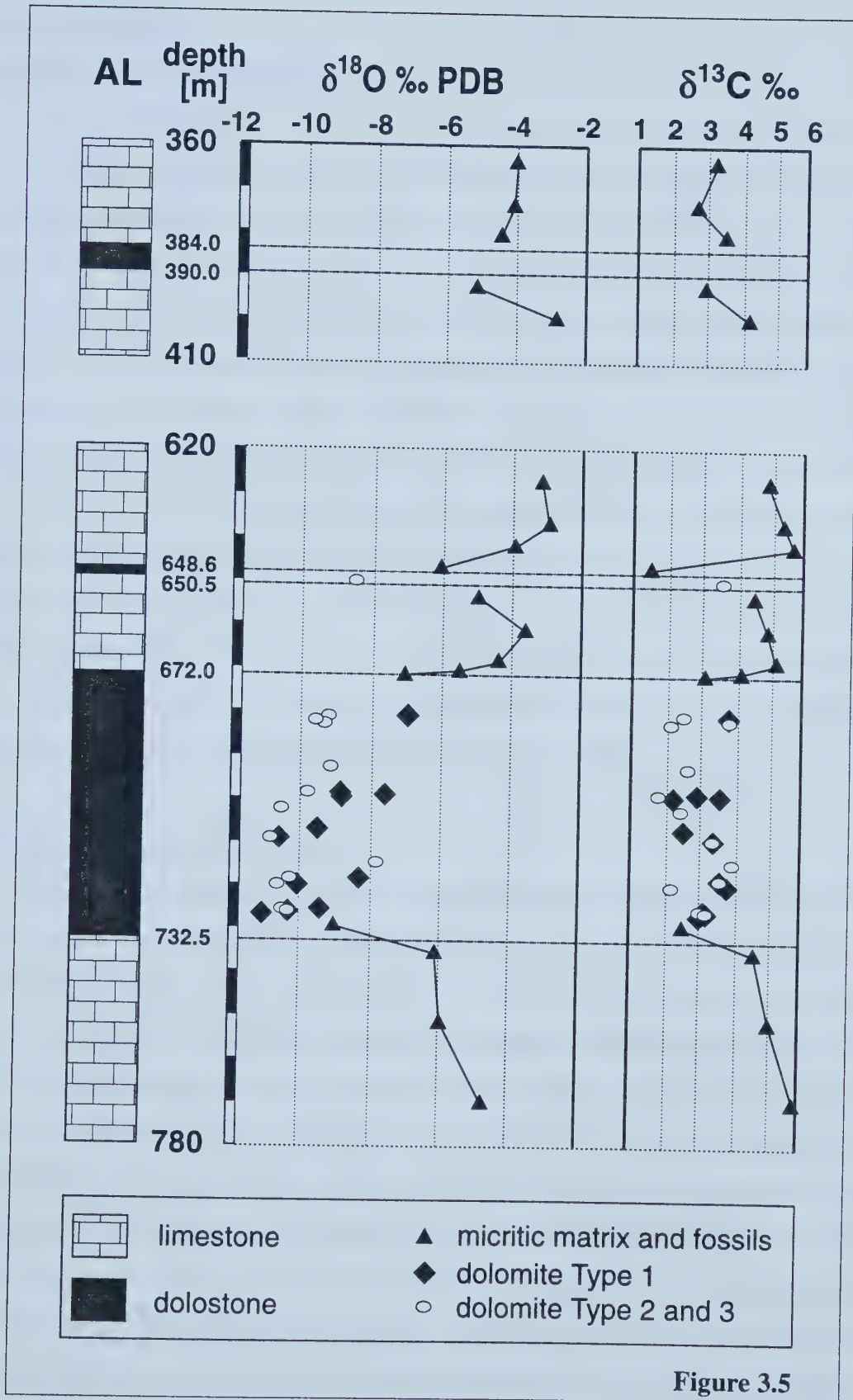
Only some of the samples that were taken within a few cm of the contact to a dolostone interval have strongly depleted  $\delta^{18}\text{O}$  values compared to the bulk of the sample set. If, however, the isotope values of the samples are plotted against the distance to their respective dolostone interval, a general trend of decreasing  $\delta^{18}\text{O}$  and  $\delta^{13}\text{C}$  values with decreasing distance to a dolostone interval can be observed. The results for the limestone host rock surrounding three dolostone intervals of the Almerfeld core (AL) are shown in Figure 3.5. The  $\delta^{18}\text{O}$  and  $\delta^{13}\text{C}$  values of the limestone samples range from -3.2 to -9.2 ‰ PDB and from +2.8 to +5.5 ‰ PDB, respectively, generally showing rapidly decreasing values closer to the dolostone intervals. Both  $\delta^{18}\text{O}$  and  $\delta^{13}\text{C}$  trends generally correlate positively, indicating a common cause for the changes in stable isotope composition. Similar trends in stable isotope composition of the host rock limestone have been observed in the core 'Auf dem Loh 7' (L7). The decrease in both  $\delta^{18}\text{O}$  and  $\delta^{13}\text{C}$  values is most pronounced very close to the contacts with the dolostone intervals. A comparison of the ranges of  $\delta^{13}\text{C}$  values of the dolomite types with the  $\delta^{13}\text{C}$  range of the host rock limestone indicates that the system was rock-buffered with respect to carbon.







**Figure 3.5:** Stable isotope (O and C) trends in limestone host rock adjacent to dolostone intervals in drill core Almerfeld (AL) from the Brilon Reef Complex resulting from recrystallization of undolomitized limestone due to dolomitization of adjacent intervals. Samples of limestone host rock include micritic matrix and calcite fossils. Within dolostone intervals, samples of dolomite Type 2 and 3 generally have lower  $\delta^{18}\text{O}$  values and the same or lower  $\delta^{13}\text{C}$  values than corresponding samples of dolomite Type 1.





### ***3.3.3 Trace elements***

#### **3.3.3.1 Pre-Variscan carbonate phases**

Average trace element concentrations for samples of limestone matrix and calcite fossils are similar, indicating that both sets of samples are representative of the carbonate fraction of the limestone host rock in the Brilon Reef Complex (Tables 3.4a and b). Electron microprobe data for Mn and Sr concentrations were obtained from the sample of a non-luminescent brachiopod shell. The Mn concentration of this sample is below the detection limit of the electron microprobe (= 130 ppm), and its Sr concentration (702 ppm) is the highest measured in the whole sample set. For the majority of the investigated pre-Variscan carbonate phases, Mn concentrations are below 300 ppm, Sr concentrations above 200 ppm, Na concentrations below 100 ppm and Zn and Pb concentrations are below 30 ppm. Samples that were taken directly at or close to dolostone intervals have trace element concentrations that fall outside those limits (i.e., higher concentrations for Mn, Na, Zn, and Pb; lower concentrations for Sr). The high Mn concentrations of these samples help to explain the observed changes in cathodoluminescence color described above, since Mn is considered to be the main activator for cathodoluminescence (Marshall 1988).

#### **3.3.3.2 Post-Variscan carbonate phases**

Bulk powder samples of the post-Variscan dolomite types are characterized by relatively high Mn (>386 ppm) and Na (>155 ppm) and relatively low Sr (<70 ppm) concentrations. Neither the trace element data determined by ICP (Tables 3.5 a, b, c, and d) nor the Mn and Fe concentrations obtained by averaging multiple spot analysis of these phases in thin sections by electron microprobe (Tables 3.6a and b) provide a clear distinction between samples of the three dolomite types. However, the microprobe data show that dolomite Type 3 has a much more restricted range of Fe (3236 to 14139 ppm) and Mn (751 to 2416 ppm) concentrations than dolomite Type 1 (Fe: 583 to 25542 ppm; Mn: 85 to 8047 ppm) or Type 2 (Fe: 3195 to 45838 ppm; Mn: 720 to 7566 ppm) but falls within their ranges. Fe/Mn ratios range between 1.0 to 6.3, with an average value of about 5 for all three dolomite types, indicating reducing conditions during their formation (Krauskopf 1957). There is no correlation between the average crystal size of dolomite Type 1 and Type 2 and



sample	depth m	n	average crystal size (μm)	MgCO <sub>3</sub> (mole %)	CaCO <sub>3</sub> (mole %)	Mn (ppm)	Fe (ppm)	Fe/Mn
AL-681.1	681.1	1	150	48.0	50.6	1355	6879	5.08
AL-699.0-.1	699	3	166	48.5	50.6	1211	4190	3.46
AL-707.3-.4	707.35	2	-	47.7	51.5	805	4046	5.02
AL-718.6	718.6	2	100	48.0	51.5	321	2666	8.30
I1-219.5	219.5	1	-	47.7	51.2	1425	5208	3.65
I1-249.45	249.45	4	50	46.7	50.5	6186	10775	1.74
I3-175.7	175.7	3	250	48.1	49.9	1626	10634	6.54
L1-262.4b	262.4	2	275	40.9	51.3	6521	37933	5.87
L1-265.9	265.9	1	100	47.8	51.1	1185	5340	4.51
L1-573.9	573.9	1	150	47.1	52.0	960	4345	4.52
L1-591.9	591.9	1	300	44.9	54.0	1092	5713	5.23
L7-166.1	166.1	1	-	48.8	50.2	1015	4679	4.61
L7-190.3	190.3	2	250	47.2	51.7	3272	3160	0.97
L7-292.3	292.3	2	250	46.7	52.5	933	3276	3.51
L7-302.5	302.5	4	150	48.5	50.2	939	6500	6.92
L7-384.6	384.6	1	150	48.9	50.3	813	4213	5.18
L7-394.7	394.7	1	150	46.7	51.1	1959	11038	5.63
L7-394.7	394.7	5	220	48.0	50.7	1265	6310	4.99
N2-461.6	461.6	2	175	46.6	51.3	1735	10960	6.32
N2-615.5	615.5	1	150	44.5	50.1	8047	25542	3.17
R1-119.5	119.5	3	300	47.3	52.6	85	583	6.84
T2-50.2	50.2	2	150	46.9	50.6	2393	13226	5.53
average			183	47.1	51.2	2052	8510	4.89

**Table 3.6a:** Results of microprobe analysis of samples of dolomite Type 1 (n = number of spot analysis).







**Table 3.6b and c:** Results of microprobe analysis of samples of dolomite Type 2 (b) and dolomite Type 3 (c).

Table 3.6b

sample	depth m	n	average crystal size (μm)	MgCO <sub>3</sub> mole %	CaCO <sub>3</sub> mole %	Mn ppm	Fe ppm	Fe/Mn
AL-681.1	681.1	3	600	49.0	50.1	769	4742	6.16
AL-699.0-.1	699.1	2	500	47.7	50.8	2265	6840	3.02
AL-718.6-.8	718.7	2	475	47.8	50.9	1235	6378	5.16
BL-387.3	387.3	1	600	46.6	50.3	2951	15671	5.31
B2-449.5	449.5	2	700	47.0	50.5	2912	12491	4.29
5B-260.5	260.5	4	500	47.5	50.8	1686	8636	5.12
I1-249.45	249.45	2	250	46.5	51.2	3876	10039	2.59
L1-265.9	265.9	3	400	48.0	51.1	1040	4366	4.20
L1-573.9	573.9	1	450	47.2	51.6	1239	5931	4.79
L1-576.8	576.8	1	450	40.3	50.5	7566	45838	6.06
L7-292.8	292.8	1	350	46.7	52.5	1216	3988	3.28
L7-375.1	375.1	1	300	49.1	50.2	720	3195	4.44
L7-384.6	384.6	5	300	48.1	51.0	987	4544	4.61
L7-394.7	394.7	6	-	47.1	50.6	2104	11377	5.41
L7-395.4	395.4	2	375	48.4	50.7	833	4143	4.98
N2-461.6	461.6	1	350	46.6	51.3	1712	11582	6.77
N2-476.4	476.4	1	500	46.9	50.3	3671	13751	3.75
N2-619.5	619.5	1	600	48.3	50.3	1355	7462	5.51
N2-638.4	638.4	2	600	47.7	50.7	1688	8690	5.15
average			461	47.2	50.8	2096	9982	4.77

Table 3.6c

AL-681.1	681.1	3	733	47.9	50.7	1149	7053	6.14
AL-699.0-.1	699.1	1	1000	48.2	50.5	1774	6296	3.55
AL-718.6-.8	718.7	2	-	47.7	51.2	1138	5262	4.62
B2-449.5	449.5	1	3000	46.4	51.2	2416	12344	5.11
I3-175.7	175.7	2	600	47.8	50.3	1816	10070	5.54
L1-265.9	265.9	1	2400	48.3	50.0	1774	8053	4.54
L1-573.9	573.9	1	900	48.6	50.5	767	4679	6.10
L1-576.8	576.8	1	1500	47.4	51.7	751	4508	6.00
L1-591.9	591.9	2	1200	46.5	52.2	1177	6386	5.42
L7-292.3	292.3	2	900	44.7	53.8	1514	7276	4.81
L7-302.5	302.5	1	2000	48.0	50.8	1092	5876	5.38
L7-375.1	375.1	3	1300	48.9	50.5	849	3236	3.81
L7-384.6	384.6	2	1800	47.9	50.6	1545	7987	4.65
L7-394.7	394.7	1	900	48.3	50.2	1301	7361	5.66
L7-395.4	395.4	3	-	48.5	50.6	904	4195	4.64
Na-461.6	461.6	1	1000	44.8	52.9	1317	7369	5.60
Na-638.4	638.4	1	1500	47.6	49.7	2176	14139	6.50
T2-50.2	50.2	1	1200	48.3	50.0	1549	9266	5.98
average			1371	47.5	51.0	1389	7298	5.23



their trace element composition. The overall similarity of the trace element compositions of the three dolomite types suggests that they were formed probably from fluids with similar trace element compositions under similar redox conditions. The significantly elevated Na concentrations in all three dolomite types compared to those of the pre-Variscan marine carbonate phases indicate fluids with higher salinities than that of seawater.

Due to the fact that no reliable data on the Fe concentration of the analyzed powder samples are available, the microprobe data were used to calculate the molar  $\text{CaCO}_3$  content of the dolomite types assuming that  $\text{MgCO}_3$ ,  $\text{CaCO}_3$ ,  $\text{MnCO}_3$ , and  $\text{FeCO}_3$  make up 100 % of the carbonate in the samples (Table 4.6 a and b). Ideal, stoichiometric dolomite has a  $\text{CaCO}_3$ -content of 50 mole %. Most modern sedimentary dolomites are non-stoichiometric (up to 62 mole %  $\text{CaCO}_3$ ) (e.g., Mazullo et al. 1987). Non-stoichiometric dolomite is thermodynamically unstable, hence recrystallization will lead to a decrease in Ca resulting in stoichiometric or nearly stoichiometric dolomite. Considering that the petrographic and stable isotope evidence presented above suggests that dolomite Type 1 has undergone recrystallization resulting in dolomite Type 2, one would expect a decrease in Ca with increasing average crystal size within Type 1 and from Type 1 to Type 2.

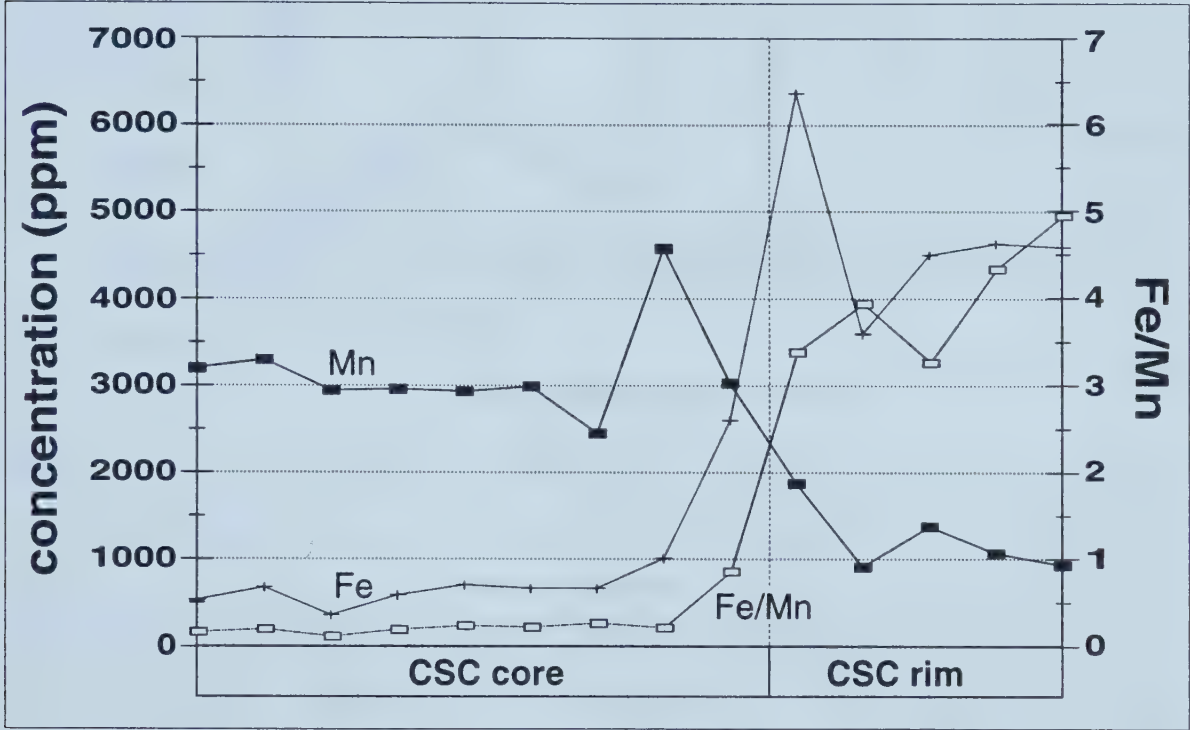
$\text{CaCO}_3$  contents of dolomite Type 1 range from 49.9 to 54.0 (average: 51.2) mole %, of dolomite Type 2 from 50.1 to 51.6 (average: 50.8) mole %, and of dolomite Type 3 from 49.7 to 52.9 (average: 51.0) mole % (Table 3.6a and b). No correlation between average crystal size and  $\text{CaCO}_3$  content could be observed in either dolomite Type 1 or dolomite Type 2. Furthermore, although the average  $\text{CaCO}_3$  content in dolomite Type 2 is more than 1 mole % lower than in dolomite Type 1, measurements of both types from a single core sample show that the difference between corresponding Type 1 and Type 2 can be positive as well as negative (Tables 3.5 a and b). Therefore, the decrease of the average  $\text{CaCO}_3$  content from dolomite Type 1 to Type 2 cannot be taken as evidence for recrystallization of dolomite Type 1.

The trace element compositions of 13 samples of post-Variscan calcite cements of phase 24 fall into two groups (Table 3.5d). Vug-filling, translucent poikilotopic calcite (TC) is characterized by Mn concentrations below 900 ppm, Sr and Na concentrations below 65 ppm, and a large range of Zn and Pb concentrations (Zn: 4 to 1090 ppm; Pb: 1 to 251 ppm). Bulk powder samples of vug-lining zoned clear euhedral calcite cement (CSC) have high Mn





concentrations (>2000 ppm), Sr concentrations above 75 ppm, Na concentrations above 52 ppm, and low Zn and Pb concentrations of < 20 and 46 ppm, respectively. A microprobe traverse across a zoned CSC shows that CSC consists of a Mn-rich/Fe-poor core and a Mn-poor/Fe-rich rim (Figure 3.6), confirming the petrographic observations, and indicating a rapid change from relatively oxidizing to relatively reducing conditions.

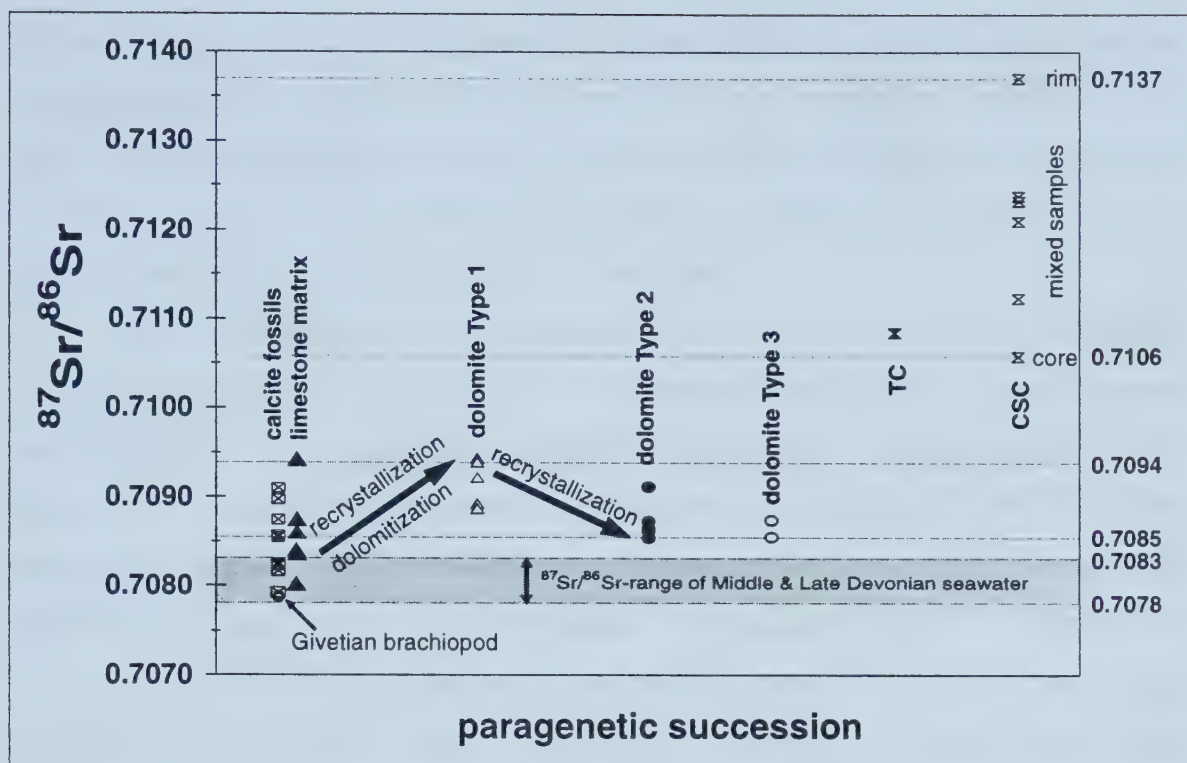


**Figure 3.6:** Trace element (Mn and Fe) concentrations and Fe/Mn-ratios along a microprobe traverse across a zoned crystal of clear scalenohedral calcite cement (CSC) from its core to its rim.

### 3.3.4 Strontium isotopes

The  $^{87}\text{Sr}/^{86}\text{Sr}$  values of samples of host rock limestone (micritic matrix,  $n = 9$ ; and calcitic fossils,  $n = 7$ ) range from 0.7079 (non-luminescent shell of Givetian brachiopod) to 0.7094 (limestone at the contact to dolostone interval), generally increasing with increasing proximity to a dolostone interval (Table 3.4a) (Figure 3.7). According to Denison et al. (1994), limestone samples with a Sr/Mn-ratio > 2 and a Mn-concentration < 300 ppm are most likely to have preserved the original marine  $^{87}\text{Sr}/^{86}\text{Sr}$  value. Using these criteria, the original  $^{87}\text{Sr}/^{86}\text{Sr}$  values for marine Devonian limestones in the Brilon Reef Complex range from 0.7079 to 0.7084 (average of 0.7081;  $n = 5$ ) (Table 3.4a). The value of 0.7079





**Figure 3.7:** Ranges in Sr isotope compositions for the investigated carbonate mineral phases from the Brilon Reef Complex. Sr isotope value for sample of non-luminescent Givetian brachiopod provides the baseline for unaltered Middle to Upper Devonian calcite fossils and limestone matrix. Shift towards more radiogenic values is the result of increasing recrystallization by fluids that, at the same time, led to the formation of dolomite Type 1. Recrystallization of dolomite Type 1 results in a decrease in  $^{87}\text{Sr}/^{86}\text{Sr}$  values, approaching that of dolomite Type 3. Range of  $^{87}\text{Sr}/^{86}\text{Sr}$  values in samples of clear scalenohedral calcite cement (CSC) is due to mixing of material from the core with material from the rim during microsampling.

corresponds with data for Givetian brachiopods from the western Rhenish Schiefergebirge by Diener et al. (1996) and the best estimate for Givetian seawater by Denison et al. (1997). The  $^{87}\text{Sr}/^{86}\text{Sr}$  values of the unaltered samples fall within the range of the best estimate for Middle to Late Devonian seawater (0.7078 to 0.7083, Denison et al. 1997). The value of 0.7084 for one sample appears rather high within the context of two other samples from the same core but neither petrographic nor geochemical data indicate any other kind of alteration.

Samples of dolomite Type 1 have  $^{87}\text{Sr}/^{86}\text{Sr}$  values between 0.7089 and 0.7094 (average 0.7092,  $n = 6$ ), increasing with decreasing average crystal size (Figure 3.7). Samples of dolomite Type 2 have  $^{87}\text{Sr}/^{86}\text{Sr}$  values between 0.7085 and 0.7091 (average 0.7087,  $n = 5$ ). In the two cases where corresponding samples of dolomite Type 1 and Type 2 were taken from the same core sample, Type 2 always has a lower  $^{87}\text{Sr}/^{86}\text{Sr}$  value. Two samples of





dolomite Type 3 have  $^{87}\text{Sr}/^{86}\text{Sr}$  values of 0.7085 and 0.7087, respectively. In the one case where corresponding samples of dolomite Type 2 and Type 3 were taken (sample B2-441.4, tables 3.5 b and c), both have the same  $^{87}\text{Sr}/^{86}\text{Sr}$  value within analytical error, which serves as further evidence that the fluid that precipitated dolomite Type 3 also led to the recrystallization of dolomite Type 1 to dolomite Type 2.

The Sr isotope trends in the limestone host rock correlate well with the petrographic and stable isotope trends described above. The increase from Middle to Upper Devonian marine  $^{87}\text{Sr}/^{86}\text{Sr}$  values in presumably unaltered limestone samples to more radiogenic values that approach that of the least recrystallized (small average crystal size, heavy  $\delta^{18}\text{O}$  value) grey matrix dolomite ( $^{87}\text{Sr}/^{86}\text{Sr} = 0.7094$ ), suggests that the fluid that led to the formation of dolomite Type 1 also caused the recrystallization of the adjacent limestones (Figure 3.7).

The  $^{87}\text{Sr}/^{86}\text{Sr}$  values of samples of late calcite cements (TC and CSC) range from 0.7106 to 0.7137 (Table 3.5d, Figure 3.7). The lowest value is that of a powder sample from the petrographically homogenous core of a CSC crystal, and the highest value is that of a powder sample from the zoned rim of the same CSC crystal (sample L7-375.1, Table 3.5d). The other samples of CSC have  $^{87}\text{Sr}/^{86}\text{Sr}$  values that fall between those two endmembers, indicating that they represent mixtures of the two. The  $^{87}\text{Sr}/^{86}\text{Sr}$  value for the rim represents an average value of several thin growth zones (see Chapter 2, Plate 2.9b). The one sample of TC has a  $^{87}\text{Sr}/^{86}\text{Sr}$  value close to that of the core of CSC.

The  $^{87}\text{Sr}/^{86}\text{Sr}$  value of a cement represents that of the fluid from which it precipitated and is not influenced by changes in element concentration, temperature, Eh and pH during precipitation. Hence, the difference in the  $^{87}\text{Sr}/^{86}\text{Sr}$  values between the core and the rim of CSC indicates that either 1) the fluid composition evolved during precipitation of the cement, or 2) two different fluids with distinctly different  $^{87}\text{Sr}/^{86}\text{Sr}$  values were involved in its formation. The rapid change in Fe and Mn concentrations from the core of CSC to its rim (Figure 3.6), and the fact that the lowest and the highest  $^{87}\text{Sr}/^{86}\text{Sr}$  value for CSC were measured in samples from the core and the rim of a single crystal, strongly suggests precipitation from two different fluids. Furthermore, despite the differences in trace element compositions between samples of TC and samples of the core of CSC, the similarity of the  $^{87}\text{Sr}/^{86}\text{Sr}$  values may indicate precipitation from the same fluid, but under different conditions. Assuming that TC and the core of CSC precipitated from the same fluid, the





similarity in stable isotope compositions (TC:  $\delta^{13}\text{C} = 2.5 \text{ ‰ PDB}$ ;  $\delta^{18}\text{O} = -7.3 \text{ ‰ PDB}$ ; core of CSC:  $\delta^{13}\text{C} = 2.8 \text{ ‰ PDB}$ ,  $\delta^{18}\text{O} = -7.8 \text{ ‰ PDB}$ ) also suggests a similar temperature of formation. Using the calcite-water fractionation equation of Friedman and O'Neil (1977), a difference in  $\delta^{18}\text{O}$  of  $0.5 \text{ ‰ PDB}$  corresponds to a temperature difference of only  $3^\circ\text{C}$ . This would limit the possible causes for the difference in trace element compositions between TC and the core of CSC to differences in trace element concentrations in the fluid(s) from which they precipitated, and/or different redox conditions. Unfortunately, no reliable data on the Fe concentration of TC are available, that could be used to determine if TC and the core of CSC were precipitated under different redox conditions.

### **3.3.5 Fluid inclusion microthermometry**

#### **3.3.5.1 Dolomite Type 3 (saddle dolomite)**

Homogenization temperatures ( $T_h$ ) in primary inclusions in two saddle dolomite crystals range from 109 to 119 (average 114)  $^\circ\text{C}$  and 105 to 111 (average 108)  $^\circ\text{C}$ , respectively (Appendix 4, Figure 3.8). The difference between the homogenization temperatures of a fluid inclusion assemblage from the center and that from the rim of one saddle dolomite crystal lies within the analytical error of  $\pm 2 \text{ }^\circ\text{C}$  (113 and 115  $^\circ\text{C}$ , respectively). The homogenization temperatures of secondary inclusions in one saddle dolomite sample range from 93 to 96.6 (average 94.7)  $^\circ\text{C}$ . Eutectic temperatures ( $T_e$ ) in primary fluid inclusions in the two saddle dolomites range from -56.4 to -65.3 (average 61.2)  $^\circ\text{C}$  and -51.0 to -56.0 (average -53.5)  $^\circ\text{C}$  (Figure 3.8a), respectively, indicating a complex cation composition of the inclusion fluid. According to Goldstein and Reynolds (1994), the aqueous system  $\text{NaCl-CaCl}_2\text{-MgCl}_2\text{-H}_2\text{O}$  has a predicted eutectic temperature at  $-57 \text{ }^\circ\text{C}$ , which agrees well with the average value for the two investigated saddle dolomites (i.e., -57.4  $^\circ\text{C}$ ). Values for  $T_m\text{-ice}$  for the primary inclusions in the two saddle dolomites range from -22.2 to -26.3 (average -24.4)  $^\circ\text{C}$  (Figure 3.8b), which corresponds to salinities of 23.7 to 26.2 (average 24.8) equivalent wt. % NaCl, using the formula by Bodnar (1992) for the  $\text{H}_2\text{O-NaCl}$  system. Although the low  $T_e$  clearly indicates a more complex composition, the  $\text{H}_2\text{O-NaCl}$  system is used because reliable temperatures for intermediate melting of other phases (such as hydrohalite and antarcticite), which would be necessary for a more precise





**Figure 3.8:** Results of microthermometric analysis of primary (p), pseudosecondary (ps), and secondary (s) two-phase fluid inclusions in dolomite Type 3, sphalerite (ZnS), and clear scalenohedral calcite (CSC). a) Eutectic temperatures ( $T_e$ ) plotted against homogenization temperatures. Characteristic stable eutectic temperatures for various aqueous systems are from Davies et al. 1990 (dashed horizontal lines). b) Temperature of final melting of ice ( $T_{m-ice}$ ) plotted against homogenization temperature. Data are given in Appendix 4. See text for further explanation.

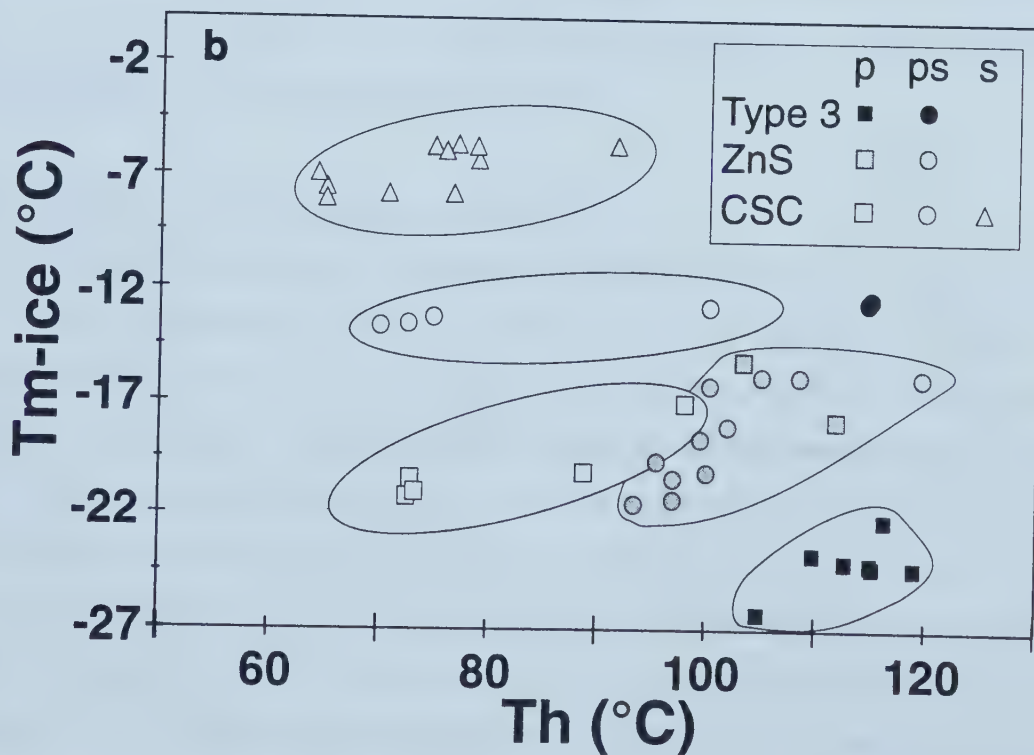
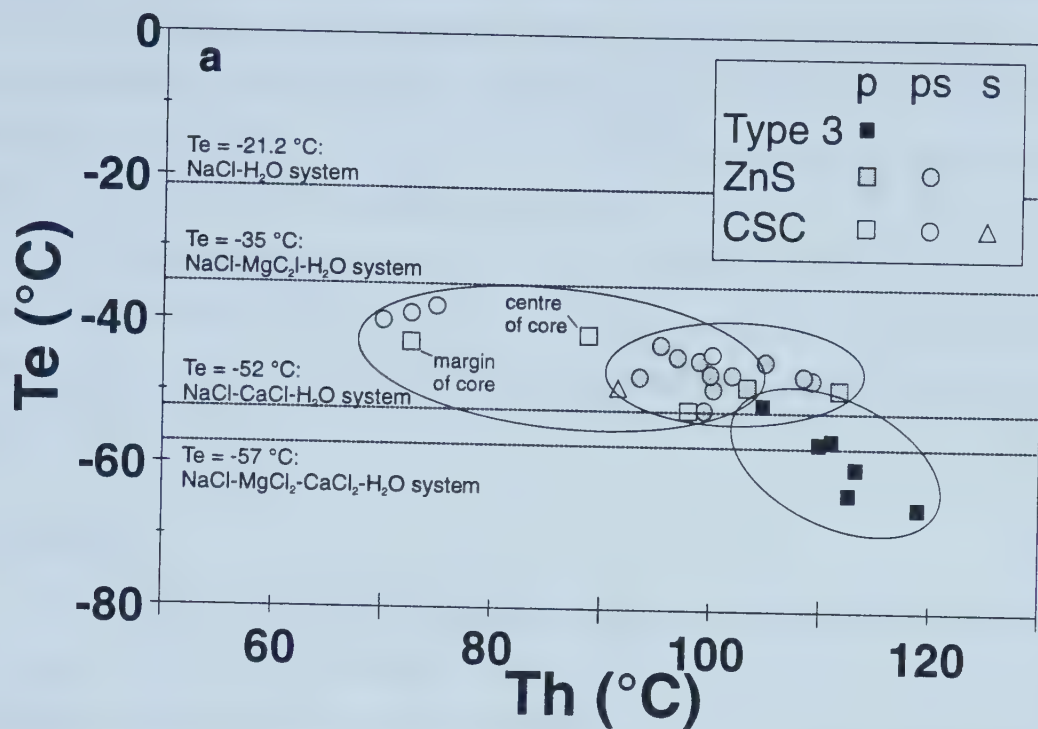


Figure 3.8





determination of the bulk salinity (Goldstein and Reynolds 1994), could not be obtained. A more complex composition will generally result in slightly lower salinities than those calculated under the assumption of the H<sub>2</sub>O-NaCl system (Goldstein and Reynolds 1994). These limitations also apply to the calculation of the bulk salinities of the investigated fluid inclusions in sphalerite and late calcite described below.

The two pseudosecondary inclusions in one dolomite sample have a Th of 115 °C (Figure 3.8b). No eutectic temperatures could be measured for the two pseudosecondary inclusions. Their average Tm-ice of -12.5 °C corresponds to a salinity of 16.3 equivalent weight % NaCl.

#### 3.3.4.2 Sphalerite

Primary and pseudosecondary fluid inclusions in sphalerite have Th between 94 and 120 (average 103) °C and Te between -43.0 and -52.0 (average -47.0) °C (Figure 3.8a), which indicates either a NaCl-CaCl<sub>2</sub>-H<sub>2</sub>O or a NaCl-MgCl<sub>2</sub>-H<sub>2</sub>O system, when compared to observed ranges of Te compiled by Goldstein and Reynolds (1994). Values for Tm-ice range from -15.1 to -21.5 (average -18.4) °C (Figure 3.8b) corresponding to salinities between 18.6 and 23.2 (average 21.1) equivalent weight % NaCl.

#### 3.3.4.3 Clear scalenohedral calcite cement (CSC)

Primary fluid inclusions in 3 samples of CSC have Th between 72 and 98 (average 81) °C and Te between -38 and -52 (average -45) °C (Appendix 4, Figure 3.8a). Pseudosecondary inclusions have Th between 70 and 100 (average 77) °C and Te between -38 and -51 (average -43) °C, and secondary inclusions have Th between 64 and 92 (average 72) °C (Figure 3.8b) and Te between -46 and -49 (average -48) °C (Appendix 4). Primary and pseudosecondary inclusions from the central part of one crystal have higher Th than those located toward the rim, but Te values do not differ with location (Figure 3.8a). Values for Tm-ice range from -16.9 to -24.8 (average -19.7) °C for primary inclusions, -10.6 to -17.7 (average -12.9) °C for pseudosecondary inclusions, and -4.6 to -11.7 (average -6.5) °C for secondary inclusions (Appendix 4, Figure 3.8b), which correspond into average salinities of 22.0, 16.7, and 9.8 equivalent weight % NaCl, respectively.



### 3.3.6 Post-Variscan fluid flow events in the Brilon Reef Complex

When interpreting geochemical data, one must bear in mind that the measured stable isotope and trace element compositions in the solid phases are not only a function of the stable isotope and trace element compositions of the fluid from which they formed, but are also dependent on temperature, the compositions of possible precursor mineral phases, the extent of water-rock interaction, and, in the case of some trace elements, on the redox conditions and precipitation kinetics. Considering that the relative importance of these factors in ancient systems is almost impossible to decipher, stable isotope and trace element data of the solid phases should not be used in isolation when trying to differentiate between fluids of different origin.

The data from this study suggest that at least four post-Variscan fluid flow events, each characterized by a distinct fluid type, were involved in dolomitization, recrystallization, dolomite cementation, sulfide mineralization and calcite cementation of the investigated core intervals (Figure 3.9).

*Fluid flow event #1* led to the formation of dolomite Type 1 by replacement of limestone, and to the partial recrystallization of adjacent undolomitized limestone. The resulting fine-crystalline, planar to nonplanar dolomite Type 1 is best characterized by a maximum  $^{87}\text{Sr}/^{86}\text{Sr}$  value of 0.7094, indicating the involvement of a fluid with a  $^{87}\text{Sr}/^{86}\text{Sr}$  value  $\geq 0.7094$ , which is significantly higher than that of Middle to Late Devonian ( $^{87}\text{Sr}/^{86}\text{Sr} = 0.7078$  to  $0.7083$ ) or any younger seawater (Burke et al. 1982; Smalley et al. 1994; Denison et al. 1997) (fluid type 1 in Figure 3.9). Values of  $\delta^{18}\text{O} < -6.5\text{‰}$  PDB for dolomite Type 1 point to its formation at elevated temperatures relative that of the limestones. A fluid bearing a large component of fresh meteoric water is unlikely on the basis of the relatively high Na concentrations in dolomite Type 1, that are comparable to those of dolomite Type 3, which definitely precipitated from highly saline fluids, as shown by the fluid inclusion study presented above. Recrystallization by the same fluid of the undolomitized limestone host rock immediately adjacent to the dolostone intervals is indicated by elevated  $^{87}\text{Sr}/^{86}\text{Sr}$  values compared to Middle to Upper Devonian marine values (0.7079 to 0.7084). The trend of increasing  $^{87}\text{Sr}/^{86}\text{Sr}$  values is accompanied by petrographic changes of the micritic limestone matrix (increasing crystal size, change from euhedral to anhedral crystal habit, decreasing







**Figure 3.9:** Fluid flow events and characteristics of fluid types that resulted in limestone recrystallization, dolomitization, dolomite recrystallization, dolomite cementation, base metal sulfide precipitation, and calcite cementation in the Devonian Reef Complex, based mainly on strontium isotope data. For the base metal sulfides, no strontium isotope data are available. See text for further explanation.

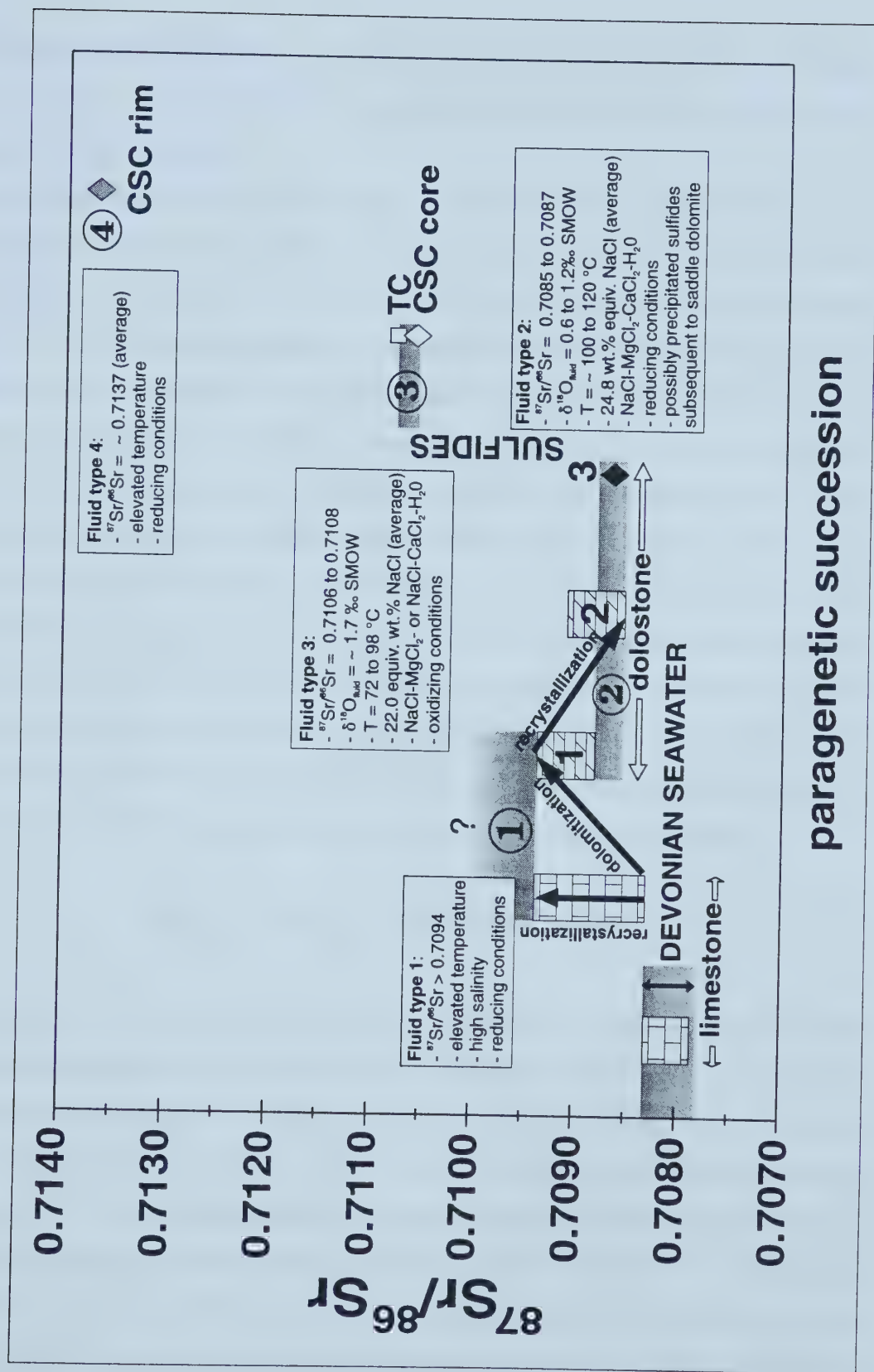


Figure 3.9



porosity, change from non-luminescent to mottled orange cathodoluminescence color), as well as by changes in other geochemical parameters (decreasing  $\delta^{18}\text{O}$  and  $\delta^{13}\text{C}$  values, increasing Mn concentration).

*Fluid flow event #2* led to the formation of dolomite Type 2 via recrystallization of dolomite Type 1 and to the precipitation of dolomite Type 3. Recrystallization of dolomite Type 1 originated at fractures and vugs and resulted in an increase in crystal size, a change in crystal habit from subhedral to anhedral, and a decrease in  $\delta^{18}\text{O}$  and  $^{87}\text{Sr}/^{86}\text{Sr}$  values. The compositional similarity between dolomite types 1 and 2 and the obvious difference in crystal size suggests reduction of surface energy as the primary drive for recrystallization, very likely catalyzed by elevated temperature and the composition of the hydrothermal fluid. The  $^{87}\text{Sr}/^{86}\text{Sr}$  values of dolomite Type 2 range between those of unrecrystallized dolomite Type 1 (up to 0.7094) and dolomite Type 3 (0.7085-0.7087), which strongly suggests that the fluid responsible for the recrystallization of dolomite Type 1 also precipitated dolomite Type 3. A range of  $\delta^{18}\text{O}$  values from +0.6 to +1.2 ‰ SMOW for the fluid that precipitated dolomite Type 3 can be derived, based on the average homogenization temperatures of primary fluid inclusions (108 °C and 114 °C) and the  $\delta^{18}\text{O}$  value of one sample of dolomite Type 3 (-10.7 ‰ PDB = 19.9 ‰ SMOW), and using the dolomite-water fractionation equation

$$\delta^{18}\text{O}_{\text{dolomite}} - \delta^{18}\text{O}_{\text{fluid}} = 2.78 \times 10^6 T^{-2} + 0.11$$

of Fritz and Smith (1970) ( $T$  = temperature in °K). Although this equation is based on data for the temperature range from 25 to 78.6 °C (Fritz and Smith 1970), it seems reasonable to assume that it can be extrapolated to slightly higher temperatures. A different dolomite-water fractionation equation was derived by Matthews and Katz (1977) for the temperature range from 252 to 295 °C, but extrapolation from this high temperature range to temperatures at about 100 °C appears questionable. The high average salinity (24.8 equiv. wt. % NaCl) and complex cation composition of the inclusion fluids suggest formation from fluids similar to deep basinal brines found in sedimentary basins around the world (Hanor 1987). The  $^{87}\text{Sr}/^{86}\text{Sr}$  value of the fluid that precipitated dolomite Type 3 was distinctively less radiogenic than that of dolomite Type 1.

*Fluid flow event #3* resulted in the precipitation of the core of the clear scalenohedral



calcite cement (CSC) and possibly also of the poikilotopic, translucent calcite cement (TC). It is characterized by a high salinity (average 22 equiv. wt. % NaCl) and a high  $^{87}\text{Sr}/^{86}\text{Sr}$  ratio ( $^{87}\text{Sr}/^{86}\text{Sr} = 0.7106$  to  $0.7108$ ) with a complex cation composition (fluid type 3 in Figure 3.9). The core of CSC is Mn-rich and Fe-poor, indicating relatively oxidizing conditions during precipitation. Fluid inclusion homogenization temperatures show a general decrease in fluid temperature during growth of the core without a change in salinity and cation composition. A calculation of the  $\delta^{18}\text{O}$  value of the fluid from the average fluid inclusion homogenization temperature ( $78\text{ }^{\circ}\text{C}$ ) and the  $\delta^{18}\text{O}$  value ( $-9.2\text{ }_{\text{PDB}} = +21.4\text{ }_{\text{SMOW}}$ ) of one sample of CSC (AL-726.8), using the calcite-water fractionation equation

$$\delta^{18}\text{O}_{\text{calcite}} - \delta^{18}\text{O}_{\text{fluid}} = 2.78 \times 10^6 T^{-2} - 2.89$$

of Friedman and O'Neil (1977) ( $T$  = temperature in  $^{\circ}\text{K}$ ; valid for a temperature range from  $0$  to  $500\text{ }^{\circ}\text{C}$ ) yields a value of  $+1.7\text{ }_{\text{SMOW}}$ . However, this value can only serve as an approximation because the  $^{87}\text{Sr}/^{86}\text{Sr}$  value of this sample ( $0.7123$ ) indicates that it represents a mixture of material from the core ( $^{87}\text{Sr}/^{86}\text{Sr} = 0.7106$ ) and from the rim ( $^{87}\text{Sr}/^{86}\text{Sr} = 0.7137$ ) of CSC.

The sulfide mineralization within the dolostone intervals is placed between dolomite Type 3 and CSC in the paragenetic sequence. Microthermometric data from fluid inclusions in sphalerite indicate slightly lower temperatures than during precipitation of dolomite Type 3, as well as lower salinities and a possible change in the cation composition of the fluids compared to dolomite Type 2, but these data are not sufficient to support a separate fluid flow event. The prevalence of reducing conditions during dolomite ( $\text{Fe}/\text{Mn} > 1$ ) and sulfide precipitation, evidence of corrosion of dolomite Type 3 and sulfide minerals prior to calcitization, and calcite cementation ( $\text{Fe}/\text{Mn} < 1$  in cores of CSC) suggests that the precipitation of sphalerite and associated pyrite is probably more closely linked to fluid flow event #2 than to fluid flow event #3.

*Fluid flow event #4* resulted in the precipitation of the Mn-poor/Fe-rich rim of CSC indicating relatively reducing conditions. A  $^{87}\text{Sr}/^{86}\text{Sr}$  value of  $0.7137$  indicates a significant increase in the radiogenic component of the dissolved Sr in fluid type 4 relative to fluid type 3. A slightly higher  $\delta^{18}\text{O}$  value of the rim compared to that of the core (difference of  $0.6\text{ }_{\text{SMOW}}$ )





in one sample, where it was possible to separate the core from the rim, could be taken as an indication of a slight drop in temperature (4 °C). However, the Sr isotope and trace element data indicate that it is more likely the result of changes in fluid composition and redox conditions than of a change in temperature.

Microthermometric data on pseudosecondary and secondary inclusions in CSC indicate a decrease in salinity between precipitation of the core and the rim and a decrease in temperature and salinity after precipitation of the rim. The growth zonation of the rim, indicating phases of corrosion followed by phases of calcite precipitation (Chapter 2, Plate 2.9b), and the presence of further types of post-CSC replacive and fracture-filling calcite generations in the Brilon Reef Complex (Moritz 1983), further suggest a continuation of the episodic character of fluid movement.

### ***3.3.6 Timing of fluid flow events, origin of fluids, and hydrologic driving mechanism***

Dolomitization in the Brilon Reef Complex occurred after the Variscan Orogeny, probably during the Late Cretaceous/Early Tertiary (Chapter 2). The observation that dolomite Types 2 and 3 seem to be restricted to the same intervals as dolomite Type 1 (Chapter 2) suggests that fluid flow events #1 and #2 used the same fault and fracture systems within the Brilon Reef Complex as pathways, probably within a short period of time. Based on paragenetic relationships, Moritz (1983) assigned a Late Cretaceous age to the formation of dolomite Type 1 (his 'Dolomit III', which includes saddle dolomite cements), invoking Sr-poor (i.e., low Sr concentration) pore waters from Cretaceous marine sediments as the Mg source for dolomitization. Late Cretaceous seawater acting as the sole dolomitizing fluid can be ruled out by the high  $^{87}\text{Sr}/^{86}\text{Sr}$  values of the dolomite types (0.7085 to 0.7094) compared to that of Upper Cretaceous seawater ( $^{87}\text{Sr}/^{86}\text{Sr} = 0.7073$  to 0.7078), but this does not exclude its participation in the formation of a dolomitizing fluid by interaction with older siliciclastic sedimentary rocks (e.g., Paleozoic shales, sandstones, and greywackes) and mixing with  $^{87}\text{Sr}$ -enriched fluids in the Paleozoic sedimentary succession.

Dolomite types 2 and 3 formed from a less  $^{87}\text{Sr}$ -enriched fluid ( $^{87}\text{Sr}/^{86}\text{Sr} = 0.7085$ -0.7087) than did dolomite Type 1, indicating that a major portion of the dissolved Sr could have been derived from a marine source (i.e., Cretaceous seawater or older marine carbonates and/or evaporites). The high salinities determined in fluid inclusions of dolomite Type 3 and,



based on similar Na concentrations, also postulated for dolomite types 1 and 2, exclude the participation of a large component of fresh meteoric and/or normal marine waters. The trace element compositions (high Mn, Fe, Na, Zn, Pb, low Sr) of all three dolomite types together with the fluid inclusion data obtained from dolomite Type 3, indicate that dolomitization, dolomite recrystallization, and dolomite cementation were the result of the introduction of highly saline subsurface fluids with a complex cation composition into the limestone hostrock along faults and fracture systems. The difference in  $^{87}\text{Sr}/^{86}\text{Sr}$  values between fluid type 1 ( $\geq 0.7094$ ) and fluid type 2 (0.7085-0.7087) reflects interaction with siliciclastic rocks (fluid type 1) and with marine carbonates and/or evaporites (fluid type 2), suggesting different pathways for these fluids prior to their injection into the Brilon Reef Complex.

The minor sulfide mineralization that followed dolomite Type 3 has been assigned a Late Cretaceous/Early Tertiary age by several workers (Schriell 1954; Brinckmann 1981; Schaeffer 1984, 1986), based on the occurrence of the same type of mineralization in Upper Cretaceous marine sandstones that overly parts of the Brilon Reef Complex. From differences in the spatial distribution and in the Pb-isotope compositions between Variscan and post-Variscan galenas from the northeastern Rhenish Schiefergebirge, Schaeffer (1984, 1986) concluded that the base metals of the post-Variscan mineralization were derived from Early Paleozoic shales or metasediments in the subsurface, and not by remobilization of Paleozoic base metal sulfide deposits, as suggested by Schneiderhöhn (1953) and Schriell (1952, 1954). The high salinities and complex cation compositions in the investigated fluid inclusions in sphalerite, and the fact that both dolomitization and sulfide precipitation require reducing conditions, are consistent with the interpretation that the post-dolomite/pre-CSC sulfide mineralization occurred as a last stage of fluid flow event #2. The differences in Fe/Mn- and  $^{87}\text{Sr}/^{86}\text{Sr}$  ratios between the core and rim of CSC, as well as decreasing salinities from primary, to pseudosecondary, to secondary fluid inclusions in the core of CSC, demonstrate rapid changes in redox-potential and fluid sources, which appear to be characteristic of the post-Variscan mineralization elsewhere in the Rhenish Schiefergebirge (Behr et al. 1987; Behr and Gerler 1987).

Independent evidence suggests that the Brilon Reef Complex was close to the surface in post-Variscan times (Chapter 2; Clausen et al. 1982). Hence, the low  $\delta^{18}\text{O}$  values and fluid inclusion homogenization temperatures between 70 and 120 °C in the investigated post-





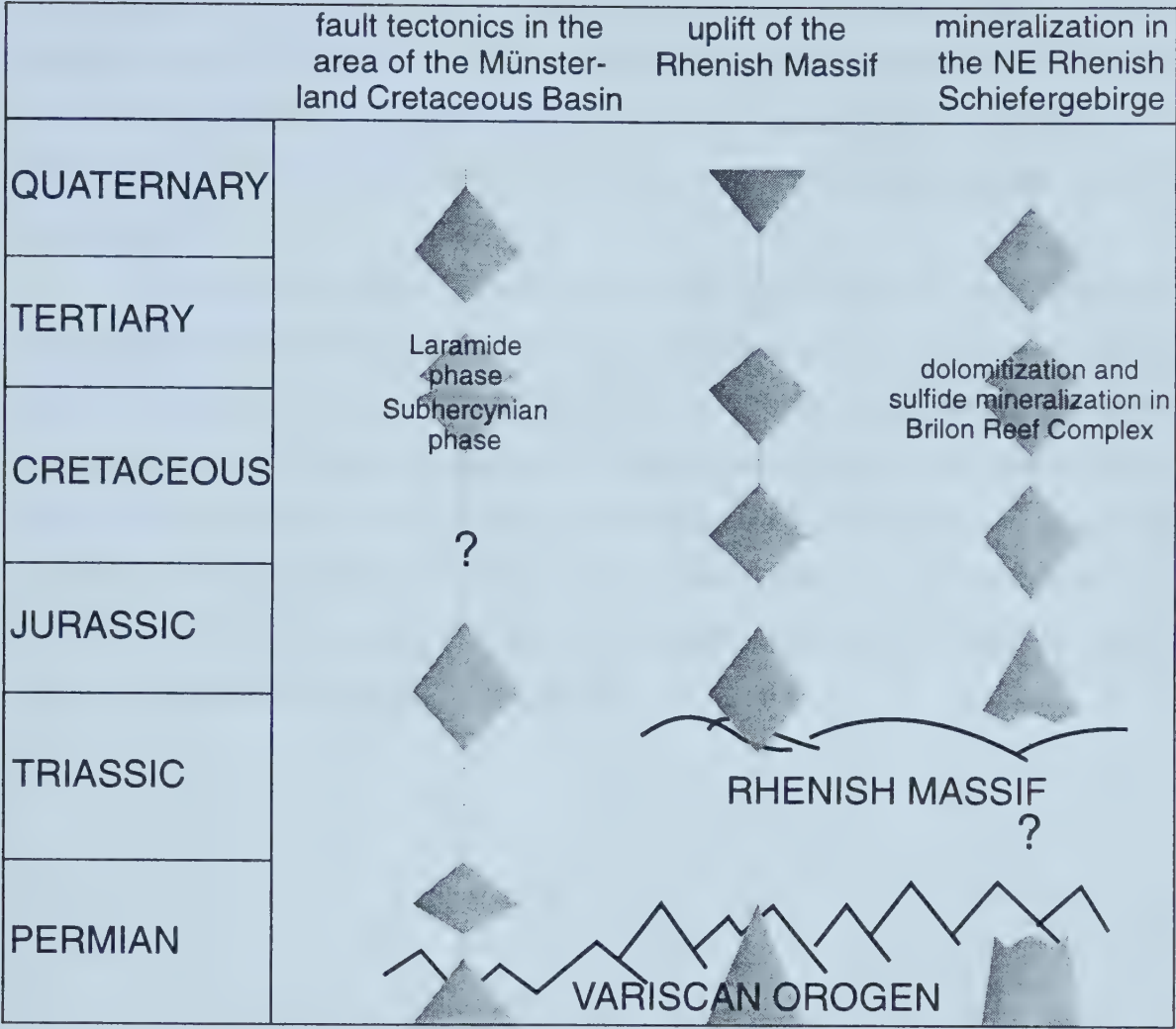
Variscan mineral phases (equivalent to burial depths between 1800 and 3500 m, assuming a normal geothermal gradient of 30 °C/km), indicate a hydrothermal origin of dolomitization, dolomite recrystallization and cementation, sulfide mineralization, and calcite cementation in the Brilon Reef Complex. Furthermore, the episodic nature of the post-Variscan mineralization in the northeastern Rhenish Schiefergebirge has been explained by tectonic (seismic) pumping of fluids derived from sedimentary brines during the Mesozoic to Tertiary regional uplift and faulting of the Variscan basement (Behr and Horn 1984a and b; Behr and Gerler 1987; Behr et al. 1987). According to Behr and Gerler (1987) and Behr et al. (1987), these sedimentary brines consisted of a mixture of Permian and Mesozoic formation waters, evaporative relict brines, and brines that resulted from the dissolution of evaporites. Because of their high density, these brines descended from the Permian to Mesozoic sedimentary troughs, that had formed at the margins of the Variscan orogen, into the underlying Variscan basement, and underwent compositional changes as the result of water-rock interaction on their way. During distinct phases of tectonic activity, these brines ascended on faults, mixed with waters in the shallower subsurface, and precipitated various types of hydrothermal vein deposits (Behr et al. 1987).

Wrede (1992) found that phases of extensional and transpressional fault tectonics in the area of the Münsterland Cretaceous Basin, which is located north of the Rhenish Schiefergebirge where it overlies the deformed Paleozoic succession of the Rhenish Schiefergebirge (Figure 3.1), coincide with phases of mineralization in the northeastern Rhenish Schiefergebirge (Schaeffer 1984) and phases of uplift of the Rhenish Schiefergebirge (Murawski et al. 1983) (Figure 3.10). The timing of mineralization in the Brilon Reef Complex coincides with the so-called Subhercynian and Laramide tectonic phases. These phases are the remote effects of the Alpine Orogeny further to the south and in the area of the Münsterland Cretaceous Basin, are characterized by a transpressional tectonic regime resulting in the inversion of faults in the basin, that previously had experienced mostly extensional tectonics (Drozdewski 1988, 1995; Drozdewski and Wrede 1994).

It might therefore be possible, that the dolomitizing and mineralizing fluids may share a common origin with saline groundwaters (TDS up to 250,000 mg/l) that have been encountered in subsurface coal-mines, wells, and artesian springs in the Münsterland







**Figure 3.10:** Schematic diagram illustrating the temporal coincidence of phases of fault tectonics in the area of the Münsterland Cretaceous Basin (Wrede 1992), phases of uplift of the Rhenish Massif (Murawski et al. 1983), and mineralization phases in the eastern Rhenish Schiefergebirge (Schaeffer 1984) (modified from Wrede 1992). The dolomitization and base metal sulfide mineralization in the Brilon Reef Complex has been constrained to the Late Cretaceous/Early Tertiary, when wrench tectonic fault movements of the Subhercynian and Laramide tectonic phases occurred in the area of the Münsterland Cretaceous Basin.

Cretaceous Basin. The brines in the Münsterland Cretaceous Basin presumably constitute a complex mixture of Paleozoic and Mesozoic formation waters, evaporative relict brines, meteoric water, and brines that resulted from the subrosive dissolution of Permian, Triassic, and Jurassic evaporites (Michel et al. 1974; Michel and Nielsen 1977; Michel 1994; Wedewardt 1995), but the questions of their origin(s) and evolution have not been satisfactorily answered yet (Wedewardt 1995). Regional wrench tectonics, hydrothermal



convection due to increased heat flow in the Late Cretaceous to Early Tertiary (Lommerzheim 1994), together with surface-controlled basin-wide groundwater movements, may have led to the episodic injection of highly saline brines along deep-reaching NNW-SSE trending fault-systems into the Brilon Reef Complex, resulting in dolomitization and sulfide mineralization.

To be able to evaluate if present-day saline groundwaters in the Münsterland Cretaceous Basin bear a genetic relationship to the dolomitization and sulfide mineralization in and around the fractures of the Brilon Reef Complex, the origin and evolution of the saline groundwaters in the Münsterland Cretaceous Basin have to be better delineated within the context of the regional geologic history. An investigation of the oxygen, hydrogen, and strontium isotopic compositions of saline groundwater samples from the Münsterland Cretaceous Basin, in conjunction with data on their chemical composition, has been carried out and is presented in Chapter 4 of this thesis.



### 3.4 References

- Allan, J. R. and Wiggins, W.D., 1993, Dolomite Reservoirs - Geochemical Techniques for Evaluating Origin and Distribution. American Association of Petroleum Geologists Continuing Education Course Note Series #36, 129 p.
- Behr, H.J. and Horn, E.E., 1984a, Quarzbildung und Verkieselungsprozesse in den Karbonatkomplexen des Rheinischen Schiefergebirges. In: Postvaristische Gangmineralisationen in Mitteleuropa. Gesellschaft Deutscher Metallhütten-Bergleute, 41, p. 27-45.
- Behr, H.J. and Horn, E.E., 1984b, Unterscheidungskriterien für Mineralisationen des varistischen und postvaristischen Zyklus, die aus der Analyse fluider Einschlüsse gewinnbar sind. Gesellschaft Deutscher Metallhütten-Bergleute, 41, p. 255-269.
- Behr, H.J. and Gerler, J., 1987, Inclusions of sedimentary brines in post-Variscan Mineralizations in the Federal Republic of Germany - A Study by neutron activation analysis. Chemical Geology, 61, p. 65-77.
- Behr, H.J., Horn, E.E., Frentzel-Beyme, K., and Reutel, Chr., 1987, Fluid inclusion characteristics of the Variscan and post-Variscan mineralizing fluids in the Federal Republic of Germany. Chemical Geology, 61, p. 273-285.
- Bodnar, R.J., 1992, Revised equation and table for freezing point depressions of H<sub>2</sub>O-salt fluid inclusions. Fourth Biennial Pan-American Conference on Research on Fluid Inclusions, Program and Abstracts, Lake Arrowhead, California, 14, p. 15.
- Brand, U. and Morrison, J.O., 1987, Paleocene #6. Biogeochemistry of fossil marine invertebrates. Geoscience Canada, 14, p. 85-107.
- Brinkmann, J., 1981, Projekt Rhenoharzynikum, Untersuchung der Metallverteilung in geosynklinalen Sedimenten des Rhenoharzynikums in stratiformen Konzentrationen. Bericht über das Kernbohrprogramm im Briloner Riffkalk-Komplex. Unpublished report by the Bundesanstalt für Geowissenschaften und Rohstoffe, Hannover, 129 p.
- Brinckmann, J., Clausen, C.-D., Müller, H., and Stoppel, D., 1989, Geologische Übersichtskarte der Brilon-Warsteiner Riffkarbonate und ihrer Umrahmung. Geologisches Jahrbuch, D95 (1990).
- Burke, W.H., Denison, R.E., Hetherington, E.A., Koepnick, R.B., Nelson, H.F., and Otto, J.B., 1982, Variation of seawater <sup>87</sup>Sr/<sup>86</sup>Sr throughout Phanerozoic time. Geology, 10, p. 516-519.
- Clausen, C.-D., Grebe, H., Leuteritz, K., Uffenorde, H., and Wirth, W., 1982, Zur Paläogeographie, Tektonik und Karstmorphologie der südlichen und östlichen Warsteiner Carbonatplattform (Warsteiner Sattel, Rheinisches Schiefergebirge). Fortschritte in der Geologie von Rheinland und Westfalen, 30, p. 241-319.
- Davies, D.W., Lowenstein, T.K., and Spencer, R.J., 1990, Melting behavior of fluid inclusions in laboratory-grown halite crystals in the systems NaCl-H<sub>2</sub>O, NaCl-KCl-H<sub>2</sub>O, NaCl-MgCl<sub>2</sub>-H<sub>2</sub>O. Geochimica et Cosmochimica Acta, 54, p. 591-601.





- Davies, G.R., 1996, Hydrothermal dolomite (HTD) reservoir facies: global perspectives on tectonic-structural and temporal linkage between MVT and SEDEX Pb-Zn ore bodies, and subsurface HTD reservoir facies. Canadian Society of Petroleum Geologists Short Course Notes, 167 p.
- Deuser, W.G., 1970, Extreme  $^{13}\text{C}/^{12}\text{C}$  variations in Quaternary dolomites from the continental shelf. *Earth and Planetary Science Letters*, 8, p. 118-124.
- Denison, R.E., Koepnick, R.B., Fletcher, A., Howell, M.W., and Callaway, W.S., 1994, Criteria for the retention of original seawater  $^{87}\text{Sr}/^{86}\text{Sr}$  in ancient shelf limestones. *Chemical Geology*, 112, p. 131-143.
- Denison, R.E., Koepnick, R.B., Burke, W.H., Hetherington, E.A., and Fletcher, A., 1997, Construction of the Silurian and Devonian seawater  $^{87}\text{Sr}/^{86}\text{Sr}$  curve. *Chemical Geology*, 140, p. 109-121.
- Diener, A., Ebner, S., Veizer, J., and Buhl, D., 1996, Strontium isotope stratigraphy of the Middle Devonian: Brachiopods and conodonts. *Geochimica et Cosmochimica Acta*, 60, p. 639-652.
- Drozdowski, T., 1988, Die Wurzel der Osning-Überschiebung und der Mechanismus herzynischer Inversionsstörungen in Mitteleuropa. *Geologische Rundschau*, 77, p. 127-141.
- Drozdowski, G., and Wrede, 1994, Faltung und Bruchtektonik - Analyse der Tektonik im Subvariscikum. *Fortschritte in der Geologie von Rheinland und Westfalen*, 38, p. 7-187.
- Drozdowski, G., 1995, Die Alpen entstehen - was geschieht im Münsterland? In: *Geologisches Landesamt Nordrhein Westfalen, 1995, Geologie im Münsterland*, p. 63-65.
- Dunham, R.J., 1962, Classification of carbonate rocks according to depositional texture. In: Ham, W. E. (editor), *Classification of Carbonate Rocks*, American Association of Petroleum Geologists Memoir 1, p. 108-121.
- Dunn, P. A. (1988), Dynamics of  $\delta^{13}\text{C}$  and  $\delta^{18}\text{O}$  variation in the Devonian-Carboniferous succession of Belgium and Ireland. Unpublished M.Sc. thesis, University of Michigan, Ann Arbor, 55 pp.
- Friedman, I. and O'Neil, J. R., 1977, Compilation of stable isotope fractionation factors of geochemical interest. In: *Data of Geochemistry*, United States Geological Survey Professional Paper 440-KK, p. 1-12.
- Fritz, P. and Smith, D. C. W., 1970, The isotopic composition of secondary dolomites. *Geochimica et Cosmochimica Acta*, 34, p. 1161-1173.
- Games, L. M. and Hayes, J. M., 1976, On the mechanism of  $\text{CO}_2$  and  $\text{CH}_4$  production in natural anaerobic environments. In: Nriagu, J. O. (editor), *Environmental Biogeochemistry I*, 51-66.



- Goldstein, R.H. and Reynolds, T.J., 1994, Systematics of fluid inclusions in diagenetic minerals. Society of Economic Paleontologists and Mineralogists Short Course 31, 199 p.
- Gregg, J.M. and Sibley, D.F., 1984, Epigenetic dolomitization and the origin of xenotopic dolomite texture. *Journal of Sedimentary Petrology*, 54, p. 908-931.
- Gregg, J.M. and Shelton, K.L., Dolomitization and dolomite Neomorphism in the back reef facies of the Bonnetterre and Davis Formations (Cambrian), southeastern Missouri. *Journal of Sedimentary Petrology*, 60, p. 549-562.
- Hanor, J. S., 1987, Origin and migration of subsurface sedimentary brines. Society of Economic Paleontologists and Mineralogists Short Course 21, 247 pp.
- Hudson, J. D., 1975, Carbon isotopes and limestone cement. *Geology*, 3, p. 19-22.
- Hurley, N. F. and Lohmann, K. C., 1989, Diagenesis of Devonian reefal carbonate in the Oscar Range, Canning Basin, western Australia. *Journal of Sedimentary Petrology*, 59, p. 127-145.
- James, N.P., Bone, Y., and Kyser, T.K., 1997, Brachiopod  $\delta^{18}\text{O}$  values do reflect ambient oceanography: Lacepede Shelf, southern Australia. *Geology*, 25, p. 551-554.
- Krauskopf, K. B., 1957, Separation of manganese from iron in sedimentary processes. *Geochimica and Cosmochimica Acta*, 12, p. 61-84.
- Lohmann, K. C., Breining-Afifi, K. A., Budai, J. M., and Cercione, K. R., 1985, Enriched carbon-13 compositions in meteoric and shallow burial calcites and dolomites: evidence of organic fermentation during early diagenesis. Society of Economic Paleontologists and Mineralogists Annual Midyear Meeting, 2, Tulsa, p. 55.
- Lohmann, K. C. and Walker, J. C. G., 1989, The  $\delta^{18}\text{O}$  record of Phanerozoic abiotic marine calcite cements. *Geophysical Research Letters*, 16, p. 319-322.
- Lommerzheim, A. J., 1994, Genese und Migration der Erdgase im Münsterländer Becken. *Fortschritte in der Geologie von Rheinland und Westfalen*, 38, p. 309-348.
- Machel, H.G., 1979, Fazies und Diagenese der devonischen Riffcarbonate der Bohrung Romberg (Briloner Riff). Unpublished Diplom-thesis, Technische Universität Braunschweig, 231 pp.
- Machel, H. G., 1990, Submarine Frühdiagenese, Spaltenbildungen und prätektonische Spätdiagenese des Briloner Riffs. *Geologisches Jahrbuch.*, Reihe D95, p. 85-137.
- Machel, H.G., 1997, Recrystallization versus neomorphism, and the concept of 'significant recrystallization' in dolomite research. *Sedimentary Geology*, 113, p. 161-168.
- Marshall, D.J., 1988, Cathodoluminescence of geological materials. 146 p.
- Matthews, A. and Katz, A., 1977, Oxygen isotope fractionation during the dolomitization of calcium carbonate. *Geochimica et Cosmochimica Acta*, 41, p. 1431-1438.





- Mazullo, S. J., Reid, A. M., and Gregg, J. M., 1987, Dolomitization of Holocene Mg-calcite supratidal deposits, Ambergris Cay, Belize. *Geological Society of America Bulletin*, 98, p. 224-231.
- McCrea, J. M., 1950, On the isotopic chemistry of carbonates and a paleotemperature scale. *Journal of Chemical Physics*, 18, p. 849-857.
- Michel, G., 1994, Wie kommt die Sole ins Revier. *Mitteilungen der Geologischen Gesellschaft Essen*, 12, p. 65-81.
- Michel, G. and Nielsen, H., 1977, Schwefel-Isotopenuntersuchungen an Sulfaten ostwestfälischer Mineralwässer. *Fortschritte der Geologie von Rheinland und Westfalen*, 26, p. 185-227.
- Michel, G., Rabitz, A., and Werner, H., 1974, (with a contribution by Scherp, A.), Betrachtungen über die Tiefenwässer im Ruhrgebiet. *Fortschritte der Geologie von Rheinland und Westfalen*, 20, p. 215-236.
- Moritz, W., 1983, Fazies und Diagenese des Briloner Karbonatkomplexes anhand einiger ausgewählter Bohrungen. Unpublished Ph.D. thesis, Technische Universität Braunschweig, 180 pp.
- Mountjoy, E.W., 1994, Dolomitization and the character of hydrocarbon reservoirs: Devonian of western Canada. In: Parker, A. and Sellwood, B. W. (editors), *Quantitative Diagenesis: Recent Developments and Applications to Reservoir Geology*, p. 33-94.
- Mountjoy, E.W. and Krebs, W., 1983, Diagenesis of Devonian reefs and buildups, western Canada and Europe - a comparison. *Zeitschrift der deutschen geologischen Gesellschaft*, 134, p. 5-60.
- Murawski, H., Albers, H. J., Bender, P., Berners, H.-P., Durr, St., Huckriede, R., Kauffmann, G., Kowalczyk, G., Meinburg, P., Müller, R., Ritzkowski, S., Schwab, K., Semmel, A., Stapf, K., Walter, R., Winter, K.-P., and Zankl, H., 1983, Regional Tectonic Setting and Geological Structure of the Rhenish Massif. In: Fuchs, K., von Gehlen, K., Mälzer, H., Murawski, H., and Semmel, A. (editors), *Plateau Uplift.*, p. 381-403.
- O'Neil, J. R., 1987, Preservation of H, C, and O isotopic ratios in the low temperature environment. In: Kyser, T. K. (editor), *Stable Isotope Geochemistry of Low Temperature Fluids*, Mineralogical Association of Canada, Short Course Handbook, 13, p. 85-128.
- Popp, B. N., Anderson, T. F., and Sandberg, P. A., 1986a, Brachiopods as indicators of original isotopic compositions in Paleozoic limestones. *Geological Society of America Bulletin*, 97, p. 1262-1269.
- Popp, B.N., Anderson, T.F., and Sandberg, P.A., 1986b, Textural, elemental, and isotopic variations among constituents in Middle Devonian limestones, North America. *Journal of Sedimentary Petrology*, 56, p. 715-727.





- Qing, H., Barnes, C.R., Buhl, D., and Veizer, J., 1998, The strontium isotopic composition of Ordovician and Silurian brachiopods and conodonts: Relationships to geological events and implications for coeval seawater. *Geochimica et Cosmochimica Acta*, 62, p. 1721-1733.
- Reitsema, R. H., 1980, Dolomite and nahcolite formation in organic-rich sediments: isotopically heavy carbonates. *Geochimica et Cosmochimica Acta*, 44, p. 1045-2049
- Roedder, E., 1984, Fluid inclusions. *Reviews in Mineralogy*, Mineralogical Society of America, 12, 664 p.
- Schaeffer, R., 1984, Die postvariszische Mineralisation im nordöstlichen Rheinischen Schiefergebirge. Braunschweiger geologisch-paläontologische Dissertationen, 3, 206 p.
- Schaeffer, R., 1986, Geochemische Charakteristika und Genese der jungmesozoisch-tertiären Vererzung im Sauerland (Rheinisches Schiefergebirge). *Fortschritte in der Geologie von Rheinland und Westfalen*, 34, p. 337-381.
- Schneiderhöhn, 1953, Fortschritte in der Erkenntnis sekundär-hydrothermalen und regenerierter Lagerstätten. *Neues Jahrbuch der Mineralogie, Monatshefte*, 1953, p. 223-237.
- Schriel, W., 1952, Die gegenseitigen Beziehungen der Erzparagenese variszischen und tertiären Alters erläutert an der Stellung des Bensberger und Ramsberger Erzbezirks zur Paffrather Kalkmulde und dem Massenkalksattel von Brilon nebst einem Vergleich mit anderen Gebieten. *Neues Jahrbuch der Mineralogie, Monatshefte*, 1952, p. 239-253.
- Schriel, W., 1954, Der Briloner Galmei-Distrikt. *Zeitschrift der deutschen Geologischen Gesellschaft*, 106, p. 308-349.
- Sharma, T. and Clayton, R.N., 1964, Measurement of  $O^{18}/O^{16}$  ratios of total oxygen of carbonates. *Geochimica et Cosmochimica Acta*, 29, p. 1347-1353.
- Sheperd, T.J., Rankin, A.H., and Alderton, D.H., 1985, A practical guide to Fluid Inclusion Studies. Glasgow, Blackie and Son, 239 p.
- Smalley, P.C., Higgins, A.C., Howarth, R.J., Nicholson, H., Jones, C.E., Swinburne, N.H. M., and Bessa, J., 1994, Seawater Sr isotope variations through time: A procedure for constructing a reference curve to date and correlate marine sedimentary rocks. *Geology*, 22, p. 431-434.
- SPSS for Windows, Release 7.0, copyright SPSS Incorporated.
- Taylor, H. P. Jr., 1979, Oxygen and hydrogen isotope relationships in hydrothermal mineral deposits. In: Barnes, H. L. (editor), *Geochemistry of Hydrothermal Ore Deposits*, 2<sup>nd</sup> ed., p. 236-277.
- Veizer, J., Fritz, P., and Jones, B., 1986, Geochemistry of brachiopods: oxygen and carbon isotope records of Paleozoic oceans. *Geochimica et Cosmochimica Acta*, 50, p. 1679-1696.



- Wahba, Y., 1978, Die Geologie des Briloner Massenkalksattels im östlichen Sauerland. Unpublished Ph.D. thesis, Universität Clausthal, 203 pp.
- Wedewardt, M., 1995, Hydrochemie und Genese der Tiefenwässer im Ruhr-Revier. Deutsche Montan Technologie-Berichte aus Forschung und Entwicklung, 39, 172 pp.
- Wizisk, U., 1995, Mikrofazielle Entwicklungsgeschichte des devonischen Briloner Riffkomplexes (Sauerland). Unpublished Dissertation, Ruhr-University Bochum, 79 pp.
- Wrede, V., 1992, Störungstektonik im Ruhrkarbon. Zeitschrift der angewandten Geologie, 38, p. 94-104.



## CHAPTER 4

# OXYGEN, HYDROGEN, AND STRONTIUM ISOTOPIC COMPOSITIONS OF SALINE GROUNDWATERS IN THE MÜNSTERLAND CRETACEOUS BASIN: CLUES TO THEIR ORIGIN AND EVOLUTION

## 4.1 Introduction

### 4.1.1 Background

Oxygen, hydrogen, and strontium isotopes of groundwaters have been frequently used to infer their origin and evolution (Chaudhuri 1978; Sunwall and Pushkar 1979, Starinsky et al. 1983; Stueber et al. 1984, 1987; Burtner 1987; Fisher and Kreitler 1987; McNutt et al. 1987; Lowry et al. 1988; Land and McPherson 1989; Egeberg and Aagaard 1989; Connolly et al. 1990; Chaudhuri et al. 1992, Chaudhuri and Clauer 1993; Moldovanyi et al. 1993; Stueber 1998). Oxygen and hydrogen isotopic data of groundwaters provide information regarding the source of water molecules and effects of water-rock interaction, whereas the strontium isotopic composition identifies sources of Sr, helps to constrain water-rock interactions, and can be used to trace the evolution and migration paths of fluids.

The term groundwater, as used herein, refers to all aqueous subsurface fluids that occur beneath the water table in soils and geologic formations that are fully saturated (Freeze and Cherry 1979). In this chapter, the term *saline groundwater* refers to all groundwaters with salinities (= total dissolved solids or TDS) higher than that of freshwater (TDS > 1,000 mg/l) (Solley et al. 1983) and includes the salinity ranges of brackish water (TDS = 1,000 to 10,000 mg/l), saline water (TDS = 10,000 to 100,000 mg/l), and brine water (TDS > 100,000 mg/l) (Carpenter 1978).

A major physical attribute of most saline groundwaters is that they have migrated over long distances prior to entering the reservoir rocks or aquifers where they presently reside and from which they can be produced. In many instances significant chemical reactions between waters and minerals seem to have occurred elsewhere in the subsurface and, hence, the chemical compositions of the waters often bear little or no relation to the mineralogical framework of the present reservoir rocks or aquifers (Chaudhuri and Clauer





1993). Furthermore, it is widely recognized that saline groundwaters play an important role in processes such as hydrocarbon migration, subsurface dolomitization, and the formation of sediment-hosted ore deposits, (e.g., Sverjensky 1984; Bethke and Marshak 1990; Kesler et al. 1997; Morrow 1998), but the origin(s) and source(s) of the water and solutes remain controversial. Saline groundwaters may originate as meteoric water that percolates into the subsurface and reacts with rocks along its path; or as interstitial seawater (connate water) trapped during original sediment deposition (Lowry et al. 1988). Subsequent chemical and isotopic changes may result from (1) dilution of the saline groundwater by meteoric water; (2) migration and mixing of different saline groundwaters with contrasting chemical and isotopic compositions; and (3) water-rock interaction. The salinity of the groundwaters has been attributed to halite dissolution (Land and Prezbindowski 1981), retention or reflux of evaporatively concentrated seawater (Rittenhouse 1967; Carpenter 1978), shale membrane filtration (Graf 1982), and/or evaporation of non-marine fluids (Hardie 1990).

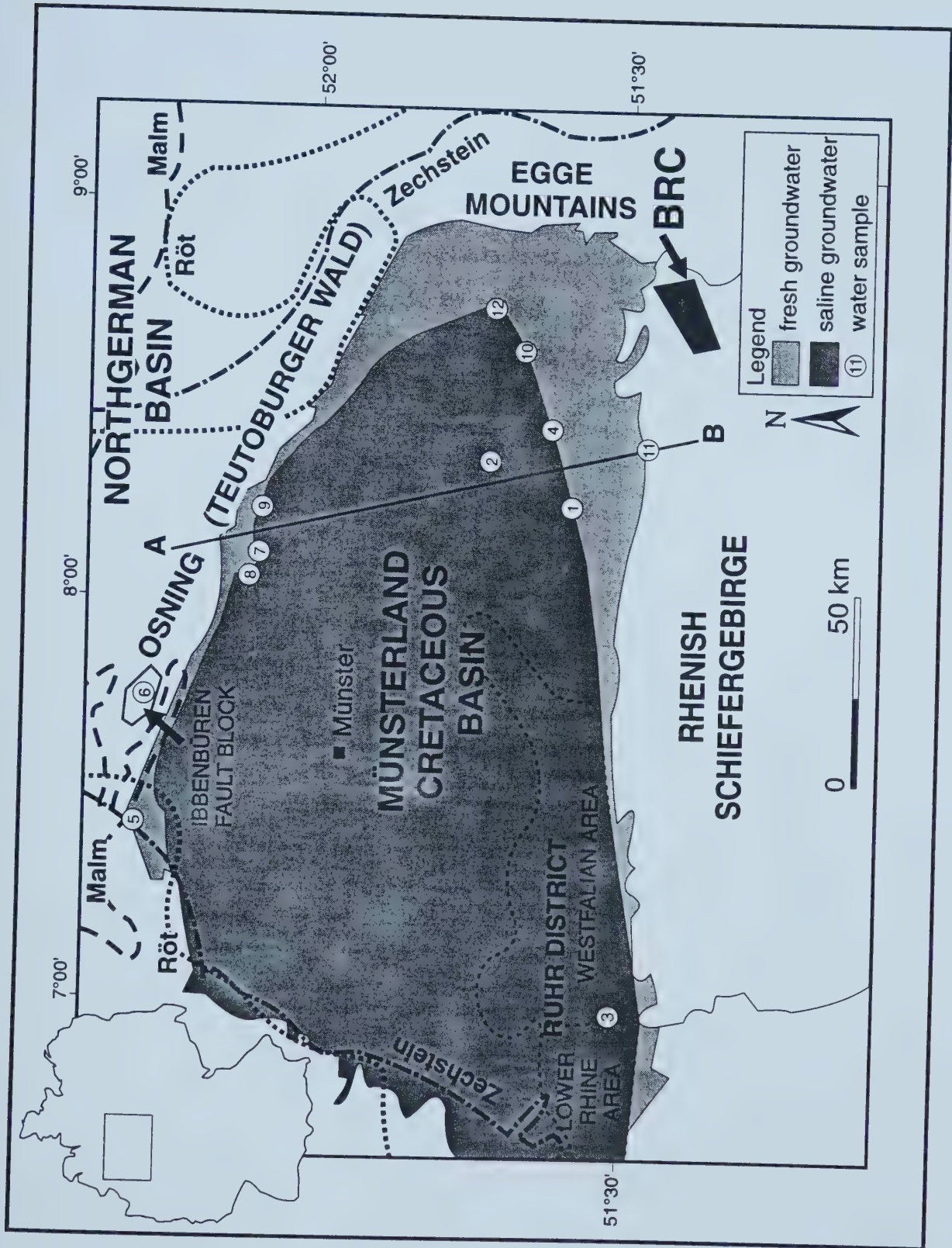
The geochemical and microthermometric investigations of the post-Variscan fault-controlled hydrothermal dolomitization and associated minor Pb-Zn sulfide mineralization in the Devonian Brilon Reef Complex in the northeastern Rhenish Schiefergebirge (Figure 4.1) show that dolomite, sphalerite, and calcite cements formed from highly saline fluids (19-26 equivalent weight % NaCl) with a complex cation composition (Chapter 3). The occurrence of saline groundwaters with salinities of up to 25 % (250,000 mg/l) in the subsurface of the so-called Münsterland Cretaceous Basin (MCB) directly north of the Brilon Reef Complex (Figures 4.1 and 4.2), gives rise to the hypothesis that the dolomitizing and mineralizing fluids may share a common origin with the present-day saline groundwaters in the MCB. Dolomitization and mineralization in the Brilon Reef Complex probably took place during the Late Cretaceous/Early Tertiary, at the same time when Saxonian tectonic movements brought the present-day shape of the MCB into existence.

The compositions and distribution of the saline groundwaters in the MCB have been the subject of numerous publications (Patteisky 1954; Fricke and Wevelmeyer 1960; Fricke 1961, 1962, 1963, 1964a, b, 1967, 1968, 1969; Puchelt 1964; Angerer et al. 1968; Michel 1963; Geyh and Michel 1974; Michel and Nielsen 1977; Wedewardt 1995), and several theories about their origin(s) exist. Puchelt (1964) suggested that the saline groundwaters are





**Figure 4.1:** Map of the Münsterland Cretaceous Basin (MCB) in Northwestern Germany showing the distribution of saline groundwater (TDS > 1000 mg/l) in the regional aquifer. Dashed lines labeled Zechstein, Röt, and Malm delineate the southernmost extent of Upper Permian, Triassic, and Jurassic halite deposits in the subsurface (modified after Michel 1983a). Solid line A-B indicates position of a schematic cross-section shown in Figure 4.2. BRC = Brilon Reef Complex.









**Figure 4.2:** Schematic cross-section A-B (see Figure 4.1) depicting the stratigraphy and present-day geological structure of the Münsterland Cretaceous Basin, as well as the position of the boundary between fresh and saline groundwater (TDS = 1000 mg/l) in the subsurface (dashed line). See text for further explanation.

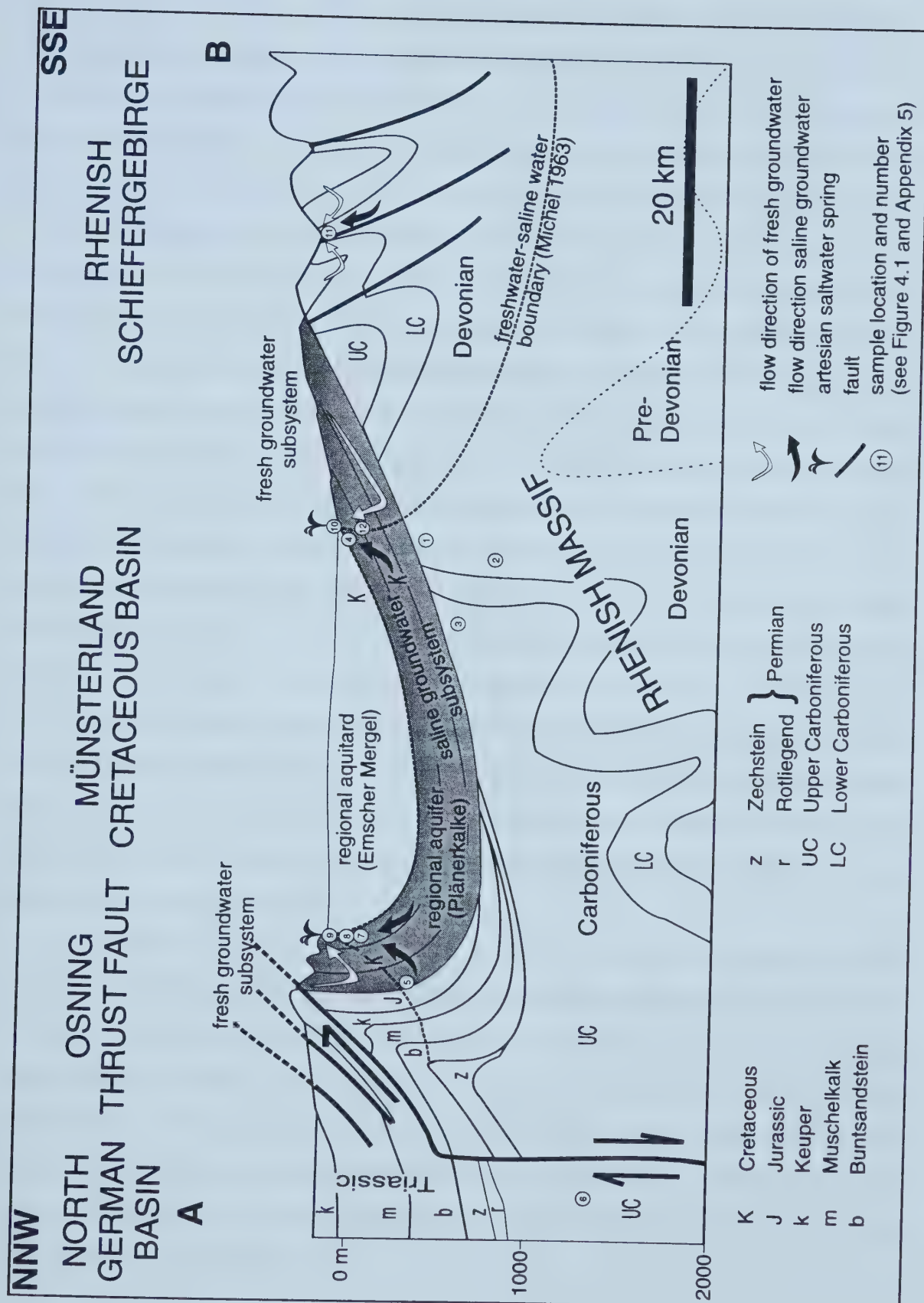


Figure 4.2



derived from the primary sedimentary pore waters (“connate water”) that underwent compositional modifications due to water-rock interaction and biological activity (e.g., sulfate reducing bacteria), whereas Fricke (1961) and Michel and Nielsen (1977) invoked the subsurface dissolution (subrosion) of halite deposits in the periphery of the MCB and migration of the resulting brines into the basin. Patteisky (1954) proposed a magmatic origin of the saline waters as so-called juvenile water. Most recent publications (Michel et al. 1974; Michel 1983 a, b, 1994; Wedewardt 1995) concluded that the present-day compositions of the saline groundwaters in the MCB are the result of the complex hydrogeologic history of the area that led to the mixing of fluids of different origins (modified sedimentary pore water, subrosion brines, meteoric water). In their study of the sulfur isotopic compositions of sulfate from saline groundwaters from the eastern part of the MCB, Michel and Nielsen (1977) were able to show that the dissolved sulfate in these groundwaters was derived from the Zechstein evaporites at the eastern margin of the MCB. Similar studies on saline groundwaters from coal mines in the Ruhr-District (Puchelt and Nielsen 1967) and the Ibbenbüren area (Bässler 1970) yielded ambiguous results, i.e., the waters were interpreted to contain sulfate from different sources (i.e., oxidation of pyrite, dissolution of evaporites of different ages). Wedewardt (1995) used the bromide/chloride systematics of the saline groundwaters from the Ruhr District (Figure 1, sample location 3) as evidence for the origin of the high salinities of the groundwaters from the subrosive dissolution of Upper Permian (Zechstein) halite deposits in the Lower Rhine area and for the subsequent migration of the resulting brines into the halite-free areas of the MCB.

This chapter presents the first data on the Sr isotopic composition of saline groundwaters from the MCB. The main objective of this part of the present study is to better delineate the origin(s) and evolution of the present-day saline groundwaters in the MCB using oxygen, hydrogen, and strontium isotopes in conjunction with their chemical compositions. Within the framework of the regional geologic history (outlined below), the hypothesis that the present-day saline groundwaters in the MCB bear a genetic relationship to the mineralization (including dolomitization) in and around the fractures of the Brilon Reef Complex can be evaluated.





#### ***4.1.2 Geographic location and geologic framework***

The MCB extends in N-S direction from 51°30' N to 52°20' N (ca. 150 km) and in W-E direction from 6°30' E to 9°E (ca. 80 km) and covers an area of close to 11000 km<sup>2</sup> (Fig. 4.1). To the south, it is bordered by the mountain range of the Rhenish Schiefergebirge. To the east and northeast, the ridges of the Egge Mountains and the Osning form a sharp morphologic boundary. In the west, northwest and north, the transitions to the neighboring Lower Rhine area and the Central-Netherlands-Basin occur without a clear morphologic change.

Morphologically, the area of the MCB can be divided into lowlands, wide valleys, ridges, and mountains (Struckmeyer 1990). The landsurface generally slopes from SE to N and NW. Elevation gradients mainly range between 0.1 to 1 %, and rarely exceed 2 %. The highest elevations occur in the SE corner of the MCB (up to 503 m a. S.L.). At the western and northwestern margins of the basin, maximum elevations reach about 50 m a. S. L. Several areas within the MCB have elevations of up to 150 m a. S. L. and exhibit a strong local relief with deeply incised valleys. The remaining area of the MCB consists of extensive lowlands with elevations between 20 and 75 m a. S. L.

An overview over the geologic history of the area of the MCB is given in Figure 4.3. In the subsurface, the MCB consists of two major geologic units: the Paleozoic basement and the overlying Mesozoic and Cenozoic strata (Figure 4.2). The Paleozoic basement, which is generally referred to as the Rhenish Massif, consists of Ordovician to Upper Carboniferous, mainly clastic sedimentary rocks that were deformed during the Late Carboniferous Variscan Orogeny, resulting in SW-NE trending folds and thrust faults. The Variscan deformation front approached from the south, hence the intensity of deformation decreases northward. Strongly deformed rocks of the Rhenish Massif crop out in the Rhenish Schiefergebirge in the south. Paleozoic rocks that were not deformed during the Variscan Orogeny occur in the subsurface of the northwestern part of the MCB.

The central part of the Rhenish Massif was exposed at the surface during most of the post-Variscan time. Upper Permian to Lower Cretaceous sedimentary rocks, including Upper Permian (Zechstein), Lower Triassic (Röt), and Upper Triassic (Malm) halite deposits, occur only in the periphery of the MCB (Figures 4.1 and 4.2). An Albian/Cenomanian









transgression resulted in the inundation of the northern Rhenish Massif and marine sedimentation resumed. During the Cenomanian and Turonian, marine limestones, the so-called “Plänerkalke” formed, followed by marls (“Emscher Mergel”) of Coniacian to Campanian age. The MCB fell dry at the end of the Late Cretaceous, due to uplift and northward tilting of the Rhenish Massif. During the Tertiary, marine sedimentation took place only in the Lower Rhine area in the western part of the basin (Figure 4.1).

Wrench tectonics during the Subhercynian and Laramide phases of the Saxonian Orogeny in the Late Cretaceous to Early Tertiary resulted in the present-day asymmetric structure of the basin, which is characterized by steeply dipping to overturned beds of the “Plänerkalke” at the northeastern and northern margins of the basin and gently sloping beds at its western, southern, and eastern margins (Figure 4.2). During the Laramide phase of the Saxonian Orogeny, southward thrusting and transpressional uplift of fault blocks (e.g., Ibbenbüren fault block; Figure 4.1, sample location 6) occurred along the so-called Osning Zone, which separates the MCB from the Northgerman Basin to the north (Rosenberg 1983) (Figure 4.2).

In the Pleistocene, the Scandinavian continental glaciers extended southward into the MCB in 3 phases during the Saale glacial period, crossing the mountain ridges of the Osning Zone (Thome 1983). Glacial erosion and deposition resulted in characteristic glacial and periglacial sediments and landforms (glacial till, erratics, drumlins, kames, ozers, sanders, loess plains), which are still present at the surface today.

#### ***4.1.3 Hydrogeological framework***

The regional hydrologic system of the MCB is that of an artesian basin that has elevated recharge areas at its margins and a thick and areally extensive aquitard overlying the regional aquifer in its center (Figure 4.1 and 4.2). The main regional aquifer in the MCB consists of Upper Cretaceous (Cenomanian/Turonian) marine carbonates (“Plänerkalke”) (Figure 4.2). Saline groundwaters also permeate the fractured bedrock of the underlying deformed Paleozoic basement, the so-called northern Rhenish Massif. In the center of the MCB, the “Plänerkalke” are overlain by Upper Cretaceous marls (“Emscher Mergel”), which form the regional aquitard that separates the regional aquifer from several local hydrologic





systems close to the surface (Struckmeyer 1990). Within the regional aquifer, two hydrologic subsystems have been recognized (Struckmeyer 1990), (1) a marginal fresh groundwater subsystem at the southern, eastern, and northern margins of the basin where the regional aquitard has been eroded; and (2) a central saline groundwater subsystem below the regional aquitard (Figure 4.2).

The sedimentary rocks of the Paleozoic basement generally have low hydraulic conductivities ( $k_f$ ) that range from  $2 \times 10^{-13}$  to  $4 \times 10^{-9}$  m/s (Wedewardt 1995) and are similar to those of the Upper Cretaceous regional aquitard ( $k_f = 10^{-12}$  to  $10^{-9}$  m/s; Struckmeier 1990). Most of the groundwater movement in the Paleozoic basement and regional carbonate aquifer is restricted to fractures and faults (Wedewardt 1995). In the marginal areas of the MCB, the karstification of the Upper Cretaceous limestones has enhanced permeabilities in the areas where the regional carbonate aquifer is not covered by the regional aquitard (Figures 4.1 and 4.2). Therefore, water movement is impeded in the central part of the regional aquifer, and the fact that the saline groundwaters in the central part of the regional aquifer have not yet been diluted to fresh water salinities has been attributed to decreasing permeabilities within the regional aquifer from the margins to the center and to the effective sealing qualities of the regional aquitard (Struckmeyer 1990).

The flow patterns within the regional saline groundwater subsystem are unknown because of the lack of pressure and hydrochemical data from the central part of the MCB (Struckmeyer 1990; Wedewardt 1995). In the few wells that penetrate the regional aquifer and the Paleozoic basement in the central part of the basin, no drill stem tests were carried out (Struckmeyer 1990). Therefore, the possibility of lateral and vertical, cross-formational recharge of saline groundwaters from the underlying Paleozoic basement and neighboring areas along faults cannot be evaluated using hydrogeologic data.

The saline groundwaters discharge at the surface in artesian springs at the interface between the regional aquifer and the regional aquitard. They are also produced from wells from the regional aquifer and the underlying Paleozoic rocks below the aquitard. For example, in the deep coal mines of the Ruhr-District in the southwestern part of the MCB, the saline groundwaters are being pumped continuously to allow mining activities to proceed and to keep abandoned sections of the mines accessible for possible reactivation (Wedewardt



1995; Heuser personal communication 1998). In response to the extraction of saline groundwaters in coal mines during the last 150 years, the boundary between the fresh groundwater subsystem at the margins of the basin and the central saline groundwater subsystem has been shifting basinward, resulting in the disappearance of saltwater springs at the surface (Struckmeyer 1990).

Presently, the pressure exerted by meteoric water recharge of the regional fresh groundwater subsystem from the highlands in the Osning fault zone, Egge Mountains and Rhenish Schiefergebirge (Figures 4.1 and 4.2) on the regional saline groundwater subsystem below the regional aquitard appears to be the driving force for the artesian discharge of the saline groundwaters. After heavy rainfalls, the rate of discharge as well as the salinity of the discharging saline groundwater has been reported to increase (Fricke 1961, 1963; 1964b; Angerer et al. 1968; Papakonstantinou 1970), which indicates that more concentrated, saline waters are mobilized from greater depth.

Points of discharge at the surface and in the subsurface are almost exclusively reported to be associated with fault-related fracture systems (e.g., Fricke 1961, 1963, 1964a, b, 1967, 1968; Michel 1963; Wolansky 1964; Wedewardt 1995). Many of these faults cut through the Paleozoic basement and overlying Cretaceous bedrock and extend southward into the Rhenish Schiefergebirge. Although the boundary between fresh and saline groundwater (TDS > 1000 mg/l) lies at greater depths in the Rhenish Schiefergebirge than in the MCB (Michel 1963; Figure 4.2), saline groundwaters ascend along fault planes and discharge at the surface, especially where NNW-SSE trending normal faults cross-cut the SW-NE trending Variscan anticlines (e.g., sample location 11 in Figure 4.2; Fricke 1967; Michel 1983b).

Locally, the faults along which saline groundwaters occur are mineralized with base metal sulfides associated with quartz, barite, and carbonate gangue minerals (calcite, dolomite, strontianite) (Pilger 1961; Scherp and Strübel 1974; Hofmann and Schürenberg 1979; Hofmann 1979; Bode 1980; Unland 1985; Schaeffer 1983, 1984). The Pb-Zn veins in the Paleozoic rocks of the Ruhr-District have been thought to have resulted from the ascent of metal-bearing, hydrothermal fluids along faults during the late phases of the Variscan Orogeny under the influence of magmatic intrusions in the deeper subsurface (Pilger 1961).





More recent investigations of the tectonic evolution of the Ruhr-District, however, indicate that many of these faults are of post-Variscan origin and that the major amount of the base metal sulfide mineralization may be of Cretaceous and Tertiary age (Drozdowski and Wrede 1994).

#### ***4.1.4 Paleohydrogeologic history***

Michel et al. (1974) developed the concept of paleohydrologic cycles to explain the origin and evolution of the present-day saline groundwaters in the MCB, based on its sedimentary and tectonic history and the present-day chemical compositions of the saline groundwaters. Each cycle begins with a marine transgression and spans the period of sedimentation, subsequent regression and erosion. Based on a large hydrogeochemical data set from saline groundwaters from the Ruhr District in the southwestern part of the MCB, Wedewardt (1995) further refined and extended the reconstruction of the paleohydrogeologic history of the MCB proposed by Michel et al. (1974) (Table 4.1). Michel et al. (1974) subdivided the paleohydrogeologic history of the MCB into 4 cycles, whereas Wedewardt (1995) recognized 5 cycles in the Lower Rhine area, and 2 cycles in the Westfalian area of the Ruhr District (Figure 4.1; Table 4.1). The two-fold subdivision of Wedewardt (1995) is generally applicable to the whole area of the MCB: the western, northern, and eastern margins of the MCB underwent a similar development as the Lower Rhine area, whereas the paleohydrogeologic history of the southern margin and the central part of the MCB corresponds to that of the Westfalian area. Nevertheless, both areas are inextricably linked with respect to their hydrogeological evolution, because migration and mixing of groundwaters to various extents has been occurring between these areas (Wedewardt 1995).

The first cycle started with the marine transgression in the Devonian and included the Carboniferous and Early Permian (Rotliegend). During the Devonian and Early Carboniferous, the area was under marine conditions, whereas humid terrestrial conditions prevailed in the Late Carboniferous, during which paralic coal swamps thrived. During the Variscan Orogeny (Westfalian/Stefanian), the compacted and lithified sediments were deformed and uplifted. Burial compaction and tectonic deformation led to the partial or complete expulsion of the original sedimentary water. In the Stefanian and Rotliegend, arid







**Table 4.1:** Schematic representation of the paleohydrogeologic evolution of the Ruhr District in the southwestern part of the Münsterland Cretaceous Basin (modified from Wedewardt 1995). Each hydrologic cycle begins with a transgression. During periods of marine sedimentation, marine pore waters became buried and were partially expelled by compaction of the sediments (ES). During times of exposure, infiltration of meteoric water occurred (IS). In contrast to Michel et al. (1974), Wedewardt (1995) distinguished between two areas, based on differences in their paleohydrogeologic evolution: (1) the Lower Rhine area with 5 paleohydrogeologic cycles; and (2) the Westfalian area with 2 paleohydrogeologic cycles. See text for further explanation.





conditions prevailed and the infiltration of surface water decreased. According to Michel et al. (1974), at the end of the first cycle, a mixture of groundwaters of marine and meteoric origin, modified by water-rock interaction during burial and tectonic deformation and by evaporation during times of arid conditions, was present in pores and fractures within the Paleozoic sedimentary rocks that now underlie the Münsterland Cretaceous Basin.

The second cycle in the Lower Rhine area and other areas in the periphery of the MCB began with the Late Permian marine ingressions of the Zechstein-Sea which encroached only on the margins of the Rhenish Massif. While Michel et al. (1974) also included the subsequent marine ingressions in the Triassic and Jurassic into the second cycle, Wedewardt (1995) distinguished two cycles (his cycle II and III; Table 4.1) because of differences in the climatic conditions. Arid conditions during the Zechstein and certain periods of the Triassic are supposed to have resulted in an increase in groundwater salinities in the exposed areas, whereas humid conditions during the remaining time until the Late Cretaceous led to the infiltration of fresh groundwater. During times of marine ingressions, seawater infiltration led to an increase in salinity of the groundwater in the respective coastal areas. Wedewardt (1995) pointed out the possible involvement of relict brines that resulted from the formation of halite during the Permian, Triassic, and Jurassic. Because of their high density, these brines descended into the underlying rocks and mixed with the groundwaters already present. Michel et al. (1974) proposed that the deep groundwaters in the Paleozoic basement probably had elevated salinities at the end of the Late Cretaceous, but not as high as they are today.

The third cycle of Michel et al. (1974) corresponding to Wedewardt's (1995) cycle IV in the Lower Rhine area and cycle II in the Westfalian area, began with the marine transgression in the Cenomanian and covered the entire area of the Münsterland Cretaceous Basin. Continuous subsidence resulted in the formation of a thick succession of limestones and marls. Compactional expulsion of most of the pore water took place during the Upper Cretaceous. Michel et al. (1974) tenuously argued that parts of the expelled water infiltrated the fractured Paleozoic basement below, where it supposedly mixed with the deep groundwater. In the Late Cretaceous, the area of the MCB fell dry, resulting in the infiltration of fresh groundwater and the dissolution of halite deposits of the Permian (Zechstein), Triassic (Röt), and Jurassic (Malm) in the subsurface at the margins of the MCB. The





subrosion brines mixed with the deep groundwater and caused a significant increase in salinity, probably reaching that of the present-day basinal brines. In contrast to Michel et al. (1974) and Michel (1994), Wedewardt (1995) states, that subrosive dissolution of halite deposits in the periphery of the MCB and migration of the resulting brines probably has been an ongoing process since the end of the Permian.

The forth cycle of Michel et al. (1974) is equivalent to cycle V of Wedewardt (1995) (Table 4.1). It encompassed the time period from the Oligocene transgression to the present. This transgression affected only the western and northwestern parts of the MCB, whereas most of the basin was exposed. Uplift of the Rhenish Schiefergebirge in the Tertiary supposedly led to the mobilization and ascent of saline groundwaters, which mixed with the shallower groundwater.

During the humid phases of the Late Tertiary, the infiltration of fresh groundwater resulted in karstification of the "Pläner Limestone" and the development of the regional fresh groundwater subsystem at the northern, eastern and southern margins of the MCB. With continuous erosion of the sealing Upper Cretaceous marls, the fresh groundwater subsystem expanded basinwards. During the Quaternary, the deep groundwater probably did not undergo significant changes. A slight "freshening" may have occurred during the interglacial periods, while no significant amount of fresh groundwater is expected to have formed during glacial periods (Michel et al. 1974).

From the above it becomes clear, that the present-day saline groundwaters in the MCB have a very complex history, and that their present-day chemical and isotopic compositions are the combined result of water-rock interaction, migration, and mixing of fluids of different origins.

The data gathered in this study (Chapters 2 and 3) suggest alternative possibilities and extended interpretations for the regional hydrogeology. In particular, the geochemical and microthermometric investigations of the post-Variscan, fault-controlled hydrothermal dolomitization and associated minor Pb-Zn sulfide mineralization in the Devonian Brilon Reef Complex suggest that the dolomitizing and mineralizing fluids may share a common origin with the present-day saline groundwaters in the MCB. Wrench tectonics during the



Late Cretaceous/Early Tertiary (Rosenberg 1983; Wrede 1992) together with an increased heatflow (Lommerzheim 1988, 1991, 1994) may have been the cause for the episodic nature of the post-Variscan mineralization in the northeastern Rhenish Schiefergebirge and possibly also in the Paleozoic and Mesozoic rocks in the area of the MCB. These tectonic events most likely had a profound impact on the regional groundwater flow systems by (1) creating and re-activating faults that acted as pathways or barriers for groundwater flow; (2) displacing pre-existing groundwaters by tectonic loading; and (3) creating a new basin geometry and surface topography resulting in a change of the regional groundwater flow patterns.

The investigation of the stable and strontium isotope compositions of the saline groundwaters from the MCB presented in this chapter provides a further parameter to better constrain their history. The results allow to evaluate the hypothesis that these groundwaters have a genetic relationship to the mineralization in the Brilon Reef Complex.

## **4.2 Data base and analytical methods**

For this study, 12 water samples were taken from locations at the margins of the Münsterland Cretaceous Basin where saline groundwaters were accessible (Figure 4.1, Appendix 5). Sample locations include subsurface coal mines in the Carboniferous of the Ruhr District (sample 3) and the Ibbenbüren District (sample 6), nine wells (6 of those artesian), and one natural artesian spring (sample 10). The samples originate from a variety of depths (0 m to approximately 1500 m below surface), stratigraphic levels (Middle Devonian to Pleistocene), and aquifer lithologies (fractured shale, sandstone, limestone, sand) (Figure 4.2; Appendix 5).

Prior to sampling, the temperature, pH, and specific electrical conductivity of the waters were measured electrometrically. The measured values have not been corrected for differences in temperature and, hence, can be used only as an approximation for the total concentration of dissociated ions.

The water samples were collected in airtight polyethylene bottles and special care was taken not to leave any headspace. Volumes taken were 500 ml for analysis of the hydrochemical composition and TDS, and 60 ml for isotopic analysis ( $^{87}\text{Sr}/^{86}\text{Sr}$ ,  $\delta^{18}\text{O}$ ,  $\delta\text{D}$ ).





The results of previous hydrochemical analyses carried out by the Fresenius Institute were available for sample locations 1, 2, 4, and 9 (Appendix 5). Michel and Nielsen (1977) published sulfur isotope data for saline groundwaters at sample locations 1, 2, 4, 8, and 10. The sulfur isotope composition for a saline groundwater at sample location 5 was determined by Bässler (1970).

#### ***4.2.1 Hydrochemistry***

The hydrochemical composition and total dissolved solids (TDS) of the water samples were determined by Dr. B. Lürer in the laboratory of the Geological Survey of the Province of Northrhine-Westfalia. Chloride and nitrate concentrations were determined by ion chromatography (IC), using a Dionex 4000i ion chromatograph, and bicarbonate concentrations by titration with 0.1 N HCl. Fluoride concentrations were measured electrochemically with an ion-selective electrode (ISE). Bromine and iodine were not analyzed. Total sulfur and phosphorus concentrations and all cation concentrations were determined by ICP(inductively coupled plasma)-spectroscopy, using a TJA(Thermo Jarrel Ash) IRIS-AP ICP equipped with a CID(charge injection device)-detector in an argon plasma. The water samples were evaporated at 180°C to determine the amount of TDS.

#### ***4.2.2 Stable isotope analysis***

Determination of the oxygen and hydrogen isotopic composition of the water samples was carried out at the University of Calgary. The isotope composition of oxygen was determined by analysis of CO<sub>2</sub> that was equilibrated isotopically with the water at ambient temperature (at 25°C). The isotope composition of hydrogen was measured by analysis of H<sub>2</sub> gas that was obtained by reacting the water samples with metallic zinc at 450°C. The isotope compositions are reported in the  $\delta$ -notation relative to the SMOW standard. In-run precision was better than  $\pm 0.2$  ‰ for  $\delta^{18}\text{O}$  and better than  $\pm 1$  ‰ for  $\delta\text{D}$ .

#### ***4.2.3 Strontium isotope analysis***

For each water sample, the volume of water required to yield 4  $\mu\text{g}$  of strontium (necessary for accurate strontium isotopic analysis) was calculated based on the strontium





concentrations of the water samples as determined by ICP. The necessary aliquot of water was evaporated and the residue dissolved in 1N HCl. Strontium was extracted from the solution using standard cation exchange techniques. The strontium isotopic analyses were carried out on a VG 354 thermal ionization mass spectrometer at the University of Alberta. The samples were loaded as a phospho-tantalate gel on a single Re ribbon bead assembly. In-run precision was better than  $4 \times 10^{-5}$  ( $2\sigma$ ). The isotopic ratios of the samples were normalized against the value of the NBS 987 standard, which yielded a  $^{87}\text{Sr}/^{86}\text{Sr}$  value of 0.71021 over the period of the analysis of the water samples.

### 4.3 Results

The results of the field measurements and of the chemical and isotopic analyses results are tabulated in Appendix 5 and plotted in Figures 4.4 to 4.13. For the purpose of comparison, the chemical composition of seawater is given in Table 4.2.

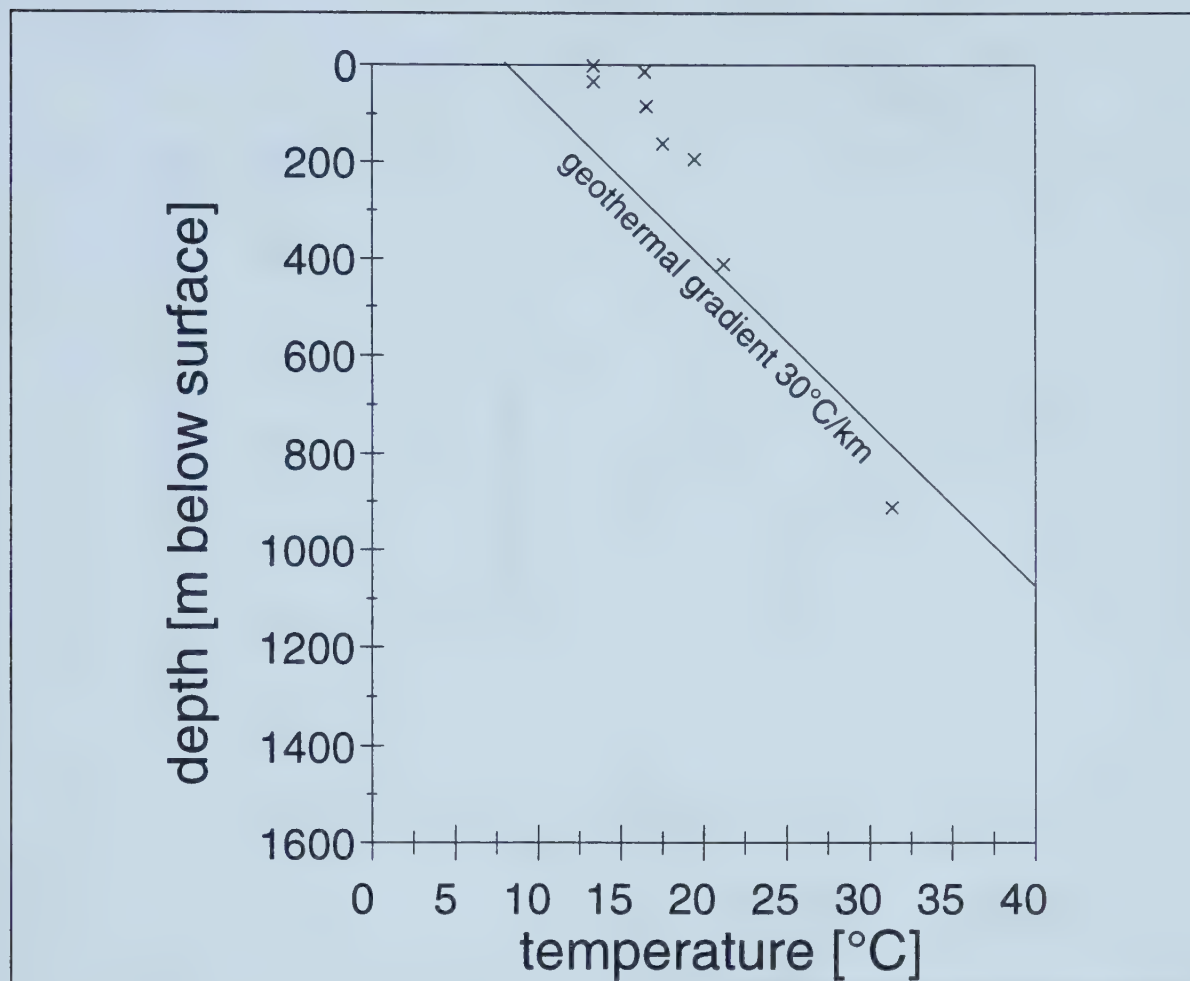
major constituents		minor and trace constituents	
	mg/l		mg/l
Cl	19350	Al	0.002
Na	10760	Ba	0.01
SO4	2710	Fe	0.002
Mg	1290	I	0.06
Ca	411	Li	0.18
K	399	Mn	0.0002
HCO3	142	Ni	0.0005
Br	67	Pb	0.00003
Sr	8	Rb	0.12
B	4.5	Zn	0.002

**Table 4.2:** Chemical composition of seawater (from Drever 1988).

#### 4.3.1 Temperature and pH

Temperature measurements could only be obtained for 8 of the samples. The temperatures of the water samples range from 13.4°C at 0 m depth to 31.4 °C at 910 m depth (Figure 4.4). The temperatures of 6 samples at shallow depths (between 0 and 192 m) are significantly elevated relative to those expected at their respective depths, based on the mean





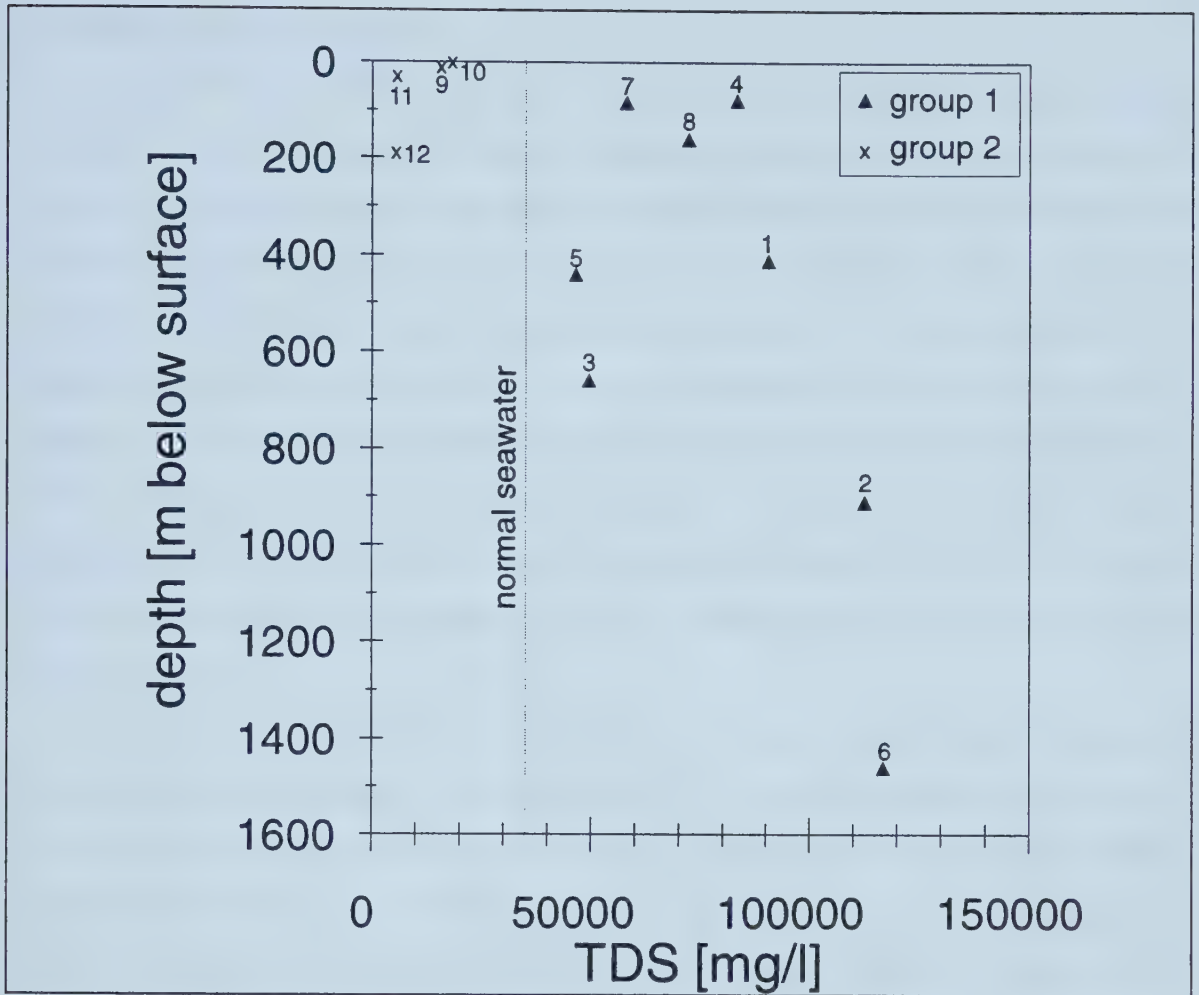
**Figure 4.4:** Temperature vs depth plot for the investigated saline groundwater samples from the MCB. The solid line represents the expected temperature increase with depth based on an average annual surface temperature of 8°C and assuming a geothermal gradient of 30°C per 1000 m.

annual surface temperature of 8°C and an assumed geothermal gradient of 3°C/100 m (Figure 4.3), whereas the temperature of one sample at 411 m depth is only slightly elevated and that of one sample at 910 m depth is lower. The pH-values show a range from 6.3 to 7.3, irrespective of aquifer lithology (Appendix 5).

#### 4.3.2 Total dissolved solids (TDS) and specific electrical conductivity

The TDS of the investigated water samples range from 5402 mg/l (sample 12) to 112674 mg/l (sample 2), with 8 out of 12 samples having higher TDS than seawater (approximately 35000 mg/l, Drever 1988). The specific electrical conductivity values





**Figure 4.5:** Depth vs total dissolved solids (TDS) plot of the saline groundwater samples from the MCB. The samples have been divided into two groups: group 1 with TDS > normal seawater, and group 2 with TDS < normal seawater.

correspond well with TDS. Generally, TDS increases with depth but the data scatter of the 12 samples is quite large (Figure 4.5). Samples with higher TDS than seawater (group 1; samples 1 to 8) are from sample locations at greater depths where active mixing between meteoric water and saline groundwater is expected to be limited or non-existing. Samples with lower TDS than seawater are from sample locations at or close to the surface (group 2; samples 9 to 12) where active mixing can be expected.





### 4.3.3 Stable isotope composition

In a  $\delta D$  versus  $\delta^{18}O$  cross plot, the isotopic compositions of meteoric waters worldwide lie along a straight line (meteoric water line = MWL) defined by the equation  $\delta D = 8\delta^{18}O + 10$ . This relationship is the result of isotope fractionation during evaporation and condensation in the hydrologic cycle (Friedman et al. 1964). With respect to seawater (SMOW), water of meteoric origin is preferentially enriched in  $^{16}O$  and has negative  $\delta^{18}O$  values, whereas silicate and carbonate rocks are enriched in  $^{18}O$  and have positive  $\delta^{18}O$  values. A shift towards more positive  $\delta^{18}O$  values in groundwaters is caused by either oxygen isotope exchange between the water and rocks or by mixing of isotopically altered groundwaters with meteoric water, or both (Kharaka and Carothers 1986). The  $\delta D$  values are less affected by water-rock interaction than the  $\delta^{18}O$  values because the hydrogen content of rocks is very low.

Oxygen and hydrogen isotopic analyses for the investigated saline groundwaters from the MCB are plotted in Figure 4.6 along with MWL. Most of the samples plot on or very close to the meteoric water line. The range of  $\delta D$  values for present-day shallow groundwaters of the area of the MCB is between -50 and -60 ‰ SMOW (Sonntag et al. 1983). Wedewardt (1995) reports a  $\delta D$  value of -52.5 ‰ SMOW and a  $\delta^{18}O$  value of -7.82 ‰ SMOW for the present-day precipitation in the Ruhr District (Figure 4.6). All samples of group 2 and the majority of samples of group 1 have  $\delta D$  values lower than that of present-day meteoric water in the Ruhr District, but fall within regional range. Samples from the northern margin of the MCB (samples 7, 8, and 9; Figures 4.1 and 4.2) have the lowest values, samples from the southeastern part have slightly higher values (samples 1, 2, 4, 10, 11, and 12; Figures 4.1 and 4.2). The data for sample 6 plot on the meteoric water line, but at higher values than present-day precipitation. The data for samples 3 and 5 plot on a trajectory between the value for present-day meteoric water in the Ruhr District and that of seawater (SMOW). Of the samples in group 1, the two samples with the least elevated TDS have the highest  $\delta D$  and  $\delta^{18}O$  values (samples 3 and 5).





**Figure 4.6:** Stable isotope compositions of saline groundwaters of the MCB. Samples from the northern and southeastern margins fall into distinct groups. See text for further explanation.

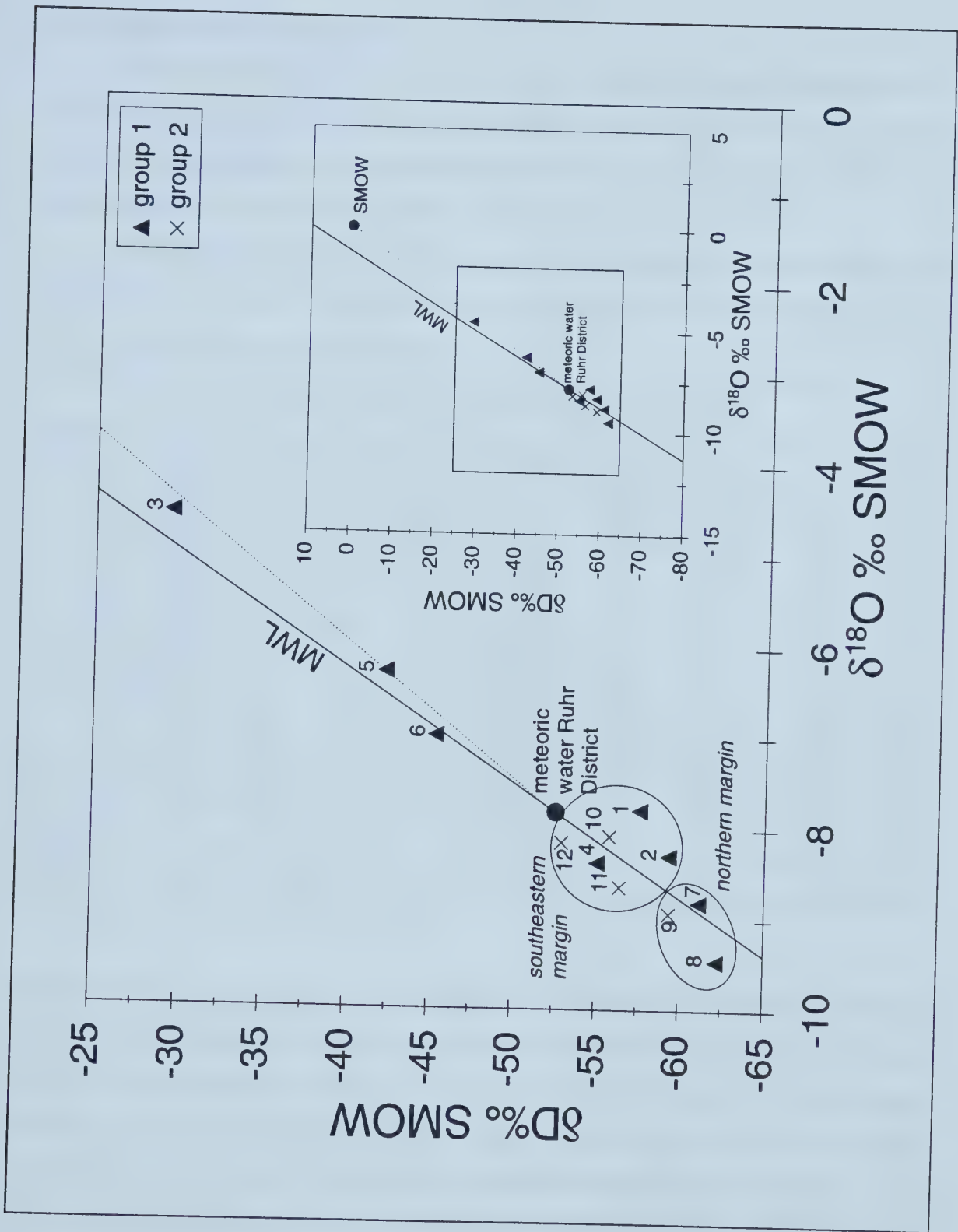


Figure 4.6





4.3.4 Hydrochemical composition

The dissolved inorganic constituents can be divided into major, minor and trace constituents, depending on their concentrations. Major constituents occur in concentrations > 5 mg/l, minor constituents in concentrations from 0.1 to 5 mg/l, and trace constituents in concentrations < 0.1 mg/l (Davies and De Wiest 1966).

The chemical composition of the analyzed water samples is characterized by the predominance of Na and Cl, which generally represent more than 90 equivalent mole % of the total cations and anions (Table 4.3).

sample	cations (equivalent mole-%)				anions (equivalent mole-%)			mNa/mCl	K/Na
	Na	K	Ca	Mg	Cl	SO4	HCO3		
1	91.77	0.93	5.45	1.84	97.48	1.12	1.40	0.94	0.017
2	92.73	0.95	5.15	1.18	97.02	1.64	1.34	0.96	0.017
3	79.51	0.42	14.24	5.83	94.35	5.32	0.33	0.85	0.009
4	90.55	1.04	6.91	1.50	95.55	2.23	2.22	0.95	0.020
5	94.97	0.33	2.89	1.81	98.60	0.00	1.40	0.98	0.006
6	94.96	0.27	2.87	1.90	98.49	1.10	0.41	0.96	0.005
7	89.01	0.72	8.17	2.09	90.39	5.72	3.89	0.99	0.014
8	90.00	0.70	7.38	1.92	91.08	5.60	3.32	0.99	0.013
9	88.13	0.82	9.12	1.92	84.92	6.69	8.39	1.05	0.016
10	90.65	0.87	7.43	1.04	90.41	3.18	6.41	1.01	0.016
11	85.45	1.49	9.90	3.16	90.61	2.27	7.12	0.96	0.030
12	76.36	0.75	20.96	1.93	84.91	3.54	11.56	0.91	0.017
seawater	77.37	1.69	3.39	17.55	90.28	9.34	0.39	0.86	0.037

**Table 4.3:** Molar percentages of major cations and anions, molar ratios of Na and Cl, and ratios of K and Na concentrations for samples from the MCB and seawater, calculated from values given in Appendix 5 and Table 4.2.

Seawater has a molar ratio of Na and Cl (mNa/mCl) of about 0.86, whereas that of halite is 1. The mNa/mCl ratios of the water samples range between 0.85 (sample 3) and 1.05 (sample 9), with most samples having ratios close to unity (Table 4.3; Figure 4.7). Further cations occurring as major constituents in the water samples include K, Ca, Mg, and Sr (Appendix 5). Ca generally is the second most important cation and can reach up to 21.0 mole % of the total cations (sample 12) (Table 4.3). The two samples with the lowest mNa/mCl ratios (samples 3 and 12) contain the largest molar quantities of Ca (14 and 21 mole % of total cations, respectively) (Table 4.3). Further anions that almost always occur as major constituents are SO<sub>4</sub> and HCO<sub>3</sub> (Appendix 5). Only sample 5 is devoid of measurable



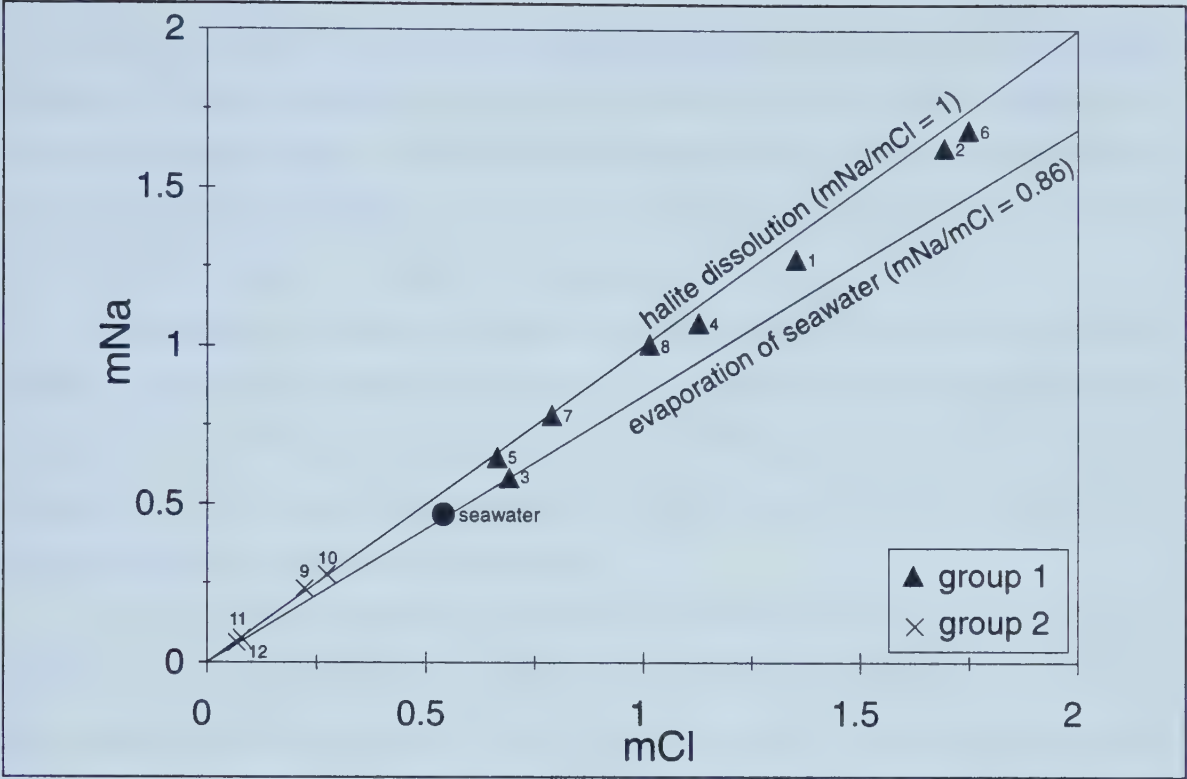


Figure 4.7: Plot of molar concentrations of Na and Cl in the investigated samples.

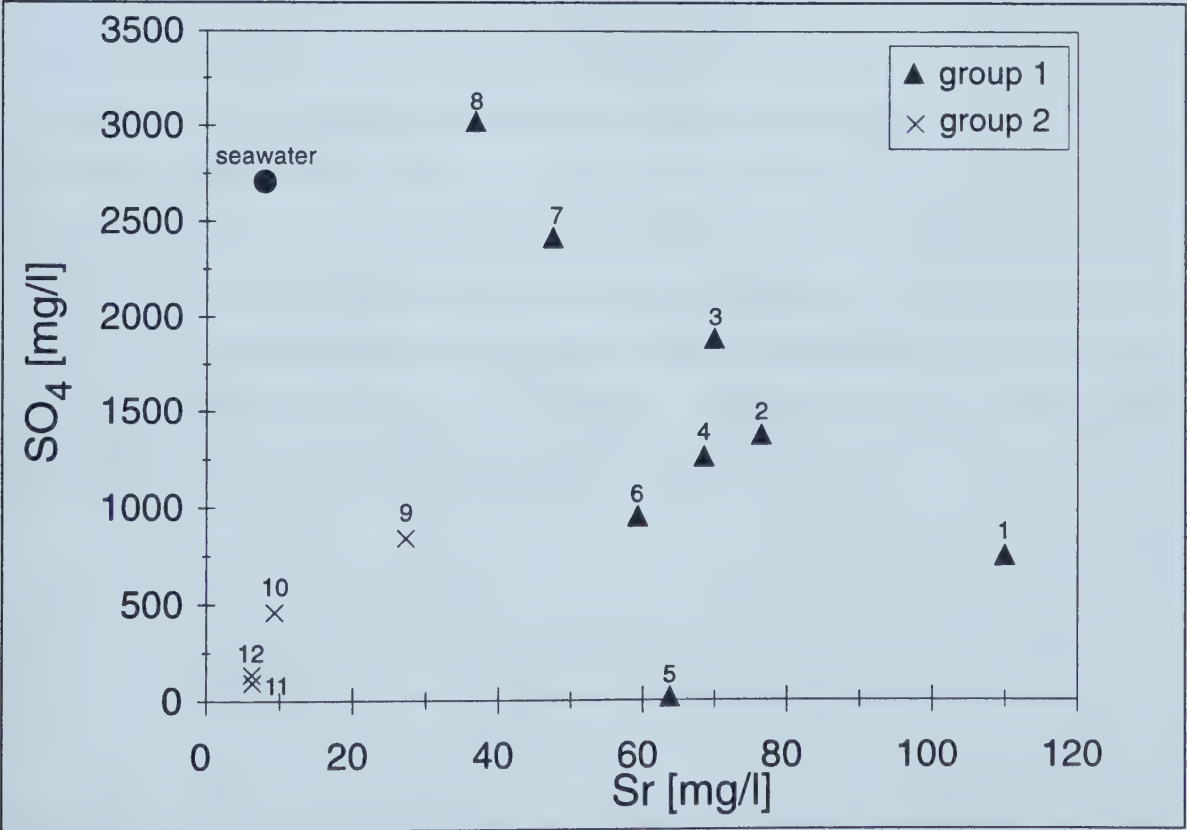


Figure 4.8: Cross plot of SO<sub>4</sub> and Sr concentrations in investigated samples.



amounts of  $\text{SO}_4$  (Figure 4.8). In the same sample, Ba occurs as a major constituent (9.7 mg/l), whereas all other samples have Ba concentrations below 0.4 mg/l (Appendix 5). Concentrations of Fe and Li exceed 5 mg/l in 50 % and 30 % of the samples, respectively. The concentrations of all other ions vary from that of minor and that of trace constituents or are below their respective detection limit (Appendix 5).

With respect to seawater, all samples are depleted in Mg (Figure 4.9a) and enriched in  $\text{HCO}_3$ , (not shown). Furthermore, the majority of samples is depleted in K (Figure 4.9b) and  $\text{SO}_4$  (Figure 4.8) and enriched in Na, Ca, Sr, and Cl (Figures 4.7, 4.8, 4.9a, b). In all samples, Zn concentrations exceed the seawater value, whereas Pb concentrations are below the detection limit (Appendix 5, Table 4.3).

Mg and K concentrations correlate positively with Cl concentrations (Figures 4.9a and b). Sample 3 in the Mg/Cl plot and samples 3, 5, and 6 in the K/Cl plot do not fall on the main trends. In the Ca/Cl and Sr/Cl plots (Figures 4.10a and b) the data scatter widely and only weak positive correlations are displayed. In the Ca/Cl plot, samples 3, 5, and 6 exhibit the largest deviations from the main trend. Since the chemical compositions of the waters are dominated by Na and Cl, very similar data distributions result when K, Mg, Ca, and Sr concentrations are plotted against Na concentrations (e.g., K/Na plot in Figure 4.11a). The K/Na ratios of all samples are below that of seawater ( $\text{K/Na} = 0.037$ ) (Table 4.3; Figure 4.11b). Regardless of the Cl concentrations, the K/Na ratios of most samples fall within a range between 0.013 and 0.020. Exceptions to this are samples 3, 5, and 6 of group 1 with very low K/Na ratios, and sample 11 of group 2 with a high K/Na ratio (Figure 4.11b). No systematic relationships between the chemical compositions and the stable isotope compositions of the investigated water samples could be identified.





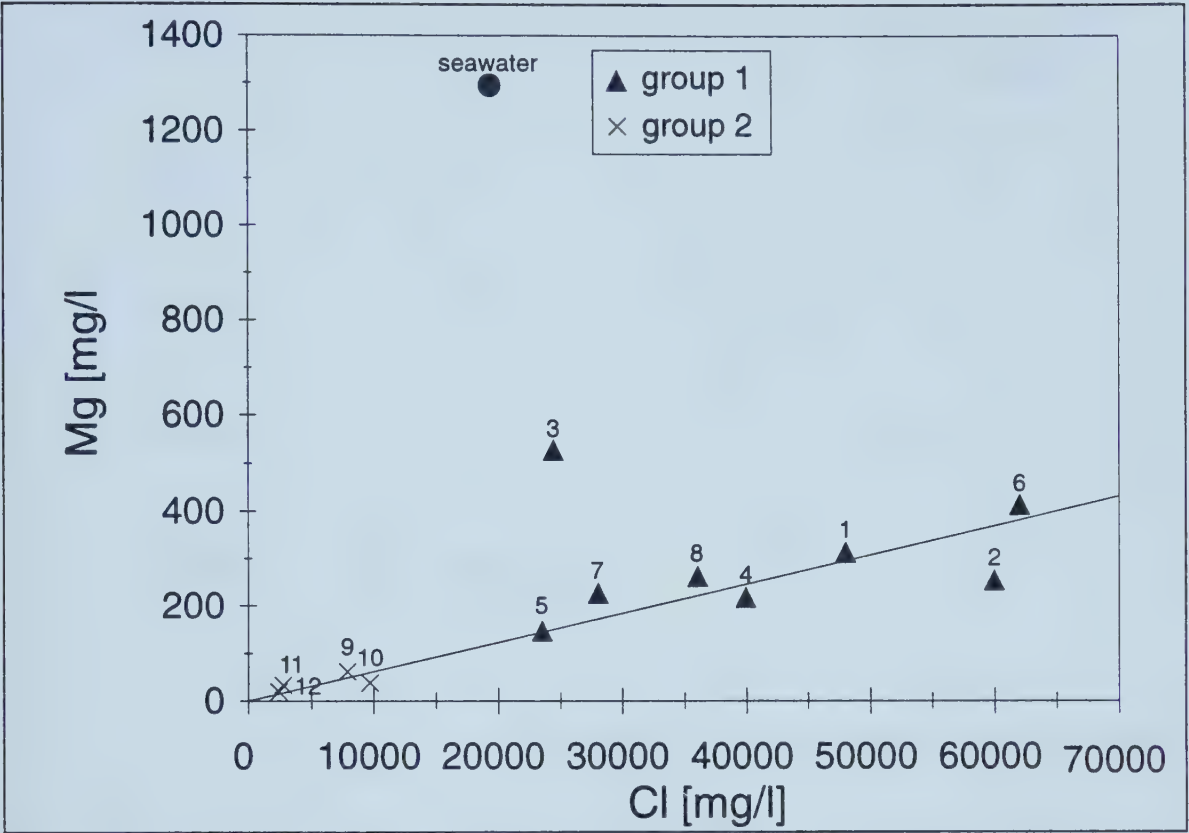


Figure 4.9a: Cross plot of Mg and Cl concentrations in the investigated samples.

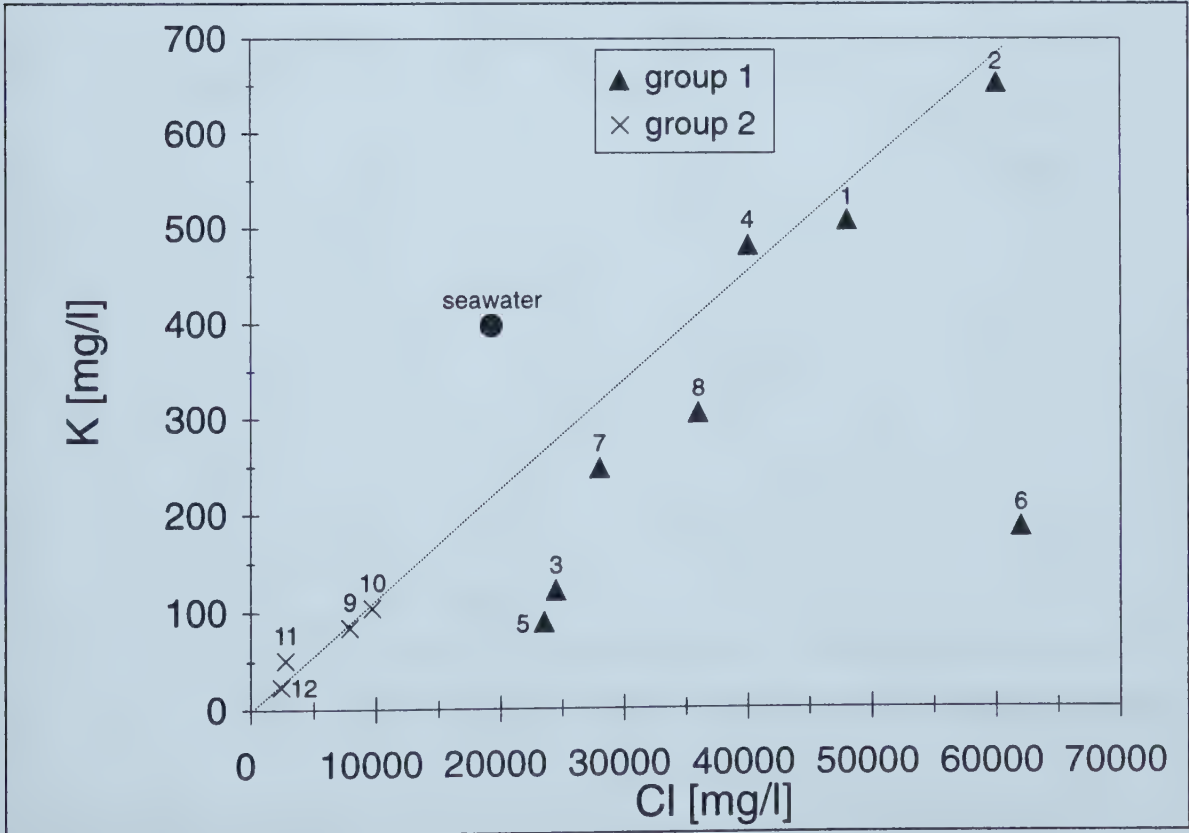


Figure 4.9b: Cross plot of K and Cl concentrations in the investigated samples.



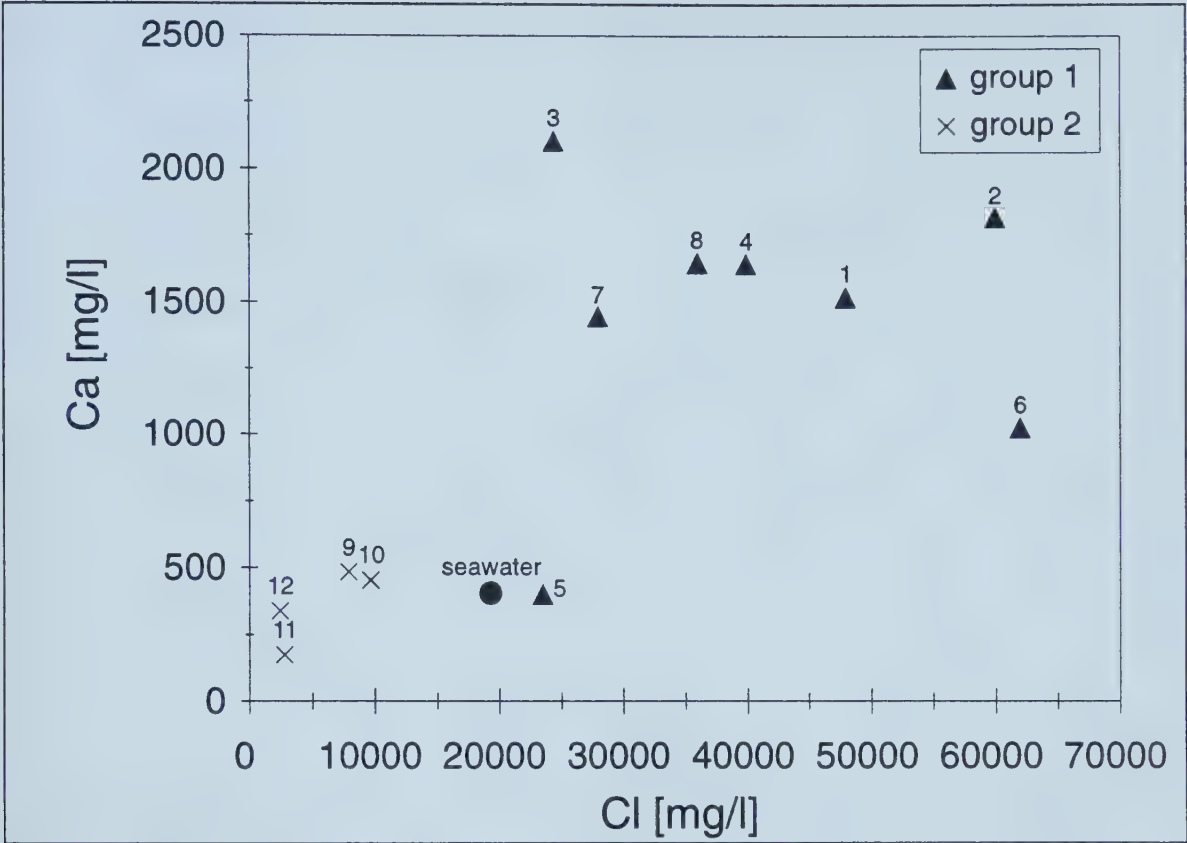


Figure 4.10a: Cross plot of Ca and Cl concentrations in the investigated samples.

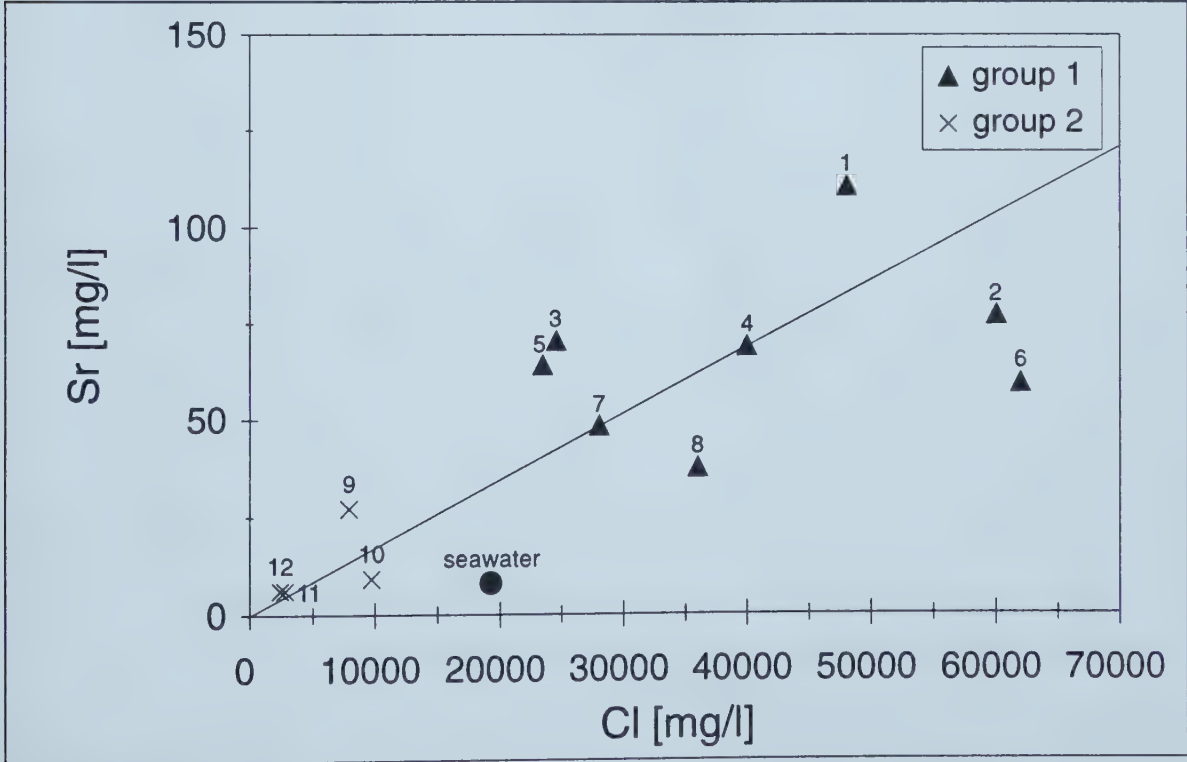
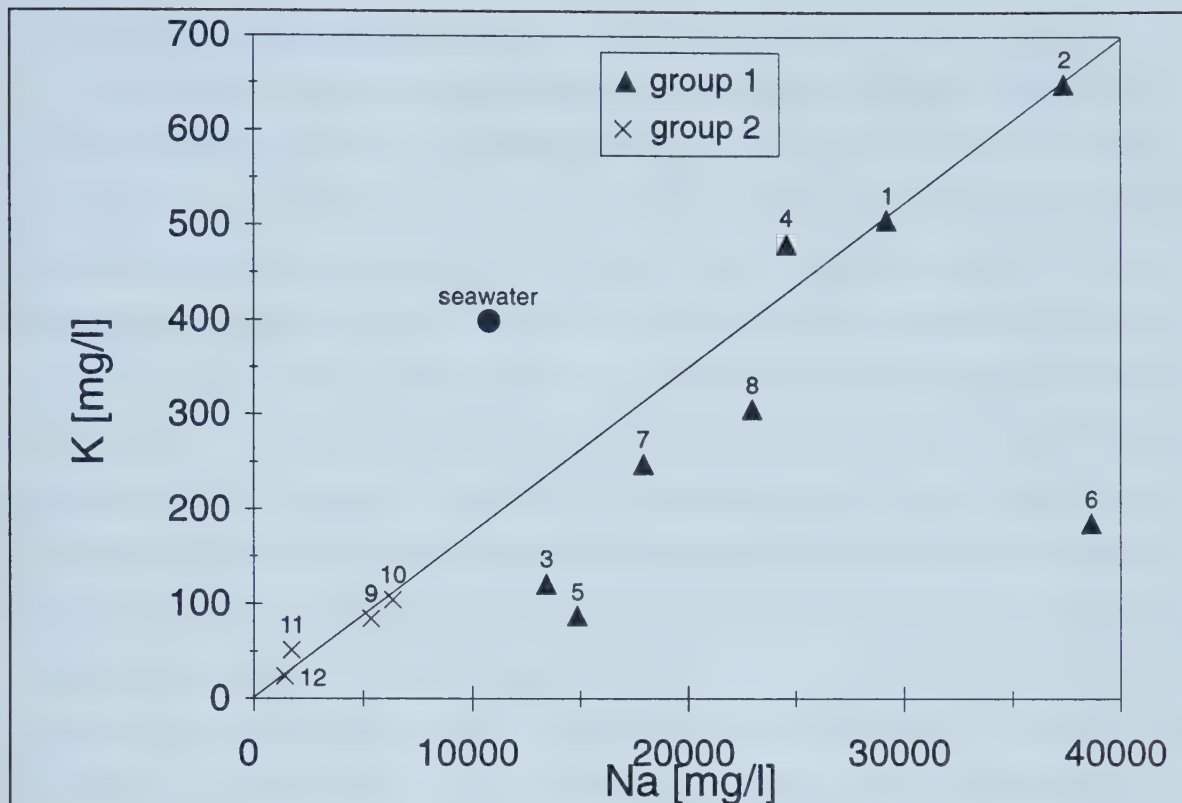
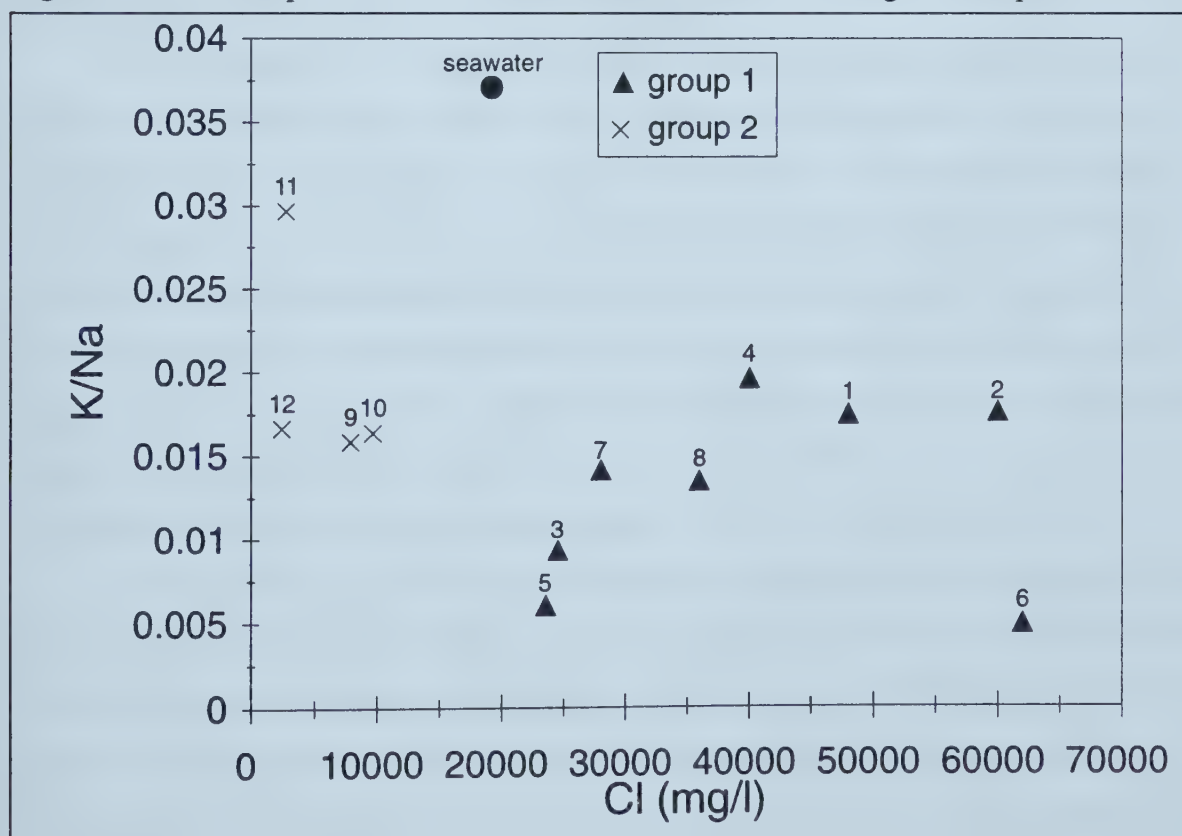


Figure 4.10b: Cross plot of Sr and Cl concentrations in the investigated samples.





**Figure 4.11a:** Cross plot of K and Na concentrations in the investigated samples



**Figure 4.11b:** Cross plot of K/Na concentration ratios and Cl concentrations.





#### 4.3.5 Strontium isotope composition

The  $^{87}\text{Sr}/^{86}\text{Sr}$  ratios of the investigated water samples range from 0.7084 to 0.7136. The values for samples from the regional aquifer (samples 4, 7, 8, 12) are above the range of values for Upper Cretaceous seawater (i.e.,  $^{87}\text{Sr}/^{86}\text{Sr} = 0.7073$  to  $0.7078$ ; Burke et al. 1982) and that for Phanerozoic seawater (i.e.,  $^{87}\text{Sr}/^{86}\text{Sr} = 0.7068$  to  $0.7090$ ; Burke et al. 1982), those from siliciclastic lithologies span a range from 0.7084 to 0.7136 (Appendix 5). With the exception of sample 3, water samples taken from the Paleozoic bedrocks have  $^{87}\text{Sr}/^{86}\text{Sr}$  ratios higher than 0.7114, whereas samples taken from the overlying regional aquifer have  $^{87}\text{Sr}/^{86}\text{Sr}$  ratios below 0.7114 (Figures 4.12 and 4.13). A water sample taken from Pleistocene sands above the steeply inclined regional aquifer at the northern margin of the MCB (sample 9; Figures 4.1 and 4.2) has a  $^{87}\text{Sr}/^{86}\text{Sr}$  ratio of 0.7088; another water sample from Pleistocene sands above the shallowly inclined regional aquifer in the southeastern part of the basin (sample 10; Figures 4.1 and 4.2) has a  $^{87}\text{Sr}/^{86}\text{Sr}$  ratio of 0.71176. Samples 7, 8, and 9 from the northern margin form a trend of increasing  $^{87}\text{Sr}/^{86}\text{Sr}$  ratios with increasing Cl concentration, which corresponds to an increase in depth.

For the samples of group 1, the  $^{87}\text{Sr}/^{86}\text{Sr}$  ratios increase with increasing Cl concentrations (Figure 4.12a). Since TDS is dominated by Na and Cl, TDS and Na concentrations exhibit the same positive correlation with the  $^{87}\text{Sr}/^{86}\text{Sr}$  ratios (not shown). With the exception of sample 6, these samples also form a trend of increasing  $^{87}\text{Sr}/^{86}\text{Sr}$  ratios with increasing K concentrations (Figure 4.12b). No correlation could be identified in the  $^{87}\text{Sr}/^{86}\text{Sr}$  ratio versus Sr concentrations (Figure 4.13a). In the plot of  $^{87}\text{Sr}/^{86}\text{Sr}$  ratios vs reciprocal Sr ( $1/\text{Sr}$ ) concentration (Figure 4.13b), the values for samples 10, 11, and 12 of group 2 form a distinct group at high  $1/\text{Sr}$  values and high  $^{87}\text{Sr}/^{86}\text{Sr}$  ratios, whereas group 1 and sample 9 of group 2 scatter from low to high  $^{87}\text{Sr}/^{86}\text{Sr}$  ratios at low  $1/\text{Sr}$  values.

Of the samples in group 1, the two samples with the lowest  $^{87}\text{Sr}/^{86}\text{Sr}$  (samples 3 and 5) have the highest  $\delta\text{D}$  and  $\delta^{18}\text{O}$  values, which corresponds to the least elevated TDS (Figure 4.6). For the samples of group 2, no obvious correlations between  $^{87}\text{Sr}/^{86}\text{Sr}$  ratios, chemical and isotopic compositions could be determined. Sample 9, however, appears to fit into the trends described for the samples of group 1, because of its low  $^{87}\text{Sr}/^{86}\text{Sr}$  ratio (Figure 4.12b, 4.13a, b).





**Figure 4.12:**  $^{87}\text{Sr}/^{86}\text{Sr}$  ratio versus Cl concentration (a) and versus K concentration (b). With the exception of sample 3, water samples taken from the Paleozoic bedrocks (P) have  $^{87}\text{Sr}/^{86}\text{Sr}$  ratios higher than 0.7114, whereas samples taken from the overlying regional aquifer (C) have  $^{87}\text{Sr}/^{86}\text{Sr}$  ratios below 0.7114 (stippled horizontal line in Figure 4.12a). See text for further explanation.

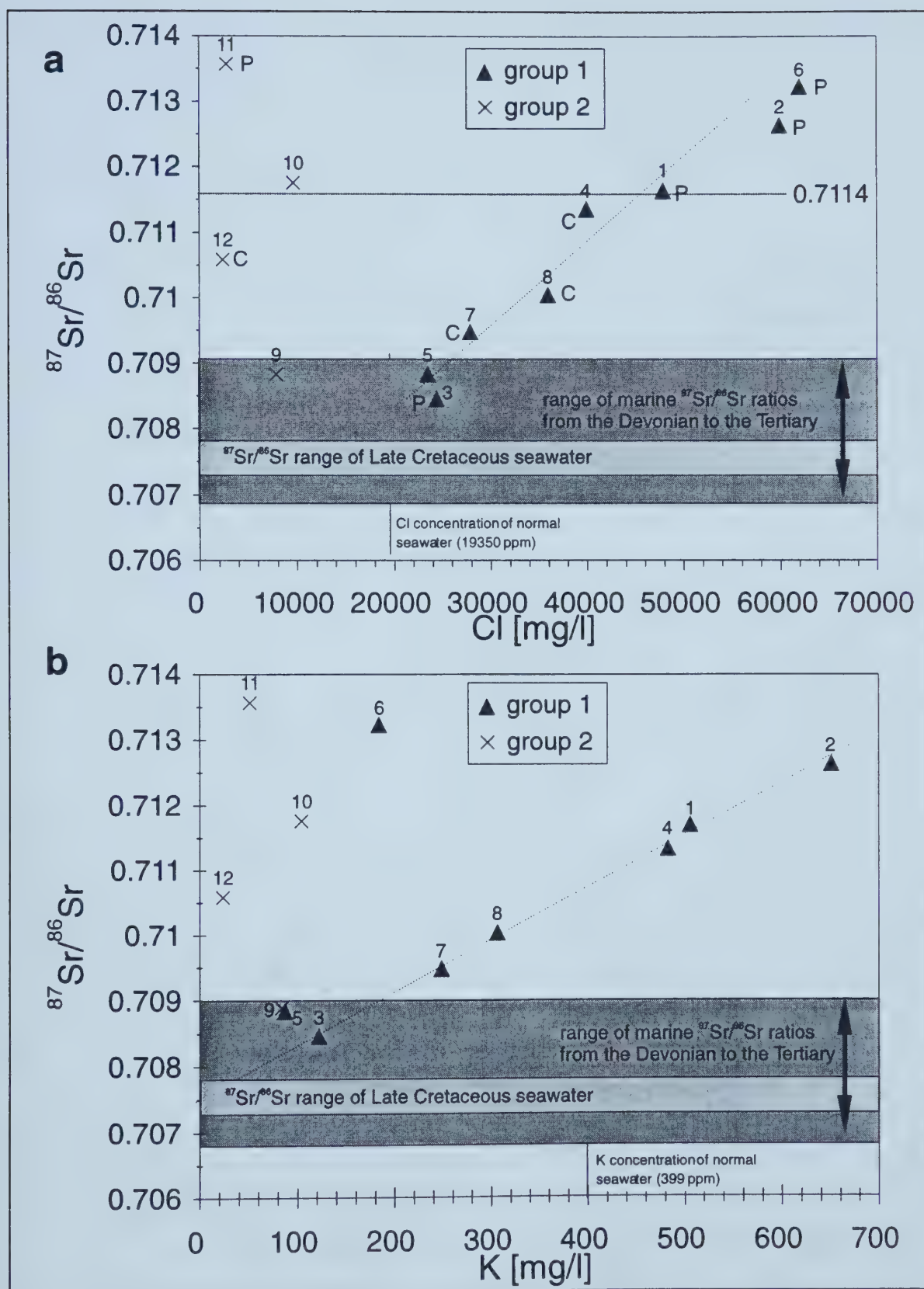
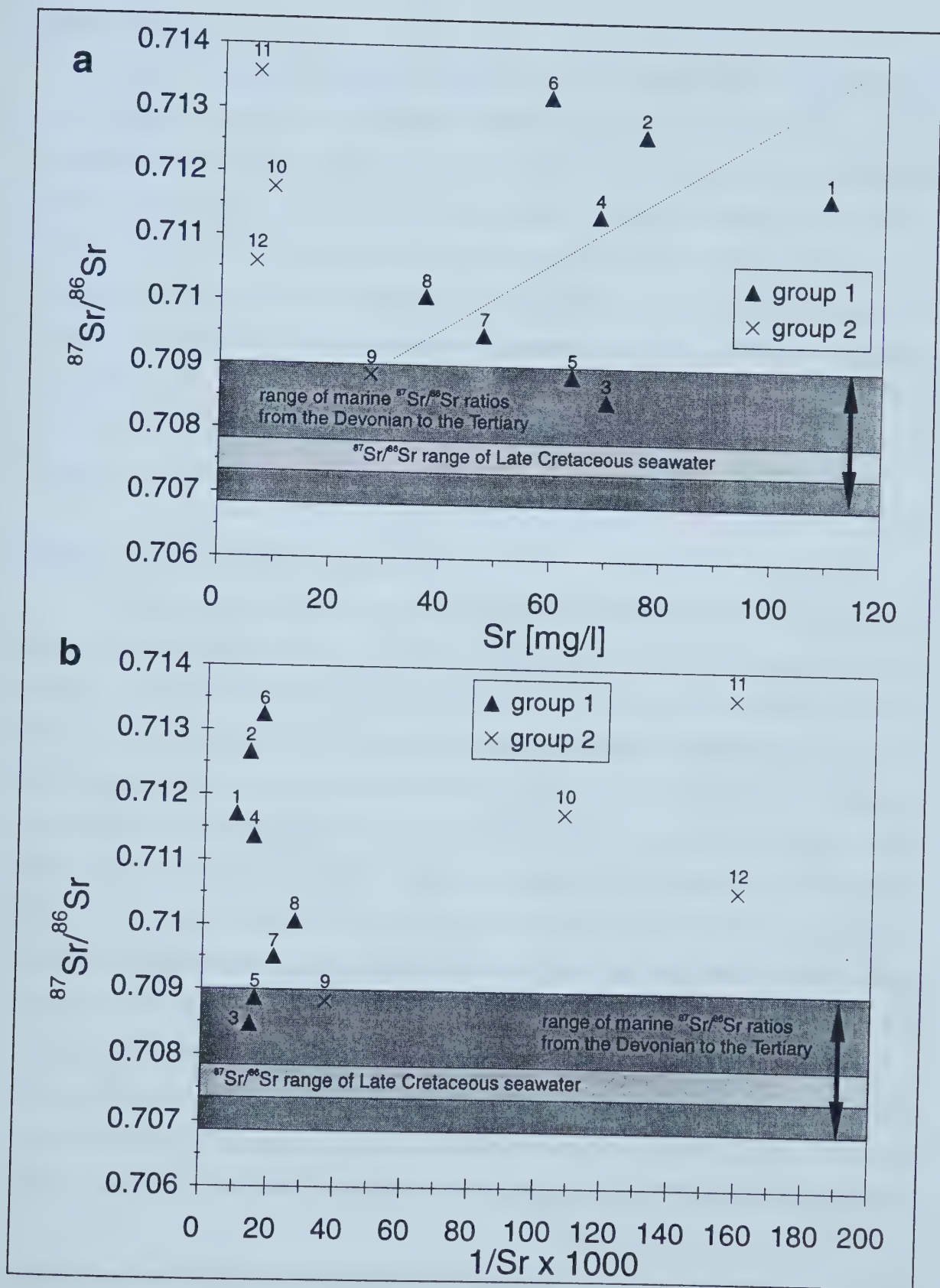


Figure 4.11







**Figure 4.13:**  $^{87}\text{Sr}/^{86}\text{Sr}$  ratio versus Sr concentration (a) and reciprocal strontium ( $1/\text{Sr}$ ) concentration. See text for further explanation.



## 4.4 Discussion

The circumstance that the groundwater samples investigated in this study were taken from a variety of locations and lithologies implies that these samples are not necessarily representative of the saline groundwaters in the MCB. With this in mind, the principal aim of this discussion is to find a plausible explanation for the hydrochemical and isotopic characteristics that is consistent with the present knowledge of the geological and hydrological history of the area, and that serves the main purpose of this part of the present study, i.e., to determine if the present-day saline groundwaters in the MCB bear any genetic relationship to the mineralization (including dolomitization) in and around the fractures of the Brilon Reef Complex. Further investigations with a much larger database will have to be carried out to confirm the tentative interpretations presented herein.

### *4.4.1 Present-day movement of brines*

The fact that the saline groundwaters at shallow depths have elevated temperatures relative to that expected at their respective depths (Figure 4.4) and discharge on vertical faults (e.g., Fricke 1961, 1963, 1964a, b, 1967, 1968; Michel 1963; Wolansky 1964; Wedewardt 1995) serves as evidence for the upward movement of the saline groundwaters from deeper parts of the basin and the underlying Paleozoic bedrock on faults. Increases in salinity and rates of discharge of the saline groundwaters after heavy rainfalls (Fricke 1961, 1963, 1964b; Angerer et al. 1968; Papakonstantinou 1970) suggest that this upward movement is driven mainly by the pressure exerted by the regional fresh groundwater subsystem at the southern, eastern, and northern margins of the MCB on the regional saline groundwater subsystem in the center of the basin (Figures 4.1 and 4.2). The relative low temperature of the one sample at 910 m depth (sample 2), together with the fact that it originates from an artesian well and has a high salinity (TDS = 112674 mg/l), suggests that it is not cooled (and diluted) by active mixing with surface-derived meteoric water, but rather that the geothermal gradient is probably lower than the assumed 30°C/km (i.e., 26°C/km).

### *4.4.2 Origin and evolution of the saline groundwaters*

Based on the hydrochemical and isotopic data, the investigated saline groundwater





samples fall into two groups. Samples in group 1 are characterized by TDS greater than seawater (Figure 4.5), a wide range of stable isotope compositions between that of regional present-day meteoric water and seawater (Figure 4.6), and increasing  $^{87}\text{Sr}/^{86}\text{Sr}$  ratios with increasing Cl concentrations (Figure 4.12a). Samples in group 2 have salinities less than seawater, stable isotope compositions in the range of present-day meteoric water in the region, and highly variable  $^{87}\text{Sr}/^{86}\text{Sr}$  ratios.

#### 4.4.2.1 Origin of the water

The fact that the oxygen and hydrogen isotope compositions of most of the investigated water samples plot on or close to the meteoric water line (MWL) (Figure 4.6) indicates that these waters are dominated by present-day meteoric water. For samples of group 2, this was to be expected, since they were obtained at locations where active mixing between present-day meteoric water and saline groundwaters is very likely (e.g., at the surface, at very shallow depths, and close to the boundary between fresh and saline groundwater (Figures 4.1 and 4.2). This is also reflected in their chemical compositions, especially their dilution below seawater salinities (Figure 4.5). The fact that most of the samples of group 1 also have stable isotope compositions in the range of present-day meteoric water suggests that most of the regional aquifer and parts of the underlying Paleozoic have been flushed by present-day meteoric water. Differences in the stable isotope compositions between samples from the southeastern margin (samples 1, 2, 4, 10, 11, and 12) and those from the southeastern margin (samples 7, 8, and 9) are probably due to regional variations in the stable isotope composition of the precipitation in the respective recharge areas, i.e., the Egge Mountains and Rhenish Schiefergebirge in the east and south, and the Osning in the north (Figures 4.1, 4.2, and 4.6).

Mixing of water of a marine origin with meteoric water is suggested by the stable isotope compositions of samples 3 and 5, which plot on a trajectory connecting the stable isotope composition of present-day meteoric water in the Ruhr-District with that of seawater (SMOW; Figure 4.6). This is in agreement with the findings of Wedewardt (1995), who found a similar mixing trend in his investigation of the isotopic composition of the deep groundwaters in the Ruhr District. The fact that samples 3 and 5 are from the southwestern





and northwestern margin of the MCB, which repeatedly experienced marine conditions during the history of the area (Figure 4.3 and Table 4.1), supports this interpretation. Other processes, such as isotope exchange during water-rock interaction, evaporation and condensation, isotope fractionation due to membrane effects, and mixing of several different fluids, also can have an impact on the isotopic compositions of waters (Kharaka and Carothers 1986). From the small data set available here, however, it is not possible to accurately evaluate the involvement of these processes.

The position of sample 6 on the meteoric water line but at higher values than present-day meteoric water (Figure 4.6) suggests the involvement of meteoric water from a time period when climatic conditions were warmer and/or when the area was located closer to the ocean (Sonntag et al. 1983; Faure 1990). The Tertiary, for example, would satisfy both criteria (Figure 4.3). Age determinations of some saline groundwaters from the MCB were carried out by Jacobshagen and Münnich (1964), Geyh and Michel (1981), and Wedewardt (1995). The absence of  $^{14}\text{C}$  and  $^3\text{H}$  in the samples with the highest salinities led Jacobshagen and Münnich (1964) and Geyh and Michel (1981) to the conclusion that the undiluted saline groundwaters are older than 40000 years. In addition, Wedewardt (1995) reported the results of the isotopic analysis of the noble gases He and Ar from pore waters in Carboniferous sandstones and siltstones from the Ruhr District. Pre-glacial  $^{40}\text{Ar}/^{36}\text{Ar}$ -ratios ( $> 300$ ) and calculated semiquantitative He-ages between 24 and 45 Ma confirm a pre-glacial age of the saline groundwaters (Wedewardt 1995).

These considerations suggest that three water components occur in the saline groundwaters of the MCB: (1) a seawater component; (2) an 'old' (pre-glacial) meteoric water component, and (3) a present-day meteoric water component. The present-day meteoric water component is dominant in most samples. In the deeper parts of the basin (sample 5) and the underlying Paleozoic (samples 3 and 6), however, undefined quantities of fluids that have the stable isotopic compositions of older meteoric water and seawater, respectively, appear to be present.

#### 4.4.2.2 Dissolution of halite

Dissolved chloride can be used as the conservative reference parameter because in



many halite-free environments few processes other than mixing affect its concentration (Hanor 1987). High sodium and chloride concentrations in groundwaters generally suggest their origin from evaporated sea water or from the dissolution of evaporites. The slight enrichment of sodium with respect to evaporated seawater (Figure 4.7) indicates an external source of sodium, provided there is no halite in the sequence that may have dissolved. Sodium is released into solution during weathering of Na-rich plagioclase (Wedepohl 1978) and by cation exchange with Ca that is attached to the surfaces of newly formed clay minerals (Matthess 1990). Alternatively, groundwaters that are enriched in Na with respect to evaporated sea water may also originate from the dissolution of halite. A brine that resulted from the dissolution of halite has a mNa/mCl ratio of about 1 (e.g., Lehmann 1974; Zhou and Li 1992). Halite dissolution is suggested by the fact that most of the investigated samples have ratios close to unity (Figure 4.7). The fact that the samples with the lowest mNa/mCl ratios (samples 3 and 12) contain the largest molar quantities of Ca (14 and 21 mole-% of total cations, respectively) (Table 4.3), suggests that, in these cases, dissolved Na was extracted from solution by exchange with Ca from clay minerals (Matthess 1990).

Dissolution of halite as the main source for the sodium and chloride in the saline groundwaters in the MCB has been suggested by several authors (e.g., Fricke 1961; Michel and Nielsen 1977; Wedewardt 1995). Supporting evidence has been provided by sulfur isotope measurements of the dissolved sulfate in saline groundwaters from the eastern and northeastern part of the MCB and adjacent areas (Bässler 1970; Michel and Nielsen 1977) (Appendix 5). Their data indicate that the sulfate in some of the saline groundwaters in the MCB originated from anhydrite in the Upper Permian (Zechstein) evaporites. The  $\delta^{34}\text{S}$  value for Upper Permian sulfate is well constrained at about  $+11 \pm 2$  ‰ CDT, and represents the minimum for marine sulfate during the Phanerozoic (e.g., Claypool et al. 1980; Kampschulte et al. 1998). The  $\delta^{34}\text{S}$  values of dissolved sulfate from saline groundwaters at the sample locations 1, 2, 4, 5, 8, and 10 range between 10.8 and 14.5 ‰ CDT (Table 4.5) (Michel and Nielsen 1977, value for sample location 5 from Bässler 1970). The samples with  $\delta^{34}\text{S}$  values between 8 and 13 ‰ CDT were considered to have obtained their dissolved sulfate from the dissolution of Upper Permian evaporites (samples 5, 8, and 10), those with slightly higher values were considered to have been influenced by influx of dissolved Upper Permian marine





sulfate (samples 1, 2, and 4) (Michel and Nielsen 1977). Higher values may be due to mixing of Upper Permian marine sulfate with older or younger marine sulfate with higher  $\delta^{34}\text{S}$  values and/or sulfate that had been affected by bacterial sulfate reduction (producing sulfide with low  $\delta^{34}\text{S}$  values and leaving sulfate with higher  $\delta^{34}\text{S}$  values).

Wedewardt (1995) used Br/Cl ratios of saline groundwaters from the Ruhr District as the main argument for the hypothesis that they derive their salinity from the subrosive dissolution of halite. Normal seawater has a Br concentration of about 67 mg/l and a Br/Cl ratio of about 0.0034. This ratio remains the same during evaporation of seawater up to halite saturation. When halite saturation is reached, Cl preferentially precipitates as NaCl, and Br preferentially remains in solution, resulting in Br/Cl ratios below that of seawater in the solid halite, and a continuous increase in the Br/Cl ratio in the remaining solution during further precipitation of chlorides. Depending on the Br concentration in the solution from which halite precipitated, the Br/Cl ratios in solid halite range between 0.0001 to 0.0004 (Rittenhouse 1967). Consequently, the Br/Cl ratio of a brine that results from the dissolution of halite is smaller than 0.0034.

Wedewardt (1995) reported Br/Cl ratios between 0.0007 and 0.0029 (average 0.0014) for the saline groundwaters in the Ruhr District. From the chemical data of saline groundwaters in the Ibbenbüren District presented in Bässler (1970), Wedewardt (1995) calculated Br/Cl ratios ranging from 0.0003 to 0.0014. Previous chemical analyses of groundwater samples from sample locations 1, 2, 4, and 9 by the Fresenius Institute give Br/Cl ratios between 0.0004 and 0.0005 (Appendix 5).

It is, therefore, most likely, that the elevated mNa/mCl ratios of the majority of samples from this study are the result of the subrosion of halite in the periphery of the MCB. In addition, there are local variations due to clay mineral exchange reactions, such as the low mNa/mCl ratios of sample 3 and 12 (Table 4.3; Figure 4.7).

#### 4.4.2.3 Sources of Sr

In the lattice of most minerals, Sr substitutes preferentially for Ca, whereas Rb, which is the source of radiogenic  $^{87}\text{Sr}$  via radioactive decay of the nuclide  $^{87}\text{Rb}$ , substitutes





preferentially for K (Faure 1990). The main sources of Sr are carbonate minerals, calcium sulfates (gypsum, anhydrite), plagioclase, and smectite, which have relatively high Sr concentrations but generally low  $^{87}\text{Sr}/^{86}\text{Sr}$  ratios similar to that of the fluid (i.e., water or magma) from which they formed. Illite, K-feldspar, and mica contribute less Sr because they are more resistant to chemical weathering, have low Sr concentrations, or both. These minerals, however, contain significant amounts of  $^{87}\text{Rb}$  and, thus, produce radiogenic  $^{87}\text{Sr}$ , resulting in  $^{87}\text{Sr}/^{86}\text{Sr}$  ratios that increase with age. In a context where evaporites are present, the mineral sylvite (KCl), which contains only small amounts of Sr but has been reported to reach  $^{87}\text{Sr}/^{86}\text{Sr}$  ratios up to 2.5 (Baadsgaard 1987) as a result of high original  $^{87}\text{Rb}$  concentrations, needs to be considered as a source of radiogenic Sr as well (Moldovanyi et al. 1993). All of the above minerals are present in the sedimentary succession of the area of the MCB and may have contributed Sr to the saline groundwaters.

In the area of the MCB, marine carbonates are the most likely source for Sr with marine  $^{87}\text{Sr}/^{86}\text{Sr}$  ratios, because of their widespread occurrence and high Sr concentrations. For example, Kramm (1985) reported extremely uniform Sr isotopic compositions ( $^{87}\text{Sr}/^{86}\text{Sr} = 0.70752 \pm 5 \times 10^{-5}$ ) from vein strontianite from carbonate-hosted deposits in the MCB. The fact that this  $^{87}\text{Sr}/^{86}\text{Sr}$  ratio of the strontianite corresponds to that of the Upper Cretaceous (Campanian) host limestones within analytical error led Kramm (1985) to the conclusion that the Sr was derived from these limestones.

Calcium sulfates (gypsum, anhydrite), which are present in the periphery of the MCB (Figure 4.3), may have contributed Sr with marine  $^{87}\text{Sr}/^{86}\text{Sr}$  ratios as well. This is supported by the sulfur isotopic compositions of dissolved sulfate in saline groundwaters from the MCB, which have been interpreted to be derived from the dissolution of Zechstein evaporites (Michel and Nielsen 1977).

The positive correlation between the  $^{87}\text{Sr}/^{86}\text{Sr}$  ratios and K concentrations for the samples in group 1 (Figure 4.12b) confirms that radiogenic Sr is derived from K-bearing minerals, but does not aid in distinguishing between the various possible sources. Clastic sedimentary rocks in the MCB make up most of the Paleozoic basement and are abundant in the Mesozoic sedimentary successions (Figure 4.3 and Table 4.1) and are therefore the most likely source for the radiogenic Sr in the saline waters in the MCB. Sylvite only occurs



along the periphery of the basin and, despite its potentially high  $^{87}\text{Sr}/^{86}\text{Sr}$  ratios (Baadsgard 1987), is probably volumetrically negligible (Heuser personal communication 1998). Furthermore, dissolution of sylvite causes enrichment of the groundwater in K relative to Na, which results in a positive correlation between the K/Na ratio and Cl concentration. For the investigated samples, such a correlation does not exist (Figure 4.11b). The fact that most of the water samples obtained from the Paleozoic basement have  $^{87}\text{Sr}/^{86}\text{Sr}$  ratios above 0.7114 while those from the overlying Cretaceous strata have lower ratios (Figures 4.12 and 4.13) suggests that the radiogenic Sr probably is derived mainly from interaction of groundwater with Paleozoic siliciclastic sediments.

#### 4.4.2.4 Mixing relations and effects of water-rock interactions

The trend of increasing  $^{87}\text{Sr}/^{86}\text{Sr}$  ratios with increasing Cl concentrations in group 1 (Figure 4.12a) suggests mixing of a highly saline,  $^{87}\text{Sr}$ -enriched water component and a less saline water component with a Sr isotope composition in the range of Phanerozoic seawater. Two-component mixing and endmember water compositions can be evaluated using plots of  $^{87}\text{Sr}/^{86}\text{Sr}$  ratio vs Sr concentration (Figure 4.13a) and  $^{87}\text{Sr}/^{86}\text{Sr}$  vs reciprocal Sr ( $1/\text{Sr}$ ) concentration (Figure 4.13b) (Faure 1990). Mixing between two endmember fluids with different Sr concentrations and different  $^{87}\text{Sr}/^{86}\text{Sr}$  ratios result in a hyperbolic mixing line in the  $^{87}\text{Sr}/^{86}\text{Sr}$  ratio vs Sr concentration plot, and in a straight line in the  $^{87}\text{Sr}/^{86}\text{Sr}$  ratio vs reciprocal Sr ( $1/\text{Sr}$ ) concentration plot (Faure 1990).

The scatter of data in the  $^{87}\text{Sr}/^{86}\text{Sr}$  ratio vs Sr concentration plot (Figure 4.13b) suggests that processes other than simple mixing of Sr derived from two sources with different Sr concentrations and different  $^{87}\text{Sr}/^{86}\text{Sr}$  ratios (e.g., carbonates and siliciclastics) have taken place. This is further confirmed by the scatter of data in the plot of  $^{87}\text{Sr}/^{86}\text{Sr}$  ratios vs  $1/\text{Sr}$  concentration (Figure 4.13b). Local processes involving addition or removal of Sr after mixing may be responsible for the lack of correlation. This is indicated by the scatter of data in the  $\text{SO}_4$  vs Sr, Ca vs Cl, and Sr vs Cl plots (Figures 4.8, 4.10a and 4.10b). Addition of Sr from interaction with carbonates, sulfates, and siliciclastics may change the  $^{87}\text{Sr}/^{86}\text{Sr}$  ratio of the groundwater (depending on the amount and the  $^{87}\text{Sr}/^{86}\text{Sr}$  ratio of the added Sr relative to those of the Sr already present), whereas removal of Sr by precipitation of





carbonates and sulfates will not affect its  $^{87}\text{Sr}/^{86}\text{Sr}$  ratio.

$^{87}\text{Sr}/^{86}\text{Sr}$  ratios of the groundwater samples from the Paleozoic bedrocks are generally high, those from the groundwater samples from the overlying regional aquifer are lower, but do not fall within the range of  $^{87}\text{Sr}/^{86}\text{Sr}$  ratios for Phanerozoic seawater (Figures 4.12 and 4.13). This suggests that the waters must have contained Sr with high  $^{87}\text{Sr}/^{86}\text{Sr}$  ratios prior to entering the regional aquifer and since then have not interacted enough with the limestones as to lower the  $^{87}\text{Sr}/^{86}\text{Sr}$  ratios to marine values, and can be taken as further evidence for the upward movement of warm, saline (and  $^{87}\text{Sr}$ -enriched) groundwaters along faults from the Paleozoic bedrock into the regional aquifer. The absence of water-rock Sr isotopic equilibration has been frequently observed in carbonate-hosted groundwaters, such as oil field brines, and has been interpreted in a similar way (e.g., Stueber et al. 1984; Chaudhuri et al. 1987; Connolly et al. 1990; Moldovanyi et al. 1993). The difference in the  $^{87}\text{Sr}/^{86}\text{Sr}$  ratios between samples 9 and 10 (e.g., Figure 4.12a) may be due to the difference in the vertical distance from the base of the regional aquifer to the point of discharge between the northern and the southeastern part of the MCB (Figure 4.2). At sample location 9, the groundwater ascended through about 800 m of Upper Cretaceous limestones, whereas at sample location 10, the groundwater passed through only a vertical distance of 300 m, resulting in a relatively low  $^{87}\text{Sr}/^{86}\text{Sr}$  ratio for sample 9 and a relatively high  $^{87}\text{Sr}/^{86}\text{Sr}$  ratio for sample 10 (Figure 4.12a).

The low  $^{87}\text{Sr}/^{86}\text{Sr}$  ratio of sample 3 (e.g., Figure 4.12) is probably due to interaction of groundwater with Paleozoic and/or Mesozoic marine carbonates or sulfates and mixing with seawater prior to entering the Carboniferous sandstone aquifer, from which the sample was obtained. For this sample, mixing with seawater-derived groundwater (either as original, syn-sedimentary pore water, or as younger seawater that infiltrated the Paleozoic sedimentary rocks) is indicated by its stable isotope composition (Figure 4.6).

In the  $^{87}\text{Sr}/^{86}\text{Sr}$  ratios vs  $1/\text{Sr}$  concentration plot (Figure 4.13b), the values for samples 10, 11, and 12 of group 2 form a distinct group at high  $1/\text{Sr}$  values and high  $^{87}\text{Sr}/^{86}\text{Sr}$  ratios, which suggests dilution by meteoric water or dilute shale water (Connolly et al. 1990; Chaudhuri and Clauer 1993). While the samples of group 2 follow the same trend in the K vs Na concentration plot like samples of group 1 (Figure 4.11a), they do not in the  $^{87}\text{Sr}/^{86}\text{Sr}$





ratio vs K concentration plot (Figure 4.11b). Assuming that the water samples in group 2 originated from waters of group 1, this indicates that these water samples were affected by a process that decreased both their Na and K concentrations, but did not significantly change their K/Na ratios and  $^{87}\text{Sr}/^{86}\text{Sr}$  ratios, which can only be achieved by dilution with meteoric water.

## 4.5 Conclusions

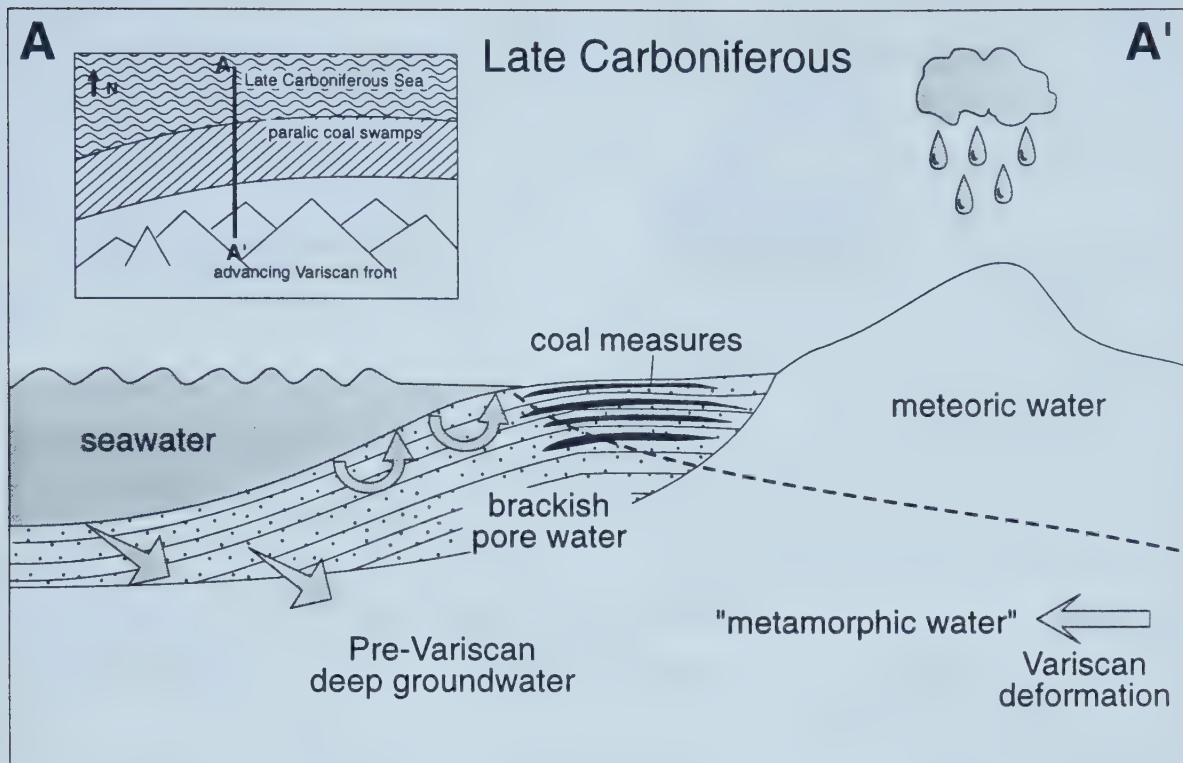
The new data presented here confirm that the present-day saline groundwaters in the MCB are the combined result of water-rock interaction, migration, and mixing of fluids of different origins. Specifically, the data provide evidence for (1) halite dissolution, (2) water-rock interaction of highly saline fluids with siliciclastic sediments, (3) mixing of highly saline fluids with less saline waters of marine isotopic compositions, (4) fault-controlled movement of warm saline  $^{87}\text{Sr}$ -enriched groundwaters from the Paleozoic bedrock into the overlying Late Cretaceous limestone aquifer, (5) water-rock interaction of ascending saline groundwater with the limestone aquifer, and (6) dilution by meteoric water. The sub-recent processes of mixing of different saline groundwaters, water-rock interaction, and dilution by modern meteoric water are volumetrically predominant, so that inferences about the early groundwater-forming processes have to remain elusive. This severely restricts the possibility that a genetic relationship between the present-day saline groundwaters in the Münsterland Cretaceous Basin and the Late Cretaceous/Early Tertiary mineralization (including dolomitization) in the Brilon Reef Complex can be detected. Nevertheless, the findings of this study are consistent with the regional paleohydrologic history (Table 4.1) and can be used to refine our understanding of the origin and evolution of the saline groundwaters in the MCB.

A series of schematic diagrams in Figure 4.14 illustrates the paleohydrologic history of the MCB with emphasis on the fluids that enter the groundwater system. Pre-Variscan sedimentary pore waters already consisted of a mixture of marine and meteoric waters, especially in the thick paralic succession of the coal-bearing, mainly siliciclastic Carboniferous sediments. These pore waters, however, are unlikely to have been preserved due to tectonic expulsion and partial to complete displacement by metamorphic fluids during

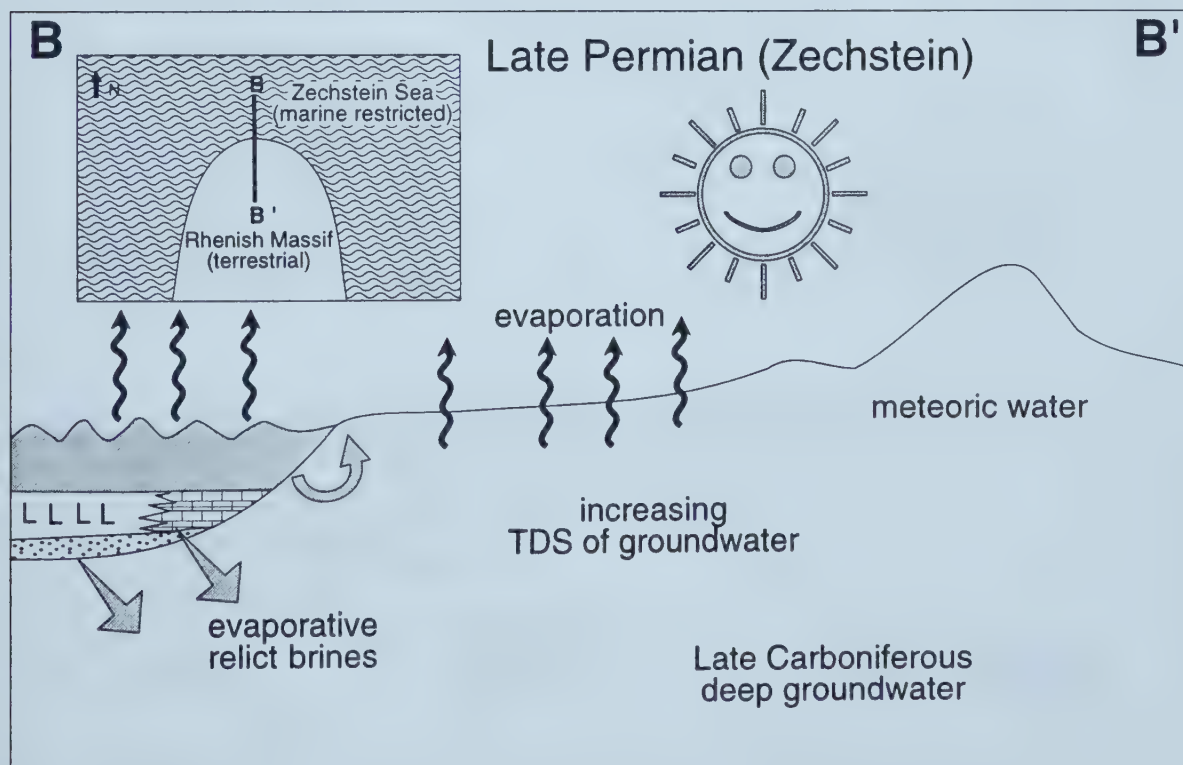




**Figure 4.14:** Schematic N-S cross sections illustrating the paleohydrogeologic history of the Münsterland Cretaceous Basin (MCB) from the Late Carboniferous to Recent. Small insert maps schematically show bird's-eye view and location of cross section line. See text for explanation.



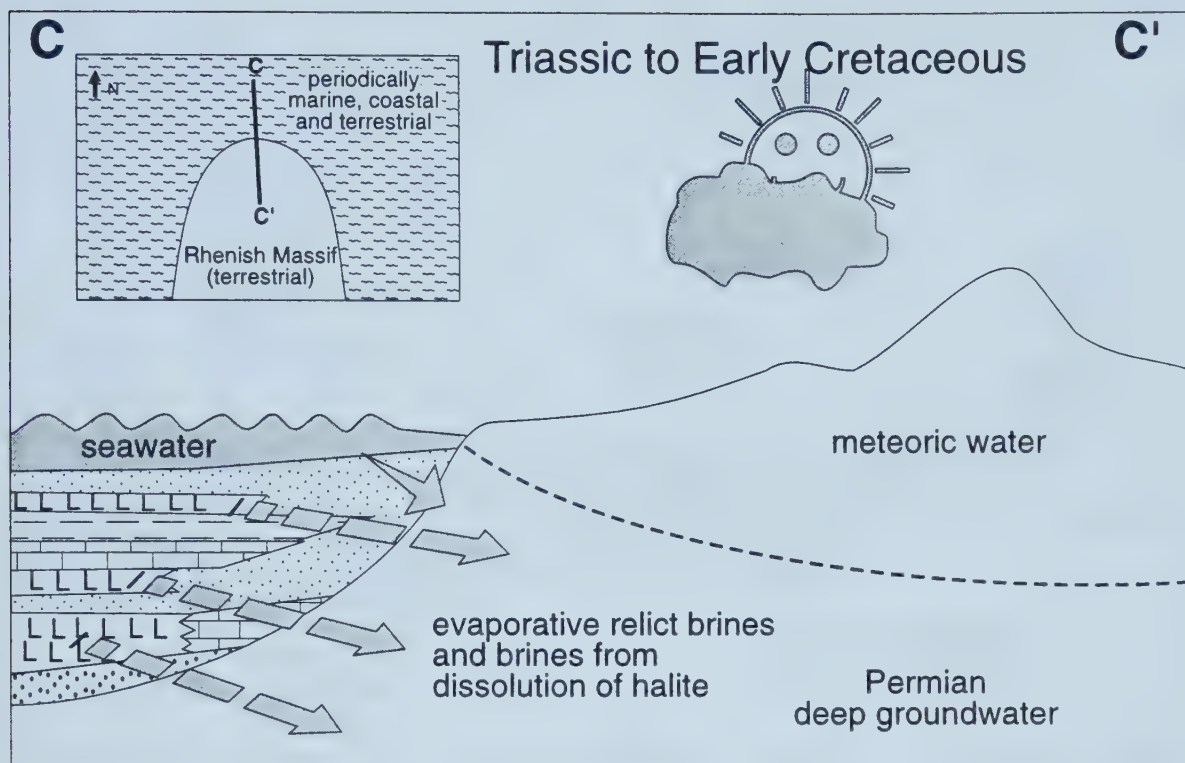
**Figure 4.14a**



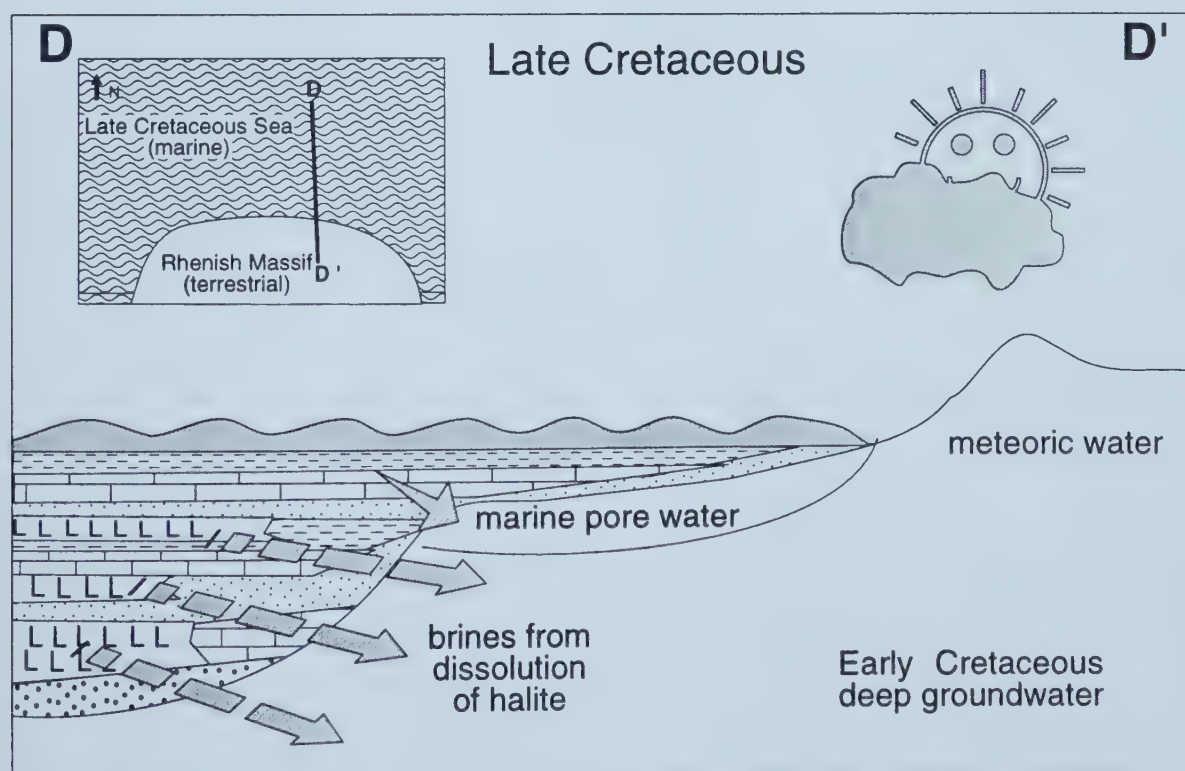
**Figure 4.14b**





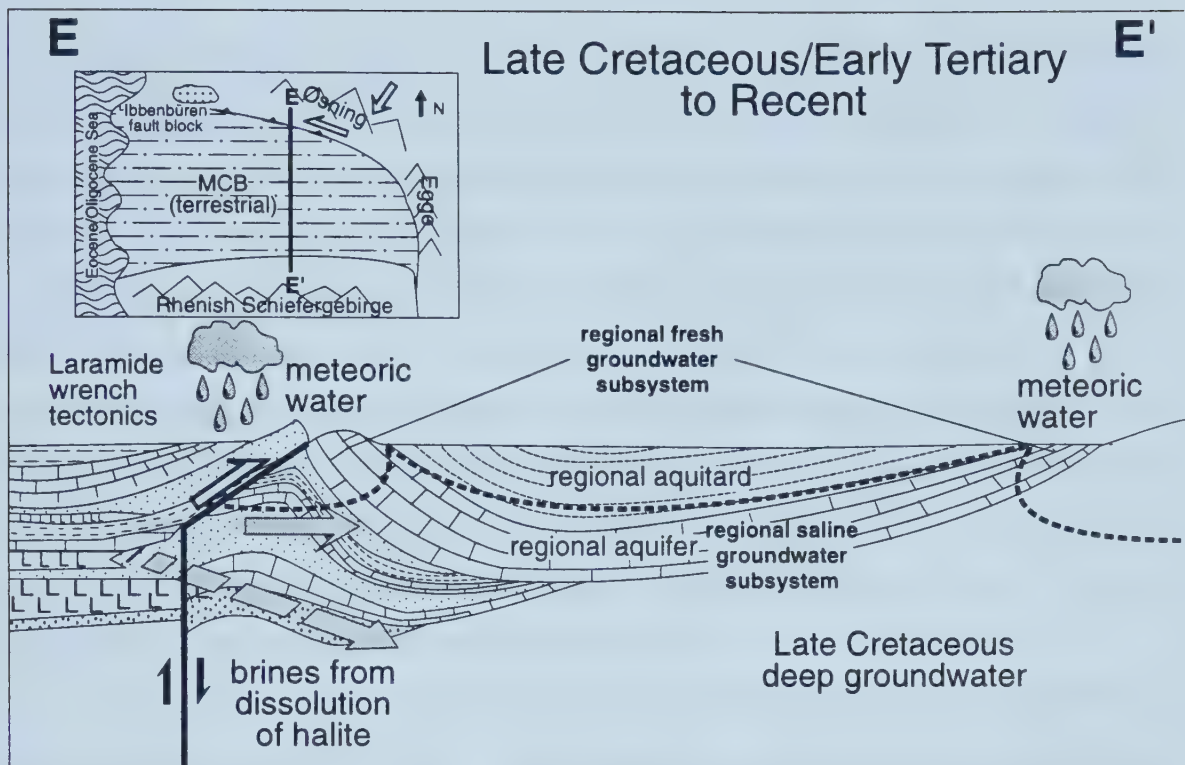


**Figure 4.14c**



**Figure 4.14d**





**Figure 4.14e**



the Variscan deformation and the subsequent infiltration of meteoric waters in most of the area of the present-day MCB (Figure 4.14a). From the end of the Variscan deformation in the Late Carboniferous until the beginning of the Late Cretaceous only the margins of the Rhenish Massif came under the direct influence of seawater (Figures 4.14b and c). In these areas, evaporation of seawater under arid conditions during the Late Permian (Zechstein), Early Triassic (Röt), and Late Jurassic (Malm) resulted in the deposition of marine evaporites, and the formation of highly concentrated, dense evaporative relict brines (Figures 4.14b and c). Because of their high density, these brines must have descended into the underlying sedimentary rocks where they blended with a mixture of post-Variscan marine pore waters and post-Variscan meteoric waters, which had already undergone rock-water interaction to various extents (Figures 4.14b and c).

Dissolution of halite in the subsurface very likely began in the Triassic and continues until today. Over time, seawater and meteoric water, as well as various mixtures of different groundwaters, must have been involved in the subsurface dissolution of the Permian, Triassic, and Jurassic halite deposits. Continuous dissolution, however, can only be achieved, if a hydraulic gradient exists that removes the solutes from the site of halite dissolution. Such a hydraulic gradient can be created by differences in fluid density, which would result in vertical as well as lateral transport of dissolved NaCl away from the halite (Wedewardt 1995). Considering that most of the area of the Rhenish Massif was under terrestrial conditions for the time between the Variscan Orogeny and the Late Cretaceous, a hydraulic gradient probably existed between the margins of the Rhenish Massif, where seawater, evaporative relict brines, and brines from the subsurface dissolution of halite occurred, and its exposed and halite-free center, where more dilute groundwaters of meteoric origin predominated (Wedewardt 1995). Over time, the saline groundwaters that formed by subsurface dissolution of halite in the periphery of the Rhenish Massif, migrated towards its halite-free center, characterized by less saline groundwaters, interacted with the surrounding rocks on their way and mixed with the groundwaters already present (Figures 4.14c and d)..

Changes in relative sea-level and variations in the climatic conditions also affected the chemical and isotopic compositions of the groundwaters. Arid climatic conditions resulted in the formation of highly saline evaporative relict brines and drastically decreased





the input of meteoric water. During times when humid climatic conditions prevailed, meteoric precipitation was relatively high and led to the dilution of groundwaters and to increased chemical weathering and the dissolution of evaporites in the subsurface (Figure 4.14c, e).

The Late Cretaceous transgression flooded the whole area of the MCB and introduced marine water into the groundwater system (Figure 4.14d). It also led to the formation of areally extensive marine calcareous sedimentary rocks (limestones and marls) which are the major lithologic components of the present-day regional hydrological system of the MCB, i.e., the limestones being the regional aquifer and the marls the regional aquitard (Struckmeyer 1990). It is likely that the seawater component in the present-day saline groundwaters of the MCB (samples 3 and 5) is derived from Late Cretaceous seawater.

The Subhercynian and Laramide phases of the Saxonian Orogeny in the Late Cretaceous/Early Tertiary had a profound impact on the geometry of the MCB (Figure 4.14e, insert map). Wrench tectonics resulted in southward thrusting at the northern margin of the MCB and the reactivation and creation of many faults within the area of the basin (Drozdewski and Wrede 1994; Figure 4.14e). These tectonic movements coincided with a major phase of uplift and northward tilting of the Rhenish Massif, a phase of increased heatflow in the eastern part of the MCB (Lommerzheim 1991), and a major phase of fault-controlled mineralization events in the northeastern Rhenish Schiefergebirge (Schaeffer 1983, 1984; chapter 3 of this thesis).

The groundwaters that were present in the subsurface of the MCB at the end of the Late Cretaceous probably consisted of two types: (1) Late Cretaceous marine sedimentary pore water within the Cretaceous sedimentary rocks and the fault and fracture systems of the uppermost parts of the deformed Paleozoic basement; and (2) highly saline deeper groundwater that originated from the previous hydrogeological history of the area (Figures 4.14a-d). Seismic pumping due to the tectonic activity, and hydrothermal circulation on faults due to increased heatflow may have resulted in the ascent and mixing of the saline groundwaters with the Cretaceous sedimentary pore waters, resulting in episodic phases of fault-controlled mineralization in the Paleozoic basement and in the overlying strata. This scenario may explain the Late Cretaceous/Early Tertiary mineralization (including



dolomitization) in and along faults in the Brilon Reef Complex.

During the Early Tertiary, subtropical terrestrial conditions predominated in the area of the MCB (Table 4.1; Figure 4.14e). Subsurface dissolution of halite under the influence of Tertiary meteoric water is suggested by the chemical and stable isotope composition of sample 6. The new surface topography and basin geometry resulted in a regional hydrologic system of an artesian basin that has elevated recharge areas at its margins and a thick and areally extensive aquitard overlying the regional aquifer in its center (Figures 4.2 and 4.14e). The development of karst in the regional aquifer at the southern, eastern, and northern margins of the MCB facilitated the establishment of a regional fresh groundwater subsystem which confines the regional saline groundwater subsystem in the center of the basin below the regional aquitard. The Eocene/Oligocene transgression affected only the westernmost part of the MCB (Figure 4.14e).

Presently, most of the regional aquifer and the shallower parts of Paleozoic bedrock appears to be dominated by sub-recent meteoric water, whereas “old” meteoric water of presumed Tertiary age (sample 6) and marine-derived water of presumed Cretaceous age (sample 3 and 5) are still present in the deeper parts of the basin and the underlying basement.



## 4.6 References

- Angerer, P., Michel, G, and Semmler, W., 1968, Das Verschließen der "Solquelle" Nateln. Glückauf (Forschungshefte), 29, p. 43-50.
- Baadsgaard, H., 1987, Rb-Sr and K-Ca isotope systematics in minerals from potassium horizons in the Prairie Evaporite Formation, Saskatchewan, Canada. Chemical Geology, 66, p. 1-15.
- Bässler, R., 1970, Hydrogeologische, chemische und Isotopen-Untersuchungen der Grubenwässer des Ibbenbürener Steinkohlenreviers. Zeitschrift der deutschen geologischen Gesellschaft, Sonderhefte Hydrogeologie Hydrogeochemie, p. 209-286.
- Bethke, C.M. and Marshak, S., 1990, Brine migration across North America - the plate tectonics of groundwater. Annual Reviews in Earth and Planetary Sciences, 18, p. 287-316.
- Bode, R., 1980, Strontianit aus dem Münsterland. Mineralogical Magazine, 4. P. 88-90.
- Burtner, R.L., 1987, Origin and evolution of Weber and Tensleep formation waters in the Green River and Uinta-Piceance basins, northern Rocky Mountain area. Chemical Geology, 65, p. 255-282.
- Carpenter, A.B., 1978, Origin and chemical evolution of brines in sedimentary basins. Oklahoma Geological Survey Circular, 79, p. 60-77.
- Chaudhuri, S., 1978, Strontium isotopic composition of several oil field brines from Kansas and Colorado. Geochimica et Cosmochimica Acta, 42, p. 329-332.
- Chaudhuri, S., Broedel, V., and Clauer, 1987, Strontium isotopic evolution of oil field waters from carbonate reservoir rocks in Bindley field, central Kansas, USA. Geochimica et Cosmochimica Acta, 51, p. 45-54.
- Chaudhuri, S. and Clauer, N., 1993, Strontium isotopic compositions and potassium and rubidium contents of formation waters in sedimentary basins: clues to the origin of the solutes. Geochimica Cosmochimica Acta, 57, p.
- Claypool, G.E., Holser, W.T., Kaplan, I.R., Sakai, H., and Zak, I., 1980, The age curves of sulfur and oxygen isotopes in marine sulfate and their mutual interpretation. Chemical Geology, 28, p. 199-260.
- Connolly, C.A., Walter, L.M., Baadsgard, H., and Longstaffe, F.J., 1990, Origin and evolution of formation waters, Alberta Basin, Western Canada Sedimentary Basin. II. Isotope systematics and water mixing. Applied Geochemistry, 5, p. 397-413.
- Davies, S.N. and De Wiest, R.J.M, 1966, Hydrogeology. 463 p.
- Drozdewski, G. and Wrede, V., 1994, Faltung und Bruchtektonik - Analyse der Tektonik im Subvariscikum. Fortschritte in der Geologie von Rheinland und Westfalen, 38, p. 7-187.





- Egeberg, P.K. and Aagaard, P., 1989, Origin and evolution of formation waters from oil fields on the Norwegian shelf. *Applied Geochemistry*, 4, p. 131-142.
- Faure, G., 1990, *Principles of Isotope Geology*. 589 p. (John Wiley & Sons)
- Fischer, R.S. and Kreitler, C.W., 1987, Geochemistry and hydrodynamics of deep-basin brines, Palo Duro Basin, Texas, USA. *Applied Geochemistry*, 2, p. 459-476.
- Freeze, R.A. and Cherry, J.A., 1979, *Groundwater*. 604 p. Prentice Hall.
- Fricke, K., 1961, Tiefenwasser, Solquellen und Solewanderung im Bereich des Münsterschen Beckens. *Zeitschrift der deutschen geologischen Gesellschaft*, 113, p. 37-47.
- Fricke, K., 1963, Die neuen Solebohrungen der Saline und Solbad Sassendorf GmbH., zugleich Beitrag zur Hydrogeologie der Solevorkommen am Südrand des Münsterschen Beckens. *Heilbad und Kurort*, 15, p. 102-108.
- Fricke, K., 1964a, Neue Bohrungen und hydrogeologische Untersuchungen im Heilquellengebiet von Solbad Ravensber/Teutoburger Wald. *Heilbad und Kurort*, 16, p. 116-118.
- Fricke, K., 1964b, Bemerkungen zu den Solquellen des Hellwegs. (Erläutert am Beispiel Bad Westernkotten, Krs. Lippstadt.) *Zeitschrift der deutschen geologischen Gesellschaft*, 116, p. 76-87.
- Fricke, K., 1967, Das Heilquellengebiet von Bad Belecke (Möhne) und die Neuerschließung von Natrium-Chlorid-Wasser 1963. *Geologisches Jahrbuch*, 84, p. 735-754.
- Fricke, K., 1968, Hydrogeologische und hydrochemische Ergebnisse der Sole-Neubohrung 1965 Bad Westernkotten. *Fortschritte der Geologie von Rheinland und Westfalen*, 16, p. 121-132.
- Fricke, K., 1969, Die Thermalbohrung Bad Lippspringe 1962 (Martinus-Quelle). *Fortschritte in der Geologie von Rheinland und Westfalen*, 17, p. 95-130.
- Fricke, K. and Wevelmeyer, W., 1960, Neue Thermal-Sole-Bohrung in Bad Waldliesborn 900 m tief. *Heilbad und Kurort*, 12, p. 158-162.
- Friedman, I., Redfield, A.C., Schoen, B., and Harris, J., 1964, The variation of the deuterium content of natural waters in the hydrologic cycle. *Reviews in Geophysics*, 2, p. 177-224.
- Geologisches Landesamt Nordrhein-Westfalen, 1995, *Geologie im Münsterland*. 195 p.
- Geyh, M. and Michel, G., 1974, Isotopen- und Hydrochemie des tieferen Grundwassers im Raum Paderborn. *Fortschritte in der Geologie von Rheinland und Westfalen*, 20, p. 67-77.
- Geyh, M. and Michel, G., 1981, Isotopen- und hydrochemischen Betrachtungen über die Süßwasser/Salzwasser-Zone am Nordostrand des Münsterländer Beckens. *Zeitschrift der deutschen geologischen Gesellschaft*, 132, p. 597-612.



- Gradstein, F.M. and Ogg, J., 1996, A Phanerozoic time scale. Episodes, 19, p.
- Graf, D.L., 1982, Chemical osmosis, reverse chemical osmosis, and the origin of subsurface brines. *Geochimica et Cosmochimica Acta*, 46, p. 1431-1448.
- Hardie, L.A., 1990, The roles of rifting and hydrothermal  $\text{CaCl}_2$  brines in the origin of potash evaporites: A hypothesis. *American Journal of Science*, 290, p. 43-106.
- Hofmann, R., 1979, Die Entwicklung der Abscheidungen in den gangförmiger Barytvorkommen in Deutschland. Monograph Series Mineral Deposits, 17, p. 81-214.
- Hofmann, R. and Schürenberg, H., 1979, Geochemische Untersuchungen gangförmiger Barytvorkommen in Deutschland. Monograph Series mineral Deposits, 17, p. 1-80.
- Jacobshagen, V. and Münnich, K. O., 1964,  $^{14}\text{C}$ -Altersbestimmung und andere Isotopen-Untersuchungen an Thermalsolen des Ruhrkarbons. *Neues Jahrbuch der Geologie und Paläontologie, Monatshefte*, 1964, p. 561-568.
- Kampschulte, A., Buhl, D., and Strauss, H., 1998, The sulfur and strontium isotopic compositions of Permian evaporites from the Zechstein basin, northern Germany. *Geologische Rundschau*, p. 192-199.
- Kharaka, Y.K. and Carothers, W.W., 1986, Oxygen and hydrogen isotope geochemistry of deep basin brines. In: Fritz, P. and Fontes, J.Ch., *Handbook of Environmental Isotope Geochemistry*, 2, p. 305-360.
- Kharaka, Y.K., Maest, A.S., Carpenter, W.W., Law, L.M., Lamothe, R.J., and Fries, T.L., 1987, Geochemistry of metal-rich brines from central Mississippi Salt Dome basins, U.S.A. *Applied Geochemistry*, 2, p. 543-561.
- Karrenberg, H., 1974, Über neuere hydrogeologische Forschungsarbeiten im Aufgabenbereich des Geologischen Landesamtes Nordrhein-Westfalen. *Fortschritte in der Geologie von Rheinland und Westfalen*, 20, p. 355-370.
- Kesler, S.E, Vennemann, T.W., Frederickson, C, Breithaupt, A., Vazquez, R., and Furman, F.C., 1997, Hydrogen and oxygen isotope evidence for origin of MVT-forming brines, southern Appalachians. *Geochimica et Cosmochimica Acta*, 61, p. 1513-1523.
- Land, L.S. and Prezbindowski, D.R., 1981, The origin and evolution of saline formation water, Lower Cretaceous carbonates, south-central Texas, USA. *Journal of Hydrogeology*, 54, p. 51-74.
- Land, L.S. and MacPherson, G.L., 1989, Geochemistry of formation water, Plio-Pleistocene reservoirs, offshore Louisiana. *Transactions of the Gulf Coast Association of the Geological Society*, 39, p. 421-430.
- Lehmann, H.-W., 1974, Geochemie und Genesis der Tiefenwässer der Norddeutschen Senke. *Zeitschrift der angewandten Geologie*, 20, p.502-509 and 551-557.





- Lommerzheim, A., 1988, Die Genese und Migration von Kohlenwasserstoffen im Münsterländer Becken. Unpublished dissertation at the University of Münster, 260 p.
- Lommerzheim, A., 1991, Die geothermische Entwicklung des Münsterländer Beckens und ihre Bedeutung für die Kohlenwasserstoff-Genese in diesem Raum. Deutsche Gesellschaft für Mineralienkunde-Berichte, 468, p. 319-372.
- Lommerzheim, A., 1994, Die Genese und Migration der Erdgase im Münsterländer Becken. Fortschritte in der Geologie von Rheinland und Westfalen, 38, p. 309-348.
- Lowry, R.M., Faure, G., Mullet, D.I., and Jones, L.M., 1988, Interpretation of chemical and isotopic compositions of brines based on mixing and dilution, "Clinton" sandstones, eastern Ohio, USA. Applied Geochemistry, 3, p. 177-184.
- Matthess, G., 1990, Die Beschaffenheit des Grundwassers. Lehrbuch der Hydrogeologie, 2, 498 p.
- McNutt, R. H., Frape, S. K., and Dollar, P., 1987, Strontium, oxygen, and hydrogen isotopic composition of brines, Michigan and Appalachian basins, Ontario and Michigan. Applied Geochemistry, 2, p. 495-505.
- Michel, G., 1963, Untersuchungen über die Tiefenlage der Grenze Süsswasser-Salzwasser im nördlichen Rheinland und anschliessenden Teilen Westfalens, zugleich ein Beitrag zur Hydrogeologie und Chemie des tiefen Grundwassers. Forschungsberichte des Landes Nordrhein-Westfalen, 1239, 131 p.
- Michel, G., 1964, Betrachtungen zur Hydrochemie des tieferen Grundwassers im Ruhrgebiet. Zeitschrift der deutschen geologischen Gesellschaft, 116, p.161-166.
- Michel, G., 1966, Über die mögliche Herkunft des mineralisierten Grundwassers im Münsterschen Becken. Zeitschrift der deutschen geologischen Gesellschaft, 116, p. 161-166.
- Michel, G., 1983a, Sole im Münsterland - woher, wohin? Heilbad und Kurort, 35, p. 66-76.
- Michel, G., 1983b, Die Sole des Münsterländer Kreide-Beckens. Neues Jahrbuch der Geologie und Paläontologie, Abhandlungen, 166, p. 139-159.
- Michel, G., 1994, Wie kommt die Sole ins Revier. Mitteilungen der Geologischen Gesellschaft Essen, 12, p. 65-81.
- Michel, G. and Nielsen, H., 1977, Schwefel-Isotopenuntersuchungen an Sulfaten ostwestfälischer Mineralwässer. Fortschritte der Geologie von Rheinland und Westfalen, 26, p. 185-227.
- Michel, G., Rabitz, A., and Werner, H., 1974, (with a contribution by Scherp, A.), Betrachtungen über die Tiefenwässer im Ruhrgebiet. Fortschritte der Geologie von Rheinland und Westfalen, 20, p. 215-236.





- Moldovanyi, E.P., Walter, L.M., and Land, L.S., 1993, Strontium, boron, oxygen, and hydrogen isotope geochemistry of brines from basal strata of the Gulf Coast sedimentary basin, USA. *Geochimica et Cosmochimica Acta*, 57, p. 2083-2099.
- Morrow, D.W., 1998, Regional Subsurface Dolomitization: Models and Constraints. *Geoscience Canada*, 25, p. 57-70.
- Papakonstantinou, A., 1970, Die hydrogeologischen Verhältnisse im Raum Bad Westernkotten, Haarstrang (unter besonderer Berücksichtigung quantitativer und qualitativer Zusammenhänge zwischen Niederschlägen und Soleführung). Unpublished Diplom-Thesis, University of Marburg, 66 p.
- Patteisky, K., 1954, Die thermalen Solen des Ruhrgebietes und ihre juvenilen Quellgase. *Glückauf*, 90, p. 1334-1348 and p. 1508-1519.
- Pilger, A., 1961, Übersicht über die Gangvererzung des Ruhrgebietes. *Geologisches Jahrbuch, Beihefte*, 40, p. 297-350.
- Puchelt, H., 1964, Zur Geochemie des Grubenwassers im Ruhrgebiet. *Zeitschrift der deutschen geologischen Gesellschaft*, 116, p. 167-203.
- Puchelt, H. and Nielsen, H., 1967, Untersuchungen über die Verteilung der Schwefelisotope in den Grubenwässern des Ruhrreviers. *Glückauf (Forschungshefte)*, 28, p. 303-310.
- Rittenhouse, G., 1967, Bromine in oil-field waters and its use in determining possibilities of origin of these waters. *American Association of Petroleum Geologists Bulletin*, 51, p. 2430-2440.
- Rosenfeld, U., 1983, Beobachtungen und Gedanken zur Osning Tektonik. *Neues Jahrbuch der Geologie und Paläontologie Abhandlungen*, 166, 34-49.
- Schaeffer, R., 1983, Vererzungen in karbonischen und tertiären Sedimenten bei Velbert (Niederbergisches Land) - eine Zeitmarke für die saxonische Mineralisation des Rheinischen Schiefergebirges. *Zeitschrift der deutschen Geologischen Gesellschaft*, 134, p. 225-245.
- Schaeffer, R., 1984, Die postvariszische Mineralisation im nordöstlichen Rheinsichen Schiefergebirge. *Braunschweiger geologisch-paläontologische Dissertationen*, 3, 206 pp.
- Scherp, A. and Strübel, G., 1974, Zur Barium-Strontium-Mineralisation. *Mineralium Deposita*, 9, p. 155-168.
- Semmler, W., 1960, Die Herkunft der Grubenwasserzuflüsse im Ruhrgebiet. *Glückauf*, 96, p. 502-511.
- Solley, W.B. et al., 1983, Estimated use of water in the United States. *United States Geological Survey Circular* 1001, 56 p.
- Sonntag, C., Münnich, H.J., and Rozanski, K., 1983, Variations of deuterium and oxygen-18 in continental precipitation and groundwater, and their causes. In: A. Street-Perrot et al. (eds.), *Variations in the Global Water Budget*, p. 107-124.



- Starinsky, A., Bielsky, M., Lazar, B., Steinitz, G., and Raab, M., 1983, Strontium isotope evidence on the history of oil field brines, Mediterranean coastal plain, Israel. *Geochimica et Cosmochimica Acta*, 47, p. 687-695.
- Stueber, A.M., Pushkar, P., and Hetherington, E.A., 1984, A strontium isotopic study of Smackover brines and associated solids, southern Arkansas. *Geochimica et Cosmochimica*, 48, p. 1637-1649.
- Stueber, A.M., Pushkar, P., and Hetherington, E.A., 1987, A strontium isotopic study of formation waters from the Illinois basin. *Applied Geochemistry*, 2, p. 477-494.
- Stueber, A.M., Saller, A.H., and Ishida, H., 1998, Origin, migration, and mixing of brines in the Permian Basin: geochemical evidence from the eastern Central Basin Platform, Texas. *American Association of Petroleum Geologists Bulletin*, 82, p. 1652-1672.
- Struckmeier, W., 1990, Wasserhaushalt und hydrogeologische Systemanalyse des Münsterländer Beckens. LWA (Landesamt für Wasser und Abfall Nordrhein-Westfalen) Schriftenreihe, 45, 72 p.
- Sunwall, M.T. and Pushkar, P., 1979, The isotopic composition of strontium in brines from petroleum fields of southeastern Ohio. *Chemical Geology*, 24, p. 189-197.
- Sverjenski, D.A., 1984, Oil field brines as ore-forming solutions. *Economic Geology*, 79, p. 23-37.
- Thome, K.N., 1983, Gletschererosion und -akkumulation im Münsterland und angrenzenden Gebieten. *Neues Jahrbuch der Geologie und Paläontologie Abhandlungen*, 166, p. 116-183.
- Unland, G., 1985, Die Strontianitlagerstätte im Münsterland. *Aufschluss*, 36, p. 371-374.
- Voigt, E., 1963, Über Randtröge vor Schollenrändern und ihre Bedeutung im Gebiet der Mitteleuropäischen Senke und angrenzender Gebiete. *Zeitschrift der deutschen geologischen Gesellschaft*, 114, p. 378-418.
- Wedewardt, M., 1995, Hydrochemie und Genese der Tiefenwässer im Ruhr-Revier. DMT-Berichte aus Forschung und Entwicklung, 39, 250 p.
- Wolansky, D., 1964, Die Hydrogeologie des Deckgebirges im niederrheinisch-westfälischen Revier in ihrer Bedeutung für den Bergbau. *Zeitschrift der deutschen geologischen Gesellschaft*, 116, p. 55-69.
- Wrede, V., 1992, Störungstektonik im Ruhrkarbon. *Zeitschrift der angewandten Geologie*, 38, p. 94-104.
- Zhou, X. and Li, C., 1992, Hydrogeochemistry of deep formation brines in the central Sichuan Basin, China. *Journal of Hydrology*, 138, p. 1-15.



## **CHAPTER 5**

### **SYNOPSIS**

#### **5.1 Restatement of objectives**

As stated in Chapter 1, the primary objective of this thesis research is to determine the spatial distribution, origin, and timing of dolomitization and associated base metal sulfide mineralization encountered in drill cores from the Middle and Upper Devonian Brilon Reef Complex. The previous chapters treated various, but interdependent, aspects of the primary objective. In particular, the objective of Chapter 2 was to determine the primary controls on dolomitization by documenting the spatial and temporal relationships between the distribution of dolostone and (1) sedimentary facies, (2) other diagenetic phases, and (3) tectonic structures. Within the framework of the spatial and temporal relationships established in Chapter 2, the objectives of Chapter 3 were (1) to determine the effects of dolomitization and associated base metal mineralization on the undolomitized limestone hostrock adjacent to the dolostone intervals by identifying petrographic and geochemical trends; (2) to geochemically characterize selected pre- and post-Variscan mineral phases; and (3) to determine the compositions and temperatures of the fluids that resulted in the dolomitization and associated base metal mineralization in the Brilon Reef Complex. The objective of Chapter 4 was to test one working hypothesis on the origin, timing, and movement of the dolomitizing and mineralizing fluids by conducting a study on the origin and evolution of saline groundwaters that presently occur in the adjacent Münsterland Cretaceous Basin. The objective of this, the final, chapter is to integrate the findings of all previous chapters.

#### **5.2 Integration of results and interpretations**

The geologic history of the Brilon Reef Complex is illustrated in a series of diagrams that represent schematic N-S and W-E cross-sections through the Brilon Reef Complex (Figures 5.1 to 5.6).



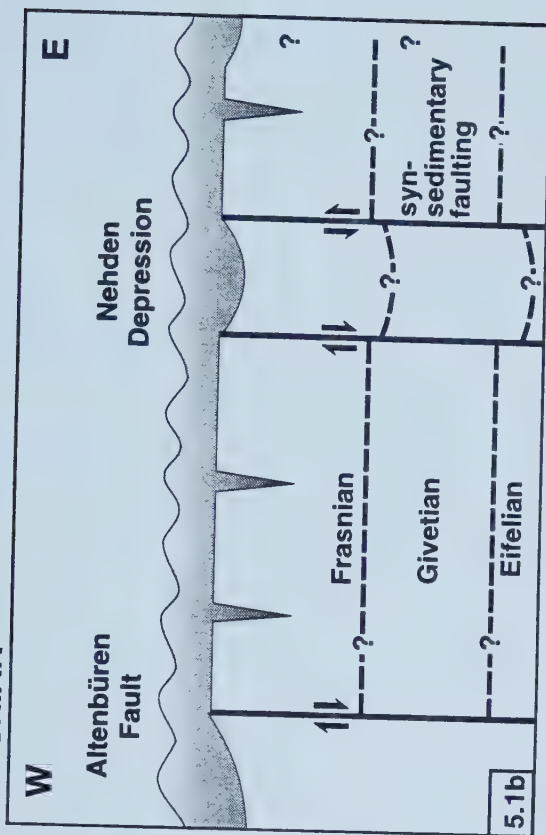
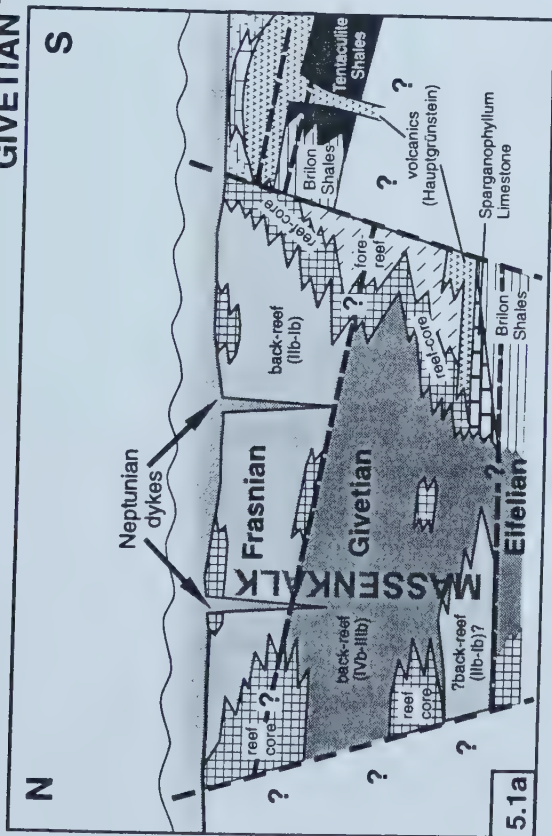




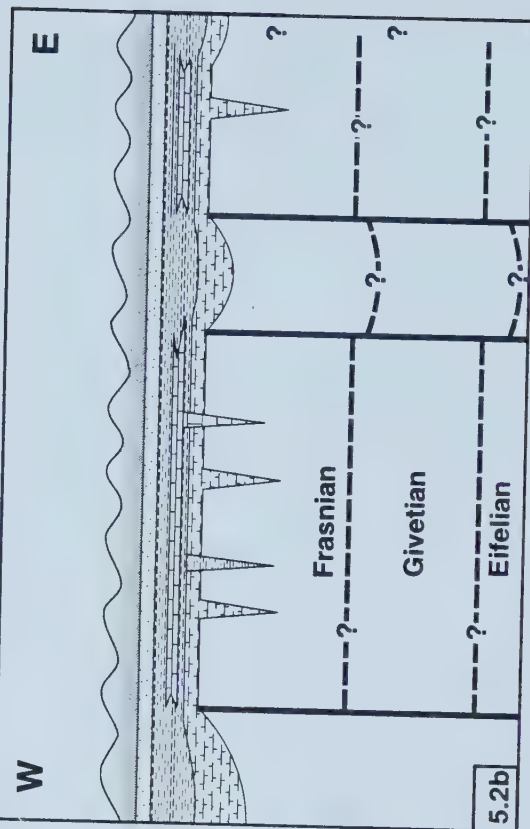
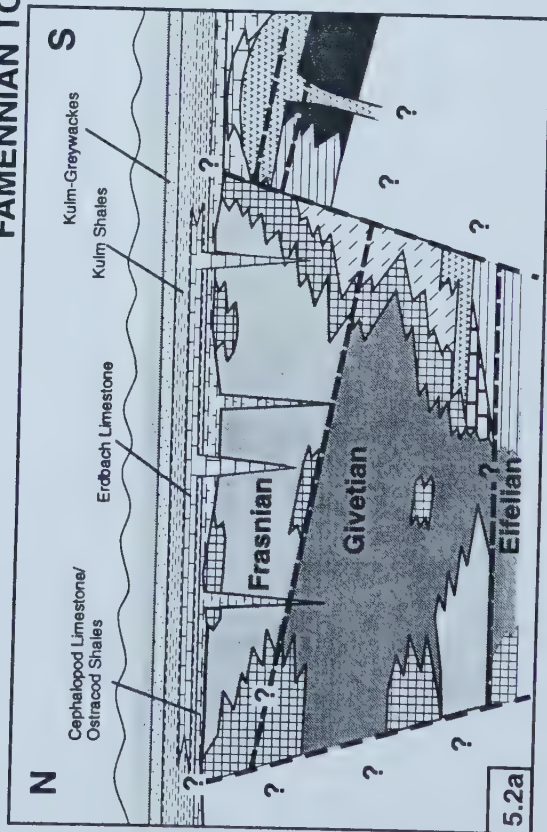
**Figure 5.1:** Schematic N-S (a) and W-E (b) cross-section through the Brilon Reef Complex in the Frasnian. Approximate location of N-S cross section is given in Chapter 2, Figure 2.1 (A-A'). Questionmarks on dashed lines signify uncertainties about the position of stratigraphic boundaries. Figure 5.1a shows carbonate facies distribution within the “Massenkalk” at the end of reef growth (for more detailed figure, see Chapter 2, Figure 2.4). In Figure 5.1b, the locations of NNW-SSE trending synsedimentary faults (e.g., Altenbüren Fault) are schematically indicated. For further explanation, see text.

**Figure 5.2:** Schematic N-S (a) and W-E (b) cross-section through the Brilon Reef Complex in the Late Carboniferous prior to the onset of the Variscan deformation in the area. Submarine fissures (Neptunian dykes) are filled with Upper Devonian and Lower Carboniferous marls and limestones. For further explanation, see text.

# GIVETIAN TO FRASNIAN



# FAMENNIAN TO WESTPHALIAN





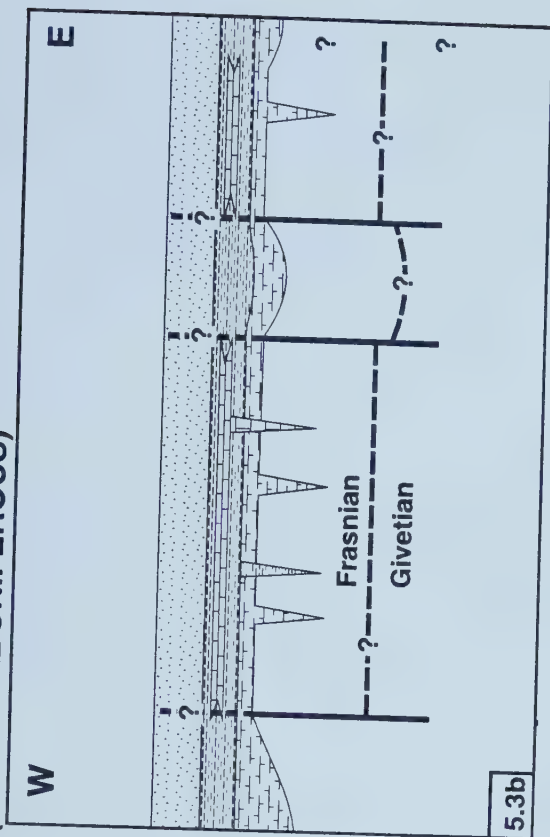
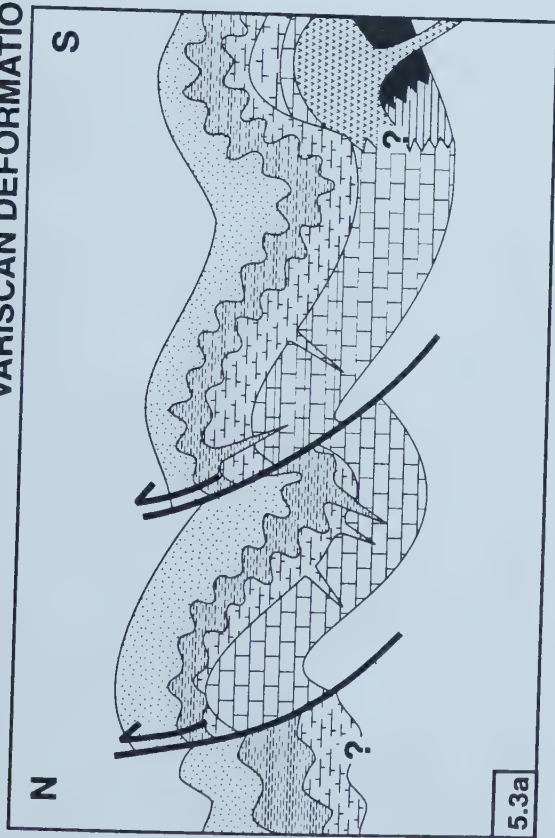




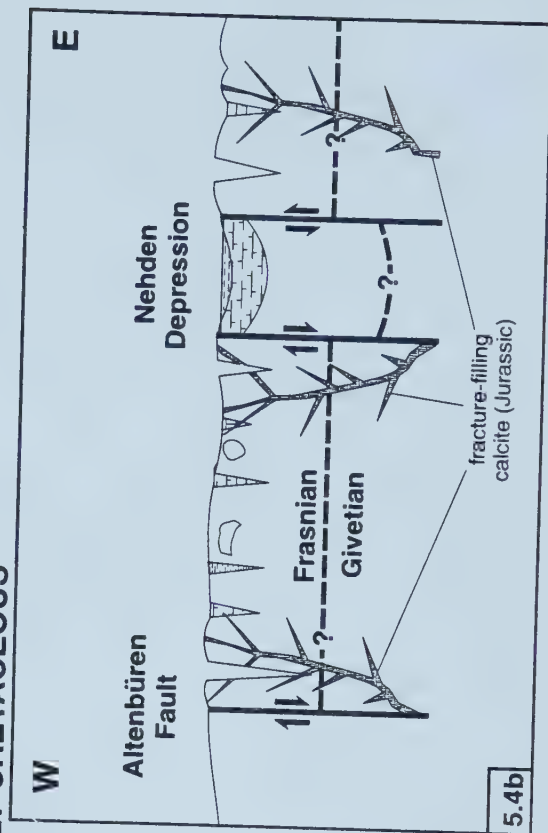
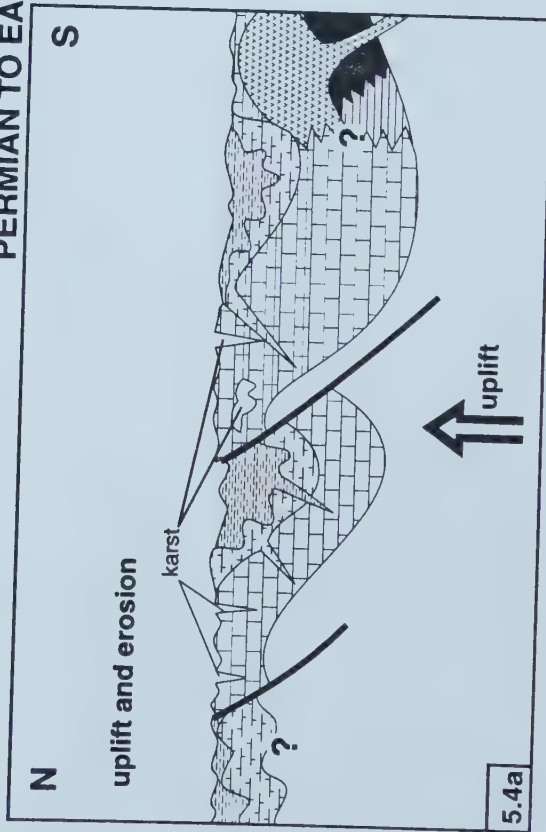
**Figure 5.3:** Schematic N-S (a) and E-W (b) cross-section through the Brilon Reef Complex during the Variscan Orogeny in the Late Carboniferous (not to scale). The Variscan deformation resulted in SW-NE trending folds that are further structured by thrust faults (5.3a). No evidence for movement of the NNW-SSE trending faults (5.3b) during the Variscan deformation has been found.

**Figure 5.4:** Schematic N-S (a) and E-W (b) cross-section through the Brilon Reef Complex from the Permian to the Early Cretaceous (not to scale). Uplift and erosion resulted in the denudation of the Variscan Orogen and the exposure of the Brilon Reef Complex at the surface. Extensional tectonics in the Jurassic caused reactivation of the NNW-SSE trending normal faults and led to fracturing and subsequent calcite cementation (5.4.b).

# VARISCAN DEFORMATION (LATE CARBONIFEROUS)



# PERMIAN TO EARLY CRETACEOUS



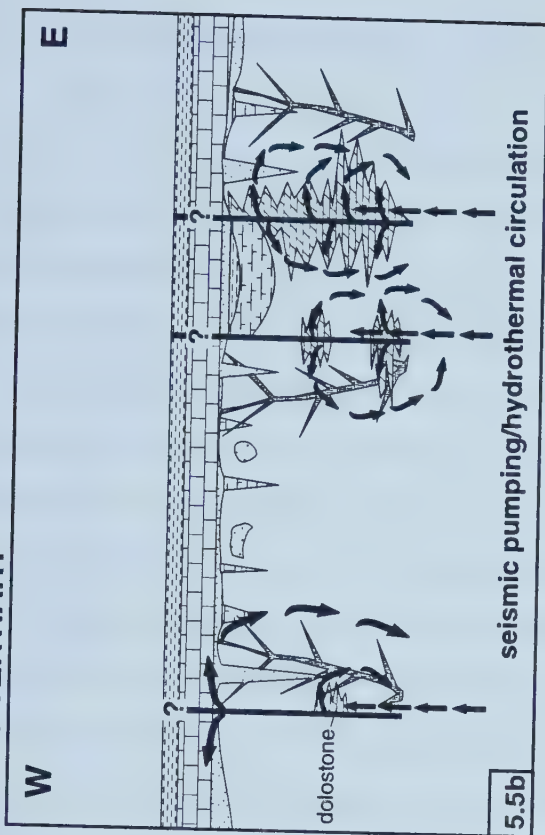
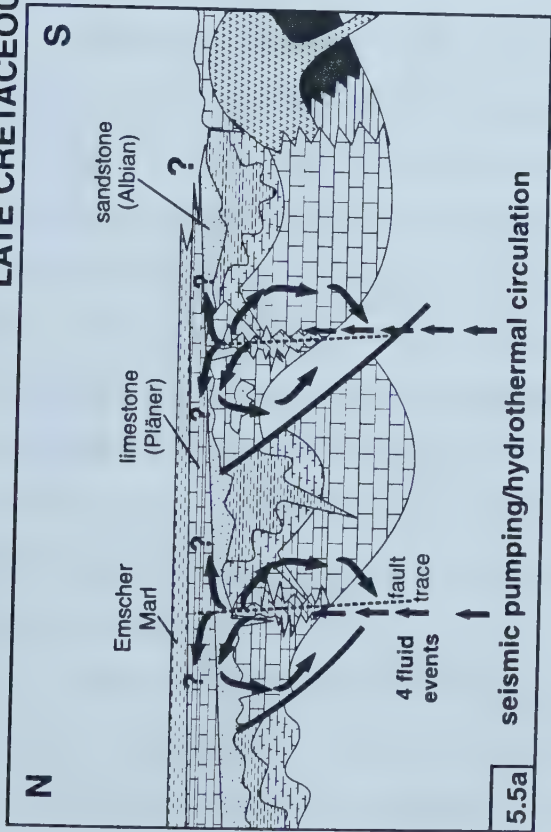




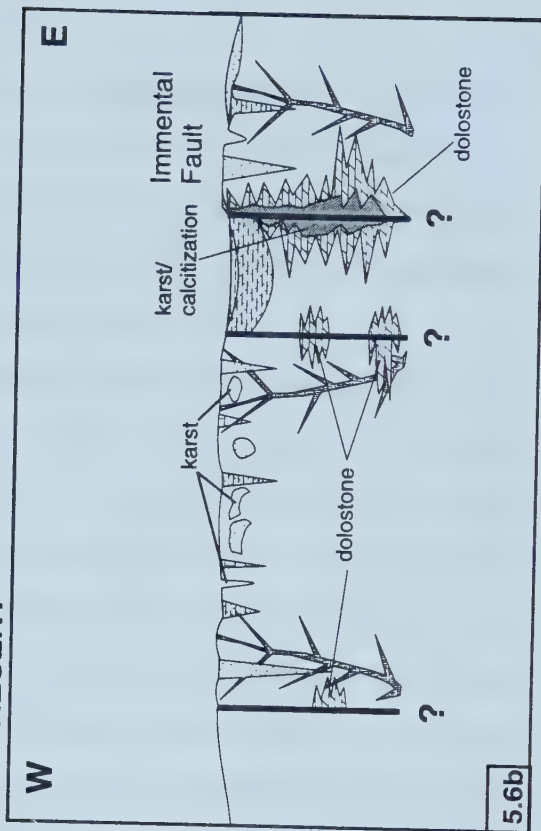
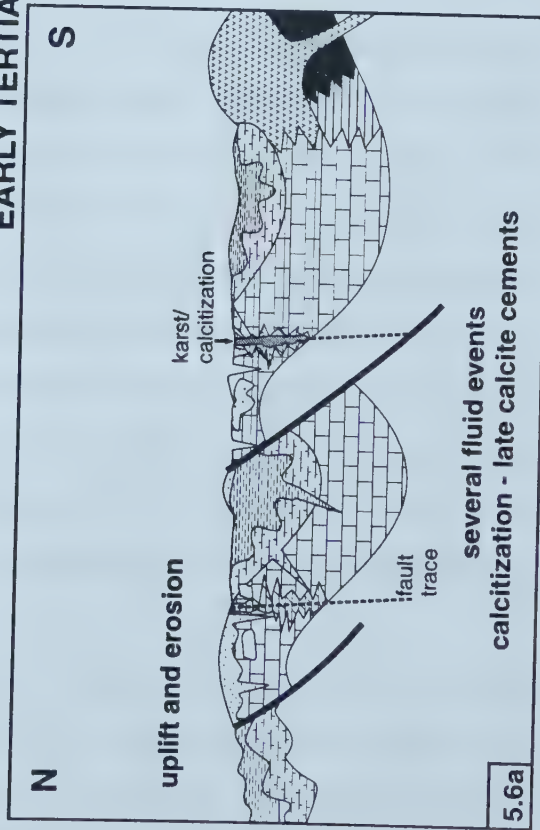
**Figure 5.5:** Schematic N-S (a) and W-E (b) cross-sections through the Brilon Reef Complex during the Late Cretaceous/Early Tertiary. The Late Cretaceous marine transgression deposited sandstones, limestones and marls on top of the Brilon Reef Complex. The southern extent of Late Cretaceous marine sediments in the Brilon area is not known. Wrench tectonics and increased heatflow resulted in seismic pumping and hydrothermal circulation of dolomitizing and ore-forming fluids in deep reaching NNW-SSE trending faults (dashed vertical lines in (a), solid vertical lines in (b)). The extent of dolomitization and mineralization within the Cretaceous sedimentary rocks is unknown, because most of these have been eroded (see Figure 5.6).

**Figure 5.6:** Schematic N-S (a) and W-E (b) cross-sections through the Brilon Reef Complex at present. Further uplift and erosion resulted in the almost complete removal of Cretaceous sediments in the area of the Brilon Reef Complex. Surface related karst, carbonate dissolution, calcitization, and several generations of fracture and cavity filling cements have affected the dolostone bodies in many places, resulting in their partial to complete obliteration (e.g., at the Immental Fault).

# LATE CRETACEOUS/EARLY TERTIARY



# EARLY TERTIARY TO PRESENT







### 5.2.1 Carbonate facies distribution and stratigraphy

The investigation of the facies distribution and stratigraphy of the “Massenkalk” facies was necessary to determine if sedimentary facies acted as a primary control on the distribution of dolostone intervals in the Brilon Reef Complex. Furthermore, it provides a more detailed insight into the facies development during the main phase of reef growth and may prove to be helpful in future attempts to correlate the drill cores.

The Middle and Upper Devonian “Massenkalk” of the Brilon Reef Complex can be mapped as facies types characteristic of fore-reef, reef-core, and back-reef (lagoonal) depositional environments (Figure 5.1a). Deposits of fore-reef character have been encountered only at the southern margin of the reef complex. Deposits of reef-core facies occur at the southern and northeastern margins, whereas the volumetrically predominant deposits of back-reef character occupy most of the central part of the reef complex (Figure 5.1a). In the investigated drill cores, matrix-rich carbonate facies types (e.g., floatstones, packstones, wackestones, mudstones) predominate, whereas grainstones and matrix-poor rudstones rarely occur.

The attempt to correlate the investigated drill cores using a biostratigraphic and lithostratigraphic approach did not yield any reliable results. Fossils allowing a high stratigraphic resolution (e.g., conodonts) are rare in the reefal carbonates. Although the occurrence of the brachiopod *Stringocephalus burtini* in drill cores from the northern part of the reef complex indicates a Givetian age, its absence elsewhere does not necessarily imply a different stratigraphic age. Lithostratigraphic correlation of the drill cores is complicated by (1) lateral changes in lithofacies, which in part may have been the result of synsedimentary faulting (Figure 5.1b); (2) displacements, fracturing, and brecciation due to Variscan (thrust) and post-Variscan (normal) faults; and (3) the effects of other post-sedimentary processes, such as the introduction of externally-derived sediments into fractures and karst cavities.

General trends in facies development have been recognized and may provide a useful tool for the stratigraphic correlation of the drill cores from the Brilon Reef Complex, if investigated in greater detail. In particular, a facies shift from subtidal facies zones (IVb and IIIb) to peritidal facies zones (IIb and Ib), following the disappearance of the Givetian brachiopod *Stringocephalus burtini* in the back-reef environment of the central and northern



part of the reef complex, may correspond to the transition from the fore-reef dominated older (Upper Givetian) part to the back-reef dominated younger (Frasnian) part of the succession at the southern margin of the reef complex (Figure 5.1a). The observed facies changes indicate a lowering of relative sea level during the main phase of reef growth, i.e., the rate of carbonate accumulation exceeded the rate of subsidence. The end of reef growth in the Late Frasnian, however, is marked by a transition from peri- and subtidal back-reef deposits to open-marine nodular limestones and cephalopod-bearing marls, suggesting a marked increase in relative sea level. It is not clear whether this deepening of the Late Devonian sea was caused by a significant eustatic sea level rise, by an increase in tectonic subsidence, or a combination of the two.

The recognition of deep-reaching fractures filled with Upper Devonian/Lower Carboniferous cephalopod limestones and Lower Carboniferous crinoidal limestones (Füchtbauer and Richter 1983; Machel 1990) provide evidence for the continuation of marine sedimentation during the Late Devonian and Early Carboniferous (Figure 5.2). Lower Carboniferous shales and cherts indicate a further deepening of the sedimentary environment prior to the advance of the deformation front of the Variscan Orogen from the south, which resulted in the deposition of flysch-type greywackes in the Brilon area (Figures 5.2a and b).

### 5.2.2 Diagenetic and tectonic framework

Machel (1979, 1990) and Moritz (1983) have studied the pre-Variscan diagenetic history of the “Massenkalk” in the Brilon Reef Complex in detail, which is not repeated here. The fact that the major amount of dolostone in the “Massenkalk” of the Brilon Reef Complex formed after the Variscan deformation (Chapter 2) resulted in the focus of the present study on the post-Variscan textural and mineralogical changes.

The Variscan deformation resulted in broad SW-NE trending folds that are further structured by thrust faults (Figure 5.3a). In drill core, macroscopic fabrics that developed in response to the Variscan deformation are rare. They include (1) deformed sutured stylolites; (2) tectonically oriented and strained fossils; (3) vertical stylolites; and (4) shear zones.

The succession of post-Variscan textural and mineralogical changes in the investigated dolostone intervals has been recognized to consist of at least 6 phases, which, in continuation of the 18 pre-kinematic (phases 1 to 18) diagenetic phases and the one syn-





kinematic phase 19 (Machel 1990), have been assigned numbers 20 to 25. These phases include: repeated fracturing (phases 20 through 25), calcite cementation (phases 20, 24, and 25), dolomitization (dolomite Type 1; phase 21), calcite dissolution (phase 21), dolomite recrystallization (dolomite Type 2; phase 22), dolomite cementation (dolomite Type 3; phase 22), minor base metal sulfide mineralization (galena, sphalerite, pyrite; phase 23), dolomite dissolution, limonitization, and calcitization (phase 24). The widespread and significant post-Variscan fracturing in the northeastern Rhenish Schiefergebirge has been attributed mainly to distinct phases of post-orogenic extensional tectonics that resulted in the formation of new faults, as well as in reactivation of the older, NNW-SSE trending faults (Figures 5.4b, 5.5b, 5.6b) during uplift and erosion of the Rhenish Massif (Schaeffer 1984, 1986). The age of the three dolomite types and subsequent sulfide mineralization and calcite cementation is constrained to the Late Cretaceous/Early Tertiary by integration of the data from this study with the paragenetic sequence by Schaeffer (1984, 1986).

### ***5.2.3 Controls on the distribution of dolostone***

Dolostone intervals in the “Massenkalk” of the Brilon Reef Complex occur at all depth levels and range in thickness from several dm to hundreds of meters (Figure 5.5). The major amount of dolostone formed in the central part of the Brilon Reef Complex along the Immental Fault. Unfortunately, subsequent fracturing, corrosion, and calcitization along this fault resulted in the partial to complete obliteration the dolostone intervals. Considering that (1) no well in the Brilon Reef Complex penetrated the full vertical extent of the “Massenkalk” from its pre-erosional top to its base and that (2) a confident stratigraphic correlation of the drill cores is still not possible, the distribution of dolostone intervals within the investigated drill cores, as shown in this study, may not be representative of their distribution within the whole carbonate body of the Brilon Reef Complex.

Within individual drill cores, the extent of dolomitization is largely controlled by the amount of post-Variscan fracturing (phases 21 and 22), both of which generally increase with increasing proximity to the prominent NNW-SSE trending, subvertical normal faults. Carbonate facies types as well as pre-Variscan diagenesis and textures related to the Variscan deformation do not appear to have any significant influence on the distribution of dolostone in the Brilon Reef Complex.





#### 5.2.4 Evidence for hydrothermal dolomitization

Several lines of evidence indicate that post-Variscan dolomitization in the Brilon Reef Complex is hydrothermal in origin. Nonplanar dolomite textures in dolomite Types 1 and 2 are indicative of dolomite formation at temperatures in excess of 50°C (Gregg and Sibley 1984). Dolomite Type 3 occurs as saddle dolomite cement, which characteristically forms in a temperature range between 60 and 150 °C (Radke and Mathis 1980, Machel 1987). This is confirmed by fluid inclusion homogenization temperatures between 105 and 120 °C for a sample of dolomite Type 3. Furthermore, strongly depleted  $\delta^{18}\text{O}$  values below -6.5 ‰ PDB of all three dolomite types suggest dolomite formation at elevated temperatures. At the time of dolomitization in the Late Cretaceous/Early Tertiary, the Middle and Upper Devonian “Massenkalk” of the Brilon Reef Complex was overlain only by a thin (probably < 200 m) cover of Cretaceous marine sandstones, limestones and marls (Figure 5.5). Assuming a maximum thickness of about 1000 m of the “Massenkalk”, a surface temperature of 20° C, and a geothermal gradient of 30 °C, burial temperatures should have ranged between 20 and about 60 °C, depending on the depth. The textural, isotopic, and microthermometric data indicate that the temperatures of formation of the dolomite types exceeded those expected at their respective depths, hence, the fluids from which these dolomite types formed were hydrothermal.

Petrographic, trace element, and isotopic trends in the undolomitized limestones within several meters of the limestone-dolostone contacts adjacent to the dolomitized intervals are suggestive of recrystallization by hydrothermal fluids. With decreasing distance from the dolomitized intervals, the sizes of calcite crystals that make up the limestone matrix increase, crystal shapes change from subhedral to anhedral, and intercrystalline porosity decreases. Changes in CL color from non-luminescent to dark red to mottled orange correspond to an increase in Mn concentrations towards the limestone-dolostone contacts. These changes also correlate with a drastic decrease in the  $\delta^{18}\text{O}$  values, and a slight decrease of the  $\delta^{13}\text{C}$  values. Sr isotope compositions correlate well with these trends showing an increase from Givetian to Frasnian marine values ( $^{87}\text{Sr}/^{86}\text{Sr} = 0.7079$  to  $0.7083$ , Burke et al. 1982) to more radiogenic values that approach that of the grey matrix dolomite ( $^{87}\text{Sr}/^{86}\text{Sr} = 0.7094$ ). These data suggest that the hydrothermal fluid that led to the formation of the grey matrix dolomite also caused the recrystallization of the adjacent limestones.



### 5.2.5 Evidence for dolomite recrystallization

In the study of carbonate rocks, the term recrystallization, as defined by Folk (1965), refers to changes in crystal size without any change of mineralogy. Machel (1997) extended the definition for recrystallization by including other textural changes (i.e., changes in the crystal shapes from planar to nonplanar), structural changes (i.e., changes in ordering and strain), compositional changes (i.e., changes in stoichiometry and trace element and isotopic composition), as well as changes in the paleomagnetic properties. Specific thermodynamic drives for recrystallization of a mineral include reduction of lattice strain (strain recrystallization), the reduction of surface free energy (Ostwald ripening), the transformation of a less thermodynamically stable composition to a more stable form (e.g., calcian dolomite to stoichiometric dolomite), and the transformation of a disordered to an ordered mineral (Sibley and Gregg 1987; Machel 1997). To accommodate for the fact that recrystallization may not change all or some of the measurable parameter in a way that recrystallization can be recognized, Machel (1997) proposed the concept of 'significant recrystallization'. According to this concept, a dolomite is considered to be 'significantly recrystallized', if changes via recrystallization in texture, structure, composition, and/or paleomagnetic properties result in data ranges that are larger than the original ones. If only some of the measured parameters have significantly changed as a result of recrystallization, the dolomite is 'significantly recrystallized' with respect to these parameters, but 'insignificantly recrystallized' with respect to those parameters that are still within the original data ranges (Machel 1997).

Correlative trends of average crystal size, oxygen isotope composition, and Sr-isotope composition (i.e., more depleted  $\delta^{18}\text{O}$  and decreasing  $^{87}\text{Sr}/^{86}\text{Sr}$  values with increasing crystal size) indicate that 'significant recrystallization' of dolomite Type 1 has occurred with respect to these parameters, whereas it is 'insignificantly recrystallized' with respect to carbon isotopes, stoichiometry, and trace elements. Various degrees of significant recrystallization are represented by (1) the spatial and petrographic relationships between dolomite Type 1 and Type 2 (i.e., coarse-crystalline Type 2 forming halos within areas of fine-crystalline Type 1); (2) the overlap of their ranges in  $\delta^{18}\text{O}$  and  $^{87}\text{Sr}/^{86}\text{Sr}$ ; (3) in the case of samples of dolomite Type 1 and Type 2 from the same core sample, dolomite Type 2 always has the same or a





more depleted  $\delta^{18}\text{O}$  value as well as the same or lower  $^{87}\text{Sr}/^{86}\text{Sr}$  value than corresponding dolomite Type 1. Reduction of surface energy as the primary thermodynamic drive for recrystallization, catalyzed by elevated temperature and the composition of the hydrothermal fluid, is suggested by the compositional similarity between dolomite types 1 and 2 and the obvious difference in crystal size. However, cation ordering as a thermodynamic drive cannot be completely discounted, since no detailed X-ray data are available.

#### ***5.2.6 Composition of dolomitizing and mineralizing fluids***

The high salinities in fluid inclusions of dolomite Type 3, sphalerite, and clear scalenohedral calcite cement (CSC) indicate that the dolomitizing and mineralizing fluids were highly saline (19 to 26 equiv. wt.-% NaCl). Furthermore, similar ranges of trace element concentrations of the three dolomite types, and average Fe/Mn ratios of about 5, suggest that the three dolomite types formed from fluids with similar trace element concentrations under relatively reducing conditions. Nevertheless, the petrographic, geochemical, isotopic and microthermometric data, the Sr-isotopic compositions of the investigated carbonate phases have been used to distinguish between 4 fluid flow events.

Fluid flow event #1 resulted in the dolomitization of limestone, and in the partial recrystallization of adjacent undolomitized limestone by a saline, hydrothermal fluid with a  $^{87}\text{Sr}/^{86}\text{Sr}$  ratio  $\geq 0.7094$  under reducing conditions. Fluid flow event # 2 resulted in the formation of dolomite Type 2 ( $^{87}\text{Sr}/^{86}\text{Sr} = 0.7085$  to  $0.7091$ ) via recrystallization of dolomite Type 1 ( $^{87}\text{Sr}/^{86}\text{Sr} = 0.7089$  to  $0.7094$ , decreasing with increasing degree of recrystallization) and the precipitation of dolomite Type 3 by a saline (25 equiv. wt. % NaCl), hydrothermal ( $105$  to  $120^\circ\text{C}$ ) fluid with a calculated  $\delta^{18}\text{O}$  value range ( $+0.6$  to  $+1.2$  ‰ SMOW) slightly above that of normal marine seawater ( $\delta^{18}\text{O} = 0$  ‰ SMOW), and  $^{87}\text{Sr}/^{86}\text{Sr}$  ratios between  $0.7085$  and  $0.7087$  under reducing conditions. No geochemical data on the subsequent sulfide minerals were obtained. The fluid inclusion data on one sphalerite sample is not sufficient to propose a separate fluid flow event for sulfide mineralization, although it may have taken place. The close association of sulfide mineralization with dolomite Type 3 and the fact that both dolomitization and sulfide precipitation require reducing conditions, may suggest that it formed in the late stages of fluid flow event # 2.

Fluid flow event # 3 led to the precipitation of the core of CSC from a saline (average





22 equiv. wt. % NaCl), hydrothermal (72 to 98 °C), and  $^{87}\text{Sr}/^{86}\text{Sr}$ -enriched fluid ( $^{87}\text{Sr}/^{86}\text{Sr} = 0.7106$ ) with a calculated  $\delta^{18}\text{O}$  value of +1.7 ‰ SMOW under relatively oxidizing conditions (Fe/Mn ratio < 1). Corrosion of dolomite and sulfide minerals, and the formation of limonite/goethite prior to or simultaneously with precipitation of the core of CSC can also be attributed to the oxidizing conditions during fluid flow event # 3. Finally, fluid flow event # 4 resulted in the precipitation of the Mn-poor/Fe-rich rim of CSC from a fluid with a  $^{87}\text{Sr}/^{86}\text{Sr}$  value of 0.7137 under relatively reducing conditions.

### 5.2.7 Origin of dolomitizing and mineralizing fluids

The relatively high Na concentrations of the dolomite types, highly saline inclusion fluids with complex compositions (Na-Ca-Mg-Cl), distinct Sr isotope compositions, and calculated O isotope compositions slightly above that of normal marine seawater, place certain constraints on the origin of the dolomitizing and mineralizing fluids (Table 5.1). At the time of dolomitization and mineralization in the Late Cretaceous/Early Tertiary, the fluids that were present in the area of the Brilon Reef Complex probably consisted of two

	Salinity (equiv. wt. % NaCl)	chemical composition	temperature (°C)	$^{87}\text{Sr}/^{86}\text{Sr}$	$\delta^{18}\text{O}$ ‰ SMOW calculated
dolomite Type 1	*similar to Types 2 and 3	**similar to Types 2 and 3	***> 50	$\geq 0.7094$	n.d.
dolomite Type 2 and 3	~ 25	Na-Mg-Ca-Cl	~ 110	~ 0.7086	~ +0.6 to +1.2
sphalerite	~ 21	Na-Mg-Ca-Cl	~ 100	n.d.	n.d.
CSC core	~ 22	Na-Mg-Ca-Cl	~ 80	0.7106	~ +1.7
CSC rim	n.d.	n.d.	n.d.	0.7137	

**Table 5.1:** Characteristics of dolomitizing and mineralizing fluids in the Brilon Reef Complex, based on petrographic, geochemical, and microthermometric data (Chapter 3). CSC = clear scalenohedral calcite cement; \* based on similar Na concentration of dolomites; \*\* based on similar major and minor element composition of dolomites; \*\*\* based on sub-to anhedral dolomite texture (crystal roughening temperature).



types: (1) Late Cretaceous seawater within the overlying Cretaceous sedimentary rocks and in the fault, fracture, and karst systems of the uppermost parts of the deformed Paleozoic bedrock, and (2) highly saline deeper groundwater that originated from the previous hydrogeological history of the area.

If the calculated, slightly enriched oxygen isotope values for the fluid that precipitated dolomite Type 3 and fracture- and vug-filling calcite cement (CSC) are taken as evidence for the involvement of slightly evaporated seawater, Cretaceous seawater is the only reasonable choice. Enrichment in  $^{18}\text{O}$  in seawater has been attributed to preferential removal of  $^{16}\text{O}$  due to evaporation and, therefore, is positively correlated with salinity (Faure 1990). For example, Craig (1966) found that an increase in salinity from 3.6 % to 4.1 % in the Red Sea corresponds to an increase in  $\delta^{18}\text{O}$  from +0.6 to +1.9 ‰ SMOW. However, considering the inferred high salinities of the dolomitizing and mineralizing fluids in the Brilon Reef Complex, the enrichment in  $^{18}\text{O}$  in the fluids is too small to be the result of evaporation of seawater. The slightly enriched oxygen isotope values for dolomite Type 3 and CSC more likely is the result of water-rock interaction of a groundwater of non-marine or more complex origin (e.g., Kharaka and Carothers 1986).

Late Cretaceous seawater acting as the sole dolomitizing fluid can also be ruled out by the high  $^{87}\text{Sr}/^{86}\text{Sr}$  values of the dolomite types compared to that of Late Cretaceous seawater ( $^{87}\text{Sr}/^{86}\text{Sr} = 0.7073$  to  $0.7078$ ; Burke et al. 1982). This, however, does not exclude the participation of Late Cretaceous seawater in the formation of a dolomitizing fluid via interaction with older siliciclastic sedimentary rocks (e.g., Paleozoic shales, sandstones, and greywackes) and mixing with  $^{87}\text{Sr}$ -enriched groundwater in the Paleozoic sedimentary succession.

The inferred differences in  $^{87}\text{Sr}/^{86}\text{Sr}$  ratios of the fluids, from which the three dolomite types and the core and rim of CSC formed, cannot be the result of mixing of a saline groundwater with a constant  $^{87}\text{Sr}/^{86}\text{Sr}$  ratio and different quantities of seawater, because seawater has a low Sr concentration (8 mg/l), and large amounts of seawater would be necessary to significantly influence the  $^{87}\text{Sr}/^{86}\text{Sr}$  ratios of the saline groundwaters. Furthermore, mixing with different quantities of seawater would result in vastly different salinities of the resulting mixtures, of which the most dilute one would be expected to have the lowest  $^{87}\text{Sr}/^{86}\text{Sr}$  ratio. For the samples investigated in this study, this is not the case (Table





5.1). Hence, the participation of Cretaceous seawater is not required to produce the calculated oxygen isotope composition and the measured  $^{87}\text{Sr}/^{86}\text{Sr}$  ratios. However, seawater may have been a source of Mg for dolomitization of the limestones in the Brilon Reef Complex.

The distinct Sr isotopic compositions of the dolomite types and the two growth phases of the subsequent fracture and vug-filling calcite cement (CSC) can be best explained by pulses of saline groundwaters with different  $^{87}\text{Sr}/^{86}\text{Sr}$  ratios. An episodic character of mineralization, especially during the Late Cretaceous/Early Tertiary, is further supported by regional fluid inclusion studies of the post-Variscan mineralization in the northeastern Rhenish Schiefergebirge (Behr and Horn 1984a and b; Behr and Gerler 1987; Behr et al. 1987). The variable  $^{87}\text{Sr}/^{86}\text{Sr}$  ratios of the fluids were most likely due to different migration pathways and/or different degrees of water-rock interaction. The mineralizing fluids are thought to have been derived from sedimentary brines that formed in the post-Variscan sedimentary troughs at the margins of the Rhenish Massif and descended into the Paleozoic basement, where they were heated and then re-ascended along faults, undergoing compositional changes due to water-rock interaction and mixing with other fluids on their way (Behr et al. 1987). Cooling, pressure decrease, water-rock interaction, and mixing with descending sulfate/bicarbonate waters probably led to precipitation of some of the solutes resulting in mineralizations (Skinner 1979, Behr and Gerler 1987). Tectonic (seismic) pumping (Sibson et al. 1975; Sibson 1994; Garven 1995), as a result of wrench tectonics, has been postulated as a mechanism to account for the episodic character of the post-Variscan mineralization in the northeastern Rhenish Schiefergebirge (Behr and Horn 1984a and b). Post-Variscan coalification anomalies (Kalkreuth 1979, Lommerzheim 1994) as well as geophysical anomalies in the northern Rhenish Massif, have been taken as evidence for the presence of deep-seated heat sources in the form of intrusions or mantle diapirs (Neugebauer et al. 1983), which could have triggered hydrothermal circulation of dolomitizing and ore forming fluids.

The influence of post-Variscan hydrothermal activity led to the thermal maturation of organic matter, which resulted in the generation of hydrocarbons (wet gases and condensates) (Lommerzheim 1994; Jochum 1998). The potential sources include Lower Devonian shales (Jochum et al. 1994) and Carboniferous coal-bearing strata (Lommerzheim 1994; Wellens 1997). These hydrocarbons may have acted as a reducing agent for the





reduction of sulphate in the metal-bearing hydrothermal solutions, thereby producing  $\text{H}_2\text{S}$  for base metal sulfide precipitation. Fluid inclusion homogenization temperatures of more than  $100^\circ\text{C}$  in sphalerite from the Brilon Reef Complex suggest thermochemical sulfate reduction (TSR) as the sulfate-reduction mechanism.

#### ***5.2.8 Origin and evolution of saline groundwaters in the Münsterland Cretaceous Basin***

The post-Variscan regional sedimentary and tectonic evolution in the northern Rhenish Massif and the adjacent Münsterland Cretaceous Basin is suggestive of a combination of tectonic pumping during phases of wrench tectonics and hydrothermal circulation due to increased heat flow as the means of long-distance fluid transport along fault and fracture systems. The hypothesis that the fault-controlled hydrothermal mineralization (including dolomitization) in the Brilon Reef Complex bears a genetic relationship to present-day saline groundwaters in the Münsterland Cretaceous Basin (MCB) was investigated in Chapter 4.

The present-day saline groundwaters in the MCB share three characteristics with the fluids that resulted in the dolomitization, minor base metal sulfide mineralization, and calcite cementation in the Brilon Reef Complex: (1) they are saline to highly saline (TDS up to 250000 mg/l), (2) they have the same range of Sr isotope compositions ( $^{87}\text{Sr}/^{86}\text{Sr} = 0.7084$  to  $0.7136$ ), and (3) they ascend on NNW-SSE trending faults. The data show that the present-day saline groundwaters in the MCB are the combined result of water-rock interaction, migration, and mixing of fluids of different origins. In particular, the data provide evidence for (1) subsurface dissolution of halite in the periphery of the MCB; (2) water-rock interaction of highly saline fluids with siliciclastic sediments in the Paleozoic bedrock; (3) mixing of highly saline fluids with less saline waters of marine isotopic compositions, (4) fault-controlled movement of warm saline  $^{87}\text{Sr}$ -enriched groundwaters from the Paleozoic bedrock into the overlying Late Cretaceous limestone aquifer; (5) water-rock interaction of ascending saline groundwater with the limestone aquifer; and (6) dilution by meteoric water. Integration of these findings into the regional paleohydrogeologic framework of the Münsterland Cretaceous Basin and the underlying Rhenish Massif suggests that halite dissolution, migration of saline groundwaters, water-rock interaction, and mixing of groundwaters of various origins and compositions must have taken place since the Late



Permian when extensive halite deposits formed in the periphery of the Rhenish Massif. Therefore, the highly saline fluids that resulted in the dolomitization and mineralization of the Brilon Reef Complex in the Late Cretaceous/Early Tertiary may have been derived from such a mixture. Different pathways and differences in water-rock interaction and fluid mixing during migration, hydrothermal circulation, and seismic pumping can account for the differences in the Sr-isotopic composition of the fluids. It is, however, important to point out, that the hydrochemical and isotopic data of the present-day saline groundwaters from the MCB show that parts of the regional aquifer in this basin and the underlying Paleozoic strata have been flushed by sub-recent meteoric water. Thus, these waters do not bear a direct genetic relationship with the fault-controlled hydrothermal mineralization in the Brilon Reef Complex. Consequently, the possibility that formation fluids from the MCB were driven into the Brilon Reef Complex to generate dolomites, sulfides, and calcites in the fracture systems remains elusive.

### **5.3 Comparison with other examples of dolomitization in Devonian carbonates**

Over the past few decades, numerous studies on the origin of dolostone have been carried out. These studies include local case studies, as well as studies on a regional scale. Although the basic requirements for the formation of dolostone are generally agreed upon (Morrow 1982; Machel and Mountjoy 1986, 1987), the plethora of publications and the controversial discussion of the various proposed models show that a variety of fluids, transport processes, and diagenetic settings can satisfy these requirements. To illustrate this point, the results of the investigation of selected examples of dolomitization of Devonian carbonates are summarized below and compared to the findings of this thesis.

#### ***5.3.1 Dornap Carbonate Complex, northern Rhenish Schiefergebirge, Germany***

Although dolomite has been described from almost all Devonian carbonate complexes in the northern Rhenish Schiefergebirge as part of the paragenetic succession (Krebs 1974), the only detailed study was carried out on dolostone bodies of the Dornap Carbonate Complex, which is located approximately 50 km west of the Brilon Reef Complex. Here, Leuchs (1985) studied the relationships between silicification,





dolomitization and lithofacies of Middle to Upper Devonian limestones. Locally, laterally extensive (ca. 1 km) dolostone bodies between 5 and 30 m in thickness occur at the base of the carbonate complex, which overlies basal shales. In the hanging wall, these dolostone bodies grade into isolated vertical dolostone bodies ranging in width from 10 to 20 m at the base to less than 1 m at the top. Within the vertical dolostone bodies Leuchs (1985) recognized three phases of silicification and one phase of dolomitization. One quartz generation formed prior to, one contemporaneously with, and one after dolomitization. While dolomite occurs as a, in many places fabric-destructive replacement of the limestone and previously formed quartz, the last generation of quartz also occurs as cement in pore spaces within the dolostone. Further mineral phases that are associated with the dolomite include pyrite and hematite as well as fracture- and void-filling calcite. The dolomite bodies follow NNW/SSE-trending tectonic joints that, according to Leuchs (1985), formed during the Variscan deformation and represent extensional features oriented perpendicular to the direction of tectonic compression. The amount of dolomite decreases from the base of the carbonate complex to the top corresponding with an increase in the amount of quartz. Both dolomite and quartz contents decrease with increasing distance from the joints.

Oxygen isotope compositions of the dolomite samples are depleted compared to that of the limestone host rock ( $\delta^{18}\text{O} = -6.5 \text{ ‰ PDB}$ ) and range from  $-8.5$  to  $-7.9 \text{ ‰ PDB}$  increasing slightly from the base to the top of the dolomite bodies. The carbon isotope compositions of the dolomite samples are similar to that of the limestone host rock. All three quartz generations show cathodoluminescence, which Leuchs (1985) interpreted as evidence for a hydrothermal origin. Differences in cathodoluminescence color and inclusion density of the quartz generations were attributed to differences in temperature and fluid composition, resulting in different growth rates.

Based on field investigations in limestone quarries, petrography, and stable isotope analysis, Leuchs (1985) suggested that silicification and dolomitization in the Dornap Reef Complex resulted from several phases of “ascending thermal fluids, possibly circulating deep groundwaters driven by hydrothermal convection cells”. Based solely on the association with the NNW/SSE-trending joints, he proposed a syn-Variscan timing. However, he did not present any data that would exclude a post-Variscan origin. More recent work on the structural geology of the Ruhr District by Drozdewski and Wrede (1994) indicates that many





of the NNW/SSE-trending structures have a much more complex post-Variscan history than previously thought. These authors strongly recommend that the timing of many of the supposedly syn-Variscan to early post-Variscan mineralizations associated with these faults needs to be reconsidered, because there is increasing evidence that these faults provided pathways for mineralizing fluids during the Mesozoic and Cenozoic, especially the Late Cretaceous and Early Tertiary. The finding of this thesis, i.e., that the fault-controlled dolomitization and associated sulfide mineralization in the Brilon Reef Complex is most like Late Cretaceous/Early Tertiary in age, corroborates the recommendation of Drozdewski and Wrede (1994).

Despite the disagreement on the timing of mineralization, Leuchs' (1985) interpretation of the origin and formation of the "vertical" dolostone bodies in the Dornap Carbonate Complex is similar in principle to that of this study on the dolostone intervals in the Brilon Reef Complex. However, saddle dolomite has not been reported from the Dornap Carbonate Complex.

### ***5.3.2 Western Canada Sedimentary Basin***

Amthor et al. (1993), Machel et al. (1994), and Mountjoy and Amthor (1994) provided the hitherto last of a series of synthesis on dolomitization of Devonian carbonates in the Western Canada Sedimentary Basin. Accordingly, dolomitization occurred in at least two main phases: 1) replacement dolomites that formed during early to intermediate burial (between 500 and 1500 m) and represent 80 to 90 % of all dolomites in the WCSB, and (2) minor coarse crystalline and saddle dolomite that formed from hydrothermal fluids (> 90°C) at greater depths (between 1500 and 3000 m or deeper). Dolomitization varies from partial to complete, and is fabric-destructive in most cases.

There also are cases of near-surface dolomitization by seawater or evaporated seawater. Such dolomitization is suggested by microcrystallinity (5-20 µm), mimetic textures, as well as marine carbon, oxygen, and strontium isotopic compositions (Martindale and Orr 1987; Theriault and Hutcheon 1987; Teare 1990; Martindale and MacDonald 1990; Qing 1991; Mountjoy and Halim-Dihardja 1991; Hübscher 1996).

The massive replacement dolomites from the Devonian of the Western Canada Sedimentary Basin typically are medium- to coarse-crystalline, subhedral to euhedral planar



mosaic dolomite and coarse-crystalline anhedral nonplanar dolomite. They crosscut depositional facies boundaries and postdate early-diagenetic features. Coarse-crystalline mosaic dolomites show relatively uniform petrography with mottled-red CL. They are significantly depleted in  $\delta^{18}\text{O}$  relative to hypothetical Upper Devonian marine dolomites ( $\delta^{18}\text{O} = -2.4$  to  $0$  ‰ PDB) and have slightly higher  $^{87}\text{Sr}/^{86}\text{Sr}$  ratios (0.7081-0.7094) than corresponding Devonian seawater. The paragenetic, petrographic, and geochemical data suggest that most of the replacement dolomites in the Upper Devonian carbonates of the Western Canada Sedimentary Basin formed from modified Devonian seawater during shallow to intermediate burial in the Devonian to Mississippian (see also: Mountjoy et al. 1992; Amthor et al. 1993; Dix 1993; Drivet and Mountjoy 1997; Wendte et al. 1998; Mountjoy and Green 1998).

Deeper-burial, coarse-crystalline dolomite cements occur as vug and fracture fillings in dolomitized and undolomitized limestones. These dolomite cements have high  $^{87}\text{Sr}/^{86}\text{Sr}$  ratios ( $> 0.7100$ ). Temperatures derived from fluid-inclusion microthermometry range from  $80^{\circ}\text{C}$  to  $200^{\circ}\text{C}$ , and salinity estimates range from 18 to 31 equivalent wt. % NaCl, respectively. In some cases, fluid inclusions indicate higher temperatures than expected from maximum burial, suggesting that hydrothermal formation waters moved along fractures and conduit systems. Some of these dolomites appear to be related to basin-wide fluid flow, probably caused by a combination of sedimentary and tectonic loading and topographically driven fluid flow during the Cretaceous and Early Tertiary (Mountjoy and Amthor 1994; Machel et al. 1996).

Wendte et al. (1998) proposed two phases of saddle dolomite formation in the Devonian Swan Hills Formation in the Wild River area, based on epifluorescence-defined stratigraphy and fluid inclusion homogenization temperatures: 1) an early phase in continuation of the early replacement dolomitization (Late Devonian to Early Carboniferous), and 2) a later phase during deep burial (Late Cretaceous to Eocene). For the early phase, Wendte et al. (1998) postulated a model of dolomitization invoking both seepage reflux and regional thermal convection of residual evaporitic brines (“thermoflux” dolomitization). Their interpretation of the timing of precipitation of the second-phase saddle dolomite cements in the Wild River area corresponds with that of Mountjoy and Amthor (1994).

In his recent review paper, Morrow (1998) cautions that the topographic recharge and





tectonic compaction models (Qing and Mountjoy 1992, 1994; Amthor et al. 1993; Drivet and Mountjoy 1997) may have been overapplied to the question of the origin of regionally extensive subsurface dolomite bodies. Topographic recharge has been shown to be extremely efficient at moving fluids and redistributing heat through foreland basins (Bethke et al. 1988; Garven et al. 1993; Garven 1995). On the other hand, the circulation of meteoric groundwater also results in the relatively quick replacement of the saline basinal fluids (Deming and Nunn 1991; Cathles 1993). The very high salinities of fluid inclusions in hydrothermal and associated subsurface dolomites, however, serve as an indication that there has been little, if any, admixture of meteoric water in the Devonian section of the Western Canada Sedimentary Basin (Morrow 1998). Morrow (1998) further argues that the topographic recharge model is not consistent with regional temperature trends derived from stable isotope and fluid inclusion homogenization temperature data (see also: Qing and Mountjoy 1992, 1994).

On the other hand, compaction flow by sedimentary (burial compaction; Machel and Mountjoy 1987) and tectonic loading (Oliver 1986; Amthor et al. 1993; Machel et al. 1996; Drivet and Mountjoy 1997) is consistent with the observed high salinities of fluid inclusions. This type of flow, however, is limited volumetrically and temporally, placing severe constraints on the amount of subsurface dolomite that can be formed. Furthermore, an extreme amount of focusing of flow would be required to satisfy thermal constraints (e.g., Cathles 1993).

The shortcomings of the topographic recharge and compaction flow models caused Morrow (1998) to suggest thermal convection initiated by high heat flow in late Paleozoic time as the driving force for regional subsurface dolomitization in the Western Canada Sedimentary Basin. His main arguments are:

- 1) thermal convection can support long-lived flow systems capable of circulating subsurface solutions many times through the rock mass, thereby satisfying mass balance, salinity, and thermal requirements;
- 2) during thermal convection in strata beneath the seabed, seawater could be continually added, thereby enhancing the dolomitization potential of the convection system;
- 3) crustal scale convection systems within subaerially exposed orogenic belts have been documented (Nesbitt and Muehlenbachs 1995);





4) both upward and downward extending bodies of hydrothermal dolomite have been documented in outcrop (Morrow et al. 1990, Morrow and Aulstead 1995).

Several authors (Aulstead and Spencer 1985; Aulstead et al. 1988; Packard et al. 1989; Morrow et al. 1990; Morrow and Aulstead 1995; Davies 1996; Wendte et al. 1998) postulated increased heatflow as a result of pre-Cordilleran thermal events, possibly coinciding with times of rifting. However, direct evidence of heat sources for regional thermal convection is lacking (Mountjoy and Green 1998).

Davies (1996) introduced the term hydrothermal dolomite reservoir facies (HTD-RF) for occurrences of dolomites composed of a large proportion of open space-filling dolospar cement (saddle dolomite) within breccia masses, fractures, or large vugs commonly associated with bodies of subsurface replacement dolomites. From his compilation of numerous case studies involving alleged hydrothermal dolomite from the Western Canada Sedimentary Basin and other parts of the world, he concluded that the occurrence of HTD-RF appears to be spatially and genetically linked to the presence of deep seated fault and fracture systems, often with strike-slip faults as a key component of the structural setting. Furthermore, he postulated that there is a close spatial and possibly a temporal linkage between HTD-hosted MVT deposits and sediment-hosted exhalative (Sedex) Pb-Zn ore bodies (Davies 1996), thereby favoring an early and relatively shallow burial emplacement. Recent discoveries of fault-controlled dolomitization in the Deep Basin of western Alberta (Green and Mountjoy 1997; Duggan 1997; Mountjoy and Green 1998) suggest that hydrothermal dolomitization and reservoir enhancement may have been more pervasive than previously thought (Berger and Davies 1999). The timing (early vs. late) and the nature of the fluid driving force (thermal convection vs. burial and tectonic compaction), however, are still being debated (Nesbitt and Prochaska 1998; Morrow 1998; Mountjoy and Green 1998; Berger and Davies 1999).

The above summary illustrates that the multitude of case studies from the Western Canada Sedimentary Basin provides a good basis for the development of various regional models. In the Rhenish Massif of Germany, there is no evidence for regionally extensive pervasive dolomitization of the Devonian carbonates. Dolomitization, however, is part of the regional post-Variscan mineral paragenesis (Schaeffer 1984, 1986) and, thus, must have been the result of regionally active processes. Unfortunately, with the exception of the Dornap and



Brilon Reef complexes, occurrences of dolostone in Devonian carbonates in the Rhenish Massif either have not been noted or have not been studied in more detail.

The dolostone intervals from the Brilon Reef Complex show striking textural similarities with many examples of dolostone from the Western Canada Sedimentary Basin. Similar to the major amount of dolostone in the Western Canada Sedimentary Basin, the petrographic, geochemical, and microthermometric data from the Brilon dolomites point to epigenetic dolomite formation at elevated temperatures from highly saline fluids. However, in contrast to many occurrences of dolostone in the Western Canada Sedimentary Basin, only a negligible amount of dolomite formed during shallow and deep burial. The bulk of the dolomite and associated sulfide mineralization clearly formed after the Variscan Orogeny and are spatially and genetically linked to deep reaching faults that have acted as pathways for dolomitizing and mineralizing fluids, probably during a distinct phase of wrench tectonics in the Late Cretaceous/Early Tertiary.

The relatively small volumes of dolostone in the Devonian carbonates of the Rhenish Massif do not place as stringent mass balance restrictions on the dolomitizing fluids and transport mechanism as do the large volumes of dolostone in the Western Canada Sedimentary Basin. Similar to the Western Canada Sedimentary Basin, dolomitizing and mineralizing fluids were highly saline, but an origin of the Brilon dolostone from evaporated Devonian seawater is highly unlikely, simply because the original formation waters very likely had been expelled during the Variscan deformation (Wedewardt 1995).

In contrast to the Western Canada Sedimentary Basin, in the area of the Northern Rhenish Massif there is evidence for increased heatflow and thermal anomalies during post-Variscan times, which are thought to have resulted in post-burial, post-tectonic coalification (Hoyer et al. 1974; Kalkreuth 1979; Lommerzheim 1994) and hydrothermal mineralization (Schaeffer 1984, 1986). Postulated deep-seated intrusions (Hoyer et al. 1974; Kalkreuth 1979; Schaeffer 1994, 1986) or a mantle plume (Neugebauer et al. 1983) may have triggered hydrothermal circulation of saline groundwater. The regional post-Variscan structural history of the Northern Rhenish Massif is characterized by fault activity due to distinct phases of extensional and transpressional tectonics related to the opening of the Atlantic Ocean and the Alpine Orogeny (Walther 1984; Schaeffer 1984, 1986; Drozdowski and Wrede 1994). Seismic pumping during the transpressional phase in the Late Cretaceous/Early Tertiary very





likely caused the episodic injection of mineralizing fluids along deep-reaching faults. A combination of seismic pumping and hydrothermal circulation therefore seems to be the most likely scenario for the fault-controlled dolomitization and associated mineralization of the Brilon Reef Complex.

The above shows, that differences in the sedimentary, diagenetic, structural, thermal, and hydrological evolution between the Western Canada Sedimentary Basin and the Rhenish Massif (including the overlying Münsterland Cretaceous Basin), make a direct comparison rather difficult. This stresses once more the point that occurrences of ancient dolostone have to be interpreted within their local and regional geologic and paleohydrogeologic context (e.g., Machel and Mountjoy 1986, 1987; Machel et al. 1994).

#### **5.4 Contributions to original knowledge**

This thesis study is the first study that focuses on the dolomitized intervals encountered in drill cores from the Devonian Brilon Reef Complex. Therefore, many aspects of this thesis constitute contributions to original knowledge. The following aspects are considered particularly noteworthy:

- (1) establishment of the first descriptive inventory of dolomitized intervals in drill cores from the Brilon Reef Complex (Appendices 1 and 2);
- (2) first representation of the spatial distribution of dolostone in the Brilon Reef Complex;
- (3) first study to investigate the relationships between dolomitization, sedimentary facies, diagenetic phases, and structural features in the Brilon Reef Complex;
- (4) recognition of a distinct facies change at the transition from the Givetian to the Frasnian, which may prove useful in future attempts of stratigraphic correlation across the Brilon Reef Complex;
- (5) recognition of fault- and fracture control of dolomitization in the subsurface;
- (6) refutation of the hypothesis that the largest volume of dolostone in the Brilon Reef Complex is concentrated at the reef margins;
- (7) establishment of a hydrothermal origin of dolomitization, limestone recrystallization, dolomite recrystallization, dolomite cementation, sulfide mineralization, calcitization, and calcite cementation in the investigated core intervals from the Brilon Reef Complex;





- (8) petrographic and geochemical evidence for significant recrystallization of undolomitized limestone and matrix dolomite;
- (9) identification of at least four fluid flow events that resulted in the textural and mineralogical changes mentioned in (8), based on petrographic, geochemical, and microthermometric data;
- (10) proposal of a dolomitization model invoking fault-controlled, episodic ascent and circulation of saline, hydrothermal fluids with distinct Sr-isotopic compositions, and mixing with descending marine-derived pore waters during the Late Cretaceous/Early Tertiary;
- (11) recognition of a marine (probably Cretaceous) water component, an “old” (probably Tertiary) meteoric water component, and a sub-recent to recent meteoric water component in the saline groundwaters from the Münsterland Cretaceous Basin from stable isotope compositions (D and O);
- (12) Sr-isotope evidence for ascending highly saline,  $^{87}\text{Sr}$ -enriched groundwaters along faults and water-rock interaction with marine Upper Cretaceous limestones in the Münsterland Cretaceous Basin;
- (13) refutation of the hypothesis that the present-day saline groundwaters in the Münsterland Cretaceous Basin bear a direct genetic relationship to the fault- and fracture-controlled mineralization (including dolomitization) in the Brilon Reef Complex.

## 5.5 Future work

Future work on the Devonian carbonates of the Brilon Reef Complex should address the lingering problem of stratigraphic correlation. Stratigraphic correlation is needed to be able to assess the direction and amount of synsedimentary tectonic movements along the NNW-SSE trending faults. This may be achieved using a combination of detailed structural analysis and possibly a sequence stratigraphic approach integrating subsurface and outcrop data. Furthermore, the volcanic activity that occurred during reef growth may have resulted in the deposition of distinct layers of volcanogenic material (tuffs, bentonites). Thin clay layers and shale partings displaying a variety of colors (black, grey, green, beige, brown, red) are relatively common within the carbonates of the Brilon Reef Complex, and a detailed investigation of their mineralogy and geochemistry may provide clues to their origin(s).

The investigation of the stable and radiogenic isotope and the geochemical



compositions of the carbonate phases carried out for this thesis project focused only on a few dolostone intervals from the Brilon Reef Complex. The analysis of more samples is needed to be able to establish geochemical trends for the post-Variscan dolomitization, host-rock alteration and sulfide mineralization. Further microthermometric work on fluid inclusions in saddle dolomite, sphalerite, and late calcite cements on a larger number of samples may provide a more detailed picture of the temperatures and compositions of the dolomitizing and mineralizing fluids. Isotopic and chemical analysis of the inclusion fluids (Yang et al. 1995; Nesbitt and Prochaska 1998) would aid in further delineating the origin and evolution of the dolomitizing and mineralizing fluids beyond the partially speculative interpretations that are presented in this thesis.

The analysis of hydrocarbons within fluid inclusions in saddle dolomites and sphalerites may shed some light on the nature and origin of the reducing agent for the reduction of sulfate in the metal-bearing hydrothermal solution producing  $H_2S$  for base metal sulfide precipitation (Jochum et al. 1995; Jochum 1998).

The age of dolomitization and sulfide mineralization in the Brilon Reef Complex has been constrained to the Late Cretaceous/Early Tertiary by integration into the regional paragenetic sequence. To further support this claim, radiometric age dating of sphalerite from the dolostone intervals of the Brilon Reef Complex using the Rb-Sr system (Nakai et al. 1993) is suggested.

A detailed regional investigation of fault-controlled hydrothermal fluid events in the northeastern Rhenish Schiefergebirge and Münsterland Cretaceous Basin, providing a larger database of chemical data on carbonate and sulfide minerals as well as on paleo- and recent fluids, is required to determine if the results of this study have more than local implications for the formation and distribution patterns of dolostone and associated base metal sulfide mineralization.





## 5.6 References

- Allan, J.R., and Wiggins, W.D., 1993, Dolomite reservoirs. Geochemical techniques for evaluating origin and distribution. American Association of Petroleum Geologists, Continuing Education Course Notes, 26, 129 p.
- Amthor, J.E., Mountjoy, E.W., and Machel, H.G., 1993, Subsurface dolomites in the Upper Devonian Leduc Formation buildups, central part of Rimbey-Meadowbrook reef trend, Alberta, Canada. *Bulletin of Canadian Petroleum Geology*, 41, p. 164-185.
- Aulstead, K.L. and Spencer, R.J., 1985, Diagenesis of the Keg River Formation, northwestern Alberta: Fluid inclusion evidence. *Bulletin of Canadian Petroleum Geology*, 33, p. 167-183.
- Aulstead, K.L., Spencer, R.J., and Krouse, H.R., 1988, Fluid inclusion and isotopic evidence on dolomitization, Devonian of western Canada. *Geochimica et Cosmochimica Acta*, 52, p. 1027-1035.
- Behr, H.J. and Horn, E.E., 1984a, Quarzbildung und Verkieselungsprozesse in den Karbonatkomplexen des Rheinischen Schiefergebirges. In: *Postvaristische Gangmineralisationen in Mitteleuropa*. Gesellschaft Deutscher Metallhütten-Bergleute, 41, p. 27-45.
- Behr, H.J. and Horn, E.E., 1984b, Unterscheidungskriterien für Mineralisationen des variskischen und postvariskischen Zyklus, die aus der Analyse fluider Einschlüsse gewinnbar sind. *Gesellschaft Deutscher Metallhütten-Bergleute*, 41, p. 255-270.
- Behr, H.J. and Gerler, J., 1987, Inclusions of sedimentary brines in post-Variscan Mineralizations in the Federal Republic of Germany - A Study by neutron activation analysis. *Chemical Geology*, 61, p. 65-77.
- Behr, H.J., Horn, E.E., Frentzel-Beyme, K., and Reutel, Chr., 1987, Fluid inclusion characteristics of the Variscan and post-Variscan mineralizing fluids in the Federal Republic of Germany. *Chemical Geology*, 61, p. 273-285.
- Berger, Z. and Davies, G.R., 1999, The development of linear hydrothermal dolomite (HTD) reservoir facies along wrench or strike slip fault systems in the Western Canadian Sedimentary Basin. *Canadian Society of Petroleum Geologists Bulletin*, 26, p. 34-38.
- Bethke, C.M., Harrison, W.H., Upson, C., and Altaner, S.P., 1988, Supercomputer analysis of sedimentary basins, *Science*, 239, p. 261-267.
- Burke, W.H., Denison, R.E., Hetherington, E.A., Koepnick, R.B., Nelson, H.F., and Otto, J.B., 1982, Variation of seawater  $^{87}\text{Sr}/^{86}\text{Sr}$  throughout Phanerozoic time. *Geology*, 10, p. 516-519.
- Cathles, L.M., 1993, A discussion of flow mechanisms responsible for alteration and mineralization in the Cambrian aquifers of the Ouachita-Arkoma basin-Ozark system. In: *Horbury, A.D. and Robinson, A.G. (eds.), Diagenesis and Basin Development*, American Association of Petroleum Geologists, AAPG Studies in Geology, 36, p. 99-112.





- Craig, H., 1966, Isotopic composition and origin of the Red Sea and Salton Sea geothermal brines. *Science*, 154, p. 1544-1548.
- Davies, G.R., 1996, Hydrothermal dolomite reservoir facies. *Canadian Society of Petroleum Geologists, Short Course book*, 167 p.
- Deming, D. and Nunn, J.A., 1991, Numerical simulations of brine migration by topographically driven recharge. *Journal of Geophysical Research*, 96, p. 2485-2499.
- Dix, G., 1993, Patterns of burial- and tectonically controlled dolomitization in an Upper Devonian Fringing-Reef complex: Leduc Formation, Peace River Arch area, Alberta, Canada.
- Drivet, E. and Mountjoy, E.W., 1997, Dolomitization of the Leduc Formation (Upper Devonian), southern Rimbey-Meadowbrook Reef Trend, Alberta. *Journal of Sedimentary Research*, 67, p. 411-423.
- Duggan, J.P., 1997, Sedimentology and diagenesis of Swan Hills Simonette oil field, west-central Alberta basin: M.Sc.thesis, McGill University, Montreal, 177p.
- Faure, G., 1990, *Principles of isotope geology*. 589 p.
- Folk, R.L., 1965, Some aspects of recrystallization in ancient limestones. In: Pray, L.C. and Murray, R.C., *Dolomitization and Limestone Diagenesis*, Society of Economic Paleontologists and Mineralogists Special Publication, 13, p. 14-48.
- Füchtbauer, H. and Richter, D.K., 1983, Relations between submarine fissures, internal breccias and mass flows during Triassic and earlier rifting periods. *Geologische Rundschau*, 72, p. 53-66.
- Garven, G., 1995, Continental-scale groundwater flow and geologic processes. In: Wetherill, G.W., Albee, A.L. and Burke, K.C. (eds.), *Annual Review of Earth and Planetary Sciences*, 23, p.89-118.
- Garven, G., Ge, S., Person, M.A., and Sverjensky, D.A., 1993, Genesis of stratabound ore deposits in the midcontinent basins of North America. 1. The role of regional groundwater flow. *American Journal of Science*, 293, p. 497-568.
- Green, D.G. and Mountjoy, E.W., 1997, Possible fault-fracture controlled dolomitization of the West-Central Alberta Deep Basin; Pine Creek (Leduc Fm., Wabamun Fm.) and Kaybob South (Swan Hills Fm.). Program with Abstracts, Canadian Society of Petroleum Geologists – Society of Economic Paleontologists and Mineralogists 1997 Joint Convention, June 1-6, 1997, Calgary.
- Gregg, J.M. and Sibley, D.F., 1984, Epigenetic dolomitization and the origin of xenotopic dolomite texture. *Journal of Sedimentary Petrology*, 54, p. 908-931.
- Hoyer, P., Clausen, C.-D., Leuteritz, K., Teichmüller, R., and Thome, K. N., 1974, Ein Inkohlungsprofil zwischen dem Gelsenkirchener Sattel des Ruhrkohlenbeckens und dem Ostsauerländer Hauptsattel des Rheinischen Schiefergebirges. *Fortschritte in der Geologie von Rheinland und Westfalen*, 24, p. 161-172.



- Huebscher, H., 1996, Regional controls on the stratigraphic and diagenetic evolution of the Woodbend Group Carbonates, North-central Alberta, Canada. Unpublished Ph.D. thesis, University of Alberta. 231 p.
- Jochum, J., 1998, Die Bedeutung von Kohlenwasserstoffen bei der Bildung hydrothermaler Buntmetallvorkommen – Neue Modelle zur Genese am Beispiel variskischer und postvariskischer Lagerstätten des Rhenischen Schiefergebirges. Habilitation thesis, Technical University Aachen, 153 p.
- Jochum, J., Friedrich, G., Germann, A., Horsfield, B., Leistner, F., and Pickel, W., 1994, Origin and chemistry of hydrocarbons in ore minerals of the Triassic sandstone-hosted lead-zinc deposits Maubach and Mechernich, Germany. In: Foster, R.P. (ed.), Abstracts Volume, Economic Geology in Europe and Beyond II with special reference to Models for Mineral Deposits in Sedimentary Basins, April 13-14, 1994, Keyworth, Nottingham, England, p. 25-27.
- Jochum, J. Germann, A., Friedrich, G., Horsfield, B., and Pickel, W., 1995, Mechanical decrepitation coupled with gas chromatography – a new method for the determination of hydrocarbons in ore minerals.
- Kalkreuth, W., 1979, Das Inkohlungsbild des Ostsauerländer Hauptsattels im rheinherzynikum mit besonderer Berücksichtigung der Trennflächenanalyse. - Fortschritte der Geologie von Rheinland und Westfalen, 27, p. 227 - 321.
- Kharaka, Y.K. and Carothers, W.W., 1986, Oxygen and hydrogen isotope geochemistry of deep basin brines. In: Fritz, P. and Fontes, J.Ch., Handbook of Environmental Isotope Geochemistry, 2, p. 305-360.
- Leuchs, W., 1985, Beziehungen zwischen Verquarzung und Dolomitisierung der devonischen Riffkalke von Dornap bei Wuppertal. Neues Jahrbuch der Geologie und Paläontologie, Monatshefte, 1985, p. 129-152.
- Lommerzheim, A. J. (1994), Genese und Migration der Erdgase im Münsterländer Becken. - Fortschritte in der Geologie von Rheinland und Westfalen, 38, p. 309-348.
- Machel, H.G., 1987, Saddle dolomite as a by-product of chemical compaction and thermochemical sulfate reduction. Geology, 15, p. 936-940.
- Machel, H.G., 1990a, Submarine Frühdiagenese, Spaltenbildungen und prätektogenetische Spätdiagenese des Briloner Riffs. Geologisches Jahrbuch, D95, p. 85-137.
- Machel, H.G., 1997, Recrystallization versus neomorphism, and the concept of 'significant recrystallization' in dolomite research. Sedimentary Geology, 113, p. 161-168.
- Machel, H. G. and Mountjoy, E. W., 1986, Chemistry and environments of dolomitization - a reappraisal. - Earth Science Reviews, 23, p. 175-222.
- Machel, H.G., and Mountjoy, E.W., 1987, General constraints on extensive pervasive dolomitization - and their application to the Devonian carbonates of western Canada. Bulletin of Canadian Petroleum Geology, 35, p. 143-158.





- Machel, H.G., Mountjoy, E.W., and Amthor, J.E., 1994, Dolomitization of Devonian Riff- and Plattformkarbonaten in West-Kanada. *Zentralblatt für Geologie und Paläontologie*, Teil I, 1993, h.7/8, p. 941-957.
- Machel, H.G., Cavell, P.A., and Patey, K.S., 1996, Isotopic evidence for carbonate cementation and recrystallization, and for tectonic expulsion of fluids into the Western Canada Sedimentary Basin. *Geological Society of America, Bulletin*, 108, p. 1108-1119.
- Martindale, W. and Orr, N.E., 1987, Middle Devonian Winnipegosis reefs in the Tablelands area, S.E. Saskatchewan. *Second International Symposium on the Devonian System, Canadian Society of Petroleum Geologists, Program with Abstracts*, p. 156.
- Martindale, W. and MacDonald, R.W., 1990, Sedimentation and diagenesis of the Winnipegosis Formation, Tableland area, southeast Saskatchewan. In: Bloy, G.R. and Hadley, M.G., *The Development of Porosity in Carbonate Reservoirs*, Canadian Society of Petroleum Geologists, Short Course Notes, Section 6, p. 6-1 to 6-19.
- Morrow, D. W., 1982, Diagenesis 2. Dolomite - Part 2: Dolomitization models and ancient dolostones. *Geoscience Canada*, 9, p. 95-107.
- Morrow, D.W., 1998, Regional Subsurface Dolomitization: Models and Constraints. *Geoscience Canada*, 25, p. 57-70.
- Morrow, D.W., Cumming, G.L., and Aulstead, K.L., 1990, The gas-bearing Devonian Manatoc facies, Yukon and Northwest Territories. *Geological Survey of Canada, Bulletin* 400, 54 p.
- Morrow, D.W. and Aulstead, K.L., 1995, The Manatoc dolomite: A Cretaceous-Tertiary or a Paleozoic event? Fluid inclusion and isotopic evidence. *Bulletin of Canadian Petroleum Geology*, 43, p. 267-280.
- Mountjoy, E.W., 1994, Dolomitization and the character of hydrocarbon reservoirs: Devonian of western Canada. In: Parker, A. and Sellwood, B.W. (eds.), *Quantitative Diagenesis: Recent Developments and Applications to Reservoir Geology*, p. 33-94.
- Mountjoy, E.W. and Halim-Dihardja, M., 1991, Multiple phase fracture and fault-controlled burial dolomitization, Upper Devonian Wabamun Group, Alberta. *Journal of Sedimentary Petrology*, p. 590-612.
- Mountjoy, E.W. and Amthor, J.E., 1994, Has burial dolomitization come of age? Some answers from the Western Canada Sedimentary Basin. - *Special Publications of the International Association of Sedimentologists*, 21, p. 203-229.
- Mountjoy, E.W. and Green, D., 1998, Burial diagenesis and dolomitization in the Western Canada Sedimentary Basin: early due to thermal convection or late due to progressive heating during burial? In: *Fluid Flow in Carbonates: Interdisciplinary Approaches*. Society of Economic Paleontologists and Mineralogists Research Conference, September 20-24, 1998. Door County, Wisconsin.





- Mountjoy, E.W., Qing, H., and McNutt, R.H., 1992, Sr isotopic composition of Devonian dolomites, Western Canada Sedimentary Basin: significance of sources of dolomitizing fluids. *Applied Geochemistry*, 7, p. 59-75.
- Nakai, S., Halliday, A.N., Kesler, S.E., Jones, H.D., Kyle, J.R., and Lane, T.E., 1993, Rb-Sr dating of sphalerites from Mississippi Valley-Type (MVT) ore deposits. *Geochimica et Cosmochimica Acta*, 57, p. 417-427.
- Nesbitt, B.E. and Muehlenbachs, K., 1995, Geochemical studies of the origins and effects of synorogenic crustal fluid in the southern Omineca Belt of British Columbia, Canada. *Geological Society of America, Bulletin* 107, p. 1033-1050.
- Nesbitt, B.E., and Prochaska, W., 1998, Solute chemistry of inclusion fluids from sparry dolomitites and magnesites in Middle Cambrian carbonate rocks of the southern Canadian Rocky Mountains. *Canadian Journal of Earth Sciences*, 35, p. 546-555.
- Neugebauer, H.-J., Woidt, W.-D., and Wallner, H., 1983, Uplift, volcanism and tectonics: evidence for mantle diapirs at the Rhenish Massif. In: Fuchs, K., von Gehlen, K., Mälzer, H., Murawski, H., and Semmel, H. (eds.), *Plateau uplift*, pp. 509-567.
- Oliver, J., 1986, Fluids expelled tectonically from orogenic belts: their role in hydrocarbon migration and other geologic phenomena. *Geology*, 14, p. 99-102.
- Packard, J.J., Pellegrin, G.J., Al-Asam, I.S., Samson, I., and Gagnon, J., 1989, Diagenesis and dolomitization associated with hydrothermal karst in Famennian upper Wabamun ramp sediments, northwestern Alberta. In: Bloy, G., Hadley, M.B., and Cutic, B.V. (eds.), *The development of porosity in carbonate reservoirs*, Canadian Society of Petroleum Geologists, Short Course, p. 54-72.
- Perkins, R.D., Dwyer, G.S., Rosoff, D.B., Fuller, J., Baker, P.A., and Lloyd, R.M., 1994, Saline sedimentation and diagenesis: West Caicos Island, British West Indies. In: Purser, B., Tucker, M., and Zenger, D. (eds.), *Dolomites - A Volume in Honour of Dolomieu*, International Association of Sedimentologists, Special Publication 21, p. 37-54.
- Qing, H., 1991, Diagenesis of Middle Devonian Presqu'ile Dolomite, Pine Point NWT and Adjacent Subsurface. Ph.D. Thesis, McGill University, 287 pp.
- Radke, B.M. and Mathis, R.L., 1980, On the formation and occurrence of saddle dolomite. *Journal of Sedimentary Petrology*, 50, p. 1149-1168.
- Schaeffer, R., 1984, Die postvariszische Mineralisation im nordöstlichen Rheinischen Schiefergebirge. Braunschweiger geologisch-paläontologische Dissertationen, 3, 206 pp.
- Schaeffer, R., 1986, Geochemische Charakteristika und Genese der jungmesozoisch-tertiären Vererzung im Sauerland (Rheinisches Schiefergebirge). *Fortschritte in der Geologie von Rheinland und Westfalen*, 34, p. 337-381.
- Sibley, D. F. and Gregg, J. M., 1987, Classification of dolomite rock textures. *Journal of Sedimentary Petrology*, 57, p. 967-975.



- Sibson, R.H., Moore, J.M.C.M., Rankin, A.H., 1975, Seismic pumping - a hydrothermal fluid transport mechanism. *Journal of the Geological Society London*, 131, p. 653-659.
- Sibson, R.H., 1994, Crustal stress, faulting and fluid flow. In: Parnell, J. (ed.), *Geofluids: origin, migration and evolution of fluids in sedimentary basins*, Geological Society Special Publication London, 78, p. 69-84.
- Skinner, B.J., 1979, The many origins of hydrothermal mineral deposits. In Barnes, H.L. (ed.), *Geochemistry of hydrothermal ore deposits*, p. 1-21.
- Theriault, F. and Hutcheon, I., 1987, Dolomitization and calcitization of the Upper Devonian Grosmont Formation, Northern Alberta. *Journal of Sedimentary Petrology*, 57, p. 955-966.
- Teare, M., 1990, Sedimentology and Diagenesis of Middle Devonian Winnipegosis Reef Complexes, Dawson Bay, Manitoba. M.Sc. Thesis, McGill University, Montreal, 150 pp.
- Walther, H.W., 1984, Alter, Genese und wirtschaftliche Bedeutung der postvaristischen Gangmineralisation in Mitteleuropa – eine Einführung. *Schriftenreihe der Gesellschaft Deutscher Metallhütten-Bergleute* 41, 1-12.
- Wedewardt, M., 1995, Hydrochemie und Genese der Tiefenwässer im Ruhr-Revier. *DMT-Berichte aus Forschung und Entwicklung*, 39, 250 p.
- Wellens, M., 1997, Genese und Migration von Kohlenwasserstoffen in paläozoischen Sedimentgesteinen am Nordrand des Linksrheinisch-Ardennischen Schiefergebirges. *Aachener Geowissenschaftliche Beiträge* 24, 280 p.
- Wellens, M. and Jochum, J., 1995, Evidence for hydrocarbon migration during Variscan and post-Variscan time in the western Rhenish Massif (Rheinisches Schiefergebirge). In: Mann, U., Poelchau, H.S., Steingrobe, B., Muller, A. (eds.), *Proceedings of the 10<sup>th</sup> Annual Meeting of the Aachen Sedimentology Group*, October 11-13, 1995, Aachen, p.125-130.
- Wendte, J., Qing, H.; Dravis, J.J., Moore, S.L.O., Stasiuk, L.D., and Ward, G., 1998, High-temperature saline (thermofluid) dolomitization of Devonian swan Hills platform and bank carbonates, Wild River area, west-central Alberta. *Bulletin of Canadian Petroleum Geology*, 46, p.210-265.
- Yang, W., Spencer, R.J., and Krouse, H.R., 1995, Stable isotope and major element compositions of fluid inclusions in Devonian and Cambrian dolomite cements, western Canada. *Geochimica et Cosmochimica Acta*, 59, 15, p. 3159-3172.



## APPENDIX 1

Schematic lithologs, gamma-ray curves, carbonate facies and stratigraphy of the investigated drill cores from the Brilon Reef Complex (in alphabetical order). Hardcopies of the gamma-ray curves were obtained from the archives of the “Bundesanstalt für Geowissenschaften und Rohstoffe”, Hannover, Germany. Drill cores were investigated at a meter-scale with respect to their gross facies distribution within the so-called “Massenkalk” using the carbonate facies model for Middle to Upper Devonian shallow-marine carbonates by Machel and Hunter (1994); see also Chapter 3, Figure 2.3. Different shades of grey in the carbonate facies column represent black to dark grey (dark shade of grey), medium grey (medium shade of grey), and light grey (light shade of grey) color of carbonate rock. For lithologic patterns, symbols, and abbreviations, refer to legend on the next page. Black bars to the right of the litholog indicate the position and vertical extent of dolostone.

### References

Machel, H. G. and Hunter, I. G., 1994, Facies Models for Middle to Late Devonian Shallow-marine Carbonates, with Comparisons to Modern Reefs: a Guide for Facies Analysis. *Facies*, 30, p. 155-176.



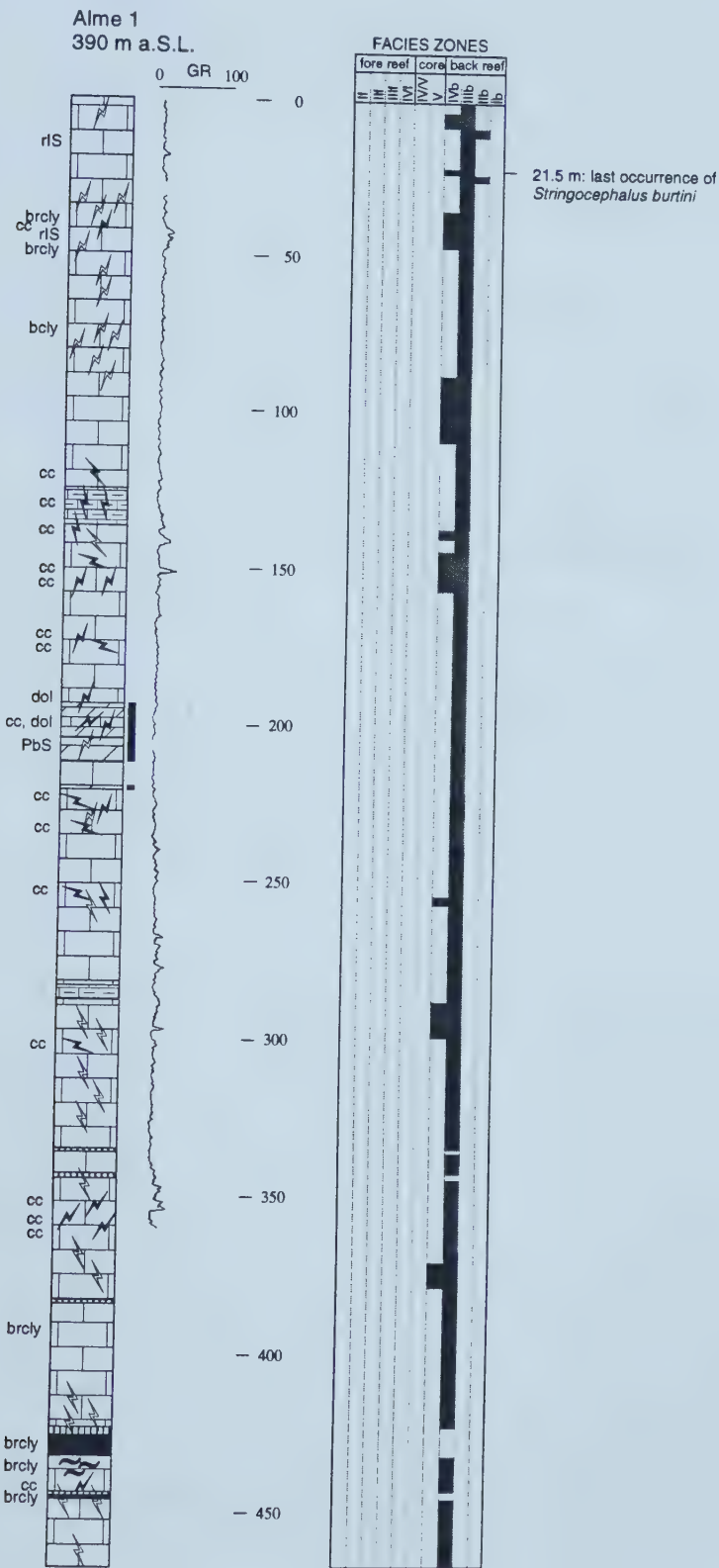


LITHOLOGY	SYMBOLS	ABBREVIATIONS
limestone		
marly limestone		
nodular limestone		
carbonaceous shale		
silty shale		
shale		
dolostone		
dolomitic limestone		
dolostone with limestone relics		
limestone breccia		
limestone breccia (matrix dolomitized)		
dolostone breccia		
dolostone breccia (matrix calcitic)		
"Schalstein" (volcanic tuff & carbonate detritus)		
massive diabase		
massive fracture filling calcite		
no recovery		
	 subhorizontal fracture (open)	
	 inclined fracture (filled)	
	 subvertical fracture (unfilled)	
	 irregular cavity (filled)	
		lim PbS py qtz r rs styl ZnS
		limonite galena pyrite quartz red red shale stylolites sphalerite
		b bg br brec cc cly dol g gr hem IS
		black beige brown breccia calcite clay dolomite grey green hematite internal sediment

Appendix 1: Legend

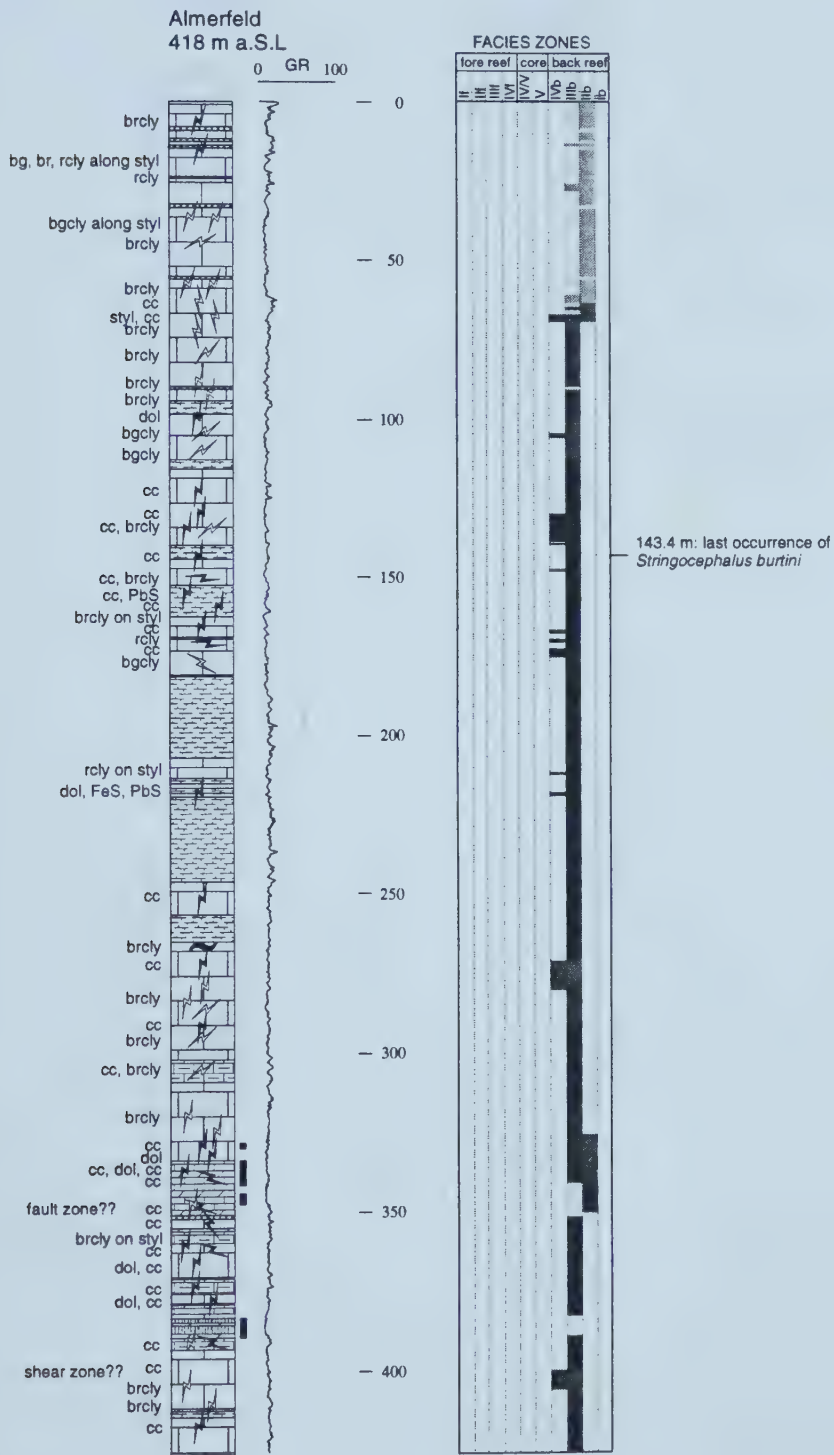


**Appendix 1:** schematic lithologs, gamma-ray curves, carbonate facies, and stratigraphy of Brilon drill cores: Alme 1 (A1) drill core.





## Appendix 1 continued: Almerfeld (AL) drill core.

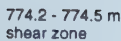


continued on next page



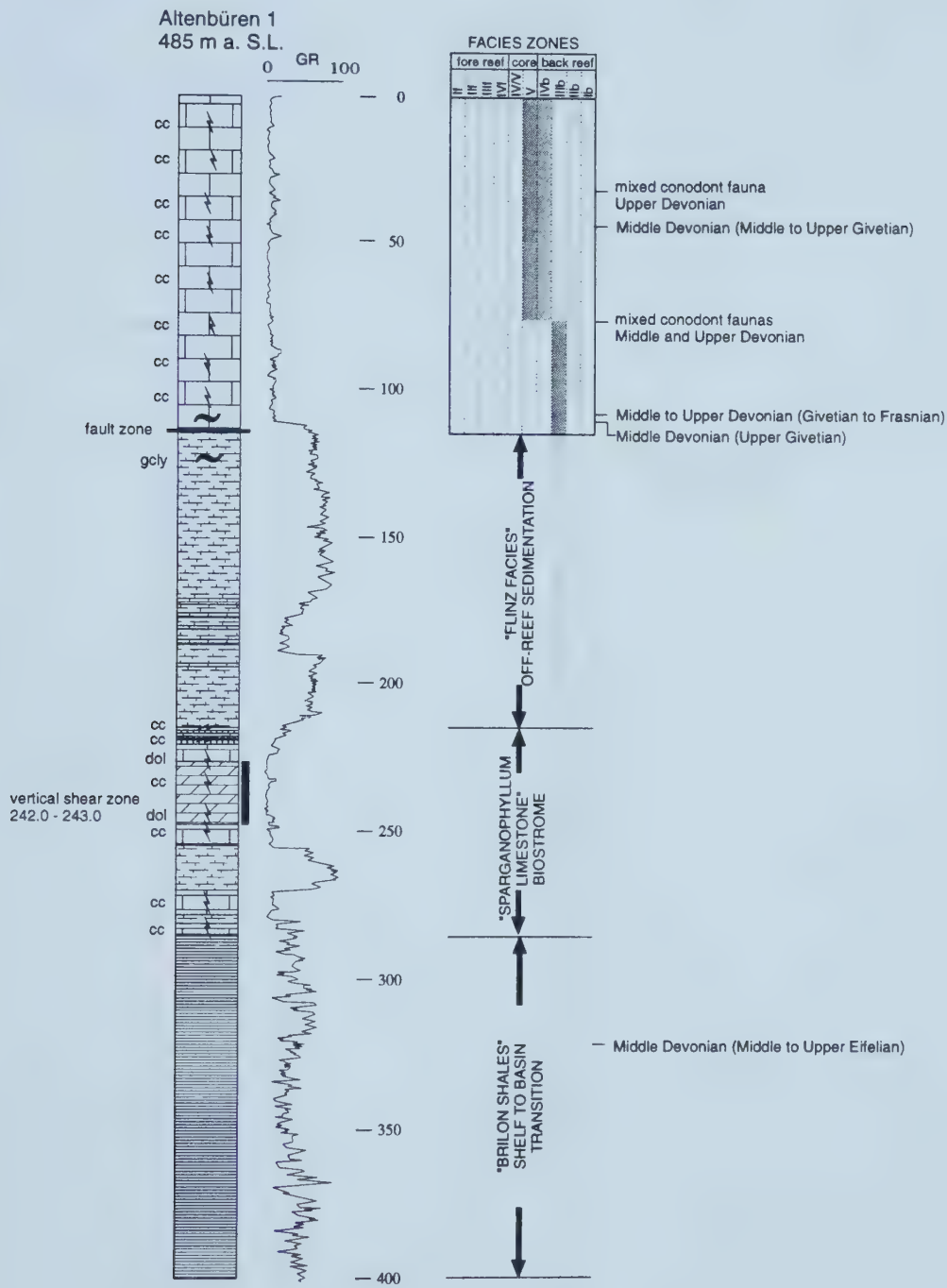


## Appendix 1 continued: Almerfeld (AL) drill core continued.



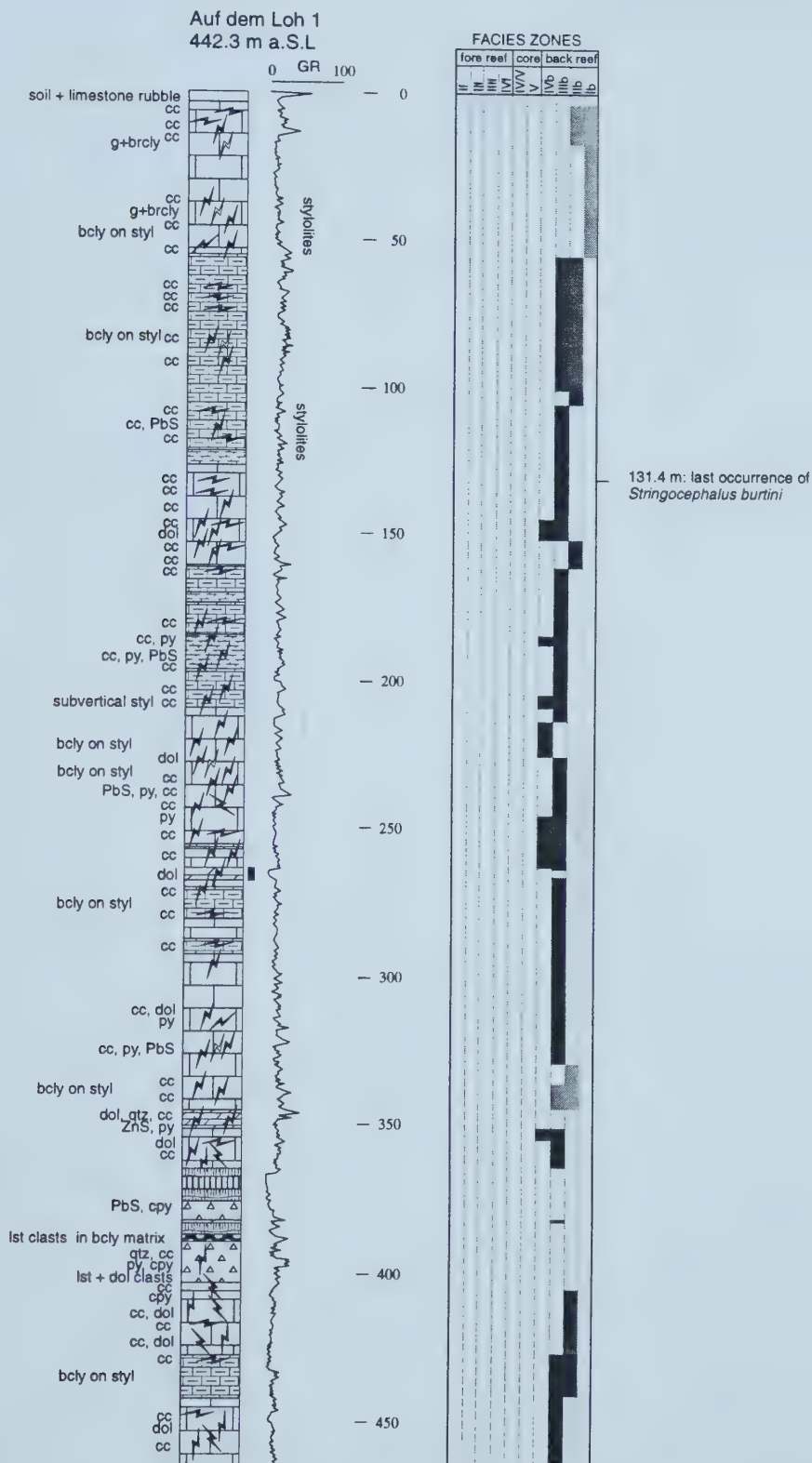


## Appendix 1 continued: Altenbüren 1 (AB1) drill core.





## Appendix 1 continued: Auf dem Loh 1 (L1) drill core.

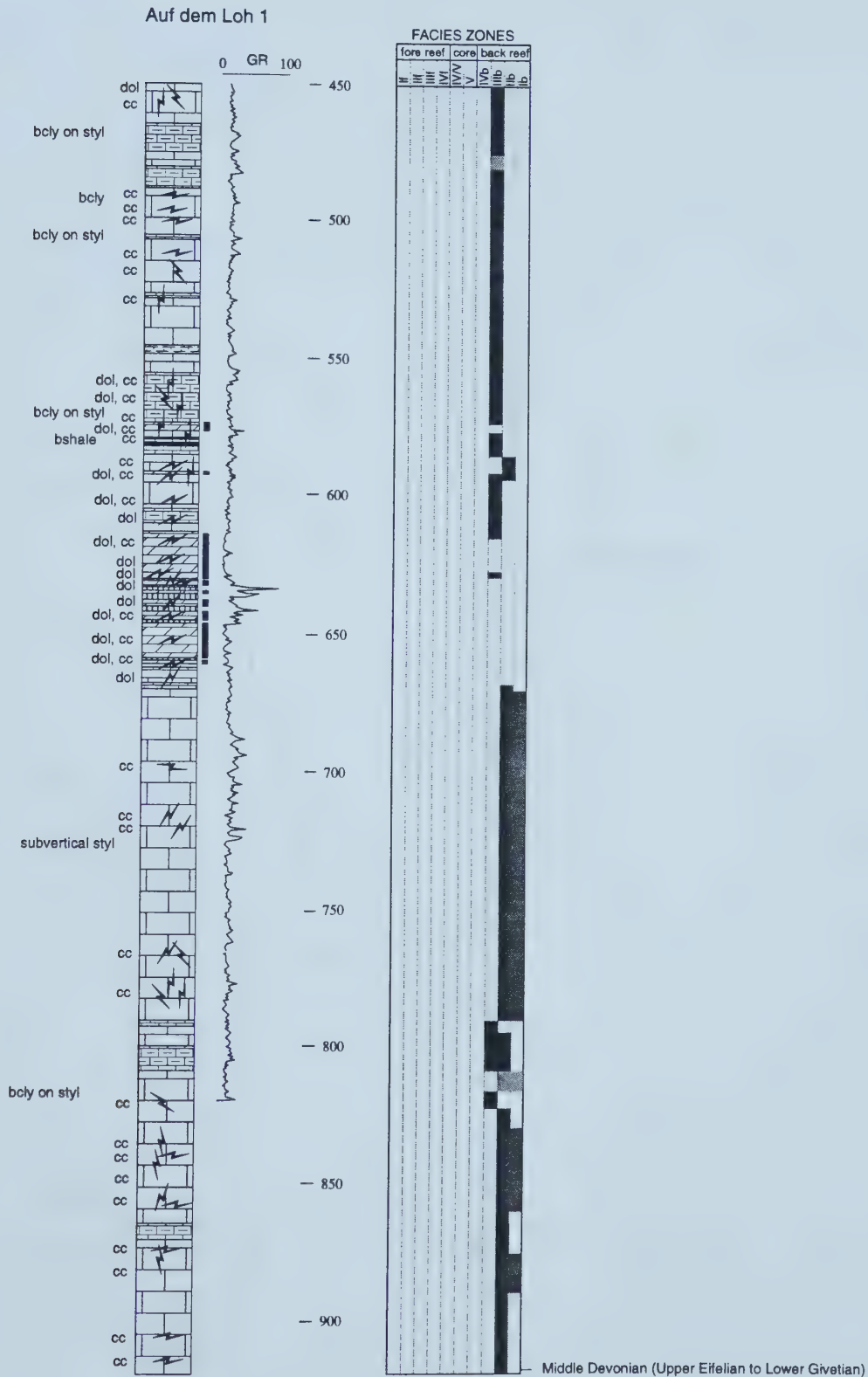


continued on next page



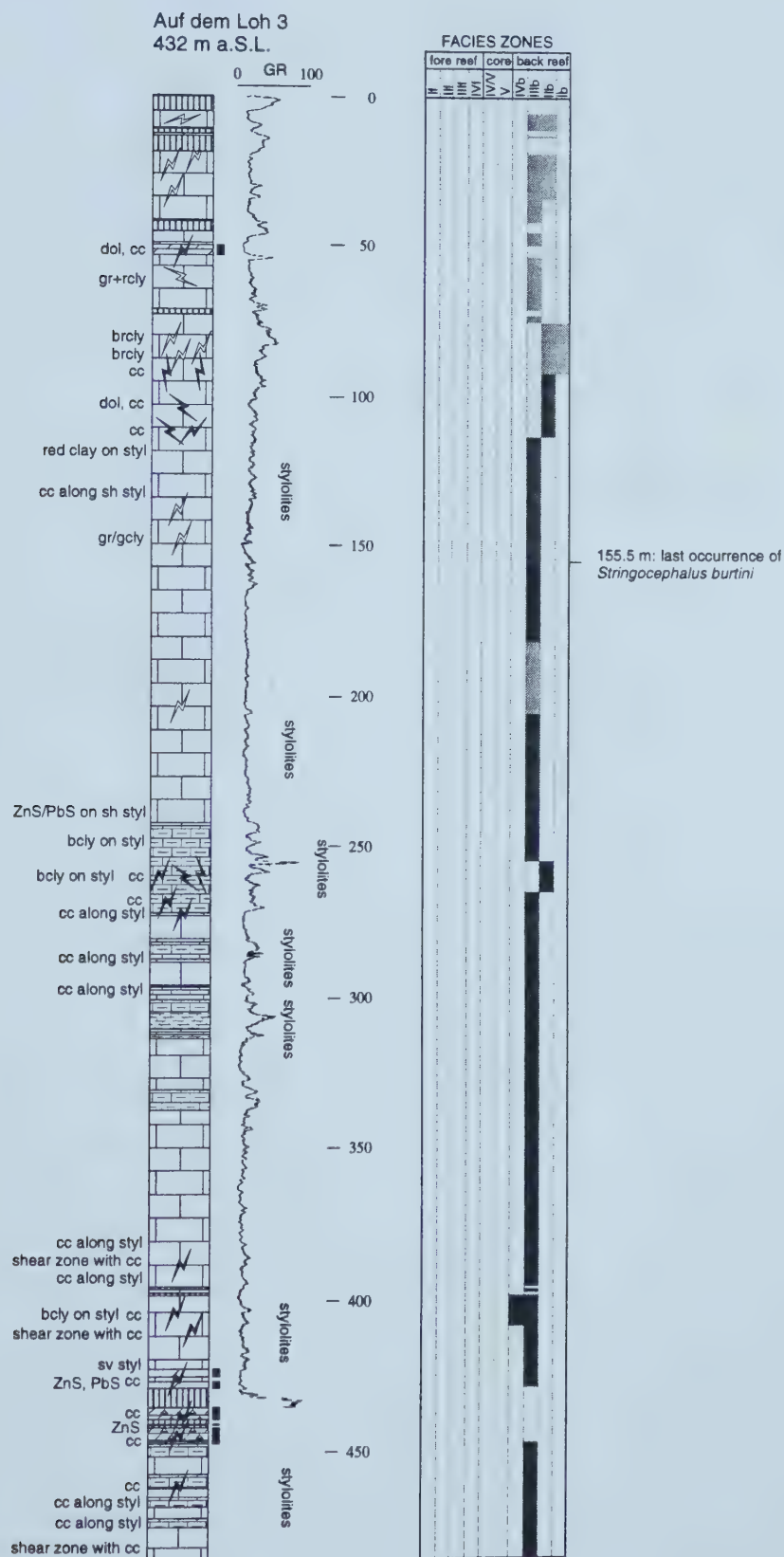


Appendix 1 continued: Auf dem Loh 1 (L1) drill core continued.



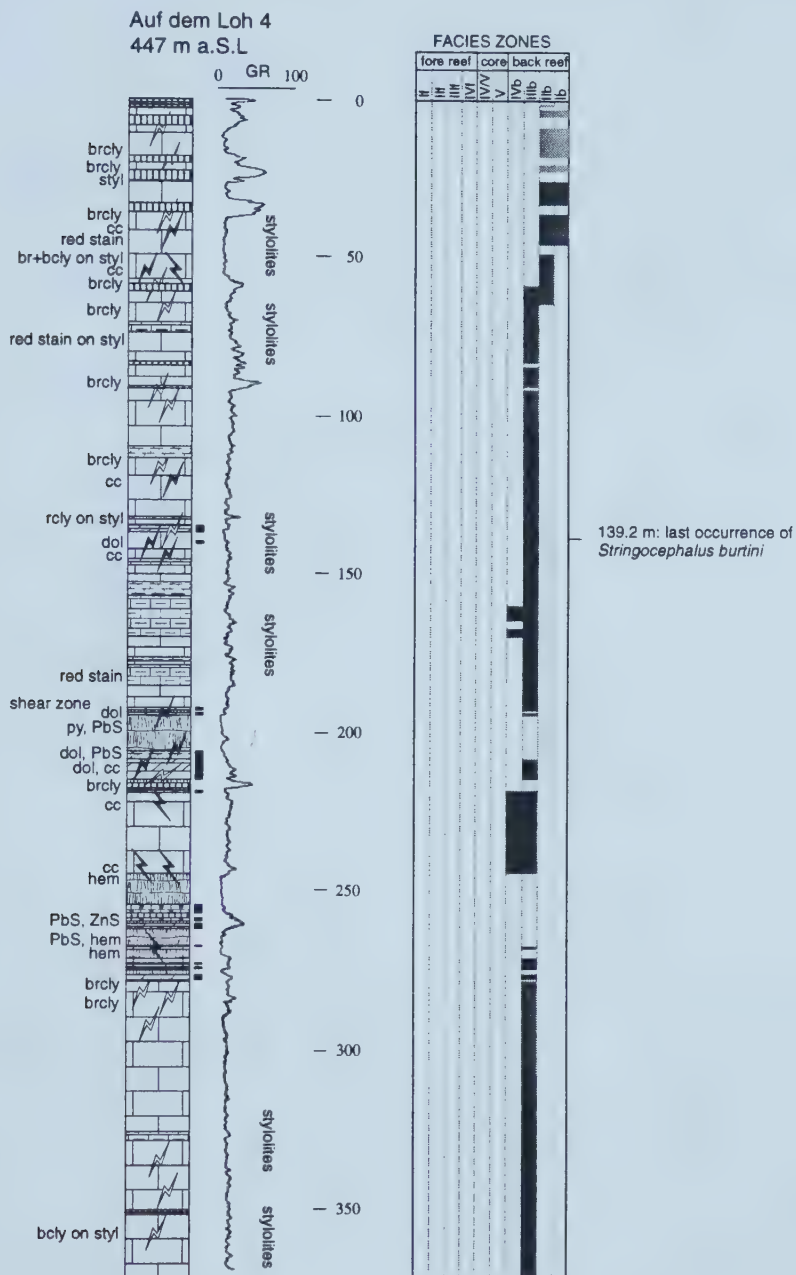


## Appendix 1 continued: Auf dem Loh 3 (L3) drill core.





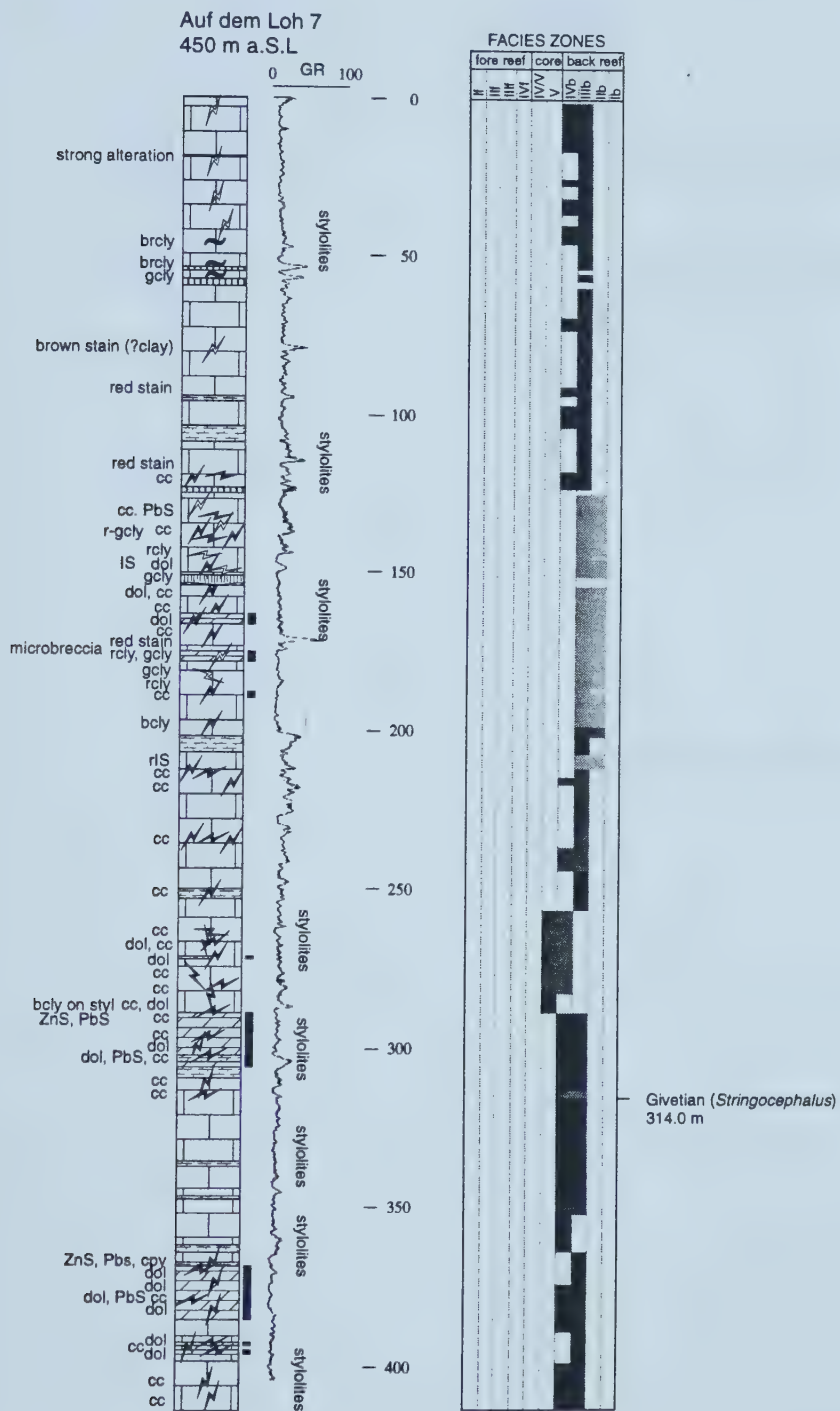
## Appendix 1 continued: Auf dem Loh 4 (L4) drill core.





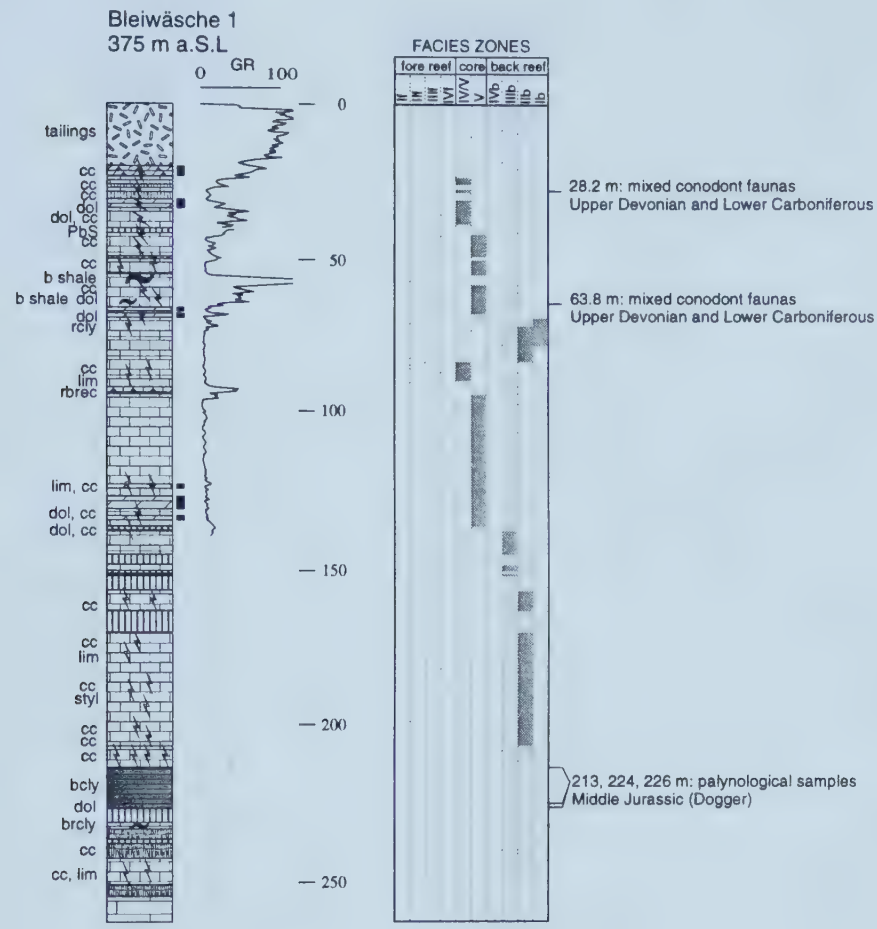


## Appendix 1 continued: Auf dem Loh 7 (L7) drill core.



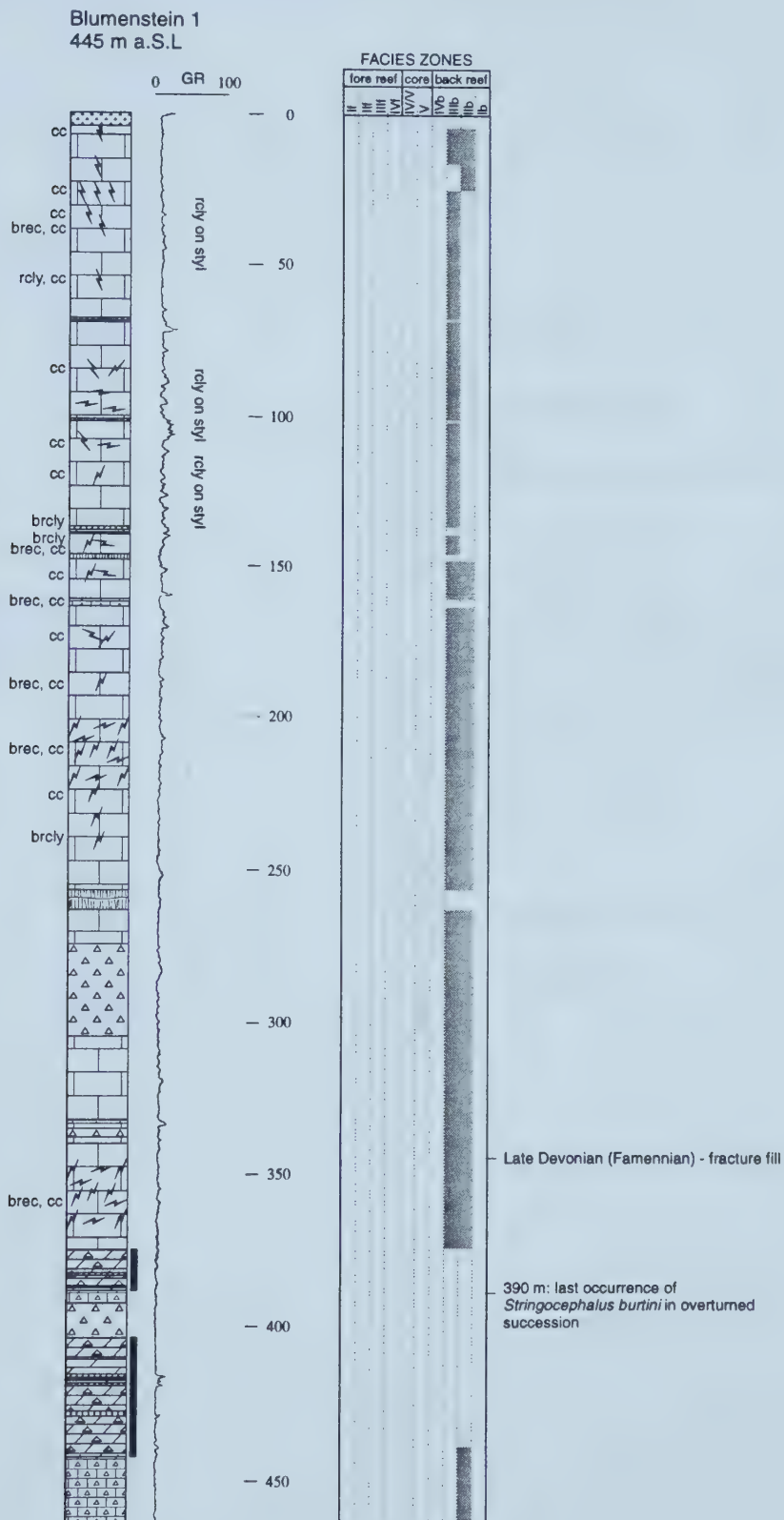


Appendix 1 continued: Bleiwäsche 1 (BW1) drill core.





## Appendix 1 continued: Blumenstein 1 (BL) drill core.

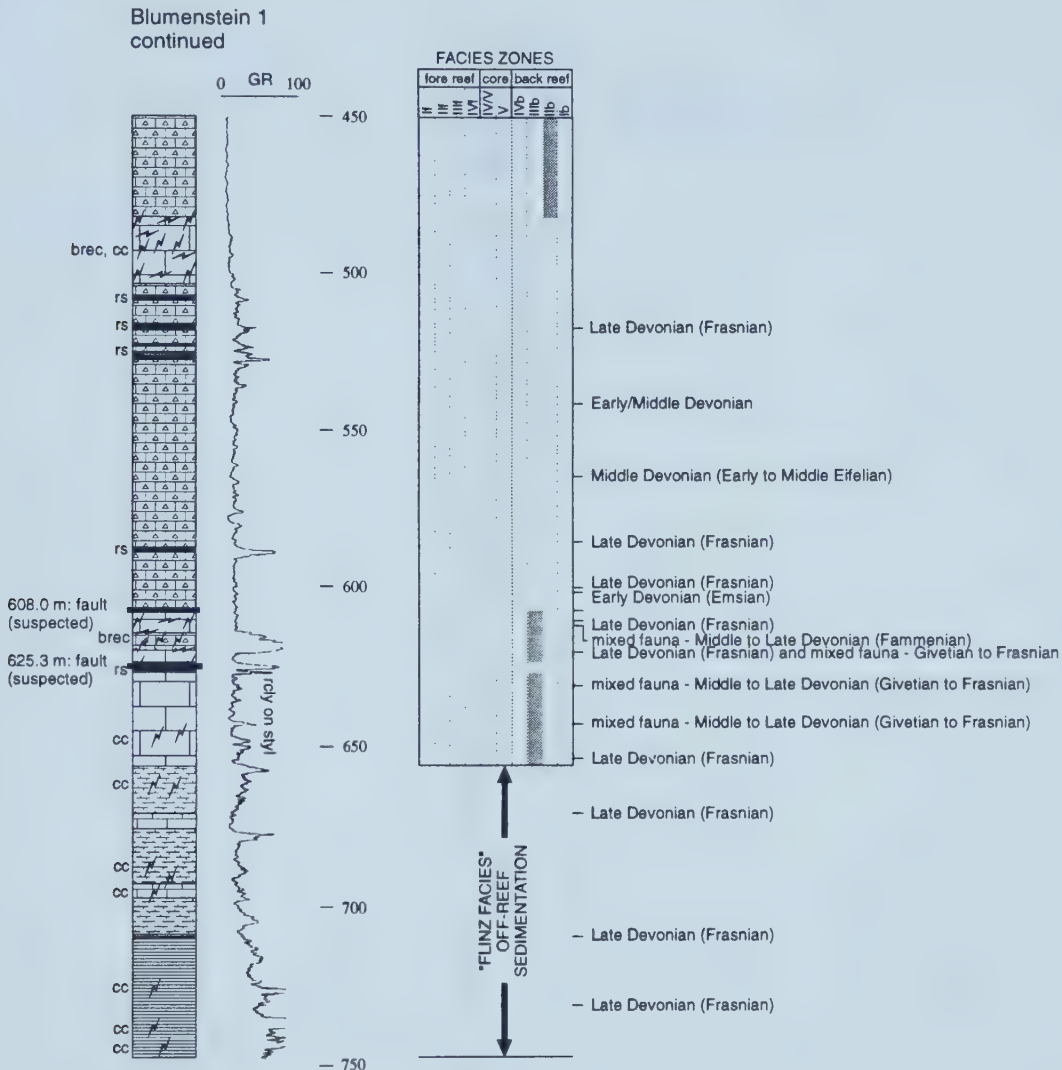


continued on next page



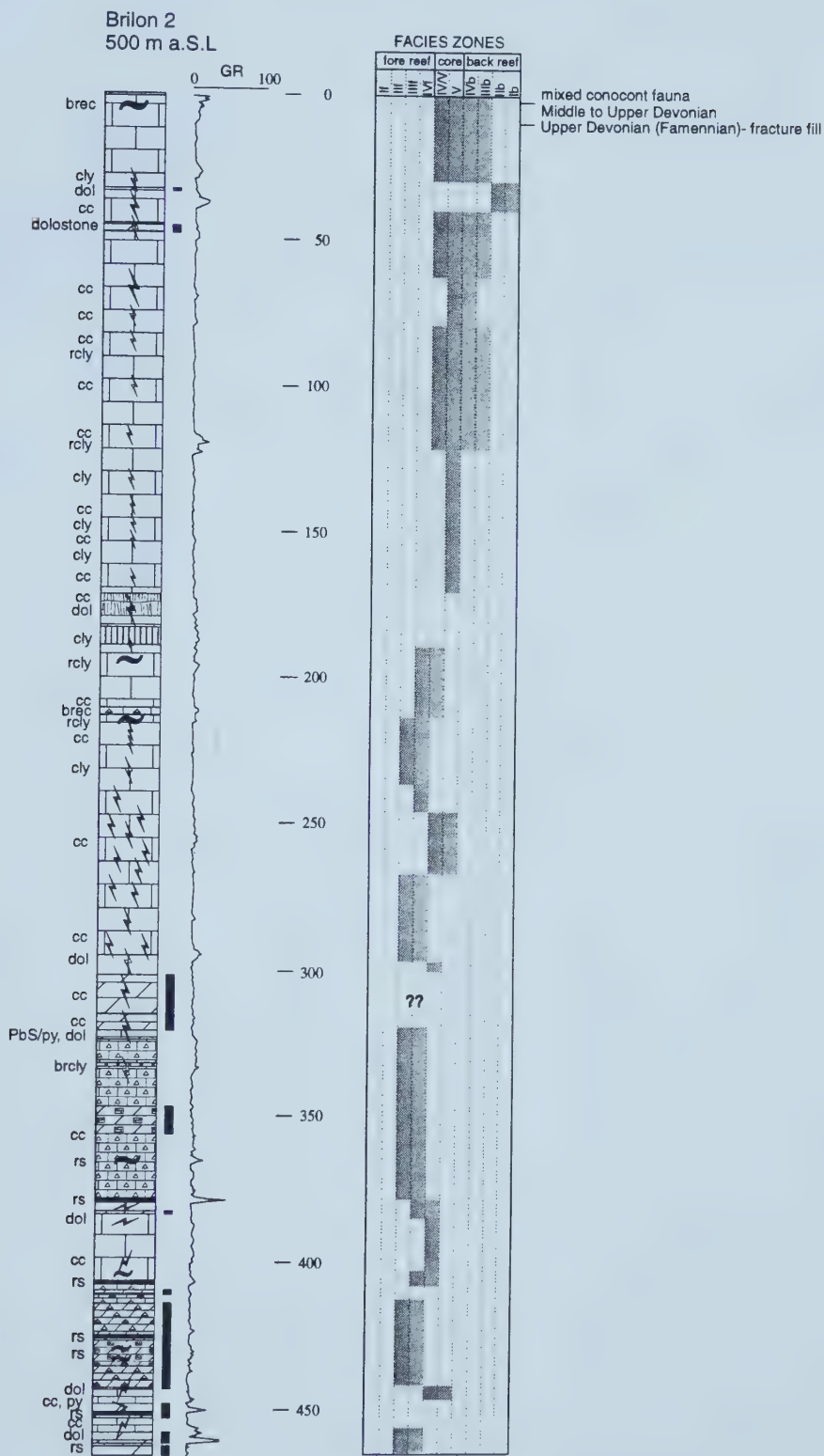


## Appendix 1 continued: Blumenstein 1 (BL) drill core continued.



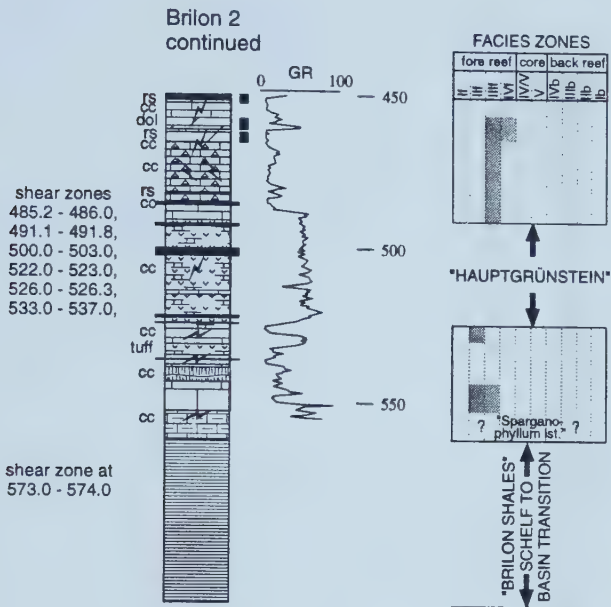


## Appendix 1 continued: Brilon 2 (B2) drill core.





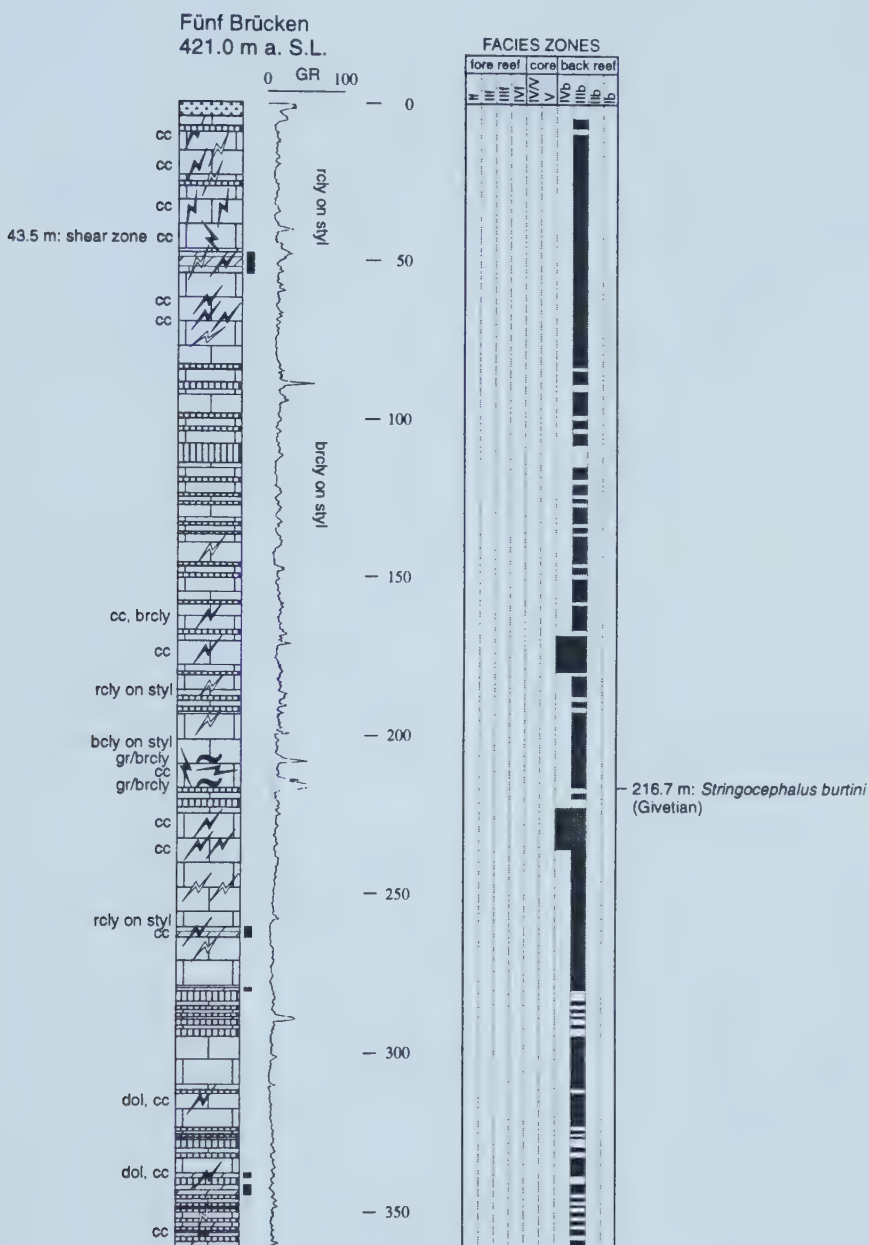
## Appendix 1 continued: Brilon 2 (B2)drill core continued.





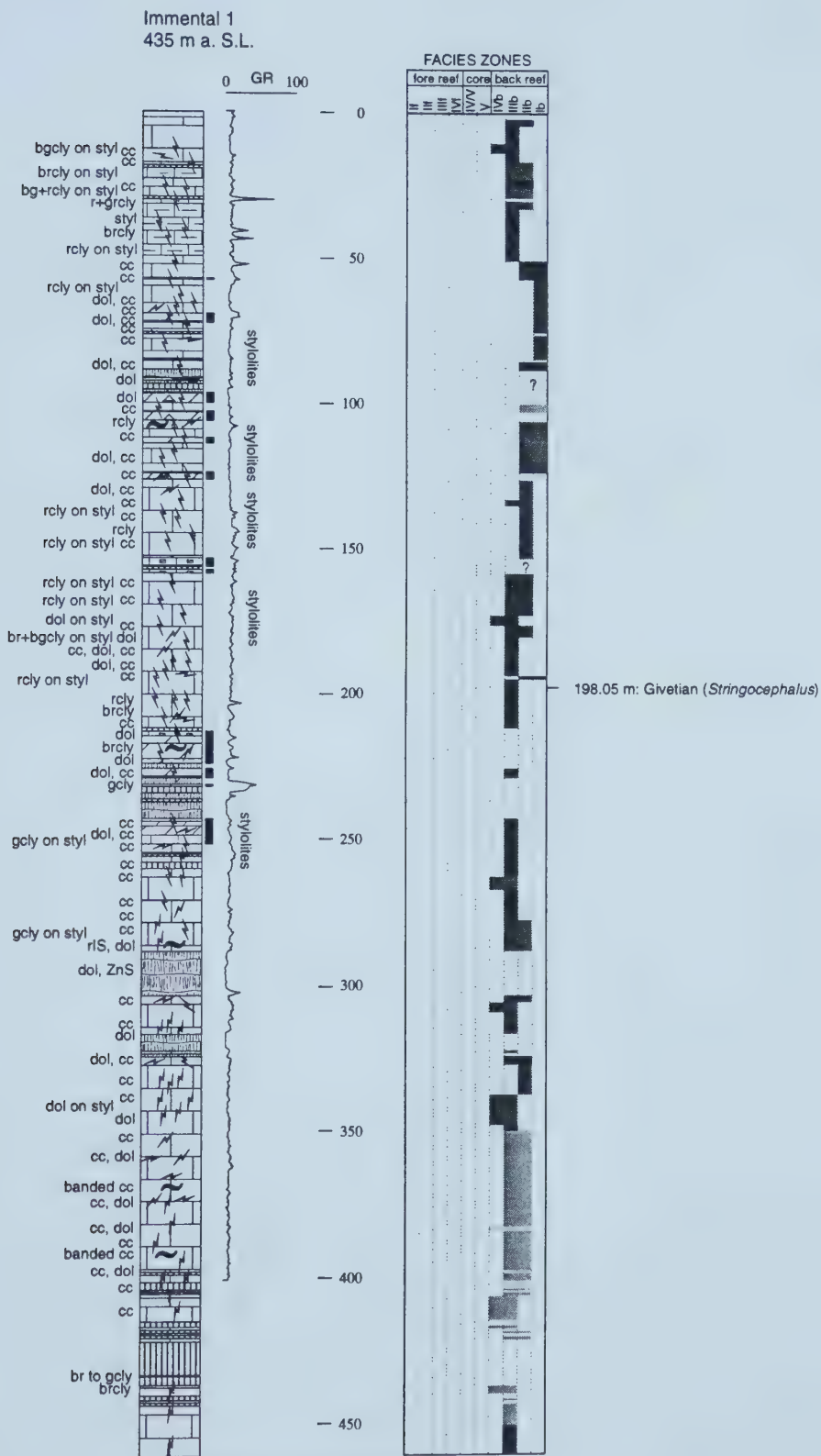


## Appendix 1 continued: Fünf Brücken (5B) drill core.



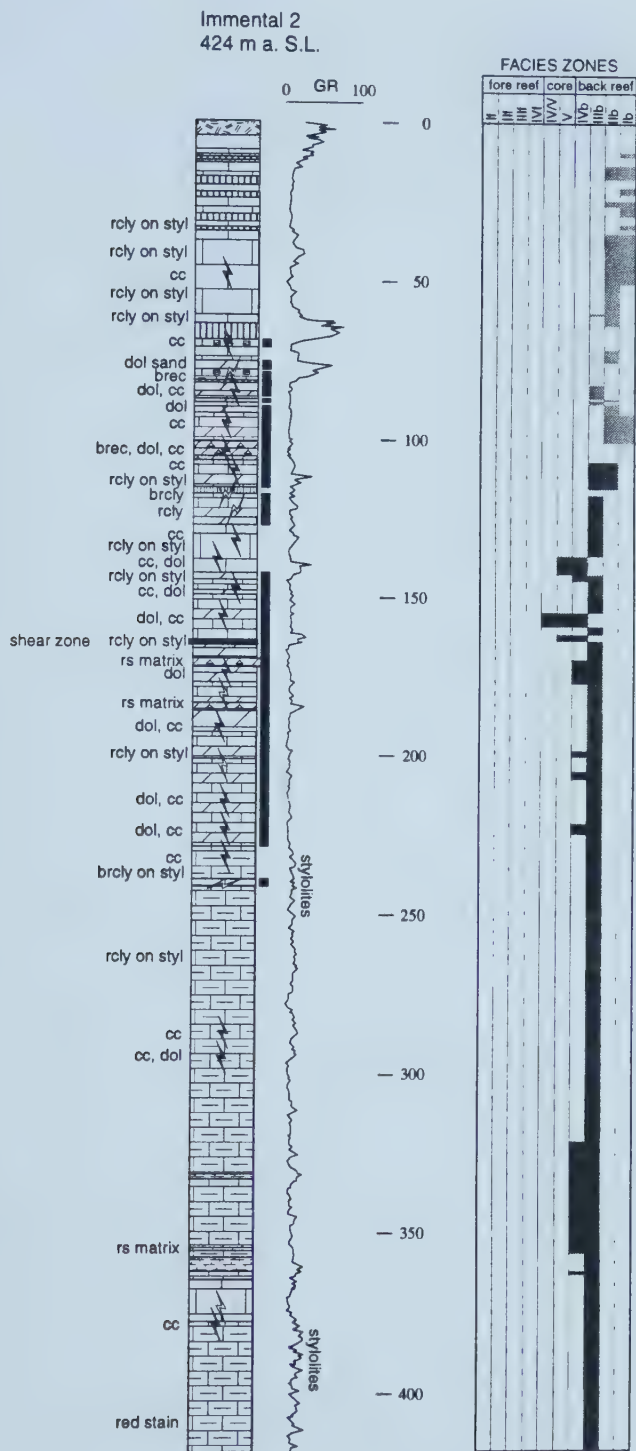


## Appendix 1 continued: Immental 1 (I1) drill core.





## Appendix 1 continued: Immental 2 (I2) drill core.

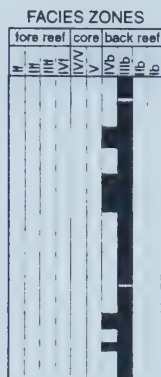
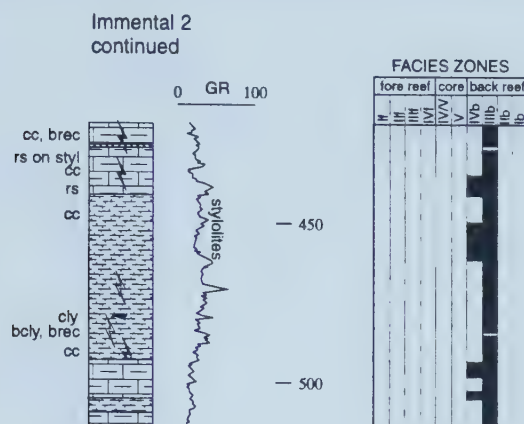


continued on next page



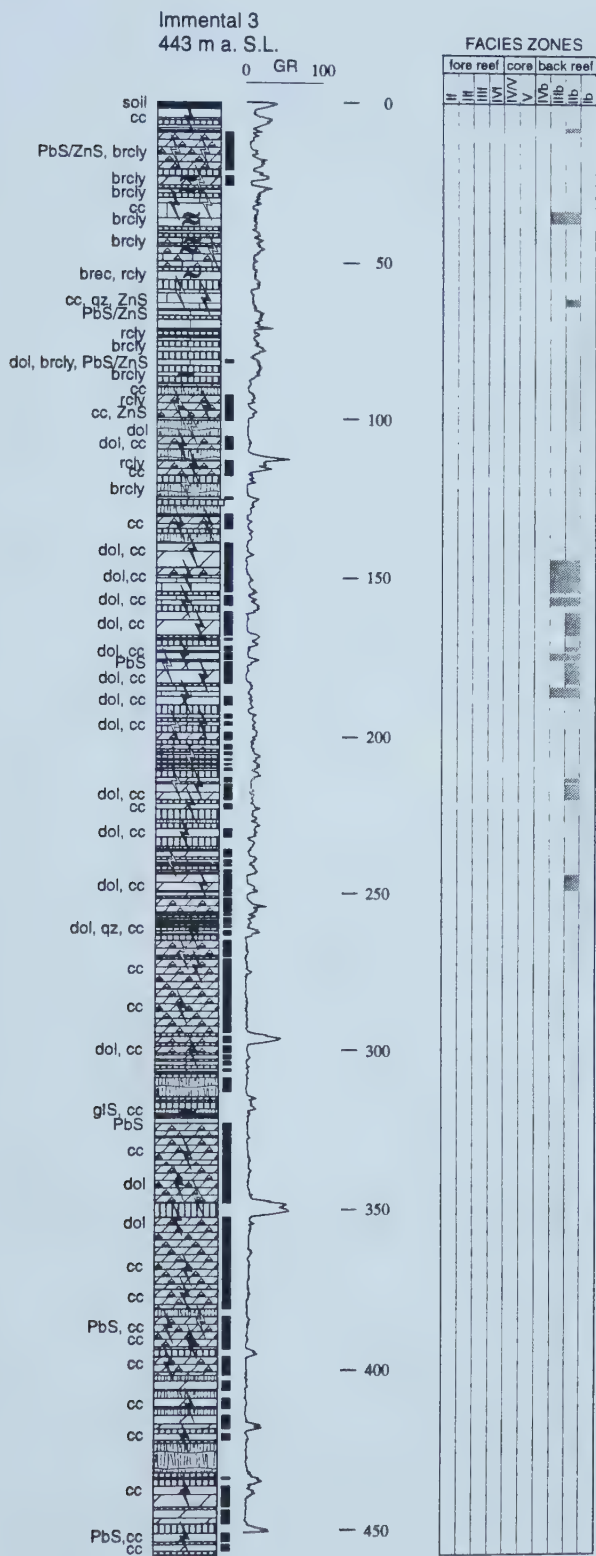


## Appendix 1 continued: Immental 2 (I2) drill core continued.



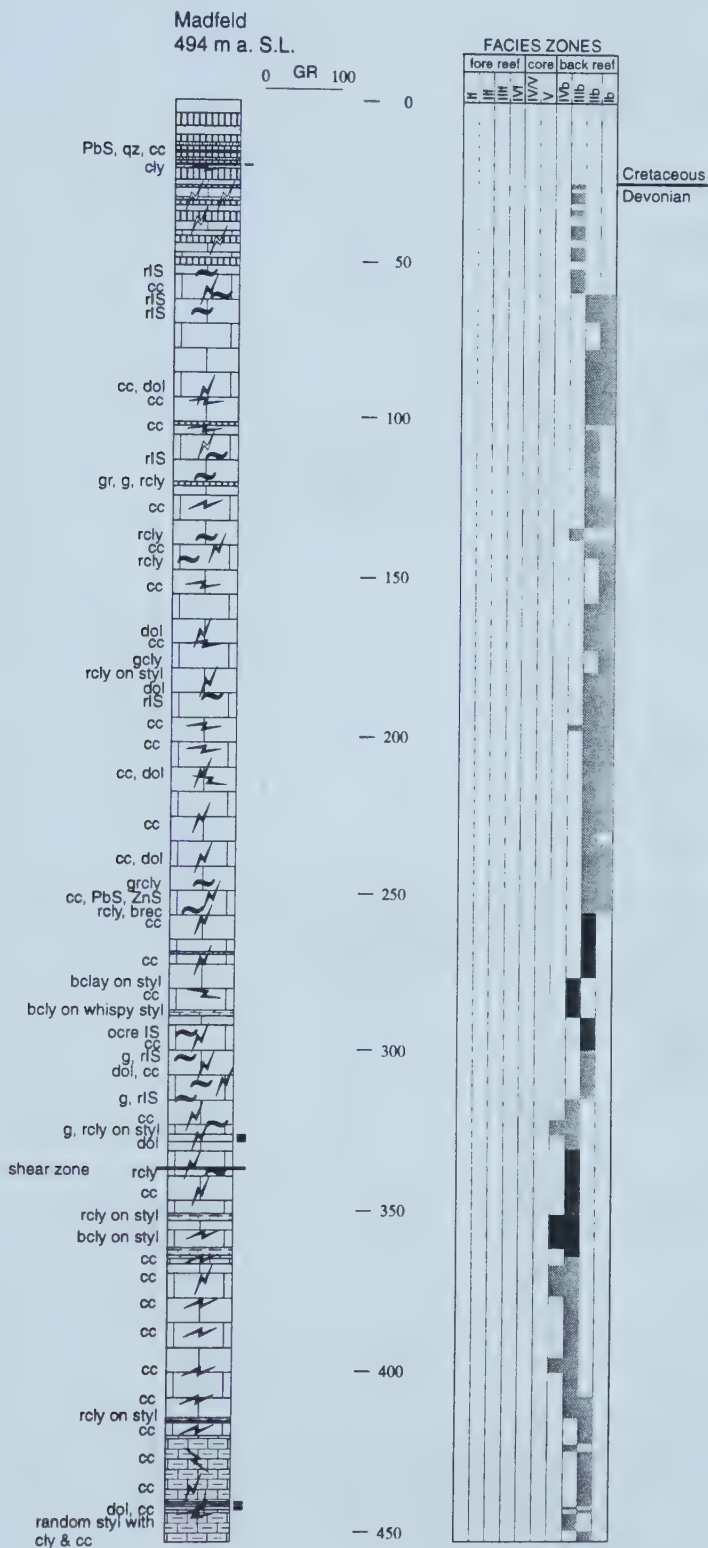


## Appendix 1 continued: Immental 3 (I3) drill core.





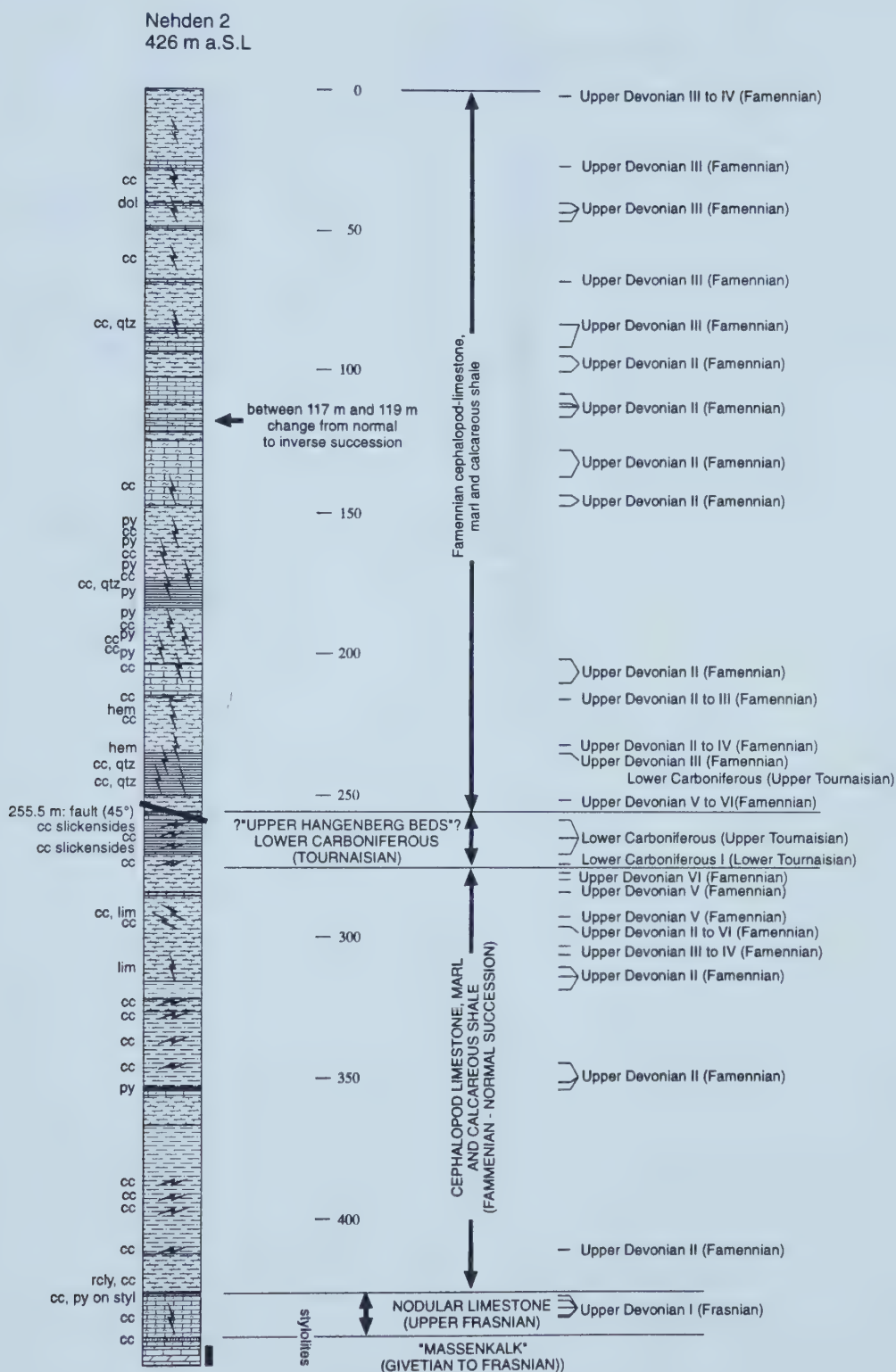
## Appendix 1 continued: Madfeld 1 (M1) drill core.







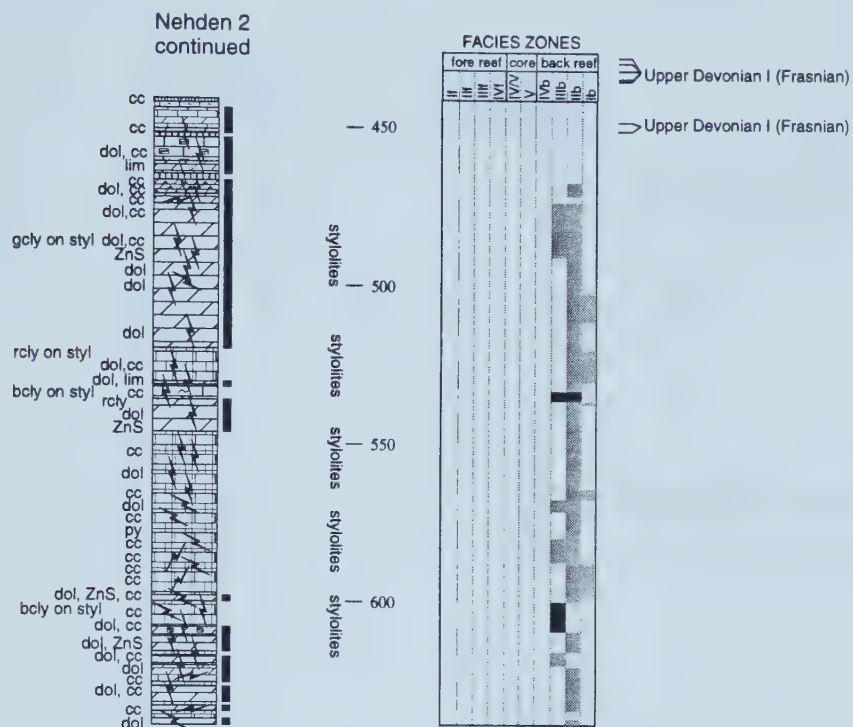
## Appendix 1 continued: Nehden 2 (N2) drill core.



continued on next page

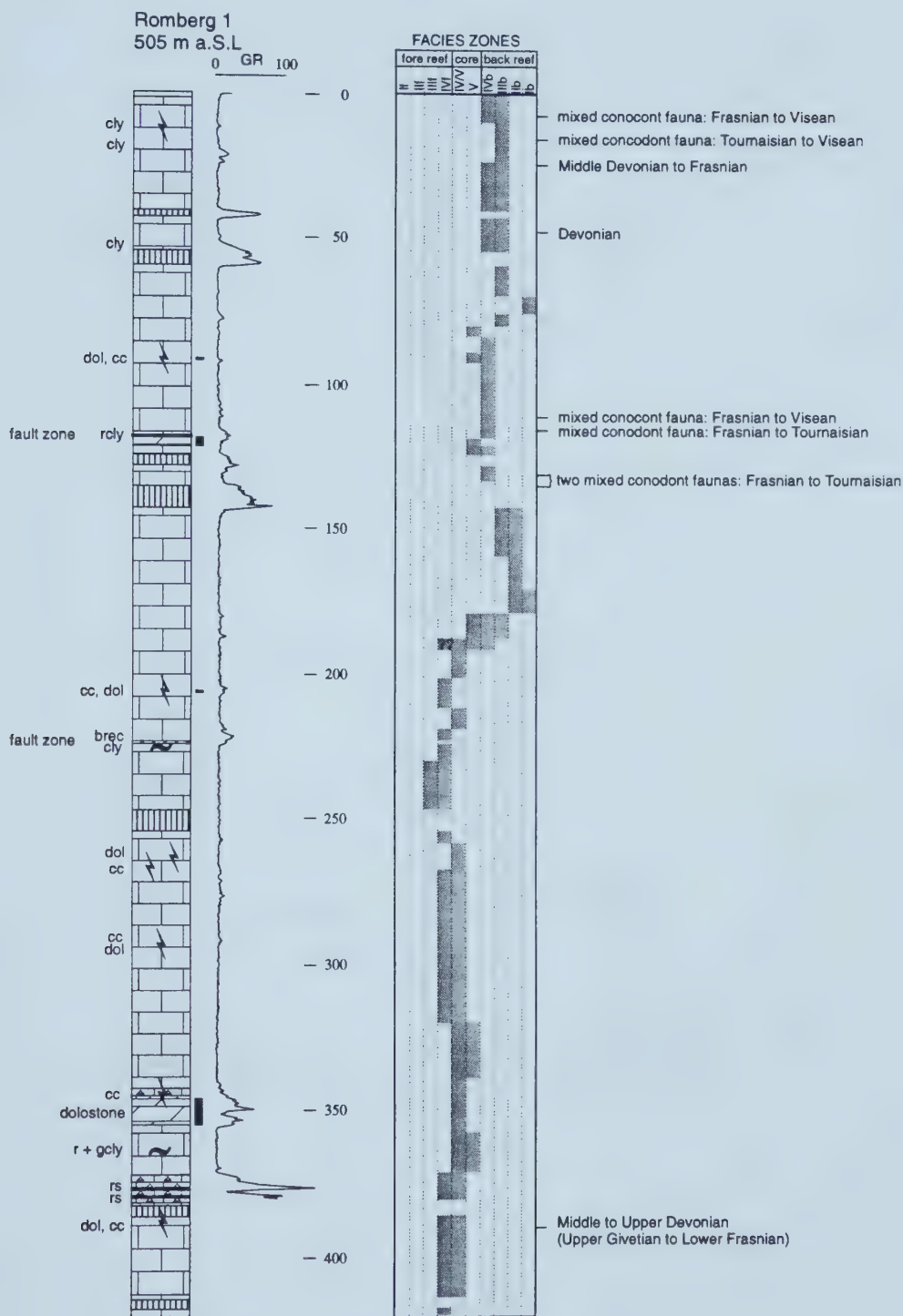


## Appendix 1 continued: Nehden 2 (N2) drill core continued.





## Appendix 1 continued: Romberg 1 (R1) drill core.



continued on next page

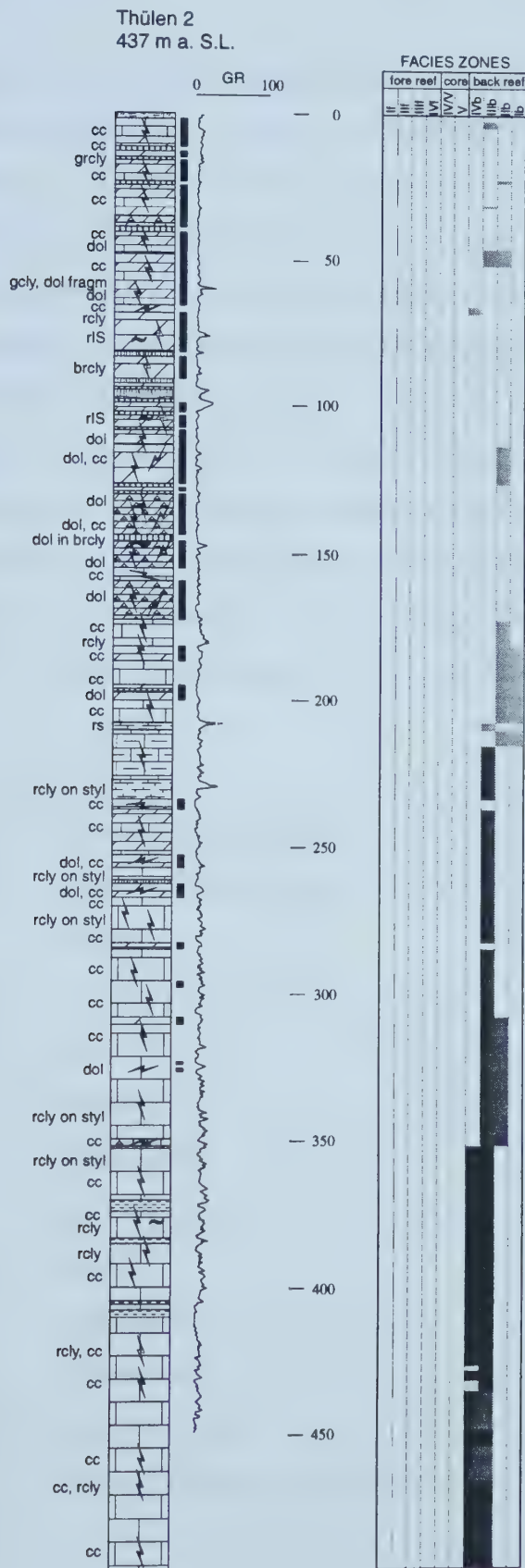








## Appendix 1 continued: Thülen 2 (TH2) drill core.





## APPENDIX 2

Table of petrographic characteristics of dolostone intervals in the investigated drill cores from the Brilon Reef Complex. For locations of drill cores, see Chapter 2, Figure 2.1 and Table 2.1. For facies context of dolostone intervals, see Appendix 1. The assignment of facies zones follows Machel and Hunter (1994). Volume % of dolomite and final porosity was estimated visually during core logging and thin section petrography. Porosity types were assigned using the classification of Choquette and Pray (1970). Dolomite types 1, 2, and 3 refer to those described in Chapter 2 (phase 21 and 22). Base metal concentrations are those reported in Brinckmann (1981) and were determined on bulk samples over 1 m core intervals. Concentrations are considered not elevated, when within the range those of the surrounding unmineralized limestone (< 50 ppm Pb, < 50 ppm Zn). Concentrations given are maximum concentrations. Average Pb and Zn concentrations of dolostone intervals are generally only slightly elevated (< 100 ppm Pb and Zn, respectively).

abbreviations:

BC	= intercrystalline porosity
CSC	= clear scalenohedral calcite (phase 24, see Chapter 2)
d	= dark
FRAC	= fracture porosity
incl	= inclined
m	= medium
n.a.	= not available
n.r.	= not recognizable
PbS	= galena
sh	= subhorizontal
sv	= subvertical
VUG	= vuggy porosity
ZnS	= sphalerite (phase 23, see Chapter 2)





## References

- Brinkmann, J., 1981, Projekt Rhenoharzynikum, Untersuchung der Metallverteilung in geosynklinalen Sedimenten des Rhenoharzynikums in stratiformen Konzentrationen. Bericht über das Kernbohrprogramm im Briloner Riffkalk-Komplex. Unpublished report by the Bundesanstalt für Geowissenschaften und Rohstoffe, Hannover, 129 p.
- Choquette, P.W. and Pray, L.C., 1970, Geological nomenclature and classification of porosity in sedimentary carbonates. American Association of Petroleum Geologists Bulletin, 54, p. 207-250.
- Machel, H. G. and Hunter, I. G., 1994, Facies Models for Middle to Late Devonian Shallow-marine Carbonates, with Comparisons to Modern Reefs: a Guide for Facies Analysis. Facies, 30, p. 155-176.



Appendix 2: Characteristics of dolostone intervals in the Brilon Reef Complex.

drill core	interval (m)	lithology/texture	facies zone	vol. % dolomite (estimated)	stylolites	fracturing	dolom. types			origin of dolomite
							1	2	3	
Alme 1	193.0-204.0	m to dgrey rudstone/ floatstone	IIlb	50 - 75	-	sv, sh fractures	+	+	+	fractures
	204.1-211.8	dgrey floatstone/ rudstone	IIlb	75	-	sv, sh fractures	+	+	+	fractures vugs
	220.1-220.5	dgrey floatstone/ rudstone	IIlb	75	-	sv fractures	+	+	+	fractures
Almerfeld	328.5-329.0	mgrey wackestone/ floatstone	IIb-IIlb	50 - 75	-	sv fractures	+	-	-	?
	333.1-341.0	mgrey wackestone/ floatstone	IIb-IIlb	75	-	sv fractures	+	-	-	?
	344.1-347.8	mgrey mudstone/ wackestone	IIb	75	-	sv fractures	+	-	-	?
	384.0-390.0	massive white calcite with relicts of dolostone wallrock	IIlb	n/a	-	fracture (?sv)	-	+	+	fracture
	648.6-650.5	m to dgrey floatstone	IIlb	75	-	sv, sh fractures	-	+	+	fractures vugs
	672.1-734.1	intensively fractured m to dgrey floatstone	IIlb-IIb	95	-	sv, sh, incl fractures	+	+	+	fractures vugs
Altenbüren 1	227.2-247.0	dgrey to black floatstone/ bindstone, in places strongly fractured and brecciated	n.r.	90	sh, sv	sv fractures vertical shear zone	+	+	+	fractures
Bleiwäsche 1	20.8-23.0	dolomitized breccia	n.r.	98	-	fault breccia?	+	-	-	?
	31.6-32.6	dolomitized breccia	n.r.	100	-	fault breccia?	+	-	-	?
	32.6-33.6	fine crystalline dolostone	n.r.	95	-	-	+	-	-	?
	35.2-35.8	dolomitized breccia	n.r.	90	-	fault breccia?	+	-	-	?
	66.0-67.2	mgrey grainstone/rudstone	V	80	-	sv fracture	+	+	-	fracture



# Appendix 2 continued

drill core	interval (m)	lithology/texture	facies zone	vol. % dolomite (estimated)	stylolites	fracturing	dol. types			origin
							1	2	3	
Bleiwäsche 1	68.3-70.0	fine crystalline dolostone	n.r.	100	-	fault breccia?	+	+	-	fractures
		around dolomitized breccia				sv fractures				
	123.4-124.5	limonitic dolostone, mgrey rudstone/grainstone	IV/V	80	-	sv fractures	+	-	-	?
	127.0-130.6	mgrey rudstone/grainstone	IV/V	95	-	sv fractures	+	+	-	vugs
Blumenstein 1	133.5-134.4	mgrey rudstone/grainstone	IV/V	95	-	sv fractures	+	+	-	vugs
	376.0-389.0	dolomitized breccia	IIb-lb?	80	-	breccia	+	+	+	fractures
						microfractures				
	403.2-443.4	dolomitized breccia	IIb-lb?	85	-	breccia	+	+	+	fractures
Brilon 2						irregular fractures				
	34.0-35.0	Igrey wackestone/ floatstone	lb-IIb	90	-	fractures	+	-	-	fractures
	47.0-49.0	Igrey floatstone	IIlb-IVb	90	-	fractures	+	-	-	fractures
	302.8-333.6	fractured and calcitized dolostone	n.r.	50	sv	sv fractures	+	-	-	fractures
	348.1-357.5	dolomitized breccia	IIIf-IIIIf	75	sv	sv fractures	+	-	-	?
	384.1-385.4	fractured Igrey floatstone/ rudstone	IVf-IV/V	90	-	-	+	+	-	?
	410.0-411.7	I to mgrey rudstone	IV/V-V	75	irregular	-	+	+	-	?
	414.0-443.9	dolomitized breccia	IIIf-IVf	85	irregular	fractures	+	+	+	fractures vugs
	448.4-453.0	fractured and calcitized dolostone	n.r.	75	-	sv, incl fractures	+	+	+	fractures vugs
	458.3-463.6	red, laminated dolomitic shale	IIIf-IVf	80	sv	sv fractures	+	+	+	fractures





Appendix 2 continued

drill core	interval (m)	lithology/texture	facies zone	vol. % dolomite (estimated)	stylolites	fracturing	dol. types			origin
							1	2	3	
Fünf Brücken	47.8-54.1	mgrey floatstone	IIlb	80	sh	sh fractures	+	-	-	?
	260.4-264.1	lgry mudstone	IIlb	80	-	fractures	+	-	-	fractures
	280.0-281.0	lgry wackestone	IIlb	75	-	-	+	-	-	?
	338.0-339.2	mgrey floatstone	n.r.	90	-	fractures	+	+	+	fractures
	341.1-344.1	mgrey floatstone	IIlb	50-75	-	sv fractures	+	-	-	?
Immental 1	56.8-57.0	mgrey floatstone	IIb-IIb	95	-	sv fracture	+	-	-	?
	69.8-71.8	mgrey mudstone	Ib	75	-	sv fracture	+	+	+	fracture
	96.9-100.0	dolomitized breccia	n.r.	80	-	sv fractures	+	+	+	fractures
	103.0-106.0	fractured mudstone/ wackestone	Ib-IIb	75	-	irregular fractures	+	-	-	?
	111.1-112.6	mgrey mudstone	Ib-IIb	75	sh	sv fractures	+	+	+	?
	123.0-126.4	mgrey mudstone/ wackestone	Ib-IIb	75	sh	irregular fractures	+	-	-	?
	153.9-154.6	calcite cemented breccia with dolostone clasts	n.r.	20	-	-	+	-	-	?
	212.2-251.5	fractured dolostone with intervals of massive calcite	IIIb	70	sh, sv	irregular fractures	+	+	+	fractures
	68.7-70.5	fractured mgrey wackestone/ floatstone	IIb	60	-	sv fractures	+	-	-	fractures
	76.0-127.7	m to lgrey mudstone/wacke- stone/floatstone, fractured, with intervals of massive calcite	Ib-IIIb	60-80	sh, incl	sv, incl fractures	+	+	+	fractures
Immental 2	142.5-229.0	m to dgrey floatstones/ rudstones, with brecciated intervals and intervals of massive calcite	IIIb-IV/V	70-90	sh	sv, incl fractures	+	+	+	fractures vugs
	239.7-240.4	m to dgrey floatstone	IIIb	95	-	incl fracture	+	+	+	fracture



Appendix 2 continued

drill core	interval (m)	lithology/texture	facies zone	vol. % dolomite (estimated)	stylolites	fracturing	dol. types			origin
							1	2	3	
Immental 3	9.6-21.5	dolomitized breccia, strongly altered (karst)	n.r.	65	-	fault breccia	+	-	-	?
	24.5-26.7	dolomitized breccia	n.r.	65	-	open fractures				
	81.0-81.9	dolomitized breccia	n.r.	85	-	fault breccia	+	-	-	?
	92.7-459.5	intervals of dolomitized breccias, mgrey mudstone, wackestone, floatstone	IIb-IIIb	50-100	-	-	+	-	-	?
		strongly fractured, pervaded by large cavities (karst) and intervals of massive calcite contain dolomite relicts				fault breccia	+	+	+	fractures
Loh 1	262.5-267.8	m to dgrey floatstone	IIIb	75-95	sh	sv fractures	+	+	+	fractures
	573.9-577.4	fractured and brecciated mineralized, fractured dgrey dolostone with interval of laminated dolomi with dolomite neomorphs	IIIb	95	-	fractures	+	+	+	fractures
	591.8-592.3	mgrey wackestone/floatstone	IIb	95	-	sh fractures	+	+	+	fractures
	613.0-660.4	fractured and brecciated m to dgrey wackestone/floatstone/rudstone, m-sized cavities	IIb	95	-	sh, incl, sv fractures	+	+	+	fractures vugs
Loh 3	48.7-53.6	dolostone relicts within massive calcite (replaces dolomite)	IIIb	50	-	fracture	-	+	+	fracture
	422.0-425.1	mgrey packstone/rudstone	IIIb	50-75	-	sv, incl fractures	+	-	-	



Appendix 2 continued

drill core	interval (m)	lithology/texture	facies zone	vol. % dolomite (estimated)	stylolites	fracturing	dol. types			origin
							1	2	3	
Loh 3	426.7-447.2	strongly fractured, brecciated, packstone/rudstone, intervals of massive calcite (replaces dolomite) m-sized cavities	IIIb	70-90	-	sv, incl fractures	+	+	+	fractures cavities
Loh 4	135.8-138.0	mgrey floatstone, wackestone limonitic alteration originating at sv open fracture (?karst)	IIIb	95	-	-	+	-	-	?
	140.2-140.6 192.8-218.3	mgrey floatstone strongly fractured floatstone/ rudstone, intervals of massive calcite (replacing dolomite)	IIIb IIIb	100 50-80	-	incl fractures sv, incl fractures	+	+	+	fractures fractures
	258.5-259.7	crystalline dolostone at bottom of cavity (strongly weathered)	n.r.	75	-	-	?	-	-	cavity
	260.0-260.9 261.5-261.6	crystalline dolostone crystalline dolostone relict	n.r.	80 80	-	-	?	-	-	cavity ?
	267.0-267.2	dgrey floatstone at bottom of massive calcite interval	IIIb	95	-	-	+	-	-	?
Loh 7	273.4-278.7	dgrey wackestone/floatstone	IIIb	85	-	sv	+	-	-	?
	163.05-167.2 175.6-179.1	lgrey mudstone/wackestone lgrey wackestone	IIb-IIIb IIb-IIIb	95 90	sh -	sv, incl fractures sv fractures	+	+	+	fractures ?
	188.6-190.3 270.6-271.1	lgrey mudstone/wackestone mgrey rudstone/bindstone	IIb-IIIb IVb	80 75	-	v fracture sv fracture	+	-	-	?
	289.2-305.5	dgrey rudstone	IIIb-IVb	90	sh, sv	irregular fractures	+	+	+	fracture fracture vugs
	368.1-384.7	m to dgrey rudstone, fractured	IIIb-IVb	95	-	sv, incl fractures	+	+	+	fractures vugs
	392.2-392.7 394.6-395.5	mgrey floatstone mgrey floatstone	IIIb IIIb	100 100	-	incl fractures incl fractures	+	+	+	fractures fractures





Appendix 2 continued

drill core	interval (m)	lithology/texture	facies zone	vol. % dolomite (estimated)	stylolites	fracturing	dol. types			origin
							1	2	3	
Madfeld 1	20.0-20.2	crystalline dolostone at bottom of cavity within Cretaceous sandstone	n.r.	65	-	-	+	-	-	cavity
	326.9-328.1	lgrey floatstone	IIlb	95	sh	sv fractures	+	+	+	fractures
	442.1-442.2	lgrey wackestone	IIb-IIIb	95	sv	sv fracture	+	+	+	fracture
	443.4-444.0	lgrey wackestone/floatstone	IIlb	95	sh	sv fracture	+	+	+	fracture
Nehden 2	445.0-520.0	reddish grey wackestone/ floatstone, rare ruststone layers some intervals strongly fractured and brecciated brown alteration around open fractures and cavities	IIb-IIIb	80-100	sh	sv, incl fractures	+	+	+	fractures vugs
	530.4-531.6	lgrey floatstone	IIlb	95	-	sv fracture	+	+	+	fracture
	533.0-533.4	mgrey floatstone,	IIb-IIIb	75	sh	-	+	-	-	?
	538.1-546.5	mgry wackestone/floatstone	IIlb	80-95	sh	irregular fractures	+	+	+	fractures vugs
	598.7-600.0	m to dgrey floatstone	IIlb	80-95	sh	irregular fractures	+	+	+	fractures vugs
	608.1-639.2	m to dgrey floatstone/ wackestone	IIlb	80-95	sh	sv fractures	+	+	+	fractures vugs
	91.1-91.4	lgrey rudstone strongly calcitized, limonitized	IVb-V	50	-	sv fractures	-	+	-	fractures vugs
	117.4-119.8	lgrey floatstone strongly calcitized, limonitized	IVb	50	-	irregular fractures	-	+	-	?
	207.1-207.4	lgrey rudstone strongly calcitized, limonitized	IVf	65	-	-	+	+	+	vugs
	347.0-351.5	lgrey rudstone strongly calcitized, limonitized	IV/V	75	-	irregular fractures (open)	-	+	-	?
Romberg 1										



Appendix 2 continued

drill core	interval (m)	lithology/texture	facies zone	vol. % dolomite (estimated)	stylolites	fracturing	dol. types			origin
							1	2	3	
Romberg 1	442.5-447.6	lgrey floatstone	IIIf-IVf	75	-	sv fractures	-	+	-	fractures vugs
	469.2-478.0	mgry wackestone/packstone, rare rudstone, dolomite only in vicinity of sv fractures	IIIf-IIIIf	25	-	sv fractures	+	+	+	fractures
	483.0-491.0	mgry wackestone/packstone, dolomite only in vicinity of fractures	IIIf-IIIf	25	-	sv fractures	+	+	+	fractures
	626.4-627.1	lgrey rudstone	?IVf-IV/V	80	-	irregular fractures	-	+	+	fractures
	633.2-666.5	crystalline dolostone, breccia- like appearance, strong brown alteration along open fractures	? IIIIf ?	75-95	-	sv fractures, in some places open	-	+	+	fractures vugs
Thülen 2	720.0-732.1	grey reddish rudstone, breccia- like appearance (?sedimentary) with reddish dolomitized matrix	?IIIIf-IVf?	35	-	-	+	-	-	breccia matrix
	7.3-154.1	mgrey fine crystalline dolostone intensively fractured and brecciated, with intervals of massive calcite (replacing dolomite and cementing fractures)	?IIb-IVb	30-95	-	fractures	+	+	+	fractures vugs
	158.8-172.3	mgrey fine crystalline dolostone intensively fractured and brecciated	n.r.	95	-	irregular fractures	+	+	+	fractures vugs
	182.0-187.7	mgrey mudstone? with intervals of fine crystalline dolostone	IIb-IIb	50	sh	sv, incl fractures	+	+	-	?
	195.5-200.0	mgrey mudstone?	IIb-IIb	95	-	sv fractures	+	+	+	fractures
	234.2-238.0	mgrey mudstone?	n.r.	75	-	irregular fractures	+	+	+	vugs



Appendix 2 continued

drill core	interval (m)	lithology/texture	facies	vol. % dolomite (estimated)	stylolites	fracturing	dol. types			origin
							1	2	3	
Thülen 2	252.7-256.8	m to dgrey wackestone/ floatstone	IIlb	90	-	sv fractures	+	+	+	vugs
	262.0-267.0	mgrey wackestone/floatstone	IIlb	75	-	incl fractures	+	+	+	fractures
	282.6-285.3	m to dgrey wackestone/ floatstone	IIlb	50-75	sh	incl fractures	+	-	-	vugs ?
	308.2-309.8	m to dgrey floatstone	IIb-IIlb	95	-	-	+	-	-	?
	321.7-323.0	m to dgrey floatstone	IIb-IIlb	95	-	-	+	-	-	?
	324.9-326.6	mgrey floatstone	IIb-IIlb	90	-	sv, incl fractures	+	+	+	fractures vugs





Appendix 2 continued

drill core	interval (m)	macroscopic mineralization	base metal concentrations over 1 m intervals (Brinckmann 1981)	post-dolomite cementation	post-dolomite alteration	porosity types	final porosity (estimated)
Alme 1	193.0-204.0	-	up to 540 ppm Pb, 90 ppm Zn	white calcite	calcitization/limonitization	BC	5 %
	204.1-211.8	-	up to 80 ppm Pb, 75 ppm Zn	CSC	calcitization/limonitization	VUG, BC	20 %
	220.1-220.5	PbS	up to 75 ppm Pb, 65 ppm Zn	clear calcite	calcitization/limonitization	BC	5 %
Almerfeld	328.5-329.0	-	n.a.	white calcite	calcitization/limonitization	BC	< 5 %
	333.1-341.0	-	n.a.	-	calcitization/limonitization	BC	< 5 %
	344.1-347.8	-	n.a.	-	calcitization/limonitization	BC	< 5 %
	384.0-390.0	-	n.a.	white calcite, CSC	calcitization/limonitization	VUG, BC	< 5 %
	648.6-650.5	-	n.a.	CSC	calcitization/limonitization	VUG, BC	15 %
Altenbüren 1	672.1-734.1	ZnS	up to 75 ppm Pb, 810 ppm Zn	white calcite, CSC	in some intervals calcitization/limonitization	FRAC, VUG, BC	< 5 to 15 %
	227.2-247.0	pyrite	up to 45000 ppm Zn and 4800 ppm Pb directly above dolostone interval	white calcite, CSC	calcitization	FRAC, BC	< 5 to 10 %
Bleiwäsche 1	20.8-23.0	-	up to 430 ppm Pb, 260 ppm Zn	white calcite	limonitization	BC	< 5 %
	31.6-32.6	-	up to 350 ppm Pb, Zn < 50 ppm	-	limonitization	BC	< 2 %
	32.6-33.6	PbS	up to 950 ppm Pb, 70 ppm Zn	white calcite	limonitization	BC	< 2 %
	35.2-35.8	-	up to 1350 ppm Pb, 180 ppm Zn	white calcite	limonitization	BC	< 2 %
	66.0-67.2	-	up to 110 ppm Pb, 215 ppm Zn	-	limonitization	BC	< 2 %



Appendix 2 continued

drill core	interval (m)	macroscopic mineralization	base metal concentrations over 1 m intervals (Brinckmann 1981)	post-dolomite cementation	post-dolomite alteration	porosity types	final porosity (estimated)
Bleiwäsche 1	68.3-70.0	-	up to 100 ppm Pb, 95 ppm Zn	-	-	VUG, BC	5 %
	123.4-124.5	-	up to 75 ppm Pb, 95 ppm Zn	white calcite	limonitization	FRAC	3 %
	127.0-130.6	-	up to 140 ppm Pb, 90 ppm Zn	white calcite	limonitization	VUG	3 to 15 %
	133.5-134.4	-	up to 65 ppm Pb, Zn < 50 ppm	white calcite	limonitization	VUG	5 %
Blumenstein 1	376.0-389.0	-	not elevated	white calcite	calcitization/limonitization	BC, VUG	5 %
	403.2-443.4	-	up to 160 ppm Pb, 140 ppm Zn	white calcite, CSC	limonitization	VUG	15 %
Brilon 2	34.0-35.0	-	n.a.	-	limonitization	BC, FRAC	5 %
	47.0-49.0	-	n.a.	-	limonitization	BC, FRAC	5 %
	302.8-333.6	ZnS, PbS	n.a.	white calcite	calcitization/limonitization	VUG, FRAC	5 %
	348.1-357.5	-	n.a.	white calcite	calcitization/limonitization	BC	5 %
	384.1-385.4	-	n.a.	-	calcitization	VUG	10 %
	410.0-411.7	-	n.a.	-	limonitization	VUG, BC	10 %
	414.0-443.9	pyrite	n.a.	-	-	VUG	10 to 20 %
	448.4-453.0	pyrite	n.a.	white calcite	calcitization/limonitization	VUG	5 %
	458.3-463.6	-	n.a.	white calcite	calcitization	VUG	2 %



# Appendix 2 continued

drill core	interval (m)	macroscopic mineralization	base metal concentrations over 1 m intervals (Brinckmann 1981)	post-dolomite cementation	post-dolomite alteration	porosity types	final porosity (estimated)
Fünf Brücken	47.8-54.1	-	not elevated	white calcite	calcitization/limonitization	VUG	5 %
	260.4-264.1	-	not elevated	white calcite	calcitization/limonitization	BC	< 2 %
	280.0-281.0	-	not elevated	-	limonitization	BC	< 2 %
	338.0-339.2	-	not elevated	white calcite	calcitization/limonitization	BC	< 2 %
	341.1-344.1	-	not elevated	white calcite	limonitization	BC	< 2 %
Immental 1	56.8-57.0	-	up to 100 ppm Pb, 160 ppm Zn	clear calcite	limonitization	-	-
	69.8-71.8	-	not elevated	clear calcite	limonitization	BC	5 to 10 %
	96.9-100.0	-	up to 105 ppm Pb, 150 ppm Zn	white calcite	calcitization/limonitization	BC	< 5 %
	103.0-106.0	-	up to 125 ppm Pb, 180 ppm Zn	white calcite	calcitization/limonitization	BC	< 5 %
	111.1-112.6	-	765 ppm Pb, 200 ppm Zn	white calcite	calcitization/limonitization	BC, VUG	5 %
Immental 2	123.0-126.4	-	145 ppm Pb, 225 ppm Zn	white calcite	calcitization/limonitization	BC	< 5 %
	153.9-154.6	-	not elevated	white calcite	calcitization/limonitization	-	-
	212.2-251.5	-	up to 150 ppm Pb, 152 ppm Zn	white calcite	calcitization/limonitization	BC, VUG	< 5 %
	68.7-70.5	-	up to 210 ppm Pb, 95 ppm Zn	white calcite	calcitization/limonitization	BC, VUG	< 3 %
	76.0-127.7	-	up to 420 ppm Pb, 240 ppm Zn, but mostly < 50 ppm for both	white calcite	calcitization/limonitization	BC, VUG	< 5 to 15 %
Immental 2	142.5-229.0	-	up to 190 ppm Pb, 1200 ppm Zn, but mostly < 50 ppm for both	white calcite	calcitization/limonitization	BC, VUG	< 5 to 15 %
	239.7-240.4	-	not elevated	white calcite	calcitization/limonitization	BC, VUG	< 5 to 15 %





## Appendix 2 continued

drill core	interval (m)	macroscopic mineralization	base metal concentrations over 1 m intervals (Brinckmann 1981)	post-dolomite cementation	post-dolomite alteration	porosity types	final porosity (estimated)
Immental 3	9.6-21.5	PbS, ZnS	580 ppm Pb, 75 ppm ZnS	-	calcitization/limonitization	FRAC	20 %
	24.5-26.7	PbS, ZnS	not elevated	-	calcitization/limonitization	BC, VUG	5 %
	81.0-81.9	-	up to 170 ppm Pb, < 50 ppm Zn	white calcite	calcitization/limonitization	BC, VUG	< 5 %
Loh 1	92.7-459.5	PbS, ZnS	up to 620 ppm Pb, 1280 ppm Zn but mostly < 50 ppm for both	clear quartz, white calcite, CSC	calcitization/limonitization	BC, VUG	< 5 to 15 %
	262.5-267.8	-	n.a.	white calcite	calcitization	BC, VUG	5 to 10 %
	573.9-577.4	pyrite, ZnS	n.a.	CSC	-	BC, VUG	5 to 10 %
Loh 3	591.8-592.3	-	n.a.	white calcite	calcitization/limonitization	BC	< 2 %
	613.0-660.4	pyrite, ZnS	n.a.	white calcite, CSC	calcitization/limonitization	VUG, BC	< 5 to 10 %
	48.7-53.6	-	n.a.	CSC, white calcite	calcitization/limonitization	BC, VUG	< 5 %
Loh 3	422.0-425.1	-	n.a.	white calcite	calcitization/limonitization dissolution	VUG	20 %



Appendix 2 continued

drill core	interval (m)	macroscopic mineralization	base metal concentrations over 1 m intervals (Brinckmann 1981)	post-dolomite cementation	post-dolomite alteration	porosity types	final porosity (estimated)
Loh 3	426.7-447.2	ZnS	up to 650 ppm Pb and 3700 ppm Zn	white calcite, CSC	massive calcitization	VUG	15 %
Loh 4	135.8-138.0	-	n.a.	-	limonitization	BC	< 5%
	140.2-140.6	-	n.a.	-	-	BC, VUG	15 %
	192.8-218.3	pyrite PbS	n.a.	white calcite	massive calcitization, limonitization	BC, VUG	< 5 to 10 %
	258.5-259.7	PbS	34000 ppm Pb, 14000 ppm Pb	-	limonitization	n.a.	n.a.
	260.0-260.9	pyrite, PbS	16500 ppm Pb, 1100 ppm Zn	-	limonitization	BC, VUG	n.a.
	261.5-261.6	-	33000 ppm Pb, 16500 ppm Zn	white calcite	calcitization/limonitization	BC	n.a.
	267.0-267.2	-	up to 55 ppm Pb, 65 ppm Zn	white calcite	calcitization	BC	n.a.
	273.4-278.7	-	1200 ppm Pb, 610 ppm Zn	white calcite	calcitization/limonitization	BC, VUG	15 %
Loh 7	163.05-167.2	-	n.a.	white calcite	-	BC	5 %
	175.6-179.1	-	n.a.	CSC	calcitization/limonitization	BC, VUG	15 %
	188.6-190.3	-	n.a.	white calcite	calcitization/limonitization	n/a	n/a
	270.6-271.1	-	n.a.	-	-	BC	< 5 %
	289.2-305.5	PbS, ZnS	up to 1180 ppm Pb, 910 ppm Zn	white calcite, CSC	calcitization	BC, VUG	10 %
	368.1-384.7	pyrite	up to 2200 ppm Pb, 1800 ppm Zn	CSC	calcitization	BC, VUG	10 %
	392.2-392.7	-	n.a.	-	-	BC, VUG	5 to 10 %
	394.6-395.5	-	n.a.	-	-	BC, VUG	5 to 10 %



## Appendix 2 continued

drill core	interval (m)	macroscopic mineralization	base metal concentrations over 1 m intervals (Brinckmann 1981)	post-dolomite cementation	post-dolomite alteration	porosity types	final porosity (estimated)
Madfeld 1	20.0-20.2	PbS	n.a.	white calcite	calcitization/limonitization	n.a.	n.a.
	326.9-328.1	-	n.a.	CSC	-	VUG	15 %
	442.1-442.2	-	n.a.	CSC	calcitization	BC	< 5 %
	443.4-444.0	-	n.a.	white calcite	calcitization	BC	< 5 %
Nehden 2	445.0-520.0	ZnS	n.a.	CSC, white calcite	calcitization/limonitization	VUG, BC	< 5 to 10 %
	530.4-531.6	-	n.a.	white calcite	limonitization	VUG, BC	5 %
	533.0-533.4	-	n.a.	-	calcitization/limonitization	BC	5 %
	538.1-546.5	ZnS	n.a.	CSC	calcitization/limonitization	VUG, BC	< 5 %
	598.7-600.0	ZnS	n.a.	CSC	calcitization/limonitization	VUG, BC	< 5 %
	608.1-639.2	ZnS	n.a.	CSC	calcitization/limonitization	VUG, BC	< 5 %
Romberg 1	91.1-91.4	-	n.a.	white calcite, CSC	calcitization/limonitization	BC, VUG	5 %
	117.4-119.8	-	n.a.	white calcite, CSC	calcitization/limonitization	BC, VUG	5 %
	207.1-207.4	-	n.a.	CSC	calcitization/limonitization	BC, VUG	5 %
	347.0-351.5	-	n.a.	white calcite	calcitization/limonitization originating at open fractures	BC, VUG	5 %





Appendix 2 continued

drill core	interval (m)	macroscopic mineralization	base metal concentrations over 1 m intervals (Brinckmann 1981)	post-dolomite cementation	post-dolomite alteration	porosity types	final porosity (estimated)
Romberg 1	442.5-447.6	-	n.a.	white calcite	calcitization/limonitization	BC, VUG	5 %
	469.2-478.0	-	n.a.	-	limonitization along fractures	n.a.	n.a.
	483.0-491.0	-	n.a.	-	limonitization along fractures	n.a.	n.a.
	626.4-627.1	-	n.a.	white calcite	limonitization along fractures	BC, VUG	5 %
	633.2-666.5	PbS	n.a.	white calcite, CSC	limonitization along open fractures	BC, VUG	5 %
Thülen 2	720.0-732.1	-	n.a.	-	-	BC, VUG	n.a.
	7.3-154.1	-	n.a.	white calcite, CSC	calcitization/limonitization	BC, VUG	< 5 %
	158.8-172.3	-	n.a.	white calcite, CSC	calcitization/limonitization	BC, VUG	< 5 %
	182.0-187.7	-	n.a.	white calcite	calcitization/limonitization	n/a	n.a.
	195.5-200.0	-	n.a.	white calcite	limonitization around cavity	VUG	< 5 %
	234.2-238.0	-	n.a.	CSC	limonitization around open vugs and thin fractures	VUG	< 5 %



Appendix 2 continued

drill core	interval (m)	macroscopic mineralization	base metal concentrations over 1 m intervals (Brinckmann 1981)	post-dolomite cementation	post-dolomite alteration	porosity types	final porosity (estimated)
Thülen 2	252.7-256.8	-	n.a.	CSC	limonitization around open vugs	VUG	n.a.
	262.0-267.0	-	n.a.	white calcite	calcitization	VUG	< 5 %
	282.6-285.3	-	n.a.	white calcite	calcitization/limonitization	n.a.	n.a.
	308.2-309.8	-	up to 80 ppm Pb, 200 ppm Zn	-	limonitization	n.a.	n.a.
	321.7-323.0	-	not elevated	-	limonitization	n.a.	n.a.
	324.9-326.6	-	< 50 ppm Pb, up to 65 ppm Zn	white calcite, CSC	calcitization/limonitization	VUG	5 %



## APPENDIX 3

### Carbonate sample dissolution procedure for ICP analysis ensuring minimum interference of non-carbonate material

1. Weigh ~50 mg sample powder into a 15 ml centrifuge tube (pyrex, no paint). With each batch of 15 samples (centrifuge holds eight 15 ml tubes at one time) include a blank, treating it exactly the same as the samples but without the sample powder.

**NOTE:** From here on, everything should be done in the laminar-flow/clean hood.

2. Add 1.0 ml 1.0 N HCl, dropwise, holding the centrifuge tube at an angle to prevent contact with the sample until all the acid is in the centrifuge tube. Remove the pipette, tip the centrifuge tube to vertical and agitate gently to dissolve the sample. When effervescence dies down tip the centrifuge tube at an angle again and add 2.0 ml 1.0 N HCl (total volume 3.0 ml). Cover with parafilm. Agitate several times over the next hour to ensure contact of acid with sample powder. Ultrasound for 10 min, twice in the next few hours. Leave the sample to dissolve overnight or for a minimum of 6 hours. **Do not use heat or stronger HCl to speed dissolution as this will increase the likelihood of contamination by leaching of clays.**
3. Centrifuge for 10 min at maximum speed.
4. Carefully remove supernatant solution from the residue, using a new clean, disposable pipette for each sample, and transfer the solution to a clean disposable beaker. Avoid transferring any residue. Cover beaker with parafilm.
5. Using a clean, calibrated disposable pipette, add 0.5 ml 1.0 N HCl dropwise to the centrifuge tube, washing the walls. Centrifuge as in step 3 and repeat step 4 adding the washings to the sample solution in the disposable beaker.
6. Repeat step 5 (washing) twice (or three times if significant solution was left in the centrifuge tube at step 4) to ensure quantitative transfer of all soluble material to the disposable beaker. Add 2 or 3 drops of Millipore water to residue, cover the centrifuge tube tightly with parafilm and set aside for step 16.
7. Attach clean, disposable filter to clean, disposable 5 ml syringe. Using clean, disposable





- pipette, transfer 1.0 ml of 1.0 HCl to syringe and push HCl through filter into waste container to ensure proper functioning of syringe and filter and to rinse filter. Remove plunger in preparation for step 8.
8. Remove parafilm from disposable beaker and pour sample solution into syringe. Make sure to transfer all the sample solution. Little droplets in the beaker can be merged to form bigger ones by tapping the beaker on the work surface holding it at a slight angle. Push sample solution through filter into a clean 23 ml Savillex container. Rinse beaker with 0.5 ml Millipore water if necessary and add to sample solution. Rinse syringe and filter with 0.5 ml Millipore to ensure quantitative transfer of soluble sample into Savillex container.
  9. Place the Savillex container with the sample solution on a hot plate in a clean hood and evaporate to dryness.
  10. Add ~0.25 ml (10 drops) Millipore water and ~0.25 ml (10 drops)  $\text{HNO}_3$  conc. (16N). Bake to dryness.
  11. Repeat step 10. Remove from hotplate and cool.
  12. To the cool, dry nitrate residue add 4.0 ml of 3:1  $\text{HNO}_3$  conc:HCl (1N) using a graduated glass pipette with a rubber bulb (could use Eppendorf, if available). Close Savillex container with screw-top. Agitate/ultrasound/heat as necessary to achieve complete solution. Let sample solution cool, if necessary.
  13. Transfer the solution to a 25 ml volumetric flask using a new clean, disposable pipette for each sample, applying numerous small washes of Millipore water (at least three times 1 ml) to achieve a quantitative transfer from the Savillex vessel. Make the solution to volume with 0.3N  $\text{HNO}_3$  (~20 ml) and mix thoroughly. Rinse Savillex container immediately and fill with Millipore water.
  14. Final transfer of sample solution into Nalgene storage bottles has to be done in two steps to avoid spilling the solution. First, transfer the final sample solution to non-wetting 30 ml teflon (Nalgene) beaker, then transfer solution from beaker into new clean Nalgene storage bottle (30 ml).
  15. Rinse volumetric flask immediately and fill with Millipore water.



### **Residues:**

16. Dry a clean, labelled glass slide (one for each sample) for about 30 min in oven at 105°C. Remove from oven using tweezers (not to leave fingerprints), place in desiccator and let cool to room temperature. Weigh.
17. Transfer the residue from step 6 onto the slide, using a minimum of Millipore water and a transfer pipette (disposable pipettes from step 4 can be re-used) to transfer successive aliquots until all is on the slide. Dry on hot plate (set heat to 1/3) in the clean hood. Dry in the oven for about 30 min at 105°C. Place in desiccator and let cool to room temperature. Weigh.
18. If residue is to be retained for future examination scrape or brush it onto a glazed weighing paper and fold up to seal. Label.

### **Time involved for batch of 16 (15 samples + 1 blank; double time for first batch):**

step 1: 90 min

step 2: 60 min

reaction overnight

step 3 to 6: 180 min

step 7 & 8: 90 min

step 9 (baking to dryness): approx. 180 min, preferably overnight.

step 10 & 11: each treatment with Millipore and  $\text{HNO}_3$  takes about 20 min for one batch, time for baking to dryness between treatments may vary (allow at least 1 hour).

step 12: 60 min

step 13: 60 min

step 14 & 15: 45 min



## APPENDIX 4

Results of fluid inclusion microthermometry.

assemblage	= fluid inclusion assemblage
incl. #	= inclusion number
lv	= liquid-vapor, 2-phase fluid inclusion
p	= primary inclusion type
ps	= pseudosecondary inclusion type
s	= secondary inclusion type
Th	= homogenization temperature upon heating
Te	= eutectic temperature or temperature of first melt in inclusion
Tmice	= temperature of final melting of ice in inclusion
equiv.wt. %	= equivalent weight percent





# Appendix 4: Results of fluid inclusion microthermometry.

sample	mineral phase	assemblage	incl. #	type	Th	Te	Tmice	equiv.wt. % NaCl	
AL-726.2a	saddle dol. rim	1	1	lv, p	113.3	-59.9	-	-	
			2	lv, p	109.9	-56.4	-23.7	24.6	
			3	lv, p	112.7	-63.2	-24.0	24.8	
			4	lv, p	109.2	-	-	-	
			5	lv, p	116.3	-	-22.2	23.7	
			6	lv, p	119.0	-65.3	-24.3	25.0	
			average		113.4	-61.2	-23.6	24.5	
		saddle dol. core	2	1	lv, p	115.0	-	-24.1	24.8
				2	lv, p	115.3	-	-24.2	24.9
				average		115.2	-	-24.2	24.9
			total average p		113.8	-61.2	-23.8	24.6	
	3	1	lv, ps	114.8	-	-12.3	16.2		
		2	lv, ps	114.7	-	-12.6	16.5		
		average		114.8	-	-12.5	16.3		
	AL-726.2b	saddle dol.	1	1	lv, p	111.1	-56.0	-	-
				2	lv, p	-	-	-24.3	25.0
				3	lv, p	104.8	-51.0	-26.3	26.2
				average		108.0	-53.5	-25.3	25.6
			2	1	lv, s	93.0	-	-	-
				2	lv, s	93.5	-	-	-
				3	lv, s	94.5	-	-	-
				4	lv, s	94.5	-	-	-
				5	lv, s	96.0	-	-	-
				6	lv, s	96.5	-	-	-
				average		94.7	-	-	-
AL-726.2b		ZnS	1	1	lv, p	103.4	-48.7	-15.1	18.6
				2	lv, p	111.8	-49.0	-17.7	20.6
				3	lv, p	-	-47.8	-18.5	21.2
				4	lv, p	-	-	-17.9	20.8
				average		107.6	-48.5	-17.3	20.3
			2	1	lv, ps	100.3	-49.0	-16.2	19.5
				2	lv, ps	100.0	-47.0	-20.1	22.3
				3	lv, ps	95.5	-43.0	-19.6	22.0
				4	lv, ps	99.5	-52.0	-18.6	21.3
				5	lv, ps	93.5	-47.5	-21.5	23.2
				6	lv, ps	109.3	-47.7	-	-
		3	7	lv, ps	102.0	-47.0	-18.0	20.9	
			8	lv, ps	97.0	-44.7	-21.3	23.1	
			9	lv, ps	97.0	-44.7	-20.4	22.5	
	10		lv, ps	-	-	-20.4	22.5		
	11		lv, ps	-	-	-20.2	22.4		
	average		99.3	-47.0	-19.6	22.0			
	1		1	lv, ps	119.6	-	-15.8	19.2	
			2	lv, ps	105.0	-45.2	-15.8	19.2	
			3	lv, ps	108.5	-47.2	-15.8	19.2	
4		lv, ps	99.0	-45.2	-	-			
average		108.0	-45.9	-15.8	19.2				
total average ps		102.0	-45.9	-18.7	21.3				
total average p and ps		102.76	-47.0	-18.4	21.1				



Appendix 4 continued: Results of fluid inclusion microthermometry.

sample	mineral phase	assemblage	incl. #	type	Th	Te	Tmice	equiv.wt. % NaCl
AL-709.5-6	CSC	1	1	lv, p	-	-47.6	-21.8	23.4
			2	lv, p	-	-47.0	-21.3	23.1
			3	lv, p	-	-44.0	-18.0	20.9
			4	lv, p	-	-39.0	-17.4	20.4
				average	-	-44.4	-19.6	22.0
		2	1	lv, p	-	-	-17.3	20.3
			2	lv, p	-	-	-16.8	20.0
			3	lv, p	-	-38.0	-24.8	25.3
			4	lv, p	-	-49.0	-23.9	24.7
			5	lv, p	-	-42.0	-20.1	22.3
				average	-	-43.0	-20.6	22.5
		7		lv, ps		-45.0	-12.3	16.2
AL-726.8	CSC margin of core	1	1	lv, p	72.9	-	-20.4	22.5
			2	lv, p	71.9	-	-	-
			3	lv, p	72.6	-43.0	-21.2	23.0
			4	lv, p	73.3	-	-21.0	22.9
				average	72.7	-43.0	-20.9	22.8
		5		lv, ps	72.6	-39.0	-13.5	17.3
			6	lv, ps	74.9	-38.0	-13.2	17.0
				average	73.8	-38.5	-13.4	17.1
		2	1	lv, p	88.8	-41.8	-20.1	22.3
			2	lv, p	-	-47.6	-20.5	22.6
			3	lv, p	87.8	-	-	-
				average	88.3	-44.7	-20.3	22.4
		3	1	lv, ps	100.2	-44.2	-12.7	16.6
			2	lv, ps	-	-46.3	-13.6	17.4
			3	lv, ps	-	-	-11.3	15.2
			4	lv, ps	-	-47.0	-10.6	14.5
				average	100.2	-45.8	-12.1	15.9
		4	1	lv, s	-	-	-4.6	7.3
			2	lv, s	91.6	-49.0	-5.6	8.7
			3	lv, s	-	-	-7.6	11.2
			4	lv, s	-	-	-5.9	9.1
			5	lv, s	74.9	-	-5.7	8.8
			6	lv, s	-	-46.0	-6.3	9.6
		5		average	83.3	-47.5	-6.0	9.1
			1	lv, s	70.7	-	-7.8	11.4
			2	lv, s	65.0	-	-7.5	11.1
			3	lv, s	64.2	-	-6.9	10.3
			4	lv, s	67.0	-	-	-
			5	lv, s	65.0	-	-8.0	11.7
		4		average	66.4	-	-7.6	11.1
			1	lv, s	78.9	-	-6.3	9.6
			2	lv, s	78.7	-	-5.7	8.8
			3	lv, s	77.0	-	-5.6	8.7
			4	lv, s	75.9	-	-5.9	9.1
			5	lv, s	76.6	-	-7.8	11.4
		for AL-726.6 CSC		average	77.4	-	-6.3	9.5
				total average p	66.8	-18.9	-14.7	16.2
				total average ps	41.3	-35.8	-12.5	16.3
				total average s	55.3	-5.9	-6.1	9.2



Appendix 4 continued: Results of fluid inclusion microthermometry.

sample	mineral phase	assemblage	incl. #	type	Th	Te	Tmice	equiv.wt. % NaCl
AL-726.2a	CSC	1	1	lv, s	68.0	-	-	-
			2	lv, s	67.0	-	-	-
			3	lv, s	67.5	-	-	-
			4	lv, s	67.5	-	-	-
			5	lv, s	67.5	-	-	-
				average	67.5	-	-	-
AL-726.2b	CSC	1	1	lv, p	98.0	-52.0	-16.9	20.0
			2	lv, p	-	-38.0	-18.1	20.9
			3	lv, p	-	-52.0	-16.1	19.4
			4	lv, p	-	-	-18.3	21.1
				average	98.0	-47.3	-17.4	20.4
		2	1	lv, ps	70.0	-40.0	-13.6	17.4
			2	lv, ps	74.5	-	-	-
			3	lv, ps	70.0	-	-	-
			4	lv, ps	74.0	-	-	-
			5	lv, ps	-	-41.0	-12.5	16.4
			6	lv, ps	-	-40.0	-17.7	20.6
			7	lv, ps	-	-51.0	-11.4	15.3
				average	72.1	-43.0	-13.8	17.4
		for all CSC	total average p		80.8	-44.7	-19.7	22.0
			total average ps		76.6	-43.2	-12.9	16.7
			total average s		71.9	-47.5	-6.5	9.8





## **APPENDIX 5**

Results of field measurements, analyses of chemical and isotopic composition of saline groundwater samples from the Münsterland Cretaceous Basin



Appendix 5: Results of field measurements, analyses of chemical and isotopic composition of saline groundwater samples from the Münsterland Cretaceous Basin.

sample number	1	2	3	4
well/spring/mine	B 14 N	Bad Waldliesborn I	Iduna-Quelle	Bad Westernkotten 1 (W. Warte)
location	Bad Sassendorf	Lippstadt	Bottrop-Kirchhellen	Erwitte
R	3441523	3454202	2560980	3455485
H	5718019	5731270	5718860	5722535
depth [m]	411	910	658.5	79
aquifer lithology	shale/sandstone	shale	sandstone	limestone
stratigraphy	Middle Devonian	Middle Devonian	Upper Carboniferous	Upper Cretaceous
temperature [°C]	21.3	31.4	n.a.	n/a
pH	6.6	6.3	n.a.	6.4
conductivity [mS/m]	6690	9630	n.a.	n/a
Na [mg/l]	29250	37420	13450	24600
K [mg/l]	506	650	121.76	482
Ca [mg/l]	1515	1811	2100	1636
Mg [mg/l]	310	251	521	215
Fe [mg/l]	15.3	16.1	7.5	17
Mn [mg/l]	0.3	0.7	0.38	0.6
Cl [mg/l]	48000	60000	24500	40000
SO4 [mg/l]	747	1370	1870	1263
HCO3 [mg/l]	1183.7	1427.7	146.44	1598.6
NO3 [mg/l]	<0.499	<0.499	<0.499	<0.499
Zn [mg/l]	0.005	0.104	0.013	0.009
Cu [mg/l]	<0.003	0.25	<0.003	<0.03
Ni [mg/l]	0.012	0.1	0.02	0.037
Co [mg/l]	<0.002	0.002	<0.002	<0.002
Sr [mg/l]	110	76.5	70	68.5
B [mg/l]	3.08	4.1	6.4	2.4
Cd [mg/l]	<0.001	<0.001	<0.001	<0.001
Cr [mg/l]	<0.004	<0.004	<0.004	<0.004
Pb [mg/l]	<0.006	<0.006	<0.006	<0.006
As [mg/l]	<0.02	<0.02	<0.02	<0.02
Ba [mg/l]	0.027	0.2	0.029	0.03
F [mg/l]	0.08	0.37	0.87	0.1
P [mg/l]	<0.099	<0.099	1.69	<0.099
N [mg/l]	29.8	39.1	12.7	20
Al [mg/l]	0.015	<0.005	0.114	0.124
Li [mg/l]	21.4	19.6	3.6	9.94
TDS [mg/l]	90764	112674	49600	83434
87Sr/86Sr	0.71165	0.71262	0.70845	0.71134
delta18O [SMOW]	-7.8	-8.29	-4.56	-8.37
delta D [SMOW]	-57.55	-59.28	-29.48	-55.01
delta34S [CDT]*	13.5	14.5	-	13.3
comments	well	well, artesian	Zeche Prosper, near Krudenberg-Sprung	well, artesian

\* from Michel and Nielsen (1977)



Appendix 5 continued: Results of field measurements, analyses of chemical and isotopic composition of saline groundwater samples from the Münsterland Cretaceous Basin.

sample number	5	6	7	8
well/spring/mine	Saline Gottesgabe	Ibbenbüren Ostfeld	Weidtmann-Sprudel	Neue Martins-Quelle
location	Rheine	Ibbenbüren	Bad Rothenfelde	Bad Laer
R	2596868	3417200	3442720	3437845
H	5796972	4796350	5775180	5775005
depth [m]	440	1360 to 1560	83	160
aquifer lithology	shale	limestone/sandstone	limestone	limestone
stratigraphy	Lower Cretaceous	Upper Carboniferous	Upper Cretaceous	Upper Cretaceous
temperature [°C]	n/a	n/a	16.6	??17.6
pH	7.2	n/a	6.6	6.6
conductivity [mS/m]	1384	n/a	5390	6300
Na [mg/l]	14890	38660	17940	23000
K [mg/l]	86.887	185	248	306
Ca [mg/l]	395	1020	1435	1643
Mg [mg/l]	150	408	223	260
Fe [mg/l]	<0.002	<0.002	21.2	16.6
Mn [mg/l]	0.05	<0.001	0.52	0.7
Cl [mg/l]	23500	62000	28000	36000
SO <sub>4</sub> [mg/l]	<0.199	939	2400	2997
HCO <sub>3</sub> [mg/l]	573.56	445.42	2074.5	2257.5
NO <sub>3</sub> [mg/l]	<0.499	<0.499	<0.499	<0.499
Zn [mg/l]	0.005	3.6	0.012	0.017
Cu [mg/l]	<0.003	<0.003	<.003	<0.003
Ni [mg/l]	0.007	0.02	0.026	0.03
Co [mg/l]	<0.002	<0.002	<0.002	<0.002
Sr [mg/l]	63.8	59.2	47.7	37
B [mg/l]	3.5	1.25	2.5	2.7
Cd [mg/l]	<0.001	<0.001	<0.001	<0.001
Cr [mg/l]	<0.004	<0.004	<0.004	<0.004
Pb [mg/l]	<0.006	<0.006	<0.006	<0.006
As [mg/l]	<0.02	<0.02	<0.02	<0.02
Ba [mg/l]	9.709	0.38	0.02	0.017
F [mg/l]	0.39	0.29	0.13	0.16
P [mg/l]	<0.099	<0.099	<0.099	<0.099
N [mg/l]	19.4	22.3	11.9	13.5
Al [mg/l]	0.021	0.064	0.07	0.117
Li [mg/l]	3.6	8.75	3.5	4.2
TDS [mg/l]	46586	116820	58208	72508
<sup>87</sup> Sr/ <sup>86</sup> Sr	0.70883	0.71319	0.70945	0.71003
delta18O [SMOW]	-6.28	-6.99	-8.8	-9.46
delta D [SMOW]	-42.2	-45.32	-61.12	-62.1
delta 34S [CDT]	**11.2	-	-	*11.4
comments	well	subsurface coal mine	well	well

\* from Michel and Nielsen (1977); \*\* from Bässler (1970)





Appendix 5 continued: Results of field measurements, analyses of chemical and isotopic composition of saline groundwater samples from the Münsterland Cretaceous Basin.

sample number	9	10	11	12
well/spring/mine	Wünschelbrunnen (Solbad Ravensberg)	Sültoid 3	Kaiser-Heinrich-Quelle	Padulus (Schloss Neuhaus)
location	Borgholzhausen	Salzkotten	Warstein-Belecke	Paderborn
R	3448035	3472965	3453595	3480360
H	5773728	5725395	5706495	5734710
depth [m]	13	0	33	192
aquifer lithology	Sand	sand	shale/sandstone	limestone
stratigraphy	Pleistocene	Pleistocene	Upper Devonian	Upper Cretaceous
temperature [°C]	16.5	13.4	13.4	19.5
pH	6.8	6.6	7.3	6.8
conductivity [mS/m]	1973	2350	701	720
Na [mg/l]	5355	6366	1735	1425
K [mg/l]	84.971	104.42	51.471	23.75
Ca [mg/l]	483	455	175.26	341
Mg [mg/l]	61.811	38.565	33.886	19.067
Fe [mg/l]	<0.002	0.42	0.71	0.44
Mn [mg/l]	0.001	0.35	0.15	0.2
Cl [mg/l]	7900	9700	2800	2423
SO4 [mg/l]	843	462	95	136.67
HCO3 [mg/l]	1342.3	1183.7	378.3	567.45
NO3 [mg/l]	<0.499	<0.499	<0.499	7.269
Zn [mg/l]	0.034	0.002	0.006	0.144
Cu [mg/l]	<0.003	<0.003	<0.003	0.008
Ni [mg/l]	0.013	0.021	0.004	0.009
Co [mg/l]	<0.002	<0.002	<0.002	<0.002
Sr [mg/l]	27.3	9.306	6.324	6.263
B [mg/l]	1.024	0.635	0.347	0.123
Cd [mg/l]	<0.001	<0.001	<0.001	<0.001
Cr [mg/l]	<0.004	<0.004	<0.004	0.019
Pb [mg/l]	<0.006	<0.006	<0.006	<0.006
As [mg/l]	<0.02	<0.02	<0.020	0.025
Ba [mg/l]	0.026	0.02	0.069	0.071
F [mg/l]	1.3	0.41	0.54	0.23
P [mg/l]	<0.099	<0.099	<0.099	<0.099
N [mg/l]	3.12	3.3	0.85	<0.5
Al [mg/l]	0.038	0.016	0.019	0.025
Li [mg/l]	1.1	2.594	1.268	0.652
TDS [mg/l]	15694	18166	5726	5402
<sup>87</sup> Sr/ <sup>86</sup> Sr	0.70883	0.71176	0.71357	0.71059
delta18O [SMOW]	-8.92	-8.07	-8.63	-8.15
delta D [SMOW]	-59.3	-55.72	-56.37	-52.79
delta 34S [CDT]	-	*10.8	-	-
comments	well, artesian	spring, artesian	well, artesian	well, artesian

\* from Michel and Nielsen (1977)



Appendix 5 continued: Results of previous field measurements and analyses of the chemical composition of saline groundwater samples from the Münsterland Cretaceous Basin, taken at some of the same sampling locations and carried out by the Institute Fresenius.

sampling date	Fresenius 1991	Fresenius 1992	Fresenius 1956	Fresenius 1996
compares to sample	1	2	4	9
well/spring/mine	B 14 N	Bad Waldliesborn I	Bad Westernkotten 1 (W. Warte)	Wünschelbrunnen (Solbad Ravensberg)
location	Bad Sassendorf	Lippstadt	Erwitte	Borgholzhausen
R	3441523	3454202	3455485	3448035
H	5718019	5731270	5722535	5773728
depth [m]	411	910	79	13
aquifer lithology	shale/sandstone	shale	limestone	Sand
stratigraphy	Middle Devonian	Middle Devonian	Upper Cretaceous	Pleistocene
temperature [°C]	20.4	34.8	23	16.3
pH	5.7	5.98	6.6	6.28
conductivity [mS/m]	n.d.	n.d.	n.d.	n.d.
Na [mg/l]	34530	45040	28160	5700
K [mg/l]	490	775	401.1	65
Ca [mg/l]	1773	2271	1807	489
Mg [mg/l]	372	318	246.7	68
Fe [mg/l]	17.1	20.6	23.14	3.1
Mn [mg/l]	0.34	0.89	0.73	0.033
Cl [mg/l]	56930	73460	45892	8568
SO <sub>4</sub> [mg/l]	758	1435	1325	823
HCO <sub>3</sub> [mg/l]	1217	1440	1628	1330
NO <sub>3</sub> [mg/l]	< D.L.	< D.L.	< D.L.	< D.L.
Zn [mg/l]	< D.L.	0.15	n.d.	< D.L.
Cu [mg/l]	0.007	0.017	n.d.	0.004
Ni [mg/l]	0.008	< D.L.	n.d.	0.002
Co [mg/l]	0.002	0.007	n.d.	< D.L.
Sr [mg/l]	129	106	n.d.	24
B [mg/l]	4.66	6.42	n.d.	2.32
Br [mg/l]	29	38	18.1	3.1
Cd [mg/l]	< D.L.	< D.L.	n.d.	< D.L.
Cr [mg/l]	< D.L.	< D.L.	n.d.	< D.L.
Pb [mg/l]	0.002	0.015	n.d.	0.002
As [mg/l]	0.003	0.052	n.d.	0.005
Ba [mg/l]	0.18	0.23	n.d.	0.034
F [mg/l]	0.37	1.1	n.d.	2.1
P [mg/l]	n.a.	n.a.	n.d.	n.a.
N [mg/l]	< D.L.	< D.L.	n.d.	< D.L.
Al [mg/l]	n.a.	n.a.	n.d.	n.a.
Li [mg/l]	16	6.7	n.d.	1.2
TDS [mg/l]	96327	125007	n.d.	16500
Br/Cl	0.00051	0.00052	0.00039	0.00036



## APPENDIX 6

### REFEREED PUBLICATIONS

- Grobe, M. & Machel, H.G., 1997, Petrographic and C and O isotope evidence for fault-controlled hydrothermal mineralization of the Devonian Brilon Reef Complex, Germany (translated title). - Zentralblatt für Geologie und Paläontologie, Teil 1, 1996, (5/6), 5 fig., 397-413, Stuttgart (Schweizerbart).
- Grobe, M. & Machel, H.G., 1996, Post-Variscan dolomitization of the Devonian Brilon Reef Complex, northeastern Rhenish Schiefergebirge, Germany (translated title). - Zentralblatt für Geologie und Paläontologie, Teil 1, 1995, (½), 4 fig., 131-143, Stuttgart (Schweizerbart).

### ABSTRACTS

- Grobe, M. & Machel, H.G., 1998, Post-Variscan pervasive dolomitization of the Devonian Brilon Reef Complex, Germany: an example of fault-controlled hydrothermal dolomitization. GEOTRIAD '98, June 16-18, 1998, Calgary.
- Grobe M. & Machel, H.G., 1998, Fault-controlled basin-scale migration of brines in the Rhenish Massif, Germany: a hypothesis. -GEOTRIAD '98, June 16-18, 1998, Calgary.
- Grobe M. & Machel, H.G., 1997, Petrographic and geochemical evidence for fault-controlled hydrothermal mineralization of the Brilon Reef Complex, Germany. - Association of American Petroleum Geologists Bulletin, 81/10, p. 1175.
- Grobe M. & Machel, H.G., 1997, Fault-controlled basin-scale fluid migration of mineralizing fluids in the northeastern Rhenish Massif, Germany. - Gaea heidelbergensis, 3, abstracts of 18<sup>th</sup> IAS Regional Meeting in Sedimentology, Heidelberg, September 1-4, 1997, 1 fig., p. 150.
- Grobe M., Machel, H.G., Riciputi, L.R., 1996, Hydrothermal mineralization of the Devonian Brilon Reef Complex, northeastern Rhenish Schiefergebirge, Germany (translated title). - Sediment '96, 11<sup>th</sup> Annual Meeting of Sedimentologists, May 10-14, 1996, Vienna, Austria, program with abstracts, p. 44.
- Grobe, M. & Machel, H.G., 1995, Dolomitization of the Devonian Brilon Reef Complex, northeastern Rhenish Schiefergebirge, Germany (translated title). - Sediment '95, 10<sup>th</sup> Annual Meeting of Sedimentologists, May 24-26, 1995, Freiberg in Sachsen, Germany, program with abstracts, p. 70-71.





## APPENDIX 7

Zbl. Geol. Paläont. Teil I	1995	H. 1/2	131–143	Stuttgart, Mai 1996
----------------------------	------	--------	---------	---------------------

### Postvariszische Dolomitisierung des devonischen Briloner Riffkomplexes, nordöstliches Rheinisches Schiefergebirge, Deutschland

Post-Variscan dolomitization of the Devonian Brilon Reef Complex,  
northeastern Rhenish Schiefergebirge, Germany

Von MATTHIAS GROBE und HANS G. MACHEL, Edmonton

Mit 4 Abbildungen im Text

GROBE, M. & MACHEL, H. G. (1996): Postvariszische Dolomitisierung des devonischen Briloner Riffkomplexes, nordöstliches Rheinisches Schiefergebirge, Deutschland. [Post-Variscan dolomitization of the Devonian Brilon Reef Complex, northeastern Rhenish Schiefergebirge, Germany.] - Zbl. Geol. Paläont. Teil I, 1995 (1/2): 131–143; Stuttgart.

**Abstract:** Pervasively dolomitized intervals from 9 cores from the eastern part of the Brilon Reef Complex were logged and sampled in detail to gain information about their spatial and temporal distribution and the conditions of their formation. The spatial distribution of the dolomitized intervals suggests that there exists a close relationship between dolomitization and subvertical, Saxonian faults. Data from thin-section petrography, XRD and stable isotope analysis define three dolomite types that may be genetically linked and probably were formed under influence of meteoric water and/or at elevated temperatures. Jurassic-Cretaceous intrusive bodies, suspected in the deep subsurface, could have served as heat sources.

**Zusammenfassung:** Pervasiv dolomitisierte Intervalle aus 9 Bohrkernen aus dem östlichen Teil des Briloner Riffkomplexes wurden makroskopisch untersucht und beprobt, um ihre räumliche und zeitliche Verteilung sowie ihre Bildungsbedingungen zu ergründen. Die räumliche Verteilung der dolomitisierten Intervalle deutet darauf hin, daß ein ursächlicher Zusammenhang zwischen der Dolomitisierung und subvertikalen saxonischen Störungen besteht. Dünnschliffuntersuchungen, Röntgendiffraktometrie und  $\delta^{18}\text{O}$ -Daten definieren Dolomittypen, die wahrscheinlich eine enge genetische Verwandtschaft aufweisen und eine Entstehung unter Einfluß von meteorischem Wasser unter erhöhten Temperaturen andeuten. Als Wärmequelle könnten in größerer Tiefe vermutete jurassisch-kretazische Intrusivkörper in Frage kommen.

0340-5109/96/1995-0131 \$ 3.25

© 1996 E. Schweizerbart'sche Verlagsbuchhandlung, D-70176 Stuttgart



## 1. Einleitung

Ausgedehnte Vorkommen devonischer Flachwasserkarbonate sind aus Westkanada, Australien, China und Mitteleuropa bekannt. Während sie in Westkanada zu einem Großteil pervasiv (= durchgreifend) dolomitisiert vorliegen und sich dort als wichtige Speichergesteine für Kohlenwasserstoffe erweisen (z. B. MACHEL & MOUNTJOY 1987), tritt Dolomit in den anderen devonischen Karbonatprovinzen nur untergeordnet auf. Der mittel- bis oberdevonische Briloner Riffkomplex im nordöstlichen Rheinischen Schiefergebirge ist insofern eine Ausnahme, daß er meter- bis zehnermeter mächtige, pervasiv dolomitisierte Intervalle aufweist, welche in mehreren Bohrkernen angetroffen wurden. In Teilen des Riffkomplexes sind diese Dolomite Träger einer stark gangartenbetonten Buntmetallvererzung mit hauptsächlich Sphalerit, Bleiglanz und Pyrit/Markasit (BRINKMANN 1981, SCHAEFFER 1986). Das Ziel der vorliegenden Studie ist es,

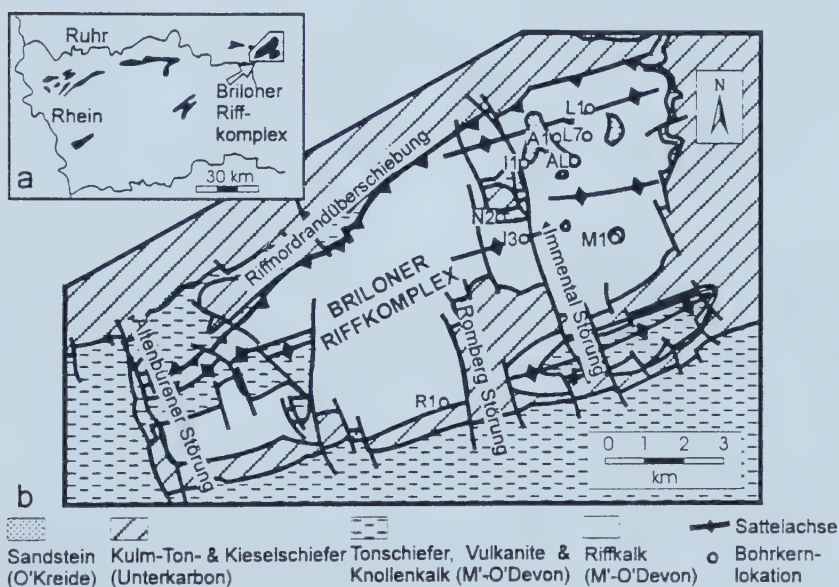


Abb. 1 a, b. Geographische Lage und vereinfachte geologische Übersichtskarte des Briloner Riffkomplexes (verändert nach BRINKMANN 1981). Die schwarzen Objekte in Abb. 1 a repräsentieren die Lagen von devonischen Karbonatkomplexen im Rheinischen Schiefergebirge. Bohrkernbezeichnungen: A1 = Alme 1, AL = Almerfeld, I1 = Immental 1, I3 = Immental 3, L1 = Auf dem Loh 1, L7 = Auf dem Loh 7, M1 = Madfeld 1, N2 = Nehden 2, R1 = Romberg 1.

Fig. 1 a, b. Location and simplified geological map of the Brilon Reef Complex (modified after BRINKMANN 1981). Black objects in Fig. 1 a represent locations of Devonian carbonate complexes in the Rhenish Schiefergebirge. Core I.D.s: A1 = Alme 1, AL = Almerfeld, I1 = Immental 1, I3 = Immental 3, L1 = Auf dem Loh 1, L7 = Auf dem Loh 7, M1 = Madfeld 1, N2 = Nehden 2, R1 = Romberg 1.



die Herkunft dieser dolomitisierten Intervalle mit Hilfe petrographischer und geochemischer Methoden näher zu beleuchten. Außerdem werden Vergleiche zu Dolomiten in anderen devonischen Karbonatprovinzen angestrebt.

### 1.1 Geologischer Rahmen

Der Briloner Riffkomplex ist Teil eines NE-SW verlaufenden Gürtels von Karbonatkomplexen, die vom Mitteldevon bis ins untere Oberdevon (Adorf) einem dem Old-Red-Kontinent südlich vorgelagerten Schelf aufwuchsen (Abb. 1). Nach dem Ende des Riffwachstums wurde der Briloner Riffkomplex von oberdevonischen Cephalopodenkalken überlagert, auf die rote und grüne Tone des höheren Oberdevons folgten. Eine weitere Vertiefung des Sedimentationsraumes im Unterkarbon führte zur Ablagerung von Kulm-Ton- und -Kieselschiefern, welche im Oberkarbon von flyschartigen Grauwacken überlagert wurden. Faltung und Hebung während der variszischen Orogenese führten zur vollständigen Erosion der karbonischen Schichten im Gebiet des Briloner Riffkomplexes, mit Ausnahme von Überresten in einer schon synsedimentär angelegten Mulde in seinem zentralen Teil sowie in zahlreichen tiefreichenden Spalten, in denen sich karbonische Sedimente sammelten. Bis auf eine marine Ingression während der Oberkreide (Cenoman), welche randlich marine, meist siliciklastische Sedimente hinterließ, verblieb das Gebiet des Briloner Riffkomplexes bis heute im terrestrischen Bereich.

Die variszische Tektogenese resultierte in der nordwärtigen Überschiebung des Karbonatkomplexes auf oberdevonische und unterkarbonische Klastika. Die Karbonatgesteine bilden gegenwärtig im allgemeinen weite, SW-NE streichende Falten, welche durch zwei Störungssysteme weiter strukturiert werden. Eines dieser Systeme verläuft WSW-ENE, subparallel zu den Faltenachsen, und ist mit seinen als Auf- oder Überschiebungen ausgebildeten Störungen auf die variszische Einengung zurückzuführen. Dagegen sind die NNW-SSE verlaufenden Abschiebungen zum Teil prävariszischen, synsedimentären Ursprungs (z. B. Altenbürener Störung, Romberg-Störung, Immental-Störung; Abb. 1) und wurden im Rahmen der postvariszischen (saxonischen) Dehnungstektonik reaktiviert, was zur heutigen strukturellen Unterteilung des Riffkomplexes in einzelne tektonische Blöcke führte (BRINKMANN 1981). Während des späten Mesozoikums und frühen Tertiärs kam es durch hydrothermale Aktivität zu Mineralisierungen entlang vieler dieser Störungen. Die Vererzungen mit Buntmetallsulfiden (Sphalerit, Bleiglanz, Pyrit/Markasit) sind mit den Gangarten Kalzit, Dolomit und Baryt vergesellschaftet (SCHAEFFER 1986).

### 1.2 Bisherige Arbeiten

Die präkinematische diagenetische Entwicklung im Briloner Riffkomplex ist recht gut untersucht (MACHEL 1979, 1990a, b, MORITZ 1983). Die postvariszische Alteration hingegen erfuhr bisher nur eine wenig detaillierte Bearbeitung, mit der Ausnahme einer regionalen Untersuchung der postvariszischen Mineralisation, welche einige Proben vom Briloner Riffkomplex beinhaltete (SCHAEFFER 1984, 1986).





Verschiedene Bearbeiter erwähnen das Vorkommen pervasiv dolomitierter Intervalle in einigen Bohrkernen des Briloner Riffkomplexes, welche im Rahmen eines von der Bundesanstalt für Geowissenschaften und Rohstoffe (BGR) durchgeführten Bohrprogrammes Ende der 70er Jahre gewonnen wurden (MACHEL 1979, 1990a, BRINKMANN 1981, MORITZ 1983, SCHAEFFER 1984, 1986). Über die Anzahl und Ursachen der Dolomitierungsereignisse sowie die räumliche und zeitliche Verteilung der Dolomitintervalle gehen die Meinungen jedoch auseinander.

### 1.3 Methoden und Datenbasis

Bislang wurden 9 Bohrkern aus dem östlichen Teil des Briloner Riffkomplexes unter faziellen und diagenetischen Gesichtspunkten untersucht. Pervasiv dolomitisierte Intervalle wurden in Hinblick auf ihre petrographischen Charakteristika detailliert aufgenommen und beprobt.

Folgende Methoden wurden angewendet:

1. Petrographie: makroskopische Untersuchung der Fazies und Diagenese; Dünnschliffpetrographie und Kathodenlumineszenzmikroskopie;
2. Kristallographie: röntgendiffraktometrische Untersuchungen von 14 Dolomitproben zur Bestimmung ihrer Zusammensetzung (Vol.-%  $\text{CaCO}_3$ ) und ihres Ordnungsgrades;
3. Geochemie: Analyse der Kohlenstoff- und Sauerstoffisotopenzusammensetzungen von Dolomit- und Kalzitproben.

## 2. Fazies und Korrelation der Bohrkern

Acht der neun bisher untersuchten Bohrkern werden hauptsächlich von lagunären Ablagerungen dominiert. Nur der Bohrkern Romberg 1, welcher am südlichen Rifftrand des Riffkomplexes gewonnen wurde, zeigt eine vertikale Abfolge vom Vorriff über den Riffkern in den Ablagerungsbecken des Hinterriffs (MACHEL 1990b).

Eine stratigraphische Korrelation der Bohrkern ist aufgrund der intensiven strukturellen Deformation extrem erschwert. Bedauerlicherweise kann die Biostratigraphie im Briloner Riffkomplex nicht für eine Korrelation benutzt werden, da, bis auf Mischfaunen in jüngeren Spalten, aus den Riffkarbonaten so gut wie keine Conodontenfaunen gewonnen werden konnten (BRINKMANN 1981). Im Rahmen dieser Arbeit wurde versucht, eine Korrelation mit Hilfe von vertikalen Fazieswechseln, welche Schwankungen des relativen Meeresspiegels widerspiegeln, zu erstellen, was jedoch bisher noch zu keinem überzeugenden Ergebnis geführt hat.

Die Verteilung der pervasiv dolomitisierten Intervalle stellte sich als unabhängig von der Ausbildung der Karbonatfazies heraus. Die Behauptung, die Hauptmasse der pervasiven Dolomitisierung sei an den Rändern des Riffkomplexes konzentriert (MORITZ 1983), wird durch das Auftreten von mächtigen dolomitisierten Intervallen in seinem zentralen Teil (Nehden 2, Almerfeld) widerlegt (Abb. 1 und 2).



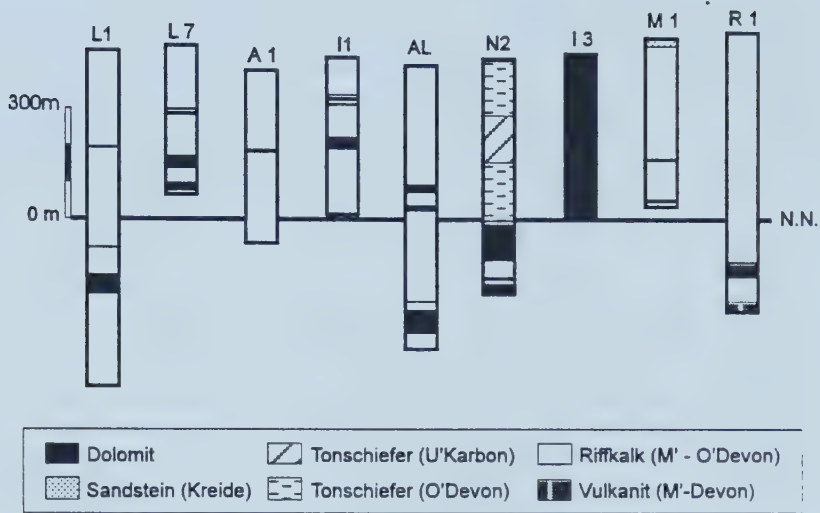


Abb. 2. Verteilung der pervasiven Dolomitintervalle in den untersuchten Bohrkernen relativ zur Lage des heutigen Meeresspiegels (Lokationen und Bezeichnungen der Bohrkern siehe Abb. 1b).

Fig. 2. Distribution of pervasive dolostone intervals within the investigated cores relative to the position of present-day sea-level (for locations and I.D.s of cores see Fig. 1b).

### 3. Postvariszische Diagenese

Alle bisher untersuchten Bohrkern zeigen mehrere pervasiv dolomitisierte Intervalle auf (Abb. 2). Diese Intervalle variieren in ihrer Mächtigkeit von einigen Zentimetern zu mehreren Zehnermetern und treten gewöhnlich in mehreren hundert Metern Tiefe (Auf dem Loh 1, Almerfeld, Nehden 2, Romberg 1) und/oder in der unmittelbaren Nähe von tiefreichenden subvertikalen, saxonischen Störungen (Immental 3) auf. Dieser Befund legt einen genetischen Zusammenhang zwischen der pervasiven Dolomitisierung und diesen Störungen nahe und kann somit, zusammen mit der Überprägung variszischer Deformationsstrukturen und dem engen paragenetischen Zusammenhang mit der posttektogenetischen Mineralisation, als ein weiteres Indiz für postvariszische Dolomitisierung gewertet werden. Das Auftreten von pervasiv dolomitisierten Intervallen in den tieferen Bereichen der längeren Bohrkern kann als ein Hinweis für die Existenz eines zusammenhängenden Dolomitkörpers großen Ausmaßes angesehen werden. Eine von BRINKMANN (1981) und MACHEL (1990b) postulierte genetische Beziehung zur postkretazischen Landoberfläche konnte jedoch bisher nicht bestätigt werden.

#### 3.1 Petrographie

Makroskopische und dünnschliffpetrographische Untersuchungen an den pervasiv dolomitisierten Intervallen führten zur Aufstellung einer vorläufig-



gen paragenetischen Abfolge. Aufgrund der Schwerpunktsetzung dieser Arbeit auf die dolomitisierten Kernintervalle konnten frühdiagenetische Phasen nicht identifiziert werden. Die paragenetisch ältesten Bildungen in den untersuchten Kernintervallen sind Styolithen. Die meisten der Styolithen sind steilstehend, was eher auf tektonische Einengung als auf Kompaktion während der Versenkung zurückzuführen ist. Auf eine Phase der Spaltenbildung und Lösung von Makrofossilien (z. B. *Amphipora*) folgte die pervasive Dolomitisierung des Kalkgesteins, welche in der Bildung von drei textuell unterschiedlichen und paragenetisch aufeinanderfolgenden Dolomittypen resultierte.

Typ 1 ist ein oftmals sedimentäre Gefüge und Fossilien enthaltender, grauer Verdrängungsdolomit. Er besteht aus planaren bis nicht planaren Mosaiken fein- bis grobkristalliner (50-300  $\mu\text{m}$ ), sub- bis anhedraler Dolomitekristalle mit einer hellroten Kathodenlumineszenz oder mit einer dünnen, hellroten Randzone um einen dunkelroten Kern. Er ist gewöhnlich der dominierende Dolomittyp in jenen Bereichen, die makroskopisch als "grauer Matrixdolomit" angesprochen werden. In einigen Fällen tritt Typ 1 auch als Verdrängung von Fossilien mit nahezu mimetischer Erhaltung auf. Die interkristallinen Poren sind gut verbunden.

Typ 2 ist ein milchig-weißer bis leicht rosafarbener, im allgemeinen grobkristalliner Verdrängungsdolomit, der, von Spalten und Lösungshohlräumen ausgehend, Typ 1 entlang diffuser Grenzen in Form von "Verdrängungshalos" mit Ausmaßen von 2 cm bis zu mehreren Metern verdrängt. Er tritt in Form nicht-planarer Mosaiken, grob- bis sehr grobkristalliner (300  $\mu\text{m}$  - 3 mm), sub- bis anhedraler, manchmal undulös auslöschender Kristalle mit dunkelroter Lumineszenz auf. Außer in der Nähe von Spalten und Lösungshohlräumen weist Typ 2 kaum interkristalline Porosität auf.

Typ 3 ist ein milchig-weißer, sehr grobkristalliner Dolomitcement (800  $\mu\text{m}$  - 5 mm), welcher meist als sub- bis euhedraler, dunkelrot lumineszierender Satteldolomit mit gebogenen Kristallflächen und undulöser Auslöschung in den verbleibenden Spalten und Lösungshohlräumen auftritt.

Auf eine zweite Spaltenbildungsphase folgte die Abscheidung geringer Mengen (<1 Vol.-% in den bearbeiteten Kernen) von Sulfiden (Pyrit/Markasit, Sphalerit, Bleiglanz). Die paragenetischen Beziehungen zwischen Dolomitlösung und Sulfidmineralisation konnten bisher noch nicht eindeutig geklärt werden. In einigen Fällen wurde vormalig dolomitisiertes Gestein in der Nähe von Spalten durch grobkristallinen Kalzit verdrängt. In den verbliebenen Lösungshohlräumen und Spalten treten bis zu 2 cm große, weißliche bis klare, euhedrale Kalzitzementkristalle auf, welche aus einer Fe-armen inneren und einer Fe-reichen äußeren Zone aufgebaut sind.

In Dünnschliffen vom Bohrkern "Auf dem Loh 1" treten längliche, euhedrale Kristalle authigenen Quarzes (60-600  $\mu\text{m}$ ) innerhalb dolomitisierter und kalzitierter Intervalle auf. Viele dieser Kristalle sind korrodiert und/oder teilweise durch spätere Phasen (z. B. Kalzit) verdrängt worden und weisen Einschlüsse von Dolomitrhomben auf, jedoch niemals von Kalzit. Diese Tatsache stellt ihre Bildung zwischen die Dolomitisierung und spätere Kalzitisierung.

### 3.2 Stöchiometrie und Ordnungsgrad der Dolomittypen

14 Dolomitproben (Typ 1: n = 5; Typ 2: n = 6; Typ 3: n = 3) vom Bohrkern "Almerfeld" wurden röntgendiffraktometrisch untersucht, um ihre





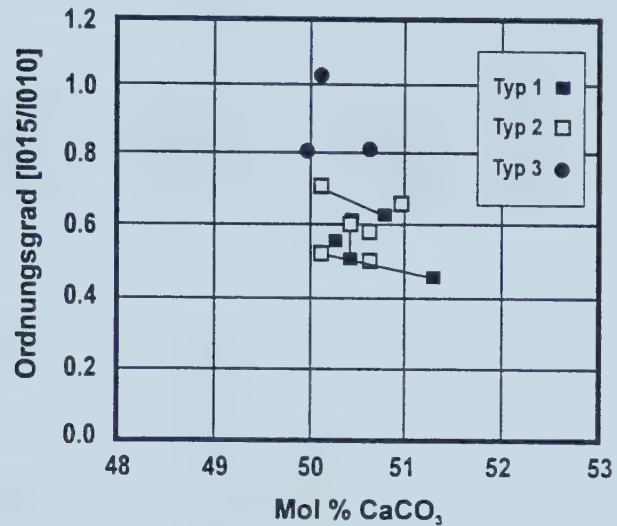


Abb. 3. Ergebnisse der röntgendiffraktometrischen Untersuchungen der drei Dolomittypen zur Bestimmung ihres CaCO<sub>3</sub>-Gehaltes (in Mol-%) und ihres Ordnungsgrades (Verhältnis der Intensitäten der Reflektionen 015 und 010). Die Linien verbinden Dolomittypen 1 und 2 aus denselben Handstücken.

Fig. 3. Results of XRD-analysis of the three dolomite types to determine their CaCO<sub>3</sub> content (in mole %) and degree of order (ratio of intensities of reflections 015 and 010). Lines connect dolomite types 1 and 2 from the same core samples.

CaCO<sub>3</sub>-Gehalte und ihre Ordnungsgrade zu bestimmen (Abb. 3). Diese Daten haben potentiell genetische Bedeutung. Dolomite mit einem hohen Ordnungsgrad (>0,5) und nahezu stöchiometrischen Ca:Mg-Verhältnissen bilden sich allgemein bei erhöhten Temperaturen und/oder sind Rekristallisationsprodukte von weniger stöchiometrischen, weniger geordneten Dolomiten, welche sich bei niedrigeren Temperaturen gebildet hatten (TUCKER & WRIGHT 1990).

Die CaCO<sub>3</sub>-Gehalte aller drei Dolomit-Typen fallen in den Bereich zwischen 49,9 und 51,3 Mol-% (Abb. 3). Während die Ordnungsgrade (errechnet aus dem Verhältnis der Reflektionsintensitäten I015/I010) der Typen 1 und 2 etwa gleich sind (0,46 bis 0,72), haben die des Typs 3 deutlich höhere Ordnungsgrade (0,82 bis 1,03). In Fällen, in denen verschiedene Dolomittypen aus einem Handstück analysiert wurden, zeigt Typ 1 immer einen niedrigeren Ordnungsgrad und den gleichen oder einen höheren CaCO<sub>3</sub>-Gehalt als die benachbarten Typen 2 und 3.

Diese Daten, zusammen mit den oben genannten petrographischen Merkmalen, deuten darauf hin, daß Typ 2 ein Rekristallisationsprodukt von Typ 1 ist. Die hohen Ordnungsgrade des Typs 3 können auf sein relativ ungehindertes Wachstum als Zement zurückgeführt werden.



### 3.3 Stabile Isotope

Bisher wurde folgendes Probenmaterial, unter der Anwendung der Standardmethoden nach McCREA (1950) und EPSTEIN et al. (1964), auf seine  $\delta^{13}\text{C}$ - und  $\delta^{18}\text{O}$ -Werte hin untersucht: Dolomittyp 1:  $n = 11$ ; Dolomittyp 2:  $n = 9$ ; Dolomittyp 3:  $n = 1$ ; euhedraler Kalzit:  $n = 4$ ; kalzitische Stromatopore:  $n = 1$ . Die analytischen Daten sind in Abb. 4 graphisch dargestellt.

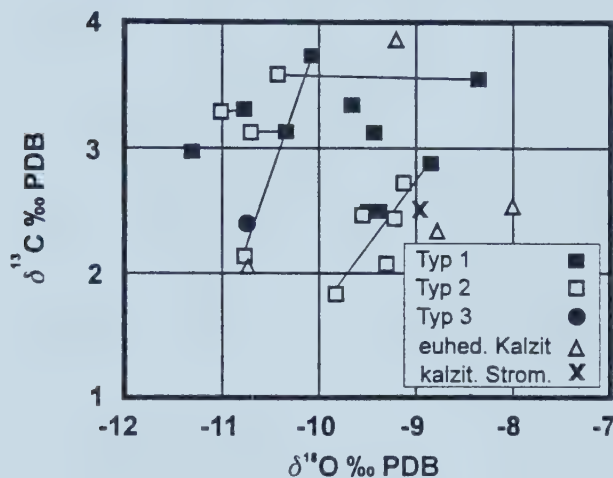


Abb. 4. Ergebnisse der Analyse der stabilen Kohlenstoff- und Sauerstoffisotopenzusammensetzungen der drei Dolomittypen, euhedralen Kalzite und einer kalzitischen Stromatopore. Die Linien verbinden Dolomittypen 1 und 2 aus denselben Handstücken.

Fig. 4. Results of the analysis of the carbon and oxygen isotope compositions of the three dolomite types, euhedral calcites and one calcitic stromatoporoid. Lines connect dolomite types 1 and 2 from the same samples.

#### 3.3.1 Kohlenstoffisotope

Die  $\delta^{13}\text{C}$ -Werte aller drei Dolomittypen fallen in den Bereich von +1,8 bis +3,7 ‰ PDB. Typ 2 scheint zwei Populationen bei +2 bzw. +3,4 ‰ PDB zu bilden. Die vier Kalzit:zementproben und die kalzitische Stromatopore weisen Werte zwischen +2,1 und +3,8 ‰ PDB auf.

Für im Gleichgewicht mit mittel- bis oberdevonischem Meerwasser gebildete Karbonate wird allgemein ein  $\delta^{13}\text{C}$ -Wert von ca. +2 ‰ PDB angenommen (POPP et al. 1986, VEIZER et al. 1986). Im Verlaufe des jüngeren Paläozoikums ist jedoch ein Anstieg des  $\delta^{13}\text{C}$ -Wertes in marinen Karbonaten auf bis zu +4 ‰ PDB zu verzeichnen (LOHMANN & WALKER 1989). Demzufolge könnte die in der vorliegenden Studie beobachtete Spannweite der  $\delta^{13}\text{C}$ -Werte auf eine Beimischung spätpaläozoischen Meerwassers zurückzuführen sein. Andere Prozesse könnten jedoch auch dafür



verantwortlich sein: (1) Reduktion von  $\text{CO}_2$  zu  $\text{CH}_4$  (SILVERMAN & OYAMA 1968, CLAYPOOL & KAPLAN 1974); (2) Spätstadien der Oxydation organischer Substanzen zu  $\text{CO}_2$  in  $\text{C}_{\text{org}}$ -armen Sedimenten (DEUSER 1970); (3) Gleichgewichtseinstellung zwischen Karbonat und  $\text{CO}_2$  (FRIEDMAN & MURATA 1979); und (4) anaerobe Fermentation (GAMES & HAYES 1976, REITSEMA 1980, LOHMANN et al. 1985).

### 3.3.2 Sauerstoffisotope

Die  $\delta^{18}\text{O}$ -Werte der analysierten Dolomitproben streuen von -8,4 bis -11,3 ‰ PDB (Abb. 4). Während Dolomittyp 1 mit seinen Werten diesen gesamten Bereich abdeckt, hat Typ 2 Werte zwischen -9,8 und -11,0 ‰ PDB. In Fällen, in denen Typ 1 und 2 aus demselben Handstück analysiert wurden, weist Typ 2 meist um bis zu 2 ‰ negativere  $\delta^{18}\text{O}$ -Werte auf. Dünnschliffuntersuchungen zeigten, daß einige Bereiche des "grauen Matrixdolomits" sowohl Dolomittyp 1 als auch Typ 2 enthalten. In diesen Fällen haben beide Typen nahezu gleiche Werte. Der bisher einzige Wert für Dolomittyp 3 hat keinerlei statistische Aussagekraft.

Basierend auf den besten Abschätzungen für marine  $\delta^{18}\text{O}$ -Werte (POPP et al. 1986, VEIZER et al. 1986, CARPENTER & LOHMANN 1989), sollten die  $\delta^{18}\text{O}$ -Werte für mittel- und oberdevonische Dolomite bei ca. 0 ‰ PDB liegen. Die viel niedrigeren  $\delta^{18}\text{O}$ -Werte der Briloner Dolomitproben deuten auf den möglichen Einfluß von an  $^{18}\text{O}$  verarmten Porenwässern (meteorisches Wasser) und/oder erhöhten Temperaturen hin. Die Abnahme der  $\delta^{18}\text{O}$ -Werte von Typ 1 nach Typ 2 kann als ein weiteres Indiz für die Interpretation des Typs 2 als ein Rekristallisationsprodukt von Typ 1 gewertet werden. Weiterhin weisen die Isotopendaten zusammen mit Dünnschliffbeobachtungen auf eine inverse Beziehung zwischen Kristallgröße und  $\delta^{18}\text{O}$ -Wert bei allen drei Dolomittypen hin, was jedoch noch quantitativ belegt werden muß.

Die  $\delta^{18}\text{O}$ -Werte der drei Kalzitemente fallen in den Bereich zwischen -8,0 und -10,7 ‰ PDB, die kalzitische Stromatopore hat einen Wert von -9,0 ‰ PDB (Abb. 4). Auch diese Werte deuten auf den Einfluß von an  $^{18}\text{O}$  verarmten Fluiden und/oder erhöhten Temperaturen hin. Vorläufige Untersuchungen der Flüssigkeitseinschlüsse von zwei euhedralen Kalziten und die Analyse ihrer Wasserstoffisotopenzusammensetzung ( $T_{\text{H}} = 73,3^\circ\text{C}$ ,  $\delta\text{D} = -44$  ‰ SMOW; GROBE & MACHEL in Vorb.) geben dafür weitere Hinweise. Der niedrige  $\delta^{18}\text{O}$ -Wert der kalzitischen Stromatopore (-9 ‰ PDB gegenüber ca. -3 ‰ PDB für devonischen marinen Kalzit (CARPENTER & LOHMANN 1989) belegt eine Rekristallisation in solchen Porenwässern.

## 4. Schlußfolgerungen

Aufgrund der vorliegenden Daten können die folgenden vorläufigen Schlußfolgerungen gezogen werden:

Eine stratigraphische Korrelation zwischen den einzelnen Bohrungen ist erforderlich, um die zeitlichen Beziehungen zwischen der Dolomitisierung und anderen Mineralisationen relativ zur Versenkungstiefe, zu tektonischen Deformationen und postkinematischen Oberflächenebenen zu bestimmen. Vertikale Faziesänderungen, welche Schwankungen des relativen Meeresspiegels widerspiegeln, können vermutlich wenigstens im südlichen Teil des





Briloner Riffkomplexes, wo die Faziesänderungen am ausgeprägtesten sind, für eine Korrelation herangezogen werden.

Im Gegensatz zu der von MORITZ (1983) geäußerten Meinung, daß der Hauptteil der pervasiven Dolomite im Briloner Riffkomplex auf die Rifffazies am Südrand des Komplexes konzentriert sei, scheint die Verteilung der Dolomitintervalle nicht durch die Ausbildung der Karbonatfazies kontrolliert zu sein. Die meisten der massiven, pervasiven Dolomitintervalle wurden entweder in größerer Tiefe (Romberg 1, Almerfeld, Auf dem Loh 1, Nehden 2) und/oder in der Nähe tiefreichender, NNW-SSE verlaufender Störungen (Immental-Störung, Romberg-Störung) angetroffen. Weiterhin treten diese Dolomitintervalle in einem etwa gleichen Tiefenbereich auf, was die Existenz eines lateral durchgängigen, sedimentäre Fazies und tektonische Strukturen durchkreuzenden Dolomitkörpers vermuten läßt. Die gegenwärtigen Tiefenunterschiede der Dolomitintervalle könnten auf Vertikalbewegungen entlang der Störungen nach der Dolomitisierung oder durch die abdichtende Wirkung dieser Störungen als Permeabilitätsbarrieren während der Dolomitisierung zurückzuführen sein.

Die bisher nur an einer kleinen Anzahl von Proben aus den pervasiv dolomitisierten Intervallen durchgeführten petrographischen Untersuchungen führten zur Identifikation von vermutlich synkinematischer Drucklösung, mindestens zwei Spaltenbildungsphasen, bevorzugter Lösung von Fossilresten, pervasiver Dolomitisierung in drei aufeinanderfolgenden Schritten, Abscheidung von euhedralem Quarz, geringer Vererzung mit Buntmetallsulfiden, Dolomitlösung, Kalzitisierung von Dolomit und Zementation der verbliebenen Lösungshohlräume und Spalten mit mindestens zwei Kalzitgenerationen. Fortlaufende Untersuchungen werden diese Daten verfeinern und in eine umfassende paragenetische Abfolge einordnen.

Die vorläufigen Ergebnisse der röntgendiffraktometrischen und isotope-geochemischen Untersuchungen der drei Dolomittypen sind vielversprechend. Sowohl Dolomittyp 1 als auch Typ 2 sind Verdrängungsformen und genetisch miteinander eng verwandt, da Typ 2 wahrscheinlich durch Rekristallisation aus Typ 1 hervorgegangen ist. Dolomittypen 2 und 3 könnten ebenfalls genetisch miteinander verwandt sein, indem Typ 3 eine frei in größere Hohlräume wachsende Variante des Typs 2 darstellt. Die Sauerstoff- und Wasserstoffisotopendaten deuten weiterhin auf eine Bildung von Typ 2 und 3 unter Einfluß von meteorischem Wasser unter erhöhten Temperaturen hin.

Die Ausbildung von Typ 3 als Satteldolomit sowie die Analyse der isotopischen Zusammensetzung der späten, euhedralen Kalzite und vorläufige Untersuchungen ihrer Flüssigkeitseinschlüsse (GROBE & MACHEL in Vorb.) erbrachten weitere Hinweise auf den möglichen Einfluß meteorischen Wassers bei erhöhten Temperaturen. Als Wärmequellen für eine entsprechende hydrothermale Aktivität könnten tiefliegende, jurassisch-kretazische Intrusivkörper, welche für die Region postuliert werden (HOYER et al. 1976, BEHR et al. 1979, KALKREUTH 1979) und für einen Teil der Vererzungen im Briloner Raum verantwortlich sein sollen (MORITZ 1983, SCHAEFFER 1984, 1986), in Frage kommen.

**Danksagung.** Wir danken D. STOPPEL (BGR) für seine enorme Hilfsbereitschaft und für die Ermöglichung der Bearbeitung und Beprobung der Bohrkern in den Bohrkernlagern der BGR und des NLfB in Wehmingen und



Grubenhagen. K.: STEUERWALD (GLA NRW) gab uns im Briloner Riffkomplex einen Überblick über den geologischen Rahmen und die vielfältigen noch ungelösten Probleme. Finanzielle Unterstützung wurde vom Deutschen Akademischen Austauschdienst und der University of Alberta (MG) sowie von der Alexander-v.-Humboldt-Stiftung und dem Natural Sciences and Engineering Research Council of Canada (HGM) gewährt.

### Literaturverzeichnis

- BEHR, H. J., HESS, H., OELSCHLEGEL, G. & LINDENBERG, H. G. (1979): Die Quarzmineralisation vom Typ Suttrop am N-Rand des rechtsrheinischen Schiefergebirges. - Aufschluß, Sonderbd. 29 (Warstein): 205-231, 13 Abb.; Heidelberg.
- BRINKMANN, J. (1981): Projekt Rhenoharzynikum, Untersuchung der Metallverteilung in geosynklinalen Sedimenten des Rhenoharzynikums in stratiformen Konzentrationen. - Ber. Kernbohrprogr. im Briloner Riffkalk-Komplex: VII u. 65 S. Anh., 129 S., 21 Abb., 5 Tab., 23 Bohrprof.; Hannover (B.-Anst. Geowiss. u. Rohstoffe). [Unveröff.]
- CARPENTER, S. J. & LOHMANN, K. C. (1989):  $\delta^{18}\text{O}$  and  $\delta^{13}\text{C}$  variations in Late Devonian marine cements from the Golden Spike and Nevis reefs, Alberta, Canada. - J. Sedim. Petrol., 59: 792-814, 14 Abb., 1 Tab.; Tulsa.
- CLAYPOOL, G. E. & KAPLAN, I. R. (1974): The origin and distribution of methane in marine sediments. - In: KAPLAN, I. R. (ed.): Natural Gases in Marine Sediments: 99-139, 16 Abb., 4 Tab.; New York (Plenum Press).
- DEUSER, W. G. (1970): Extreme  $^{13}\text{C}/^{12}\text{C}$  variations in Quaternary dolomites from the continental shelf. - Earth Planet. Sci. Letters, 8: 118-124, 3 Tab.; Amsterdam.
- EPSTEIN, S., GRAF, D. L. & DEGENS, E. T. (1964): Oxygen isotope studies on the origin of dolomites. - In: CRAIGH, H., MILLER, S. L. WASSERBURG, G. J. (eds.): Isotopic and cosmic chemistry: 169-180, 2 Abb., 7 Tab.; Amsterdam (North-Holland Publ. Co.).
- FRIEDMAN, I. & MURATA, K. J. (1979): Origin of dolomite in Miocene Monterey Shale and related formations in the Temblor Range, California. - Geochim. Cosmochim. Acta, 43: 1357-1365, 3 Abb., 1 Tab.; New York.
- GAMES, L. M. & HAYES, J. M. (1976): On the mechanism of  $\text{CO}_2$  and  $\text{CH}_4$  production in natural anaerobic environments. - In: NRIAGU, J. O. (ed.): Environmental Biogeochemistry, I: 51-66, 4 Abb., 4 Tab.; Ann Arbor, Mich. (Ann Arbor Sci. Publ. Inc.).
- HOYER, P., CLAUSEN, C.-D., LEUTERITZ, K., TEICHMÜLLER, R. & THOME, K. N. (1976): Ein Inkohlungsprofil zwischen dem Gelsenkirchener Sattel des Ruhrkohlenbeckens und dem Ostsauerländer Hauptsattel des Rheinischen Schiefergebirges. - Fortschr. Geol. Rheinl. u. Westf., 24: 161-162, 1 Abb., 1 Taf.; Krefeld.
- KALKREUTH, W. (1979): Das Inkohlungsbild des Ostsauerländer Hauptsattels im Rhenoharzynikum mit besonderer Berücksichtigung der Trennflächenanalyse. - Fortschr. Geol. Rheinl. u. Westf., 27: 277-321, 13 Abb., 3 Tab., 1 Taf.; Krefeld.



- LOHMANN, K. C., BREINING-AFIFI, K. A., BUDAI, J. M. & CERCONE, K. R. (1985): Enriched carbon-13 compositions in meteoric and shallow burial calcites and dolomites: evidence of organic fermentation during early diagenesis. - SEPM Ann. Midyear Meet., 2: 55; Tulsa.
- LOHMANN, K. C. & WALKER, J. C. G. (1989): The  $\delta^{18}\text{O}$  record of Phanerozoic abiotic marine calcite cements. - Geophys. Res. Lett., 16: 319-322, 5 Figs.; Washington.
- MACHEL, H. G. (1979): Fazies und Diagenese der devonischen Riffcarbonate der Bohrung Romberg (Briloner Riff). - Diplomarb., TU Braunschweig: 231 S., 81 Abb., 6 Tab., 14 Taf.; Braunschweig. [Unveröff.]
- (1990a): Faziesinterpretation des Briloner Riffs mit Hilfe eines Faziesmodells für devonische Riffkarbonate. - Geol. Jb., D95: 43-83, 5 Abb., 6 Taf.; Hannover.
- (1990b): Submarine Frühdiagenese, Spaltenbildungen und prätektonische Spätdiagenese des Briloner Riffs. - Geol. Jb., D95: 85-137, 2 Abb., 5 Taf.; Hannover.
- MACHEL, H. G. & HUNTER, I. G. (1994): Facies Models for Middle to Late Devonian Shallow-Marine Carbonates, with Comparison to Modern Reefs: a Guide for Facies Analysis. - Facies, 30: 155-176, 5 Abb., 7 Taf.; Erlangen.
- MACHEL, H. G. & MOUNTJOY, E. W. (1987): General constraints on extensive pervasive dolomitization - and their application to the Devonian carbonates of Western Canada. - Bull. Canad. Petr. Geol., 35: 143-158, 6 Figs.; Calgary.
- McCREA, J. M. (1950): On the isotopic chemistry of carbonates and a paleotemperature scale. - J. Chem. Physics, 18: 849-857, 5 Figs., 11 Tab.; New York.
- MORITZ, W. (1983): Fazies und Diagenese des Briloner Karbonatkomplexes anhand einiger ausgewählter Bohrungen. - Diss., TU Braunschweig: 180 S., 26 Abb., 4 Tab., 10 Taf.; Braunschweig. [Unveröff.]
- POPP, B. N., ANDERSON, T. F. & SANDBERG, P. A. (1986): Brachiopods as indicators of original isotopic compositions in Paleozoic limestones. - Geol. Soc. Amer. Bull., 97: 1262-1269, 7 Abb., 2 Taf.; Baltimore.
- REITSEMA, R. H. (1980): Dolomite and nahcolite formation in organic-rich sediments: isotopically heavy carbonates. - Geochim. Cosmochim. Acta, 44: 2045-2049, 1 Tab.; New York.
- SCHAEFFER, R. (1984): Die postvariszische Mineralisation im nordöstlichen Rheinischen Schiefergebirge. - Braunsch. geol.-paläont. Diss., 3: 206 S., 43 Abb., 9 Tab., 4 Anl.; Braunschweig.
- (1986): Geochemische Charakteristika und Genese der jungmesozoisch-tertiären Vererzung im Sauerland (Rheinisches Schiefergebirge). - Fortschr. Geol. Rheinl. u. Westf., 34: 337-381, 7 Abb., 11 Tab., 3 Taf.; Krefeld.
- SILVERMAN, M. P. & OYAMA, V. I. (1968): Automatic apparatus for sampling and preparing gases for mass-spectral analysis in studies of carbon isotope fractionation during methane metabolism. - Analyt. Chem., 40: 1833-1837; New York.
- TUCKER, M. E. & WRIGHT, V. P. (1990): Carbonate Sedimentology. - XII u. 482 S., 392 Abb., 4 Tab.; Oxford (Blackwell Sci. Publ.).





VEIZER, J., FRITZ, P. & JONES, B. (1986): Geochemistry of brachiopods: oxygen and carbon isotope records of Paleozoic oceans. - *Geochim. Cosmochim. Acta*, **50**: 1679-1696, 9 Abb., 3 Tab.; New York.

Anschrift der Verfasser:

Dipl.-Geol. MATTHIAS GROBE und Prof. Dr. HANS G. MACHEL, Department of Earth and Atmospheric Sciences, University of Alberta, Edmonton, AB, T6G 2E3, Kanada.



## APPENDIX 8

Zbl. Geol. Paläont. Teil I	1996	H. 5/6	397 – 413	Stuttgart, Juni 1997
----------------------------	------	--------	-----------	----------------------

### Petrographische und stabile Isotopendaten (C und O) für störungskontrollierte hydrothermale Mineralisation im devonischen Briloner Riffkomplex, Deutschland

Petrographic and C and O isotope evidence for fault-controlled hydrothermal  
mineralization of the Devonian Brilon Reef Complex, Germany

Von MATTHIAS GROBE und HANS G. MACHEL, Edmonton

Mit 5 Abbildungen im Text

GROBE, M. & MACHEL, H. G. (1997): Petrographische und stabile Isotopendaten (C und O) für störungskontrollierte hydrothermale Mineralisation im devonischen Briloner Riffkomplex, Deutschland. [Petrographic and C and O isotope evidence for fault-controlled hydrothermal mineralization of the Devonian Brilon Reef Complex, Germany.] - Zbl. Geol. Paläont. Teil I, 1996 (5/6): 397-413; Stuttgart.

**Abstract:** Pervasive dolomitization and minor base metal sulfide mineralization in the Brilon Reef Complex are associated with Saxonian faults. The succession of post-Variscan diagenetic/hydrothermal processes and their impact on the limestone host rocks were investigated using petrographic and geochemical ( $\delta^{13}\text{C}$ ,  $\delta^{18}\text{O}$ ) methods. The  $\delta^{18}\text{O}$ -value of -6.5 ‰ PDB defines the boundary between pre- and posttectogenetic calcites and dolomites. The lower  $\delta^{18}\text{O}$ -values of the posttectogenetic carbonate phases and a drastic decrease of the  $\delta^{18}\text{O}$ -values of the limestone host rocks adjacent to the dolomitized intervals point to the involvement of hydrothermal fluids and the possible influence of meteoric water. Questions about the origin and genesis of these fluids, as well as their transport processes, are under further investigation.

**Zusammenfassung:** Pervasiv dolomitisierte und gering mit Buntmetallsulfiden vererzte Intervalle im Briloner Riffkomplex sind an saxonische Störungen gebunden. Unter Anwendung von petrographischen und isotopengeochemischen ( $\delta^{13}\text{C}$ ,  $\delta^{18}\text{O}$ ) Methoden wurde die Abfolge der postvariszischen diagenetischen/hydrothermalen Prozesse sowie deren Auswirkung auf das Karbonatnebengestein untersucht. Der  $\delta^{18}\text{O}$ -Wert von -6,5 ‰ PDB bestimmt die Grenze zwischen prä- und posttektogenetischen Kalziten und Dolomiten. Niedrigere  $\delta^{18}\text{O}$ -Werte der posttektogenetischen Karbonatphasen sowie

0340-5109/97/1996-0397 \$ 4.25

© 1997 E. Schweizerbart'sche Verlagsbuchhandlung, D-70176 Stuttgart



eine drastische Abnahme der  $\delta^{18}\text{O}$ -Werte des Kalkgesteins in unmittelbarer Nähe der dolomitisierten Bereiche geben Hinweise auf eine Beteiligung von hydrothermalen Lösungen und den möglichen Einfluß von meteorischem Wasser. Die Fragen nach der Herkunft und Genese dieser Lösungen sowie ihrer Transportprozesse werden weiter untersucht.

## 1. Einleitung

Der im nordöstlichen Rheinischen Schiefergebirge gelegene devonische Briloner Riffkomplex weist mehrere, offensichtlich an tiefreichende saxonsche Störungen gebundene Zonen von Rekristallisation, Karbonatzementation und Vererzung auf. Pervasive (= durchgreifende) Dolomitisierung und Rekristallisation des Nebengesteins kommen mit Mächtigkeiten von Metern bis Zehnermetern vor und sind in vielen Fällen mit einer Buntmetallvererzung (Pyrit/Markasit, Zinkblende, Bleiglanz) vergesellschaftet (BRINKMANN 1981). Die dolomitisierten Intervalle weisen viele petrographische Ähnlichkeiten mit Dolomitvorkommen in West-Kanada auf, die oftmals Kohlenwasserstoff- und in einigen Fällen Buntmetallsulfidlagerstätten von wirtschaftlicher Bedeutung enthalten (MOUNTJOY 1994). Der Briloner Riffkomplex kann daher als Fallstudie dienen, um die Entstehung ähnlicher Vorkommen näher zu beleuchten. Nachdem sich eine vorhergehende Arbeit (GROBE & MACHEL 1996) hauptsächlich mit der Charakterisierung der postvariszischen Dolomittypen befaßt hat, ist es das Ziel der vorliegenden Arbeit, die Abfolge der diagenetischen/hydrothermalen Prozesse mittels petrographischer und isotopengeochemischer Methoden mit Schwerpunkt auf deren Auswirkung auf die isotopische Zusammensetzung der Karbonatgesteine im Briloner Riffkomplex zu ermitteln. Aus den Ergebnissen können Rückschlüsse auf die Herkunft und Zusammensetzung der dolomitisierenden und erzbringenden Lösungen sowie auf mögliche hydrologische Transportprozesse und die Bedingungen, unter denen diese Lösungen zur Rekristallisation, Karbonatzementation und Vererzung geführt haben, gezogen werden.

### 1.1 Geologischer Rahmen

Vom Mitteldevon bis ins untere Oberdevon kam es auf einem dem Old Red-Kontinent südlich vorgelagerten Schelf zur Bildung von Karbonatkomplexen (Abb. 1a). Der Briloner Riffkomplex entstand am Schelfrand zeitgleich mit basischer vulkanischer Aktivität im südlich davon gelegenen Becken. Auf ein biostromales Initialstadium folgte die Ausbildung eines biohermalen Riffkomplexes. Die biostromalen und biohermalen Gesteine werden allgemein unter dem Begriff "Massenkalk" zusammengefaßt (KREBS 1967). Das Riffwachstum kam im unteren Oberdevon (Adorf) vermutlich durch ein Zusammenspiel mehrerer, für die Produktivität der Rifforganismen ungünstiger Faktoren, wie z. B. einer Zunahme der Wassertiefe (BÄR 1966, MACHEL 1979, 1990a) und einer klimatischen Abkühlung (MALMSHEIMER et al. 1991), zum Erliegen. Auf dem abgestorbenen Riffkomplex wurden im weiteren Verlauf des Oberdevons Cephalopodenkalke und dann rote und grüne tonige Siltsteine abgelagert, die eine Vertiefung des Ab-





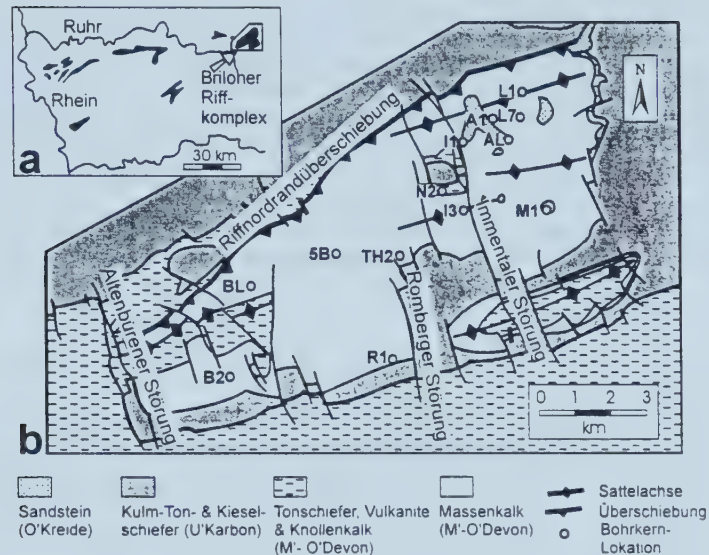


Abb. 1 a und b. Geographische Lage und vereinfachte geologische Übersichtskarte des Briloner Riffkomplexes (verändert nach BRINKMANN 1981). Die schwarzen Objekte in Abb. 1a repräsentieren die Lagen von devonischen Karbonatkomplexen im Rheinischen Schiefergebirge. Bohrkernbezeichnungen: A1 = Alme 1, AL = Almerfeld, B2 = Brilon 2, BL = Blumenstein, 5B = Fünf Brücken, I1 = Immental 1, I3 = Immental 3, L1 = Auf dem Loh 1, L7 = Auf dem Loh 7, M1 = Madfeld 1, N2 = Nehden 2, R1 = Romberg 1, TH2 = Thülen 2.

Fig. 1 a and b. Location and simplified geological map of the Brilon Reef Complex (modified after BRINKMANN 1981). Black objects in Fig. 1a represent locations of Devonian carbonate complexes in the Rhenish Schiefergebirge. For core I.D.'s see German legend.

lagerungsraumes anzeigen. Darauf folgen im Unterkarbon pelagische (Kulm-)Ton- und Kiesel-schiefer, die im Verlaufe des Oberkarbons durch flyschartige Grauwacken abgelöst wurden, die auf das Herannahen der variszischen Deformationsfront von Süden her zurückzuführen sind. Diese erreichte das nordöstliche Rheinische Schiefergebirge im Westfal/Stefan und führte zur Auffaltung des Briloner Riffkomplexes in WSW-ENE streichenden Falten und zu seiner nordwärtigen Überschiebung auf klastische Gesteine des Oberdevons und Unterkarbons (BRINKMANN 1981). Mehrere Hebungsphasen führten seitdem zur Erosion der karbonischen Schichten auf großen Teilen des Briloner Riffkomplexes. In der Oberkreide wurde das Gebiet letztmalig in den marinen Sedimentationsbereich einbezogen, was z. B. durch Plänerkalke in Spalten und durch Erosionsreste randlich-mariner, meist siliziklastischer Sedimente, die den devonischen Massenkalk im Ostteil des Riffkomplexes diskordant überlagern, belegt ist (Abb. 1b).

Im Briloner Riffkomplex treten zwei Störungssysteme besonders hervor: 1. ein WSW-ENE, subparallel zu den Faltenachsen verlaufendes System von



Auf- sowie Überschiebungen, die ihren Ursprung in der variszischen Deformation haben, und 2. ein NNW-SSE verlaufendes System von Abschiebungen (Altenbürener Störung, Romberger Störung, Immentaler Störung, s. Abb. 1b) zum Teil prävariszischen, synsedimentären Ursprungs, die durch postvariszische (saxonische) tektonische Bewegungen reaktiviert wurden (BÄR 1966, BRINKMANN 1981). Die NNW-SSE gerichteten Störungen dienten nach der variszischen Deformation bis ins frühe Tertiär offenbar wiederholt als Aufstiegswege für hydrothermale Lösungen, die zur lokalen Vererzung mit Buntmetallsulfiden (Zinkblende, Bleiglanz, Pyrit/Markasit) mit Kalzit, Dolomit und Baryt als Hauptgangarten führten (SCHAEFFER 1986, WERNER 1990).

## 1.2 Bisherige Arbeiten

Die Buntmetallsulfidvererzungen des Briloner Galmeidistriktes wurden zuerst von SCHRIEL (1954) aufgrund ihres Auftretens in unmittelbarer Nähe saxonischer Störungen und der überlagernden Reste kretazischer Sandsteine als saxonische hydrothermale Bildungen interpretiert. Er beschrieb Buntmetallvererzungen in Kalzit- (untergeordnet Baryt-) Gangspalten und Karsthohlräumen des Massenkalkes und in Gangspalten in Gesteinen der Kreide sowie metasomatische Vererzungen, welche im Massenkalk mit Dolomit, jedoch in Gesteinen der Kreide häufig mit Baryt vergesellschaftet sind. Die postvariszischen Buntmetallsulfidvererzungen im Briloner Raum wurden durch BRINKMANN (1981), SCHAEFFER (1984, 1986) und WERNER (1990) weiter bearbeitet. Diese Arbeiten haben ihren Schwerpunkt in der Untersuchung der Erzminerale und Gangarten und befassen sich nur am Rande mit den Auswirkungen der hydrothermalen Mineralisation auf das Nebengestein (z. B. Rekristallisation, pervasive Dolomitisierung). Das Auftreten pervasiv dolomitisierter Intervalle wurde zuerst von GROBE & MACHEL (1996) in einen ursächlichen Zusammenhang mit den subvertikalen, schwach vererzten saxonischen Störungen gestellt. Mit Hilfe von petrographischen, kristallographischen und isotopengeochemischen Untersuchungen definierten sie drei, offenbar genetisch eng miteinander verwandte Dolomittypen, die wahrscheinlich bei erhöhten Temperaturen unter dem möglichen Einfluß von meteorischem Wasser gebildet wurden. Ziel der hier vorliegenden Arbeit ist es, die isotopengeochemischen Auswirkungen der postvariszischen diagenetischen/hydrothermalen Prozesse auf die Karbonatgesteine genauer zu charakterisieren.

## 1.3 Datenbasis und Methoden

Für die vorliegende Studie wurden pervasiv dolomitisierte Intervalle sowie deren Nebengesteinsbereiche (bis jeweils 20 m oberhalb und unterhalb der Dolomitintervalle) aus 13 Bohrkernen vom Briloner Riffkomplex (Abb. 1b) unter diagenetischen Gesichtspunkten beprobt und untersucht. An ausgewählten Proben wurden petrographische (Dünnschliffpetrographie, Kathodenlumineszenzmikroskopie) und geochemische (C- und O-Isotopenanalysen) Untersuchungen durchgeführt.



2. Ablauf der Diagenese im Briloner Riffkomplex

Abb. 2 zeigt einen schematischen Überblick über den Ablauf der Diagenese und hydrothermalen Mineralisation (hier zur Vereinfachung kollektiv "Diagenese" genannt) im Briloner Riffkomplex. Hierzu wurden die Daten von MACHEL (1979, 1990b), MORITZ (1983) und GROBE & MACHEL (1996) verwendet und durch die Ergebnisse der vorliegenden Studie ergänzt. MACHEL (1979, 1990b) unterteilte die "Diagenese" des Briloner Riffkomplexes in fünf Stadien. Stadien I bis III sind prätektonogenetisch bezüglich der variszischen Deformation und schließen syndimentäre Frühdiagenese (Stadium I), Diagenese unter einer geringen Sedimentbedeckung (<30 m) (Stadium II) und Diagenese bei zunehmender Versenkung (Stadium III) ein. Über die maximale Versenkungstiefe des Briloner Riffkomplexes am Ende von Stadium III liegen bislang nur Schätzungen vor, jedoch betrug sie sicherlich mehr als 2000 m (MACHEL 1990b, BÜKER et al. 1995). Stadium IV umfaßt die syntektonogenetischen mineralogischen und textuellen Veränderungen und Stadium V die posttektonogenetische "Diagenese". Die meisten diagenetischen Phasen der Stadien I bis III sind in den Arbeiten von MACHEL (1979, 1990b) und MORITZ (1983) bereits beschrieben. Eine von GROBE & MACHEL (1996) vorgestellte vorläufige paragenetische Abfolge der postvariszischen "Diagenese" wird durch weitere petrographische Untersuchungen hiermit weitgehend bestätigt (s. u.).

STRATIGRAPHIE	DEVON BIS UNTERKARBON			OBER-KARB.	PERM BIS REZENT
DIAGENESE-STADIUM DIAGENESE-PHASE TIEFE	PRATEKTOGENETISCHE DIAGENESE			SYN-TEKT.	POST-TEKTOGENET.
	I	II	III	IV	V
		max. 30 m	30m bis >2000 m	?	?
Mikritisierung	■				
Karbonatlösung	■				■ ■
Internsediment	■ ■	■ ■			■
Kalzitcement	■ ■ ■ ■ ■ ■ ■ ■		■ ■	■ ■	■ ■ ■ ■
Spaltenbildung		■ ■ ■ ■ ■ ■ ■ ■	■ ■	■ ■	■ ■ ■ ■
Dolomit		■ ■	■ ■		■ ■
Quarz		■ ■		■ ■	■ ■
Limonit/Goethit		■ ■	■ ■		■ ■
Dedolomitisierung		■ ■	■ ■		■ ■
Rekristallisation		■ ■		■ ■	■ ■ ■ ■
Styloolithisation			■ ■	■ ■	
Pyrit/Markasit			■ ■	■ ■	■ ■
Zinkblende					■ ■
Bleiglanz					■

Abb. 2. Schematische Darstellung der paragenetischen Abfolge im Briloner Riffkomplex, erstellt und ergänzt aufgrund von Daten von MACHEL (1979, 1990b), MORITZ (1983) und GROBE & MACHEL (1996).

Fig. 2. Schematic representation of the paragenetic sequence of the Brilon Reef Complex based on data from this study and data from MACHEL (1979, 1990b), MORITZ (1983), and GROBE & MACHEL (1996).





## 2.1 Petrographie

In den pervasiv dolomitisierten Bohrkernbereichen sind die Diagenese-produkte der prätektonischen Diagenesestadien durch posttektonische Prozesse überprägt. Durch makroskopische Untersuchungen an 13 Bohrkernen und petrographische Untersuchungen an 51 Dünnschliffen von 8 Bohrkernen konnten drei Spaltenbildungsphasen, zwei Phasen von Karbonatlösung, mindestens zwei direkt aufeinanderfolgende Dolomitierungsphasen, mehrere Phasen der Kalzitisierung und Kalzitcementation, eine Bildungsphase von authigenem Quarz und Abscheidungsphasen von Pyrit/

Abb. 3. a: Bohrkern Almerfeld (AL), Teufe 681,1 m: Von subhorizontaler Spalte ausgehende Verdrängung von grauem Matrixdolomit (Typ 1) durch weißlichen grobkristallinen Dolomit (Typ 2). Maßstab = 1 cm.

b: Bohrkern Almerfeld (AL), Teufe 713,8 m: Offener Lösungshohlraum innerhalb eines pervasiv dolomitisierten Bereiches. Fast vollständige Verdrängung von Dolomittyp 1 (1) durch Dolomittyp 2 (2). Als Satteldolomit ausgebildeter Dolomittyp 3 (3) konnte frei in den Lösungshohlraum hineinwachsen, gefolgt von Zinkblende (4) und klarem, euhedralem Kalzitcement (5). Maßstab = 1 cm.

c: Bohrkern Almerfeld (AL), angefärbter Dünnschliff, Teufe 709,5 m: Als Satteldolomit ausgebildeter Dolomittyp 3 (1) gefolgt von Zinkblende (2). Anschließend Lösung und/oder Kalzitisierung der Außenzonen der Dolomitekristalle sowie eines unbestimmten rundlichen Objektes (Pfeile), in dessen Zentrum und auf dessen Rand Zinkblende abgeschieden wurde. Maßstab = 0,5 mm.

d: Bohrkern Nehden 2 (N2), Teufe 482,6 m: Limonit/Goethit (Pfeil) auf angelösten Flächen von Dolomittyp 3 (1), welcher einen Lösungshohlraum innerhalb eines pervasiv dolomitisierten Bereiches (Dolomittyp 1) auskleidet. Der verbleibende Hohlraum ist mit klarem Kalzit (2) zementiert. Maßstab = 1 cm.

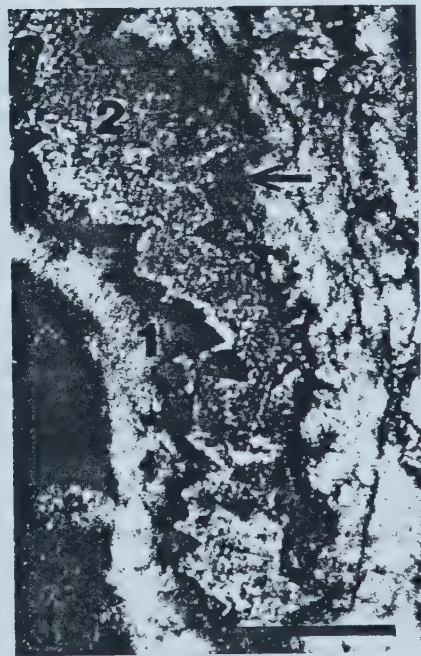
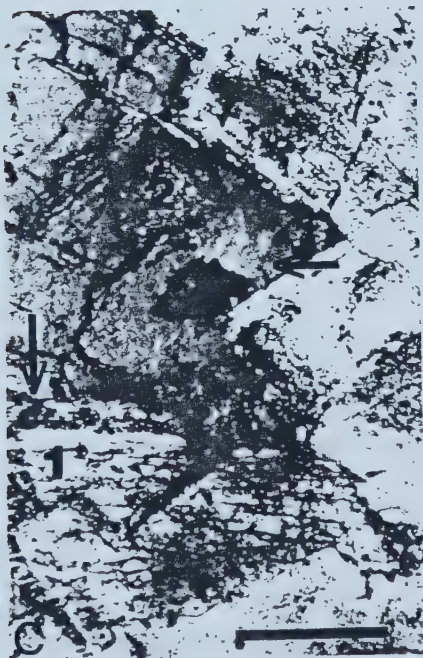
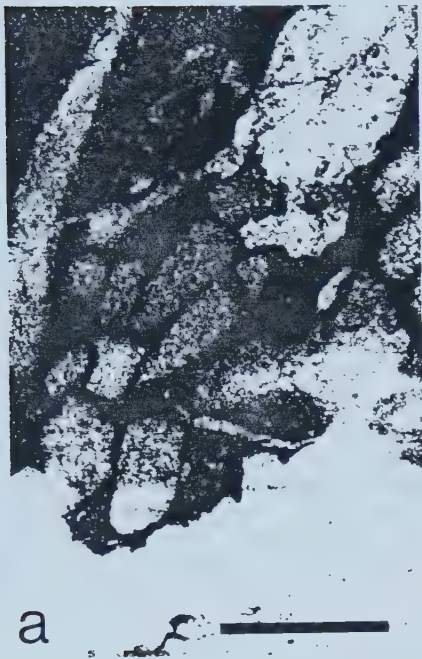
Fig. 3. a: Drillcore Almerfeld (AL), depth 681.1 m: Replacement of grey matrix dolomite (Type 1) by whitish coarse-crystalline dolomite (Type 2) originating at subhorizontal fracture. Scale bar = 1 cm.

b: Drillcore Almerfeld (AL), depth 713.8 m: Open solution vug within pervasively dolomitized interval. Almost complete replacement of Dolomite Type 1 (1) by Dolomite Type 2 (2). Dolomite Type 3 (3) is present as saddle dolomite that grew into the open vug space, followed by sphalerite (4) and clear, euhedral calcite cement (5). Scale bar = 1 cm.

c: Drillcore Almerfeld (AL), stained thin section, depth 709.5 m: Saddle dolomite (Type 3) (1) followed by sphalerite (2). Subsequent dolomite dissolution and/or calcitization of outer zones of saddle dolomite crystals and of an unidentified round object (arrows) with sphalerite in its centre and on its rim. Scale bar = 0.5 mm.

d: Drillcore Nehden 2 (N2), depth 482.6 m: Limonite/goethite (arrow) on corroded surfaces of Dolomite Type 3 (1) lining a solution vug within a pervasively dolomitized interval (Dolomite Type 2). The remaining pore space is cemented by clear calcite (2). Scale bar = 1 cm.









Markasit, Zinkblende und Bleiglanz für das Diagenesestadium V identifiziert werden (Abb. 2). Der Anteil der Buntmetallsulfide ist mit durchschnittlich weniger als 1 Vol.-% unbedeutend. Die zwei postvariszischen Dolomitierungsphasen resultierten in der Bildung von drei Dolomittypen (GROBE & MACHEL 1996) (Abb. 3a und b): grauer, feinkristalliner ( $<300\text{ }\mu\text{m}$ ), den Kalkstein verdrängender Matrixdolomit (Typ 1); weißlicher, grobkristalliner ( $300\text{ }\mu\text{m} - 3\text{ mm}$ ) Dolomit (Typ 2), der Typ 1 von Spalten und Lösungshohlräumen ausgehend verdrängt; und weißlicher, grobkristalliner ( $800\text{ }\mu\text{m} - 5\text{ mm}$ ), meist als Satteldolomit ausgebildeter, in den Spalten und Lösungshohlräumen auftretender Dolomitcement (Typ 3). Alle drei Dolomittypen scheinen genetisch eng miteinander verwandt zu sein (GROBE & MACHEL 1996), wobei nicht auszuschließen ist, daß Typ 1 zumindest teilweise auf eine noch ältere Dolomitierungsphase zurückzuführen ist. Zur Dolomit- und Kalzitlösung kam es nach der sich an Dolomit Typ 3 anschließenden Buntmetallsulfidvererzung (Abb. 3c). In vielen Fällen tritt rostig-brauner Limonit/Goethit auf den angelösten Flächen auf (Abb. 3d). Zudem wurde das Massenkalkgestein von den Spalten ausgehend rekristallisiert und Teile der dolomitisierten Bereiche kalzitisiert. Zuletzt kam es zur Abscheidung von euhedralen Kalzitcementkristallen, welche in einigen Fällen aus einem Fe-armen Kern und einer Fe-reichen äußeren Zone aufgebaut sind (GROBE & MACHEL 1996).

### 3. Stabile Isotope

Die isotopengeochemischen Untersuchungen sollten zeigen, ob und inwieweit sich prätektogenetische Karbonatphasen von denen des posttektogenetischen Stadiums isotopisch unterscheiden lassen und ob sich die Auswirkungen von posttektogenetischen diagenetischen/hydrothermalen Lösungen im Nebengestein der pervasiv dolomitisierten Bereiche erkennen lassen. Hierzu wurden nicht alle beobachteten Karbonatphasen, sondern nur eine Auswahl von prä- und posttektogenetischen Karbonatphasen beprobt. Folgendes Probenmaterial wurde unter Anwendung der Standardmethoden nach McCREA (1950) und EPSTEIN et al. (1964) auf seine  $\delta^{13}\text{C}$ - und  $\delta^{18}\text{O}$ -Werte hin untersucht:

1. prätektogenetische Karbonatphasen: mikritisches Kalkgestein ( $n = 30$ ); kalzitische Fossilien ( $n = 10$ ); radiaxial-fibröser Kalzitcement ( $n = 1$ ).
2. posttektogenetische Karbonatphasen: grauer Matrixdolomit (Dolomit Typ 1:  $n = 23$ ); weißlicher, grobkristalliner Dolomit (Dolomit Typen 2 und 3:  $n = 20$ ); spättektogenetischer Kalzitcement ( $n = 11$ ).

Die im Massenspektrometer gemessenen Isotopenverhältnisse werden in der  $\delta$ -Notation in permil relativ zum PDB-Standard angegeben. Die Reproduzierbarkeit der Messungen ist besser als 0,2 ‰ für  $\delta^{13}\text{C}$  und  $\delta^{18}\text{O}$ .

#### 3.1 Prätektogenetische Karbonatphasen

Die Ergebnisse der isotopengeochemischen Untersuchungen an prätektogenetischen Karbonatphasen sind in Abb. 4a dargestellt. Die  $\delta^{13}\text{C}$ - und  $\delta^{18}\text{O}$ -Werte der Kalksteinproben fallen in den Bereich zwischen +1,4 und





+5,5 ‰ PDB und -2,8 und -8,8 ‰ PDB. Die untersuchten Proben kalzitischer Fossilien weisen  $\delta^{13}\text{C}$ -Werte zwischen +1,3 und +3,6 ‰ PDB und  $\delta^{18}\text{O}$ -Werte zwischen -3,6 und -9,0 ‰ PDB auf, die Probe des radiaxial-fibrösen Kalzitiments einen  $\delta^{13}\text{C}$ -Wert von +2,1 ‰ PDB und einen  $\delta^{18}\text{O}$ -Wert von -4,0 ‰ PDB.

Ein  $\delta^{13}\text{C}$ -Wert von ca. +2,0 ( $\pm 1,0$ ) ‰ PDB kann allgemein als Richtwert für im isotopischen Gleichgewicht mit mittel- bis oberdevonischen Meerwasser gebildete Karbonate angenommen werden (VEIZER et al. 1986, HURLEY & LOHMANN 1989, LOHMANN & WALKER 1989). Die  $\delta^{13}\text{C}$ -Werte des radiaxial-fibrösen Kalzitiments, der meisten kalzitischen Fossilproben und 40 % der Kalksteinproben fallen in diesen Bereich. Die übrigen untersuchten Kalksteinproben sind im Vergleich dazu an  $^{13}\text{C}$  angereichert (Abb. 4a). Diese Anreicherung kann entweder durch frühdiagenetische Fermentationsprozesse (GAMES & HAYES 1976, LOHMANN et al. 1985) entstanden sein, die bis zu einer maximalen Versenkungstiefe von 1000 m ablaufen können (ALLAN & WIGGINS 1993), oder durch Oxidation organischer Substanzen zu  $\text{CO}_2$  in  $\text{C}_{\text{org}}$ -armen Sedimenten bei größerer Versenkungstiefe (DEUSER 1970).

Generell werden die schwersten  $\delta^{18}\text{O}$ -Werte innerhalb eines Datensets als beste Einschätzungen der primären  $\delta^{18}\text{O}$ -Werte von marinen Karbonaten angesehen (O'NEIL 1987). Für die als primär interpretierten  $\delta^{18}\text{O}$ -Werte wird oft ein Bereich von maximal  $\pm 1$  ‰ als Variationsbreite angegeben (z. B. HURLEY & LOHMANN 1989, ALLAN & WIGGINS 1993). Demzufolge liegt der Bereich primärer  $\delta^{18}\text{O}$ -Werte für die mittel- bis oberdevonischen Karbonate des Briloner Riffkomplexes zwischen -4,8 und -2,8 ‰ PDB (Abb. 4a). Die  $\delta^{18}\text{O}$ -Werte des radiaxial-fibrösen Kalzitiments und der Mehrzahl der Kalkstein- und kalzitischen Fossilproben vom Briloner Riffkomplex fallen in diesen Bereich. Untersuchungen von MORITZ (1983) ergaben für oberdevonische radiaxial-fibröse Kalzite vom Briloner Riffkomplex einen fast deckungsgleichen  $\delta^{18}\text{O}$ -Wertebereich zwischen -4,9 und -2,9 ‰ PDB. Basierend auf einer umfangreichen Zusammenstellung der publizierten  $\delta^{18}\text{O}$ -Werte mariner kalzitischer Invertebraten und Zemente geben ALLAN & WIGGINS (1993) einen Bereich von -3,7 bis -5,8 ‰ PDB für  $\delta^{18}\text{O}$  von "am wenigsten veränderten" ("least altered") devonischen marinen Kalziten an (Abb. 4a). Dieser Bereich deckt sich ebenfalls mit der Mehrzahl der untersuchten Proben. Die Ursache für die gegenüber dem von ALLAN & WIGGINS (1993) angegebenen Bereich um ca. 1 ‰ angereicherten maximalen  $\delta^{18}\text{O}$ -Werte im Briloner Riffkomplex ist bisher noch unbekannt, jedoch mögen lokale Faktoren (Wassertemperatur, Salinität, Einfluß juvenilen Wassers durch Vulkanismus) eine Rolle gespielt haben. Demgegenüber reflektieren die niedrigeren  $\delta^{18}\text{O}$ -Werte der übrigen Proben Rekristallisation bei erhöhten Temperaturen und/oder unter der Beteiligung von an  $^{18}\text{O}$ -verarmten Lösungen.

### 3.2 Posttektogenetische Karbonatphasen

In Abb. 4b sind die Ergebnisse der isotopengeochemischen Untersuchungen der posttektogenetischen Karbonatphasen graphisch dargestellt. Die  $\delta^{13}\text{C}$ -Werte aller untersuchten posttektogenetischen Karbonatproben fallen zwischen +1,8 und +3,9 ‰ PDB, ihre  $\delta^{18}\text{O}$ -Werte zwischen -6,7 und -11,3 ‰ PDB. Die gemessenen  $\delta^{13}\text{C}$ -Werte fallen in den gleichen Bereich wie die



Werte der Mehrzahl der prätektogenetischen Karbonatphasen. Dieses deutet darauf hin, daß es zum Zeitpunkt der Abscheidung der untersuchten posttektogenetischen Karbonatphasen zu einer Gleichgewichtseinstellung der C-Isotope zwischen dem Kalkgestein und den diagenetischen/hydrothermalen Lösungen gekommen war.

Andererseits sind die posttektogenetischen Karbonatphasen gegenüber denen der Mehrzahl der prätektogenetischen Karbonate stark an  $^{18}\text{O}$  verarmt. Dies deutet auf eine Bildung dieser Karbonate bei erhöhten Temperaturen und/oder unter Beteiligung von an  $^{18}\text{O}$ -verarmten Lösungen hin (meteorische Wässer). Die relativ große Spannbreite der  $\delta^{18}\text{O}$ -Werte posttektogenetischer Karbonatphasen kann auf unterschiedliche Temperaturen bei ihrer Bildung bzw. der Verdrängung und Rekristallisation älterer Karbonatphasen und/oder auf Unterschiede im Mengenverhältnis Lösung zu Gestein zurückzuführen sein (TAYLOR 1979).

Aus der diese Ergebnisse zusammenfassenden Abb. 4c ist ersichtlich, daß der  $\delta^{18}\text{O}$ -Wert von ca.  $-6,5\text{‰}$  PDB die untersuchten Karbonatphasen des Briloner Riffkomplexes in eine prätektogenetische ( $\delta^{18}\text{O} > -6,5\text{‰}$  PDB) und eine posttektogenetische Gruppe ( $\delta^{18}\text{O} < -6,5\text{‰}$  PDB) aufteilt. Proben mit einem  $\delta^{18}\text{O}$ -Wert  $< -6,5\text{‰}$  PDB sind bei erhöhten Temperaturen und/oder dem Einfluß von an  $^{18}\text{O}$  verarmten Lösungen rekristallisiert (Kalkgestein, Fossilien) oder gebildet worden (Matrixdolomit, weißlicher Dolomit, spätdiagenetische Kalzitmente). Nach ALLAN & WIGGINS (1993) liegt bei diesem Wert auch die Grenze zwischen fröhdagenetischem Dolomit ( $\delta^{18}\text{O} > -6,5\text{‰}$  PDB) und Dolomit, der unter erhöhten Temperaturen gebildet wurde ( $\delta^{18}\text{O} < -6,5\text{‰}$  PDB). Dies steht mit den Befunden der vorliegenden Arbeit und der von GROBE & MACHEL (1996) im Einklang.

### 3.3 Isotopen-Trends

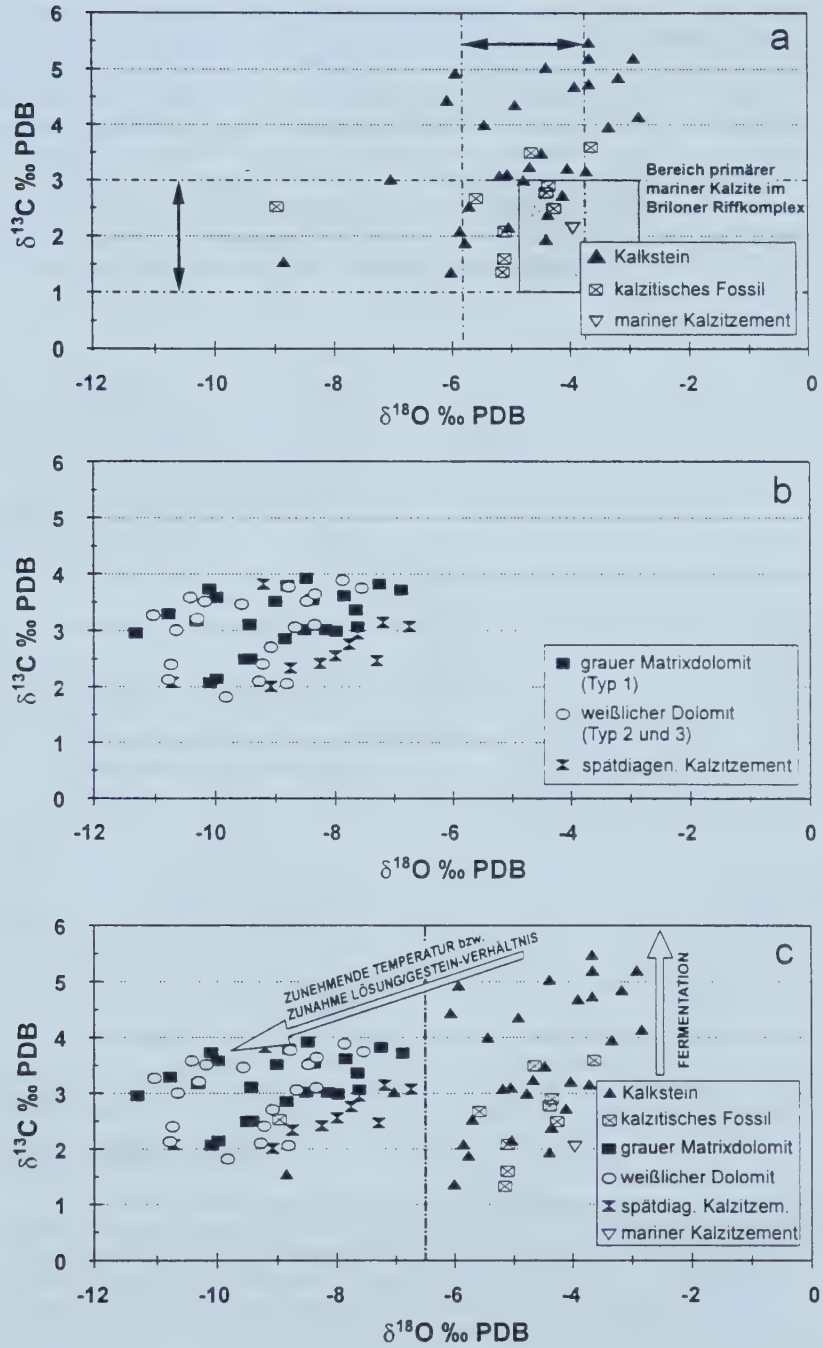
Massenkalkproben wurden auch entlang der Bohrkerne in Abständen von dm bis mehreren m zu den dolomitisierten Intervallen genommen, um die Auswirkungen der diagenetischen/hydrothermalen Lösungen auf die

---

Abb. 4 a-c. C- und O-Isotopenzusammensetzung von prätektogenetischen (a) und posttektogenetischen Karbonatphasen (b) aus dem Briloner Riffkomplex. Der vertikale Doppelpfeil kennzeichnet den  $\delta^{13}\text{C}$ -Wertebereich für devonische marine Kalzite (VEIZER et al. 1986, HURLEY & LOHMANN 1988, LOHMANN & WALKER 1989), der horizontale Doppelpfeil den  $\delta^{18}\text{O}$ -Wertebereich von "least altered" devonischen marinen Kalziten (ALLAN & WIGGINS 1993). Siehe Text zur weiteren Erläuterung.

Fig. 4 a-c. Carbon and oxygen isotope compositions of pre-tectogenetic (a) and post-tectogenetic carbonates (b) from the Brilon Reef Complex. The vertical double-pointed arrow indicates the range in  $\delta^{13}\text{C}$ -values of Devonian marine calcites (VEIZER et al. 1986, HURLEY & LOHMANN 1988, LOHMANN & WALKER 1989), the horizontal double-pointed arrow the range in  $\delta^{18}\text{O}$ -values of least altered Devonian marine calcites (ALLAN & WIGGINS 1993). See text for further explanation.









isotopische Zusammensetzung des Kalknebengesteins zu untersuchen. In Abb. 5 sind die Ergebnisse dieser Untersuchungen am Beispiel des Bohrkerns Almerfeld (AL) dargestellt. Die  $\delta^{13}\text{C}$ -Werte der Massenkalkproben liegen zwischen +1,4 und +5,5 ‰ PDB, ihre  $\delta^{18}\text{O}$ -Werte zwischen -3,2 und -7,3 ‰ PDB. Die  $\delta^{18}\text{O}$ -Werte dieser Kalke sind in unmittelbarer Nähe der dolomitisierten Intervalle relativ niedrig und nehmen mit zunehmender Entfernung davon zu. Die  $\delta^{13}\text{C}$ -Werte sind mit diesem Trend meist (aber nicht immer) positiv korreliert. Ähnliche Trends in der isotopischen Zusammensetzung des Kalknebengesteins treten auch im Bohrkern Auf dem Loh 7 auf. Sie sind sehr wahrscheinlich durch die Einwirkung von hydrothermalen Lösungen entstanden, die entlang von Störungen aufstiegen und

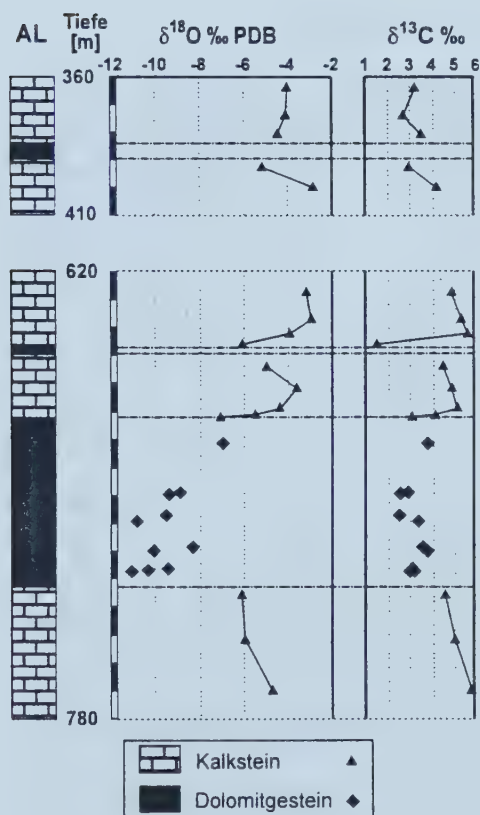


Abb. 5. Stabile Isotopenzusammensetzung von pervasiv dolomitisierten Intervallen und angrenzendem Kalknebengestein im Bohrkern Almerfeld (AL). Trends in  $\delta^{18}\text{O}$ - und  $\delta^{13}\text{C}$ -Werten des Kalknebengesteins werden auf die Einwirkung von diagenetischen/hydrothermalen Lösungen zurückgeführt.

Fig. 5. Stable isotope composition of pervasively dolomitized intervals and adjacent limestone host rock in the core Almerfeld (AL). Trends in  $\delta^{18}\text{O}$ - and  $\delta^{13}\text{C}$ -values of the limestone host rock reflect the influence of diagenetic/hydrothermal fluids.



zur pervasiven Dolomitisierung der umgebenden Karbonate führten sowie die isotopische Zusammensetzung des unmittelbar angrenzenden, nicht dolomitisierten Massenkalks durch Rekristallisation veränderten.

Vorläufige Ergebnisse mikrotehromometrischer Untersuchungen an Flüssigkeitseinschlüssen von posttektogenetischen Kalzitcementen deuten auf hochsalinare hydrothermale  $\text{CaCl}_2$ -( $\text{MgCl}_2$ -)NaCl-Lösungen hin (16–22 äquiv. Gew.-% NaCl,  $T_h = 70$  bis  $90^\circ\text{C}$ ,  $T_e = -40$  bis  $-50^\circ\text{C}$ ). Erste Berechnungen der  $\delta^{18}\text{O}$ -Werte der Lösungen mit Hilfe der  $\delta^{18}\text{O}$ -Werte dieser Kalzitcementen und der Homogenisierungstemperaturen und  $\delta\text{D}$ -Werte von Flüssigkeitseinschlüssen ergeben, daß die hydrothermalen Lösungen wahrscheinlich durch die Beimischung von meteorischem Wasser an  $^{18}\text{O}$  verarmt gewesen sind.

#### 4. Zusammenfassung und Schlußfolgerungen

Die fortgesetzten petrographischen Untersuchungen der posttektogenetischen "Diagenese"-Geschichte des Briloner Riffkomplexes bestätigen und ergänzen die von GROBE & MACHEL (1996) aufgestellte vorläufige paragenetische Abfolge. Die Integration mit bereits veröffentlichten Daten zum "Diagenese"-Ablauf ermöglichen eine Einordnung in eine umfassendere paragenetische Abfolge. Im Bereich der in dieser Arbeit untersuchten Bohrkernintervalle haben posttektogenetische Prozesse (Spaltenbildung, pervasiv Dolomitisierung, Karbonatlösung, Rekristallisation, geringe Vererzung mit Buntmetallsulfiden, Kalzitisierung und Kalzitcementation) die Produkte der prätektogenetischen Diagenese weitgehend überprägt. Die offenbar an tiefreichende saxonische Störungen gebundene pervasiv Dolomitisierung führte zur Verdrängung und/oder Rekristallisation des Massenkalks ausgehend von Spalten und Lösungshohlräumen (Dolomittypen 1 und 2) und zur Abscheidung von meist als Satteldolomit ausgebildetem Dolomitcement (Dolomittyp 3). Im Anschluß daran kam es zu einer geringfügigen Vererzung mit Buntmetallsulfiden (Pyrit/Markasit, Zinkblende, Bleiglanz), der eine ebenfalls von Spalten ausgehende Rekristallisation des Massenkalkgesteins sowie eine Kalzitisierung von Teilen der dolomitisierten Bereiche folgte. In verbliebenen Spalten und Resthohlräumen schieden sich dann euhedrale Kalzitcemente ab.

Die Ergebnisse der isotopengeochemischen Untersuchungen liefern wichtige Informationen über mögliche diagenetische Prozesse sowie über die mögliche Herkunft und Zusammensetzung der posttektogenetischen diagenetischen/hydrothermalen Lösungen. Anhand der  $\delta^{18}\text{O}$ -Werte lassen sich die prätektogenetischen Karbonatphasen ( $\delta^{18}\text{O} > -6,5\text{‰ PDB}$ ) von den posttektogenetischen Karbonatphasen ( $\delta^{18}\text{O} < -6,5\text{‰ PDB}$ ) unterscheiden. Die  $\delta^{13}\text{C}$ - und  $\delta^{18}\text{O}$ -Werte der Mehrzahl der untersuchten prätektogenetischen Karbonatphasen liegen innerhalb der normalen Bandbreite für mittel- bis oberdevonischen Karbonate. Kalksteinproben und Proben kalzitischer Fossilien zeigen jedoch einen Trend zu schwereren  $\delta^{13}\text{C}$ -Werten, was sehr wahrscheinlich auf den Ablauf von Fermentationsprozessen während der frühen Diagenese-Stadien (Versenkungstiefe  $< 1000\text{ m}$ ) zurückzuführen ist. Die  $\delta^{13}\text{C}$ -Werte der posttektogenetischen Karbonatphasen fallen in den Bereich der Mehrzahl der prätektogenetischen Karbonatphasen, was darauf hindeutet, daß sie den Kohlenstoff hauptsächlich aus dem prätektogenetischen anorganischen Kohlenstoffreservoir bezogen haben. Die relativ niedri-



gen  $\delta^{18}\text{O}$ -Werte aller untersuchten posttektonischen Karbonatphasen weisen auf eine Bildung bei erhöhten Temperaturen und/oder unter der Beteiligung von an  $^{18}\text{O}$ -verarmten Lösungen hin. Die Auswirkungen dieser hydrothermalen Lösungen auf das nicht dolomitisierte Kalknebengestein lassen sich durch eine drastische Abnahme der  $\delta^{18}\text{O}$ -Werte (und meist auch der  $\delta^{13}\text{C}$ -Werte) in unmittelbarer Nähe der dolomitisierten Bereiche nachweisen. Die beobachteten Trends können mit einer Abnahme der Temperatur und/oder einer Abnahme des Lösung/Gestein-Verhältnisses mit zunehmendem Abstand zu diesen Bereichen erklärt werden. Vorläufige Untersuchungen von Flüssigkeitseinschlüssen (Mikrothermometrie,  $\delta\text{D}$ ) von posttektonischen Kalzitkemen deuten auf eine hydrothermale Entstehung aus hochsalinaren  $\text{CaCl}_2$ -( $\text{MgCl}_2$ -) $\text{NaCl}$ -Lösungen hin und liefern weitere Hinweise auf einen möglichen Einfluß von an  $^{18}\text{O}$ -verarmten Lösungen (meteorisches Wasser).

Die salinaren hydrothermalen Lösungen bestanden vermutlich aus einer komplexen Mischung von paläozoischen und mesozoischen Formationswässern, meteorischem Wasser, salinaren Reliktlösungen und Lösungen aus der Ablaugung von permischen und triassischen Evaporiten. Eine solche Entstehung wird für die heute in dem dem Ostrheinischen Schiefergebirge vorgelagerten Münsterländer Kreidebecken auftretenden salinaren Lösungen postuliert (MICHEL 1983). Nach MICHEL (1983) lagen diese Lösungen bereits im Alttertiär in ihrer heutigen Zusammensetzung vor. Sie könnten durch ein Zusammenwirken von oberflächengesteuerten beckenweiten Grundwasserbewegungen (MICHEL 1994) und durch erhöhten Wärmefluß verursachte hydrothermale Konvektion im Verlaufe des Mesozoikums und Alttertiärs (NEUGEBAUER et al. 1983, SCHAEFFER 1986) entlang der NNW-SSE verlaufenden saxonischen Störungssysteme in den Briloner Riffkomplex eingewandert sein und dort zur hydrothermalen Mineralisation geführt haben. Zur genaueren Eingrenzung der Herkunft und Zusammensetzung dieser Lösungen werden z. Zt. weitere geochemische Untersuchungen (Haupt- und Spurenelemente,  $^{87}\text{Sr}/^{86}\text{Sr}$ ) sowie mikrothermometrische und geochemische Untersuchungen von Flüssigkeitseinschlüssen durchgeführt.

**Danksagung.** Wir danken D. STOPPEL (BGR) für seine unermüdliche Hilfsbereitschaft und die Ermöglichung der Bearbeitung und Beprobung der Bohrkern in den Bohrkernlagern der BGR und des NLfB in Wehmingen und Grubenhagen. H. R. KROUSE (University of Calgary) stellte freundlicherweise sein Isotopen-Labor zur Aufbereitung und Messung eines Großteils der Karbonatproben zur Verfügung. D. K. RICHTER und C. SPÖTL danken wir für ihre kritischen Kommentare als Gutachter des Manuskriptes. Finanzielle Unterstützung wurde vom Deutschen Akademischen Austauschdienst, der University of Alberta und der Geological Society of America (MG) sowie von der Alexander-v.-Humboldt-Stiftung und dem Natural Sciences and Engineering Research Council of Canada (HGM) gewährt.

#### Literaturverzeichnis

- ALLAN, J. R. & WIGGINS, W. D. (1993): Dolomite Reservoirs - Geochemical Techniques for Evaluating Origin and Distribution. - AAPG Continuing Education Course Note Ser., 36: 129 S., 96 Abb., 2 Anh.; Tulsa.





- BÄR, P. (1966): Stratigraphie, Fazies und Tektonik am Briloner Massenkalk-Sattel (Ostsauerland). - Diss., Univ. Gießen: 29 S., 9 Abb., 3 Taf., 1 Kt.; Gießen.
- BRINKMANN, J. (1981): Projekt Rhenoharzynikum, Untersuchung der Metallverteilung in geosynklinalen Sedimenten des Rhenoharzynikums in stratiformen Konzentrationen. - Bericht über das Kernbohrprogramm im Briloner Riffkalk-Komplex: VII u. 65 S. Anh., 129 S., 21 Abb., 5 Tab., 23 Bohrprof.; Hannover (BGR). [Unveröff.]
- BÜKER, C., LITTKE, R. & WELTE, D. H. (1995): 2D-modelling of the thermal evolution of Carboniferous and Devonian sedimentary rocks of the eastern Ruhr basin and northern Rhenish Massif, Germany. - Z. dt. geol. Ges., 146: 321-339, 7 Abb., 7 Tab.; Hannover.
- DEUSER, W. G. (1970): Extreme  $^{13}\text{C}/^{12}\text{C}$  variations in Quaternary dolomites from the continental shelf. - Earth Planet. Sci. Letters, 8: 118-124, 3 Tab.; Amsterdam.
- EPSTEIN, S., GRAF, D. L. & DEGENS, E. T. (1964): Oxygen isotope studies on the origin of dolomites. - In: CRAIGH, H., MILLER, S. L. & WASSERBURG, G. J. (eds.): Isotopic and cosmic chemistry: 169-180, 2 Abb., 7 Tab.; Amsterdam (North-Holland Publ. Co.).
- GAMES, L. M. & HAYES, J. M. (1976): On the mechanism of  $\text{CO}_2$  and  $\text{CH}_4$  production in natural anaerobic environments. - In: NRIAGU, J. O. (ed.): Environmental Biogeochemistry, I: 51-66, 4 Abb., 4 Tab.; Ann Arbor, Mich. (Ann Arbor Sci. Publ. Inc.).
- GROBE, M. & MACHEL, H. G. (1996): Postvariszische Dolomitisierung des devonischen Briloner Riffkomplexes, nordöstliches Rheinisches Schiefergebirge, Deutschland. - Zbl. Geol. Paläont. Teil I, 1995 (1/2): 131-143, 4 Abb.; Stuttgart.
- HURLEY, N. F. & LOHMANN, K. C. (1989): Diagenesis of Devonian reefal carbonates in the Oscar Range, Canning Basin, western Australia. - J. Sedim. Petrol., 59: 127-145; Tulsa.
- KREBS, W. (1967): Reef development in the Devonian of the eastern Rhenish Slate Mountains, Germany. - Int. Symp. on the Devon. Syst.: 295-306, 4 Abb., 2 Tab.; Calgary.
- LOHMANN, K. C., BREINING-AFIFI, K. A., BUDAI, J. M. & CERCONE, K. R. (1985): Enriched carbon-13 compositions in meteoric and shallow burial calcites and dolomites: evidence of organic fermentation during early diagenesis. - SEPM Ann. Midyear Meet., 2: 55; Tulsa (S. E. P. M.).
- LOHMANN, K. C. & WALKER, J. C. G. (1989): The  $\delta^{18}\text{O}$  record of Phanerozoic abiogenic marine calcite cements. - Geophys. Res. Lett., 16: 319-322, 5 Fig.; Washington.
- MACHEL, H. G. (1979): Fazies und Diagenese der devonischen Riffkarbonate der Bohrung Romberg (Briloner Riff). - Dipl.-Arb., TU Braunschweig: 231 S., 81 Abb., 6 Tab., 14 Taf.; Braunschweig. [Unveröff.]
- (1990a): Faziesinterpretation des Briloner Riffs mit Hilfe eines Faziesmodells für devonische Riffkarbonate. - Geol. Jb., D95: 43-83, 5 Abb., 6 Taf.; Hannover.
- (1990b): Submarine Frühdiagenese, Spaltenbildungen und prätektonische Spätdiagenese des Briloner Riffs. - Geol. Jb., D95: 85-137, 2 Abb., 5 Taf.; Hannover.
- MALMSHEIMER, K. W., MENSINK, H. & STRITZKE, R. (1991): Gesteinsvielfalt im Riffgebiet um Brilon. - Geol. Paläont. Westf., 18: 67-83; Münster.



- McCREA, J. M. (1950): On the isotopic chemistry of carbonates and a paleotemperature scale. - *J. Chem. Physics*, **18**: 849-857, 5 Fig., 11 Tab.; New York.
- MICHEL, G. (1983): Die Sole des Münsterländer Kreide-Beckens. - *N. Jb. Geol. Paläont., Abh.*, **166**: 139-159, 5 Abb., 2 Tab.; Stuttgart.
- (1994): Wie kommt die Sole ins Revier? - *Mitt. Geol. Ges. Essen*, **12**: 65-81, 5 Abb.; Essen.
- MORITZ, W. (1983): Fazies und Diagenese des Briloner Karbonatkomplexes anhand einiger ausgewählter Bohrungen. - Diss., TU Braunschweig: 180 S., 26 Abb., 4 Tab., 10 Taf.; Braunschweig. [Unveröff.]
- MOUNTJOY, E. W. (1994): Dolomitization and the character of hydrocarbon reservoirs: Devonian of Western Canada. - In: PARKER, A. & SELLWOOD, B. W. (eds.): *Quantitative Diagenesis: Recent Developments and Applications to Reservoir Geology*: 33-94, 27 Abb., 5 Tab.; Amsterdam (Kluwer Acad. Publ.).
- NEUGEBAUER, H. J., WOIDT, W.-D. & WALLNER, H. (1983): Uplift, Volcanism and Tectonics: Evidence for Mantle Diapirs at the Rhenish Massif. - In: FUCHS, K., VON GEHLEN, K., MÄLZER, H., MURAWSKI, H. & SEMMEL, A. (eds.): *Plateau Uplift*: 381-403, 14 Abb., 2 Tab.; Berlin/Heidelberg/New York/Tokyo (Springer).
- O'NEIL, J. R. (1987): Preservation of H, C, and O isotopic ratios in the low temperature environment. - In: KYSER, T. K. (ed.): *Stable Isotope Geochemistry of Low Temperature Fluids*. *Miner. Assoc. Canada, Short Course Handb.*, **13**: 85-128, 12 Abb.; Saskatoon (M. A. C.).
- SCHAEFFER, R. (1984): Die postvariszische Mineralisation im nordöstlichen Rheinischen Schiefergebirge. - *Braunschweiger geol.-paläont. Diss.*, **3**: 206 S., 43 Abb., 9 Tab., 4 Anl.; Braunschweig.
- (1986): Geochemische Charakteristika und Genese der jungmesozoisch-tertiären Vererzung im Sauerland (Rheinisches Schiefergebirge). - *Fortschr. Geol. Rheinld. u. Westf.*, **34**: 337-381, 7 Abb., 11 Tab., 3 Taf.; Krefeld.
- SCHRIEL, W. (1954): Der Briloner Galmei-Distrikt. - *Z. dt. geol. Ges.*, **106**: 308-349, 7 Abb., 5 Taf.; Hannover.
- TAYLOR, H. P. Jr. (1979): Oxygen and hydrogen isotope relationships in hydrothermal mineral deposits. - In: BARNES, H. L. (ed.): *Geochemistry of Hydrothermal Ore Deposits*, 2nd ed.: 236-277, 9 Abb.; New York (Wiley & Sons).
- VEIZER, J., FRITZ, P. & JONES, B. (1986): Geochemistry of brachiopods: oxygen and carbon isotope records of Paleozoic oceans. - *Geochim. Cosmochim. Acta*, **50**: 1679-1696, 9 Abb., 3 Tab.; New York.
- WERNER, W. (1990): Die epigenetische Markasit-Schwefspat-Zinkblende-Vererzung "Altenbüren" (nordöstliches Rheinisches Schiefergebirge). - *Geol. Jb.*, **D95**: 139-176, 10 Abb., 2 Tab.; Hannover.

Anschrift der Verfasser:

MATTHIAS GROBE und HANS G. MACHEL, Department of Earth and Atmospheric Sciences, University of Alberta, Edmonton, AB, Kanada.

















University of Alberta Library



0 1620 1136 8220

**B45362**